Engineering Materials

Mohammad Khalid
Andrews Nirmala Grace
Arunachalam Arulraj
Arshid Numan *Editors*

Fundamental Aspects and Perspectives of MXenes

Springer

Engineering Materials

This series provides topical information on innovative, structural and functional materials and composites with applications in optical, electrical, mechanical, civil, aeronautical, medical, bio- and nano-engineering. The individual volumes are complete, comprehensive monographs covering the structure, properties, manufacturing process and applications of these materials. This multidisciplinary series is devoted to professionals, students and all those interested in the latest developments in the Materials Science field, that look for a carefully selected collection of high quality review articles on their respective field of expertise.

Indexed at Compendex (2021)

More information about this series at https://link.springer.com/bookseries/4288

Mohammad Khalid · Andrews Nirmala Grace ·
Arunachalam Arulraj · Arshid Numan
Editors

Fundamental Aspects and Perspectives of MXenes

Springer

Editors
Mohammad Khalid
Graphene and Advanced 2D Materials
Research Group
Sunway University
Subang Jaya, Selangor, Malaysia

Arunachalam Arulraj
Faculty of Engineering
Universidad de Concepción Edmundo
Laren
Concepción, Chile

Andrews Nirmala Grace
Centre for Nanotechnology
Vellore Institute of Technology
Vellore, Tamil Nadu, India

Arshid Numan
Graphene and Advanced 2D Materials
Research Group
Sunway University
Subang Jaya, Malaysia

ISSN 1612-1317 ISSN 1868-1212 (electronic)
Engineering Materials
ISBN 978-3-031-05005-3 ISBN 978-3-031-05006-0 (eBook)
https://doi.org/10.1007/978-3-031-05006-0

This Springer imprint is published by the registered company Springer Nature Switzerland AG
The registered company address is: Gewerbestrasse 11, 6330 Cham, Switzerland

Preface

MXene: Fundamental Aspects and its Perspectives presents the state-of-the-art research on MXenes—a class of two-dimensional (2D) metal carbides and nitrides discovered in the past decade. This book describes the development in fundamentals, innovations, emerging discoveries, and applications of 2D MXenes. Due to their unique physicochemical characteristics and abundant surface chemistries, MXenes continue to outperform other novel materials and dominate every sector of life, ranging from energy harvesting, storage, and conversion to portable and flexible electronics; from environmental remediation to electromagnetic interference shielding; and from space to medical and biomedical applications. Their most recent cutting-edge applications include the development of artificial heart and kidneys, high-capacity and long-life batteries, printable microstrip antennas, portable sensors, and thin membranes for air and water purification. This book provides up-to-date research and development in MXene's distinct electronic, optical, mechanical, thermal, electrochemical, topological, and other related properties. Furthermore, various emerging applications of MXenes in a diverse field, including batteries, supercapacitors sensors, catalysts, electromagnetic interference shielding, hydrogen storage, biological and environmental remediation, have been thoroughly discussed in different chapters of this book. In addition, for commercial viability, a significant emphasis has been placed on theoretical conceptualization, safety measures, and scale-up of MXene during synthesis and processing. This book will be essential reading for young and future generations of researchers, materials scientists, biochemists, electrochemists, solid-state physicists, engineers, and industry experts working in the subject of 2D materials, as it bridges academic research and industrial development.

Subang Jaya, Malaysia — Mohammad Khalid
Vellore, India — Andrews Nirmala Grace
Concepción, Chile — Arunachalam Arulraj
Subang Jaya, Malaysia — Arshid Numan

Contents

About the Editors

Dr. Mohammad Khalid is a Research Professor and Head of Graphene and Advanced 2D Materials Research Group at Sunway University, Malaysia. His research interests lie in the area of advanced nanomaterial synthesis, heat transfer fluids, energy harvesting, and storage. With over 200 research articles in peer-reviewed international journals, he is among the top 2% of scientists in the field of Material Science. He has supervised more than 30 postgraduate students and has over 15 years of research and teaching experience. He is also a Fellow of the Higher Education Academy (FHEA), UK.

Andrews Nirmala Grace is a Professor and Director at the Centre for Nanotechnology Research, Vellore Institute of Technology (VIT), Vellore, India. She received her Ph.D. degree from the University of Madras, India and worked as a Postdoctoral/Senior Researcher Fellow at the Korea Institute of Energy Research, South Korea on Renewable Energy. She is a Fellow of the Royal Society of Chemistry (FRSC), Fellow of the Academy of Sciences, Chennai (FASCh) and member of International Solar Energy Society (ISES). Her current research interests include Energy materials, design and fabrication of electrodes for dye sensitized, perovskite solar cells; Electrodes for supercapacitors - Morphological studies of supercapacitor electrodes and study of electrochemical redox reactions at the interface of electrodes and electrolytes; Engineering of inter-layer spaces in 2D materials to improve the ion accessibility; Tuning the structure and porosity of electrode materials; Transparent photovoltaics for device and surface integration; Flexible energy devices for conversion and storage—flexible and printable supercapacitors for wearable devices such as sensors and energy conversion. She has more than 150 International Peer reviewed publications, one patent published and has edited a book, authored three book chapters (h-index of 40 and i-10 index of 95).

Dr. Arunachalam Arulraj received his Ph.D. in Nanotechnology (Energy) from Anna University, Tamil Nadu, India. For his academic achievements, he received the meritorious award (TEQIP-II Fellowship) from the Government of India for the

years 2013 and 2016. Currently, he is working as an ANID-FONDECYT Postdoctoral Fellow at the Department of Materials Engineering, University of Concepcion, Concepcion, Chile. His research interests are focused on designing and studying various two-dimensional functional materials, including chalcogenides, MXenes, graphene that perform energy conversion reactions (solar energy conversion, H_2 production), and energy storage (supercapacitors).

Dr. Arshid Numan obtained his M.Sc. degree in Electrical Engineering from COMSATS University, Pakistan, and Ph.D. in Experimental Physics from the Center for Ionics, Department of Physics, University Malaya, Kuala Lumpur, Malaysia. Currently, he is working as a Senior Research Fellow at Graphene and Advanced 2D Materials Research group (GAMRG), School of Engineering and Technology, Sunway University Malaysia. He has over 6 years of research and teaching experience. He has more than 95 publications and edited 2 books. His research interest is mainly focused on the development of 2D heterostructure nanomaterials for energy storage and electrochemical sensors application.

MXene: Pioneering 2D Materials

Arunachalam Arulraj, R. V. Mangalaraja, and Mohammad Khalid

Abstract Two-dimensional (2D) nanomaterials such as graphene and chalcogenides have been appealing candidates for their desired applications owing to their demonstrated intriguing properties. Besides these 2D materials, discovering new types of 2D materials such as MXene aids in broadening the flatland research. MXenes with general formula $M_{n+1}X_nT_x$ are a relatively new class of emerging materials discovered a decade back (since 2011) and are 2D transitional carbides, nitrides, and carbonitrides based materials. From its discovery, MXene becomes popular owing to its unique physicochemical properties and diverse chemistries. Several different types of MXenes and their combinations with other materials have been discovered using computational and experimental methods. Due to their compositional versatility, 2D gallery spaces, ordered structures, controlled surface chemistry, etc. these materials (MXene and its composition) are found to be suitable materials for various applications, including but not limited to energy storage, catalysis, optoelectronics, smart textiles, antennas, and electromagnetic interference shielding. In this chapter, a brief introduction to the evolution of MXene and a glimpse into its field of applications have been emphasized.

Keywords MXene · Evolution · Properties · Applications · Safety measures · Perspectives

A. Arulraj · R. V. Mangalaraja (✉)
Advanced Ceramics and Nanotechnology Laboratory, Faculty of Engineering, Department of Materials Engineering, University of Concepcion, Concepcion, Chile
e-mail: mangal@udec.cl

M. Khalid
Graphene and Advanced 2D Materials Research Group (GAMRG), School of Engineering and Technology, Sunway University, Selangor, Malaysia

A. Arulraj · R. V. Mangalaraja
Faculty of Engineering and Sciences, Universidad Adolfo Ibañez, Diagonal Las Torres 2640, Peñalolén, Santiago, Chile

M. Khalid et al. (eds.), *Fundamental Aspects and Perspectives of MXenes*, Engineering Materials, https://doi.org/10.1007/978-3-031-05006-0_1

1 Introduction

Emerging confined structures and the unusual properties of the two-dimensional (2D) materials have drawn huge attention to their family. Among the different family members, MXenes have been pioneering in the past decade (since 2011) due to their fascinating properties, which include but are not limited to their metallic electrical conductivity. This significant property lacks largely in the other palette of the 2D family. MXenes comprise 2D transitional metal carbides/nitrides/carbonitrides, which can be achieved by selective etching of bonded (strong) layers in solid materials such as MAX phases. MAX phases are layered ternary carbides, and nitrides with layers of 'A' element (Group 13–16) bonded between them [1, 2]. Recent reports also evidence that transition metals from groups 8–12 (Fe, Cu, Zn, Cd, Ir, and Au) can also form the A layer of MAX phases, either as solid solutions or as pure A elements, in Fig. 1, all the investigated A elements in MAX phases are highlighted in rose color [3]. $M_{n+1}X_n$ layers are held together by metallic bonding between the M-A layers, which is usually weaker than the M-X bonds, allowing selective etching of the A layers. $M_{n+1}X_nT_x$ is the general formula for MXene materials, where M represents early transition metal (Mo, W, Ti, V, Sc, Y, Zr, Hf, Nb, Ta, or Cr), X denotes carbon or nitrogen, and n is between 1 and 3 [4–6]. The transition metals (M) used as a precursor for MXenes are represented in olive green color (Fig. 1) in the periodic table. T denotes the surface termination groups, which are mostly O, F, and OH, some rare cases Cl termination will also exist, and x in T_x represents the number of surface functionalities [7, 8], the blue color in the periodic table denotes the variously reported surface terminations of MXenes (Fig. 1).

Aforementioned, MXenes are layered sheet-like structures with thickness ranging from 1 nm, which can be fine-tuned by changing the proposition of n in MXenes. Upon a change in the "n" ($M_{n+1}X_nT_x$), a wide variety of compositions ranging from M_2XT_x, $M_3X_2T_x$, $M_4X_3T_x$, etc., has been developed employing both computational

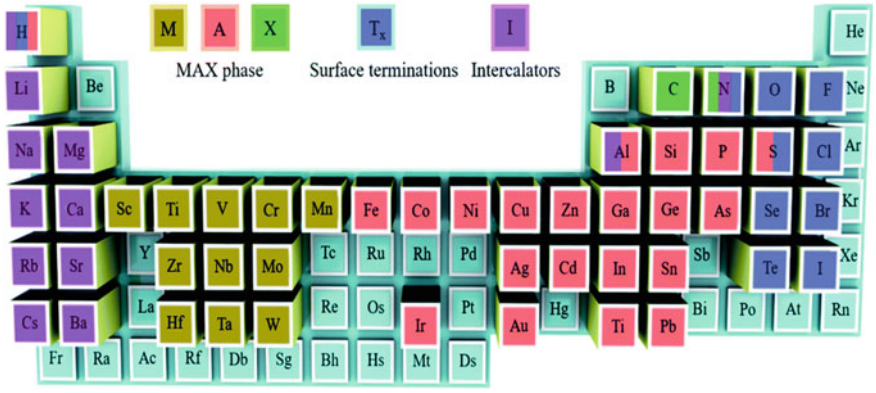

Fig. 1 Reported materials on MXene, surface terminations, and intercalant cations in the periodic table [1]

and experimental approaches [9, 10]. Unlike most 2D materials, which rely on van der Waals bonding to hold the layered structures (sheets) together, however, 3D layered MXenes (carbides and nitrides), including MAX phases, rely on primary bonding (supported by A element) between the layers. As a result, the production of MXenes can be achieved only with the chemical exfoliation approach [11–13]. The chemical exfoliation route includes fluoride-containing acidic solutions, such as hydrofluoric acid (HF) or a mixture of lithium fluoride and hydrochloric acid (HCl). On the other hand, electrochemical selective etching, for instance, etching Ti_2AlC in chloride-containing solutions, allows fluoride-free etching routes [14–16]. The different synthesis and processing strategies of the MXene from MAX are discussed briefly in chapter "Synthesis and Processing Strategies".

MXenes offer unique properties that make them intriguing materials with a wide range of uses. MXenes (exfoliation of MAX product) are hydrophilic in form, which aids in the possible dispersion of materials (MXenes) in water and other organic solvents such as ethanol, dimethyl sulfoxide, N, N-dimethylformamide, and propylene carbonate [17]. As a function of pH and variety of compositions during the synthesis process, the zeta potential values of MXenes are obtained to be negative in the range of 30–80 mV [4]. MXene colloidal solutions are stable due to their high negative zeta potential, which allows for the fabrication of MXene films and patterns using nearly any ink-based process. Filtration, spray coating, spin coating, dip coating, printing, etc., have been used to fabricate MXene films [17–19]. MXene characteristics are a unique combination of features, and while we've learned a lot about them over the past decade, there's still a lot more work to be done to comprehend them completely. Like their MAX precursors, all bare MXenes are metallic; however, they can be anticipated as metals or semiconductors due to their surface terminations during the synthesis process [4, 20]. Most of the experimental reports on MXenes are pointed to it as metallic, and few reports anticipate MXenes as topological insulators [7]. The electronic properties of MXenes are largely influenced by their surface chemistry (M, X, and T), structure (M_2XT_x, $M_3X_2T_x$, $M_4X_3T_x$), and surface termination position [21]. $Ti_3C_2T_x$ film has one of the highest electrical conductivities among solution-processed nanomaterials that can afford up to 20,000 S/cm, making it the optimum material for emerging applications such as shielding and antenna applications [22]. Next to graphene and hexagonal boron nitride (h-BN), the elastic moduli (2D) of the MXene (specifically single-layered) measured from indentation are found to be 326–329 N/m, which makes them the next strongest material (after G and h-BN) through exploring Young's modulus of 330 ± 30 GPa. Surprisingly, the explored Young's modulus of MXene ($Ti_3C_2T_x$) surpasses other materials in the 2D family, which includes graphene oxide, metal chalcogenides [23]. Likewise, MXene exhibits excellent mechanical properties; however, most of its mechanical properties are yet to explore. These distinct features are not only limited to their mechanical properties; it also includes optical properties; by means of changing their surface chemistry, the absorption range of the MXene can be fine-tuned. For instance, single-layered MXene with a one nm thickness absorbs ~3% visible light at the wavelength of ~550 nm. The optical properties of the MXenes

have been explored since 2016, which paved the path for developing advanced applications such as mode-locked lasers, photothermal therapy, and surface-enhanced Raman spectroscopy (SERS) [24, 25]. MXenes' electrochemical characteristics have been researched extensively, and almost 50% of the reports on MXenes are based on their electrochemical energy storage applications [26]. The electrochemical energy storage applications of the MXenes are detailed later in this chapter. Likewise, the fascinating properties of MXenes in correspondence with their surface chemistry are provided in-depth in chapter "Properties of MXenes" (Fig. 2).

The quick progress of MXene chemistry has enthralled the MAX community, and the desire to synthesize additional (novel) MXenes led to the identification of new subfamilies of MAX phases like ordered double transition metal carbides. Ordered MAX phases can be achieved by combining two metals (a preferably heavy metal with a light one) in the out-plane ordered structure; sandwiching of two layers from similar or different kinds of carbide-based metals (M) can be done. For instance, Mo_2TiAlC_2 and $Mo_2Ti_2AlC_3$, by selective etching of the element "Al" double ordered MXenes are obtained (marked in red in Fig. 3) [27, 28]. By considering the reports of the in-plane ordering of structures, the basal planes comprised of two types of "M" elements in a separate row, for instance, $(Mo_{2/3}Sc_{1/3})_2AlC$, $(Mo_{2/3}Y_{1/3})_2AlC$,

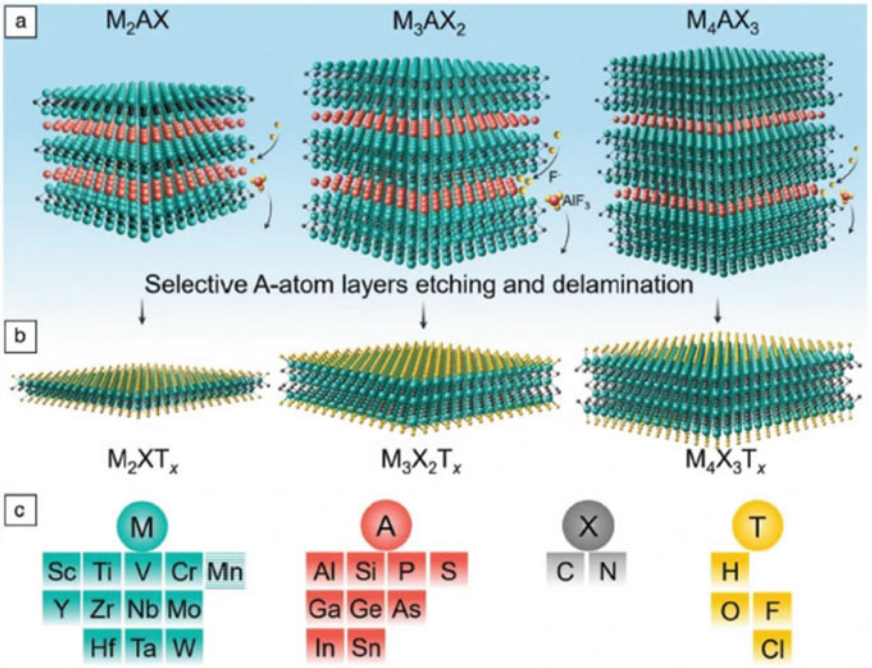

Fig. 2 **a** Different MAX precursors (M_2AX, M_3AX_2, M_4AX_3) with selective etching (A) for producing, **b** MXenes (M_2XT_x, $M_3X_2T_x$, $M_4X_3T_x$), and **c** possible elements for M, A, X, and T [27]

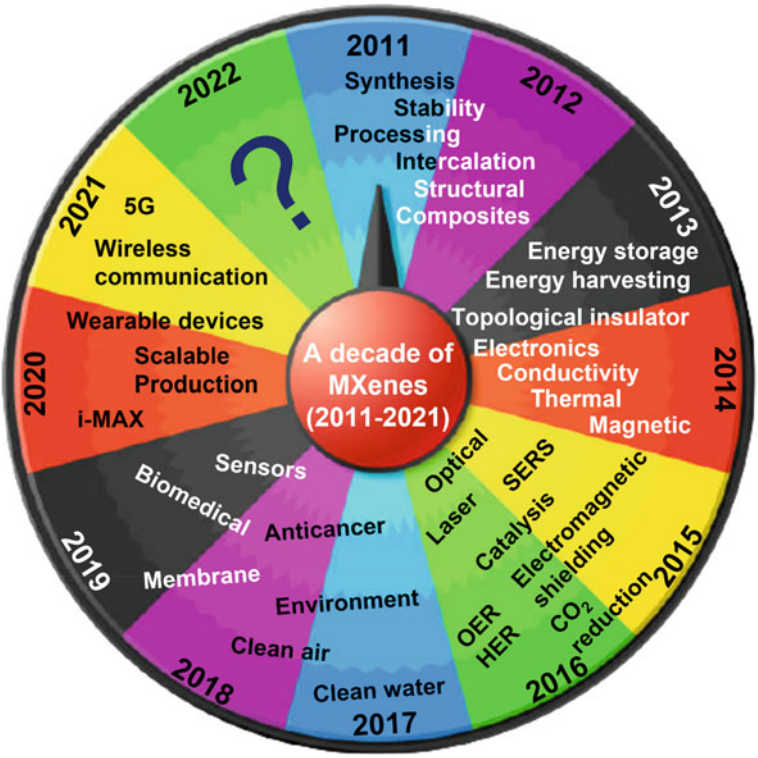

Fig. 3 Schematics representation for applications of MXenes

etc. These in-plane ordering of the MAX phase materials can be selectively etched, resulting in the formation of two different kinds of MXenes such as $(Mo_{2/3}Y_{1/3})_2CT_x$ or $Mo_{1.33}CT_x$, by etching lighter transition metal in MAX phases (i.e., Sc or Y) with ordered divacancies [6, 27]. However, the MXene with selective etching of light transition metal will not fall under the formula of $M_{n+1}X_nT_x$, since the atomic vacancies of the transition metals are about 33%, thereby representing it to be $M_{1.33}XT_x$. Besides these layered ordered structures, MXene can be composited with different materials such as semiconducting nanoparticles, conducting polymers, etc. [6]. The surface terminations (T_x) in the MXenes support functionalizing the materials and can form composites with carbonaceous materials such as graphene or carbon nanotubes [29]. These kinds of different interactions/composites of MXenes with other materials are detailed in chapter "MXene-Based Composites and Their Applications".

All the 2D materials do not require van der Waal forces that can be appreciated to discover new classes of materials, including MXenes. It was well known that the MXene can be achieved by selectively etching out the A element from the MAX phases. This kind of selective etching also contributes to ease of access in producing large-scale fabrication. Till now, most of the MXenes (except Mo_2N) have been synthesized through these selective etching processes [30–32]. Although various

MXenes have been discovered in the recent decade, stoichiometry and delamination can be modified using various cationic intercalants. For instance, in the case of in-situ etching (LiF + HCl), the MXene can be delaminated by raising its pH, or it can say that no additional intercalants are required [33–36]. However, the in-situ route of chemical etching may leave traces of more surface terminations than the direct fluoride (HF) etching route. Furthermore, using more harsh solvents (etchants) increases the defects in MXenes [37, 38].

Hence, etching and the etchant need to be significantly considered in achieving high-quality MXenes flakes. During the etching process, intercalation of ions takes place that intends to separate and/or delaminate the MXene flakes. The different ions including Li^+, Al^{3+}, Ca^{2+}, and Na^+ are reported to be widely used intercalant in MXene delamination [1, 13, 38, 39]. Sometimes, MXenes also absorb heavy metallic ions from these intercalated ions during the delamination as M-X bonding is short and strong, ions cannot penetrate through their flakes [1, 40]. Following the delamination process (intercalation), the storage of colloidal suspension, also referred to as post-synthesis of MXenes, needs to be considered in achieving high-quality MXenes. Generally, the colloidal suspension will be stored in either water or organic solvents (as inks). The temperature and ambient condition of the stored colloidal solution significantly impact the oxidation rate of the delaminated MXenes. Recently a report suggested that the hydrolysis of MXene and water contributes a vital role in their degradation. For instance, the storage of MXene ($Ti_3C_2T_x$) in an aqueous (water) medium with dissolved oxygen exhibits stability for a month (~30 days). Even though the stability of MXene colloidal was reasonably good, the oxidation rate of MXene may change due to the dissolved oxygen in colloidal suspension. It can overcome the oxidation issue by purging inert gases such as argon to lower the dissolved oxygen content. In addition to the MXene suspension, the films fabricated using spray coating or filtration exhibits similar stability over a month [32, 33, 35]. Likewise, different aspects of delamination and the storage process are available in chapter "Stability and Degradation of MXene".

Because of their intriguing features, different types of MXenes can be produced by expanding the available combinations of M and A with carbon or nitrogen in MAX phases. As discussed earlier, single and double ordered transition metals were achieved with MAX phase materials to produce the ordered MXenes. However, the possibility of combining different elements and metals cannot be executed directly by an experimental approach due to their cost and time constraints. At this juncture, the possible combination for the formation of MXene and MAX phases can predict with the computational approach, including MD simulation, DFT, etc. These computational approaches can subsequently guide the experimentalist to synthesize the novel MXenes. Specifically, the quantum calculations (theoretical) and other property evaluations carried out for the different combinations of materials are feasible in exploring novel materials. Recently, Khalediali dusti et al. conducted a series of fundamental computational analyses of different combinations of MAX phases (around 1122 materials). Based on their elemental information and high-throughput density functional theory (DFT) results, 466 MAX phase compounds out of 1122 are experimentally possible to synthesize.

Further, the theoretical calculation has been extended to determine the formation of MXene from MAX and found that only 26 MXenes compounds can be experimentally synthesized among 136 MAX phases. From these computational results, it can be clear that the computational results are equally important in determining the formation of the compounds, specifically when a novel composition of elements or compounds has been proposed [41]. Such computational approaches and the determination of their properties are described in a detailed way in chapter "Simulative Molecular Modelling of MXene". Furthermore, it was known that the distinct composition of the MXenes relies upon their surface terminations that can keep increasing/decreasing with the magnitude of order in its composition. The tendency with change in order can transform the MXenes into carbonitrides; thereby, infinite compositions (of MXene) can predict with computation, which opens a new era in atomistic 2D materials design through a computational approach.

MXene possesses unique properties, including its hydrophilic nature, interlayer spacing, ease of access structure, controllable thickness, metallic conductivity, tuneable Fermi energy levels, etc., rendering them valuable applications. Moreover, the stacking/restacking of the MXene sheets (interlayers or interlayer spacing) can be controlled by adding various spacers between their layers [42–44]. For instance, the surface terminations (specifically –O) make MXenes more active redox materials, higher electrical conducting nature of MXenes aids rapid electronic transportation to the electrochemical sites. Further, by fine-tuning its properties using different fabrication/processing strategies, one can develop electronic circuits for sensors, batteries, supercapacitors, biomedical devices, etc. Besides these applications, the higher electronic conductivity of the MXene paves the path in a new stream of applications, including but not limited to MXetronics (combination of MXene and optoelectronics), allowing them to be employed as interconnectors and current collectors in the electronic devices. The strong electromagnetic interaction of MXenes with different frequencies ranging from tera- to giga-hertz renders them in interference shielding and higher-end communications. The gas separation, hydrolysis, and/or dialysis (water purification) are achieved by controlling the interlayer stacking space of the MXene layers. The liquid crystal formation can be done in association with the processing of surface functionalization of MXenes [45]. With all these aspects, the new class of MXene materials has been highly under research in recent decades with a comprehensive list of applications.

The most explored application of MXenes has remained dedicated to electrochemical energy storage devices. The ease of ionic intercalation (cations) in MXene supports faster ionic transportation during the electrochemical reaction in the energy storage devices. Thus, the combined properties of redox ability, conductivity, and ionic intercalation of MXenes endorses them as a potentially viable candidate for energy storage applications. The modification of surface and suitable intercalant (for intercalation of cations) enhances the capacitance value of MXene by 200% compared with the normal approach of the same [46]. For instance, the MXene ($Ti_3C_2T_x$) fabrication from the MAX phase (Ti_3AlC_2) will have the surface terminations of F and/or OH functional groups, which then be treated with different kinds of bases with varied cationic radii like KOH. By treating with such bases results in

the replacement of surface termination elements with the cationic element (i.e., F with K^+) using weakening the bond is existing between the surface termination (F) and the transition metal (Ti). The presence of K^+, in the case of MXene treated with KOH, enhances the capacitive performance of the energy storage devices due to the intercalation of K^+ ions in the interlayer spacing between the MXene stacks, which emphasize drastic change over in the internal structure of the host by bringing larger cations. Hence, one of the best ways to boost the energy storage device's performance can achieve by combining the mechanism of surface modification and intercalation of cations [47–49]. Besides these modifications, the charge storage performance in the electrochemical devices varies concerning the electrolytes used in the electrochemical reactions. The same theme was applicable for MXenes in the acidic medium exhibiting pseudocapacitive behavior.

In contrast, double-layered capacitance (EDLC) will be displayed while carrying out the reaction in alkaline or aqueous neutral-based electrolytes, respectively. As mentioned above, the surface modification of MXene can be done with various metallic cations such as Li, Mg, Al, Na, and K, which explore the material in several types of energy storage devices, including ionic batteries. Furthermore, the dynamics of ions existing between the MXenes layers paves the way for a possible replacement for electrolytic capacitors too, which induces the increase in voltage window and thereby extends their cyclic stability and performance [50]. The detailed exploration of the materials in the various kind of energy storage devices are discussed in chapter "Energy Storage Applications of MXene".

Likewise, the effective intercalation of metallic cation suits MXenes for diversified environmental applications such as pollutant removal, heavy metal ions removal, etc. The major concern with the growth of the industrial sector is their wastewater discharge in water bodies, which contains several heavy metallic ions, including lead, copper, arsenic, zinc, chromium, lead, mercury, etc. Several remedies have been explored, and some are still under research to resolve such issues. In general, the atomic weight of such heavy metals in the water bodies lies between ~63 and ~200 with 5 g/cm^3 density [51, 52]. Therefore, the release of such heavy metals is non-biodegradable and is a major concern to the environment. Developing novel materials, including MXene with its thin interlayer spacing, presented effective trapping of heavy metallic ions adsorption such as barium, cadmium, lead, chromium, etc., from the discharged wastewater [53]. Additionally, the MXene surface-functionalized properties also played a vital role in enhancing the adsorption efficiency. For instance, the most explored material, MXene ($Ti_3C_2T_x$), is used as an adsorbent to remove barium (Ba) ions from the aqueous solution. The adsorbent ($Ti_3C_2T_x$) records removal or adsorption efficiency of 90% (55 mg/L initial concentration) within 10 min of the initial reaction, which are observed to be superior to the other reported carbonaceous materials. Such superior activity of MXene can be attributed to their combined characteristics such as hydrophilicity, active sites, negative surface area, chemical stability, and ease of ionic intercalation. The report also suggests that the adsorption of Ba ions is not affected by other associated existence of heavy metallic ions, including chromium, calcium, lead, etc. Further, the

experimentation model (i.e., Dubinin-Radushkevich) evidence that in addition to the adsorption (physisorption), chemisorption also happened during the reaction owing to the chemical bonding that takes place between the surface termination of MXene with Ba ions [53].

MXenes, adsorption kinetics relies largely on the charge of the organic contaminants; very recently, Kim et al. reported the adsorption property of $Ti_3C_2T_x$ under different pH towards numerous pharmaceutical compounds. Among the different elements present in the pharmaceutical compound, the MXene adsorbed the AMT heavily with the capacity of 58.7 mg/g at a pH of 7.0. Such high adsorption occurs due to their electrostatic attraction between the positively charged AMT and negatively charged MXene. Besides the electrostatic force of attraction, the adsorption capacity of the MXene can be enhanced by fine-tuning their interlayer spacing. Several processing strategies can enhance the interlayer spacing; here, in the same report, Kim et al. investigated the adsorption performance of MXene under different sonication frequencies (128, and 580 kHz). It was observed that the 214 mg/g recorded to be high in the frequency range over 28 kHz as compared to other frequencies 1 kHz (138 mg/g) and 580 kHz (172 mg/g), respectively. The significant enhancement in the adsorption performance of the MXenes was credited to the well-dispersed MXene with more surface functional groups through cavitation creation (sonication) [54].

The superior activity of MXenes in environmental applications is not only limited to the adsorption of heavy metals; it also shows excellent kinetics adsorption against different dyes. For instance, the adsorption activity of $Ti_3C_2T_x$ against methylene blue (MB) dye under different alkaline conditions is carried out and found that NaOH treated MXene shows a higher rate of adsorption (189 mg/g). The faster kinetic reaction attributed to the charge interaction and intercalation of ions is the main cause for the higher adsorption rate [55, 56]. Further enhancement in kinetic adsorption of MXene is achieved by compositing MXene with other nanomaterials. Recently, Kang et al. experimented with the adsorption activity of $Ti_3C_2T_x$-GO composite membrane towards the removal of different dyes such as MB, Rose Bengal (RB), methylene red (MR), coomassie brilliant blue (CBB). $Ti_3C_2T_x$-GO composites exhibit a 100% removal rate with CBB, 99% with MB, 94% with RB, and 68% with MR, respectively. Likewise, the removal efficiencies of MXenes for different ionic salts such as Na_2SO_4, $MgCl_2$, NaCl, and $MgSO_4$ were also reported with different adsorption rates. The adsorption kinetics of the MXenes in correlation with different dyes varies concerning the ionic size, interlayer spacing, electrostatic interaction [57]. The complete aspect of the environmental remedial application of MXenes is discussed in chapter "Environmental Applications of MXenes".

Besides energy and environmental-related applications of MXenes, another dominant application of MXenes is electromagnetic interference shielding (EMI). The first study on MXene for EMI was published soon after discovering the first MXene (i.e., Ti_3C_2). Since then, the $Ti_3C_2T_x$ was claimed to be one of the superior materials for EMI [58, 59]. The higher electrical conducting (~20,000 S/cm) property was one of the state-of-art to forefront MXene as EMI shielding materials, comparable to those of other conventional and synthetic metals. The superior shielding performance of

MXenes is determined by its intrinsic activity and the extrinsic modification of materials such as pores, structures, and dielectric inclusions [60, 61]. We are all much aware of the rapid pace of industrial technologies, specifically in the area of electronic and communication, where fifth-generation (5G) technologies are emerging in commercialization with big technological data and the internet of things (IoT) [62, 63]. As the 5G technology receives huge interest in the telecommunication industries, the electromagnetic waves generate and/or receive/transmit in a wide range of frequencies; the interference associated with the electromagnetic waves (referred to as electromagnetic interference) is a serious threat and prone to escalate by deteriorating the device performance and system security [59, 60, 64]. Thus, the unperturbed operation of 5G technologies can be ensured by addressing the major challenge posed by EMI using the advancement of materials like MXenes [59, 65–67]. Aforementioned, the fascinating properties of MXenes, which include high metallic conductivity, flexibility, higher electronic density, ease of processability, electrical conductivity, etc., outweigh their benefits in the field of EMI shielding [59, 68, 69]. Further, the laminated (stacked) architecture of MXene sheets supports incident electromagnetic waves absorption within the layers (shield), which differentiates them from other conventional materials. The energy attenuation of electromagnetic waves in the multi-layered MXene stacks plays a constructive role in demonstrating effective shielding performance. The excellent interference shielding was achieved by properly fabricating materials with low thickness and maximum thickness absorption [70]. Apart from these properties, the surface chemistry of MXenes also plays a significant contribution in the enhancement of electromagnetic waves absorption through polarization losses. For instance, dipolar or oriental polarizations dominate at the frequency range of over GHz. The individual layers in the multi-layered MXene stacks create dipoles under applied electromagnetic waves associated with the negatively charged surface terminations (T_x), resulting in the energy reduction of electromagnetic waves with capacitive loss. Additionally, the large surface area of 2D MXenes benefits the facile processability and higher flexibility, specifically for the next-generation foldable electronics [59, 71, 72] (see chapter "MXenes for Electromagnetic Interference (EMI) Shielding"). Such unique properties make them an ideal candidate for EMI shielding.

Apart from the dominant applications (energy, environment, and EMI) of MXenes, the large number of its compositions with various surface terminations suits them in other fields of applications, including medicine. For each material, its end-users application is one of the important factors to step over the next stage in terms of commercialization or scaling-up with an advancement. Many experimental, computational, and review reports exist in briefing the growing library of 2D MXenes and their composition. Along with the experimental results, the computational approach such as molecular dynamics simulations is necessary to identify or develop the classic potential or phase field to identify their exfoliation route with different etchants for performing large-scale. The computational results support designing the experimental passage by understanding its fundamental mechanism between the interlayer spacing [73]. Unlike most other 2D materials, MXene can be scaled up, which holds as an additional benefit for achieving immediate nearby commercialization.

However, the preparation routes for achieving large-scale production are crucial to its advancement. In order to design the appropriate equipment for reaction, the reaction field's stress gradient and temperature are needed to consider for yielding large proportions of MXenes. The most commonly used and very first etchant used in the synthesis of MXene (i.e., HF) was the only possible route so far to scale up their production. Despite the environmental concern on the usage of HF, it was the only etchant that could yield ~50 g of MXene without comprising their purity. However, the delamination and intercalation of large-scale MXene synthesis are still awaiting in-depth investigation. Also, the scaling up of other possible routes of etching, including LiF/HCl molten salts, is necessary to use their facile delamination process, safety, cost, and environmental protection. Once the etching routes are achieved, an adequate quantity of sheets can be produced from ultrasonic treatment. Recent and future generations are looking for a smart and flexible device, particularly in the energy and electronic sectors. In this regard, the derivatives of MXenes such as fibers and flexible membranes are mostly preferred, unlike their powder (sheets) [74]. MXenes will be widely used in future additive manufacturing technologies; if large-scale, environmentally acceptable synthesis processes can be developed. Theoretically anticipated intrinsically semiconducting, ferromagnetic, and topologically insulating, as well as other discoveries in MXene physics and chemistry, should be possible with precise control of the structure and surface chemistry, including defects and strain engineering. MXenes, which are mechanically strong, environmentally stable, and electrically conductive, could have a big impact on self-powered devices that are flexible, printable, and wearable. However, using MXenes in conjunction with other 2D materials to self-assemble heterostructures and electronics is a viable option [73].

Although the MXenes are emerging in recent decades with advancements in commercialization, the safety measures in their synthesis are highly questionable. The base precursor used for MXene is MAX phase powders, which are pyrophoric forms of fine metal powders, especially when the size of the metal powders is at the nanoscale. Such pyrophoric metal powders involve safety risks in handling and storing. Numerous metal powders (nanopowders) with this type of nature (pyrophoric) require special handling and have their own safety data sheet (SDS). Because of the large surface area to volume ratio, nanoparticles exhibit distinct phenomena that are not seen in coarse powders. As a result of these differences in chemical structure, nanopowders have significantly lower ignition temperatures/energies, implying an increased risk of self-ignition and thermal explosions in the air. Chemical passivation is one of the common routes to reduce pyrophoricity by reforming their oxide shell. Moreover, different preparation routes are used to synthesize MXenes, and each route necessitates the critical examination of all risks involved. Also, the biotoxicity of MXenes is still underway; even though some studies exist on their toxicity and biosafety, they are not exhaustive, so the further in-depth investigation is necessary [75]. The detailed caution on handling and safety measures with the advancement of MXenes are discussed in chapter "Biomedical Applications of MXenes".

While progressive research has been made on MXene from the past decades, most of the reported materials on MXenes are based on carbides, and there is a trail behind nitrides synthesis. In addition, most of their dominant applications reported so far are limited to two fields: (i) energy storage and (ii) EMI. The effect of interfacial physics and associated van der Waals interactions on stability is a frequently encountered challenge. The accumulation of electrons and/or holes of the surface of MXenes and their interfaces are needed to be examined for making next-generation flexible devices [73]. The most encountered bottlenecked issue in the commercialization and large-scale synthesis of MXenes is its stability. As the oxidation rate (MXene) relies upon the temperature and humidity, it can oxidize easily in humid conditions. Compared to their monolayer counterparts, multilayer MXenes have a lower tendency to oxidize. Because the evidence suggests that MXenes surface oxidation begins near edges, shielding these edges is a viable choice. The antioxidation ability and storage life of the produced MXene dispersion might be improved by controlled edge-adsorption of different cations. For instance, coating carbon on the MXene surface in energy storage applications supports resisting oxidation and boosts their performance (capacitive). Thus, the inclusion of foreign species via the engineering of MXenes can pave a new path to stop oxidation. Besides shielding, removing water molecules, lowering the temperature, or deoxygenation are additional choices to prevent surface oxidation. Although effective, anionic salt edge adsorption could harm its performance due to salt anions interference. As a result, eliminating excess salt ions without jeopardizing MXenes' optimal application performance is a topic that needs more research. In general, laboratory-scale etching of MAX precursors is still limited, with only a few promising approaches with preparative scaled capabilities. The rapid advancement in etching engineering and the expanding application domains of delaminated MXenes, on the other hand, point to a near-future advanced technology that could offer durable MXenes materials for industrial applications [74]. It is gratifying to see that several issues on MXenes raised for a decade are resolved almost with continuous research made. However, these efforts are notwithstanding as the mitigation strategies on oxidation are unknown, especially long-term effectiveness [61]. Likewise, many factors associated with MXenes remain challenging and need to be addressed. A detailed note on the same is provided in chapters "Advancements in MXenes and Novel MXenes—Advanced Synthesis and Tailored Material-Property Design.

2 Prospects

The ability to manipulate the surface terminations of MXenes' led to exhibit highly conductive, large strength with good absorption and reflectivity trends. Therefore, it is one of the promising candidates for diversified applications. The results of the possible applications of MXenes are reported in numerous scientific reports. However, the current knowledge in MXenes is yet to be explored. For instance, MXene is regarded as one of the best materials for energy storage devices, although its underlying process has yet to be completely investigated. Moreover, stability is

one of the major concerns associated with them. It can degrade upon exposure to the air (oxygen) and/or water medium, making them difficult to apply in various fields. The other major challenge was there are no precursor materials (MAX phase) for most of the reported materials (MXenes) since most of them are explored only through a computational approach. Hence, most attention needs to be paid to synthesizing (experimental) new-layered materials. Similarly, many MXenes and MXene based composites are proposed for environmental applications like water purification, desalination, etc. But removing pollutants from the environment remains a challenge yet, which can be resolved by exploring more studies on MXenes. Besides all these facts, the safety measures of MXenes need to be considered. Perhaps, the biggest challenge yet, though, is the experimental validation of all the theoretical studies and the verification of the predicted properties of MXenes.

Acknowledgements The authors (AA and RVM) duly acknowledge FONDECYT Postdoctoral project (No.: 3200076), the Government of Chile, and the University of Concepcion, Concepcion, Chile, for the financial support.

References

1. Jiang, J., Zou, Y., Arramel, Li, F., Wang, J., Zou, J., Li, N.: Intercalation engineering of MXenes towards highly efficient photo(electrocatalytic) hydrogen evolution reactions. J. Mater. Chem. A **9**, 24195–24214 (2021)
2. Barsoum, M.W.: MAX Phases: Properties of Machinable Ternary Carbides and Nitrides. Wiley, Weinheim (2013)
3. Fu, L., Xia, W.: MAX phases as nanolaminate materials: chemical composition, microstructure, synthesis, properties, and applications. Adv. Eng. Mater. **23**, 2001191 (2021)
4. Bhat, A., Anwer, S., Bhat, K.S., Mohideen, M.I.H., Liao, K., Qurashi, A.: Prospects challenges and stability of 2D MXenes for clean energy conversion and storage applications, Npj 2D Mater. Appl. **5**, 61 (2021)
5. Gogotsi, Y., Anasori, B.: The rise of MXenes. ACS Nano **13**, 8491–8494 (2019)
6. Anasori, B., Lukatskaya, M.R., Gogotsi, Y.: 2D metal carbides and nitrides (MXenes) for energy storage. Nat. Rev. Mater. **2**, 16098 (2017)
7. Jiang, X., Kuklin, A.V., Baev, A., Ge, Y., Ågren, H., Zhang, H., Prasad, P.N.: Two-dimensional MXenes: from morphological to optical, electric, and magnetic properties and applications. Phys. Rep. **848**, 1–58 (2020)
8. Hadler-Jacobsen, J., Fagerli, F.H., Kaland, H., Schnell, S.K.: Stacking sequence, interlayer bonding, termination group stability and Li/Na/Mg diffusion in MXenes. ACS Mater. Lett. **3**, 1369–1376 (2021)
9. Meshkian, R., Näslund, L.-Å., Halim, J., Lu, J., Barsoum, M.W., Rosen, J.: Synthesis of two-dimensional molybdenum carbide, Mo_2C, from the gallium based atomic laminate Mo_2Ga_2C. Scr. Mater. **108**, 147–150 (2015)
10. Zhan, C., Sun, W., Kent, P.R.C., Naguib, M., Gogotsi, Y., Jiang, D.: Computational screening of MXene electrodes for pseudocapacitive energy storage. J. Phys. Chem. C. **123**, 315–321 (2019)
11. Duong, D.L., Yun, S.J., Lee, Y.H., van der Waals: Layered materials: opportunities and challenges. ACS Nano. **11**, 11803–11830 (2017)
12. Magnuson, M., Mattesini, M.: Chemical bonding and electronic-structure in MAX phases as viewed by X-ray spectroscopy and density functional theory. Thin Solid Films **621**, 108–130 (2017)

13. Li, X., Ran, F., Yang, F., Long, J., Shao, L.: Advances in MXene films: synthesis, assembly, and applications. Trans. Tianjin Univ. **27**, 217–247 (2021)
14. Zhao, X., Radovic, M., Green, M.J.: Synthesizing MXene nanosheets by water-free etching. Chem. **6**, 544–546 (2020)
15. Sun, W., Shah, S.A., Chen, Y., Tan, Z., Gao, H., Habib, T., Radovic, M., Green, M.J.: Electrochemical etching of Ti_2AlC to Ti_2CT (MXene) in low-concentration hydrochloric acid solution. J. Mater. Chem. A **5**, 21663–21668 (2017)
16. Natu, V., Pai, R., Sokol, M., Carey, M., Kalra, V., Barsoum, M.W.: 2D Ti_3C_2Tz MXene synthesized by water-free etching of Ti_3AlC_2 in Polar organic solvents. Chem **6**, 616–630 (2020)
17. Abdolhosseinzadeh, S., Jiang, X., Zhang, H., Qiu, J., Zhang, C.(J.).: Perspectives on solution processing of two-dimensional MXenes. Mater. Today **48**, 214–240 (2021)
18. Natu, V., Sokol, M., Verger, L., Barsoum, M.W.: Effect of edge charges on stability and aggregation of $Ti_3C_2T_z$ MXene colloidal suspensions. J. Phys. Chem. C **122**, 27745–27753 (2018)
19. Wang, X., Ong, G.M.C., Naguib, M., Wu, J.: Theoretical insights into MXene termination and surface charge regulation. J. Phys. Chem. C. **125**, 21771–21779 (2021)
20. Champagne, A., Charlier, J.-C.: Physical properties of 2D MXenes: from a theoretical perspective. J. Phys. Mater. **3**, 032006 (2020)
21. Hart, J.L., Hantanasirisakul, K., Lang, A.C., Anasori, B., Pinto, D., Pivak, Y., van Omme, J.T., May, S.J., Gogotsi, Y., Taheri, M.L.: Control of MXenes' electronic properties through termination and intercalation. Nat. Commun. **10**, 522 (2019)
22. Qiao, C., Wu, H., Xu, X., Guan, Z., Ou-Yang, W.: Electrical conductivity enhancement and electronic applications of 2D $Ti_3C_2T_x$ MXene materials. Adv. Mater. Interf. 2100903 (2021)
23. Lipatov, A., Lu, H., Alhabeb, M., Anasori, B., Gruverman, A., Gogotsi, Y., Sinitskii, A.: Elastic properties of 2D $Ti_3C_2T_x$ MXene monolayers and bilayers. Sci. Adv. **4** (2018)
24. Fu, B., Sun, J., Wang, C., Shang, C., Xu, L., Li, J., Zhang, H.: MXenes: synthesis, optical properties, and applications in ultrafast photonics. Small **17**, 2006054 (2021)
25. Jeon, J., Yang, Y., Choi, H., Park, J.-H., Lee, B.H., Lee, S.: MXenes for future nanophotonic device applications. Nanophotonics **9**, 1831–1853 (2020)
26. Das, P., Wu, Z.-S.: MXene for energy storage: present status and future perspectives. J. Phys. Energy **2**, 032004 (2020)
27. Hong, W., Wyatt, B.C., Nemani, S.K., Anasori, B.: Double transition-metal MXenes: atomistic design of two-dimensional carbides and nitrides. MRS Bull. **45**, 850–861 (2020)
28. Dahlqvist, M., Rosen, J.: Order and disorder in quaternary atomic laminates from first-principles calculations. Phys. Chem. Chem. Phys. **17**, 31810–31821 (2015)
29. Mozafari, M., Soroush, M.: Surface functionalization of MXenes. Mater. Adv. **2**, 7277–7307 (2021)
30. Frisenda, R., Niu, Y., Gant, P., Muñoz, M., Castellanos-Gomez, A.: Naturally occurring van der Waals materials. Npj 2D Mater Appl. **4**, 38 (2020)
31. Di Bartolomeo, A.: Emerging 2D materials and their Van Der Waals heterostructures. Nanomaterials **10**, 579 (2020)
32. Verger, L., Xu, C., Natu, V., Cheng, H.-M., Ren, W., Barsoum, M.W.: Overview of the synthesis of MXenes and other ultrathin 2D transition metal carbides and nitrides. Curr. Opin. Solid State Mater. Sci. **23**, 149–163 (2019)
33. Iqbal, A., Hong, J., Ko, T.Y., Koo, C.M.: Improving oxidation stability of 2D MXenes: synthesis, storage media, and conditions. Nano Converg. **8**, 9 (2021)
34. Luo, J., Matios, E., Wang, H., Tao, X., Li, W.: Interfacial structure design of MXene-based nanomaterials for electrochemical energy storage and conversion. InfoMat **2**, 1057–1076 (2020)
35. Naguib, M., Barsoum, M.W., Gogotsi, Y.: Ten years of progress in the synthesis and development of MXenes. Adv. Mater. **33**, 2103393 (2021)
36. Wang, H., Zhang, J., Wu, Y., Huang, H., Li, G., Zhang, X., Wang, Z.: Surface modified MXene Ti_3C_2 multilayers by aryl diazonium salts leading to large-scale delamination. Appl. Surf. Sci. **384**, 287–293 (2016)

37. Persson, I., Halim, J., Hansen, T.W., Wagner, J.B., Darakchieva, V., Palisaitis, J., Rosen, J., Persson, P.O.Å.: How much oxygen can a mxene surface take before it Breaks? Adv. Funct. Mater. **30**, 1909005 (2020)
38. Persson, I., Näslund, L.-Å., Halim, J., Barsoum, M.W., Darakchieva, V., Palisaitis, J., Rosen, J., Persson, P.O.Å.: On the organization and thermal behavior of functional groups on Ti_3C_2 MXene surfaces in vacuum. 2D Mater. **5**, 015002 (2017)
39. Li, X., Wang, C., Cao, Y., Wang, G.: Functional MXene materials: progress of their applications. Chem. Asian J. **13**, 2742–2757 (2018)
40. Idumah, C.I., Obele, C.M., Enwerem, U.E.: On interfacial and surface behavior of polymeric MXenes nanoarchitectures and applications. Curr. Res. Green Sustain. Chem. **4**, 100104 (2021)
41. Khaledialidusti, R., Khazaei, M., Khazaei, S., Ohno, K.: High-throughput computational discovery of ternary-layered MAX phases and prediction of their exfoliation for formation of 2D MXenes. Nanoscale **13**, 7294–7307 (2021)
42. Simon, P.: Two-dimensional MXene with controlled interlayer spacing for electrochemical energy storage. ACS Nano **11**, 2393–2396 (2017)
43. Naguib, M., Mochalin, V.N., Barsoum, M.W., Gogotsi, Y.: 25th anniversary article: MXenes: a new family of two-dimensional materials. Adv. Mater. **26**, 992–1005 (2014)
44. Naguib, M., Kurtoglu, M., Presser, V., Lu, J., Niu, J., Heon, M., Hultman, L., Gogotsi, Y., Barsoum, M.W.: Two-dimensional nanocrystals produced by exfoliation of Ti_3AlC_2. Adv. Mater. **23**, 4248–4253 (2011)
45. VahidMohammadi, A., Rosen, J., Gogotsi, Y.: The world of two-dimensional carbides and nitrides (MXenes). Science (80–), 372 (2021)
46. Li, J., Yuan, X., Lin, C., Yang, Y., Xu, L., Du, X., Xie, J., Lin, J., Sun, J.: Achieving high pseudocapacitance of 2D titanium carbide (MXene) by cation intercalation and surface modification. Adv. Energy Mater. **7**, 1602725 (2017)
47. Kajiyama, S., Szabova, L., Sodeyama, K., Iinuma, H., Morita, R., Gotoh, K., Tateyama, Y., Okubo, M., Yamada, A.: Sodium-ion intercalation mechanism in MXene nanosheets. ACS Nano **10**, 3334–3341 (2016)
48. Yu, Y.-X.: Prediction of mobility, enhanced storage capacity, and volume change during sodiation on interlayer-expanded functionalized Ti_3C_2 MXene anode materials for sodium-ion batteries. J. Phys. Chem. C **120**, 5288–5296 (2016)
49. Ghidiu, M., Halim, J., Kota, S., Bish, D., Gogotsi, Y., Barsoum, M.W.: Ion-exchange and cation solvation reactions in Ti_3C_2 MXene. Chem. Mater. **28**, 3507–3514 (2016)
50. Xie, Y., Naguib, M., Mochalin, V.N., Barsoum, M.W., Gogotsi, Y., Yu, X., Nam, K.-W., Yang, X.-Q., Kolesnikov, A.I., Kent, P.R.C.: Role of surface structure on Li-ion energy storage capacity of two-dimensional transition-metal carbides. J. Am. Chem. Soc. **136**, 6385–6394 (2014)
51. Srivastava, N.K., Majumder, C.B.: Novel biofiltration methods for the treatment of heavy metals from industrial wastewater. J. Hazard. Mater. **151**, 1–8 (2008)
52. Ihsanullah, Abbas, A., Al-Amer, A.M., Laoui, T., Al-Marri, M.J., Nasser, M.S., Khraisheh, M., Atieh, M.A.: Heavy metal removal from aqueous solution by advanced carbon nanotubes: critical review of adsorption applications. Sep. Purif. Technol. **157**, 141–161 (2016)
53. Fard, A.K., Mckay, G., Chamoun, R., Rhadfi, T., Preud'Homme, H., Atieh, M.A.: Barium removal from synthetic natural and produced water using MXene as two dimensional (2-D) nanosheet adsorbent. Chem. Eng. J. **317**, 331–342 (2017)
54. Kim, S., Gholamirad, F., Yu, M., Park, C.M., Jang, A., Jang, M., Taheri-Qazvini, N., Yoon, Y.: Enhanced adsorption performance for selected pharmaceutical compounds by sonicated Ti_3C_2TX MXene. Chem. Eng. J. **406**, 126789 (2021)
55. Vidyasagar, D., Gupta, A., Balapure, A., Ghugal, S.G., Shende, A.G., Umare, S.S.: 2D/2D Wg-C_3N_4/g-C_3N_4 composite as "Adsorb and Shuttle" model photocatalyst for pollution mitigation. J. Photochem. Photobiol. A Chem. **370**, 117–126 (2019)
56. Wei, Z., Peigen, Z., Wubian, T., Xia, Q., Yamei, Z., ZhengMing, S.: Alkali treated Ti_3C_2Tx MXenes and their dye adsorption performance. Mater. Chem. Phys. **206**, 270–276 (2018)

57. Kang, K.M., Kim, D.W., Ren, C.E., Cho, K.M., Kim, S.J., Choi, J.H., Nam, Y.T., Gogotsi, Y., Jung, H.-T.: Selective Molecular Separation on $Ti_3C_2T_x$–graphene oxide membranes during pressure-driven filtration: comparison with graphene oxide and MXenes. ACS Appl. Mater. Interf. **9**, 44687–44694 (2017)
58. Han, M., Yin, X., Wu, H., Hou, Z., Song, C., Li, X., Zhang, L., Cheng, L.: Ti_3C_2 MXenes with modified surface for high-performance electromagnetic absorption and shielding in the X-band. ACS Appl. Mater. Interf. **8**, 21011–21019 (2016)
59. Shahzad, F., Alhabeb, M., Hatter, C.B., Anasori, B., Man Hong, S., Koo, C.M., Gogotsi, Y.: Electromagnetic interference shielding with 2D transition metal carbides (MXenes). Science (80–), **353**,1137–1140 (2016)
60. Han, M., Shuck, C.E., Rakhmanov, R., Parchment, D., Anasori, B., Koo, C.M., Friedman, G., Gogotsi, Y.: Beyond $Ti_3C_2T_x$: MXenes for electromagnetic interference shielding. ACS Nano **14**, 5008–5016 (2020)
61. Mathis, T.S., Maleski, K., Goad, A., Sarycheva, A., Anayee, M., Foucher, A.C., Hantanasirisakul, K., Shuck, C.E., Stach, E.A., Gogotsi, Y.: Modified MAX phase synthesis for environmentally stable and highly conductive Ti_3C_2 MXene. ACS Nano **15**, 6420–6429 (2021)
62. Mudigonda, P., Abburi, S.K.: A survey: 5G in IoT is a boon for big data communication and its security. In: Kumar, A., Paprzycki, M., Gunjan, V. (eds.) ICDSMLA 2019. Lecture Notes in Electrical Engineering, vol. 601. Springer, Singapore (2020). https://doi.org/10.1007/978-981-15-1420-3_33
63. Médard, M.: Is 5 just what comes after 4? Nat. Electron. **3**, 2–4 (2020)
64. Iqbal, A., Shahzad, F., Hantanasirisakul, K., Kim, M.-K., Kwon, J., Hong, J., Kim, H., Kim, D., Gogotsi, Y., Koo, C.M.: Anomalous absorption of electromagnetic waves by 2D transition metal carbonitride Ti_3CNT_x (MXene). Science (80–), **369**, 446–450 (2020)
65. Yun, T., Kim, H., Iqbal, A., Cho, Y.S., Lee, G.S., Kim, M., Kim, S.J., Kim, D., Gogotsi, Y., Kim, S.O., Koo, C.M.: Electromagnetic shielding of monolayer MXene assemblies. Adv. Mater. **32**, 1906769 (2020)
66. Kumar, P., Yu, S., Shahzad, F., Hong, S.M., Kim, Y.-H., Koo, C.M.: Ultrahigh electrically and thermally conductive self-aligned graphene/polymer composites using large-area reduced graphene oxides. Carbon N.Y. **101**, 120–128 (2016)
67. Kumar, P., Shahzad, F., Yu, S., Hong, S.M., Kim, Y.-H., Koo, C.M.: Large-area reduced graphene oxide thin film with excellent thermal conductivity and electromagnetic interference shielding effectiveness. Carbon N.Y. **94**, 494–500 (2015)
68. Zeng, Z., Wang, C., Siqueira, G., Han, D., Huch, A., Abdolhosseinzadeh, S., Heier, J., Nüesch, F., Zhang, C.(J.), Nyström, G.: Nanocellulose-MXene biomimetic aerogels with orientation-tunable electromagnetic interference shielding performance. Adv. Sci. **7**, 2000979 (2020)
69. Xu, B., Gogotsi, Y.: MXenes–the fastest growing materials family in the two-dimensional world. Chin. Chem. Lett. **31**, 919–921 (2020)
70. Iqbal, A., Kwon, J., Kim, M.-K., Koo, C.M.: MXenes for electromagnetic interference shielding: experimental and theoretical perspectives. Mater. Today Adv. **9**, 100124 (2021)
71. Xu, H., Yin, X., Li, X., Li, M., Liang, S., Zhang, L., Cheng, L.: Lightweight Ti_2CT_x MXene/Poly(vinyl alcohol) composite foams for electromagnetic wave shielding with absorption-dominated feature. ACS Appl. Mater. Interf. **11**, 10198–10207 (2019)
72. Gogotsi, Y., Huang, Q.: MXenes: two-dimensional building blocks for future materials and devices. ACS Nano **15**, 5775–5780 (2021)
73. Khazaei, M., Mishra, A., Venkataramanan, N.S., Singh, A.K., Yunoki, S.: Recent advances in MXenes: from fundamentals to applications. Curr. Opin. Solid State Mater. Sci. **23**, 164–178 (2019)
74. Wei, Y., Zhang, P., Soomro, R.A., Zhu, Q., Xu, B.: Advances in the synthesis of 2D MXenes. Adv. Mater. **33**, 2103148 (2021)
75. Shuck, C.E., Ventura-Martinez, K., Goad, A., Uzun, S., Shekhirev, M., Gogotsi, Y.: Safe synthesis of MAX and MXene: guidelines to reduce risk during synthesis. ACS Chem. Heal. Saf. **28**, 326–338 (2021)

Synthesis and Processing Strategies

Sandhya Venkateshalu and Andrews Nirmala Grace

Abstract With the discovery of MXenes in 2011, they have been widely explored for a myriad of applications due to their hydrophilic nature, excellent electrical conductivity, and ease of large-scale synthesis in water. The properties of the MXenes are influenced by the synthesis route adopted. The etching agents used in the synthesis of MXenes will affect the surface terminations, morphology, and structural defects. The first MXene Ti_3C_2 was discovered using the method of hydrofluoric acid (HF) etching. However, in the urge to discover new MXenes and avoid the use of toxic HF, new etching procedures and synthesis pathways were introduced. The synthesized MXenes can be deposited through various coating techniques and fabricated into different devices. The synthesis method also determines the yield and quality of MXenes. With the various synthesis and processing techniques reported in the literature, it is evident that MXenes are evolving rapidly. This chapter summarizes the important breakthroughs in the synthesis and processing of MXenes, which includes the latest trends in etching and delamination procedures. The effects of the etching methods on the charge storage capabilities in MXenes are further discussed.

Keywords MXene · 2D materials · Etching · MXene synthesis · Processing of MXenes

1 Introduction

It is well known that 2D materials were obtained from layered bulk materials (graphite, hexagonal boron nitride, Mo_2S) by separating the atomic layers, utilizing the weak bonds between the layers compared to the bonds that are present within the layers [1]. The layers in these solid materials are held together by either van der Waals forces or hydrogen bonds. However, the new class of two-dimensional (2D) materials known as MXenes is obtained by selective removing certain layers from a precursor material known as MAX phases that belong to a large family of layered

S. Venkateshalu · A. N. Grace (✉)
Centre for Nanotechnology Research, Vellore Institute of Technology (VIT), Vellore 632014, Tamil Nadu, India
e-mail: anirmalagrace@vit.ac.in

M. Khalid et al. (eds.), *Fundamental Aspects and Perspectives of MXenes*, Engineering Materials, https://doi.org/10.1007/978-3-031-05006-0_2

ternary carbides and nitrides. MAX phase has a general formula: $M_{n+1}AX_n$ where n = 1, 2, or 3, M is the early transition metal, A is group 13 or 14 elements, and X is either or both carbon and nitrogen. These MAX phases have relatively strong interlayer bonds compared to other layered bulk materials [2, 3].

The parent MAX phases are formed by ball milling particular ratios of M, A, and X elemental powders for a certain period of time and then heating them to high temperatures. The milled samples are pressed (hot or cold) to increase the material density and eliminate structural defects. The pressure applied during pressing helps in influencing the gain growth in a preferred orientation. The milled powders can also be sintered without applying pressure, known as pressure-less sintering [4]. The formed MAX phases are treated with a suitable etchant for a specific concentration and time to remove the A element from it. The treated solution will be further centrifuged (till the suspension has a pH 6) and filtered to obtain multi-layered (ML) MXene, which has an accordion-like structure similar to exfoliated graphite. The layered structures will be further subjected to delamination to obtain few-layered (FL) MXenes (<5 layers) [5].

This chapter discusses the various etchants explored in producing new MXenes. The type of etchant used determines the surface terminations, yield, and purity of the MXene obtained. The use of HF and HF in-situ etching methods needs careful handling due to the toxic nature of HF. Hydrothermal and electrochemical etching methods are environmentally friendly alternatives. The water-free etching method is highly beneficial in applications whose performance is hindered by the presence of water. Synthesis and processing of MXenes is a crucial step in imparting various properties to the MXenes, thereby enabling them to be used in a myriad of applications.

2 Etching

Unlike the weak van der Waals force of attraction acting between the layers in transition metal dichalcogenides (TMDs) and graphite, the layers in MAX phases are strongly held; thus, mechanical exfoliation is not suitable to produce 2D layers [6]. The bond existing between M-X is strong ionic/covalent/metallic, while the bond existing between M-A is metallic. The M-A bonds are chemically active, and utilizing the relative strengths of the bonds, 'A' layers can be selectively etched to form MXene ($M_{n+1}X_nT_x$). During the etching process, the surface of the metal atoms (M) gets attached with functional groups (T_x) such as –O, –OH, or –F [7]. A schematic representing the general synthesis of $Ti_3C_2T_x$ MXene using a fluorine-based etching method is shown in Fig. 1. The schematic here shows the existence of surface terminating functional groups after the etching process [8].

Various etching methods such as acid with fluorine, molten salts, hydrothermal, electrochemical, water-free, and Lewis acid have been used to date to synthesize MXenes [9, 10]. The type of etchant used will significantly influence the surface chemistry and the material's behaviour.

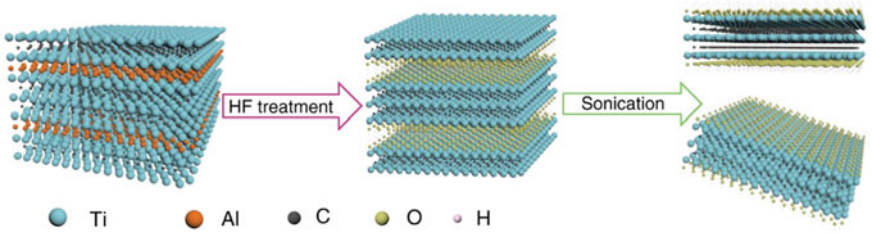

Fig. 1 General synthesis of $Ti_3C_2T_x$ MXene using a fluorine-based etching method. Ti_3AlC_2 MAX phase (left), etched (middle) and delaminated MXene (right) [8]

a. **Acid with fluorine**

Though many reagents have been identified for etching, fluoride-based materials remain the widely used reagents in the synthesis of MXenes. For the synthesis of carbide-based MXenes, HF and in-situ HF are the majorly used etchants. The etching in carbide-based MAX phases is obtained by treating them with aqueous solutions of HF or in-situ HF taken in a specific concentration and for a particular duration. The majority of carbide-based MXenes described to date have all been effectively synthesized with HF [11–14]. The reaction of HF with the MAX phase forming MXenes with surface terminations can be described by the following equations [3]:

$$M_{n+1}AX_n + 3HF \rightarrow AF_3 + {}^3/_2H_2 + M_{n+1}X_n \quad (1)$$

$$M_{n+1}X_n + 2H_2O \rightarrow M_{n+1}X_n(OH)_2 + H_2 \quad (2)$$

$$M_{n+1}X_n + 2HF \rightarrow M_{n+1}X_nF_2 + H_2 \quad (3)$$

Equation (1) represents the formation of MXene from its MAX phase, while Eqs. (2) and (3) describe the surface terminations such as –OH and –F onto the surface of the material. The etching conditions will vary for each parent MAX phase depending on its chemistry and structure. For example, Naguib et al. reported nanocrystalline ternary titanium aluminum fluoride (Ti_2AlF_9) was formed when Ti_2AlC was treated with 100% HF and the MAX phase Ti_2AlC dissolved when it was treated with 50% HF solution. However, a decrease in the concentration of HF to 10% leads to the successful formation of Ti_2C [15]. In the detailed report given by Alhabeb et al. on the effect of concentration and reaction time of HF on $Ti_3C_2T_X$, it was shown that though 5% HF could help in the removal of Al from Ti_3AlC_2; however, a perfect accordion-like structure was obtained only for $\geq$ 10% HF solutions [16]. When the MAX phases are reduced in size through ball milling, the reaction time and concentrations of HF can be reduced [17]. Also, the bond

energies of M-A play a crucial role in determining the reaction time and concentration of the etchant HF [18]. Table 1 summarizes the etching conditions required for the successful synthesis of MXenes from their MAX phases and their c-lattice parameters, respectively.

Vahid Mohammadi et al. reported the formation of V_2CT_x MXene from its MAX phase V_2AlC by treating it with 50% HF for 92 h at RT, as shown in Fig. 2. A typical accordion-like morphology can be observed here for V_2CT_x MXene, indicating its successful synthesis (Fig. 2c). Furthermore, the XRD pattern of the MXene (Fig. 2d)

Table 1 Summary of HF etching conditions to obtain MXenes from their MAX phases

MAX	MXene	HF conc.(%)	Reaction time (h)	*c*- lattice parameter (Å) (MAX)	*c*-lattice parameter (Å) (MXene)	References
Ti_2AlC	Ti_2CT_x	10	10	13.6	15.04	[15]
Ti_3AlC_2	$Ti_3C_2T_x$	40	20	18.62	20.89	[17]
Ti_3AlCN	Ti_3CNT_x	30	18	18.41	22.28	[15]
V_2AlC	V_2CT_x	50	90	13.13	23.96	[13]
Nb_2AlC	Nb_2CT_x	50	90	13.88	22.34	[19]
Nb_4AlC_3	$Nb_4C_3T_x$	50	90	24.19	30.47	[13]
Ta_4AlC_3	$Ta_4C_3T_x$	50	72	24.08	30.34	[15]

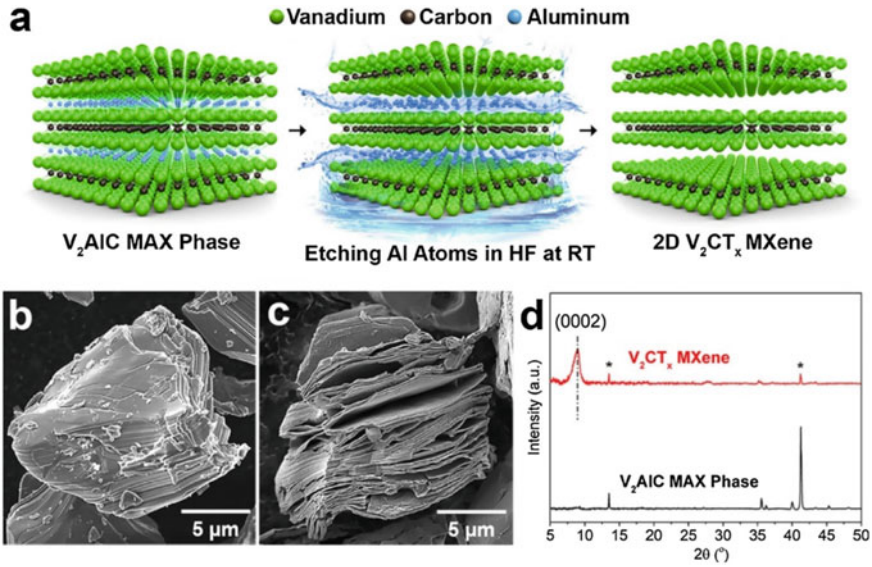

Fig. 2 Schematic indicating the formation of 2D V_2CT_x MXene from V_2AlC MAX phase (**a**), SEM images of V_2AlC and V_2CT_x respectively (**b**, **c**) and their XRD patterns (**d**). Reproduced with permission from [20] copyright 2017, American Chemical Society

shows the presence of (0002) peak, and the intensity of the peaks corresponding to the MAX phase is diminished but not completely eliminated, indicating the presence of small amounts of unreacted MAX phase [20].

Hydrofluoric acid is highly corrosive in nature and can penetrate through skin, bones, and muscles [21]. Therefore, HF needs careful handling and disposal. Thus, various other methods were designed to minimize or avoid the use of HF. A mixture consisting of an acid (HCl, H_2SO_4) and a fluoride salt (NaF, KF, LiF, NH_4F) is one such method wherein the formation of in-situ HF occurs. This method of acid–fluoride salt etching was introduced for the first time by Ghidiu et al., using LiF and HCl to etch Al from Ti_3AlC_2. The MXene obtained through this method was in the form of wet clay that could be molded into different shapes [22].

The effect of different fluoride salts such as LiF, NaF, KF, and NH_4F with HCl in etching Al from Ti_3AlC_2 and Ti_2AlC was reported extensively by Liu et al. [23]. Halim et al. reported NH_4HF_2 as an alternative to HF in etching Al from Ti_3AlC_2. It was noticed that the etching duration was longer when compared to HF. As a result, the NH_4^+ ions intercalate into the layers of MXene, thereby delaminating them without using a separate delaminating agent [24]. Intercalating cations such as Na^+, NH_4^+, Mg_2^+, K^+ and Al_3^+ into the MXene layers further helps in increasing the volumetric capacitance in supercapacitors [25]. The increase in the d spacing with the intercalation of cations into the layers of Ti3C2 MXene is schematically shown in Fig. 3 [4].

Carbide and carbonitride-based MXenes can be easily produced with aqueous acidic solutions, but the same is not possible for nitride-based MXenes. It is reported that the formation energies of nitride MXene from its MAX phase are higher compared to the carbide-based one. This means that the 'A' atoms in the nitride MAX phases are strongly bonded, requiring more energy for their removal. In addition, the cohesive energy of nitride MAX phases is less when compared to carbide-based ones. This implies that the nitride MAX phases are less stable, and thus they can dissolve easily in the widely used etchant HF [26]. To overcome these issues,

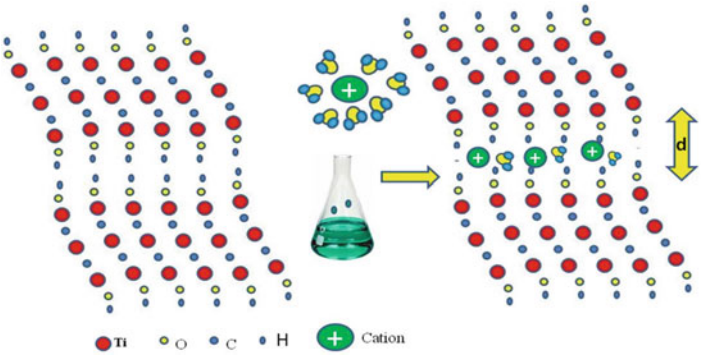

Fig. 3 Schematic illustrating the effect on the d spacing with the intercalation of cations. Reproduced with permission from [4] copyright 2020, Elsevier Ltd.

etchants other than HF are generally used to synthesize nitride-based MXenes. In this regard, Ti_2N MXene was successfully synthesized using KF–HCl mixture, which was later used as a substrate for Surface-Enhanced Raman Scattering. The FESEM images of the synthesized Ti_2N MXene through this method showed the typical layered morphology (Fig. 4) [27].

In the work reported by Urbankowski et al., nitride MXenes were synthesized from carbide MXenes, which were obtained through HF etching method. In this method, carbide MXenes Mo_2CT_x and V_2CT_x were subjected to ammonization by treating them with NH_3 gas at 550 °C to obtain nitride MXenes, Mo_2NT_x and V_2NT_x, respectively [28]. Kim et al. reported the etching mechanisms in polycrystalline Ti_3AlC_2 using LiF/HCl and HF etchants (Fig. 5). It was observed that there was spontaneous delamination with LiF/HCl etchant, but the mild etchant could not break the grain boundaries resulting in incomplete etching of MAX phases (Fig. 5b). In

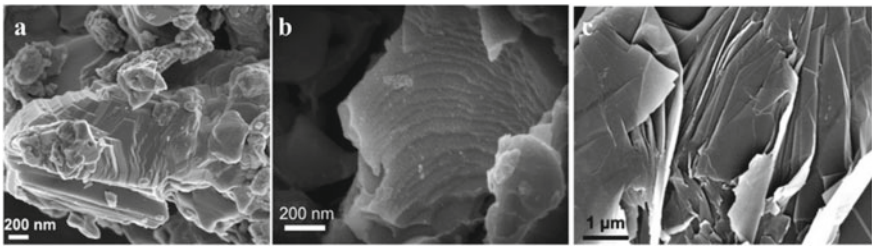

Fig. 4 FESEM images of MAX phase Ti_2AlN (**a**), KF-HCl etched MXene Ti_2N (**b**), delaminated MXene using dimethyl sulfoxide (**c**). Reproduced with permission from [27] copyright 2017, American Chemical Society

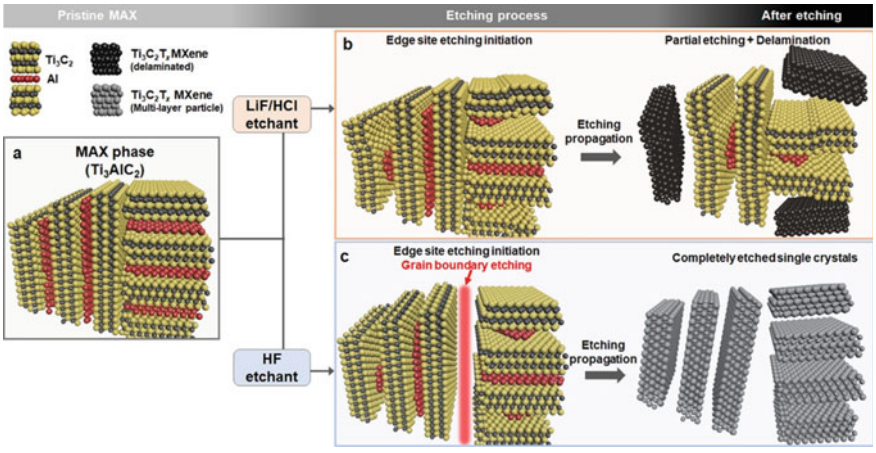

Fig. 5 Schematic representing the etching mechanism of pristine Ti_3AlC_2 MAX phase (**a**) in LiF/HCl (**b**) and HF (**c**) etching solutions. Reproduced with permission from [29] copyright 2021, American Chemical Society

the case of HF etching, it was observed that the polycrystals were broken into single crystals resulting in high etching yield (Fig. 5c). However, with the use of HF etchant, the $Ti_3C_2T_x$ sheets were not delaminated due to the absence of intercalant. This difference in the etching behavior between both the etchants could be attributed to the ability of the HF to etch grain boundaries in Ti_3AlC_2 crystals. Also, the HF is highly concentrated compared to the HF, which is gradually formed by the reaction between LiF and HCl [29].

b. **Molten salts**

Though the HF in-situ etching method is less hazardous, traces of HF will remain in the etching solution. Therefore, to overcome this issue, Urbankowski et al. introduced the molten salt etching method in which Ti_4N_3 MXene was synthesized using a eutectic molten salt mixture consisting of 59 wt% of KF, 29 wt% of LiF and 12 wt% of NaF. The MAX phase Ti_4AlN_3 was treated with this mixture at 550 °C for 30 min under Ar. After this treatment, different Al containing fluoride phases were observed; however, Ti containing fluorides were absent, confirming selective etching. The treated mixture was washed with H_2SO_4 to remove impurities, resulting in multi-layered Ti_4N_3, which was further delaminated to few layers using tetrabutylammonium hydroxide (TBAOH). The MXene obtained through this molten salt etching method has increased atomic defects compared to the HF etching method [30]. Additionally, Djire et al. have reported the successful synthesis of Ti_2N and Ti_4N_3 MXenes through molten salt etching procedure. It was seen that Ti_4N_3 synthesized through this technique exhibited both metallic and semiconducting behavior [31, 32]. The molten salt etching method has been mostly used to synthesize nitride-based MXenes, and the yields are relatively low. However, a few reports exist on synthesizing carbide-based MXenes using this method [33, 34].

c. **Hydrothermal**

The hydrothermal method used in the synthesis of MXenes is less harmful and environmentally friendly when compared to the HF etching method [35]. Thus, they are of prime importance in practical applications of MXenes. Wang et al. reported the synthesis of $Ti_3C_2T_x$ MXene from their MAX phase Ti_3AlC_2 using NH_4F through a hydrothermal method (150 °C for 24 h). The structure and morphology of the synthesized MXene can be modified by optimizing the amount of NH_4F, hydrothermal temperature, and time. With the increasing NH_4F amount and hydrothermal reaction time, the thickness of the layers decreases while the interlayer spacing increases. For low reaction temperatures such as 90 °C, etching was not observed, and for higher temperatures such as 180 °C, $Ti_3C_2T_x$ MXene was oxidized [36].

Peng et al. reported using $NaBF_4$ and HCl to synthesize Ti_3C_2 and Nb_2C MXenes through a hydrothermal route. The Ti_3C_2 MXene synthesized through this route had a large interlayer distance and BET surface area, which was attributed to the slow release mechanism during the hydrothermal reaction. Figure 6 shows the SEM images of the Nb_2C MXenes obtained for different reaction times from its MAX phase [37]. A fluorine-free, alkali-assisted hydrothermal synthesis method was used to synthesize Ti_3C_2Tx MXene, inspired by the Bayer process used widely in refining bauxite.

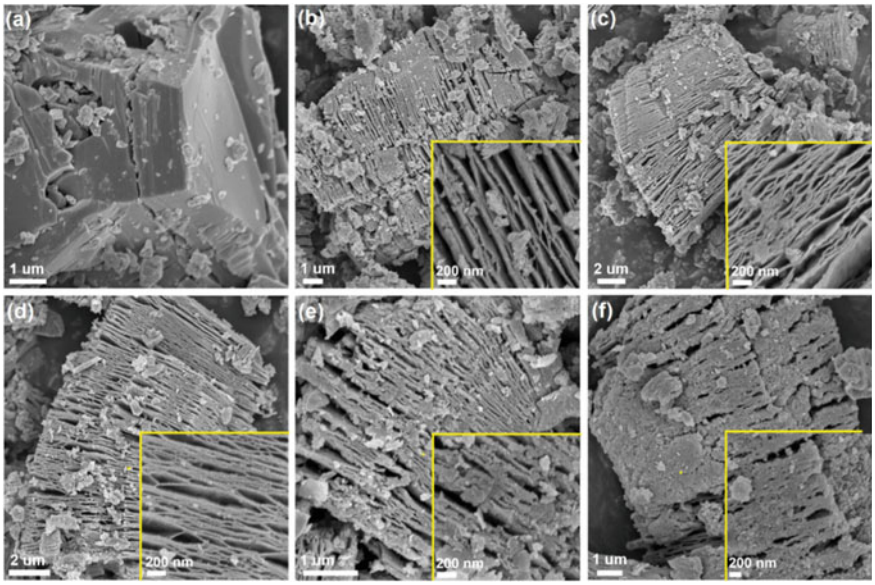

Fig. 6 SEM images of **a** MAX phase Nb_2AlC and **b–f** Nb_2C prepared from hydrothermal method, 180 °C for various reaction times (15–35 h). Reproduced with permission from [37] copyright 2018, Elsevier Ltd.

Typically, Ti_3AlC_2 was added with 27.5 M NaOH solution and heated hydrothermally (270 °C) to obtain $Ti_3C_2T_x$ MXene, which had a purity of 92 wt%. During this process, the hydroxide anions (OH^-) oxidizes the Al atoms in the Al layer producing $Al(OH)_4^-$, which gets dissolved in the alkali. As a result, the surface terminations of Ti in the MXene were only –OH and –O without –F. MXenes obtained through such a synthesis technique will contain more–OH and –O terminations when compared to those obtained through the HF etching method and thus provide better performance as supercapacitor electrodes [38].

d. **Electrochemical**

Chemical etching processes used to produce MXenes are electrochemical processes wherein electrons transfer from 'A' to other elements of the MAX phase [39]. Thus, another possible alternative approach is electrochemical etching. Sun et al. [40] reported the synthesis of Ti_2CT_x MXene for the first time using electrochemical etching in dilute HCl. The MXenes synthesized through this method had –Cl surface terminations along with –O and –OH. In this electrochemical etching method, there is a possibility that both M and A layers can be removed, producing carbide-derived carbons (CDC) due to over-etching. Thus, a careful balance of etching parameters is necessary. When the MAX phase Ti_2AlC was taken as a working electrode in a 3-electrode system, HCl electrolyte facilitates the removal of Al forming Ti_2CT_x MXene. Continuous etching leads to conversion of the outer layer of MXene to CDC and the inner MAX core to MXene. Thus, a three-layered, unique core–shell

structure consisting of an inner unetched MAX core, intermediate MXene layer, and outer CDC is obtained (Fig. 7). The MXene layers can be separated from the 3-layered structure through sonication. The report claimed that the formation of CDC is difficult to be avoided during etching. It was also suggested that the CDC formed onto the MXene could help protect it against oxidation [40].

In another report, $Ti_3C_2T_x$ (T_x = O, OH) MXene was synthesized based on the anodic corrosion of its MAX phase in a binary aqueous electrolyte, 1 M NH_4Cl and 0.2 M tetramethylammonium hydroxide (TMAOH, pH > 9). A binary aqueous electrolyte was used to allow the electrolyte ions to penetrate deep into the layers so that etching does not take place only onto the surface. In this typical fluorine-free electrochemical process, the MAX phase Ti_3AlC_2 was taken as both anode and cathode in a 2-electrode system with a binary aqueous electrolyte. The anode alone was involved in the etching reactions in which the chlorine ions from the electrolyte enable the etching of Al by breaking the Ti–Al bonds. As a result, NH_4OH intercalates into the layers and facilitates further etching by widening the edges of the etched anode. There is no reaction on the cathode side, and it is used as a counter electrode. MXenes synthesized through the electrochemical etching method pose superior electrical conductivity compared to acid with fluorine etching method. This method can obtain a high yield of >90%, making it a promising etching procedure [41]. MXenes prepared through the electrochemical etching method are widely used in energy storage applications [42, 43].

e. **Water free and Lewis acid**

In most of the etching methods reported for MXenes, water is the main solvent used, hindering their use in water-sensitive applications. However, the presence of water makes it harder for some polymerization reactions and synthesis of certain quantum dots onto MXenes [44, 45]. Moreover, the presence of trace amounts of water in Na and Li-ion batteries using organic electrolytes will significantly impede their performance [46]. Natu et al. reported the first water-free synthesis of $Ti_3C_2T_x$

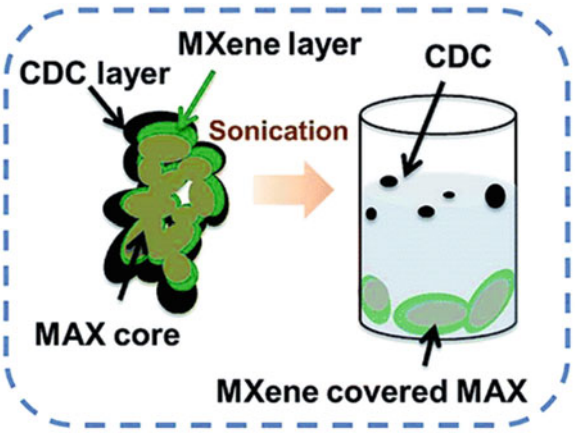

Fig. 7 Schematic representing the formation of a core–shell structure. Reproduced with permission from [40] copyright 2017, The royal society of chemistry

using various organic polar solvents and NH_4HF_2. The Al salts formed during the etching of MXenes are less soluble in organic solvents, and thus they needed acidic propanol to be washed away thoroughly. With the exchange of ammonium cations with the protons present in the acidic propanol, the d spacing reduced significantly after washing [47].

Recently, the Lewis acid molten salt method of producing MXenes with only Cl terminations has gained importance. This provides a green route in preparing MXenes without using HF [48, 49]. In the work reported by Li et al., novel MAX phases and MXenes were synthesized by exchanging the elements in the 'A' layer of the MAX phase. This is done with the help of late transition metal halides such as $ZnCl_2$, which are known as Lewis acids in their molten state. The Zn element replaces the Al element in the MAX phase Ti_3AlC_2 (as shown in Fig. 8) to form a novel MAX phase Ti_3ZnC_2. Further, in the presence of excess $ZnCl_2$, MXenes terminated with Cl, $Ti_3C_2Cl_2$ were obtained [50].

A modified general method to produce a large variety of MXenes from their MAX phases using the redox coupling between the cation in the Lewis acid molten salt and the 'A' element was proposed by Li et al. In this method, $CuCl_2$ molten salt was used in the preparation of Ti_3C_2 from Ti_3SiC_2. With the immersion of the MAX phase in $CuCl_2$ at 750 °C, $Ti_3C_2T_x$ MXene was obtained after washing out impurities like Cu particles using ammonium persulfate solution. The use of ammonium persulfate results in the addition of O groups onto the surface of Ti along with Cl groups [51]. A summary of different etching methods used to synthesize MXenes from their MAX phases since its discovery is tabulated in Table 2.

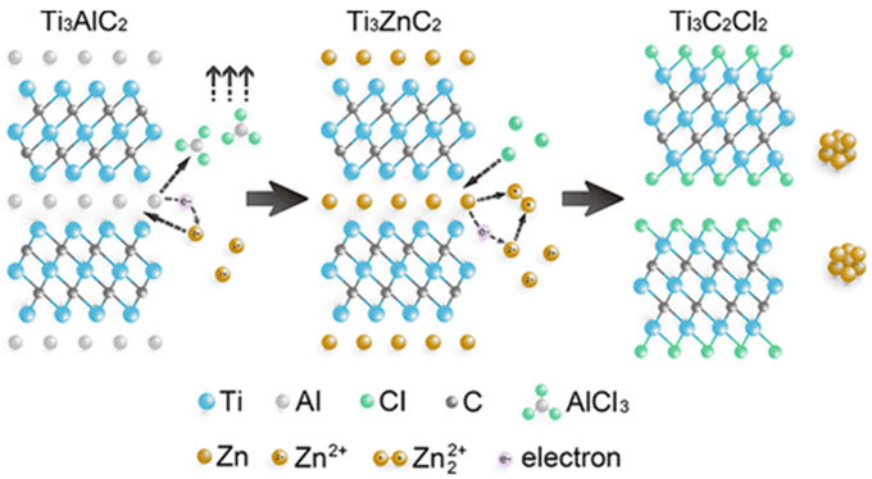

Fig. 8 Schematic representation of the formation of novel MAX phase and MXenes through Lewis acid molten salts. Reproduced with permission from [50] copyright 2019, American Chemical Society

Table 2 Different etching methods used in the synthesis of MXenes

Method	Etchant	References
Acid with Fluorine	HF	[11–17]
	LiF + HCl	[22]
	KF + HCl	[27]
	Na, LiF, K or NH_4F + HCl	[23]
	NH_4HF_2	[24]
Molten salts	LiF + NaF + KF	[30–32]
Hydrothermal	NH_4F	[36]
	$NaBF_4$ and HCl	[37]
	NaOH	[38]
Electrochemical	HCl	[40]
	NH_4Cl and TMAOH	[41]
Water free	Organic polar solvents and NH_4HF_2	[47]
Lewis acid	$ZnCl_2$	[50]
	$CuCl_2$	[51]

3 Delamination/Intercalation

The multi-layered MXenes obtained after the etching can be delaminated/exfoliated into a few or single layers through intercalating or delaminating agents. During this process, various parameters such as surface functional groups, crystallinity, defects, and the number of layers present in the material undergo changes. As seen in the case of graphene, mechanical exfoliation can also be used to obtain few-layered MXenes however, the yield is very low. There have been only two reports that claim the use of the scotch tape method for the exfoliation of multilayer MXene into few layers [52, 53]. The exfoliation methods used to produce few-layered MXenes typically depend on the (a) etching method used and (b) composition of the MXene. Based on these, the exfoliation of MXenes is achieved through intercalation of cations, handshaking or sonication and intercalation through organic molecules.

When the acid fluoride salt (KF, NaF or LiF with HCl/H_2SO_4) is used as an etchant, the cations in the fluoride salts will intercalate into the MXene layers, simultaneously delaminating them without the use of a separate delaminating agent. Sonication can help delaminate samples in some cases; however, prolonged sonication can damage the MXenes' edges, causing the sheets to break [25]. This mild sonication or simple handshaking leading to in-situ delamination is achieved when the pH of the etched MXene is neutral. In addition, MXenes have negative zeta potential due to which the aqueous colloidal MXene suspensions do not aggregate [54].

When MXenes are obtained through the HF etching method, their exfoliation is possible with the intercalation of organic molecules or ions into the layers, which helps in increasing the interlayer spaces thereby, weakening the interlayer

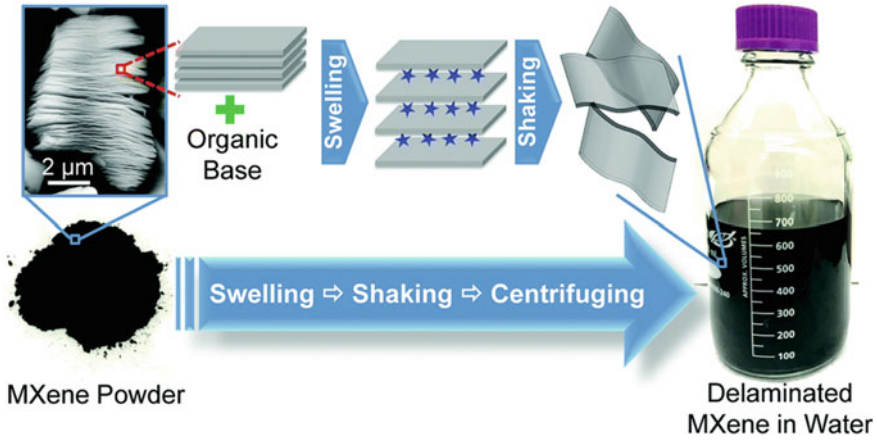

Fig. 9 Schematic representing the delamination of MXenes with organic solvents. Reproduced with permission from [57] copyright 2015, The Royal Society of Chemistry

interactions leading to exfoliation [9]. The common polar organic solvents used are dimethyl sulfoxide, tetrabutylammonium hydroxide, *n*-butylamine, hydrazine, choline hydroxide, isopropylamine and urea [55–57].

Mashtalir et al. reported hydrazine monohydrate and hydrazine monohydrate dissolved in dimethylformamide (DMF) used as the intercalating agent in Ti_3C_2 increased the c-lattice parameter from 19.5 to 25.48 and 26.8 Å, respectively. An increase in the c-lattice parameter means that the interlayer spacing increases in MXenes, leading to the weakening of bonds and producing single-layered MXenes [55]. Mechanical milling of MXene powders with organic solvents also produces few-layered MXenes. The produced delaminated MXenes helps in preventing oxidation and enable fast ion transport useful for sodium-ion batteries [58]. In the study reported by Naguib et al., various organic solvents were used as delaminating agents, and slight agitation aided in the delamination of MXene sheets. A schematic of this process is shown in Fig. 9 [57].

The delaminated colloidal suspension of MXenes in water can be further processed using vacuum filtration, spin coating, or spraying onto different substrates based on the type of application.

4 Processing of MXenes

Delaminating MXenes after synthesis, as described in the previous section, is a crucial processing step and to reduce the size of the flakes, sonication is a standard processing method [59]. Therefore, various parameters such as power output of the sonicator, sonication time, temperature of sonication, etc., will affect the concentration, quality and size distribution of the flakes [16]. It is seen that centrifugation can also help

control the size of the MXenes flakes. For example, when $Ti_3C_2T_x$ MXene was centrifuged at different RPMs like 2500, 5000, and 10,000, different sized flakes such as 2, ~1 μm and ~200 nm were obtained, respectively.

Different deposition methods such as vacuum filtration, spin coating, spray coating, rolling, and painting [60–63] can be used for solution-processed MXenes, as shown in Fig. 10. Each of these processing methods is used for a particular type of application [64]. When the spin coating is used, thin uniform coatings are produced, which are used in electronics [63]. In contrast, the rolling method produces thick films useful in making flexible electrodes for electrochemical applications [65]. MXene inks can be used to obtain particular patterns through printing or stamping methods where the thickness can be varied by increasing the number of layers [66]. A vacuum-assisted filtration setup consists of a Buchner Funnel with a filtration membrane whose pore size is small enough to prevent the MXene flakes from passing through them. The vacuum filtration method produces free-standing flexible films, which could be used as electrodes for supercapacitors or batteries [55, 67]. The spin coating technique can be used to produce uniform films which are suitable for optical applications [63]. In addition, the spray coating technique can make films with large areas useful in electromagnetic interference shielding. Although the spray

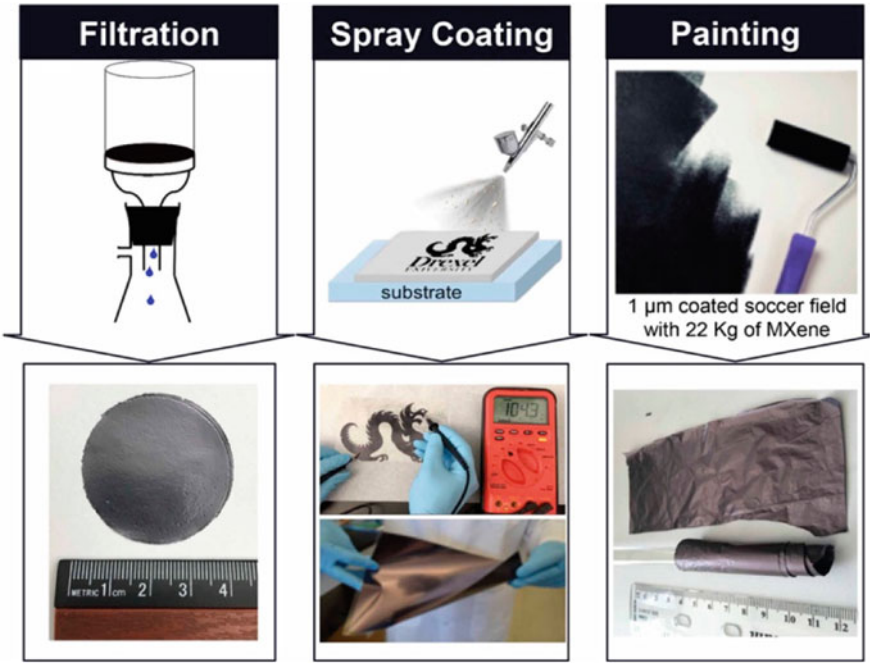

Fig. 10 Fabrication of $Ti_3C_2T_x$ MXene films produced through vacuum filtration, spray coating and painting techniques. Reproduced with permission from [16] copyright 2017, American Chemical Society

coating method is a convenient technique that can be used on any surface, the drawback is it produces non-uniform coatings and rougher films [68]. Compared to the vacuum filtration process, thinner coatings can be produced through the spray and spin-coating techniques.

5 Storage Mechanism

Intercalation and delamination are important steps that impart the energy storage properties in MXenes. During the etching procedure, the functional groups (such as –O, –OH, and –F) attached to the MXene surface serve as energy storage sites at the surface and between the layers [69].

MXenes have been shown to store energy via the adsorption–desorption mechanism. Tang et al. demonstrated that in Ti_3C_2 MXene, lithium occupies the top of the carbon atoms, which is their preferred location, and provides a theoretical capacity of 320 mA/g [70]. Therefore, it was predicted that the theoretical gravimetric capacity depends on the formula weights of MXenes. MXenes such as M_2X with low formula weight is predicted to pose higher capacity than M_3X_2 and M_4X_3 MXenes, because of the strong bonds between M and X [6].

MXenes with –O terminations exhibits higher theoretical capacity when compared to those with –OH terminations [71]. Further, Xie et al. reported that MXenes with –O terminations might react with the Na^+ or K^+ ions to form bare MXenes and metal oxides through conversion reactions. Thus all the existing storage mechanisms such as conversion reactions, stripping, and insertion may be present in MXenes [72].

With the introduction of cations (Li^+, Na^+, K^+) into the layers of MXene during etching, the interlayer spacing increases, thereby providing a wide access path for the electrolyte, which in turn helps in improving the storage capabilities of the MXene [25, 73]. Furthermore, this intercalation of ions into the MXene layers makes them suitable for non-lithium-ion batteries with limited electrode materials [72]. It is also known that delamination can also be done using organic solvents like hydrazine, DMF and urea. In these cases, there is the introduction of N-containing groups into the MXenes, which further enhances the electrochemical behavior of MXenes [55]. A similar phenomenon can also be observed in S-containing MXenes [74].

The processing step also plays a crucial role in improving the charge storage capabilities in MXenes. The electrodes made from single-layered flakes pose higher storage capabilities due to the increased exposure to the electrolyte solution. In this regard, free-standing films obtained through the vacuum filtration method contains densely packed layers, which exhibit poor performance when used as electrodes [54]. The main mechanisms of charge storage in supercapacitors are pseudocapacitance and double-layer capacitance. MXene poses the pseudocapacitive charge storage mechanism due to the surface terminated functional groups involved in redox reactions and exhibits improved capacitance than RuO_2 [9].

6 Safety Measures for MXene

With the continuous efforts to scale up the production of MXenes, guidelines for safe MXene synthesis have become very important. Identifying the hazard before scaling up will help develop safe designs before its implementation. The synthesis of MXene is a multistep process that includes the usage of combustible powders like aluminium, graphite, titanium carbide and so on to produce the parent MAX phase. Further, exothermic reactions are involved in obtaining MXene from the MAX phase. HF is the widely used etchant in the synthesis of MXenes. HF and in situ-HF etching procedures must be carried out carefully, considering the risks involved. Calcium gluconate and emergency wash stations must be available in the laboratory. Protective personal equipment must be worn while synthesizing MXenes to minimize accidents [75].

Safety Triad: Prevention, Mitigation and Response

The synthesis of MXene involves multiple steps. Thus, safety guidelines for each process step should be evaluated, including preventive and mitigating measures, emergency responses, and procedures [21]. In order to implement the preventive measures, the hazards in the synthesis process have to be first identified. The major hazards are exposure to toxic chemicals, toxic gas formation, combustible dust and runaway reactions. The hazard preventive measures include (i) safe designs, (ii) engineering and administrative controls and (iii) personal protective gear [75]. Upon the failure of preventive measures, mitigating measures should be implemented to reduce the outcome of the incident. The main aim of the mitigating measures is to reduce the effects of the undesirable event that occurs when the preventive measures fail. The mitigating measures are proper training, usage of the hood, sensors, alarms, automation of the hazardous steps, and emergency evacuation plans. With the failure of both preventive and mitigating measures, emergency response mechanisms have to be panned to reduce the impact of the undesirable incident. The emergency plans include educating the individuals working with the facility about the risks and hazards involved in the process, repair, recovery and access to the emergency response personnel.

7 Summary and Outlook

New MXenes are being formed from their MAX phases on a regular basis with the discovery of new etchants. In this chapter, we have discussed various synthesis and processing techniques of MXenes. The most effective and widely reported etchant is HF, but with their high levels of toxicity and the –F terminations onto the MXene surface (which are not suitable in biomedical applications), research on alternate etchants are required. In this regard, various etching methods such as molten salt, hydrothermal, electrochemical, water-free, Lewis acid etc., have been briefly discussed. Each of these methods has its advantages and disadvantages over

the other in terms of toxicity, yield and purity. While the molten salt synthesis technique is mostly used to synthesize nitride-based MXenes, the other synthesis methods discussed in this chapter are used to synthesize carbide-based MXenes. The various processing methods involved in obtaining MXenes desired for a particular type of application is detailed. Synthesis and processing steps play a crucial role in imparting and improvising the charge storage capabilities of MXenes. Though many MAX phases are said to exist, only a few MXenes are derived from them. Overall, discovering new MXenes for various applications via new synthesis techniques is a daunting yet exciting process.

References

1. Nicolosi, V., Chhowalla, M., Kanatzidis, M.G., Strano, M.S., Coleman, J.N.: Liquid exfoliation of layered materials. Science **340**(6139), 1226419 (2013). https://doi.org/10.1126/science.1226419
2. Barsoum, M.W.: The MN+1AXN phases: anew class of solids: thermodynamically stable nanolaminates. Prog. Solid State Chem. **28**(1), 201–281 (2000). https://doi.org/10.1016/S0079-6786(00)00006-6
3. Chaudhari, N.K., Jin, H., Kim, B., San Baek, D., Joo, S.H., Lee, K.: MXene: an emerging two-dimensional material for future energy conversion and storage applications. J. Mater. Chem. A **5**(47), 24564–24579 (2017). https://doi.org/10.1039/C7TA09094C
4. Venkateshalu, S., Grace, A.N.: MXenes—a new class of 2D layered materials: synthesis, properties, applications as supercapacitor electrode and beyond. Appl. Mater. Today **18**, 100509 (2020). https://doi.org/10.1016/j.apmt.2019.100509
5. Naguib, M., Mochalin, V.N., Barsoum, M.W., Gogotsi, Y.: 25th anniversary article: mxenes: a new family of two-dimensional materials. Adv. Mater. **26**(7), 992–1005 (2014). https://doi.org/10.1002/adma.201304138
6. Anasori, B., Lukatskaya, M.R., Gogotsi, Y.: 2D metal carbides and nitrides (MXenes) for energy storage. Nat. Rev. Mater. **2**(2), 16098 (2017). https://doi.org/10.1038/natrevmats.2016.98
7. Hong Ng, V.M., Huang, H., Zhou, K., Lee, P.S., Que, W., Xu, J.Z., et al.: Recent progress in layered transition metal carbides and/or nitrides (MXenes) and their composites: synthesis and applications. J. Mater. Chem. A **5**(7), 3039–3068 (2017). https://doi.org/10.1039/C6TA06772G
8. Li, Z., Yu, L., Milligan, C., Ma, T., Zhou, L., Cui, Y., et al.: Two-dimensional transition metal carbides as supports for tuning the chemistry of catalytic nanoparticles. Nat. Commun. **9**(1), 5258 (2018). https://doi.org/10.1038/s41467-018-07502-5
9. Verger, L, Natu, V., Carey, M., Barsoum, M.: MXenes: an introduction of their synthesis, select properties, and applications. Trends Chem. **1** (2019). https://doi.org/10.1016/j.trechm.2019.04.006
10. Verger, L., Xu, C., Natu, V., Cheng, H.-M., Ren, W., Barsoum, M.W.: Overview of the synthesis of MXenes and other ultrathin 2D transition metal carbides and nitrides. Curr. Opin. Solid State Mater. Sci. **23**(3), 149–163 (2019). https://doi.org/10.1016/j.cossms.2019.02.001
11. Naguib, M., Kurtoglu, M., Presser, V., Lu, J., Niu, J., Heon, M., et al.: Two-dimensional nanocrystals produced by exfoliation of Ti_3AlC_2. Adv. Mater. **23**(37), 4248–4253 (2011). https://doi.org/10.1002/adma.201102306
12. Zhou, J., Zha, X., Chen, F.Y., Ye, Q., Eklund, P., Du, S., et al.: A two-dimensional zirconium carbide by selective etching of Al_3C_3 from Nanolaminated $Zr_3Al_3C_5$. Angew. Chem. Int. Ed. **55**(16), 5008–5013 (2016). https://doi.org/10.1002/anie.201510432

13. Naguib, M., Halim, J., Lu, J., Cook, K.M., Hultman, L., Gogotsi, Y., et al.: New two-dimensional niobium and vanadium carbides as promising materials for Li-ion batteries. J. Am. Chem. Soc. **135**(43), 15966–15969 (2013). https://doi.org/10.1021/ja405735d
14. Mashtalir, O., Naguib, M., Dyatkin, B., Gogotsi, Y., Barsoum, M.W.: Kinetics of aluminum extraction from Ti_3AlC_2 in hydrofluoric acid. Mater. Chem. Phys. **139**(1), 147–152 (2013). https://doi.org/10.1016/j.matchemphys.2013.01.008
15. Naguib, M., Mashtalir, O., Carle, J., Presser, V., Lu, J., Hultman, L., et al.: Two-dimensional transition metal carbides. ACS Nano **6**(2), 1322–1331 (2012). https://doi.org/10.1021/nn204153h
16. Alhabeb, M., Maleski, K., Anasori, B., Lelyukh, P., Clark, L., Sin, S., et al.: Guidelines for synthesis and processing of two-dimensional titanium carbide (Ti_3C_2Tx MXene). Chem. Mater. **29**(18), 7633–7644 (2017). https://doi.org/10.1021/acs.chemmater.7b02847
17. Chang, F., Li, C., Yang, J., Tang, H., Xue, M.: Synthesis of a new graphene-like transition metal carbide by de-intercalating Ti_3AlC_2. Mater. Lett. **109**, 295–298 (2013). https://doi.org/10.1016/j.matlet.2013.07.102
18. Sun, Z., Li, S., Ahuja, R., Schneider, J.M.: Calculated elastic properties of M2AlC (M=Ti, V, Cr, Nb and Ta). Solid State Commun. **129**(9), 589–592 (2004). https://doi.org/10.1016/j.ssc.2003.12.008
19. Zhang, Y.-Z., El-Demellawi, J.K., Jiang, Q., Ge, G., Liang, H., Lee, K., et al.: MXene hydrogels: fundamentals and applications. Chem. Soc. Rev. **49**(20), 7229–7251 (2020). https://doi.org/10.1039/D0CS00022A
20. VahidMohammadi, A., Hadjikhani, A., Shahbazmohamadi, S., Beidaghi, M.: Two-dimensional vanadium carbide (MXene) as a high-capacity cathode material for rechargeable aluminum batteries. ACS Nano **11**(11), 11135–11144 (2017). https://doi.org/10.1021/acsnano.7b05350
21. Lakhe, P., Prehn, E.M., Habib, T., Lutkenhaus, J.L., Radovic, M., Mannan, M.S., et al.: Process safety analysis for Ti_3C_2Tx MXene synthesis and processing. Ind. Eng. Chem. Res. **58**(4), 1570–1579 (2019). https://doi.org/10.1021/acs.iecr.8b05416
22. Ghidiu, M., Lukatskaya, M.R., Zhao, M.-Q., Gogotsi, Y., Barsoum, M.W.: Conductive two-dimensional titanium carbide 'clay' with high volumetric capacitance. Nature **516**(7529), 78–81 (2014). https://doi.org/10.1038/nature13970
23. Liu, F., Zhou, A., Chen, J., Jia, J., Zhou, W., Wang, L., et al.: Preparation of Ti_3C_2 and Ti_2C MXenes by fluoride salts etching and methane adsorptive properties. Appl. Surf. Sci. **416**, 781–789 (2017). https://doi.org/10.1016/j.apsusc.2017.04.239
24. Halim, J., Lukatskaya, M.R., Cook, K.M., Lu, J., Smith, C.R., Näslund, L.-Å., et al.: Transparent conductive two-dimensional titanium carbide epitaxial thin films. Chem. Mater. **26**(7), 2374–2381 (2014). https://doi.org/10.1021/cm500641a
25. Lukatskaya, M.R., Mashtalir, O., Ren, C.E., Dall'Agnese, Y., Rozier, P., Taberna, P.L., et al.: Cation intercalation and high volumetric capacitance of two-dimensional titanium carbide. Science **341**(6153), 1502–1505 (2013). https://doi.org/10.1126/science.1241488
26. Shein, I.R., Ivanovskii, A.L.: Graphene-like titanium carbides and nitrides Tin+1Cn, Tin+1Nn (n=1, 2, and 3) from de-intercalated MAX phases: first-principles probing of their structural, electronic properties and relative stability. Comput. Mater. Sci. **65**, 104–114 (2012). https://doi.org/10.1016/j.commatsci.2012.07.011
27. Soundiraraju, B., George, B.K.: Two-dimensional titanium nitride (Ti_2N) MXene: synthesis, characterization, and potential application as surface-enhanced raman scattering substrate. ACS Nano **11**(9), 8892–8900 (2017). https://doi.org/10.1021/acsnano.7b03129
28. Urbankowski, P., Anasori, B., Hantanasirisakul, K., Yang, L., Zhang, L., Haines, B., et al.: 2D molybdenum and vanadium nitrides synthesized by ammoniation of 2D transition metal carbides (MXenes). Nanoscale **9**(45), 17722–17730 (2017). https://doi.org/10.1039/C7NR06721F
29. Kim, Y.-J., Kim, S.J., Seo, D., Chae, Y., Anayee, M., Lee, Y., et al.: Etching mechanism of monoatomic aluminum layers during MXene synthesis. Chem. Mater. **33**(16), 6346–6355 (2021). https://doi.org/10.1021/acs.chemmater.1c01263

30. Urbankowski, P., Anasori, B., Makaryan, T., Er, D., Kota, S., Walsh, P.L., et al.: Synthesis of two-dimensional titanium nitride Ti_4N_3 (MXene). Nanoscale **8**(22), 11385–11391 (2016). https://doi.org/10.1039/C6NR02253G
31. Djire, A., Bos, A., Liu, J., Zhang, H., Miller, E.M., Neale, N.R.: Pseudocapacitive storage in nanolayered Ti_2NTx MXene using Mg-ion electrolyte. ACS Appl. Nano Mater. **2**(5), 2785–2795 (2019). https://doi.org/10.1021/acsanm.9b00289
32. Djire, A., Zhang, H., Liu, J., Miller, E.M., Neale, N.R.: Electrocatalytic and optoelectronic characteristics of the two-dimensional titanium nitride Ti_4N_3Tx MXene. ACS Appl. Mater. Interf. **11**(12), 11812–11823 (2019). https://doi.org/10.1021/acsami.9b01150
33. Wu, M., Wang, B., Hu, Q., Wang, L., Zhou, A.: The synthesis process and thermal stability of V_2C MXene. Materials **11**(11), 2112 (2018)
34. Yan, M., Yang, L., Li, C., Zou, Y.: Preparation of two-dimensional Ti_2CTx by Molten fluorinated salt method. J. Wuhan Univ. Technol.-Mater. Sci. Ed. **34**(2), 299–302 (2019). https://doi.org/10.1007/s11595-019-2050-x
35. Wang, C., Shou, H., Chen, S., Wei, S., Lin, Y., Zhang, P., et al.: HCl-based hydrothermal etching strategy toward fluoride-free MXenes. Adv. Mater. **33**(27), 2101015 (2021). https://doi.org/10.1002/adma.202101015
36. Wang, L., Zhang, H., Wang, B., Shen, C., Zhang, C., Hu, Q., et al.: Synthesis and electrochemical performance of Ti_3C_2Tx with hydrothermal process. Electron. Mater. Lett. **12** (2016). https://doi.org/10.1007/s13391-016-6088-z
37. Peng, C., Wei, P., Chen, X., Zhang, Y., Zhu, F., Cao, Y., et al.: A hydrothermal etching route to synthesis of 2D MXene (Ti_3C_2, Nb_2C): enhanced exfoliation and improved adsorption performance. Ceram. Int. **44**(15), 18886–18893 (2018). https://doi.org/10.1016/j.ceramint.2018.07.124
38. Li, T., Yao, L., Liu, Q., Gu, J., Luo, R., Li, J., et al.: Fluorine-free synthesis of high-purity Ti_3C_2Tx (T=OH, O) via Alkali treatment. Angew. Chem. Int. Ed. **57**(21), 6115–6119 (2018). https://doi.org/10.1002/anie.201800887
39. Srivastava, P., Mishra, A., Mizuseki, H., Lee, K.-R., Singh, A.K.: Mechanistic Insight into the chemical exfoliation and functionalization of Ti_3C_2 MXene. ACS Appl. Mater. Interf. **8**(36), 24256–24264 (2016). https://doi.org/10.1021/acsami.6b08413
40. Sun, W., Shah, S.A., Chen, Y., Tan, Z., Gao, H., Habib, T., et al.: Electrochemical etching of Ti_2AlC to Ti_2CTx (MXene) in low-concentration hydrochloric acid solution. J. Mater. Chem. A **5**(41), 21663–21668 (2017). https://doi.org/10.1039/C7TA05574A
41. Yang, S., Zhang, P., Wang, F., Ricciardulli, A.G., Lohe, M.R., Blom, P.W.M., et al.: Fluoride-free synthesis of two-dimensional titanium carbide (MXene) using a binary aqueous system. Angew. Chem. Int. Ed. **57**(47), 15491–15495 (2018). https://doi.org/10.1002/anie.201809662
42. Yin, T., Li, Y., Wang, R., Al-Hartomy, O.A., Al-Ghamdi, A., Wageh, S., et al.: Synthesis of Ti_3C_2Fx MXene with controllable fluorination by electrochemical etching for lithium-ion batteries applications. Ceram. Int. (2021). https://doi.org/10.1016/j.ceramint.2021.07.023
43. Li, X., Li, M., Yang, Q., Liang, G., Huang, Z., Ma, L., et al.: In situ electrochemical synthesis of MXenes without acid/Alkali usage in/for an aqueous zinc ion battery. Adv. Energy Mater. **10**(36), 2001791 (2020). https://doi.org/10.1002/aenm.202001791
44. Vicic, D.A., Jones, G.D.: 1.07—experimental methods and techniques: basic techniques. In: Mingos, D.M.P., Crabtree, R.H. (eds.) Comprehensive Organometallic Chemistry III, pp. 197–218. Elsevier, Oxford (2007)
45. Laufersky, G., Bradley, S., Frécaut, E., Lein, M., Nann, T.: Unraveling aminophosphine redox mechanisms for glovebox-free InP quantum dot syntheses. Nanoscale **10**(18), 8752–8762 (2018). https://doi.org/10.1039/c8nr01286e
46. Xu, K.: Electrolytes and interphases in Li-ion batteries and beyond. Chem. Rev. **114**(23), 11503–11618 (2014). https://doi.org/10.1021/cr500003w
47. Natu, V., Pai, R., Sokol, M., Carey, M., Kalra, V., Barsoum, M.W.: 2D Ti_3C_2Tz MXene synthesized by water-free etching of Ti_3AlC_2 in Polar organic solvents. Chem **6**(3), 616–630 (2020). https://doi.org/10.1016/j.chempr.2020.01.019

48. Xiu, L.-Y., Wang, Z.-Y., Qiu, J.-S.: General synthesis of MXene by green etching chemistry of fluoride-free Lewis acidic melts. Rare Met. **39**(11), 1237–1238 (2020). https://doi.org/10.1007/s12598-020-01488-0
49. Xu, J., Peng, T., Qin, X., Zhang, Q., Liu, T., Dai, W., et al.: Recent advances in 2D MXenes: preparation, intercalation and applications in flexible devices. J. Mater. Chem. A **9**(25), 14147–14171 (2021). https://doi.org/10.1039/D1TA03070A
50. Li, M., Lu, J., Luo, K., Li, Y., Chang, K., Chen, K., et al.: Element replacement approach by reaction with lewis acidic molten salts to synthesize nanolaminated MAX phases and MXenes. J. Am. Chem. Soc. **141**(11), 4730–4737 (2019). https://doi.org/10.1021/jacs.9b00574
51. Li, Y., Shao, H., Lin, Z., Lu, J., Liu, L., Duployer, B., et al.: A general Lewis acidic etching route for preparing MXenes with enhanced electrochemical performance in non-aqueous electrolyte. Nat. Mater. **19**(8), 894–899 (2020). https://doi.org/10.1038/s41563-020-0657-0
52. Xu, J., Shim, J., Park, J.-H., Lee, S.: MXene electrode for the integration of WSe_2 and MoS_2 field effect transistors. Adv. Func. Mater. **26**(29), 5328–5334 (2016). https://doi.org/10.1002/adfm.201600771
53. Lai, S., Jeon, J., Jang, S.K., Xu, J., Choi, Y.J., Park, J.-H., et al.: Surface group modification and carrier transport properties of layered transition metal carbides (Ti_2CTx, T: –OH, –F and –O). Nanoscale **7**(46), 19390–19396 (2015). https://doi.org/10.1039/C5NR06513E
54. Xie, X., Zhao, M.-Q., Anasori, B., Maleski, K., Ren, C.E., Li, J., et al.: Porous heterostructured MXene/carbon nanotube composite paper with high volumetric capacity for sodium-based energy storage devices. Nano Energy **26**, 513–523 (2016). https://doi.org/10.1016/j.nanoen.2016.06.005
55. Mashtalir, O., Naguib, M., Mochalin, V.N., Dall'Agnese, Y., Heon, M., Barsoum, M.W., et al.: Intercalation and delamination of layered carbides and carbonitrides. Nat. Commun. **4**(1), 1716 2013. https://doi.org/10.1038/ncomms2664
56. Mashtalir, O., Lukatskaya, M.R., Zhao, M.-Q., Barsoum, M.W., Gogotsi, Y.: Amine-assisted delamination of Nb_2C MXene for Li-ion energy storage devices. Adv. Mater. **27**(23), 3501–3506 (2015). https://doi.org/10.1002/adma.201500604
57. Naguib, M., Unocic, R.R., Armstrong, B.L., Nanda, J.: Large-scale delamination of multilayers transition metal carbides and carbonitrides "MXenes." Dalton Trans. **44**(20), 9353–9358 (2015). https://doi.org/10.1039/C5DT01247C
58. Wu, Y., Nie, P., Wang, J., Dou, H., Zhang, X.: Few-Layer MXenes delaminated via high-energy mechanical milling for enhanced sodium-ion batteries performance. ACS Appl. Mater. Interf. **9**(45), 39610–39617 (2017). https://doi.org/10.1021/acsami.7b12155
59. Backes, C., Higgins, T.M., Kelly, A., Boland, C., Harvey, A., Hanlon, D., et al.: Guidelines for exfoliation, characterization and processing of layered materials produced by liquid exfoliation. Chem. Mater. **29**(1), 243–255 (2017). https://doi.org/10.1021/acs.chemmater.6b03335
60. Hantanasirisakul, K., Zhao, M.-Q., Urbankowski, P., Halim, J., Anasori, B., Kota, S., et al.: Fabrication of Ti_3C_2Tx MXene transparent thin films with tunable optoelectronic properties. Adv. Electron. Mater. **2**(6), 1600050 (2016). https://doi.org/10.1002/aelm.201600050
61. Shuck, C.E., Sarycheva, A., Anayee, M., Levitt, A., Zhu, Y., Uzun, S., et al.: Scalable synthesis of Ti_3C_2Tx MXene. Adv. Eng. Mater. **22**(3), 1901241 (2020). https://doi.org/10.1002/adem.201901241
62. Shahzad, F., Alhabeb, M., Hatter, C.B., Anasori, B., Man Hong, S., Koo, C.M., et al.: Electromagnetic interference shielding with 2D transition metal carbides (MXenes). Science **353**(6304), 1137–1140 (2016). https://doi.org/10.1126/science.aag2421
63. Dillon, A.D., Ghidiu, M.J., Krick, A.L., Griggs, J., May, S.J., Gogotsi, Y., et al.: Highly conductive optical quality solution-processed films of 2D titanium carbide. Adv. Func. Mater. **26**(23), 4162–4168 (2016). https://doi.org/10.1002/adfm.201600357
64. Abdolhosseinzadeh, S., Jiang, X., Zhang, H., Qiu, J., Zhang, C.: Perspectives on solution processing of two-dimensional MXenes. Mater. Today (2021). https://doi.org/10.1016/j.mattod.2021.02.010
65. Ling, Z., Ren, C.E., Zhao, M.-Q., Yang, J., Giammarco, J.M., Qiu, J., et al.: Flexible and conductive MXene films and nanocomposites with high capacitance. Proc. Natl. Acad. Sci. **111**(47), 16676–16681 (2014). https://doi.org/10.1073/pnas.1414215111

66. Abdolhosseinzadeh, S., Heier, J., Zhang, C.: Printing and coating MXenes for electrochemical energy storage devices. J. Phys.: Energy. **2**(3), 031004 (2020). https://doi.org/10.1088/2515-7655/aba47d
67. Zhao, M.-Q., Ren, C.E., Ling, Z., Lukatskaya, M.R., Zhang, C., Van Aken, K.L., et al.: Flexible MXene/carbon nanotube composite paper with high volumetric capacitance. Adv. Mater. **27**(2), 339–345 (2015). https://doi.org/10.1002/adma.201404140
68. Peng, Y.-Y., Akuzum, B., Kurra, N., Zhao, M.-Q., Alhabeb, M., Anasori, B., et al.: All-MXene (2D titanium carbide) solid-state microsupercapacitors for on-chip energy storage. Energy Environ. Sci. **9**(9), 2847–2854 (2016). https://doi.org/10.1039/C6EE01717G
69. Bao, Z., Lu, C., Cao, X., Zhang, P., Yang, L., Zhang, H., et al.: Role of MXene surface terminations in electrochemical energy storage: a review. Chin. Chem. Lett. (2021). https://doi.org/10.1016/j.cclet.2021.02.012
70. Tang, Q., Zhou, Z., Shen, P.: Are MXenes promising anode materials for Li ion batteries? Computational studies on electronic properties and Li Storage capability of Ti_3C_2 and $Ti_3C_2X_2$ (X = F, OH) monolayer. J. Am. Chem. Soc. **134**(40), 16909–16916 (2012). https://doi.org/10.1021/ja308463r
71. Karlsson, L.H., Birch, J., Halim, J., Barsoum, M.W., Persson, P.O.Å.: Atomically resolved structural and chemical investigation of single MXene sheets. Nano Lett. **15**(8), 4955–4960 (2015). https://doi.org/10.1021/acs.nanolett.5b00737
72. Xie, Y., Dall'Agnese, Y., Naguib, M., Gogotsi, Y., Barsoum, M.W., Zhuang, H.L., et al.: Prediction and characterization of MXene nanosheet anodes for non-Lithium-Ion batteries. ACS Nano **8**(9), 9606–9615 (2014). https://doi.org/10.1021/nn503921j
73. Garg, R., Agarwal, A., Agarwal, M.: A review on MXene for energy storage application: effect of interlayer distance. Mater. Res. Exp. **7**(2), 022001 (2020). https://doi.org/10.1088/2053-1591/ab750d
74. Liang, X., Rangom, Y., Kwok, C.Y., Pang, Q., Nazar, L.F.: Interwoven MXene nanosheet/carbon-nanotube composites as Li–S cathode hosts. Adv. Mater. **29**(3), 1603040 (2017). https://doi.org/10.1002/adma.201603040
75. Shuck, C.E., Ventura-Martinez, K., Goad, A., Uzun, S., Shekhirev, M., Gogotsi, Y.: Safe synthesis of MAX and MXene: guidelines to reduce risk during synthesis. ACS Chem. Health Saf. **28**(5), 326–338 (2021). https://doi.org/10.1021/acs.chas.1c00051

Properties of MXenes

Guoyin Zhu and Yizhou Zhang

Abstract MXene, a 2D transition metal carbides/nitrides, have attracted heated attention in various fields, such as supercapacitors, batteries, catalysis, solar cell, and senor, because of their outstanding properties. The coexistence of metallic and covalent bonds contributes to the intrinsic properties of MXenes, such as unique structural, surface-chemical, thermo-physical, and optoelectronic properties. These new physics and chemistry properties of MXene will open up new possibilities for applications.

Keywords MXene · Structural and surface-chemistry · Thermo-physical · Optoelectronic properties

1 Introduction

2D nanomaterials are drawing attention from diverse research fields in the past decade due to their interesting physical and chemical properties different from their bulk counterparts [1]. Up to date, a series of 2D nanomaterials have been successfully developed, including graphene [2], transition metal dichalcogenides (TMDs) [3], black phosphorus (BP) [4], and MXenes [5].

MXenes, also known as 2D transition metal carbides and nitrides, has drawn heated attention as a fast-growing family of 2D materials since their invention in 2011 [6]. They have shown great potential in many applications, such as energy conversion (such as photocatalysis, solar cell, and water splitting), energy storage (such as supercapacitor and battery), electromagnetic interference shielding, sensors, and photothermal therapy, because of their intriguing mechanical, electronic, thermal, and optical properties with various structure and surface chemistries. This chapter discusses the structural and surface-chemistry, thermo-physical, and optoelectronic properties of MXenes.

G. Zhu · Y. Zhang (✉)
School of Chemistry and Materials Science, Institute of Advanced Materials and Flexible Electronics (IAMFE), Nanjing University of Information Science and Technology, Nanjing 210044, China
e-mail: yizhou.zhang@nuist.edu.cn

M. Khalid et al. (eds.), *Fundamental Aspects and Perspectives of MXenes*, Engineering Materials, https://doi.org/10.1007/978-3-031-05006-0_3

2 Structural and Surface-Chemistry

The structure of MAX precursors and resulting MXenes have been systematically explored. Generally, MAX phases, a kind of densely layer-stacked materials, display hexagonal lattice structures. The general formula of MAX is $M_{n+1}AX_n$ (n can be 1, 2, and 3), in which M represents groups VI-transition metal (such as Ti, Mo, V, Zr, Nb, Ta, W, and Hf), A is an element belongs to groups III-VI (such as Al, Si, In, Ga and Ge), X stands for carbon and nitrogen [7–9]. In theory, the crystalline structures of MAX precursors can keep stable [10–13].

As schematically shown in Fig. 1a, MXenes were initially etched from MAX phases, which inherits hexagonal symmetry with $P6_3/mmc$ space group. The M-X bonds are still complete, whereas the M-A bonds are broken using acid treatment [14]. After A atomic layers are etched from MAX precursors by strong acid solution, the resulting layer structure materials are MXene nanosheets (Fig. 1b).

Some groups (such as F-, O- and OH-) would be formed on the surface of MXene after HF or fluoride-based salt etching [15, 16]. Based on this, Khazaei et al. investigated the geometrical structures, magnetic and electronic properties of three types of MXene systems (including M_2XF_2, $M_2X(OH)_2$, and M_2XO_2) by using first-principles calculations [17].

As shown in Fig. 2a-i,ii two kinds of hollow sites may exist on the surface of M_2X MXene: one is hollow sites A, where "X" atom is not available under the transition metals. The other is hollow site B, where an "X" atom is available. Then, four different configurations would be concluded in terms of the relative positions of the termination groups ("T") to the transition metal atoms ("M"). (1) two functional groups were located on the top of two metal atoms ("M"); (2) two functional groups were on top of the hollow sites A; (3)one functional group was on the top of hollow

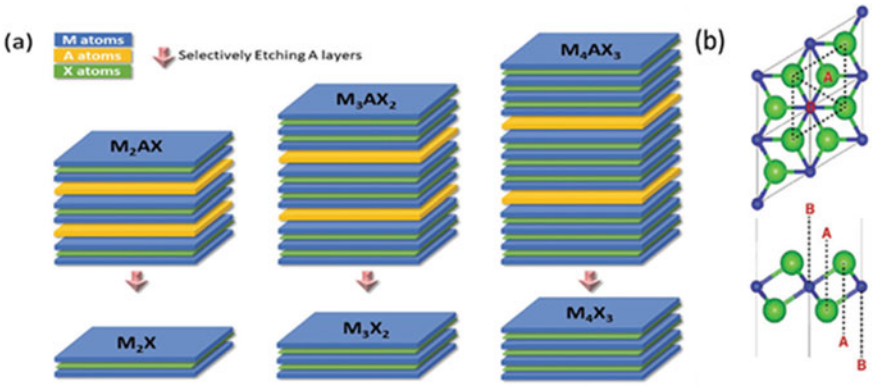

Fig. 1 Schematic structures of MAX and MXenes. **a** Three types of MAX precursors (M_2AX, M_3AX_2 and M_4AX_3) and the resulting MXenes (M_2X, M_3X_2 and M_4X_3) after selectively etching. **b** Top and side views of the atomic structure of M_2X MXene. The A and B stand for two types of hollow sites at the surface [14]

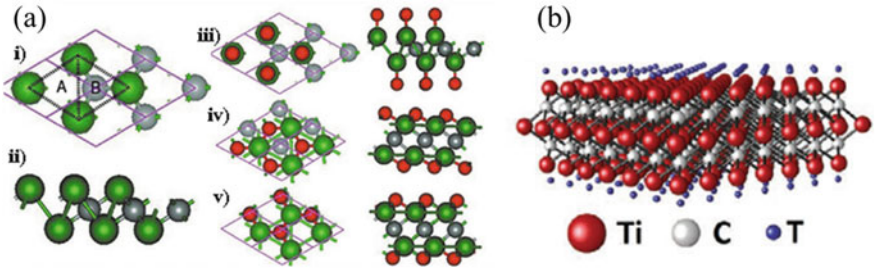

Fig. 2 **a** Structure of M_2X and M_2XT_x, **i, ii** top view and side view of M_2X layer, respectively; **iii–v** top and side views of 3 models of the functionalized MXene systems, respectively. Green, gray, and red spheres represent transitional metals, the carbon or nitrogen element, and the functionalized terminations, respectively [17]. **b** Atomic structure of $Ti_3C_2T_x$ with different surface terminations (labeled as "T") [16]

sites A and another one was on the top of hollow sites B; (4) two functional groups were located on the top of hollow sites B (Fig. 2a-iii–v) [17]. Due to the influence of functional groups with the electronic structure of MXene, some MXenes, including Hf_2CO_2, Zr_2CO_2, Sc_2CF_2, and Ti_2CO_2, were predicted to be 2D semiconductors, whereas most of the other MXenes were metallic. $Ti_3C_2T_x$, the first experimentally synthesized MXene, has been the most representative among tens of MXenes. The crystal structure decorated with functional groups is shown in Fig. 2b [16]. In addition to F, O, and OH groups, Yamada et al. found that Ti_2CT_x and $Ti_3C_2T_x$ surface can also be terminated with Cl atoms when using Cl-containing acid treatment (such as LiF/HCl) [18]. Analogous reports on the structure of V_2C and V_2CX_2 monolayers were studied with similar results as Ti_3C_2 [19].

As the existence of the large negative formation energy that keeps the transition metals and the surface terminations strongly connected, MXenes are predicted to be fully terminated. Generally, there are three possible sites for these groups on the surface of MXene (such as $Ti_3C_2T_x$). As shown in Figs. 3a, b. the three different adsorption sites can be directly above transition metal atoms, the hollow site I between three neighboring X atoms following metal atoms, and hollow site II above X atoms, respectively [20]. According to the density functional theory (DFT) calculations, the most stable structure may be the condition that the surface groups adsorbed at the hollow site I on each side of MXenes because of low steric hindrance [17, 21, 22]. However, when X atoms and surface groups cannot obtain sufficient electrons from the transition metals, site II could be more favorable for MXenes. Compared with OH- and F-group, which just need one electron, O-group requires two electrons from the transition metal to stabilize its adsorption position. Therefore, site II or the mix of site I and II configuration is more suitable for O-group in MXenes.

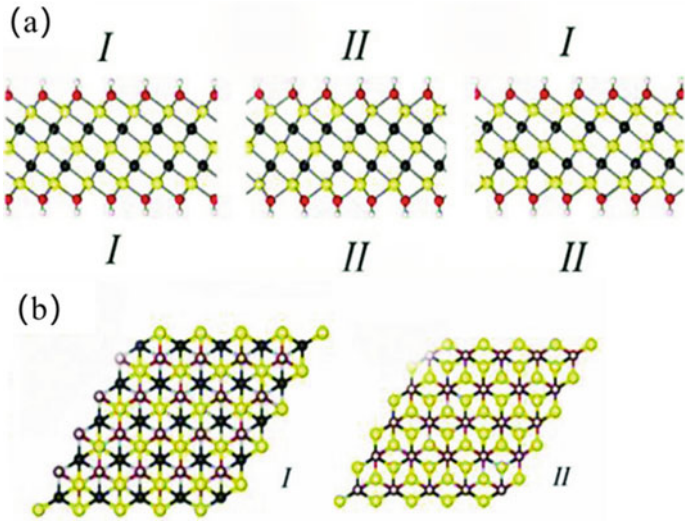

Fig. 3 Side view **a** and top views **b** of the atomic structure of $Ti_3C_2T_x$ MXene. Yellow, white, black, green, and red balls represent titanium, hydrogen, carbon, fluorine, and oxygen elements, respectively [20]

In the experiments, MXenes surfaces are quite complex and can be influenced by the nature of the transition metal on the surface and preparation conditions; it is essential for identification and quantification of the surface groups to use different characterization methods including, X-ray diffraction (XRD) [23–25], X-ray photoelectron spectroscopy (XPS) [26, 27], nuclear magnetic resonance spectroscopy (NMR) [28, 29], scanning electron microscope (SEM) and scanning transmission electron microscopy (STEM) with Energy-dispersive X-ray spectroscopy (EDX) [30, 31], X-ray atomic pair distribution function (X-ray PDF) [32, 33], Raman spectroscopy [34, 35], and energy loss spectroscopy (EELS) [36, 37].

As a structural characterization technique, XRD was used to study and identify the crystallinities and surface compositions of materials or composites. Thus, it is a useful tool to determine the successful MXene formation from the MAX phase. For example, all crystallographic peaks of MAX can be observed from the XRD pattern, which is consistent with the $p6_3/mmc$ structure. When converting the MAX to MXene, broadened (00 l) peaks and many other broad peaks from lattice reflections will be shown. Huang prepared Ti_3C_2 MXenes from Ti_3SiC_2 by the Lewis acid etching route [25], in contrast to the more conventional HF or HCl + LiF etching method. They measured the XRD peaks of the pristine Ti_3SiC_2 as well as the resultant material and reported the successful reduction of Ti_3SiC_2 into layered Ti_3C_2. Moreover, because of the 2D feature and hydrophilicity of MXenes, the interlayer spacing can be used as accommodated intercalants. To absorb K ion on the surface of MXenes (V_2C), Ye et al. treated V_2CTx MXenes by KOH. From the XRD patterns before the alkalization [24], the (002) plane of V_2CTx MXenes was located at 8.25°.

After KOH treatment, the (002) peak will shift to 6.98°, suggesting the expanded interlayer space induced by the K^+ intercalation. As a result, while XRD is an important tool for displaying MXene surface bonding, in situ techniques can be used to examine the surface chemistry of MXenes in the future.

XPS is also an important tool to detect the surface chemical compositions of the materials and observe the chemical states of the various elements. Thus, the information of MXenes' surface terminations can be identified and separated from the O1s and F1s regions from high-resolution XPS results. These elements may be assigned to different surface species or impurities such as TiO_2 particles from the aqueous etching process. However, when the difference in binding energy is less than 1 eV, such as O- and OH-groups, it would be difficult to distinguish these species [26, 38].

A recent in-situ temperature-programmed XPS investigation of $Ti_3C_2T_x$ MXene etched with 10% HF was reported by Persson et al. [27]. The XPS results measured between room temperature and 750 °C suggested that the F atom was just adsorbed on-site during the heating process, whereas O was adsorbed on two different sites. Moreover, they reported that the binding energy of 529.9 eV corresponds to the O atom bridging two titanium atoms (TiO_2). The peaks assigned to O-groups in the absence and presence of F atoms (C–Ti–O_x and C–Ti–OH_x) set at the binding energies of 531.2, and 532.0 eV, respectively. Hence, Halim et al. concluded that the general formula for $Ti_3C_2T_x$ MXene prepared by 50% HF solution should be determined to be $Ti_3C_2O_{0.3}(OH)_{0.32}F_{1.2}$ [26]. To study the surface chemistry of MXenes in-depth still need more well-designed XPS measures.

With the high sensitivity of ^1H, ^{19}F, and ^{13}C nuclei, NMR spectroscopy is a complementary technique for analyzing the chemical structure of the surface groups. It can also be applied to detect the surface chemistry of MXene, such as $Ti_3C_2T_x$ and V_2CT_x [28, 29]. For example, Hope et al. have employed the ^1H and ^{19}F NMR spectra of $Ti_3C_2T_x$ to identify –OH and –F terminations and H_2O present between the MXene nanosheets [28]. Another NMR study conducted on V_2CT_x MXene confirms that water can be hydrogen bonded to the surface hydroxide layer and that the F-group was bonded to the MXene surface [29]. However, O- terminations cannot be detected by NMR, but it can be calculated when the total amount of surface groups is assumed to be 2 ($n_{OH} + n_F + 2n_O = 2$).

As O and F elements on the MXenes' surface can be observed in EDX measures, EDX in SEM can be a complementary technique [33, 39]. However, it is difficult for EDX to identify O- and OH- groups. Light elements can also not be detected. Moverover, the signal is strongly dependent on the experimental conditions for accurate EDX quantification.

Complementary to SEM with EDX, STEM combined with EELS can directly detect the surface terminations of MXenes [37, 40]. It can be used in both quantification and site identification of the functionalizing species. Based on a detailed study of the role of surface groups, Bilyk et al. showed that the C-K edge is a clear marker for surface-induced electronic structure modifications in the Ti_3C_2 conducting core of MXenes [41]. However, STEM with EELS can be used to identify the atomic structure of the MXene sheets and intrinsic defects, surface, and edge terminations.

It shows partial coverage of surface groups and not the overall surface termination. Moreover, it is unable for STEM to detect light atoms like carbon, oxygen, and fluorine.

Neutron/X-ray PDF analysis can be used to explore the structural modeling of MXenes that includes the local arrangement of atoms terminations [32, 33]. Compared with XPS, EDX analysis, neutron/X-ray PDF analysis is more favorable to observe hydrogen atoms on the surface of MXenes. Wang et al. studied the "third-generation" structure model of $Ti_3C_2T_x$ by using neutron PDF analysis, which takes the 2D periodicity of the bare MXene and the random distribution of functional groups on the MXene surfaces [32]. From the neutron PDF results, it can find that the number of F-groups is larger than O-terminations on the surface of the HF-etched $Ti_3C_2T_x$ MXene, which agrees with the XPS and NMR results mentioned above [26, 28]. However, different from the XPS and NMR results, many OH-terminations can also be observed in the $Ti_3C_2T_x$ MXenes from the neutron PDF report. The difference might be attributed to the etching environment and sample preparation conditions. The XPS test needs a high vacuum, but PDF analyses are measured in the ambient environment. In addition, the limitations of different characterization techniques can also influence the result. The neutron/X-ray PDF analysis provides a new territory of designing novel MXene materials with controlled surface chemistry and properties.

Nowadays, The research of Raman spectroscopy of MXene's surface chemistry is still in its early stages, and the reports are only a few [34, 35, 42–44]. Hu et al. predicted the Raman (E_g and A_{1g}) vibrational modes, and they concluded that the surface terminations would influence the vibrational frequencies [34]. However, as termination species on MXenes' surfaces are mixed and random, it is still challenging to precisely assign the Raman modes of MXenes.

As mentioned above, MXene surface termination groups occupy an important place in the stability of the MXene structure and evaluation of many exciting properties. However, it is one of the most challenging problems to understand and control MXenes' surface termination groups in experiment, and research about the dynamics of the terminations is still lacking. Currently, due to the surface termination groups may be affected by the etching techniques and sample preparation, it is preferable to design the etching protocols and post-synthesis processing carefully.

3 Thermo-Physical Properties

Due to the intrinsic ceramic nature, MXenes derived from MAX Phases may be employed as thermoelectric materials in energy conversion fields. The thermophysical property of MXenes, especially the thermoelectric performance, can be evaluated through the figure of merit (ZT, $ZT = S^2\sigma T/K$), which is dimensionless. In this expression, S stands for the electrical conductivity, σ is the Seebeck coefficient, T represents temperature, and K ($K = k_l + k_e$) corresponds to thermal conductivity. Thus, ZT can be increased with the increase of the power factor ($S^2\sigma$), and the thermal conductivity (K) would simultaneously decrease [45]. Generally, the thermal

conductivity of MXenes is anisotropic along the zigzag and armchair edges. Nowadays, the thermal conductivity of various MXenes has been theoretically investigated by considering both phonon and electron contributions, such as Ti_2CO_2, Hf_2CO_2, Zr_2CO_2 [46, 47], Sc_2CF_2, Sc_2CO_2, $Sc_2C(OH)_2$ [48], and Mo_2C [49].

Among M_2CO_2 (M = Ti, Zr, Hf), Schwingenschlögl et al. reported that the lattice thermal conductivity of Ti_2CO_2 and Hf_2CO_2 is the lowest and highest, respectively, between the temperature of 300 and 700 K [47]. Moreover, the semiconducting states for different function groups were studied through DFT calculation and the projector augmented wave approach. Among Sc_2CT_2 (T = F, O, OH), $Sc_2C(OH)_2$ displayed the lowest lattice thermal conductivity due to the existence of OH functionalization [48]. The room-temperature thermal conductivity of Sc_2CF_2 along the armchair direction was about 472 W m^{-1} K^{-1}, which is even higher than that of silver. The thermal conductivity of $Sc_2C(OH)_2$ along this direction was estimated as 173 W m^{-1} K^{-1}, which is lower than that of Sc_2CF_2 and higher compared to most metals [50].

The pristine Mo_2C, which is metallic, shows a small molar volume, outstanding electrical conductivity, and attractive thermal conductivity. To explore the thermal conductivity of Mo_2C, Du et al. studied the electron and phonon contributions with first-principles density functional theory. The calculated electrical conductivity of Mo_2C MXene is about 10^6 Ω^{-1} m^{-1}, which could be remarkably influenced by doping. The room-temperature thermal conductivity of Mo_2C is estimated to be 48.4 Wm^{-1} K^{-1}, and it can reach 64.7 Wm^{-1} K^{-1} with the introduction of n-type dopants [49].

The thermal conductivity of several MXene materials mentioned in the above literature is predicted in theory, and there are few experimental reports. Liu et al. synthesize $Ti_3C_2T_x$ film and $Ti_3C_2T_x$/poly(vinyl alcohol) (PVA) film using the laser flash technique. Due to the introduction of strong Ti − O bonds, PVA can significantly improve the thermal stability of MXene. Meanwhile, With the laser thermal conductivity test instrument, the thermal conductivities of $Ti_3C_2T_x$ and $Ti_3C_2T_x$/PVA films were measured to be 55.8 and 47.6 Wm^{-1} K^{-1}, respectively [51]. Chen et al. prepared $Ti_3C_2T_x$ films from delaminated $Ti_3C_2T_x$ nanosheets by vacuum-assisted filtration. The thickness of the prepared film was about tens μm, lower than that of the commercial laser flash instruments (larger than 100 μm). Thus, the thermal conductivity of the prepared film was measured through the advanced T-type method. Figure 4a displays the schematic of the T-type method. One platinum (Pt) wire was put at the ends to copper electrodes. The test sample was supported at the center of the Pt wire. The following formula calculated the thermal conductivity of the sample ((s)).

$$\lambda_s = \frac{L_s L_{hh} A_h \left(L_h^3 qv - 12 L_{hh} \Delta T_V\right)}{L_{h1} L_{h2} A_s \left[12 L_{hh} \Delta T_V - qv\left(L_{h1}^3 + L_{h2}^3\right)\right]}$$

where L_s, L_h, A_h, and A_s correspond to the length of the test sample (MXenes), the length of the Pt wire ($L_h = L_{h1} + L_{h2}$), the cross-sectional areas of the Pt wire and the test sample (MXenes), respectively, as shown in Fig. 4b. λ_h represents the thermal

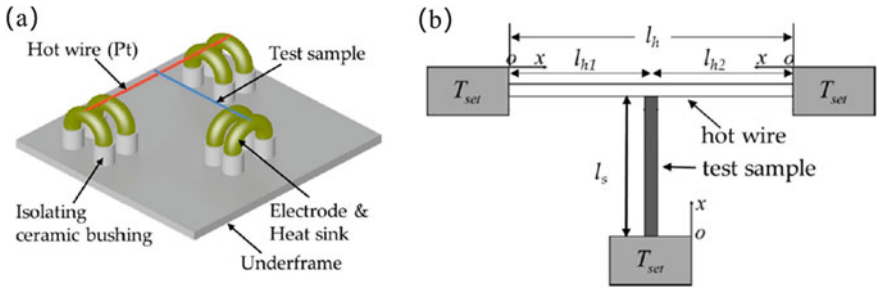

Fig. 4 A Schematic and Physical model of the advanced T-type method that the test sample located at the center of hot wire

conductivity of hot wire (Pt), $qV = UI/L_hA_h$ the volumetric heating power of the Pt wire, and ΔT_V the volumetric average temperature change of the Pt wire.

The thermal conductivity of the films was 1.26 and 2.84 Wm^{-1} K^{-1} at the temperature of 80 and 290 K, respectively, as measured by the T-type method mentioned above [52].

Due to the high thermal conductivity, MXenes can be used in heat transfer applications. Jin et al. designed PVA/MXene composite films to improve thermo-physical properties with the multilayered casting. Due to the existence of the continuous MXene layer, the resulted films showed a high in-plane thermal conductivity of 4.57 Wm^{-1} K^{-1}, almost 23 times that of the neat PVA films [53]. Moreover, multilayer and single layer $Ti_3C_2T_x$ MXene solution with ethylene glycol (EG) were prepared successfully as nanofluids by Yu et al., and they both displayed excellent thermal conductivity. As shown in Fig. 5a, the thermal conductivity of MXene nanofluids is almost stable between the temperature of 10 and 60 °C because of the viscosity of EG. At room temperature, the thermal conductivity would increase linearly when

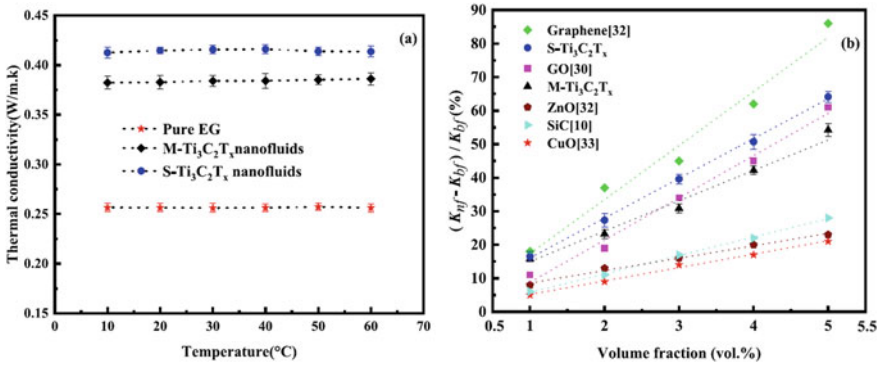

Fig. 5 **a** Thermal conductivity of MXene-based nanofluids at the temperature range from 10 to 60 °C; **b** Enhancement in thermal conductivity with the increase of the volume fraction [54]

the volume fraction of the nanofluids increased from 1 to 5% (Fig. 5b). The corresponding values of nanofluids with 5 vol% of multilayer and single layer $Ti_3C_2T_x$ MXene would increase by 53.1 and 64.9% compared to EG, respectively [54].

MXene also shows specific surface area and rich surface termination with a hydrophilic feature. These properties provide a strong adsorption effect and hydrogen bonding interactions between the polyethylene glycol (PEG) molecular chains and MXene. To obtain excellent form-stable phase change material (FSPCM), Qu et al. designed PEG/MXene composites through the simple vacuum impregnation approach, in which MXene was used as the thermally conductive supporting skeleton. The thermal conductivity of the prepared PEG/MXene would reach 2.052 Wm^{-1} K^{-1}, which is higher compared to pure PEG [55]. Rafieerad et al. comprehensively studied the thermophysical properties of $Ti_3C_2T_x$ MXene with few-layered non-covalent graphene nanoplatelets (GNPs) and covalently functionalized COOH- and NH_2- GNP nanofluids. The thermal conductivities of the water-based MXene with 0.1 and 0.2 mass% Ti_3C_2Tx were both higher (0.732 and 0.828 Wm^{-1} K^{-1}, respectively) compared to non-covalent GNPs (0.679 and 0.702 Wm^{-1} K^{-1}, respectively) [56].

The abovementioned results indicate that MXene-based materials with high thermal conductivity would have a great potential application in thermal conversion and storage fields, such as thermoelectric devices, fluorescent nanofluid, and seawater desalinization.

4 Optoelectronics Properties

As mentioned above, MXene with certain molecular structures could be theoretically calculated to be semiconducting. These MXenes have been revealed to possess greatly enhanced optical and electrical characteristics for optoelectronic applications [57–59]. A series of experimental research about the optoelectronics properties of MXenes has been reported. Among them, $Ti_3C_2T_x$ and Ti_2CT_x are outstanding representatives. After being deposited on substrates with controlled thicknesses, the resulting $Ti_3C_2T_x$ and Ti_2CT_x Mxenes can be used as transparent conductive thin films [59–64].

Gogotsi et al. first prepared transparent $Ti_3C_2T_x$ MXene film prepared by epitaxially growth and subsequently etching [61]. Ti_3AlC_2 precursor was magnetron-sputtered on the sapphire substrate and then etched by HF or NH_4HF_2. The thickness of the resulting $Ti_3C_2T_x$ film was about 19 nm, and the transmittance would reach∼90% in the visible-to-infrared range. Interestingly, the MAX film with the same thickness is also transparent in the visible light, and the transmittance would be only 30%. Moreover, the resulting films displayed metallic conductivity at 100 K. When the temperature drops below 100 K, the resistivity will increase with the temperature decrease, as shown in Fig. 6.

Many solution-processing methods, including spray-coating, spin-casting, and dip-coating, were also used to turn aqueous solutions of MXenes into thin films for

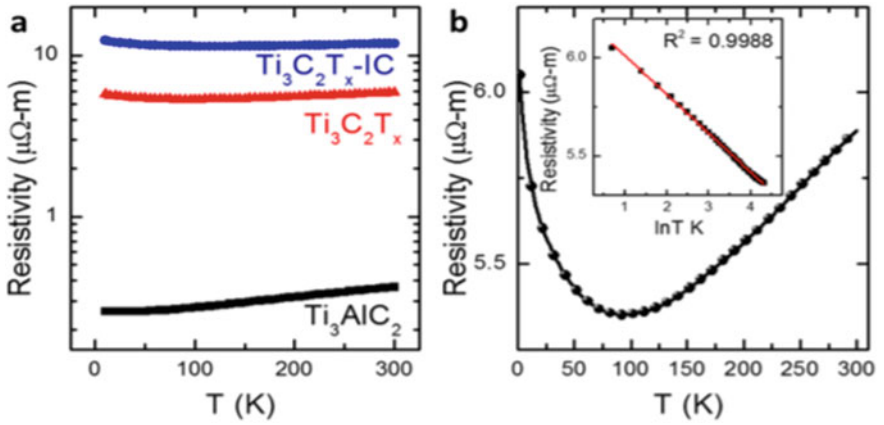

Fig. 6 **a** Resistivity of three MXene films (Ti_3AlC_2, $Ti_3C_2T_x$, and $Ti_3C_2T_x$−IC, IC represent NH_3 or NH_4^+) from 0 to 300 K. **b** Resistivity versus temperature for $Ti_3C_2T_x$. Inset shows the fitting of resistivity between the temperature of 2 and 74 K to the weak localization model ($\rho \sim \ln T$) [61]

optoelectronic devices [16, 58–60, 62, 63, 65]. Fafarman et al. synthesized flexible MXene films with high conductivity and optical quality through a low-cost spin casting approach (Fig. 7). The electrical conductivity of nanometer-thin films with >97% transparency, measured by the four-probe technique, could reach 6500 S cm^{-1}. The result surpassed the values of other solution-processed 2D materials under similar conditions. Additionally, the sheet resistance of films with 2 nm thickness could reach 1000 Ω sq^{-1}, suggesting that the percolative transport path would be formed and the film is in the bulk-conductivity regime [16].

In 2016, $Ti_3C_2T_x$ films, synthesized by Mariano et al., displayed a relatively low resistivity of 437 Ω sq^{-1} at about 77% of transmittance over a wide wavelength range from visible to near-infrared light. Remarkably, the figure of merit (FOM) of the resulting MXene films was twice that of graphene, implying excellent optoelectronic

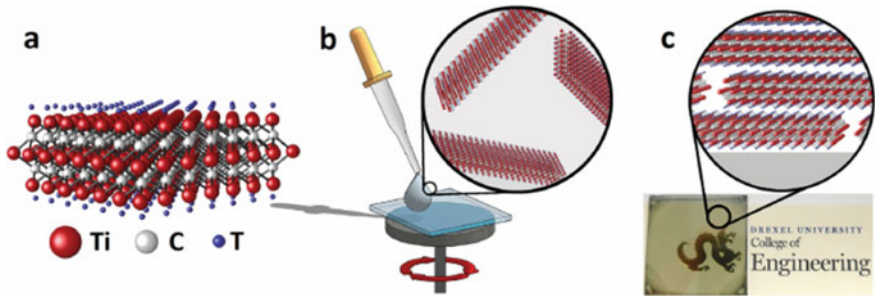

Fig. 7 Schematic illustration of $Ti_3C_2T_x$ MXene film fabrication. **a** $Ti_3C_2T_x$ atomic structure. "T" represents F, O, and OH surface terminations. **b** The spin-casting process that aqueous dispersions of $Ti_3C_2T_x$ would be deposited onto various substrates. **c** a Photo of $Ti_3C_2T_x$ film on glass [16]

properties. In addition, vacuum annealing would improve the conductivity of the films without decreasing their transparency. Hence, a drying process (typically vacuum annealing) can be employed to achieve films with better performance [62]. Zhang et al. prepared a d-$Ti_3C_2T_x$ (hand-shaken, nonsonicated) film with high conductivity of 9880 S cm^{-1} by spin-casting and following vacuum annealing at 200 °C. When the flexible substrate was bent to a small radius, the conductivity would be slightly lower compared to the glass substrate. However, the conductivity would keep stable during the bending cycles [63].

Although the spin-casting approach can achieve better-performing films in the reports mentioned above, it needs a high-concentration delaminated MXene (d-MXene) solution (usually >5 mg ml^{-1}) for considerably thick films [66, 67]. In addition, the substrate should be flat for the excellent conductivity of films, whereas the spin chamber limits the substrate size. Consequently, these restrictions of the spin-casting method could restrict the application of MXene thin films for large-scale production. The spray-coating technique is a simpler and more controllable alternative for large-scale film deposition compared with spin casting. This method allows relatively low concentrations (0.5–3 mg ml^{-1}) of $Ti_3C_2T_x$ MXene solution to be deposited on a large area substrate [68]. Moreover, Through the control of spray times, the thickness of the films can be varied from a few nanometers to several micrometers. The disadvantage of this method is that the surface of prepared films is rough with grain boundaries, which may limit industrial production [65]. The dip-coating technique can also be used to synthesize MXene thin films with high quality. With the simple sip-coating method, Lee et al. prepared thin (~5 nm) Ti_2CT_x films on the wafer-scale Al_2O_3 substrate (Fig. 8). The resistance of the resulting thin film could be about 70 Ω sq^{-1} when the transmittance reaches 86% [64]. Furthermore, the thickness of the films in this work can be controlled by the plasma treatment process.

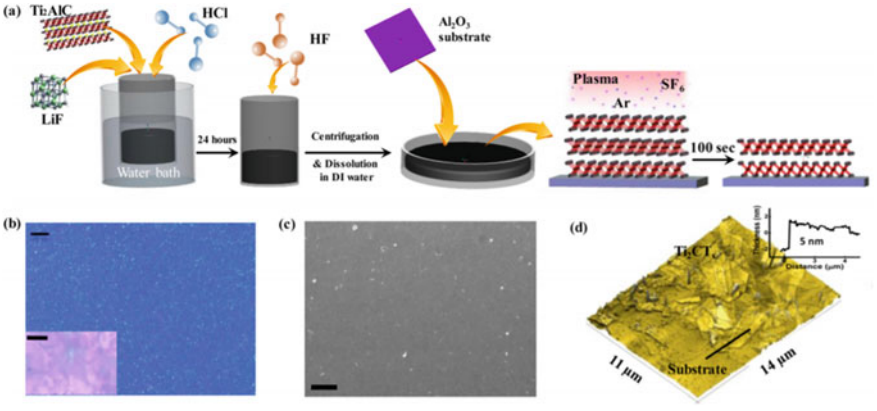

Fig. 8 **a** Schematic of the synthesis of Ti_2CT_x film with plasma treatment. **b** Optical microscope (OM) image of MXene thin film. The scale bar of the main image 100, and 5 μm for the inserted image. **c** SEM image. The scale bar is 10 μm. **d** Atomic Force Microscope (AFM) image of Ti_2CT_x thin film on the Al_2O_3 substrate [64]

In the plasma treatment process, Ti_2CT_x film can be etched layer by layer, and the surface oxidized layer could be removed without sacrificing the bottom layer.

The electronic conductivity of Ti_3CNT_x (T is a mixture of carbon and nitrogen elements) is lower than that of $Ti_3C_2T_x$. In the UV–visible spectrum, the result of Ti_3CNT_x displays a blue shift. Hantanasirisakul et al. prepared Ti_3CNT_x film with a high-concentration of d-Ti_3CNT_x solution (5–20 mg mL^{-1}) by a spin-casting technique [69]. When the concentration of the solution decreases to 5 mg mL^{-1}, the transmittance of the prepared thin films can reach 94% with a thickness of 2.5 nm. The room-temperature resistivity of Ti_3CNT_x film dispersed in tetrabutylammonium hydroxide (TBAOH) would reach 2.0×10^{-2} Ω cm after being treated at 400 °C for three hours.

Recently, Ying et al. prepared V_2CT_x MXene films through spin-casting technique with the same dispersant (TBAOH) [70]. When the thicknesses of the films increased from 11 to 116 nm, the transmittance at the wavelength of 550 nm would decrease from 89 to 27%. The sheet resistance of the prepared films in this work was about 10^4–10^6 Ω sq^{-1}. A decrease of two orders of magnitude can be observed after annealing at 150 °C, which may be attributed to TBAOH decomposition. So far, among the reports on optical-electronic properties of MXenes, Ti-based MXenes (Ti_3C_2Tx and Ti_2CTx) aqueous solution has attached the most attention. The relationship between the surface terminations, interlayer spacing, and solvents for film formation with optical-electronic properties of MXenes also needs to be explored.

Due to the high transmittance and electrical conductivity, the MXene films could be widely used in optoelectronics and photonic devices, such as photodetectors, light-emitting diodes, fiber laser, and solar cells. However, the applications of MXenes in the above fields are still in the initial stage, and there is still a long way to go to investigate the photoelectric properties of MXenes.

5 Conclusions and Perspectives

Since the discovery of MXene in 2011, the new two-dimensional transition metal carbides have built a wide range of applications due to their unique properties. When designing the novel MXene materials for potential applications, including transparent conductors, supercapacitors, Li-ion batteries, electromagnetic shielding, catalysis, and photocatalytic water splitting, thermoelectric device, fluorescent nanofluid, it is necessary to consider the properties carefully, especially structural and surface-chemistry, thermo-physical properties, and optoelectronic properties. In this chapter, we reviewed the three properties of MXenes. These properties are discussed in terms of thermal conductivity, surface terminations, transmittance, and electronic conductivity combined with various characterization methods, test methods, and theoretical calculations. Currently, there are still some challenges in the study of the MXenes' properties. Firstly, one of the most challenging tasks is understanding and controlling

MXenes' surface chemistry in experiments. Secondly, designing advanced MXene-based materials with controllable and tunable thermo-physical properties is necessary. Lastly, theoretical research about the optoelectronics properties of MXenes has been very few. Future investigations of the three properties may include in situ experimental characterizations with accurate theoretical predictions.

References

1. Tan, C., Cao, X., Wu, X.J., He, Q., Yang, J., Zhang, X., Chen, J., Zhao, W., Han, S., Nam, G.H., Sindoro, M., Zhang, H.: Recent advances in ultrathin two-dimensional nanomaterials. Chem. Rev. **117**, 6225–6331 (2017)
2. Novoselov, K.S., Geim, A.K., Morozov, S.V., Jiang, D., Zhang, Y., Dubonos, S.V., Grigorieva, I.V., Firsov, A.A.: Electric field effect in atomically thin carbon films. Science **306**, 666–669 (2004)
3. Mak, K.F., Lee, C., Hone, J., Shan, J., Heinz, T.F.: Atomically thin MoS_2: a new direct-gap semiconductor. Phys. Rev. Lett. **105**, 136805 (2010)
4. Sui, Y., Zhou, J., Wang, X., Wu, L., Zhong, S., Li, Y.: Recent advances in black-phosphorus-based materials for electrochemical energy storage. Mater. Today **42**, 117–136 (2021)
5. Zhang, Y.-Z., Wang, Y., Jiang, Q., El-Demellawi, J.K., Kim, H., Alshareef, H.N.: MXene printing and patterned coating for device applications. Adv. Mater. **32**, 1908486 (2020)
6. Naguib, M., Kurtoglu, M., Presser, V., Lu, J., Niu, J., Heon, M., Hultman, L., Gogotsi, Y., Barsoum, M.W.: Two-dimensional nanocrystals produced by exfoliation of Ti_3AlC_2. Adv. Mater. **23**, 4248–4253 (2011)
7. Mei, J., Ayoko, G.A., Hu, C., Sun, Z.: Thermal reduction of sulfur-containing MAX phase for MXene production. Chem. Eng. J. **395**, 125111 (2020)
8. Deysher, G., Shuck, C.E., Hantanasirisakul, K., Frey, N.C., Foucher, A.C., Maleski, K., Sarycheva, A., Shenoy, V.B., Stach, E.A., Anasori, B.: Synthesis of Mo_4VAlC_4 MAX phase and two-dimensional Mo_4VC_4 MXene with five atomic layers of transition metals. ACS Nano **14**, 204–217 (2019)
9. Fashandi, H., Dahlqvist, M., Lu, J., Palisaitis, J., Simak, S.I., Abrikosov, I.A., Rosen, J., Hultman, L., Andersson, M., Lloyd Spetz, A., Eklund, P.: Synthesis of Ti_3AuC_2, $Ti_3Au_2C_2$ and Ti_3IrC_2 by noble metal substitution reaction in Ti_3SiC_2 for high-temperature-stable Ohmic contacts to SiC. Nat. Mater. **16**, 814–818 (2017)
10. Ashton, M., Hennig, R.G., Broderick, S.R., Rajan, K., Sinnott, S.B.: Computational discovery of stable MAX phases. Phys. Rev. B **94**, 054116 (2016)
11. Mo, Y., Rulis, P., Ching, W.Y.: Electronic structure and optical conductivities of 20 MAX-phase compounds. Phys. Rev. B **86**, 165122 (2012)
12. Cover, M.F., Warschkow, O., Bilek, M.M.M., McKenzie, D. R.: A comprehensive survey of M_2AX phase elastic properties. J. Phys.: Condens. Matter **21**, 305403.
13. Jiang, C., Chroneos, A.: Ab initio modeling of MAX phase solid solutions using the special quasirandom structure approach. Phys. Chem. Chem. Phys. **20**, 1173–1180 (2018)
14. Xu, H., Ren, A., Wu, J., Wang, Z.: Recent advances in 2D MXenes for photodetection. Adv. Funct. Mater. **30**, 2000907 (2020)
15. Soundiraraju, B., Raghavan, R., George, B.K.: Chromium carbide nanosheets prepared by selective etching of aluminum from Cr_2AlC for hydrazine detection. ACS Appl. Nano Mater. **3**, 11007–11016 (2020)
16. Dillon, A.D., Ghidiu, M.J., Krick, A.L., Griggs, J., May, S.J., Gogotsi, Y., Barsoum, M.W., Fafarman, A.T.: Highly conductive optical quality solution-processed films of 2D titanium carbide. Adv. Funct. Mater. **26**, 4162–4168 (2016)

17. Khazaei, M., Arai, M., Sasaki, T., Chung, C.-Y., Venkataramanan, N.S., Estili, M., Sakka, Y., Kawazoe, Y.: Novel electronic and magnetic properties of two-dimensional transition metal carbides and nitrides. Adv. Funct. Mater. **23**, 2185–2192 (2013)
18. Kajiyama, S., Szabova, L., Iinuma, H., Sugahara, A., Gotoh, K., Sodeyama, K., Tateyama, Y., Okubo, M., Yamada, A.: Enhanced Li-ion accessibility in MXene titanium carbide by steric chloride termination. Adv. Energy Mater. **7**, 1601873 (2017)
19. Hu, J., Xu, B., Ouyang, C., Yang, S.A., Yao, Y.: Investigations on V_2C and V_2CX_2 (X = F, OH) monolayer as a promising anode material for Li ion batteries from first-principles calculations. J. Phys. Chem. C **118**, 24274–24281 (2014)
20. Hantanasirisakul, K., Gogotsi, Y.: Electronic and optical properties of 2D transition metal carbides and nitrides (MXenes). Adv. Mater. **30**, 1804779 (2018)
21. Khazaei, M., Ranjbar, A., Arai, M., Sasaki, T., Yunoki, S.: Electronic properties and applications of MXenes: a theoretical review. J. Mater. Chem. C **5**, 2488–2503 (2017)
22. Enyashin, A.N., Ivanovskii, A.L.: Two-dimensional titanium carbonitrides and their hydroxylated derivatives: structural, electronic properties and stability of MXenes $Ti_3C_{2-x}N_x(OH)_2$ from DFTB calculations. J. Solid State Chem. **207**, 42–48 (2013)
23. Cockreham, C. B., Zhang, X., Eakin, J. A., Dewa, M., Li, H., Li, N., Sun, J., Ha, S., Ivory, C. F.and Wang, Y.: Unveiling the interfacial and structural heterogeneity of $Ti_3C_2T_x$ MXene etched with CoF_2/HCl by integrated in situ thermal analysis. ACS Appl. Mater. Interfaces https://doi.org/10.1021/acsami.1c10021
24. Zhu, X., Cao, Z., Wang, W., Li, H., Dong, J., Gao, S., Xu, D., Li, L., Shen, J., Ye, M.: Superior-performance aqueous Zinc-ion batteries based on the in situ growth of MnO_2 Nanosheets on V_2CT_X MXene. ACS Nano **15**, 2971–2983 (2021)
25. Li, Y., Shao, H., Lin, Z., Lu, J., Liu, L., Duployer, B., Persson, P.O., Eklund, P., Hultman, L., Li, M.: A general lewis acidic etching route for preparing MXenes with enhanced electrochemical performance in non-aqueous electrolyte. Nat. Mater. **19**, 894–899 (2020)
26. Halim, J., Cook, K.M., Naguib, M., Eklund, P., Gogotsi, Y., Rosen, J., Barsoum, M.W.: X-ray photoelectron spectroscopy of select multi-layered transition metal carbides (MXenes). Appl. Surf. Sci. **362**, 406–417 (2016)
27. Persson, I., Näslund, L.-Å., Halim, J., Barsoum, M.W., Darakchieva, V., Palisaitis, J., Rosen, J., Persson, P.O.Å.: On the organization and thermal behavior of functional groups on Ti_3C_2 MXene surfaces in vacuum. 2D Mater. 5, 015002 (2017)
28. Hope, M.A., Forse, A.C., Griffith, K.J., Lukatskaya, M.R., Ghidiu, M., Gogotsi, Y., Grey, C.P.: NMR reveals the surface functionalisation of Ti_3C_2 MXene. Phys. Chem. Chem. Phys. **18**, 5099–5102 (2016)
29. Harris, K.J., Bugnet, M., Naguib, M., Barsoum, M.W., Goward, G.R.: Direct measurement of surface termination groups and their connectivity in the 2D MXene V_2CT_x using NMR spectroscopy. J. Phys. Chem. C **119**, 13713–13720 (2015)
30. Wang, X., Shen, X., Gao, Y., Wang, Z., Yu, R., Chen, L.: Atomic-scale recognition of surface structure and intercalation mechanism of Ti_3C_2X. J. Am. Chem. Soc. **137**, 2715–2721 (2015)
31. Anasori, B., Shi, C., Moon, E.J., Xie, Y., Voigt, C.A., Kent, P.R.C., May, S.J., Billinge, S.J.L., Barsoum, M.W., Gogotsi, Y.: Control of electronic properties of 2D carbides (MXenes) by manipulating their transition metal layers. Nanoscale Horiz. **1**, 227–234 (2016)
32. Wang, H.-W., Naguib, M., Page, K., Wesolowski, D.J., Gogotsi, Y.: Resolving the structure of $Ti_3C_2T_x$ MXenes through multilevel structural modeling of the atomic pair distribution function. Chem. Mater. **28**, 349–359 (2016)
33. Shi, C., Beidaghi, M., Naguib, M., Mashtalir, O., Gogotsi, Y., Billinge, S.J.L.: Structure of nanocrystalline Ti_3C_2 MXene using atomic pair distribution function. Phys. Rev. Lett. **112**, 125501 (2014)
34. Hu, T., Wang, J., Zhang, H., Li, Z., Hu, M., Wang, X.: Vibrational properties of Ti_3C_2 and $Ti_3C_2T_2$ (T = O, F, OH) monosheets by first-principles calculations: a comparative study. Phys. Chem. Chem. Phys. **17**, 9997–10003 (2015)
35. Hu, M., Li, Z., Hu, T., Zhu, S., Zhang, C., Wang, X.: High-capacitance mechanism for $Ti_3C_2T_x$ MXene by in situ electrochemical raman spectroscopy investigation. ACS Nano **10**, 11344–11350 (2016)

36. Magne, D., Mauchamp, V., Célérier, S., Chartier, P., Cabioc'h, T.: Site-projected electronic structure of two-dimensional Ti_3C_2 MXene: the role of the surface functionalization groups. Phys. Chem. Chem. Phys. **18**, 30946–30953 (2016)
37. Karlsson, L.H., Birch, J., Halim, J., Barsoum, M.W., Persson, P.O.Å.: Atomically resolved structural and chemical investigation of single MXene sheets. Nano Lett. **15**, 4955–4960 (2015)
38. Yamamoto, S., Bluhm, H., Andersson, K., Ketteler, G., Ogasawara, H., Salmeron, M., Nilsson, A.: In situx-ray photoelectron spectroscopy studies of water on metals and oxides at ambient conditions. J. Phys. Condens. Matter. 20, 184025 (2008)
39. Alhabeb, M., Maleski, K., Anasori, B., Lelyukh, P., Clark, L., Sin, S., Gogotsi, Y.: Guidelines for synthesis and processing of two-dimensional titanium carbide ($Ti_3C_2T_x$ MXene). Chem. Mater. **29**, 7633–7644 (2017)
40. Sang, X., Xie, Y., Lin, M.-W., Alhabeb, M., Van Aken, K.L., Gogotsi, Y., Kent, P.R.C., Xiao, K., Unocic, R.R.: Atomic defects in monolayer titanium carbide ($Ti_3C_2T_x$) MXene. ACS Nano **10**, 9193–9200 (2016)
41. Bilyk, T., Benchakar, M., Bugnet, M., Loupias, L., Chartier, P., Pazniak, H., David, M.-L., Habrioux, A., Celerier, S., Pacaud, J.: Electronic structure sensitivity to surface disorder and nanometer-scale impurity of 2D titanium carbide MXene sheets as revealed by electron energy-loss spectroscopy. J. Phys. Chem. C **124**, 27071–27081 (2020)
42. Sarycheva, A., Makaryan, T., Maleski, K., Satheeshkumar, E., Melikyan, A., Minassian, H., Yoshimura, M., Gogotsi, Y.: Two-dimensional titanium carbide (MXene) as surface-enhanced raman scattering substrate. J. Phys. Chem. C **121**, 19983–19988 (2017)
43. Urbankowski, P., Anasori, B., Makaryan, T., Er, D., Kota, S., Walsh, P.L., Zhao, M., Shenoy, V.B., Barsoum, M.W., Gogotsi, Y.: Synthesis of two-dimensional titanium nitride Ti_4N_3 (MXene). Nanoscale **8**, 11385–11391 (2016)
44. Champagne, A., Shi, L., Ouisse, T., Hackens, B., Charlier, J.-C.: Electronic and vibrational properties of V_2C-based MXenes: from experiments to first-principles modeling. Phys. Rev. B **97**, 115439 (2018)
45. Zebarjadi, M., Esfarjani, K., Dresselhaus, M.S., Ren, Z.F., Chen, G.: Perspectives on thermoelectrics: from fundamentals to device applications. Energy Environ. Sci. **5**, 5147–5162 (2012)
46. Zha, X.-H., Huang, Q., He, J., He, H., Zhai, J., Francisco, J.S., Du, S.: The thermal and electrical properties of the promising semiconductor MXene Hf_2CO_2. Sci. Rep. **6**, 27971 (2016)
47. Gandi, A.N., Alshareef, H.N., Schwingenschlögl, U.: Thermoelectric performance of the MXenes M_2CO_2 (M = Ti, Zr, or Hf). Chem. Mater. **28**, 1647–1652 (2016)
48. Kumar, S., Schwingenschlögl, U.: Thermoelectric performance of functionalized Sc_2C MXenes. Phys. Rev. B **94**, 035405 (2016)
49. Zha, X.-H., Yin, J., Zhou, Y., Huang, Q., Luo, K., Lang, J., Francisco, J.S., He, J., Du, S.: Intrinsic structural, electrical, thermal, and mechanical properties of the promising conductor Mo_2C MXene. J. Phys. Chem. C **120**, 15082–15088 (2016)
50. Zha, X.-H., Zhou, J., Zhou, Y., Huang, Q., He, J., Francisco, J.S., Luo, K., Du, S.: Promising electron mobility and high thermal conductivity in Sc_2CT_2 (T = F, OH) MXenes. Nanoscale **8**, 6110–6117 (2016)
51. Liu, R., Li, W.: High-thermal-stability and high-thermal-conductivity $Ti_3C_2T_x$ MXene/Poly(vinyl alcohol) (PVA) composites. ACS Omega **3**, 2609–2617 (2018)
52. Chen, L., Shi, X., Yu, N., Zhang, X., Du, X., Lin, J.: Measurement and analysis of thermal conductivity of $Ti_3C_2T_x$ MXene films. Materials **11**, 1701 (2018)
53. Jin, X., Wang, J., Dai, L., Liu, X., Li, L., Yang, Y., Cao, Y., Wang, W., Wu, H., Guo, S.: Flame-retardant poly(vinyl alcohol)/MXene multilayered films with outstanding electromagnetic interference shielding and thermal conductive performances. Chem. Eng. J. **380**, 122475 (2020)
54. Bao, Z., Bing, N., Zhu, X., Xie, H., Yu, W.: $Ti_3C_2T_x$ MXene contained nanofluids with high thermal conductivity, super colloidal stability and low viscosity. Chem. Eng. J. **406**, 126390 (2021)

55. Lu, X., Huang, H., Zhang, X., Lin, P., Huang, J., Sheng, X., Zhang, L., Qu, J.: Novel light-driven and electro-driven polyethylene glycol/two-dimensional MXene form-stable phase change material with enhanced thermal conductivity and electrical conductivity for thermal energy storage. Compos. Part B-Eng. **177**, 107372 (2019)
56. Rafieerad, M., Rafieerad, A.R., Mehmandoust, B., Dhingra, S., Shanbedi, M.: New water-based fluorescent nanofluid containing 2D titanium carbide MXene sheets: a comparative study of its thermophysical, electrical and optical properties with amine and carboxyl covalently functionalized graphene nanoplatelets. J. Therm. Anal. Calorim. **146**, 1491–1504 (2021)
57. Kim, H., Alshareef, H.N.: MXetronics: MXene-enabled electronic and photonic devices. ACS Materials Letters **2**, 55–70 (2020)
58. Dong, Y., Chertopalov, S., Maleski, K., Anasori, B., Hu, L., Bhattacharya, S., Rao, A.M., Gogotsi, Y., Mochalin, V.N., Podila, R.: Saturable absorption in 2D Ti_3C_2 MXene thin films for passive photonic diodes. Adv. Mater. **30**, 1705714 (2018)
59. Hantanasirisakul, K., Zhao, M.-Q., Urbankowski, P., Halim, J., Anasori, B., Kota, S., Ren, C.E., Barsoum, M.W., Gogotsi, Y.: Fabrication of $Ti_3C_2T_x$ MXene transparent thin films with tunable optoelectronic properties. Adv. Electron. Mater. **2**, 1600050 (2016)
60. Ying, G., Dillon, A.D., Fafarman, A.T., Barsoum, M.W.: Transparent, conductive solution processed spincast 2D Ti_2CT_x (MXene) films. Mater. Res. Lett. **5**, 391–398 (2017)
61. Halim, J., Lukatskaya, M.R., Cook, K.M., Lu, J., Smith, C.R., Näslund, L.-Å., May, S.J., Hultman, L., Gogotsi, Y., Eklund, P., Barsoum, M.W.: Transparent conductive two-dimensional titanium carbide epitaxial thin films. Chem. Mater. **26**, 2374–2381 (2014)
62. Mariano, M., Mashtalir, O., Antonio, F.Q., Ryu, W.-H., Deng, B., Xia, F., Gogotsi, Y., Taylor, A.D.: Solution-processed titanium carbide MXene films examined as highly transparent conductors. Nanoscale **8**, 16371–16378 (2016)
63. Zhang, C., Anasori, B., Seral-Ascaso, A., Park, S.-H., McEvoy, N., Shmeliov, A., Duesberg, G.S., Coleman, J.N., Gogotsi, Y., Nicolosi, V.: Transparent, flexible, and conductive 2D titanium carbide (MXene) films with high volumetric capacitance. Adv. Mater. **29**, 1702678 (2017)
64. Yang, Y., Umrao, S., Lai, S., Lee, S.: Large-area highly conductive transparent two-dimensional Ti_2CT_x film. J. Phys. Chemi. Lett. **8**, 859–865 (2017)
65. Ali, A., Belaidi, A., Ali, S., Helal, M., Mahmoud, K.: Transparent and conductive $Ti_3C_2T_x$ (MXene) thin film fabrication by electrohydrodynamic atomization technique. J. Mater. Sci. Electron. **27**, 5440–5445 (2016)
66. Zhou, J., Zha, X., Zhou, X., Chen, F., Gao, G., Wang, S., Shen, C., Chen, T., Zhi, C., Eklund, P., Du, S., Xue, J., Shi, W., Chai, Z., Huang, Q.: Synthesis and electrochemical properties of two-dimensional hafnium carbide. ACS Nano **11**, 3841–3850 (2017)
67. Akuzum, B., Maleski, K., Anasori, B., Lelyukh, P., Alvarez, N.J., Kumbur, E.C., Gogotsi, Y.: Rheological characteristics of 2D titanium carbide (MXene) dispersions: a guide for processing MXenes. ACS Nano **12**, 2685–2694 (2018)
68. Tang, Q., Zhou, Z., Shen, P.: Are MXenes promising anode materials for li ion batteries? computational studies on electronic properties and li storage capability of Ti_3C_2 and $Ti_3C_2X_2$ (X = F, OH) monolayer. J. Am. Chem. Soc. **134**, 16909–16916 (2012)
69. Hantanasirisakul, K., Alhabeb, M., Lipatov, A., Maleski, K., Anasori, B., Salles, P., Ieosakulrat, C., Pakawatpanurut, P., Sinitskii, A., May, S.J., Gogotsi, Y.: Effects of synthesis and processing on optoelectronic properties of titanium carbonitride MXene. Chem. Mater. **31**, 2941–2951 (2019)
70. Ying, G., Kota, S., Dillon, A.D., Fafarman, A.T., Barsoum, M.W.: Conductive transparent V_2CT_x (MXene) films. FlatChem **8**, 25–30 (2018)

MXene-Based Composites and Their Applications

Prakash Krishnaiah, Hafiz Taimoor Ahmed Awan, Rashmi Walvekar, and Sivakumar Manickam

Abstract MXenes have received remarkable attention due to their outstanding physical and chemical properties. They exhibit exceptional tunable performance due to their 2D structure and rich functional group, making them easy to combine with other materials such as polymers, metal oxides, 2D chalcogenides, carbonaceous, and organic hybrid materials to meet the high-performance requirements. Furthermore, MXenes and their composites have shown outstanding electrical, mechanical, and optical properties due to their functional groups and surface chemistry. This chapter covers the synthesis, surface mechanism, and applications of MXenes and related composites. For a better understanding, we address the fundamentals of MXenes to their associated fabrication techniques, including HF etching, exfoliation delamination, in-situ polymerisation, hydrothermal, etc. Then, applications of MXenes are discussed, such as energy storage in supercapacitors, batteries, solar cells, and sensors. Moreover, EMI shielding performance, water remediation, and catalytic activity of MXene/composite are highlighted. In the last part, the challenges and prospects of the MXenes and composites have been addressed to evaluate the general complications, problems, and possible solutions of the materials during synthesis and applications.

P. Krishnaiah
Centre for Nano and Material Sciences, Jain Global Campus, Jain University, Kanakapura, Bangalore 562112, India

H. T. A. Awan
Graphene and Advanced 2D Materials Research Group (GAMRG), School of Engineering and Technology, Sunway University, No. 5, Jalan Universiti, Bandar Sunway, 47500 Petaling Jaya, Selangor, Malaysia

R. Walvekar
Department of Chemical Engineering, School of Energy and Chemical Engineering, Xiamen University Malaysia, Jalan Sunsuria, Bandar Sunsuria, 43900 Sepang, Selangor, Malaysia

S. Manickam (✉)
Petroleum and Chemical Engineering Department, Faculty of Engineering, Universiti Teknologi Brunei, Bandar Seri Begawan 1410, Brunei Darussalam
e-mail: manickam.sivakumar@utb.edu.bn

M. Khalid et al. (eds.), *Fundamental Aspects and Perspectives of MXenes*, Engineering Materials, https://doi.org/10.1007/978-3-031-05006-0_4

Keywords Two-dimensional materials · MXene · Metal oxides · Polymers · Chalcogenides · Composite materials · Energy storage

1 Introduction

Two-dimensional (2D) materials have been intensively researched recently owing to their large specific surface area, high catalytic behavior, highly tunable wide-bandgap, etc. 2D materials have two dimensions outside the nanoscale range [1]. The quest to develop 2D nanostructured materials has accelerated since Novoselov and Geim discovered graphene in 2004 [2]. The 2D family encompasses a diverse range of materials, including graphene, silicene, borophene, transition metal oxides, layered double hydroxides (LDH), and MXenes, as well as hybrid materials and composites based on 2D materials [3–5]. MXenes, a unique 2D material developed in 2011 by Gogotsi and Barsoum [6]. MXenes belong to the transition metal carbides, nitrides and carbonitrides and are synthesized by the selective etching of 'A' layers from their MAX phases that have a general formula $M_{n+1}AX_n$, where n = 1, 2 or 3; M stands for transition metals like (Ti, Ta, Nb, Zr, Cr, Mo, V or Mn) while A represents IIIA and IVA group elements (Al, Si, Ga, Ge, Sn, In, Pb or As), and X can be both carbon and nitrogen elements [7].

The newly synthesized 2D materials, MXenes, are obtained by losing A layers from their original MAX phase, and their 2D nature is identical to that of graphene. It was reported that during the etching process, the surfaces of $M_{n+1}X_n$ units are always covered with functional groups such as oxygen, hydroxyl (–OH) and/or fluorine (–F). Hence, the chemical formula of MXenes is represented as $M_{n+1}X_nT_x$, where T_x shows the surface functional groups in MXenes [8]. The multifaceted chemistry of MXenes with interesting mechanical, electronic, magnetic, and electrochemical properties make them special among 2D materials. 2D morphological features with layered structures and high flexibility make MXene a suitable filler material for generating different composite materials, providing an opportunity to assimilate the tremendous properties of several 2D materials in a complementary manner. Because of this, MXenes and MXene related composites have also drawn significant attention to the scientific community in recent years for many applications. MXenes and MXene-based composites materials primarily found applications in energy storage as excellent-performance electrode materials for sodium (Na)-ion batteries, lithium-sulfur (LiS) batteries, and supercapacitors because of their splendid electrochemical performance and greater conductivity [9–11].

Besides its metal oxides, polymers and hybrid materials also play a vital role in the region of physical sciences, such as physics, chemistry, material sciences, and a variety of applications. The oxide materials acquire the broad composition of structural geometries and electronic structures, yielding to its insulator, metallic and semiconductor specification [12–15]. Oxide particles have exhibited distinctive physical and chemical characteristics due to their large density and small particle size [16]. These oxides materials include Al_2O_3, V_2O_5, TiO_2, Fe_2O_3, CeO_2 and

many more [17–23]. Furthermore, polymers and hybrid materials are the formation and combination of two or more materials and compounds (organic and inorganic) having large macromolecules and repeat ting of large molecular chain because of its identical chemical amalgamation of particles. These kinds of hybrid materials are mostly present under the scale range of 1 μm which helps these materials for the sort of various composites of this scale range [24–26]. These materials are the combination of many polymers associated with cold mixture and precondensate. Hybrid materials also exhibit many excellent properties such as chemical resistance, acid toughness, surface adhesion, rapid changing of room temperature, corrosion resistance etc. [27–30]. These polymers and hybrid materials include polysulfides, polyesters, polyurethanes, alkyds, cellulose, polyvinyl alcohol and others [31–36].

This chapter is divided into five sections; each section will cover the comprehensive details of 2D materials based on MXenes, and their composite with metal oxides, polymers, carbonaceous material, chalcogenides and hybrid materials. Furthermore, every section contains tabular information on Mxenes and their composite, including their comprehensive properties, specific parameters, and, most importantly, their applications. Various types of applications mentioned in this section include supercapacitors, batteries, sensors, photocatalysis, solar cells, thermal, dielectric, EMI shielding, bio medicines, aerospace, and many other energy-related applications [37–43].

2 Metal Oxide Doped MXene Composites

With the growing need for smart, compact, wearable, and stretchable electronic items, it is essential to develop suitable rechargeable energy storage devices that are inexpensive to manufacture, resulting in less pollution and increased safety [44, 45]. MXene displays an outstanding electrical conductivity and unique layered structure, enabling it as an attractive supporting material for many metal-ion based battery applications. Xu et al. [46] prepared vanadium pentoxide/MXene ($V_2O_5{\cdot}nH_2O/Ti_3C_2T_x$) composite as a cathodic material for zinc-ion batteries with a simple hydrothermal method. They reported a significant enhancement of electrochemical performance with the addition of MXene into metal oxide (V_2O_5), mainly due to the smart 3D structure of MXene that facilitates the high charge transport and effectively accommodates the zinc ion insertion/desertion with outstanding structural modifications.

Song et al. [47] proposed incorporating MXene composites with manganese oxide (MnO_x) for lithium-sulfur batteries. Figure 1 shows the synthesis of MnO_x/MXene composites and mechanism of their alteration of polysulfides on MnO_x/MXene. Composites of metal oxides with MXene act as chemically active support for the interaction between MnOx and MXene, significantly increasing the oxygen vacancy in the MnO_x materials. The stronger support interaction of oxide between MXene and MnO_x boosted the higher adsorption of polysulfides, and their modification occurred in the cathode. The higher adsorption and conversion of polysulfides formed

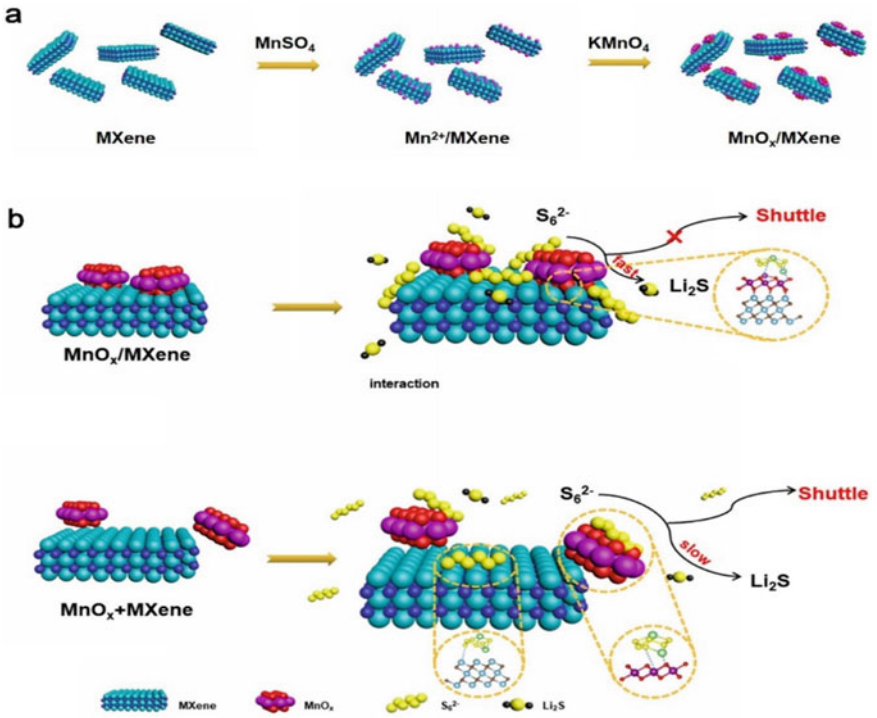

Fig. 1 Synthesis of MnO_x/MXene composites (**a**); the mechanism of conversion of polysulfides on MnO_x/MXene (**b**) [47] (reproduced with permission)

on the cathode surface overcome their loss due to diffusion, leading to enhanced electrochemical performance and stability.

It is well-known that metal oxide-based electrode materials, especially transition metal oxides, have attracted researchers by their easy synthesis in large scale and rich redox reactions, contributing to higher specific capacitance than many carbon-based materials. However, their poor dimensional stability and inherent semi-conductive properties lead to lower specific capacitance and rate capability after a few hundred cycles [48].

Due to excellent stability, rich surface-active sites and the pseudocapacitive contribution of MXene and their composites with different metal oxides have been largely attracted. Wu et al. [49] synthesized nanosheets of heterostructured $NiCo_2S_4$ composites decorated with ultrathin MXene sheets for advanced electrode material in supercapacitors. They found that the surface-functionalized MXene composites (N-Ti_3C_2/$NiCo_2S_4$) showed exceptional electrochemical properties with a specific capacitance of 1879 $F.g^{-1}$, which is far better than the pristine metal oxides or MXenes. They also noticed that the materials retained the cycling stability of 76.3%

even after 5000 cycles, demonstrating remarkable stability. This is mainly due to N-$Ti_3C_2/NiCo_2S_4$ composites with significant specific surface areas, accessible hierarchical 2D structure, and good contact with the electrolyte, allowing more charge/ions transport networks. Huang et al. [50] proposed nanobelt like metal oxide into MXene to prepare sandwich and layered structured composites composed of growing belt-like structure of amorphous $Na_{0.23}TiO_2$ on the surface of MXene sheets. The as-prepared $Na_{0.23}TiO_2$/MXene composite was utilized as a LIB anode electrode material. They reported that the composite material gave impressive cycling life and excellent rate capability. The discharge capacity of the material exhibited an upward trend with the enhancement in continuous 4000 charge–discharge cycles. The excellent stability and rate capability even after 4000 cycles are attributed to a sandwich-like structure with nanobelt of MXene composites that lowers the transfer of ions and successfully releases the electrode strain upon cycling.

Besides the electrode material, metal-oxide doped MXene composites are increasingly used in other important applications such as catalysis, EMI shielding, electromagnetic wave absorption, coatings, sensors, etc. Yin et al. [51] introduced a self-assembled sandwich-like structure of $Cu_2O/TiO_2/Ti_3C_2$ composites which showed outstanding catalytic properties for the degradation of nitro compounds. Generally, the catalytic degradation rate of nitro compounds is used to determine the catalytic properties of any material (Fig. 2).

In $Cu_2O/TiO_2/Ti_3C_2$ composites, no catalytic activity was found in the presence of TiO_2/Ti_3C_2, which clearly shows that the Ti_3C_2 and TiO_2/Ti_3C_2 were failed to perform catalytic degradation of nitro compounds. This occurs due to the poor electrical conductivity of TiO_2, limiting its catalytic activity. However, $Cu_2O/TiO_2/Ti_3C_2$ with the optimized quantity of Cu_2O showed excellent catalytic properties. Cu_2O enables the easy transport of electrons from an electron donor such as $NaBH_4$ to TiO_2 through the surface of Ti_3C_2 (MXene). They also found that the ternary composites ($Cu_2O/TiO_2/Ti_3C_2$) show excellent dimensional stability by more than 92% efficiency after 8 cycles. The main reason for the exceptional stability was due to the larger specific surface area of MXene composite (TiO_2/Ti_3C_2),

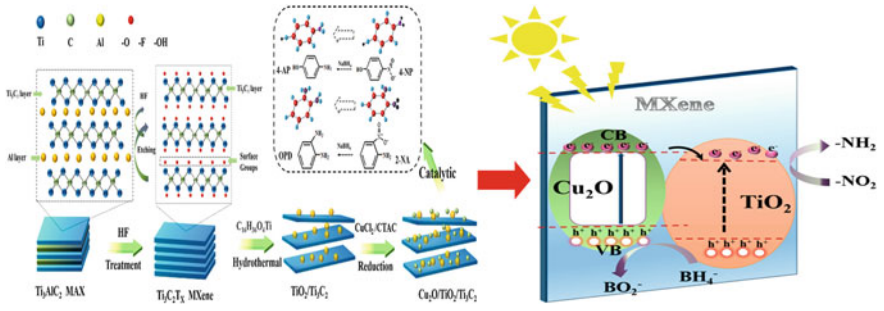

Fig. 2 Synthesis of MXene composites ($Cu_2O/TiO_2/Ti_3C_2$) and their mechanism of catalytic degradation of nitro compounds [51] (reproduced with permission)

enabling Cu_2O to adhere to the surface. Hou et al. [52] synthesized Co_9S_8 decorated MXene hybrid composites using a simple hydrothermal and high-temperature carbonization technique. The as-prepared MXene metal oxide hybrid composites ($Co_9S_8/C/Ti_3C_2T_x$) exhibited excellent electromagnetic (EM) wave absorption properties. MXene composites showed good storage capacity of EM waves and exhibited significant dissipation of EM waves, indicating improved dielectric characteristics of the composite material. The hybrid material of MXene composites with good impedance matching with EM waves makes it easier to dissipate within the material instead of reflection (Fig. 3).

The multilayered composites with many interfaces between MXene and metal oxide increase the loss of conductivity and formation of interfacial polarization, leading to excellent dissipation of EM waves. Liu et al. [53] introduced indium oxide (In_2O_3) nanocubes into MXene composites to examine the methanol gas sensing application at ambient temperature. The In_2O_3 nanocubes decorated MXene composite showed outstanding gas sensing characteristics compared to other pristine metal oxides or pristine MXene. The $In_2O_3/Ti_3C_2T_x$ composites exhibited gas sensitivity from 5 to 100 ppm of methanol concentration within 6.5 s and 3.5 s of response time and recovery time, respectively. This is an outstanding gas sensing performance compared to other gas sensing materials. Comparatively, $In_2O_3/Ti_3C_2T_x$ composites illustrated excellent gas sensitivity because of the unique and large mesoporous surface area of MXenes, enabling the accumulation of many oxygen molecules that significantly improved the sensor response and selectivity. A huge number of hidden functional groups, like −O, −OH, and −F etc., within the multilayered MXene material act as active sites for the adsorption of methanol molecules. The possible mechanism of gas sensing application of $In_2O_3/Ti_3C_2T_x$ as proposed by the authors is shown in Fig. 4.

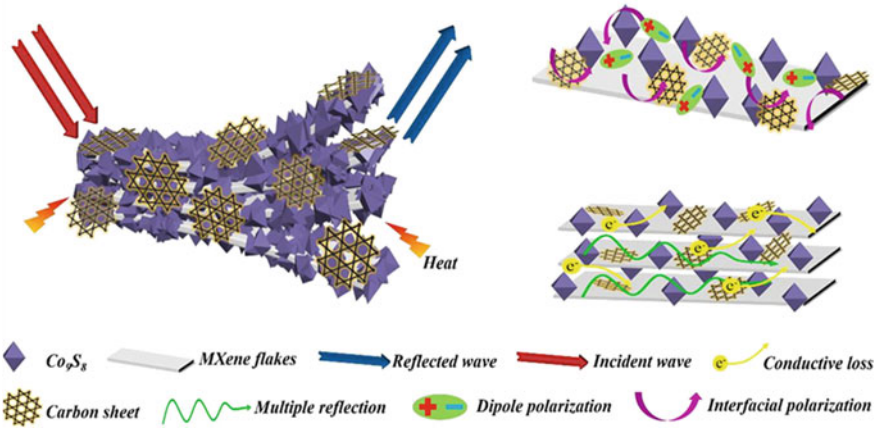

Fig. 3 Schematic representation of the possible mechanism of electromagnetic absorption of MXene composites ($Co_9S_8/C/Ti_3C_2T_x$) [52] (reproduced with permission)

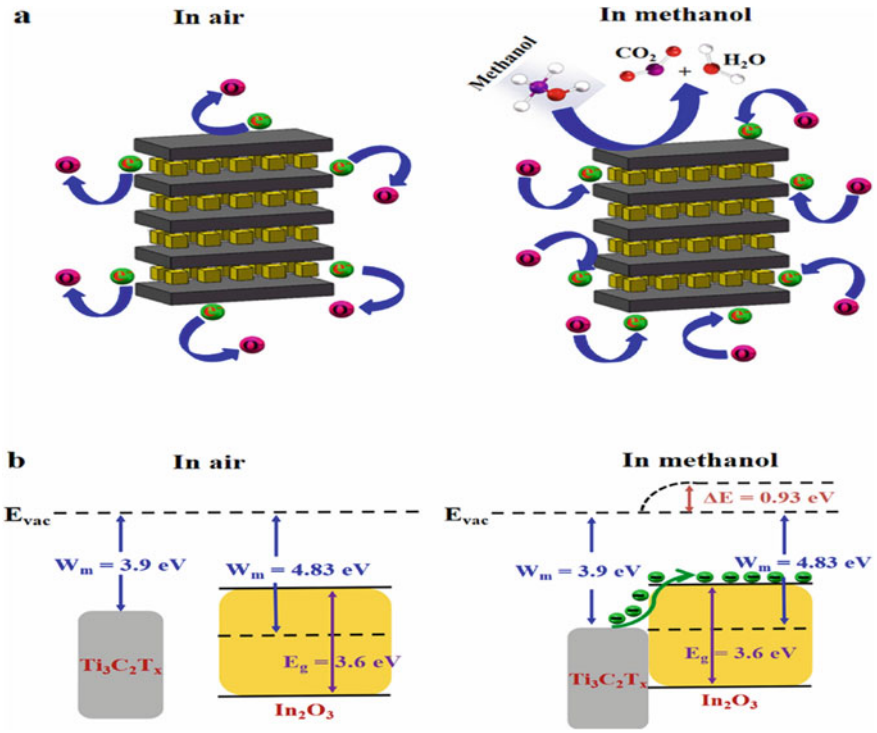

Fig. 4 Possible mechanism of gas sensitivity (**a**) and energy band diagram (**b**) of $In_2O_3/Ti_3C_2T_x$ composites in air and methanol [53] (reproduced with permission)

Similarly, Zhang et al. reported the CoO_x-NiO incorporated with MXene nanosheets prepared via atomic layer deposition route for the potential energy storage supercapacitor applications [54]. The synthesized device based on CoO_x-$NiO/Ti_3C_2T_x$ MXene nanosheet achieved the specific capacitance of 1960 F/g along with the cyclic life of 90.2% after the 8000 cycles. Liu et al. mentioned the MXene composite with rGO and CuO hybrid aerogel for sensing technology. The as prepared MXene/rGO/CuO materials obtained excellent acetone sensing performance at ambient temperature and recorded the 52.09% acetone response toward the 100 ppm [55]. The reported metal oxides to generate composites with MXenes are mainly transition metal oxides, showing excellent properties for various applications such as the battery, supercapacitor, sensing, catalysis, coating, etc. and have illustrated superior performance than their pristine materials as mentioned in Table 1.

Lin et al. [66] proposed a simple method to synthesise a novel 2D photocatalytic composite membrane of $Bi_2O_2CO_3$@MXene with multi-functional material that enables efficient water treatment. They showed that the MXene composite membrane has ultrahigh water flux due to incorporating nitrogen-doped $Bi_2O_2CO_3$ nanoparticles. The MXene composite membrane helps increase the adsorption of dye molecules by electrostatic interaction. The presence of negatively charged functional

Table 1 Describes the MXene and MXene doped oxide and its composite materials according to its potential applications and measuring parameters

S. no	MXenes	Oxides	Measuring parameters	Applications	References
1	$Ti_3C_2T_x$	$LiMn_2O_4$	243 F g^{-1} capacitance 88% life span	Supercapacitors	[56]
2	$Ti_3C_2T_x$	TiO_2	2650 $\mu molh^{-1}g_{cat}^{-1}$	Photocatalysis	[57]
3	Ti_3C_2	SnO_2	126 F g^{-1} capacitance 82% capacity retention	Supercapacitors	[58]
4	Ti_3C_2	TiO_2	43 $\mu molh^{-1}g_{cat}^{-1}$	Photocatalytic activity	[59]
5	$Ti_3C_2T_x$	MnO_2	212 F g^{-1} capacitance 88% cyclic life	Supercapacitors	[60]
6	N-Ti_3C_2	Fe_2O_3	1065 mAh g^{-1} Specific capacity	Li-Ion batteries	[61]
7	N-$Ti_3C_2T_x$	RGO	1180 mAh g^{-1} specific capacity 82.5% capacity retention	Li-Sul batteries	[62]
8	$Ti_3C_2T_x$	RGO hybrid aerogel	23.3 Sm^{-1} electrical conductivity 27.3 dB EMI shielding effect	EMI shielding	[63]
9	$Ti_3C_2T_x$	Metal/ZnO/MXene and Metal/ZnO: Pd/MXene	19,400 nm RIU^{-1} and 8350 nm RIU^{-1} sensitivities	SPR biosensors	[64]
10	$Ti_3C_2T_x$	FTO/TiO_2/$MAPbI_3$	13.83% efficiency	Perovskite solar cell	[65]

groups on the surface of the MXene can adsorb cationic dyes. Moreover, the presence of specific hydroxyl groups and the large specific surface area of MXene play a major role in its adsorption capacity. The sponge-like MXene nanocomposites were synthesized with Gd^{3+} doped vanadium oxide (GVO/MXene) to degrade industrial effluents and pathogens [67]. As compared to the undoped vanadium oxide (VO), the GVO/MXene nanocomposites showed outstanding dye degradation performance of 92% due to the presence of Gd^{3+} and MXene nanosheets in the nanocomposites. Gd^{3+} in the composites improve the light harnessing photodegradation. In addition to this, the high surface area and a large number of active sites on the surface of the MXene enhances the photodegradation ability of GVO/MXene nanocomposites. The GVO/MXene nanocomposites also show superior inhibition of bacterial growth in the presence of GVO/MXene nanocomposites as compared to VO nanoparticles.

3 Polymer-MXene Composites

Polymer-based materials are broadly utilized in our day-to-day life due to their remarkable performance and comfortable processing. In contrast, a single polymer cannot satisfy a range of intended applications. Recent developments in nanotechnology offer solutions for developing composite materials based on polymers with other nanofillers with excellent physical and thermal properties. Significant attempts have been made to tune polymer composites' thermal and mechanical properties by changing the type of filler. In recent years, MXene has been a widely used filler material in the preparation of polymer composites. Due to the excellent hydrophilic surfaces, mechanical properties, and metallic conductivity of MXenes, polymer composites with MXenes could achieve highly enhanced mechanical and thermal properties. It is also reported that incorporating many terminal active sites on the surface of MXenes during etching can increase the correlation between MXene flakes and polymer chains, offering a suitable environment for manufacturing high-performance MXene/polymer composites [68].

Furthermore, MXene possesses covalent and metallic bonds from the bonding point of view, which further tunes the conductive properties and bandgap in the MXene structure. Similarly, the existence of the defect on the MXene surface may advance the charge mobility of the MXene [69–71]. On the other hand, Polymer and MXene contain nanofiller that possess covalent bonding. Hydrogen (H) bonding can also interact with MXene, which assists uniformly and firmly dispersed among the MXene and polymer composite materials and helps create the 3D structure of MXene-polymer. Such as, the composite of MXene with xanthan yielded the hydrophilic polysaccharide $(C_6H_{10}O_5)_n$ with −O functional group was utilized to fabricate this material. Due to the strong H-bonding amidst xanthan and MXene, the MXene can be uniformly divided in the xanthan matrix [72]. Besides it's the oxygen (−O) and hydroxyl (−OH) functional group on surface MXene made the MXene surface negatively (−ve) charged, which yields to make the strong bond, i.e., positive (+ve) charged polymers, like polyethyleneimine and poly-diallyldimethylammonium chloride through an electrostatic interaction [35].

MXene incorporated polymers led to different types of composite materials such as laminated composites/structure [73], MXene coated polymeric fiber [74], composite fiber [75], aerogel, foam/sponge [76], spin-coated electrospun fiber membranes [77], etc. Generally, the preparation methods of composite materials are highly influenced by their end-use applications. Till now, multiple varieties MXene and polymer-based composite materials have been prepared due to synergetic outcomes of inorganic and organic MXene and polymers, respectively. The solution blending technique is commonly used to prepare thin-film types of composites involving the dissolution of both fillers and the polymer in a solvent. The composite materials are formed after mold pouring and evaporation of solvent. To obtain the good dissolution of polymer and filler, thorough stirring is required during solution casting process. Solution blending is the preferred method for the synthesis of MXene-polymer composites due to excellent hydrophilicity of MXene and is also

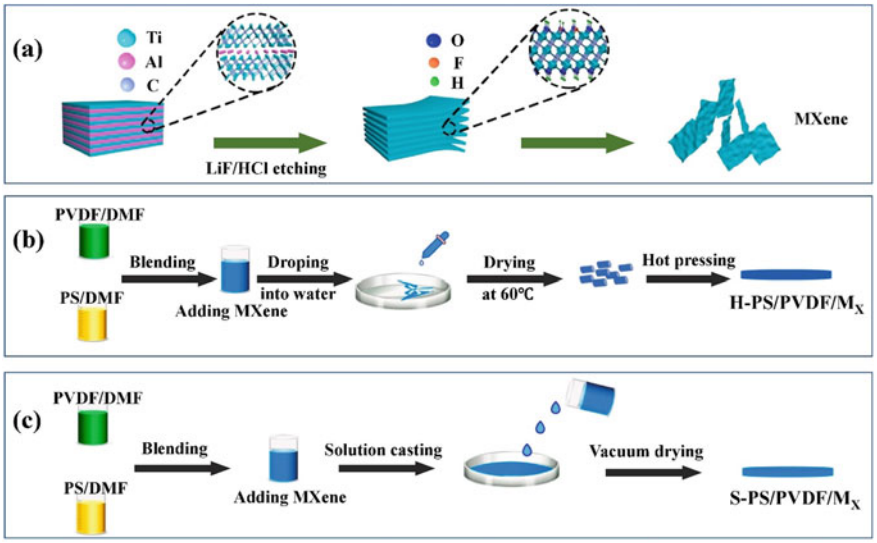

Fig. 5 Preparation methods for $Ti_3C_2T_x$ (MXene) nanosheets and their polymer composites [79] (reproduced with permission)

easy and flexible to manage filler and polymer ratio which improves the dispersion between MXene and polymer [78]. A typical solution blending method for the synthesis of MXene/PS/PVDF hybrid polymer composites is shown in Fig. 5.

Jin et al. [80] synthesized poly(vinyl alcohol) (PVA)/MXene multilayered films by solution blending method. This alternative arrangement of MXene and PVA multilayered and continuous thin films is excellent for the conduction of heat and electrons, which endows excellent electromagnetic interference (EMI) shielding and thermal conductivity. Liu et al. [81] used solution casting and vacuum-assisted filtration to synthesize MXene/chitosan films to apply for high-performance EMI shielding. Vacuum-assisted filtration was the best method to achieve the required thickness of MXene/Chitosan films and well-aligned MXene sheets on chitosan. The maximum shielding effect can be achieved due to tunable film thickness, aligned nanosheet structure, and outstanding metallic conductivity. The 37-micron thick MXene/chitosan at a $T_3C_2T_x$ content of 50% reached the specific shielding effectiveness to 15,153.9 ± 153 dB/cm, which outperformed the testified biomass-based EMI shielding composites in the X-band frequency. In most cases, it is necessary to adopt multi fabrication techniques such as solution blending and melt blending to achieve excellent dispersion and reduce agglomeration [82]. Melt blending is a highly preferred fabrication method for preparing high-performance polymer composites where high mechanical, thermal and flame-retardant properties are required due to their excellent dispersion and low agglomeration of nanofillers (Fig. 6).

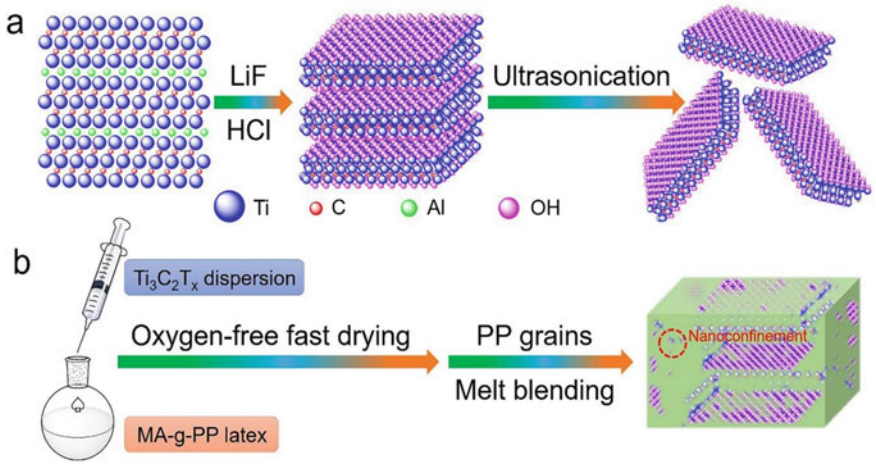

Fig. 6 Schematic diagram exhibiting the fabrication of MXene and preparation of MXene/PP composites by melt blending [82] (reproduced with permission)

Ming-Ke Xu et al. reported the $Ti_3C_2T_x$ MXene/polypropylene (PP) nanocomposite for highly effective EMI shielding [83]. The nanocomposite yielded an electrical conductivity of 437.5 C/cm along with the EMI shielding effect of 60 dB, confirming the tremendous performance of this material. Xue et al. [84] reported the fabrication of Polyphosphoramide (PPDA)-intercalated MXene incorporated polylactide (PLA) biocomposites with excellent mechanical, thermal and flame retardant properties. They found that the combination of PPDA and MXene filled PLA composites showed good flame retardant and excellent mechanical properties. This is mainly because of the homogeneous dispersion of PPDA and MXene nanofillers across the PLA matrix, offering effective load transfer and enabling fracture energy dissipation when the external load is applied to the matrix. The major advantage of using MXene as a filler in any polymer matrices is its enormous negative charge sites across the MXene surface. These charged sites and functional groups of polymer surface can form an interlinked network, leading to efficient transportation of electron and load transfer, resulting in excellent electrical conductivity and improved mechanical and thermal properties [85, 86].

Like graphene oxide, vast numbers of functional groups on the surface of MXene nanosheets present higher possibilities to interlink between nanosheets and polymer matrices, leading to improved mechanical properties. A larger number of hydrogen bonds on the surface of MXene nanosheets and polymer matrices easily form rigid and cross-linked networks between them, leading to significantly improved thermal, mechanical, and flame retardant properties of the resultant polymer composites [87]. Zhao et al. [88] demonstrated that rich hydroxyl groups bonding together in MXene and PVA made it possible to get highly stable and flexible polymer composites. They found that the tensile modulus significantly increased by 100 times for adding 30% MXene into PVA compared with pristine MXene thin film (2.87 MPa). This is

highly significant since elastic modulus was calculated based on interfacial cross-linking between filler and polymer. When the delaminated MXene nanosheet was chemically blended with PVA, the hydrogen bonds were formed with the surface functional groups of polymer matrix and MXene nanosheets, which enhanced the interfacial binding energy (BE) to increase the mechanical properties of resultant composites. In addition, the unchanging dispersion of d-Ti_3C_2 in polyvinyl alcohol was helpful to increase the intermolecular forces to further enhance the mechanical properties of MXene-polymer composites. Zhou et al. prepared the nanocellulose polymer mixed with MXene with the help of the spray coating technique [89]. The nanocellulose nanofiber and MXene composite were employed for the EMI shielding effect and electro-photothermal performance. The synthesized Ti_3C_2 MXene/cellulose nanofiber, when tested, it yields a mechanical strength of more than 250 MPa, excellent desirable toughness of 20 Mj/cm^3 and EMI effect of 60 Db. Similarly, Shi et al. [82] developed a high-performance polymer composite relying on PP and MXene inspired by natural 3D networks such as silkworm net, honeycomb and spider web. They used solution casting followed by melt blending to fabricate ultra-thin 2D nanocomposites of PP and MXene. They reported that the tensile strength of MXene/PP composites enhanced with increasing the loading of MXene. This is mainly due to hydrogen bonding between PP polymer and MXene filler, hindering the free mobility of the polymer chains and causing an enhancement in the tensile properties of the composites as compared to pristine polymer. By adding 2 wt% Mxene nanosheets, they achieved an increase of 35.3%, 674.6% and 102.2% in the tensile strength, ductility and modulus, respectively. A large number of hydrogen bonds induced nanoconfinement is responsible for the increased mechanical properties. However, elongation at break reduced with a small loading of MXene filler and then significantly increased mainly due to bond slippage in the interface of filler and polymer and reduced number of hydrogen bonds due to the agglomeration of filler. In in-situ polymerization tactic, the mixture containing polymer precursors, fillers and curing agents (or initiators) are initially premixed in solutions, and then it polymerized to create macromolecules under specific conditions. The major advantage of this technique is that good dispersion of functionalized nanoparticles could be achieved within the polymer matrices [90]. Carey et al. synthesized MXene/Nylon-6 nanocomposites by in situ ring-opening polymerization of ε-caprolactam and achieved well-exfoliated nanocomposites with significantly improved water transporting properties of the resultant nanocomposites. Due to the rapid growth of technology, adopting conventional manufacturing methods brings huge challenges to end-use applications. Hence, it is necessary to think out of the box to utilize the unlimited potential of materials properties to convert them into required end-use applications. Zheng et al. [91] reported a unique particle construction strategy called heterogeneous agglomeration to fabricate highly conductive and stable MXene incorporated polystyrene (PS) composites (MXene/PS composites), where PS emulsion converted into uniform sized 3D microspheres (PS particles), and MXene sheets were then incorporated into PS particles (Fig. 7). MXene nanosheets were completely filled between the PS particles along with strong adsorption of MXene sheets on the surface of PS particles during the strong suction filtration process, enabling strong orientation of MXene

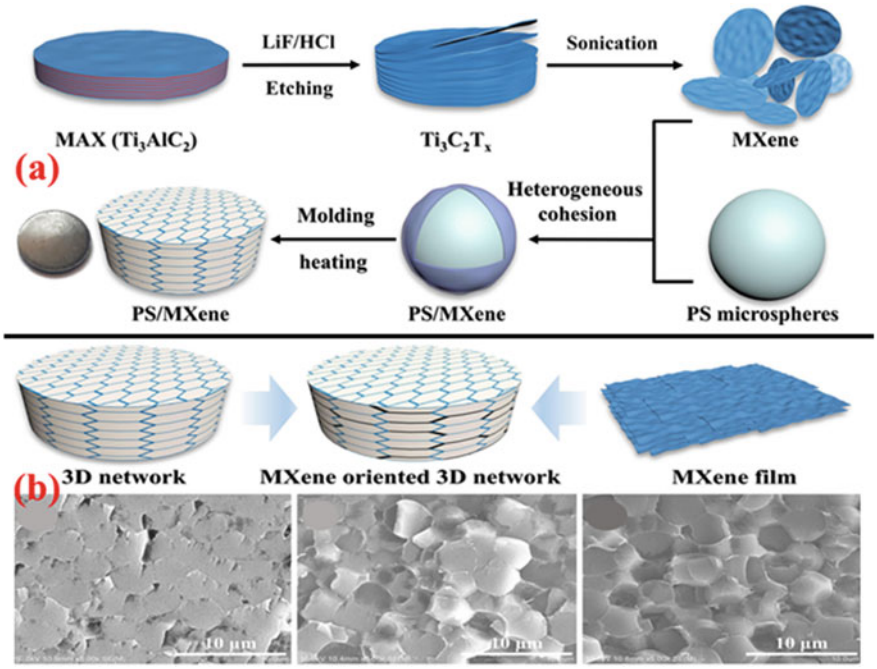

Fig. 7 Synthesis of MXene (**a**) and schematic illustration of MXene oriented 3D network structure and their cross-sectional SEM image of polystyrene composites (**b**) [91] (reproduced with permission)

sheets within the composites. This strong orientation of MXene nanosheets across the polymer composites drastically enhanced the resultant composite's mechanical, physical, thermal, and electrical performance. Due to the efficient and well-ordered structure of MXene/PS composites, the conductivity increased significantly to 3846.15 S m^{-1} with the addition of just 1.81% of MXene filler. The obtained conductivity is significantly higher than other PS composites reported so far. The flame-retardant and EMI shielding nanocoatings onto cotton fabrics were applied by layer-by-layer self-assembled technology using tannic acid modified MXene synthesized P, N-co-doped cellulose nanocrystals (TA-Mxene and PA@PANI@CNC) [92]. The resultant nanocoatings show that cotton fabric's EMI shielding efficiency (SE) with 20 bilayers coatings (Cotton-20BL) reaches up to 21 dB over the X- band frequency range. Moreover, the Cotton-20BL reaches an excellent limited oxygen index of 32. More importantly, the peak heat release rate and total smoke production are reduced by 63.0% and 98.3%, respectively. As compared to pristine cotton fabrics, the high absorbance intensities of flammable volatiles and toxic gas, including carbonyl compounds, aliphatic ethers, CO and CO_2, are markedly reduced due to the nanobarrier effect of 2D MXene and catalytic carbonization effect of PA. The Mxene nanocomposite coatings also shows good electrical conductivity and improve

chemical stability due to presence of 2D $Ti_3C_2T_x$ nanosheets which contribute to the dissipation of electromagnetic microwaves.

For more clarification regarding MXene and polymer materials, Table 2 describes several MXene and polymers regarding their unique characteristics, measurements values, and applications.

4 Carbon-Based MXene Composites

Numerous types of carbon-based nanomaterials like graphene oxide (GO), porous carbon (PC), carbon nanotubes (CNTs), carbon dots (CDs), fullerene, and carbon nanohorns (CNHs) have been exploited for potential applications in the areas of electronics, biology, medicine, environment, etc., owing to their unique physical and chemical characteristics [102–104]. The novelty of the material plays a vital role in the new technological advancements. Sun et al. [105] proposed a novel composite of MXene incorporated nitrogen-doped carbon foam (NCF) with 3D hallow neurons like architecture for solid-state supercapacitors. The authors claimed that the as-prepared MXene/NCF demonstrated a remarkable (332 F g^{-1}) capacitance, 3162 mF cm^{-3} volumetric capacitance of 64% rate capacity, which is more than 99% retention of its capacity after ten thousand cycles. The remarkable electrochemical performance was achieved due to the as-prepared 3D hollow interconnected neuron-like architecture with highly compressible, large specific surface area and highly flexible electrode of MXene/NCF composites. Zhao et al. [106] fabricated $Ti_3C_2T_x$-CNT composites and utilized this for ECs. As-prepared composites having $Ti_3C_2T_x$ and CNT layers were alternately deposited on top of each other until the total number of layers reached 6–10, which looked like a sandwich-like superposition of the MXene and CNT layers. The as-prepared electrode material for the supercapacitor, these layers exhibited superior volumetric capacitance and rate performance compared to pristine MXene. The volumetric capacitance of the $Ti_3C_2T_x$-CNT electrode increased from 340 F cm^{-3} to 370 F cm^{-3} after the 10,000 charge discharge cycles, and exhibits 55% rate which is much higher than as compared to $Ti_3C_2T_x$ electrode. A key reason for the outstanding electrochemical performance exhibited by the $Ti_3C_2T_x$-CNT composite is that CNT expands its interlayer space for an intercalation of cation, and therefore enhances the diffusion paths for electrolyte ions.

Zhou et al. [107] used V_2C and Mo_2C based MXenes, and nitrogen-doped graphene to obtain MXene/graphene composites and used them as hydrogen evolution reaction (HER) and bifunctional electrocatalysts for oxygen reduction reaction (ORR. They noticed that a minimal overpotential for ORR could be as low as 0.3 V, including a kinetic barrier of 0.2 eV. The HER process had free energy of hydrogen adsorption ($\Delta GH*$) close to one, and the reaction barrier to Tafel was as low as 1.3 eV. Graphene heterostructures exhibit favorable properties due to the strong electron transition between the MXene and graphitic sheet, altering the graphene band profile and the band center relative to the Fermi level.

Table 2 MXenes and their composite materials according to their potential applications and measuring parameters

S. no	MXenes	Polymer	Measuring parameters	Applications	References
1	$Ti_3C_2T_x$	Polypyrrole	9.5 mF/cm^2 capacitance 250 mWh/cm^3 energy density	Micro-supercapacitors	[93]
2	$Ti_3C_2T_x$	PVA	17–716 S m^{-1} electrical conductivity 0.1–4.5 W m^{-1} K^{-1} thermal conductivity	EMI shielding and thermal conductive	[94]
3	$Ti_3C_2T_x$ carbon nanotube	Polycaprolactone	30–50 mF/cm^2 areal capacitance	Flexible energy storage	[77]
4	d-Ti_3C_2	PVC	11,800 dielectric constant 3.48 W m K^{-1} thermal conductivity	Dielectric properties	[95]
5	Ti_3C_2	PANI	164 F g^{-1} specific capacitance	Supercapacitors	[96]
6	$Ti_3C_2T_x$	PEDOT:PSS	30.8 F g^{-1} specific capacitance	Supercapacitors	[97]
7	$Ti_3C_2T_x$	PDMS/Au/Ti$_3C_2T_x$/SiO_2/*n*-Si/In:Ga	10.22% efficiency	Photovoltaic cell	[98]
8	$Ti_3C_2T_x$	PANI	−56.30 dB reflection loss	EMI shielding and microwave absorption	[99]
9	Ti_3C_2	Thermoplastic polyurethane	47.1% tensile strength 39.8% storage modulus	Thermo related industries	[100]
10	$Ti_3C_2T_x$	PVA	528 F/cm^3 volumetric capacitance	Supercapacitors	[101]

MXene/GO composites can be utilized for many potential applications owing to their good electrical conductivity and enormous specific surface area [108]. The low thermal conductivity and poor flame retardant properties of graphene have limited its potential applications, such as thermal management. Micro-processing devices are used in many modern-day electronics, tend to generate a lot of waste heat and create high energy hot spots, causing lower performance and long life of the electronic devices [109]. The combination of MXene and GO 2D materials offers thermal management in the microprocessors in many electronic devices. Wan et al. reported the 2D bi-metal (Fe-Te) oxide/carbon/$Ti_3C_2T_x$ MXene for high performance Li-ion storage [110]. The synthesized prepared material having the composition of $(Fe_{2.5}Ti_{0.5})_{1.04}O_4$/C/$Ti_3C_2T_x$ MXene obtained the 757.2 mAh/g discharge capacity after the 800 charge–discharge cycles. Liu et al. [111] reported that paper-like composite material synthesized from GO and MXene composites showed excellent thermal conductivity and flame retardant properties. The authors found that by adding 40% MXene sheets into GO, the thermal conductivity increased by 184% compared to the pristine GO. In GO, the heat conduction occurs through phonon diffusion through lattice vibrations of its covalent sp^2 hybridization. The GO sheets were thermally resistant to phonon scattering due to many surface defects and grain boundaries. However, the addition of MXene nanosheets and the reduction of GO content in the MXene/GO composite film exhibit more sp^2 hybridized carbon structure that offers effective channels for phonon migration, leading to increased thermal conductivity (Fig. 8). Concerning flame retardancy properties, the presence of a large number of hydroxyl groups on the surface of GO leads to poor flame resistance ability. However, the addition of MXene nanosheets into nanosized TiO_2 acts as an effective thermal barrier at the high-temperature flame. It assists in removing hydroxyl groups on the GO surface, leading to increased fire resistance and conversion of GO into RGO (reduced graphene oxide) [111]. The authors noticed that 40% of MXene nanosheets into GO showed an extremely low heat release rate, and char residue was 91.36%, 10 times higher than pristine GO.

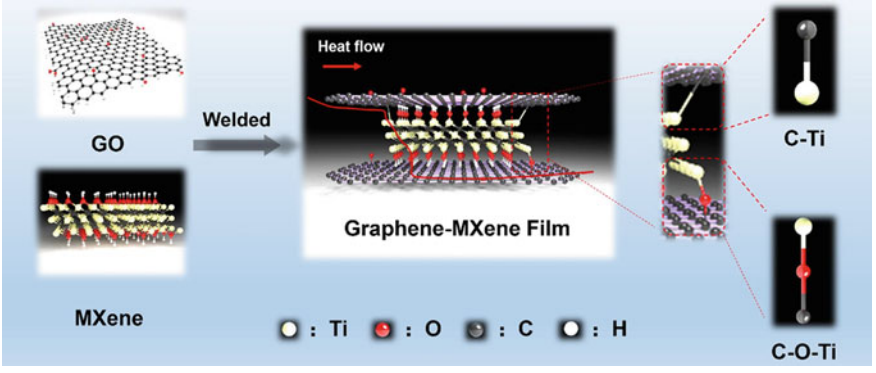

Fig. 8 Schematic representation of LED and its subsequent IR thermal image [111] (reproduced with permission)

Recently, Qi et al. reported the $Ti_3C_2T_x$ MXene composite with starch-derived carbon foam (MPCF) for thermal insulation and electromagnetic interference shielding effect [112]. The as-prepared carbonized PCF electrical conductivity of 21.8 S/cm and compression strength of 4.9 MPa at 1400 °C. Moreover, this material gained the specific shielding effect and EMI shielding effect of 216 cm^3/g and 75 dB, respectively. Aissa et al. [113] synthesized a sandwich type of composite structure using MXene and graphene nanoplatelets (GNPs) by electrohydrodynamic atomization deposition method as a potential thin film for EMI shielding applications in extremely high-frequency M-band from 60 to 80 GHz. The as-prepared thin films below 2 μm showed good electrical conductivity, outstanding electron mobility and very high EMI shielding properties. The outstanding properties of MXene/GNPs composite thin films were due to the deposition of GNPs on the surface of MXene nanosheets, creating a cross-linked conductive network across the thin film that offers extra electrons and conductive pathways within the composite layers. GNPs have also increased the electron flow of the composite film by closing pin-holes on the surface of MXene nanosheets (Fig. 9).

Friction and wear materials are becoming crucial for technological developments to reduce material losses caused by friction and wear. Few 2D materials such as molybdenum disulfide (MoS_2), graphene and graphene oxide (GO) are used in lubricant applications in the transportation and industrial sectors [114, 115]. Some reports claim that MXene is an excellent 2D solid lubricant material [116]. However, the hydrophilic nature of MXene and high reactivity towards water vapor and other gases lead to structural degradation [117]. The above problem can be overcome by incorporating other 2D materials into MXene [118]. A unique heterostructure

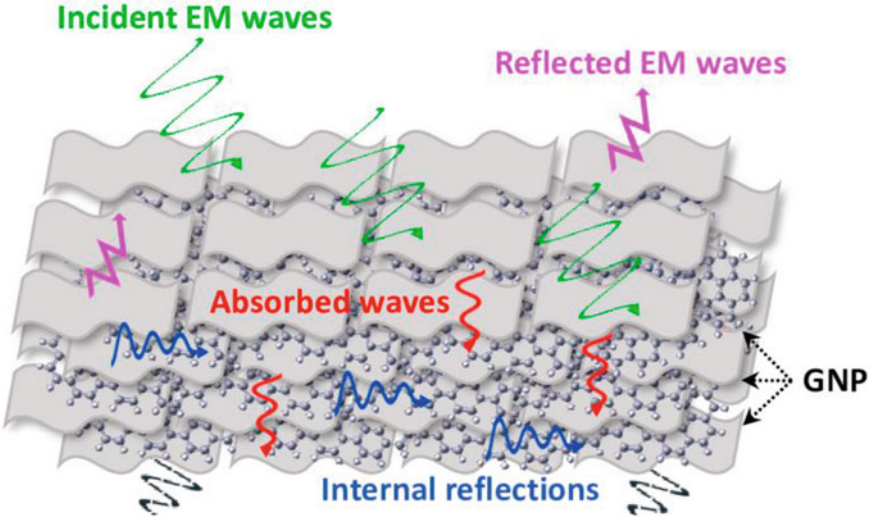

Fig. 9 Schematic representation of different governing phenomena during EMI shielding of 2D sandwiched MXene/GNPs composite thin films [113] (reproduced with permission)

can be obtained by mixing MXene nanosheets and GO. These distinctive composites of MXene/GO offer excellent tribological performance in both air and nitrogen atmosphere. Apart from individual merits of MXene and GO, the heterostructure of MXene/GO coating displayed improved stability at dry nitrogen atmosphere due to their existence of continuous and even distribution of composite layers [119]. Huang et al. [118] introduced MXene/graphene coatings to achieve superlubricity under a nitrogen atmosphere. They coated MXene/graphene composite on SiO_2 coated silicon (Si) substrate and subjected to wear by sliding against diamond-like carbon-coated steel ball to check the friction of coefficient (COF) and wear properties. COF was significantly reduced by 3.3 times compared to Si substrate, and with the addition of graphene by 37%, COF was further reduced by 37.7% compared to pristine MXene. Yang et al. [120] reported 3D MXene carbon nanotube (3D MXene-CNT architecture electrode by gel assembly and chemical vapor deposition method for Li-ion batteries (LIBs) as anode materials. The as-synthesized 3D Mxene-CNT electrode shows a good reversible capacity of 590 mA h g^{-1} at 0.1 A g^{-1} and outstanding rate performance with a capacity of 191 mA h g^{-1} at 5.0 A g^{-1}. The LIB device with 3D Mxene-CNT electrode demonstrates a high energy density of 201 Wh kg^{-1} at a power density of 210 W kg^{-1}, and an excellent energy density of 92 Wh kg^{-1} even at a high-power density of 21 000 W kg^{-1}, as well as good capacity retention of 84.7% after 3500 cycles at 2.0 A g^{-1}. The excellent performance of The LIB device with 3D Mxene-CNT electrode was due to exposure of a high number of Ti atoms on the surface of the MXene, which boosted the redox reaction. Table 3 specifies the various carbon materials synthesized with MXene for different applications.

5 Chalcogenides-Based MXene Composites

MXene 2D materials have many advantages: large specific surface area, large interlayer distance, superior electrical and thermal conductivity. However, layer restacking is one of the major drawbacks of MXene owing to hydrogen bonding or van der Waals forces between the layers which considerably hinder the utilization of MXenes for their full potential. Transition metal chalcogenides and dichalcogenides (TMCs) based nanomaterials such as sulfides (S), selenides (Se), tellurides (Te), MoS_2, WS_2, and $MoSe_2$ have been explored significantly as electrode materials in recent years owing to their excellent specific surface area, atomically thin layered arrangement, superior electrical properties, and stability [129, 130]. These chalcogenide-based nanomaterials can be used to overcome the shortcomings arising from MXene by dispersing uniformly on the surface of each layer of MXene, reducing the restacking of the MXenes and enhancing the electrochemical properties due to their synergistic interaction between MXene and TMCs [131]. Li and co-workers proved that the MXene alone is ineffective for aluminium batteries and also mentioned that conductivity increased significantly with MXene composites doped with cetyltrimethylammonium bromide (CTAB) and selenium. The MXene alone in an aluminium battery initially exhibits the specific capacity of 150 mAh

Table 3 Carbon-based MXene composites

S. no	MXenes	Carbon type	Measuring parameters	Applications	References
1	$Ti_3C_2T_x$	CNTs	130 S/cm conductivity 58 and 187 dB $cm^2\ g^{-1}$	EMI shielding	[121]
2	$Ti_3C_2T_x$	Cellulose	−43.4 dB reflection loss	Microwave absorption and aeronautics	[122]
3	Mixed-$Ti_3C_2T_x$	SWCNT	300 F/cm^3 volumetric capacitance 286 S/cm conductivity	Electrochemical capacitors	[106]
4	Sandwich-like $Ti_3C_2T_x$	SWCNT	390 F/cm^3 volumetric capacitance 385 S/cm conductivity	Electrochemical capacitors	[106]
5	$Ti_3C_2T_x$	CNTs	103.9 dB reflection loss	EMI shielding effect	[123]
6	2D $Ti_3C_2T_x$	Cellulose fiber	35 mg/g desalination capacity	CDI water desalination	[124]
7	Ti_3C_2	Nanodots-interspersed	1957 mAh cm^{-3} volumetric capacity 13.7 mAh cm^{-2} areal capacity	Li–S batteries	[125]
8	Ti_3C_2	CNTs	0.043% fading rate	Li–S cathode	[126]
9	$Ti_3C_2T_x$	CNTs	130% ctretchability 772.6 gauge factor 30–130% sensing range	Sensors	[127]
10	Ti_3C_2	CNTs and cellulose	97.9 ± 5.0 MPa tensile strength 4.6 ± 0.2% fracture strain 2506.6 S/m electrical conductivity and 38.4 dB loss	EMI shielding effect	[128]

g^{-1}. However, after 100 cycles, the specific capacity reduced drastically to 42.8 mAh g^{-1}. MXene composites with CTAB and Selenium (Ti_3C_2@CTAB-Se) showed significant improvement of specific capacity even after 100 cycles. They reported that MXene composites (Ti_3C_2@CTAB-Se) showed a 583.7 mAh g^{-1} specific capacity of 100 mA g^{-1}. Its capacity was still retained to 132.6 mAh g^{-1} even after 400 cycles, showing excellent electrochemical performance of MXene composites (Ti_3C_2@CTAB-Se) compared to pristine MXene. This is due to the reduction of conductivity and stability of MXene, which shows a drastic drop in the specific capacity. However, for MXene composites, specific capacity increased due to increased stability and more active sites, leading to increased electron transfer [132].

Huang et al. [133] synthesized 3D architectures of a few-layered like MXene composites (Ti_3C_2@$NiCo_2Se_4$) anchoring bimetallic nanoparticles of Nickel cobaltous selenide as anode material for SIBs. To fabricate MXene nanosheets, they adopted a novel and a facile solvothermal methodology to support a solution-phase flocculation approach to evade the restacking problem of few-layered Ti_3C_2 MXene nanosheets. In addition, to further stop the self-restacking of MXene nanosheets, they uniformly decorated the zero-dimensional bimetallic selenide $NiCo_2Se_4$, which acts as Na^+ ion reservoir and leads to superior redox activity onto the surface of MXene composite nanosheets and also avoids restacking issues in the MXene sheets as shown in Fig. 10.

The presence of functionalized MXene (f-MXene) nanosheets in f-Ti_3C_2@$NiCo_2Se_4$ composites have a great advantage which endows the composite materials to a rapid electron-Na^+ ion transport capability and, due to the high specific surface of MXene sheets, it enhances the quick charge transfer kinetics and increased interfacial contact between electrolyte–electrode within the battery system. Besides,

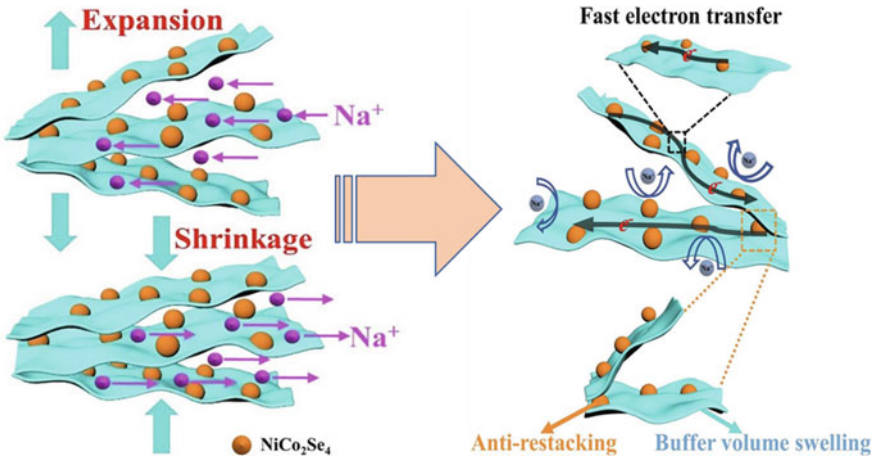

Fig. 10 Schematic representation of expansion and shrinkage abilities and excellent cycling/rate performance mechanism of Ti_3C_2@$NiCo_2Se_4$ composites (reproduced with permission) [133]

as shown in Fig. 11, f-MXene nanosheets were highly flexible to the presence of many surface functional groups that act as a flexible skeleton to dissipate strain caused by $NiCo_2Se_4$ nanoparticles during cycling and restrain pulverization. These excellent properties of MXene nanosheets are responsible for the excellent stability and outstanding electrochemical performance of f-Ti_3C_2@$NiCo_2Se_4$ composites in the sodium-ion battery systems.

Chen and co-workers proposed a novel one-step hydrothermal method to prepare MXene composites with in situ growth of CuSe nanoparticles on the surface of MXene nanosheets. The as-synthesized MXene composites (Ti_3C_2@CuSe) were used as highly efficient counter electrode (CE) material for quantum dot (QD) sensitized solar cells (SCs), showing superior electrical conductivity and polysulfide electrolyte reduction due to their large specific surface area compared to pristine MXene and CuSe nanoparticles [134]. Zong et al. [135] proposed bifunctional electrode materials for lithium storage based on metal–organic frameworks (MOFs) derived CoP anchored MXene composites. They claimed that MXene nanosheets in the MOFs-CoP@MXene/S composites act as a highly stable template for MOFs-CoP, avoiding the enlargement of MOFs-CoP materials on the surface of MXene, yields to exerting its catalytic capability. In addition, since MXene nanosheets have a large number of surface functional groups and high specific surface area, which enhance the possession of LiPS and inhibit the dissolution of polysulfide in the electrolyte. The graphene-like structure of MXene nanosheets exhibits excellent properties such

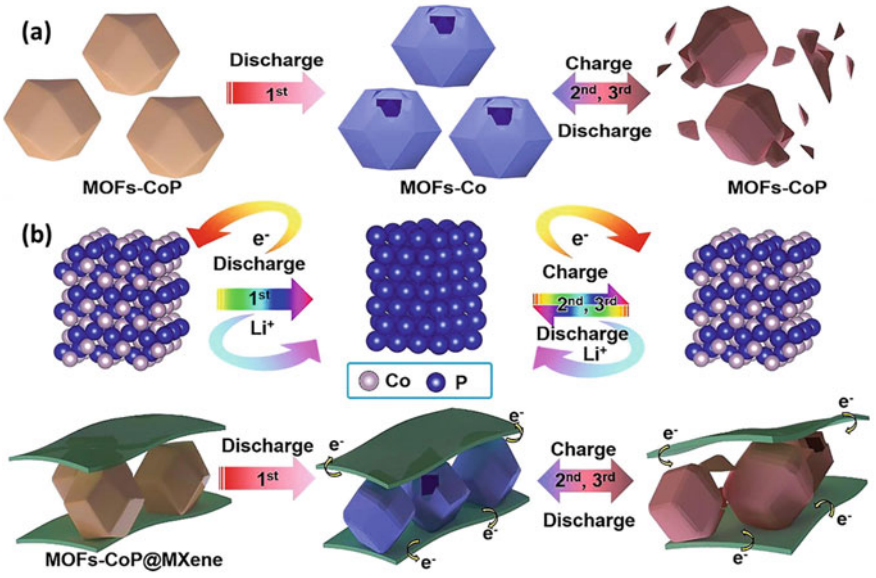

Fig. 11 Schematic representation of MOFs-CoP nanoparticles showing instability (**a**) and their protection and enhanced structural stability under the protection of MXene during cycling (**b**) [135] (reproduced with permission)

as high dimensional stability and superior conductivity within a 3D network of decorating materials on its surface, resulting in excellent electrochemical activities of MXene based composites. The authors demonstrated that MXene composites (MOFs-CoP@MXene/S) as anode material for Li-ion batteries display a high capacity of 706.5 mAh g^{-1} even after 200 cycles at 0.2 A g^{-1}, indicating that MOFs-CoP@MXene/S composites as anode material have robust Li-ion storage capacity. This indicates that it can increase the charge transfer rate and improve Li^+ diffusion kinetics with greater electrochemical activity. The authors proposed a stability mechanism, as shown in Fig. 11. The polyhedral morphology of MOFs-CoP alone showed poor structural stability and got damaged due to charge/discharge cycles since it undergoes large volume changes as an anode material. However, when made composite with Mxene, MXene acted as a substrate to MOFs-CoP nanoparticles and retained their dimensional stability.

Li and co-workers proposed synthesizing MXene nanosheets based composites by combining two or more dichalcogenides which was an effective strategy to exploit their performance as anode materials for Li-ion batteries [136]. They confirmed that SnS_2/Sn_3S_4 dichalcogenides hybrid nanoparticles restricted restacking issues in MXene nanosheets and significantly improved composite's performance. The multilayered Ti_3C_2 MXene nanosheets improved electron mobility, prevented dichalcogenide nanoparticles' agglomeration, and accommodated their volume change during the charge and discharge cycles. They reported that the dichalcogenide based MXene composites showed the best cycling performance (462.3 mAh g^{-1} at 100 mA g^{-1} after 100 cycles) and good rate performance (216.5 mAh g^{-1} at 5000 mA g^{-1}). Recently, Geun Oh and co-workers reported N-doped C-coated $CoSe_2$ incorporated with Ti_3C_2 MXene for electrochemical sodium (Na) and potassium (K) ion storages [137]. $CoSe_2$@NC/MXene attained the reversible capacities of 358 mAh g^{-1} and 317 mAh g^{-1} for potassium and sodium ion storage. In addition, this material achieves the capacitive contribution of 93%, which helps to enhance the kinetic charge transfer performance under the charging and discharging process. Moreover, in Table 4, we also mentioned other chalcogenides materials with MXene and its applications. A ZnCdS/TiO_2/Na-MXene nanocomposites were synthesized by a facile hydrothermal method in which Na^+ and ZnCdS nanoparticles were wrapped by MXene nanosheets [138]. This novel ZnCdS/TiO_2/Na-MXene nanocomposites shows an excellent photocatalyst with a photo-corrosion resistant property. The MXene restacking was minimized due to the intercalation of ZnCdS, which could facilitate the transportation and adsorption of organic pollutants in ZnCdS/TiO_2/Na-MXene nanocomposites. It is evident that the ZnCdS/TiO_2/Na-MXene nanocomposites show an excellent separation competence of electron–hole pairs and outstanding transfer efficiency of electrons on the surface of the MXene nanosheets because of their high electron conductive property.

Table 4 Chalcogenides-based MXenes composites

S. no	MXenes	Chalcogenides	Measuring parameters	Applications	References
1	$Ti_3C_2T_x$	MoS_2	290.7 mAh g^{-1} capacity	K-Ion batteries	[139]
2	$Ti_3C_2T_x$	Co-NiS	911 mAh g^{-1} capacity for Li-Storage 542 mAh g^{-1} capacity for Na-Storage	Li and Na storage batteries	[140]
3	$Ti_3C_2T_x$@C	$MoSe_2$	355 mAh g^{-1} capacity	K-Ion batteries	[141]
4	3D $Ti_3C_2T_x$	N-$CoSe_2$	1084 Wh kg^{-1} energy density	Zn-air batteries	[142]
5	Mo_2CT_x	2H-MoS_2	-450 mA $cm^{-2}{}_{geom}$	Hydrogen evolution reaction (HER) And water splitting application	[143]
6	$Ti_3C_2T_x$	MoS_2	0.39 pg mL^{-1} limit of detection (LOD)	Electrochemical aptasensor	[144]
7	$Ti_3C_2T_x$	MoS_2	-65.51 dB reflection loss	Microwave absorption	[145]
8	$Ti_3C_2T_x$	CdS-MoS_2	9679 μmol.g^{-1} h^{-1} 2.63 ns photoluminescence life time	Photocatalytic H_2 generation	[146]
9	Ti_3C_2	1 T-MoS_2	386.7 F g^{-1} specific capacitance 91.1% retention	Supercapacitors	[147]
10	$Ti_3C_2T_x$	BlueP/MoS_2	203°/RIU sensitivity	Biosensors	[148]

6 Organic Hybrid-MXene Composites

Hybrid composites of two or more materials are always effective for enhancing structural stability and overall performance. Moreover, it is well known that the MXene nanosheets alone are not enough for the required performance in many applications such as batteries, EMI shielding, dielectric materials, etc. Zhang et al. [149] proposed a 3D hybrid composite synthesized by a facile and simple method involving TiO@nitrogen doped carbon/Fe_7S_8 with in situ polymerization of polypyrrole monomer on alkalized MXene for lithium-ion batteries anode material. This MXene hybrid composite (TiO_2@NC/Fe_7S_8) has exceptional architecture where 3D urchin-like TiO_2 with good dimensional stability offers suitable space to improve the contact between electrode–electrolyte. In addition to this, the MXene hybrid composite limits the diffusion rate of lithium-ion and improves the volume change. Nitrogen-doped carbon shell layer increases the electrical conductivity, enables the transportation of electrons, and avoids the accumulation of Fe_7S_8. Fe_7S_8 provides high specific capacity during the charge and discharge process. The MXene composites (TiO_2@NC/Fe_7S_8) showed excellent electrochemical activity such as the reversible capacity of 516 mAh g^{-1} after continuous 100 charge/discharge cycles at 0.1 A g^{-1},

terrific rate capability of 337 mAh g^{-1} at 1 A g^{-1} current density and also a robust long-life span of 282 mAh g^{-1} after the 1000 charge and discharge cycles at 4 A g^{-1}.

Yao et al. [150] made the 3D hierarchical porous hybrid MXene composites derived from CoS based MOF for advanced alkali-ion batteries. The in situ formed MOF structure between the MXene nanosheets can effectively restrict the restacking of nanosheets, as indicated in Fig. 12. This enables the formation of an ordered 3D porous conductive network with a lightweight quality. The hierarchical structure of MOFs@MXene composites is a highly interlocked MXene system with ultra-fine nano-crystallization of the electrochemically active phase of CoS nanoparticles. The hybrid MXene composite system demonstrated excellent electron transport and ions transport properties. Benefiting from the synergistic effect of the individual components, CoS NP@NHC of MXene composite demonstrated exceptional electrochemistry properties as an active electrode material for many battery systems such as the sodium-ion batteries (SIBs), lithium-ion batteries (LIBs), and potassium-ion batteries (PIBs). The hierarchical structure of MOFs@MXene composites displays excellent cyclic life and rate capacities of 420 mAh g^{-1} at 2 A g^{-1} after 650 cycles for SIBs, 1145.9 mAh g^{-1} at 1 A g^{-1} after 800 cycles and 574.1 mAh g^{-1} at 5 A g^{-1} after 1000 cycles for LIBs, and 210 mAh g^{-1} at 2 A g^{-1} after 500 cycles for PIBs.

Polymer-based composites were mainly used for electric insulation and dielectric applications for many years. However, many polymer composites are found to have a low dielectric response with semiconductors. To overcome this issue and increase the dielectric constant, hybrid polymer composites with MXene nanosheets are effective. Deng et al. [151] synthesized special polymer and ceramic doped hybrid vanadium-based MXene composites with excellent dielectric properties. The as-prepared composites showed good dielectric and excellent properties dielectric properties due to strong electron polarization at heterojunction between ceramic and

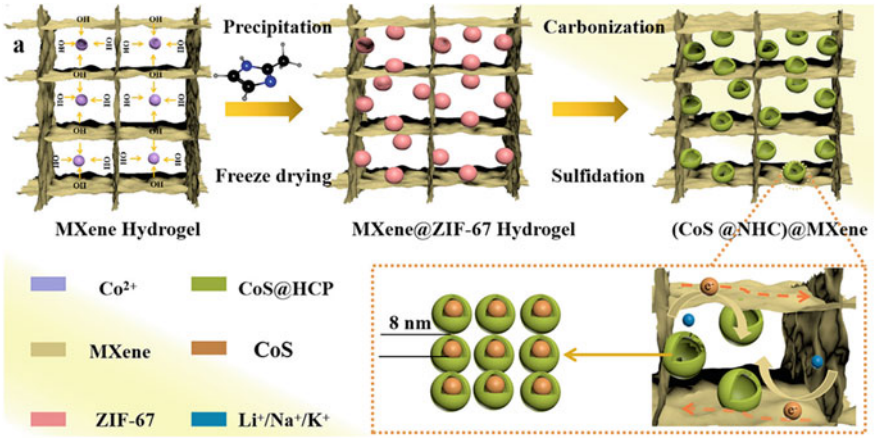

Fig. 12 Schematic representing the synthesis steps of MXene and its hybrid composites with CoS NP@NHC [150] (reproduced with permission)

MXene materials and fluorine-induced electron trap effect. MXene hybrid composites (polymer/V_2C-CuO) demonstrated enhanced electrical properties compared to polymer/Cuo composites. The authors claimed that the hybrid composite with 10 wt% CuO@MXene (V_3C) nanosheets displays a low dielectric loss of 0.23, high dielectric constant of 89, high breakdown strength of 204 MV m^{-1} and low conductivity of 6.8×10^{-7} S m^{-1} at 100 Hz.

Flexible and wearable electronic devices such as artificial electronic skins, motion detection, biomedical monitors and pressure sensors are very common nowadays and important for our day-to-day lives. MXene based hybrid composites are more effective and easy to fabricate with good mechanical stability, high sensitivity, cost-effective and high detection range [152]. Peng et al. [153] introduced highly stable hydrophobic hybrid composites of MXene/rGO/polymer to use pressure sensors for health monitoring. A simple spin-coating method was employed to fabricate MXene composites thin sheet with reduced graphene oxide (rGO) and polymer hybrid materials (PVDF-TrFE). The device displayed a good sensitivity of 2298 k/Pa, less detection limit 8 Pa, and response time of 10 ms, respectively, and it demonstrated excellent stability even after 10,000 cycles. Piezoresistive sensors comprised of Mxene/rGO/P(VDF-TrFE) composite can easily obtain signals less than 8 Pa so that it can test adult pulses randomly. The device's high sensitivity is mainly due to polymer, which acts as an aerogel. When squeezed, the pores were formed to increase the contact area, resulting in an increased current. The authors claimed that the MXene nanosheets in the composite system enhance the sensor's metallic conductivity, leading to an increase in the pressure sensing property. Furthermore, the polymer (P(VDF-TrFE)) in the composite can generate a recoverable 3D network structure, which can promptly deform to form a corresponding signal when receiving pressure and quickly back to the original state after the pressure is removed. The authors further explained that the sensor has exceptional sensitivity due to the high-pressure area because several micropores in the (P(VDF-TrFE)) sample bend only under higher pressure, which results in the higher sensitivity in the greater force region. The Mxene/rGO/P(VDF-TrFE) composite thin film sensor can check the human physiological signals (pulse rate and finger touch) in real-time. Table 5 identifies the organic-based hybrid MXene materials related to its applications and other parameters.

7 Challenges and Prospects

There are various challenges in preparing MXenes and their composites. The first challenge is linked to the synthesis of the MAX phases itself. At present, the preparation process of MAX phase material has not yet reached maturity, and it is still challenging to prepare single-phase MAX phase material that is free from impurities, thermodynamically, and mechanically stable. The Next challenge is the safe synthesis of MXenes, from their precursors (MAX) to the final product (delaminated MXene). Generally, the majority of MXene is synthesized using HF-based etching

Table 5 Organic hybrid based MXenes composite

S. no	MXenes	Organic hybrid	Measuring parameters	Applications	References
1	Nb_2CT_x	Bi_2WO_6	99.8%, 92.7% and 83.1% Photodegradation efficiency for Rhb, MB and TC-HCl	Photocatalytic activity	[154]
2	$Ti_3C_2T_x$	Quinone-coupled viologen and pyridiniumium derivatives	−2.77 eV binding energy	Pseudocapacitive interaction	[155]
3	$Ti_3C_2T_x$	NiCoOOH-NiCoS	58.2 mV dec^{-1} tafel slope 7.9 nm d_{pore}	Electrocatalytic oxygen evolution Zinc-air batteries	[156]
4	$Ti_3C_2T_x$	Ni chain/ZnO	−35.1 dB reflection loss	Microwave absorption	[157]
5	$Ti_3C_2T_x$	Phenothiazine@RGO	77% Retention 17.4 Wh/Kg energy density	Supercapacitors	[158]
6	Ti_3C_2	Bi_2WO_6	72.8 charge density 85.3 $\mu mol.g^{-1}$ h^{-1}	Photodegradation	[159]
7	$Ti_3C_2T_x$	Polytetrafluoroethylene and CuO	Vg/Va = 24.8 @ 100 ppm 810 V open-circuit voltage 34 μA short-circuit current	Sensors	[160]
8	Ti_3C_2	Ni-Co@NiCo-MOF/NF	2137.5 F g^{-1} specific capacitance 75.3% retention	Hybrid supercapacitors	[161]
9	Ti_3C_2	NH_2-MIL-125(Ti)(TiO_2)	0.9494 ns fluorescence life time 0.034 min^{-1} rate constant	Photocatalytic activity	[162]
10	Ti_3C_2	/CNHs/β-CD-MOFs	3.0 nM to 10.0 μM linear range 1.0 nM (S/N = 3) limit of detection (LOD)	Electrochemical sensing	[163]

approaches, and safe handling and waste treatment are necessary for the HF-based etchant. The next challenge relates to fewer applications of MXene in polymer and organic hybrid composites due to material compatibility and dispersion issues. The majority of applications are related to the dielectric, electrical, mechanical, and EMI shielding performance. Therefore, to derive the full potential of MXene, it is necessary to exploit MXene and its related composites in various other fields like energy, construction, automotive, etc. In addition, more research needs to be directed to the products catering to industrial and commercial needs.

8 Conclusion

This chapter summarises MXenes and their composites and then addresses their performance, fabrication, and applications. The importance of MXenes fabrication with various composites is the main theme of this chapter. Updated information of MXene and composites, namely MXene/metal oxide, MXene/polymer, MXene/carbon, MXene/chalcogenides, and MXene/organic hybrid along with their relevant applications, are highlighted in detail. Due to the large functional group and surface chemistry, MXene/composite has shown many fascinating properties owing to their unique characteristics such as conductivity, biocompatibility, cost-effectiveness, and excellent interlayer spacing. These are the keys behind the enormous attraction of MXenes and their composites. It is worth highlighting that the synthesis routes, surface characterisation, and properties of MXene/composites play a vital role in the performance of 2D materials to employ them as a newly efficient, cost-effective, and excellent friendly environment for the future generation.

References

1. Mas-Ballesté, R., et al.: 2D materials: to graphene and beyond. Nanoscale **3**(1), 20–30 (2011)
2. Novoselov, K.S., et al.: Electric field effect in atomically thin carbon films. Science **306**(5696), 666–669 (2004)
3. Oughaddou, H., et al.: Silicene, a promising new 2D material. Prog. Surf. Sci. **90**(1), 46–83 (2015)
4. Mannix, A.J., et al.: Synthesis and chemistry of elemental 2D materials. Nat. Rev. Chem. **1**(2), 0014 (2017)
5. Kalantar-zadeh, K., et al.: Two dimensional and layered transition metal oxides. Appl. Mater. Today **5**, 73–89 (2016)
6. Naguib, M., et al.: Two-dimensional nanocrystals produced by exfoliation of Ti_3AlC_2. Adv. Mater. **23**(37), 4248–4253 (2011)
7. Zhan, X., et al.: MXene and MXene-based composites: synthesis, properties and environment-related applications. Nanoscale Horiz. **5**(2), 235–258 (2020)
8. Berdiyorov, G.R., Mahmoud, K.A.: Effect of surface termination on Ion intercalation selectivity of bilayer $Ti_3C_2T_2$ (T = F, O and OH) MXene. Appl. Surf. Sci. **416**, 725–730 (2017)
9. Liang, X., Garsuch, A., Nazar, L.F.: Sulfur cathodes based on conductive MXene nanosheets for high-performance lithium-sulfur batteries. Angew. Chem. Int. Ed. **54**(13), 3907–3911 (2015)
10. Mashtalir, O., et al.: Amine-assisted delamination of Nb_2C MXene for Li-Ion energy storage devices. Adv. Mater. **27**(23), 3501–3506 (2015)
11. Xie, X., et al.: Porous heterostructured MXene/carbon nanotube composite paper with high volumetric capacity for sodium-based energy storage devices. Nano Energy **26**, 513–523 (2016)
12. Valden, M., Lai, X., Goodman, D.W.: Onset of catalytic activity of gold clusters on titania with the appearance of nonmetallic properties. Science **281**(5383), 1647–1650 (1998)
13. Rodriguez, J., Dvorak, J., Maiti, A., et al.: J. Am. Chem. Soc. **124**, 5247 (2002)
14. Bäumer, M., Freund, H.-J.: Metal deposits on well-ordered oxide films. Prog. Surf. Sci. **61**(7–8), 127–198 (1999)

15. Trudeau, M., Ying, J.: Nanocrystalline materials in catalysis and electrocatalysis: structure tailoring and surface reactivity. Nanostruct. Mater. **7**(1–2), 245–258 (1996)
16. Ayyub, P., et al.: Effect of crystal size reduction on lattice symmetry and cooperative properties. Phys. Rev. B **51**(9), 6135 (1995)
17. Zhang, H., Banfield, J.F.: Thermodynamic analysis of phase stability of nanocrystalline titania. J. Mater. Chem. **8**(9), 2073–2076 (1998)
18. Nabavi, M., Sanchez, C., Livage, J.: Structure and properties of amorphous V_2O_5. Philos. Mag. B **63**(4), 941–953 (1991)
19. Samsonov, V., Sdobnyakov, N.Y., Bazulev, A.: On thermodynamic stability conditions for nanosized particles. Surf. Sci. **532**, 526–530 (2003)
20. Ayyub, P., et al.: Size-induced structural phase transitions and hyperfine properties of microcrystalline Fe_2O_3. J. Phys. C Solid State Phys. **21**(11), 2229 (1988)
21. Hernández-Alonso, M.D., et al.: Confinement effects in quasi-stoichiometric CeO_2 nanoparticles. Phys. Chem. Chem. Phys. **6**(13), 3524–3529 (2004)
22. Skandan, G., et al.: Phase characterization and stabilization due to grain size effects of nanostructured Y_2O_3. Nanostruct. Mater. **1**(4), 313–322 (1992)
23. Cammarata, R., Sieradzki, K.: Effects of surface stress on the elastic moduli of thin films and superlattices. Phys. Rev. Lett. **62**(17), 2005 (1989)
24. Landfester, K.: Miniemulsion polymerization and the structure of polymer and hybrid nanoparticles. Angew. Chem. Int. Ed. **48**(25), 4488–4507 (2009)
25. Amancio-Filho, S., Dos Santos, J.: Joining of polymers and polymer–metal hybrid structures: recent developments and trends. Polym. Eng. Sci. **49**(8), 1461–1476 (2009)
26. Ovsianikov, A., et al.: Two photon polymerization of polymer–ceramic hybrid materials for transdermal drug delivery. Int. J. Appl. Ceram. Technol. **4**(1), 22–29 (2007)
27. Kickelbick, G.: Hybrid Materials: Synthesis, Characterization, and Applications. Wiley & Sons (2007)
28. Kickelbick, G.: Hybrid Materials-Past, Present and Future (2014)
29. Kickelbick, G.: Introduction to hybrid materials. Hybrid Mater. **1**, 2 (2007)
30. Pyun, J., Matyjaszewski, K.: The synthesis of hybrid polymers using atom transfer radical polymerization: homopolymers and block copolymers from polyhedral oligomeric silsesquioxane monomers. Macromolecules **33**(1), 217–220 (2000)
31. Irfan, M.: Chemistry of polymers. In: Chemistry and Technology of Thermosetting Polymers in Construction Applications, pp. 8–77. Springer (1998)
32. Beachell, H.C., Son, C.N.: Color formation in polyurethanes. J. Appl. Polym. Sci. **7**(6), 2217–2237 (1963)
33. Yu, B., et al.: Interface decoration of exfoliated MXene ultra-thin nanosheets for fire and smoke suppressions of thermoplastic polyurethane elastomer. J. Hazard. Mater. **374**, 110–119 (2019)
34. Beachell, H.C., Son, C.N.: Stabilization of polyurethane to thermal degradation. J. Appl. Polym. Sci. **8**(3), 1089–1096 (1964)
35. Boota, M., et al.: Interaction of polar and nonpolar polyfluorenes with layers of two-dimensional titanium carbide (MXene): intercalation and pseudocapacitance. Chem. Mater. **29**(7), 2731–2738 (2017)
36. Kagan, C.R., Mitzi, D.B., Dimitrakopoulos, C.D.: Organic-inorganic hybrid materials as semiconducting channels in thin-film field-effect transistors. Science **286**(5441), 945–947 (1999)
37. Glavin, N.R., et al.: Emerging applications of elemental 2D materials. Adv. Mater. **32**(7), 1904302 (2020)
38. Lin, Z., et al.: 2D materials advances: from large scale synthesis and controlled heterostructures to improved characterization techniques, defects and applications. 2D Mater. **3**(4), 042001 (2016)
39. Jayakumar, A., Surendranath, A., Mohanan, P.: 2D materials for next generation healthcare applications. Int. J. Pharm. **551**(1–2), 309–321 (2018)

40. Luo, B., Liu, G., Wang, L.: Recent advances in 2D materials for photocatalysis. Nanoscale **8**(13), 6904–6920 (2016)
41. Shi, L., Zhao, T.: Recent advances in inorganic 2D materials and their applications in lithium and sodium batteries. J. Mater. Chem. A **5**(8), 3735–3758 (2017)
42. Yu, S., et al.: 2D materials for optical modulation: challenges and opportunities. Adv. Mater. **29**(14), 1606128 (2017)
43. Han, Y., et al.: Recent progress in 2D materials for flexible supercapacitors. J. Energy Chem. **27**(1), 57–72 (2018)
44. Li, Y., et al.: V_2O_5 nanopaper as a cathode material with high capacity and long cycle life for rechargeable aqueous zinc-ion battery. Nano Energy **60**, 752–759 (2019)
45. Li, J., et al.: K-Ion storage enhancement in Sb_2O_3/reduced graphene oxide using ether-based electrolyte. Adv. Energy Mater. **10**(5), 1903455 (2020)
46. Xu, G., et al.: Three-dimensional hydrated vanadium pentoxide/MXene composite for high-rate zinc-ion batteries. J. Colloid Interface Sci. **593**, 417–423 (2021)
47. Song, C., et al.: Enhanced polysulfide conversion through metal oxide-support interaction in MnOx/MXene. Chem. Eng. J. **420**, 130452 (2021)
48. Long, C., et al.: High-performance asymmetric supercapacitors with lithium intercalation reaction using metal oxide-based composites as electrode materials. J. Mater. Chem. A **2**(39), 16678–16686 (2014)
49. Wu, W., et al.: Ultrathin N-doped Ti_3C_2-MXene decorated with $NiCo_2S_4$ nanosheets as advanced electrodes for supercapacitors. Appl. Surf. Sci. **539**, 148272 (2021)
50. Huang, J., et al.: Sandwich-like Na0.23TiO_2 nanobelt/Ti_3C_2 MXene composites from a scalable in situ transformation reaction for long-life high-rate lithium/sodium-ion batteries. Nano Energy **46**, 20–28 (2018)
51. Yin, J., et al.: Self-assembled sandwich-like MXene-derived composites as highly efficient and sustainable catalysts for wastewater treatment. Langmuir **37**(3), 1267–1278 (2021)
52. Hou, T., et al.: MXene-based accordion 2D hybrid structure with Co_9S_8/C/$Ti_3C_2T_x$ as efficient electromagnetic wave absorber. Chem. Eng. J. **414**, 128875 (2021)
53. Liu, M., et al.: In_2O_3 nanocubes/Ti_3C_2Tx MXene composites for enhanced methanol gas sensing properties at room temperature. Ceram. Int. (2021)
54. Zhang, X., et al.: Improved electrochemical performance of CoOx-NiO/$Ti_3C_2T_x$ MXene nanocomposites by atomic layer deposition towards high capacitance supercapacitors. J. Alloy Compd. **862**, 158546 (2021)
55. Liu, M., et al.: Flexible MXene/rGO/CuO hybrid aerogels for high performance acetone sensing at room temperature. Sens. Actuators B Chem. **340**, 129946 (2021)
56. Zhu, K., et al.: Two-dimensional titanium carbide MXene as a capacitor-type electrode for rechargeable aqueous Li-Ion and Na-Ion capacitor batteries. ChemElectroChem **4**(11), 3018–3025 (2017)
57. Su, T., et al.: Monolayer $Ti_3C_2T_x$ as an effective co-catalyst for enhanced photocatalytic hydrogen production over TiO_2. ACS Appl. Energy Mater. **2**(7), 4640–4651 (2019)
58. Zheng, W., et al.: Microwave-assisted synthesis of SnO_2-Ti_3C_2 nanocomposite for enhanced supercapacitive performance. Mater. Lett. **209**, 122–125 (2017)
59. Gao, Y., et al.: Hydrothermal synthesis of TiO_2/Ti_3C_2 nanocomposites with enhanced photocatalytic activity. Mater. Lett. **150**, 62–64 (2015)
60. Rakhi, R.B., et al.: Direct chemical synthesis of MnO_2 nanowhiskers on transition-metal carbide surfaces for supercapacitor applications. ACS Appl. Mater. Interfaces **8**(29), 18806–18814 (2016)
61. Zhang, Z., et al.: Highly-dispersed iron oxide nanoparticles anchored on crumpled nitrogen-doped MXene nanosheets as anode for Li-ion batteries with enhanced cyclic and rate performance. J. Power Sources **439**, 227107 (2019)
62. Wang, Z., et al.: Photo-synergetic nitrogen-doped MXene/reduced graphene oxide sandwich-like architecture for high-performance lithium-sulfur batteries. Int. J. Energy Res. **45**(2), 2728–2738 (2021)

63. Zhao, S., et al.: Highly electrically conductive three-dimensional $Ti_3C_2T_x$ MXene/reduced graphene oxide hybrid aerogels with excellent electromagnetic interference shielding performances. ACS Nano **12**(11), 11193–11202 (2018)
64. Sudheer, V., SarathKumar, S., Sankararaman, S.: Nanostructured ZnO and ZnO: Pd with MXene overlayer SPR biosensors. Opt. Quant. Electron. **53**(6), 1–14 (2021)
65. Cao, J., et al.: Alternative electrodes for HTMs and noble-metal-free perovskite solar cells: 2D MXenes electrodes. RSC Adv. **9**(59), 34152–34157 (2019)
66. Lin, Q., et al.: Self-cleaning photocatalytic MXene composite membrane for synergistically enhanced water treatment: oil/water separation and dyes removal. Chem. Eng. J. **427**, 131668 (2022)
67. Tahir, T., et al.: Synthesis of sponge like Gd3+ doped vanadium oxide/2D MXene composites for improved degradation of industrial effluents and pathogens. Ceram. Int. **48**(2), 1969–1980 (2022)
68. Ji, C., et al.: Ice-templated MXene/Ag–epoxy nanocomposites as high-performance thermal management materials. ACS Appl. Mater. Interfaces **12**(21), 24298–24307 (2020)
69. Novoselov, K.S., et al.: A roadmap for graphene. Nature **490**(7419), 192–200 (2012)
70. Geim, A.K., Novoselov, K.S.: The rise of graphene. In: Nanoscience and Technology: A Collection of Reviews From Nature Journals, pp. 11–19. World Scientific (2010)
71. Zhang, Z., et al.: Mechanically strong MXene/Kevlar nanofiber composite membranes as high-performance nanofluidic osmotic power generators. Nat. Commun. **10**(1), 1–9 (2019)
72. Sun, Y., et al.: MXene-xanthan nanocomposite films with layered microstructure for electromagnetic interference shielding and Joule heating. Chem. Eng. J. **410**, 128348 (2021)
73. Yang, H., et al.: Layered PVB/$Ba_3Co_2Fe_{24}O_{41}$/Ti_3C_2 Mxene composite: enhanced electromagnetic wave absorption properties with high impedance match in a wide frequency range. Mater. Chem. Phys. **200**, 179–186 (2017)
74. Jiang, C., et al.: All-electrospun flexible triboelectric nanogenerator based on metallic MXene nanosheets. Nano Energy **59**, 268–276 (2019)
75. Shao, W., et al.: Polyester@MXene nanofibers-based yarn electrodes. J. Power Sources **396**, 683–690 (2018)
76. Xu, H., et al.: Lightweight Ti_2CT_x MXene/Poly(vinyl alcohol) composite foams for electromagnetic wave shielding with absorption-dominated feature. ACS Appl. Mater. Interfaces **11**(10), 10198–10207 (2019)
77. Zhou, Z., et al.: Layer-by-layer assembly of MXene and carbon nanotubes on electrospun polymer films for flexible energy storage. Nanoscale **10**(13), 6005–6013 (2018)
78. Zhang, C., et al.: Two-dimensional transition metal carbides and nitrides (MXenes): synthesis, properties, and electrochemical energy storage applications. Energy & Environ. Mater. **3**(1), 29–55 (2020)
79. Wang, J., et al.: A new strategy for high-performance electromagnetic interference shielding by designing a layered double-percolated structure in PS/PVDF/MXene composites. Eur. Polymer J. **151**, 110450 (2021)
80. Jin, X., et al.: Flame-retardant poly(vinyl alcohol)/MXene multilayered films with outstanding electromagnetic interference shielding and thermal conductive performances. Chem. Eng. J. **380**, 122475 (2020)
81. Liu, F., et al.: Well-aligned MXene/chitosan films with humidity response for high-performance electromagnetic interference shielding. Carbohyd. Polym. **243**, 116467 (2020)
82. Shi, Y., et al.: Strengthening, toughing and thermally stable ultra-thin MXene nanosheets/polypropylene nanocomposites via nanoconfinement. Chem. Eng. J. **378**, 122267 (2019)
83. Xu, M.-K., et al.: Electrically Conductive $Ti_3C_2T_x$ MXene/polypropylene nanocomposites with an ultralow percolation threshold for efficient electromagnetic interference shielding. Ind. Eng. Chem. Res. **60**(11), 4342–4350 (2021)
84. Xue, Y., et al.: Polyphosphoramide-intercalated MXene for simultaneously enhancing thermal stability, flame retardancy and mechanical properties of polylactide. Chem. Eng. J. **397**, 125336 (2020)

85. Luo, J.-Q., et al.: Flexible, stretchable and electrically conductive MXene/natural rubber nanocomposite films for efficient electromagnetic interference shielding. Compos. Sci. Technol. **182**, 107754 (2019)
86. Hatter, C.B., et al.: Micromechanical response of two-dimensional transition metal carbonitride (MXene) reinforced epoxy composites. Compos. B Eng. **182**, 107603 (2020)
87. Pan, Y., et al.: Flammability, thermal stability and mechanical properties of polyvinyl alcohol nanocomposites reinforced with delaminated $Ti_3C_2T_x$ (MXene). Polym. Compos. **41**(1), 210–218 (2020)
88. Zhao, L., et al.: Highly-stable polymer-crosslinked 2D MXene-based flexible biocompatible electronic skins for in vivo biomonitoring. Nano Energy **84**, 105921 (2021)
89. Zhou, Z., et al.: Facile fabrication of densely packed Ti_3C_2 MXene/nanocellulose composite films for enhancing electromagnetic interference shielding and electro-/photothermal performance. ACS Nano **15**(7), 12405–12417 (2021)
90. McDaniel, R.M., et al.: Well-dispersed nanocomposites using covalently modified, multilayer, 2D titanium carbide (MXene) and in-situ "Click" polymerization. Chem. Mater. **33**(5), 1648–1656 (2021)
91. Zheng, Y., et al.: High conductivity and stability of polystyrene/MXene composites with orientation-3D network binary structure. J. Colloid Interface Sci. **595**, 151–158 (2021)
92. Mao, Y., Wang, D., Fu, S.: Layer-by-layer self-assembled nanocoatings of Mxene and P, N-co-doped cellulose nanocrystals onto cotton fabrics for significantly reducing fire hazards and shielding electromagnetic interference. Compos. A Appl. Sci. Manuf. **153**, 106751 (2022)
93. Qin, L., et al.: Polymer-MXene composite films formed by MXene-facilitated electrochemical polymerization for flexible solid-state microsupercapacitors. Nano Energy **60**, 734–742 (2019)
94. Jin, X., et al.: Flame-retardant poly (vinyl alcohol)/MXene multilayered films with outstanding electromagnetic interference shielding and thermal conductive performances. Chem. Eng. J. **380**, 122475 (2020)
95. Mazhar, S., et al.: Promising PVC/MXene based flexible thin film nanocomposites with excellent dielectric, thermal and mechanical properties. Ceram. Int. **46**(8), 12593–12605 (2020)
96. Ren, Y., et al.: Synthesis of polyaniline nanoparticles deposited on two-dimensional titanium carbide for high-performance supercapacitors. Mater. Lett. **214**, 84–87 (2018)
97. Zhang, J., et al.: MXene: a potential candidate for yarn supercapacitors. Nanoscale **9**(47), 18604–18608 (2017)
98. Yu, L., et al.: $Ti_3C_2T_x$ (MXene)-silicon heterojunction for efficient photovoltaic cells. Adv. Energy Mater. **9**(31), 1901063 (2019)
99. Wei, H., et al.: $Ti_3C_2T_x$ MXene/polyaniline (PANI) sandwich intercalation structure composites constructed for microwave absorption. Compos. Sci. Technol. **169**, 52–59 (2019)
100. Sheng, X., et al.: Properties of two-dimensional Ti_3C_2 MXene/thermoplastic polyurethane nanocomposites with effective reinforcement via melt blending. Compos. Sci. Technol. **181**, 107710 (2019)
101. Ling, Z., et al.: Flexible and conductive MXene films and nanocomposites with high capacitance. Proc. Natl. Acad. Sci. **111**(47), 16676–16681 (2014)
102. Karousis, N., et al.: Structure, properties, functionalization, and applications of carbon nanohorns. Chem. Rev. **116**(8), 4850–4883 (2016)
103. Rao, R., et al.: Carbon nanotubes and related nanomaterials: critical advances and challenges for synthesis toward mainstream commercial applications. ACS Nano **12**(12), 11756–11784 (2018)
104. Olabi, A.G., et al.: application of graphene in energy storage device—a review. Renew. Sustain. Energy Rev. **135**, 110026 (2021)
105. Sun, L., et al.: MXene/N-doped carbon foam with three-dimensional hollow neuron-like architecture for freestanding, highly compressible all solid-state supercapacitors. ACS Appl. Mater. Interfaces **12**(40), 44777–44788 (2020)
106. Zhao, M.-Q., et al.: Flexible MXene/carbon nanotube composite paper with high volumetric capacitance. Adv. Mater. **27**(2), 339–345 (2015)

107. Zhou, S., et al.: Heterostructures of MXenes and N-doped graphene as highly active bifunctional electrocatalysts. Nanoscale **10**(23), 10876–10883 (2018)
108. Dwivedi, N., et al.: Emergent 2D materials for combating infectious diseases: the potential of MXenes and MXene–graphene composites to fight against pandemics. Mater. Adv. **2**(9), 2892–2905 (2021)
109. Liu, Y., et al.: graphene enhanced flexible expanded graphite film with high electric, thermal conductivities and EMI shielding at low content. Carbon **133**, 435–445 (2018)
110. Wan, L., et al.: construction of two-dimensional bimetal (Fe-Ti) oxide/carbon/MXene architecture from titanium carbide MXene for ultrahigh-rate lithium-ion storage. J. Colloid Interface Sci. **588**, 147–156 (2021)
111. Liu, Y., et al.: Highly thermal conductivity and flame retardant flexible graphene/MXene paper based on an optimized interface and nacre laminated structure. Compos. A Appl. Sci. Manuf. **141**, 106227 (2021)
112. Qi, F., et al.: Robust $Ti_3C_2T_x$ MXene/starch derived carbon foam composites for superior EMI shielding and thermal insulation. Mater. Today Phys. **21**, 100512 (2021)
113. Aïssa, B., et al.: Nanoelectromagnetic of a highly conductive 2D transition metal carbide (MXene)/graphene nanoplatelets composite in the EHF M-band frequency. Carbon **173**, 528–539 (2021)
114. Rasheed, A.K., et al.: graphene based nanofluids and nanolubricants—review of recent developments. Renew. Sustain. Energy Rev. **63**, 346–362 (2016)
115. Kinoshita, H., et al.: Tribological properties of monolayer graphene oxide sheets as water-based lubricant additives. Carbon **66**, 720–723 (2014)
116. Rosenkranz, A., et al.: Multi-layer $Ti_3C_2T_x$-nanoparticles (MXenes) as solid lubricants—role of surface terminations and intercalated water. Appl. Surf. Sci. **494**, 13–21 (2019)
117. Zhao, X., et al.: pH, nanosheet concentration, and antioxidant affect the oxidation of $Ti_3C_2T_x$ and Ti_2CT_x MXene dispersions. Adv. Mater. Interfaces **7**(20), 2000845 (2020)
118. Huang, S., et al.: Achieving superlubricity with 2D transition metal carbides (MXenes) and MXene/graphene coatings. Mater. Today Adv. **9**, 100133 (2021)
119. Lian, W., et al.: Ti_3C_2/graphene oxide heterostructural coating with enhanced dry tribological performance. Appl. Nanosci. **11**(5), 1471–1479 (2021)
120. Yang, B., et al.: Realizing high-performance lithium ion hybrid capacitor with a 3D MXene-carbon nanotube composite anode. Chem. Eng. J. **429**, 132392 (2022)
121. Weng, G.M., et al.: Layer-by-layer assembly of cross-functional semi-transparent MXene-carbon nanotubes composite films for next-generation electromagnetic interference shielding. Adv. Func. Mater. **28**(44), 1803360 (2018)
122. Jiang, Y., et al.: Hierarchically structured cellulose aerogels with interconnected MXene networks and their enhanced microwave absorption properties. J. Mater. Chem. C **6**(32), 8679–8687 (2018)
123. Sambyal, P., et al.: Ultralight and mechanically robust $Ti_3C_2T_x$ hybrid aerogel reinforced by carbon nanotubes for electromagnetic interference shielding. ACS Appl. Mater. Interfaces **11**(41), 38046–38054 (2019)
124. Anwer, S., et al.: 2D $Ti_3C_2T_x$ MXene nanosheets coated cellulose fibers based 3D nanostructures for efficient water desalination. Chem. Eng. J. **406**, 126827 (2021)
125. Xiao, Z., et al.: Ultrafine Ti_3C_2 MXene nanodots-interspersed nanosheet for high-energy-density lithium–sulfur batteries. ACS Nano **13**(3), 3608–3617 (2019)
126. Liang, X., et al.: Interwoven MXene nanosheet/carbon-nanotube composites as Li–S cathode hosts. Adv. Mater. **29**(3), 1603040 (2017)
127. Cai, Y., et al.: Stretchable $Ti_3C_2T_x$ MXene/carbon nanotube composite based strain sensor with ultrahigh sensitivity and tunable sensing range. ACS Nano **12**(1), 56–62 (2018)
128. Cao, W., et al.: Ultrathin and flexible CNTs/MXene/cellulose nanofibrils composite paper for electromagnetic interference shielding. Nano-Micro Lett. **11**(1), 1–17 (2019)
129. Gao, M.-R., et al.: Nanostructured metal chalcogenides: synthesis, modification, and applications in energy conversion and storage devices. Chem. Soc. Rev. **42**(7), 2986–3017 (2013)

130. Choi, W., et al.: Recent development of two-dimensional transition metal dichalcogenides and their applications. Mater. Today **20**(3), 116–130 (2017)
131. Zhang, F., et al.: Interface engineering of MXene composite separator for high-performance Li–Se and Na–Se batteries. Adv. Energy Mater. **10**(20), 2000446 (2020)
132. Li, Z., et al.: Two-dimensional Ti_3C_2@CTAB-Se (MXene) composite cathode material for high-performance rechargeable aluminum batteries. Chem. Eng. J. **398**, 125679 (2020)
133. Huang, P., et al.: Few-layered Ti_3C_2 MXene anchoring bimetallic selenide $NiCo_2Se_4$ nanoparticles for superior Sodium-ion batteries. Chem. Eng. J. **417**, 129161 (2021)
134. Chen, Y., et al.: In suit growth of CuSe nanoparticles on MXene (Ti_3C_2) nanosheets as an efficient counter electrode for quantum dot-sensitized solar cells. Electrochim. Acta **316**, 248–256 (2019)
135. Zong, H., et al.: Metal-organic frameworks-derived CoP anchored on MXene toward an efficient bifunctional electrode with enhanced lithium storage. Chem. Eng. J. **416**, 129102 (2021)
136. Li, J., et al.: MXene-decorated SnS_2/Sn_3S_4 hybrid as anode material for high-rate lithium-ion batteries. Chem. Eng. J. **380**, 122590 (2020)
137. Oh, H.G., et al.: N-doped carbon-coated $CoSe_2$ nanocrystals anchored on two-dimensional MXene nanosheets for efficient electrochemical sodium-and potassium-ion storage. Int. J. Energy Res. **45**(12), 17738–17748 (2021)
138. Qin, X., et al.: Hydrothermal growth of ZnCdS/TiO_2 nanoparticles on the surface of the Ti_3C_2 MXene sheet to enhance photocatalytic performance under visible light. J. Solid State Chem. **306**, 122750 (2022)
139. Li, J., et al.: Nanosheets assembled layered MoS_2/MXene as high performance anode materials for potassium ion batteries. J. Power Sources **449**, 227481 (2020)
140. Zou, Z., et al.: Versatile interfacial self-assembly of $Ti_3C_2T_x$ MXene based composites with enhanced kinetics for superior lithium and sodium storage. ACS Nano **15**(7), 12140–12150 (2021)
141. Huang, H., et al.: Carbon-coated $MoSe_2$/MXene hybrid nanosheets for superior potassium storage. ACS Nano **13**(3), 3448–3456 (2019)
142. Zeng, Z., et al.: Bifunctional N-$CoSe_2$/3D-MXene as highly efficient and durable cathode for rechargeable Zn–air battery. ACS Mater. Lett. **1**(4), 432–439 (2019)
143. Lim, K.R.G., et al.: 2h-Mos_2 on Mo_2CT_x Mxene nanohybrid for efficient and durable electrocatalytic hydrogen evolution. ACS Nano **14**(11), 16140–16155 (2020)
144. Kashefi-Kheyrabadi, L., et al.: A MoS_2@ $Ti_3C_2T_x$ MXene hybrid-based electrochemical aptasensor (MEA) for sensitive and rapid detection of thyroxine. Bioelectrochemistry **137**, 107674 (2021)
145. Wang, J., et al.: Hierarchical carbon fiber@ MXene@ MoS_2 core-sheath synergistic microstructure for tunable and efficient microwave absorption. Adv. Func. Mater. **30**(45), 2002595 (2020)
146. Chen, R., et al.: Synergetic effect of MoS_2 and MXene on the enhanced H_2 evolution performance of CdS under visible light irradiation. Appl. Surf. Sci. **473**, 11–19 (2019)
147. Wang, X., et al.: 2D/2D 1T-MoS_2/Ti_3C_2 MXene heterostructure with excellent supercapacitor performance. Adv. Func. Mater. **30**(15), 0190302 (2020)
148. Pal, S., et al.: Sensitivity analysis of surface plasmon resonance biosensor based on heterostructure of 2D BlueP/MoS_2 and MXene. Layer. 2D Adv. Mater. Their Allied Appl. 103–129 (2020)
149. Zhang, X., et al.: 3D TiO_2@nitrogen-doped carbon/Fe_7S_8 composite derived from polypyrrole-encapsulated alkalized MXene as anode material for high-performance lithium-ion batteries. Chem. Eng. J. **385**, 123394 (2020)
150. Yao, L., Gu, Q., Yu, X.: Three-Dimensional MOFs@MXene aerogel composite derived MXene threaded hollow carbon confined CoS nanoparticles toward advanced Alkali-Ion batteries. ACS Nano **15**(2), 3228–3240 (2021)
151. Deng, Q., et al.: Remarkably improving dielectric response of polymer/hybrid ceramic composites based on 0D/2D-stacked CuO/V2C MXene heterojunction. Appl. Surf. Sci. **545**, 149008 (2021)

152. Pei, Y., et al.: $Ti_3C_2T_x$ MXene for sensing applications: recent progress, design principles, and future perspectives. ACS Nano **15**(3), 3996–4017 (2021)
153. Peng, Z., et al.: Hydrophobic and stable MXene/reduced graphene oxide/polymer hybrid materials pressure sensors with an ultrahigh sensitive and rapid response speed pressure sensor for health monitoring. Mater. Chem. Phys. 124729 (2021)
154. Cui, C., et al.: Bi_2WO_6/Nb_2CT_x MXene hybrid nanosheets with enhanced visible-light-driven photocatalytic activity for organic pollutants degradation. Appl. Surf. Sci. **505**, 144595 (2020)
155. Boota, M., et al.: Mechanistic understanding of the interactions and pseudocapacitance of multi-electron redox organic molecules sandwiched between MXene layers. Adv. Electron. Mater. **7**(4), 2001202 (2021)
156. Zou, H., et al.: Metal–organic framework-derived nickel–cobalt sulfide on ultrathin mxene nanosheets for electrocatalytic oxygen evolution. ACS Appl. Mater. Interfaces **10**(26), 22311–22319 (2018)
157. Wang, S., et al.: Hierarchical $Ti_3C_2T_x$ MXene/Ni Chain/ZnO array hybrid nanostructures on cotton fabric for durable self-cleaning and enhanced microwave absorption. ACS Nano **14**(7), 8634–8645 (2020)
158. Boota, M., Bécuwe, M., Gogotsi, Y.: Phenothiazine–MXene aqueous asymmetric pseudocapacitors. ACS Appl Energy Mater **3**(4), 3144–3149 (2020)
159. Huang, G., et al.: Ti_3C_2 MXene-modified Bi_2WO_6 nanoplates for efficient photodegradation of volatile organic compounds. Appl. Surf. Sci. **503**, 144183 (2020)
160. Wang, D., et al.: Multifunctional latex/polytetrafluoroethylene-based triboelectric nanogenerator for self-powered organ-like MXene/Metal–organic framework-derived CuO nanohybrid ammonia sensor. ACS Nano **15**(2), 2911–2919 (2021)
161. Wang, J., et al.: Construction of hexagonal nickel-cobalt oxide nanosheets on metal-organic frameworks based on MXene interlayer ion effect for hybrid supercapacitors. J. Alloy. Compd. **870**, 159466 (2021)
162. Wu, Y., et al.: Mxene-modulated dual-heterojunction generation on a metal-organic framework (MOF) via surface constitution reconstruction for enhanced photocatalytic activity. Chem. Eng. J. **390**, 124519 (2020)
163. Tu, X., et al.: Mxene/carbon nanohorn/β-cyclodextrin-metal-organic frameworks as high-performance electrochemical sensing platform for sensitive detection of carbendazim pesticide. J. Hazard. Mater. **396**, 122776 (2020)

Stability and Degradation of MXene

G. Murali, Jeevan Kumar Reddy Modigunta, Young Ho Park, Sung Young Park, and Insik In

Abstract Novel materials with intriguing qualities, which emerge from time to time as a result of the research community's tireless efforts, are cornerstones for the advancement of science and technology. MXenes, a class of two-dimensional (2D) materials reported for the first time in 2011, tremendously upgraded the devices used for electromagnetic shielding, optoelectronics, light-emitting diodes, transparent electrodes, electrochemical storage, etc. While MXenes continue to make progress in a wide range of application fields, their tendency to oxidize easily to corresponding metal oxides when exposed to air, water, and light remain a focal point to skepticism on the long-term stability of devices prepared with MXenes. MXene's 2D morphology, metallic electrical conductivity, and several other intrinsic properties deteriorate vehemently with respect to their oxidation degree. Hence, a comprehensive understanding of MXene's stability and procedures to effectively mitigate their oxidation in environmental conditions are critical to exploiting the full potential of MXenes in practical applications. It has been established that each stage in the MXene synthesis, from the parent MAX phase through the storage of the as-synthesized MXenes, has a major impact on their oxidation stability. Further, by determining the potential sources of MXenes oxidation, several strategies that are effective in mitigating the spontaneous oxidation of MXenes in the colloidal dispersion and thin-film state have been developed over the years. Here, we provide a brief review of the root causes of MXenes oxidation and factors that accelerate the oxidation phenomena, the advantages and disadvantages of MXenes oxidation, and effective synthesis/storage procedures to improve oxidation stability.

G. Murali · J. K. R. Modigunta · Y. H. Park · I. In (✉)
Department of Polymer Science and Engineering, Department of IT-Energy Convergence (BK21 FOUR), Chemical Industry Institute, Korea National University of Transportation, Chungju 27469, Republic of Korea
e-mail: in1@ut.ac.kr

S. Y. Park
Department of Green Bio Engineering, Department of Chemical and Biological Engineering, Department of IT-Energy Convergence (BK21 FOUR), Korea National University of Transportation, Chungju 380702, Republic of Korea

M. Khalid et al. (eds.), *Fundamental Aspects and Perspectives of MXenes*, Engineering Materials, https://doi.org/10.1007/978-3-031-05006-0_5

Keywords MXenes · Oxidation · Shelf-life · Defects · Synthesis conditions · Storage

1 Stability of MXene

MXenes, a family of two-dimensional (2D) transition metal carbides and nitrides, attracted considerable research interests in various application fields owing to their 2D morphology and fascinating properties such as high metallic conductivity, surface hydrophilicity, and excellent thermoelectric, electrochemical, and optoelectronic properties [1–6]. However, one of the major issues for device application is the undesired oxidation of MXenes when exposed to humid air, water, and light. The progressive oxidation transforms the 2D MXene nanosheets into corresponding metal oxide nanoparticles, rendering their outstanding properties useless. In general, several parameters including the precursor MAX phase, etchant solution, composition of the MXene, morphology (size and single- or multilayered structure) and defect structure of MXene flakes, and storing state (solution, powder, and thin-film) and conditions (temperature and environment) crucially influence the oxidation stability of MXenes [7]. The degree of MXenes oxidation can be identified through various indicators. For example, in the case of widely studied $Ti_3C_2T_x$ MXene, the following factors were closely monitored to determine the oxidation: **(1) Color of the MXene solution**: black or dark green MXene solution turns into white titanium dioxide (TiO_2) solution, **(2) UV–vis absorption spectra**: with the progress of oxidation, the MXene flake size and concentration in the solution declines and eventually the prominent optical absorption peak located in the UV region becomes narrower while the intensity of absorption peak located in the NIR region decreases, **(3) Conductivity of the MXene film**: conductivity decreases with the increased oxidation of MXene flakes [8], **(4) Morphology**: 2D MXene flakes turn into TiO_2 nanoparticle morphology [9], **(5) XPS analysis**: the relative TiO_2 composition detectable in the Ti2p region of XPS increases with the increase of MXene oxidation [10], **(6) Raman Spectroscopy**: rise in the intensity of vibrational bands of anatase and/or rutile TiO_2 (for example, anatase ~149 cm^{-1}) and a gradual decline in the MXene related peak intensity (~205 cm^{-1}) [10, 11], and **(7) XRD**: structural transformation from $Ti_3C_2T_x$ to anatase and /or rutile TiO_2 [12].

The oxidation starts at the defects or edges of the MXene flake and then spreads to other parts of the flake [13]. As the flake size defines the perimeter to surface area, MXenes having smaller flake size are susceptible to quick oxidation [10]. The defect formation in MXene nanosheets is unavoidable due to the standard acid-assisted chemical etching and mechanical washing procedures involved in synthesizing MXenes from their parent MAX phase precursors. The presence of metal cation vacancies and adatoms can be directly confirmed using atomic-resolution scanning transmission electron microscopy (STEM) (Fig. 1a and b) [14]. Further, the theoretical simulations predict that atomic defects of anions, which are difficult to identify in STEM images owing to their negligible contrast, also possible to

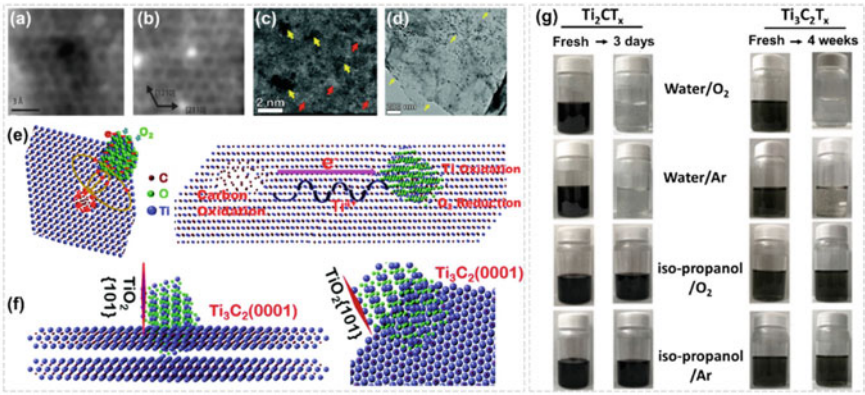

Fig. 1 STEM images showing **a** Ti vacancy (dark contrast), **b** Ti adatom (bright contrast), and **c** Ti–rich (marked by red arrows) and Ti-vacancy (marked by yellow arrows) areas in $Ti_3C_2T_x$ MXene nanosheet. **d** TEM image showing the formation of TiO_2 nanoparticles on basal plane and edges of $Ti_3C_2T_x$ MXene nanosheets (marked by yellow arrows). **e** Growth mechanism of TiO_2 cluster in MXene nanosheets having Ti vacancies and **f** an illustration showing TiO_2-(101) plane perpendicular to the MXene basal plane (0001). **g** Visual appearance of Ti_2CT_x and $Ti_3C_2T_x$ colloidal solutions stored in different environments over time. **a** and **b** are reproduced with permissions from Ref. [14]. **c–f** are reproduced with permissions from Ref. [7]. **g** is reproduced with permissions from Ref. [18]

exist in MXene nanosheets [15–17]. Xia et al. [13], in their STEM-assisted study on Ti_3C_2 MXene flakes oxidation at ambient conditions, suggested that structural defects are the nucleation centers for the oxidation of MXenes (Fig. 1c–f). They proposed that carbon atoms at positively charged Ti vacancies undergo oxidation (from C^{4-} to C^0) by losing electrons to form the aggregations of amorphous carbon, resulting in the accumulation of positively charged holes at this area (positively charged area). In the meantime, excess electrons are quickly transported in Ti_3C_2 prior to their accumulation as a net negative charge at immediate convex locations created by the atomic steps/crumpled surface. In this way, an internal electric field of a few nanometers is developed in the MXene nanosheet between accumulated positive and negative charge regions (Fig. 1e). The available O_2 enters into the MXene lattice as O^{2-} by withdrawing two electrons from the location of accumulated electrons. At the same time, the internal electric field pushes Ti cations towards this region, which allows the formation of anatase TiO_2 and oxidation of more carbon atoms (Fig. 1e). Hence, with the increased growth of TiO_2, the number of holes and their size also increases, which eventually disintegrates the 2D morphology. Further, TiO_2 preferentially grows along the (101) plane perpendicular to the (0001) basal plane of MXene (Fig. 1f). However, a study on oxidation of two types of titanium carbide MXenes (Ti_2CT_x and $Ti_3C_2T_x$) in water/O_2, water/Ar, iso-proponal/O_2, and iso-proponal/Ar environments demonstrated that water is a primary reagent that oxidizes the MXene, and oxidation of MXene is composition-dependent, thin MXene (Ti_2CT_x) is more vulnerable to oxidation than the thicker one ($Ti_3C_2T_x$) (Fig. 1g) [18]. The hydrolysis

reaction that converts $Ti_3C_2T_x$ MXene into TiO_2 is speculated to be accompanied by several gaseous species, including CO, CO_2, CH_4, and H_2 as shown in the following reactions.

$$2Ti_3C_2O_2 + 11H_2O \rightarrow 6TiO_2 + CO\uparrow + CO_2\uparrow + 2CH_4\uparrow + 7H_2\uparrow \quad (1)$$

Or

$$2Ti_3C_2(OH)_2 + 11H_2O \rightarrow 6TiO_2 + CO\uparrow + CO_2\uparrow + 2CH_4\uparrow + 9H_2\uparrow \quad (2)$$

However, later in a different report, the authors confirmed that the reactions of carbide MXenes ($Ti_3C_2T_x$) with water yield only CH_4, while the oxidation of carbonitride MXene (Ti_3CNT_x) facilitates the formation of both CH_4 and NH_3 gases [19].

Overall, it is reasonable to believe that intrinsic defects, water, and oxygen are causing the oxidation of MXene. The degradation phenomena are very quick in aqueous solution compared to powder form because the hydrophilic surface functional groups assist good aqueous dispersing ability and accelerate the interaction with water or dissolved oxygen in the water. Therefore, transforming aqueous MXene solutions into dried powders is one of the helpful approaches to enhance the shelf-life of MXenes by avoiding oxidation. The MXene oxidation is slower if the solution is converted into a thin film of well-aligned flakes because the compact morphology avoids inner flakes' interaction with the air [10]. Theoretically, multilayered MXene powders formed immediately after etching and before the delamination process are expected to exhibit stability identical to MXene films [20]. However, transforming MXene solution into powder or films through the drying process leads to the re-stacking of MXene flakes. As a result, the re-dispersion of dried powders/thin films into solvent media to form the delaminated MXene solutions is hindered when the application demands a solution-based processing. Although sonication enhances the re-dispersion of powders in the solution, it reduces the flakes size and eventually speeding up the oxidation. Therefore, the possible approach to prevent the oxidation of MXenes while retaining the monolayer and large size flakes in a good solution dispersion state is removing factors that are initiating the oxidation i.e., defects, dissolved oxygen, and water.

1.1 Stability of MXene in Aqueous Solution

De-aerating the MXene solution with inert gases such as argon to remove the oxygen from the solution and storing it at low temperatures are the widely applied strategies to enhance the shelf-life of aqueous MXene dispersion [9, 10]. As shown in Fig. 2a, b, d, and e, the aging of aqueous MXene in the air at room temperature (Air@RT) for 7 days led to the formation of 2–3 nm size particles on the basal plane along with some branches on edge sites. After prolonging the aging time in Air@RT to 30 days, MXene nanosheets completely decomposed to amorphous carbon and anatase TiO_2

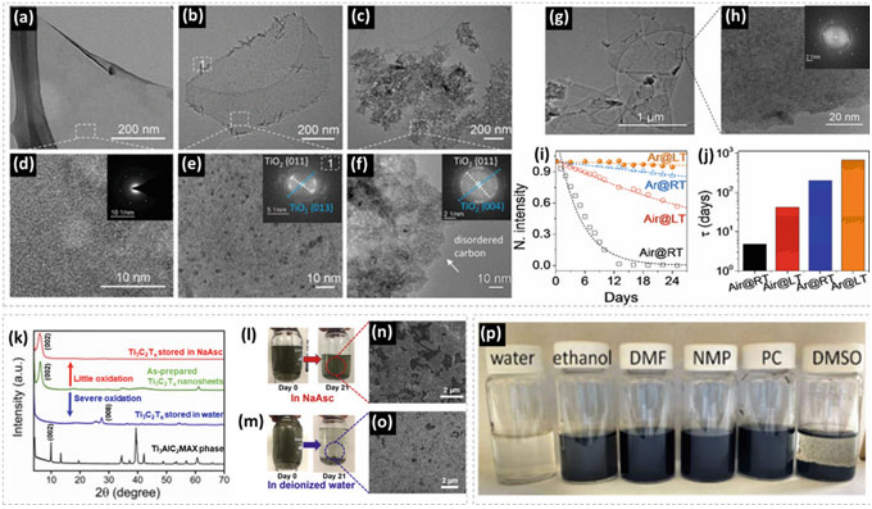

Fig. 2 TEM images of **a**, **d** MXene flakes from fresh d-$Ti_3C_2T_x$ solution and aged solutions in Air@RT for **b**, **e** 7 days and **c**, **f** 30 days. Inset in panel **d** is the corresponding SAED pattern, and those in panels **e** and **f** are the corresponding FFT patterns. **g** Low- and **h** high-magnification TEM images of aged d-$Ti_3C_2T_x$ flakes in Ar@LT for 30 days. Inset in panel **h** is the corresponding FFT pattern. **i** Stability of colloidal d-$Ti_3C_2T_x$ in different environments. The dotted lines are the fitting results according to the empirical equation $A = A_{unre} + A_{re}e^{-t/\tau}$. **j** Time constants of colloidal d-$Ti_3C_2T_x$ in different environments. **k** Crystalline structural properties of Ti_3AlC_2 and $Ti_3C_2T_x$ characterized using X-ray diffraction. Digital images of dispersions at day 0 and day 21 in **l** sodium L-ascorbate (NaAsc) and **m** deionized water. Scanning electron microscopy (SEM) images of $Ti_3C_2T_x$ nanosheets after being stored in **n** NaAsc solution and **o** deionized water for 21 days. **p** Long term stability (after 40 days) of $Ti_3C_2T_x$ MXene in organic solvents and water. **a–j** are reproduced with permissions from Ref. [10]. **k–o** are reproduced with permissions from Ref. [21]. **p** is reproduced with permissions from Ref. [22]

(Fig. 2c and f). However, aqueous MXene nanosheets stored in Ar-filled bottles at low temperatures (5 °C) (Ar@LT) retained their well-defined nanosheet morphology even after 30 days (Fig. 2g and h). In addition, decay constant measured from the empirical function $A = A_{unre} + A_{re}e^{-t/\tau}$ (A_{unre} and A_{re} represent the stable/unreactive and reactive/unstable MXene nanosheets, respectively; τ is the time constant) using the UV–visible absorption peak's intensity of aqueous MXene stored in Air@RT, air at low temperature (Air@LT), argon at room temperature (Ar@RT), and Ar@LT for over 24 days, further ascertained that the synergetic effect of inert atmosphere and low temperature (Ar@LT storage condition) can maximize the shelf-life of stored MXene (Fig. 2i and j). Further, the time constant of aqueous MXene stored at four different conditions followed the order Ar@LT > Ar@RT > Air@LT > Air@RT, indicating the dissolved oxygen supremacy in oxidizing MXene.

Maintaining the acidic pH and increasing the colloidal concentration are also proficient at hindering aqueous MXene oxidation. Zhao et al. [23] investigated the oxidation stability of both $Ti_3C_2T_x$ and Ti_2CT_x aqueous dispersions by tuning their

pH from 2 to 10 with the addition of either 0.1 M HCl or 0.1 M KOH. The higher pH of colloidal dispersion due to the addition of KOH drastically decreased in 48 h and then gradually declined with increased storage time. The abrupt decrease in pH was due to the MXene reaction with hydroxyl anions released from the added KOH as shown below

$$Ti_3C_2OH + OH^- \rightarrow Ti_3C_2O^- + H_2O \quad (3)$$

Especially, the positively charged edges of MXene nanosheets allow excessive interaction with the negatively charged hydroxyl anions and encourage the edge-driven oxidation of MXenes. On the other hand, in the acidic environment maintained with the HCl addition, owing to the positive charge of MXene edges and H_3O^+ intermediate species produced due to protons (released from HCl) interaction with water molecules, very minimal oxidation (similar to pristine MXene) is noticed. However, excessive addition of strong acid may cause surface defect formation by reacting with the MXene surface, which is detrimental to the oxidation stability of MXenes. Further, diluted MXene solutions are prone to oxidize quickly compared to highly concentrated aqueous solutions. The capping and steric shielding effects among nanosheets in highly concentrated solutions retarded the water reaction with the MXene nanosheet edges and reasoned to slow oxidation kinetics. Further, as the agitation disturbs the steric shielding effect, static or undisturbed solutions exhibit higher oxidation stability compared to agitated solutions [23].

Antioxidants such as L-ascorbate and citric acid were employed to extend the shelf-life of aqueous MXene dispersions [21]. In the absence of antioxidant, the $Ti_3C_2T_x$ MXene flakes were quickly oxidized into TiO_2 and formed large-scale aggregations, and films formed from these samples showed loss of electrical conductivity. But, the presence of antioxidant assists $Ti_3C_2T_x$ flakes to preserve their colloidal stability, chemical composition, morphology, crystal structure, and electrical conductivity even after their three weeks' storage in water (Fig. 2k–o). The enhanced oxidation stability was assigned to the suppressed oxidation reaction owing to the association of L-ascorbate anions to the edges of $Ti_3C_2T_x$ nanosheets.

1.2 Organic Media to Increase the Oxidation Stability of Colloidal MXene

Replacing the water medium with an organic solvent (that minimizes the water and dissolved oxygen interaction with MXene) is considered as an efficient approach to tackle the uncontrollable oxidation of MXenes. Yury and co-workers [22] confirmed that pristine $Ti_3C_2T_x$ MXenes have excellent dispersibility in specific organic solvents such as ethanol, N-methyl-2-pyrrolidone (NMP), dimethylformamide (DMF), dimethyl sulfoxide (DMSO), and propylene carbonate (PC). Further, after monitoring the oxidation stability of both aqueous and organic solvent dispersed

MXene for 40 days, they ascertain that organic solvents retarding the oxidation of MXene and preserving the intrinsic dark black/green color of MXene, while aqueous MXene completely converted into cloudy white color TiO_2 solution (Fig. 2p). Carey et al. [24] exchanged intercalated lithium ions in interlayers of pristine MXene with di(hydrogenated tallow)benzyl methyl ammonium chloride (DHT) to form colloidal suspensions in nonpolar solvents such as chloroform, decalin, hexane, cyclohexane, toluene, and p-xylene. These $Ti_3C_2T_x$ dispersions are stable for at least 10 days. Especially, DHT-$Ti_3C_2T_x$ dispersed in decalin is stable over DI water for more than 30 days. However, the organic dispersions are often limited to very less concentrations of MXene (below 0.5 mg mL^{-1}), which encourage the chances for a higher amount of dissolved oxygen that may speed up the oxidation phenomena. Therefore, attaining MXene organic solvent dispersions with high concentration is also a challenging task to store the MXene for a long duration. Recently, Zhang et al. [25] reported a tuned microenvironment method (TMM) by employing tetrabutylammonium hydroxide (TBAOH) as an intercalant and surface modifier to the multilayered $Ti_3C_2T_x$ produced using HF (40%) to enable concentrated $Ti_3C_2T_x$ organic dispersions in various organic solvents. It was noticed that solvents such as N,N-dimethylacetamide, DMF, and PC enabled MXene dispersions with concentrations higher than 5 mg mL^{-1}. Furthermore, PC was demonstrated to be the best suitable organic solvent to mitigate the oxidation of MXene, as the MXene-PC dispersions stored at room temperature for 30 days didn't show any degradation.

1.3 Surface Modification of MXenes

Physical or chemical surface modification of MXenes that enable the dispersion in organic solvents and encapsulation of edges and defects has also been utilized to improve the oxidation stability of MXenes. Krecker et al. [26] demonstrated the enhanced shelf-life of MXenes through bioencapsulation with uniform coatings of silk, while Wu et al. [27] employed a carbon nanoplating strategy for the effective stabilization of MXene surface against oxygen-induced structural degradation. Kim et al. [28] chemically grafted alkylphosphonic acid ligands on the surface of the $Ti_3C_2T_x$ flakes that assisted good dispersion in nonpolar organic solvents such as hexanol and chloroform. They observed the complete degradation of water dispersed pristine MXene in 1 month, while alkylphosphonic acid functionalized MXenes dispersed in chloroform exhibited resistance to oxidation up to 3 months owing to the absence of dissolved oxygen and water in the water-immiscible organic solvent [28]. Further, Lee et al. [29] demonstrated binding of polydopamine to the MXene flake surfaces through spontaneous interfacial charge transfer to yield MXene films having highly aligned flakes with greatly improved ambient stability (Fig. 3a–e). Interestingly, the MXene/polydopamine hybrid film (denoted as PDTMx (x = 2.5, 5, 10, and 15), where x denotes the mass ratio of dopamine hydrochloride precursor) prepared with optimum concentration of polydopamine hydrochloride exhibited higher electrical conductivity compared to pristine MXene film (Fig. 3d). The hydrophobic

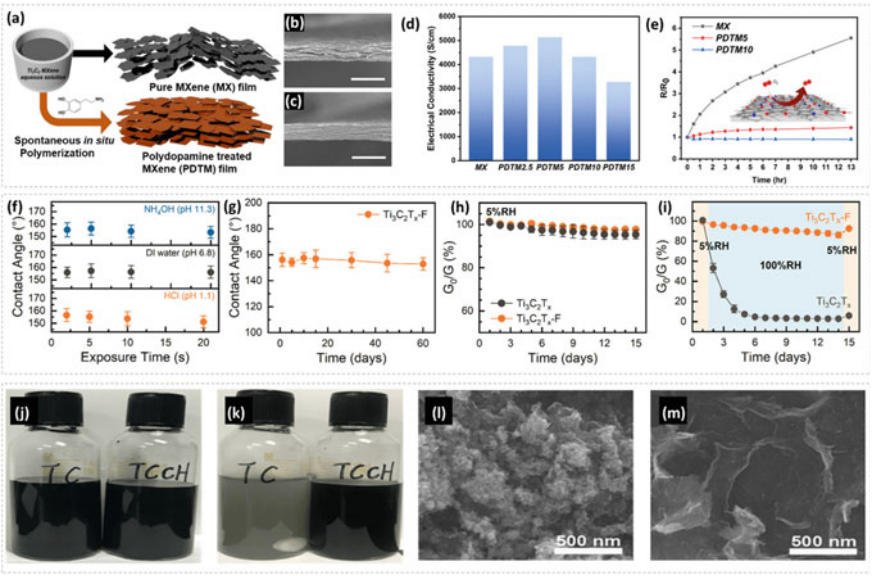

Fig. 3 Mussel-inspired MXene assembled film. **a** Schematic illustration of fabrication procedure and the morphological difference between pure MXene (MX) film and polydopamine-treated MXene (PDTM) film. Cross-sectional SEM images of **b** MXene and **c** PDTM5 (scale bar: 20 μm). **d** Electrical conductivity for each film. **e** Electrical resistance change upon heating (170 °C) in air. **f** Water contact angle measurements for $Ti_3C_2T_x$-F films after exposure to NH_4OH (pH 11.3), DI water (pH 6.8), and HCl (pH 1.1) for 2, 5, 10, and 20 s. **g** $Ti_3C_2T_x$-F film's water contact angle variations for 2 month storage at ambient conditions. **h**, **i** Change in electrical conductivity of $Ti_3C_2T_x$ and $Ti_3C_2T_x$-F stored in 5 and 100% RH over a period 2 weeks. Digital images of TC and TCCH **j** before and **k** after oxidation for 7 days. SEM images of **l** TC and **m** TCCH after oxidation for 7 days. **a–e** are reproduced with permissions from Ref. [29]. **f–i** are reproduced with permissions from Ref. [33]. **j–m** are reproduced with permissions from Ref. [34]

coating is also capable to protect MXenes from moisture induced oxidation [30]. In contrast to pristine MXene, the PDTMx films exhibited resistance to oxidation at a high temperature of 170 °C under ambient conditions, showing much lower electrical resistance change (Fig. 3e). Recently, the hybridization of MXenes with the transition metal dichalcogenide in which the chalcogenide material occupies the surface and edges of MXene is reported as an effective strategy to restrict the oxidation of MXene by hindering the interaction of water with the edges of MXene [31]. Chemical treatment with the L-ascorbic acid increased the oxidation stability of $Ti_3C_2T_x$ MXene nanosheets [11]. Further, inorganic polyanionic salts were also utilized to cap the edges of MXenes in order to improve the colloidal oxidation stability [32].

Chen and co-workers [33] reported the facile functionalization of 1H,1H,2H,2H-perfluorooctyltriethoxysilane (FOTS) on MXene surface as an effective protective layer. The hydrophobic FOTS functionalized MXene (denoted as $Ti_3C_2T_x$-F) films displayed an excellent stability against humidity, strong acidic solution (HCl, pH ~ 1.1), basic solution (NH_4OH, pH ~11.3), and deionized water (pH ~6.8) (Fig. 3f–i).

Figure 3h and i show variation in the electrical conductivity of both pristine and FOTS functionalized MXene films stored over two weeks in 5 and 100% relative humidity (RH) environments. At 5% RH, the change in electrical conductivity is very small for both films, indicating excellent stability in dry conditions. However, after being stored at 100% RH for 15 days, the pristine MXene film preserved only 2.7% of its initial conductivity, while FOTS functionalized MXene film preserved 86.2% of its initial conductivity. When films were stored back at 5%RH, the retained electrical conductivity of FOTS functionalized MXene film improved from 86.2 to 92.5% of its initial conductivity. These results confirmed the efficiency of FOTS in retarding the degradation of MXenes at extremely high humid conditions. Further, the surface of MXene was also modified through the covalent functionalization of diazonium salts [34, 35]. To establish the proficiency of diazonium salt functionalization in inhibiting the oxidation kinetics of MXene, pristine MXene (denoted as TC) and diazonium salt functionalized MXene (denoted as TCCH) nanosheets were subjected to intentional oxidation by stirring in ambient air for 7 days (Fig. 3j and k). The TC solution was completely converted into a cloudy white solution with its nanosheet morphology reduced to a cluster of nanoparticles, whereas the TCCH solution retained the intrinsic black/dark green color and nanosheet morphology (Fig. 3j–m) [34].

1.4 Advantages of MXenes Oxidation

On a positive note, the partial degradation of MXenes to corresponding oxides is favorable for forming the hybrid structure of MXene supported metal oxides or other derivatives of MXene in a facile manner without requiring multi-step synthesis protocols. The better physical and chemical properties of these MXene derived hybrid structures than the pristine MXene have led to immense research interests on controlled oxidation of MXenes intended for various applications [36–41]. Several approaches, including aging in air, high energy ball milling, thermal oxidation in air and CO_2 atmosphere, and chemical reactions, have been utilized to oxidize the MXenes [36, 42, 43]. Furthermore, the structure of MXene degradation is not restricted to metal oxides, carbons, and their composites; depending on the degrading techniques used, a wide range of MXene derivatives can be generated [36].

2 Degradation with Respect to Temperature

Several research investigations concluded that the temperature and light exposures could accelerate the interaction between oxygen or water with the MXenes [44]. Low storage temperature can minimize the influence of water or oxygen and does not require either degassing or purging inert gases [45]. Chae et al. [46] investigated the oxidation stability of MXenes at controlled temperatures by storing the MXene in anhydrous ethanol at 5 °C, and the air-filled aqueous MXene solution bottles

at 5 °C (cold storage temperature), −18 °C (freezing temperature), and −80 °C (cryogenic temperature). Raman spectroscopy, sheet resistance, and XPS analyses were utilized to assess the oxidation of the stored MXene solutions. It was evident that the air-filled aqueous MXene solution stored at −80 °C exhibited superior stability up to 39 weeks, similar to MXene dispersed in anhydrous ethanol stored at 5 °C. While both the aqueous solutions stored at 5 and −18 °C degraded eventually, the degradation was quicker in the case of 5 °C storage temperature due to the more frequent interaction of the dissolved oxygen and water with the MXene flakes. Habib et al. [8] studied the oxidation of MXene in ice (formed through freezing aqueous $Ti_3C_2T_x$ MXene solution to below 0 °C) using the conductivity of MXene films as an indicator to measure the degree of MXene oxidation; here, thin films were obtained by liquefying the ice and subsequent vacuum filtration. They have noticed only 23% drop in electrical conductivity after 21 days of storage, which was superior to the 65% drop after 14 days and 93% drop after 27 days observed in the case of MXene stored at room temperature in the form of aqueous dispersion and thin film, respectively. This concludes that the interaction of MXene with the oxygen and water depends on the storage temperature.

However, the stability of MXenes at high-temperature depends on the composition of MXenes and the environment [47, 48]. The thermal stability of $Ti_3C_2T_x$ is superior compared to fewer-atomic-layered Mo_2CT_x or Nb_2CT_x [49]. When Ti_2CT_x MXene powders are annealed in air at 225 °C, they transform to graphitic carbon and TiO_2 nanoparticles, whereas annealing at the same temperature in N_2 or Ar or N_2/H_2 atmosphere produces no visible changes in the MXene morphology [50]. Furthermore, annealing under an H_2 atmosphere effectively retarded the oxidation of $Ti_3C_2T_x$ in extremely humid conditions (100% relative humidity, 70 °C) [51]. However, the formation of TiO_2 was observed when $Ti_3C_2T_x$ was annealed in an argon atmosphere at 500 °C, which was attributed to the possible reaction of MXene with the –O and –OH functional groups attached on the surface [52]. In a different report, it was shown that surface terminal groups could also influence the oxidation stability of MXenes [53]. MXenes terminated with –O functional groups are prone to exhibit superior thermodynamic stability than the –OH or –F terminated counterparts [53]. Further, annealing at 1200 °C resulted in the defect elimination in the preserved Ti_3C_2 structure, while the XRD studies demonstrated a transformation of Ti_3C_2 into TiC structure [52]. Naguib et al. [12] reported the oxidation of MXene through heating of MXene free-standing film or powders in the air at 1150 °C for 30 s and using CO_2 at temperatures of 150, 300, and 500 °C for 1 h, while the aqueous dispersions were oxidized using hydrothermal treatment at 150, 200, and 250 °C for 48 h, 8–20 h, and 2 h, respectively. The thermal stability also depends on the etching method utilized during the synthesis process. The Ti_3C_2 prepared using NH_4HF_2 etchant required a higher annealing temperature of 500 °C in the air than the HF-etched counterpart (350 °C) to exhibit complete transformation from Ti_3C_2 to anatase TiO_2 [54].

3 Synthesis Parameters

The control over the reagents and reaction parameters, including the type of etchant, reaction time, and temperature used in the MXene synthesis reaction, undeniably influences the stability of MXenes [2, 6].

3.1 Influence of MAX Phase Precursor

The MXene flake size, purity, and defect structure, which are decisive for oxidation stability, depends on the precursor MAX phase because MXene synthesis is mainly a top-down approach of eliminating the IIIA or IVA group element layers from the parent MAX phase. It has been found that the Ti_3AlC_2 MAX phase is prone to easy formation of mono- and di-vacancies of Al and divacancies comprising Al and C atoms [55]. The presence of C vacancies may lead to the loss of associated Ti atoms present in their vicinity during the acid etching process, resulting in MXenes with a high concentration of structural defects. However, Mathis et al. [56] speculated that the formation of C vacancies in the Ti_3AlC_2 MAX phase could be avoided by using an excess amount of Al for the Ti_3AlC_2 MAX phase synthesis. They concluded that the excess Al causes the formation of molten metal at an early stage of sintering reaction that allows the better diffusion of reactants and enables the formation of Ti_3AlC_2 grains with enhanced structural ordering and morphology. However, the as-obtained product from sintering should be washed with HCl to remove the $TiAl_3$ impurity formed along with the dominant Ti_3AlC_2 MAX phase. The aqueous MXenes synthesized from the resultant MAX phase (denoted as Al-Ti_3C_2) exhibited excellent oxidation stability up to 10 months in ambient conditions, while MXene derived from the conventional MAX phase precursor lasted no longer than a few weeks (Fig. 4a–d) [18]. After being stored for 10 months, Al-Ti_3C_2 flakes exhibited sharp edges but with a small number of pinholes on the surface (Fig. 4a and b). However, the electrical conductivity of these MXene flakes varied in the range of 10,000–20,000 S cm^{-1} depending on the volume of water employed in the delamination step of their synthesis, which confirms that every step of MXene synthesis needs to be controlled carefully to obtain high-quality MXene.

The carbon precursor used for the MAX phase synthesis also significantly impacts the phase purity and particle size of the MAX phase. Shuck et al. [57] synthesized three kinds of Ti_3AlC_2 MAX phases at an identical reaction conditions using three different carbon sources such as titanium carbide (TiC), carbon lampblack, and graphite (Fig. 4e–g). The carbon precursor influenced the particle size and purity of the MAX phase formed, with graphite-MXene (4.2 μm) > TiC-MXene (2.6 μm) > carbon lampblack-MXene (0.5 μm) as the order of particle size, and Ti_3AlC_2 MAX phase purity of 95, 93, and 72 at.% for graphite, carbon lampblack, and TiC produced samples, respectively. Three different MAX phases resulted in MXenes with dissimilar flake sizes (Fig. 4h–j). As a result, the properties and

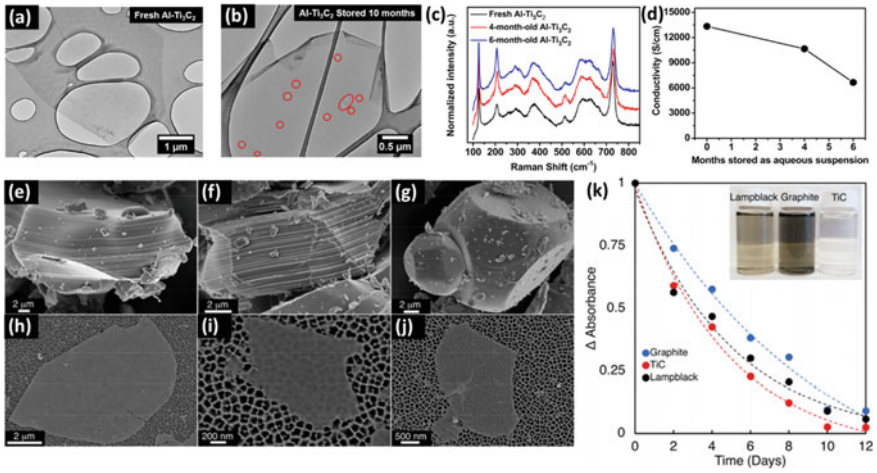

Fig. 4 TEM images of **a** a fresh Al–Ti_3C_2 flake and **b** Al–Ti_3C_2 flake from a 10-month-old solution (The red circles mark pinholes in the flake). **c** Raman spectra of films made from solutions stored for different periods of time. **d** Electronic conductivity of free-standing Al–Ti_3C_2 films made from solutions stored for different periods of time. SEM images of Ti_3AlC_2 synthesized by using **e** graphite, **f** TiC, and **g** carbon lampblack as carbon source. SEM images of $Ti_3C_2T_x$ MXene produced by a MILD-like process (40 h etching in 12 M HCl and 9 M LiF) using **h** graphite, **i** TiC, and **j** carbon lampblack-derived MAX phases. **k** Solution stability of the 0.15 mg mL^{-1} MXene colloidal solutions dispersed in deionized water calculated by the change in solution absorbance (Δ Absorbance) over 12 days. The lines represent fitting results calculated from the exponential decay function ($f(x) = y_0 + Ae^{-x/\tau}$, where y_0 is the offset value, A is the amplitude, and τ is the time constant) for aqueous solutions stored in air. All samples were stored at ambient temperature in a lab drawer away from sunlight. The digital image (inset) displays the differences in concentration of lampblack-, graphite-, and TiC-produced $Ti_3C_2T_x$ samples (left to right) after 12 days. **a–d** are reproduced with permissions from Ref. [56]. **e–k** are reproduced with permissions from Ref. [57]

oxidation stability of MXenes derived from these MAX phases varied significantly, with the oxidation stability order of Graphite-MXene > lampblack-MXene > TiC-MXene (Fig. 4k). Therefore, selecting MAX phase precursor of high-quality and large particle size is significant to achieve better oxidation stability. Further, the raw materials and their composition and sintering conditions of the MAX phase are very significant as they can result in the formation of unwanted Al_2O_3, TiC, and Ti_2AlC impurities along with the formation of intended Ti_3AlC_2 MAX phase, which ultimately affects the quality of MXene [58]. The interaction of precursor materials (of MAX phase) with the atmospheric air is enough to generate the impurities such as α-Al_2O_3 in the MAX phase that remain in MXenes even after the etching processes [59].

3.2 Etchant and Delamination Process Effects

The choice of etchants and the delamination procedures used to obtain the multilayered, few-layered, or mono-layered MXene structure directly influences the oxidation stability of MXene by causing the formation of defect structures or resulting in fragmentation of nanosheets. Because of their direct contact with the strong acids during etching, the top and bottom metallic sublayers of MXene are more likely to have vacancies, but defects in the middle atomic layer cannot be entirely ruled out because such vacancies can be inherited from the parent MAX phase. In general, concentrated HF or *in-situ* formed HF were utilized in a top-down synthesis strategy to remove A-layers from the MAX phase to form MXene flakes. The concentrated HF etchant is observed to increase the density of defects that are prone to cause MXene oxidation [60]; the higher the HF concentration, the greater the formation of defects on the surface of MXenes (Fig. 5a–d). For example, the HF etching protocol resulted in Nb_2C MXene decorated with Nb adatoms from the Nb_2AlC precursor. These Nb adatoms react with the atmospheric oxygen and destabilize the MXene structure, leading to Nb_2C MXene degradation [61]. Further, the concentrated HF etchant-assisted synthesis requires an additional synthesis step of intercalation with organic molecules such as DMSO, TBAOH, and tetramethylammonium hydroxide (TMAOH), and subsequent sonication to delaminate the multilayered MXene to monolayer nanosheets [2, 6]. This causes fragmentation of MXene nanosheets or results in the formation of holes in the nanosheet morphology, which increases the defect concentration that declines the oxidation stability [62]. On the other hand, the in-situ formed HF from LiF and HCl demonstrated less defective structure of MXene, especially, the synthetic approach which employs LiF:Ti_3AlC_2 molar ratio ≥ 7.5 and does not require any further delamination process, such as organic molecule intercalation or sonication, yields high-quality MXene flakes exhibiting excellent stability against oxidation [63–65]. Further, the intercalant ions introduced by the etchants also influence the oxidation process of MXenes. For example, the Fe^{3+} ions introduced by the FeF_3/HCl etchant solution accelerated the oxidation of MXenes and favoured the formation of anatase phase TiO_2, while the Li^+ ions introduced by the LiF/HCl etchant solution are causing less oxidation and favoured the formation of rutile phase TiO_2 [66].

The functional groups terminated on the MXene surface to ensure the surface charge neutrality after the chemical etching and washing processes alter the defect formation energy in MXenes. Density functional theory calculations predicted the easy Ti vacancy formation in $Ti_3C_2T_x$ MXene terminated with –OH and –F functional groups (similar to bare MXene), while the Ti vacancy formation energy of –O terminated MXene is much higher owing to the stronger interaction between –O and –Ti (Fig. 5e) [60]. However, functional groups are sensitive to the synthesis method, LiF-HCl synthesis method generates much higher –O terminations in $Ti_3C_2T_x$ MXene in comparison to HF synthesis method (Fig. 5f) [67]. As a result, MXenes synthesized using the LiF-HCl technique are expected to have substantially improved oxidation stability. However, He and co-workers [68] observed a higher oxidation degree in

–O rich ultrathin $Ti_3C_2T_x$ MXene (U-$Ti_3C_2T_x$) synthesized using LiF-HCl etchant compared to –F rich multilayered $Ti_3C_2T_x$ MXene (M-$Ti_3C_2T_x$) synthesized using HF as an etchant. The higher accessible area of ultrathin MXene for water and air interaction accelerates its oxidation rate compared to multilayered MXene, where water interaction with stacked flakes is restricted (Fig. 5).

3.3 Etching Temperature and Etching Time

In MXene synthesis reaction parameters such as etching temperature and etching time are also significant for getting high-quality MXene nanosheets [2, 6]. Although etching at high temperature for an extended period in LiF-HCl etchant medium

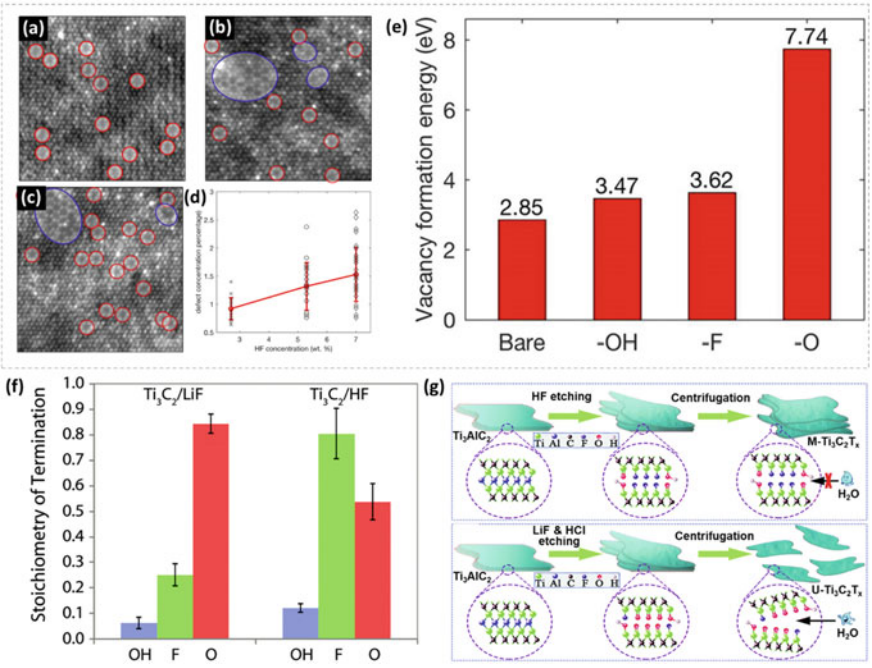

Fig. 5 HAADF-STEM images of single-layer $Ti_3C_2T_x$ MXene flakes prepared using different concentrations of HF etchant: **a** 2.7 wt.% HF, **b** 5.3 wt.% HF, and **c** 7 wt.% HF (Single V_{Ti} vacancies are indicated by red circles, while vacancy clusters $V_{Ti}{}^{C}$ are shown by blue circles). **d** Scatter plot of defect concentration from images acquired from samples produced using different HF concentrations. The red line shows the error plot with the average and standard deviation for different HF concentrations. **e** V_{Ti} formation energy on bare Ti_3C_2 and terminated single-layer $Ti_3C_2T_x$. **f** Composition of the $Ti_3C_2T_x$ surface functional groups produced by etching of the Ti_3AlC_2 in HF and LiF-HCl solutions, per Ti_3C_2 formula unit, i.e. $Ti_3C_2(OH)_xF_yO_z$. **g** Synthetic illustration of M-$Ti_3C_2T_x$ and U-$Ti_3C_2T_x$ MXenes. **a–e** are reproduced with permissions from Ref. [60]. **f** is reproduced with permissions from Ref. [67]. **g** is reproduced with permissions from Ref. [7]

assists the complete conversion of MAX phase to MXene, the quality of flakes was observed to be very poor owing to higher defect concentration [65]. Further, the tendency to form metal oxides together with MXenes increases with increasing the etching temperature [69]. Hence, shorter etching durations, low etching temperature, and maintaining the inert atmosphere during the etching process may prevent the oxidation and formation of over-etching induced defects and pinholes in the as-formed MXenes.

3.4 Water-Free MXene Synthesis

As water is one of the main oxidizing agents of MXene in a colloidal dispersion state, an entirely water-free MXene synthesis may help minimize water interaction with the MXene. *Natu* et al. [70] demonstrated that it is possible to etch and delaminate MXenes in the absence of water by using organic polar solvents (PC, acetonitrile (ACN), dioxane (DXN), DMF, DMSO, and NMP) in the presence of NH_4HF_2. The manipulation of surface functional groups from generally observed (–OH, –F, –O, –Cl, etc.) functional groups to other kinds of terminations may offer more opportunities to overcome challenges in grafting methods of MXenes. Recently, Jawaid et al. [71] reported the synthesis of $Ti_3C_2X_n$ (X = Br or I) MXene by treating the parent Ti_3AlC_2 precursor with halogens (Br_2, I_2, ICl, and IBr) in an anhydrous media (cyclohexane) at room temperature. The halogenated $Ti_3C_2X_n$ (X = Br or I) MXenes are readily dispersible in organic solvents with low dielectric constants, including chloroform, tetrahydrofuran (THF), and ACN. The dispersibility in anhydrous solvents will enable the post-synthetic modification of MXene surfaces via a molecular hybridization with organic moieties such as reversible addition-fragmentation chaintransfer (RAFT) polymerization or direct S_N2-type reactions on the labile Ti−X bond.

4 Synthesis Conditions

It is predicted that strong etchants and longer etching durations are needed to produce $M_{n+1}X_nT_x$ MXenes having larger "n" values and M is of higher atomic number element [2]. Because higher atomic number elements usually have more valence electrons, they create a stronger M-A bonding in the parent MAX phase. Hence, defect concentration may vary depending on the synthesis conditions employed to etch each particular MAX phase. However, most of the MXene's research, which is now extensively focused on the $Ti_3C_2T_x$ MXene, has used an HF etching method and revealed that increased HF concentration and etching duration leads to more defects. Further, employing ultrasonication during the etching process is recognized to produce high-quality MXenes at short reaction times. However, excessive ultrasonication could drastically decrease the flake size, which is not favorable to maintain higher oxidation stability [72, 73]. In a fluorine-free hydrothermal synthesis of $Ti_3C_2T_x$ MXene using alkali treatment, the concentration of NaOH and reaction temperature are crucial to

inhibit the oxidation of Ti from forming $Na_2Ti_3O_7$ and $Na_2Ti_5O_{11}$ phases [74, 75]. On the other hand, a chemical vapor deposition (CVD) method, which is a bottom-up synthesis strategy, could yield MXenes with larger lateral size and less or no defects [76, 77]. For example, Xu et al. [77] fabricated high-quality few nanometers thick and defect-free 2D ultrathin α-Mo_2C crystals with a size in the range of 100 μm by a CVD method.

5 Challenges and Perspectives

It is highly challenging to completely avoid the oxidation of MXenes in ambient conditions. But, the control over all pre-and post-synthesis procedures/conditions can mitigate the oxidation vulnerability of MXenes to the maximum extent. The inevitable formation of atomic defects in MXene nanosheets during their synthesis via wet chemical etching is the primary oxidation reaction source that converts 2D MXenes to their corresponding metal oxide nanoparticles. Exposure to water, oxygen, and light fuels the oxidation phenomena in MXenes. Further, larger-sized flakes are more oxidation resistant than smaller-sized flakes. As the MXene synthesis is mainly a top-down approach, many factors, including MXene sheet size, purity, and defect structure, directly depend on the precursor MAX phase. Therefore, phase purity of the MAX phase alone should not be considered as an exclusive qualification for its selection as a precursor for the MXene synthesis, additional parameters including the stoichiometric composition, grain size, and crystallinity of MAX phase are significant to yield high-quality MXenes. The conversion of MAX phase into MXene using MILD or TMM synthesis methods guarantees the formation of larger-size flakes with fewer defects, which are prone to exhibit higher oxidation stability, owing to the easy delamination procedures that do not require harsh ultrasonication step. As water is one of the oxidizing reagents of MXene, water-free MXene synthesis methods can help produce MXenes with higher oxidation stability. Further, the change in etching solvent from water to organic solvent tunes the surface functional groups type and composition, which in turn tune the defect formation in resultant MXene flakes. Therefore, new water-free synthesis strategies should be investigated to improve the oxidation stability of MXenes. Additionally, chemical and physical surface grafting of MXenes with organic molecules or semiconductors retards oxidation kinetics by allowing dispersion in organic solvents and preventing the interaction of MXenes' edges and surface defects with water or dissolved oxygen. However, so far developed surface grafting techniques are sacrificing intrinsic properties of MXenes such as electrical conductivity that is crucial in their applications. Hence, finding new chemistry and the corresponding organic ligands assisting MXenes in exhibiting high oxidation resistance while maintaining their excellent electrical conductivity and other intrinsic properties is still an urgent need. For prolonged storage of as-synthesized MXenes, the synergetic effect of organic dispersing media, high colloidal MXene concentration, inert atmosphere, and low temperature should be utilized.

6 Conclusions

Herein, we have reviewed the so far achieved progress in understanding the oxidation stability of MXenes as well as various techniques adopted to prevent or slow down oxidation kinetics of MXenes. Being a critical concern for MXenes applications, stability enhancement of MXenes against ambient atmosphere exposure deserves more attention. Still, there are numerous opportunities for breakthroughs in this area of MXene research. Starting from raw materials and synthesis conditions utilized for MAX phase preparation, etchant solution type and its concentration as well as etching duration employed to remove the 'A' layers of MAX phase in order to synthesize MXene, and storage conditions including temperature and atmosphere, dispersing media, and concentration of the colloidal solution significantly impacted the oxidation stability of MXenes. Effective strategies to completely avoid the oxidation of MXene flakes remain elusive, especially for those dispersed in water media. We expect this book chapter is informative to the reader intended to understand the stability of MXenes and investigate new approaches to enhance the shelf-life of MXene based on the outcomes of previous contributions.

Acknowledgements This research was supported by the Basic Science Research Program through the National Research Foundation of Korea (NRF) funded by the Ministry of Education (2018R1A6A1A03023788, 2019R1A2C1010692, 2021R1I1A1A01055790), and the Korea Institute for Advancement of Technology (KIAT) grant funded by the Korea Government (MOTIE) (P00008500, The Competency Development Program for Industry Specialist).

References

1. Hasan, M.M., Hossain, M.M., Chowdhury, H.K.: Two-dimensional MXene-based flexible nanostructures for functional nanodevices: a review. J. Mater. Chem. A **9**, 3231–3269 (2021)
2. Anasori, B., Lukatskaya, M.R., Gogotsi, Y.: 2D metal carbides and nitrides (MXenes) for energy storage. Nat. Rev. Mater. **2**(2), 16098 (2017)
3. Tang, X., Murali, G., Lee, H., Park, S., Lee, S., Oh, S.M., Lee, J., Ko, T.Y., Koo, C.M., Jeong, Y.J., An, T.K., In, I., Kim, S.H.: Engineering aggregation-resistant mxene nanosheets as highly conductive and stable inks for all-printed electronics. Adv. Funct. Mater. **31**, 2010897 (2021)
4. Park, Y.H., Murali, G., Modigunta, J.K.R., In, I., In, S.-I.: Recent advances in quantum dots for photocatalytic CO_2 reduction: a mini-review. Front. Chem. **9**, 734108 (2021). https://doi.org/10.3389/fchem.2021.734108
5. Vu, M.C., Mani, D., Kim, J.-B., Jeong, T.-H., Park, S., Murali, G., In, I., Won, J.-C., Losic, D., Lim, C.-S., Kim, S.-R.: Hybrid shell of MXene and reduced graphene oxide assembled on PMMA bead core towards tunable thermoconductive and EMI shielding nanocomposites. Compos. A: Appl. Sci. Manuf. **149**, 106574 (2021)
6. Murali, G., Rawal, J., Modigunta, J.K.R., Park, Y.H., Lee, J.-H., Lee, S.-Y., Park, S.-J., In, I.: A review on MXenes: newgeneration 2D materials for supercapacitors. Sustain. Energ. Fuels. **5**(22), 5672–5693 (2021)
7. Iqbal, A., Hong, J., Ko, T.Y., Koo, C.M.: Improving oxidation stability of 2D MXenes: synthesis, storage media, and conditions. Nano Converg. **8**(1), 9 (2021)

8. Habib, T., Zhao, X., Shah, S.A., Chen, Y., Sun, W., An, H., Lutkenhaus, J.L., Radovic, M., Green, M.J.: Oxidation stability of $Ti_3C_2T_x$ MXene nanosheets in solvents and composite films. NPJ 2D Mater. Appl. **3**(1), 8 (2019)
9. Seyedin, S., Zhang, J., Usman, K.A.S., Qin, S., Glushenkov, A.M., Yanza, E.R.S., Jones, R.T., Razal, J.M.: Facile solution processing of stable MXene dispersions towards conductive composite fibers. Glob. Chall. **3**(10), 1900037 (2019)
10. Zhang, C.J., Pinilla, S., McEvoy, N., Cullen, C.P., Anasori, B., Long, E., Park, S.-H., Seral-Ascaso, A., Shmeliov, A., Krishnan, D., Morant, C., Liu, X., Duesberg, G.S., Gogotsi, Y., Nicolosi, V.: Oxidation stability of colloidal two-dimensional titanium carbides (MXenes). Chem. Mater. **29**(11), 4848–4856 (2017)
11. Limbu, T.B., Chitara, B., Orlando, J.D., Garcia Cervantes, M.Y., Kumari, S., Li, Q., Tang, Y., Yan F.: Green synthesis of reduced $Ti_3C_2T_x$ MXene nanosheets with enhanced conductivity, oxidation stability, and SERS activity. J. Mater. Chem. C **8**(14), 4722–4731 (2020)
12. Naguib, M., Mashtalir, O., Lukatskaya, M.R., Dyatkin, B., Zhang, C., Presser, V., Gogotsi, Y., Barsoum, M.W.: One-step synthesis of nanocrystalline transition metal oxides on thin sheets of disordered graphitic carbon by oxidation of MXenes. Chem. Commun. **50**(56), 7420–7423 (2014)
13. Xia, F., Lao, J., Yu, R., Sang, X., Luo, J., Li, Y., Wu, J.: Ambient oxidation of Ti_3C_2 MXene initialized by atomic defects. Nanoscale **11**(48), 23330–23337 (2019)
14. Karlsson, L.H., Birch, J., Halim, J., Barsoum, M.W., Persson, P.O.Å.: Atomically resolved structural and chemical investigation of single MXene sheets. Nano Lett. **15**(8), 4955–4960 (2015)
15. Cui, W., Hu, Z.-Y., Unocic, R.R., Van Tendeloo, G., Sang, X.: Atomic defects, functional groups and properties in MXenes. Chin. Chem. Lett. **32**(1), 339–344 (2021)
16. Wu, H., Guo, Z., Zhou, J., Sun, Z.: Vacancy-mediated lithium adsorption and diffusion on MXene. Appl. Surf. Sci. **488**, 578–585 (2019)
17. Bandyopadhyay, A., Ghosh, D., Pati, S.K.: Effects of point defects on the magnetoelectronic structures of MXenes from first principles. Phys. Chem. Chem. Phys. **20**(6), 4012–4019 (2018)
18. Huang, S., Mochalin, V.N.: Hydrolysis of 2D transition-metal carbides (MXenes) in colloidal solutions. Inorg. Chem. **58**(3), 1958–1966 (2019)
19. Huang, S., Mochalin, V.N.: Understanding chemistry of two-dimensional transition metal carbides and carbonitrides (MXenes) with gas analysis. ACS Nano **14**(8), 10251–10257 (2020)
20. Deysher, G., Sin, S., Gogotsi, Y., Anasori, B.: Oxidized 2D titanium carbide MXene: flash oxidized powders. Mater. Today **21**(10), 1064–1065 (2018)
21. Zhao, X., Vashisth, A., Prehn, E., Sun, W., Shah, S.A., Habib, T., Chen, Y., Tan, Z., Lutkenhaus, J.L., Radovic, M., Green, M.J.: Antioxidants Unlock Shelf-Stable $Ti_3C_2T_x$ (MXene) Nanosheet Dispersions. Matter. **1**(2), 513–526 (2019)
22. Maleski, K., Mochalin, V.N., Gogotsi, Y.: Dispersions of two-dimensional titanium carbide MXene in organic solvents. Chem. Mater. **29**(4), 1632–1640 (2017)
23. Zhao, X., Vashisth, A., Blivin, J.W., Tan, Z., Holta, D.E., Kotasthane, V., Shah, S.A., Habib, T., Liu, S., Lutkenhaus, J.L., Radovic, M., Green, M.J.: pH, Nanosheet concentration, and antioxidant affect the oxidation of $Ti_3C_2T_x$ and Ti_2CT_x MXene dispersions. Adv. Mater. Interf. **7**(20), 2000845 (2020)
24. Carey, M., Hinton, Z., Natu, V., Pai, R., Sokol, M., Alvarez, N.J., Kalra, V., Barsoum, M.W.: Dispersion and stabilization of alkylated 2D MXene in nonpolar solvents and their pseudocapacitive behavior. Cell Rep. Phys. Sci. **1**(4), 100042 (2020)
25. Zhang, Q., Lai, H., Fan, R., Ji, P., Fu, X., Li, H.: High concentration of $Ti_3C_2T_x$ MXene in organic solvent. ACS Nano **15**(3), 5249–5262 (2021)
26. Krecker, M.C., Bukharina, D., Hatter, C.B., Gogotsi, Y., Tsukruk, V.V.: Bioencapsulated MXene flakes for enhanced stability and composite precursors. Adv. Funct. Mater. **30**(43), 2004554 (2020)
27. Wu, X., Wang, Z., Yu, M., Xiu, L., Qiu, J.: Stabilizing the MXenes by carbon nanoplating for developing hierarchical nanohybrids with efficient lithium storage and hydrogen evolution capability. Adv. Mater. **29**(24), 1607017 (2017)

28. Kim, D., Ko, T.Y., Kim, H., Lee, G.H., Cho, S., Koo, C.M.: Nonpolar organic dispersion of 2D $Ti_3C_2T_x$ MXene flakes via simultaneous interfacial chemical grafting and phase transfer method. ACS Nano **13**(12), 13818–13828 (2019)
29. Lee, G.S., Yun, T., Kim, H., Kim, I.H., Choi, J., Lee, S.H., Lee, H.J., Hwang, H.S., Kim, J.G., Kim, D.-W., Lee, H.M., Koo, C.M., Kim, S.O.: Mussel inspired highly aligned $Ti_3C_2T_x$ MXene film with synergistic enhancement of mechanical strength and ambient stability. ACS Nano **14**(9), 11722–11732 (2020)
30. Bian, R., Xiang, S., Cai, D.: Fast treatment of MXene films with isocyanate to give enhanced stability. ChemNanoMat **6**(1), 64–67 (2020)
31. Chen, W.Y., Jiang, X., Lai, S.-N., Peroulis, D., Stanciu, L.: Nanohybrids of a MXene and transition metal dichalcogenide for selective detection of volatile organic compounds. Nat. Commun. **11**(1), 1302 (2020)
32. Natu, V., Hart, J.L., Sokol, M., Chiang, H., Taheri, M.L., Barsoum, M.W.: Edge capping of 2D-MXene sheets with polyanionic salts to mitigate oxidation in aqueous colloidal suspensions. Angew. Chem. **58**(36), 12655–12660 (2019)
33. Chen, W.Y., Lai, S.-N., Yen, C.-C., Jiang, X., Peroulis, D., Stanciu, L.A.: Surface functionalization of $Ti_3C_2T_x$ MXene with highly reliable superhydrophobic protection for volatile organic compounds sensing. ACS Nano **14**(9), 11490–11501 (2020)
34. Zhang, P., Wang, L., Du, K., Wang, S., Huang, Z., Yuan, L., Li, Z., Wang, H., Zheng, L., Chai, Z., Shi, W.: Effective removal of U(VI) and Eu(III) by carboxyl functionalized MXene nanosheets. J. Hazard. Mater. **396**, 122731 (2020)
35. Jing, H., Yeo, H., Lyu, B., Ryou, J., Choi, S., Park, J.-H., Lee, B.H., Kim, Y.-H., Lee, S.: Modulation of the electronic properties of MXene ($Ti_3C_2T_x$) via surface-covalent functionalization with diazonium. ACS Nano **15**(1), 1388–1396 (2021)
36. He, S., Zhu, Q., Soomro, R.A., Xu, B.: MXene derivatives for energy storage applications. Sustain. Energy Fuels **4**(10), 4988–5004 (2020)
37. Sun, Y., Meng, X., Dall'Agnese, Y., Dall'Agnese, C., Duan, S., Gao, Y., Chen, G., Wang, X.-F.: 2D MXenes as co-catalysts in photocatalysis: synthetic methods. Nano-Micro Lett. **11**(1), 79 (2019)
38. Dall'Agnese, C., Dall'Agnese, Y., Anasori, B., Sugimoto, W., Mori, S.: Oxidized Ti_3C_2 MXene nanosheets for dye-sensitized solar cells. New J. Chem. **42**(20), 16446–16450 (2018)
39. Low, J., Zhang, L., Tong, T., Shen, B., Yu, J.: TiO_2/MXene Ti_3C_2 composite with excellent photocatalytic CO_2 reduction activity. J. Catal. **361**, 255–266 (2018)
40. Chertopalov, S., Mochalin, V.N.: Environment-sensitive photoresponse of spontaneously partially oxidized Ti_3C_2 MXene thin films. ACS Nano **12**(6), 6109–6116 (2018)
41. Zhong, Q., Li, Y., Zhang, G.: Two-dimensional MXene-based and MXene-derived photocatalysts: recent developments and perspectives. Chem. Eng. J. **409**, 128099 (2021)
42. Mashtalir, O., Cook, K.M., Mochalin, V.N., Crowe, M., Barsoum, M.W., Gogotsi, Y.: Dye adsorption and decomposition on two-dimensional titanium carbide in aqueous media. J. Mater. Chem. A **2**(35), 14334–14338 (2014)
43. Thakur, R., VahidMohammadi, A., Moncada, J., Adams, W.R., Chi, M., Tatarchuk, B., Beidaghi, M., Carrero, C.A.: Insights into the thermal and chemical stability of multilayered V_2CT_x MXene. Nanoscale **11**(22), 10716–10726 (2019)
44. Li, J., Qin, R., Yan, L., Chi, Z., Yu, Z., Li, N., Hu, M., Chen, H., Shan, G.: Plasmonic light illumination creates a channel to achieve fast degradation of $Ti_3C_2T_x$ nanosheets. Inorg. Chem. **58**(11), 7285–7294 (2019)
45. Liaw, B.Y., Roth, E.P., Jungst, R.G., Nagasubramanian, G., Case, H.L., Doughty, D.H.: Correlation of Arrhenius behaviors in power and capacity fades with cell impedance and heat generation in cylindrical lithium-ion cells. J. Power Sources **119–121**, 874–886 (2003)
46. Chae, Y., Kim, S.J., Cho, S.-Y., Choi, J., Maleski, K., Lee, B.-J., Jung, H.-T., Gogotsi, Y., Lee, Y., Ahn, C.W.: An investigation into the factors governing the oxidation of two-dimensional Ti_3C_2 MXene. Nanoscale. 11(17), 8387–8393 (2019)
47. Cui, C., Guo, R., Ren, E., Xiao, H., Lai, X., Qin, Q., Jiang, S., Shen, H., Zhou, M., Qin, W.: Facile hydrothermal synthesis of rod-like Nb_2O_5/Nb2CT_x composites for visible-light driven photocatalytic degradation of organic pollutants. Environ Res.193, 110587 (2021)

48. Liu, B., Yu, L., Yu, F., Ma, J.: In-situ formation of uniform V O nanocuboid from V_2C_5 MXene as electrodes for capacitive deionization with higher structural stability and ion diffusion ability. Desalination. 500, 114897 (2021)
49. Seredych, M., Shuck, C.E., Pinto, D., Alhabeb, M., Precetti, E., Deysher, G., Anasori, B., Kurra, N., Gogotsi, Y.: High-temperature behavior and surface chemistry of carbide mxenes studied by thermal analysis. Chem. Mater. 31(9), 3324–3332 (2019)
50. Rakhi, R.B., Ahmed, B., Hedhili, M.N., Anjum, D.H., Alshareef, H.N.: Effect of postetch annealing gas composition on the structural and electrochemical properties of Ti_2CT_x MXene electrodes for supercapacitor applications. Chem. Mater. **27**(15), 5314–5323 (2015)
51. Lee, Y., Kim, S.J., Kim, Y.-J., Lim, Y., Chae, Y., Lee, B.-J., Kim, Y.-T., Han, H., Gogotsi, Y., Ahn, C.W.: Oxidation-resistant titanium carbide MXene films. J. Mater. Chem. A **8**(2), 573–581 (2020)
52. Wang, K., Zhou, Y., Xu, W., Huang, D., Wang, Z., Hong, M.: Fabrication and thermal stability of two-dimensional carbide Ti_3C_2 nanosheets. Ceram. Int. **42**(7), 8419–8424 (2016)
53. Fu, Z.H., Zhang, Q.F., Legut, D., Si, C., Germann, T.C., Lookman, T., Du, S.Y., Francisco, J.S., Zhang, R.F.: Stabilization and strengthening effects of functional groups in two-dimensional titanium carbide. Phys. Rev. B **94**(10), 104103 (2016)
54. Feng, A., Yu, Y., Jiang, F., Wang, Y., Mi, L., Yu, Y., Song, L.: Fabrication and thermal stability of NH_4HF_2-etched Ti_3C_2 MXene. Ceram. Int. **43**(8), 6322–6328 (2017)
55. Meng, Z., Wang, C., Liu, J., Wang, Y., Zhu, X., Yang, L., Huang, L.: New insight into the interaction between divacancy and H/He impurity in Ti_3AlC_2 using first-principles studies. Phys. Chem. Chem. Phys. **22**(32), 18040–18049 (2020)
56. Mathis, T.S., Maleski, K., Goad, A., Sarycheva, A., Anayee, M., Foucher, A.C., Hantanasirisakul, K., Shuck, C.E., Stach, E.A., Gogotsi, Y.: Modified MAX phase synthesis for environmentally stable and highly conductive Ti_3C_2 MXene. ACS Nano **15**(4), 6420–6429 (2021)
57. Shuck, C.E., Han, M., Maleski, K., Hantanasirisakul, K., Kim, S.J., Choi, J., Reil, W.E.B., Gogotsi, Y.: Effect of Ti_3AlC_2 MAX phase on structure and properties of resultant $Ti_3C_2T_x$ MXene. ACS Appl. Nano Mater. **2**(6), 3368–3376 (2019)
58. Li, C., Kota, S., Hu, C., Barsoum, M.W.: On the synthesis of low-cost, titanium-based MXenes. J. Ceram. Sci. Tech. **7**(3), 301–306 (2016)
59. Scheibe, B., Kupka, V., Peplińska, B., Jarek, M., Tadyszak, K.: The influence of oxygen concentration during MAX phases (Ti_3AlC_2) preparation on the α-Al_2O_3 microparticles content and specific surface area of multilayered MXenes ($Ti_3C_2T_x$). Materials **12**(3), 353 (2019)
60. Sang, X., Xie, Y., Lin, M.-W., Alhabeb, M., Van Aken, K.L., Gogotsi, Y., Kent, P.R.C., Xiao, K., Unocic, R.R.: Atomic defects in monolayer titanium carbide ($Ti_3C_2T_x$) MXene. ACS Nano **10**(10), 9193–9200 (2016)
61. Palisaitis, J., Persson, I., Halim, J., Rosen, J., Persson, P.O.Å.: On the structural stability of MXene and the role of transition metal adatoms. Nanoscale **10**(23), 10850–10855 (2018)
62. Naguib, M., Mashtalir, O., Carle, J., Presser, V., Lu, J., Hultman, L., Gogotsi, Y., Barsoum, M.W.: Two-dimensional transition metal carbides. ACS Nano **6**(2), 1322–1331 (2012)
63. Lipatov, A., Alhabeb, M., Lukatskaya, M.R., Boson, A., Gogotsi, Y., Sinitskii, A.: Effect of synthesis on quality, electronic properties and environmental stability of individual monolayer Ti_3C_2 MXene flakes. Adv. Electron. Mater. **2**(12), 1600255 (2016)
64. Halim, J., Kota, S., Lukatskaya, M.R., Naguib, M., Zhao, M.-Q., Moon, E.J., Pitock, J., Nanda, J., May, S.J., Gogotsi, Y., Barsoum, M.W.: Synthesis and characterization of 2D molybdenum carbide (MXene). Adv. Funct. Mater. **26**(18), 3118–3127 (2016)
65. Ghidiu, M., Lukatskaya, M.R., Zhao, M.-Q., Gogotsi, Y., Barsoum, M.W.: Conductive two-dimensional titanium carbide 'clay' with high volumetric capacitance. Nature **516**(7529), 78–81 (2014)

66. Wang, X., Garnero, C., Rochard, G., Magne, D., Morisset, S., Hurand, S., Chartier, P., Rousseau, J., Cabioc'h, T., Coutanceau, C., Mauchamp, V., Célérier, S.: A new etching environment (FeF_3/HCl) for the synthesis of two-dimensional titanium carbide MXenes: a route towards selective reactivity vs. water. J. Mater. Chem. A **5**(41), 22012–22023 (2017)
67. Hope, M.A., Forse, A.C., Griffith, K.J., Lukatskaya, M.R., Ghidiu, M., Gogotsi, Y., Grey, C.P.: NMR reveals the surface functionalisation of Ti_3C_2 MXene. Phys. Chem. Chem. Phys. **18**(7), 5099–5102 (2016)
68. He, P., Wang, X.-X., Cai, Y.-Z., Shu, J.-C., Zhao, Q.-L., Yuan, J., Cao, M.-S.: Tailoring $Ti_3C_2T_x$ nanosheets to tune local conductive network as an environmentally friendly material for highly efficient electromagnetic interference shielding. Nanoscale **11**(13), 6080–6088 (2019)
69. Kumar, S., Kang, D., Hong, H., Rehman, M.A., Lee, Y.-J., Lee, N., Seo, Y.: Effect of $Ti_3C_2T_x$ MXenes etched at elevated temperatures using concentrated acid on binder-free supercapacitors. RSC Adv. **10**(68), 41837–41845 (2020)
70. Natu, V., Pai, R., Sokol, M., Carey, M., Kalra, V., Barsoum, M.W.: 2D $Ti_3C_2T_z$ MXene synthesized by water-free etching of Ti_3AlC_2 in polar organic solvents. Chem **6**(3), 616–630 (2020)
71. Jawaid, A., Hassan, A., Neher, G., Nepal, D., Pachter, R., Kennedy, W.J., Ramakrishnan, S., Vaia, R.A.: Halogen etch of Ti_3AlC_2 MAX phase for MXene fabrication. ACS Nano **15**(2), 2771–2777 (2021)
72. Rajavel, K., Ke, T., Yang, K., Lin, D.: Condition optimization for exfoliation of two dimensional titanium carbide ($Ti_3C_2T_x$). Nanotechnology **29**(9), 095605 (2018)
73. Maleski, K., Ren, C.E., Zhao, M.-Q., Anasori, B., Gogotsi, Y.: Size-dependent physical and electrochemical properties of two-dimensional MXene flakes. ACS Appl. Mater. Interf. **10**(29), 24491–24498 (2018)
74. Li, T., Yao, L., Liu, Q., Gu, J., Luo, R., Li, J., Yan, X., Wang, W., Liu, P., Chen, B., Zhang, W., Abbas, W., Naz, R., Zhang, D.: Fluorine-free synthesis of high-purity $Ti_3C_2T_x$ (T=OH, O) via Alkali treatment. Angew. Chem. Int. Ed. **57**(21), 6115–6119 (2018)
75. Zou, G., Zhang, Q., Fernandez, C., Huang, G., Huang, J., Peng, Q.: Heterogeneous Ti_3SiC_2@C-containing $Na_2Ti_7O_{15}$ architecture for high-performance sodium storage at elevated temperatures. ACS Nano **11**(12), 12219–12229 (2017)
76. Gogotsi, Y.: Transition metal carbides go 2D. Nat. Mater. **14**(11), 1079–1080 (2015)
77. Xu, C., Wang, L., Liu, Z., Chen, L., Guo, J., Kang, N., Ma, X.-L., Cheng, H.-M., Ren, W.: Large-area high-quality 2D ultrathin Mo_2C superconducting crystals. Nat. Mater. **14**(11), 1135–1141 (2015)

Simulative Molecular Modelling of MXene

Nasim Hassani and Mehdi Neek-Amal

Abstract Mxenes, among two-dimensional materials, exhibits amazing physical and chemical properties in addition to their applications. The MXenes are promising materials with great value in the engineering and industrial context. MXenes are shown by "$M_{n+1}X_nT_x$" formula, where "M" is a transition metal, "X" is carbon and/or nitrogen, "n" varies between 1 and 3, and different functional groups attached to the MXenes surface are indicated by "T_x". In addition to the experimental efforts, enormous theoretical studies are done for determining the different properties of MXenes. The vast majority of theoretical works were conducted using various levels of modeling and simulations. Molecular dynamics (MD) simulations based on reactive bond order potentials and ab-initio methods, including density functional theory (DFT), are the common theoretical methods for studying physical and chemical properties of these novel materials. After a brief introduction of the relevant modeling and simulation methods, this chapter reviews the most recent theoretical studies about MXenes and their applications.

Keywords MXene · Molecular dynamics simulations · Mxene's application · MD analysis

1 Introduction

The wonderful optical, thermodynamic, plasmonic, and electronic properties of two-dimensional (2D) materials, such as graphene, hexagonal boron nitrides, metal oxides, meta hydroxide, and transition metal dichalcogenides (TMDs), have drawn tremendous attention using 2D layered materials in various devices can significantly improve their performance in many applications, such as fuel production, solar steam production, photodetectors, and alkaline batteries.

In particular, MXenes, a family of 2D layered materials, with the general formula of $M_{n+1}X_nT_x$ (T = O, OH, F, Cl; $n = 1 - 3$) are a-few-atoms-thick materials made

N. Hassani · M. Neek-Amal (✉)
Department of Physics, Shahid Rajaee Teacher Training University, 16875-163 Lavizan, Tehran, Iran
e-mail: mehdi.neekamal@gmail.com

M. Khalid et al. (eds.), *Fundamental Aspects and Perspectives of MXenes*, Engineering Materials, https://doi.org/10.1007/978-3-031-05006-0_6

from the carbides, nitrides, and carbonitrides of the ternary transition metal that was discovered and developed in 2011 [1, 2]. These 2D materials are produced by removing the "*A*" layer from the corresponding MAX phase ($M_{n+1}AX_n$). For example, the first MXene, Ti_3C_2, was synthesized by removing the Al layer from the Ti_3AlC_2 phase selectively when this powder was soaked in the hydrofluoric acid solution at room temperature [1]. For a decade, researchers have predicted/synthesized various MXenes that are a combination of different transition metals (Ti, V, Cr, Y, Zr, Nb, Mo, Hf, Ta, W) and their alloys, as well as C and N. The MXenes nanosheets contain functional groups (O, OH, F, Cl) on their surface where the functionalized MXenes ($M_{n+1}X_nT_x$) are semiconductor whereas the pristine MXenes ($M_{n+1}X_n$) exhibit metallic characteristics.

Because of the layered structure of MXenes, they exhibit unique and unusual physical properties, including inherently good conductivity, flexibility, and excellent volumetric capacitance. As a result, numerous experimental investigations are examining the applicability of MXenes. Also, various computational techniques are used to study MXenes, such as molecular dynamics (MD) simulations and density functional theory (DFT) calculations for determining their different properties.

In this chapter, we first briefly introduce MD and DFT simulation techniques, then review some of the MD and DFT simulations based studies to find their applications, including energy storage [3], gas sensors [4], hybrid nanocomposite fabrication [5], and supercapacitors for water purification and catalytic applications [6, 7], mainly literature that was published in the last five years. It should be noted that the present chapter is focused on the review of the literature that was used computational methods for exploring the application of MXene.

2 Molecular Dynamics Simulation Technique

Molecular Dynamics (MD) simulations enable us to investigate the physical motion of interacting particles over a period of time at the molecular level. The basic principle of MD simulations is to specify the trajectories of atoms. The latter is determined by solving Newton's equation of motion numerically. In MD simulation, at each iteration of the simulation, the forces between atoms/molecules, their positions, potential energies, and velocities are determined by employing suitable interatomic potential, or in general, relevant molecular mechanics force fields. The main concepts of typical MD simulation are the following:

(i) Force field (FF) is a potential energy function that describes the interaction between atoms/molecules. It contains a set of parameters and usually is a function of coordinates and bond angles of atoms/molecules. The parameters of FFs are often determined by fitting to experimental data and/or by semi-empirical or *ab initio* quantum mechanical calculations. Nowadays, many force fields are developed such as CHARMM [8], universal ((UFF) [9], COMPASS [10], OPLS [11], ReaxFF [12]. These FFs have different degrees

of complexity and can be applied to a variety of systems. A simple expression for a typical non-bonded FF is given by Eq. (1).

$$\begin{aligned} FF = & \sum_{bonds} \frac{1}{2} k_b (r - r_0)^2 + \sum_{angles} \frac{1}{2} k_a (\theta - \theta_0)^2 \\ & + \sum_{torsions} \frac{V_n}{2} [1 + \cos(n\emptyset - \delta)] + \sum_{improper} V_{imp} \\ & + \sum_{LJ} 4k\epsilon_{ij} \left(\frac{\sigma_{ij}^{12}}{r_{ij}^{12}} - \frac{\sigma_{ij}^{6}}{r_{ij}^{6}} \right) + \sum_{elec} \frac{q_i q_j}{r_{ij}} \end{aligned} \tag{1}$$

where the first four terms comprise the local contributions to the total energy, namely bond stretching, angle bending, dihedral, and improper torsions, while the repulsive, coulombic, and van der Waals interactions are described in the final two terms using a 12-6 Lennard-Jones potential.

Because of the presence of transition metal elements in the structure of MXene, simulating MXene structures has vastly been done by using reactive force fields (ReaxFF), which provide us bond breaking and bond formation during simulation. Unfortunately, the reactive bond order (REBO) force fields depending on the size of the simulated system, can be computationally very expensive. Therefore, a critical task in studying large systems long time is parameterization of the traditional non-REBO force fields.

(ii) The force between atoms by finding the gradient of the chosen FF function. This is not usually easy in REBO FF because of the presence of many body terms. The obtained forces are used to determine the dynamics of atoms/molecules using Newton's second law.

(iii) The time step is a crucial parameter in an MD simulation which is to be ten times less than the frequency of the highest vibration of the chemical bond but on the same scale as it is on the femtosecond scale. The time step restricts the simulation length and the number of trajectories.

(iv) Updating the positions, velocities of atoms/molecules using the appropriate time step of the simulation. This is usually done by adopting a fast enough algorithm.

(v) Various thermostats and barostats for controlling the temperature and pressure of the system, which is the tricky step of a typical MD.

In fact, various thermodynamic conditions can be simulated using different so called ensembles: a collection of probable systems with the same macroscopic state while containing different microscopic states. There are different ensembles with various characteristics [13].

- Microcanonical Ensemble (NVE): The simulation system can be isolated from the rest of the world by fixing the number of particles (N), volume (V), and total energy (E).

- Isobaric-Isothermal Ensemble (NPT): A collection of systems whose thermodynamic states are determined by constant N, P (pressure), temperature (T).
- Grand canonical Ensemble (μVT): This ensemble can be used for a system considering a fixed V and T, as well as a fixed chemical potential (μ).
- Canonical Ensemble (NVT): The thermodynamic states of the system can be characterized by constant N, V, and T.

After finishing an MD simulation, one has trajectories of atoms, i.e., sequential snapshots of the system that contain the coordination of all atoms in a specific period of time. An average corresponding to these characteristics is taken over the trajectories to characterize the simulated system, known as the ensemble average. Also, the observable parameters such as temperature (pressure) can be modeled by scaling the velocities of the atoms/molecules (changing the simulation box volume) in the simplest way.

When a more accurate molecular dynamic simulation is desired (for example, for the study of chemical reactions or excited states), electronic behavior of the system can be achieved from the first-principles calculations, then the system's dynamic is characterized classically through MD. This definition refers to the ab-initio Molecular Dynamics (AIMD) [14], where the electrons are treated in a quantum mechanical way (within the DFT approach), and the ions are treated classically (within the MD approach). However, the computational cost of a typical AIMD is higher than that of classical MD. Therefore, the corresponding applicability is restricted.

2.1 The Analysis of MD Results

For a system containing atoms ranging from thousands to millions, the MD data becomes huge due to the saving coordinates and velocities of each atom extracted at each time step of the simulation. In the following, we discuss analyzing MD data using cartesian coordinates of each atom.

RMSD and RMSF

The average distance of a group of atoms in a system can be quantified by calculating the root-mean-square deviation of the atomic positions (RMSD), shown in Eq. (2). Using the RMSD, one can evaluate the deviation of the system from the initial positions (or reference structure):

$$RMSD = \sqrt{\frac{1}{N}\sum_{i=1}^{N}\delta_i^2} \tag{2}$$

where δ_i represents the distance between atom i and a reference structure. The RMDS has a unit of length. Moreover, by involving time, one can measure root-mean-square

fluctuation (RMSF), where the average deviation of a reference position is calculated over time. The RMSF can be used for studying melting phenomena and diffusion coefficient.

By aide of mean square displacement (MSD) technique and carrying out an average over time and all atoms of the system, the diffusion coefficient (D) can be calculated using Eq. (3)

$$D = \lim_{r\to\infty} \frac{\left\langle [r(t) - r(t_0)]^2 \right\rangle}{6t} \tag{3}$$

where r is the position of an atom, t and t_0 are time of the system and the time origin, respectively.

RDF

To describe the thermodynamics phase, one can analyze the system by calculating radial distribution functions (RDF) ($g(r)$, which sometimes is called pair distribution functions or pair correlation function). If the reference atom (atom a) is located at the origin O and the average number of atom b (neighbour of atom a at distance r) is given by $N_{ab}(r)$, then, the local time-averaged density of atom b is $g(r)$. The normalized RDF between atoms a and b can be calculated using Eq. (4)

$$g_{ab}(r) = (N_a N_b)^{-1} \sum_{i=1}^{N_a} \sum_{j=1}^{N_b} \langle \delta(\left|\overrightarrow{r}_i - \overrightarrow{r}_j\right| - \overrightarrow{r}) \rangle \tag{4}$$

For a homogenous system, $g_{ab}(r)$ approaches 1 when $\left|\overrightarrow{r}\right| \to \infty$. Also, the radial cumulative distribution function $G_{ab}(r)$ and, consequently, $N_{ab}(r)$ for the appropriate density (ρ) are given by Eqs. (5) and (6), respectively.

$$G_{ab}(r) = \int r_0 dr' 4\pi r'^2 g_{ab}(r) \tag{5}$$

$$N_{ab}(r) = \rho G_{ab}(r) \tag{6}$$

In fact, $g_{ab}(r)$ can be plotted as a function of r, which provides valuable information about the system's structure. For instance, if the first minimum in RDF plot is located at r_1. Then, by using Eq. 5, the coordination number ($N(r_1)$) can be calculated for a solvent the first solvation shell.

In the case of solids, the structure is specific even on a long range. The particles in a solid vibrate around their lattice site. Accordingly, the peaks of solid's RDF are located at a specific position based on the lattice constant. In contrast, gases do not have a regular structure that significantly impresses their RDF peaks.

H-bond analyses

A hydrogen bond (H-bond) is formed between a donor (D) and an acceptor (A) atoms at distance A-D and angle D-H-A less than cut off values. The cut-off values for distance and angle are usually considered 3 Å and 20 degrees, respectively. By considering these two hypotheses and defining atoms A and D, a new script can be written, or the scripts that have been written can be used to count the number of H (NH-B) bonds along a path. Then NH-B can be plotted as a function of time.

Gas flow measurements

One of the important applications of porous 2D materials is separating a gas mixture, where different gases penetrate through the pores with a translocation energy barrier leading to different gas flow rates. The latter depends on the diffusivity, size, and solubility of the gases.

In microscopic scale (100 to 1 μm) [15], if the mean free path of the molecules (λ) is greater than the characteristic length scale of system (l) continuum hydrodynamic is valid. In a channel with short length scales, the interaction of the molecules with the channel wall is stronger than the interaction of the molecules with one another.

With the aid of the ideal gas law and the use of Knudsen number ($K_n = \frac{\lambda}{l}$, l the length of the channel) at the microscopic level, the mean free path (λ) of molecules can be defined using Eq. (7).

$$\lambda = \frac{k_B T}{\sqrt{2}\pi d^2 P} \tag{7}$$

where k_B, d, T, and P are Boltzmann constant, the diameter of the gas molecule, the temperature and the pressure, respectively. In 2017, Schaff [16], based on the K_n value, categorized different flow models, i.e. $K_n<10^{-3}$, $10^{-3} < K_n<10^{-1}$, $10^{-1} < K_n<10$, $K_n>10$ refers to a continuous flow stage, a slip flow, a transition zone, and an area of molecule diffusion, respectively.

In a common MD simulation relevant to nanofluidics for a cylindrical channel and continuity assumptions, the volume flow rate (Q) can be expressed by Eq. (8)

$$Q = \frac{1}{6}\sqrt{2\pi}\,\Delta P \frac{l^3}{l\sqrt{\rho}} \tag{8}$$

where ΔP is the pressure difference between the feed and flowed sides, and ρ is the ratio of density and pressure. Also, for the slip flow [17], the flow velocity (V^*) can be calculated by using Eq. (9)

$$V^* = \frac{1}{(t_N - t_M + 1)N} \sum_{t=t_M}^{t_N} \sum_{i=1}^{N} v_{i.t}^x \tag{9}$$

where v_{i-t}^{x} is the velocity of the ith particle at time t in the x-direction, t_N, t_M are respectively the initial and the final time step, and N is the number of particles. Then, the flow velocity profile can be plotted as a function of temperature and other parameters.

Mechanical properties

The Young's modulus is calculated in MD to give insight into the compressive stiffness of solid systems. In a common MD simulation, the mechanical properties can be determined by applying a displacement to a group of atoms at a specific point and then allowing all the atoms to be relaxed. The Young's modulus can be calculated using Eq. (10).

$$E = \frac{1}{V}\frac{\partial^2 U}{\partial^2 \varepsilon} \tag{10}$$

where V, U, and ε are the volume of the simulated system, the obtained energy as a result of applied displacement (strain), and tensile strain, respectively. By plotting U versus strain and fitting a curve with the appropriate relation, the second derivation of the strain energy gives us Young's modulus.

The shear modulus (G) can also be calculated using Eq. (11).

$$G = \frac{1}{V}\frac{\partial^2 U}{\partial^2 \gamma} \tag{11}$$

where γ refer to the shear strain. The unit of both Young's and shear modulus is pascal (Pa), gigapascals (GPa), or pound per square inch (ksi). For instance, Young's modulus of Ti_3C_2 was found to be 80–100 GPa [18].

Thermal properties

In an ideal system, according to the second law of thermodynamics, the total work (W) performed on a system from initial point A to the final point B is independent of the path. In such a system, the work applied to the system is the difference between the Helmholtz free energy of states A and B ($\Delta F = F_B - F_A = W$). In common MD, where a finite rate evolves through the system, the second law of thermodynamics is no longer valid, i.e., $\Delta F \neq W$. Because in the latter, the system parameters change along a path and depend on the system's microscopic conditions. Jarzynski [19] derived an expression between the total work and Helmholtz free energy of two different thermodynamic states, shown in Eq. (12).

$$\Delta F = -\beta^{-1} \ln\langle \exp(-\beta W)\rangle \tag{12}$$

where $\beta = 1/k_B T$. Equation 12 is valid for a system independent of both path and evolution rate.

The linear coefficient of thermal expansion (α_L) and its volumetric counterparts (α_V) can be obtained using Eqs. (13) and (14)

$$\alpha_L = \frac{1}{L_0}\frac{\partial L}{\partial T} \tag{13}$$

$$\alpha_V = \frac{1}{V_0}\frac{\partial V}{\partial T} \tag{14}$$

where L_0 and V_0 denote length and volume of the system at zero temperature.

To calculate the specific heat (C_V) capacity, Eq. (15) can be applied.

$$C_V = \frac{1}{m}\left(\frac{\partial Q}{\partial T}\right)_V \tag{15}$$

where m and Q are the mass and the amount of heat of the simulated system, respectively and C_V is the heat required to increase the temperature by one degree for a unit mass of the system.

3 Density Functional Theory Approach

The quantum mechanical wave function contains all of the necessary information about a system's electrical structure. The Schrödinger equation can be quantitatively solved to give the wave function and the allowable energy. However, even with reasonable approximations, the Schrödinger equation for an N-electron system cannot be solved exactly. One of such approximations useful for many-electron systems is made based on the Density Functional Theory (DFT) approach. In fact, for a given many-electron system using various functionals, especially Perdew-Burke-Ernzerhof (PBE) [20, 21] and Heyd–Scuseria–Ernzerhof (HSE) [22–28], one can study the MXenes. These functionals are functions of the electron density, which are potentials that act on the electrons of the system.

The DFT potentials consist of two external and effective potentials that can be determined by the coordination of elements and interelectronic interactions, respectively. Accordingly, an N-electron can be treated as n one-electron equations, i.e., Kohn–Sham equations [29–31].

The wavefunctions are a linear combination of basis functions that are finite due to their size limit, allowing us to solve the problem in a linear algebra scheme. There are various basis functions (basis sets), such as atomic basis sets (linear combination of the atomic orbitals) and plane-wave basis sets. Moreover, the many-electron system can be solved by considering pseudo-potentials that divide the system's electrons into two groups, i.e., core and valence electrons. The valance electrons are responsible for the chemical binding, while core electrons do not play an important role in such

bonding. In other words, if the number of electrons is large, the core electrons can be neglected.

The long-range interactions are not taken into account in the DFT computations. Therefore, certain long-range corrections for total molecule energy, energy gradient, and frequencies are available, such as the Grimme (DFT-D3) [32, 33] or Tkatcheno–Scheffler (DFT-TS) [34] schemes, which are added to the results obtained using DFT. The latter has incorporated these interactions in DFT calculations to connect the main results. In the following sections, we review researches that used both MD and DFT approaches to explore different properties and applications of MXenes.

4 MXenes Applications

4.1 Energy storage

MXenes have a multilayer structure, where a large interlayer spacing leads to dispersion in water and intercalation of ions into their structure. The latter leads to forming composites of MXene with silicon, graphene, transition metal dichalcogenides, and other 2D materials. The intercalated MXenes exhibit good pseudocapacitance features that allow these structures and their composite counterparts to be applied as electrodes to deliver specific capacities during a cyclic process.

The advantages of employing lithium-ion (Li-ion) batteries are well known in many applications, including portable devices and electric vehicles. However, producing an anode material with longer working life and durability remains one of the most challenging issues for future Li-ion battery development. Carbon-supported TiO2 (titania–carbon) hybrids with high volumetric capacity displayed outstanding Li-ion battery performance as well as photocatalyst capabilities. The oxidation of two-dimensional Ti3C2 MXene structures is advantageous for creating hybrid carbon-supported nano titania structures.

For example, Lotfi et al. [35] evaluated the influence of an oxidizing agent on the oxidation of Ti_3C_2 MXene. They used ReaxFF to perform MD simulations at temperatures ranging from 1000 to 3000 K for 100 picoseconds (ps) in three different environments: wet air (oxygen and water molecules), dry air (oxygen molecules), and H_2O_2 (hydrogen peroxide molecules). The necessary ReaxFF parameters can be found in Reference [36]. According to their results, by diffusing Ti atoms to the surface of MXene structures, carbon-supported titania can be formed if the temperature is controlled during oxidation. Moreover, it was found that the MXene oxidation rate increases with increasing temperature in the following order of environments: hydrogen peroxide > wet air > dry air. The comparison between these three environments is demonstrated in Fig. 1.

It is clear that the presence of oxidation agents at higher temperatures leads to the migration of some Ti atoms to the MXene surface and the functionalization of MXene with functional groups -O and -OH. The MD results were further confirmed by heat

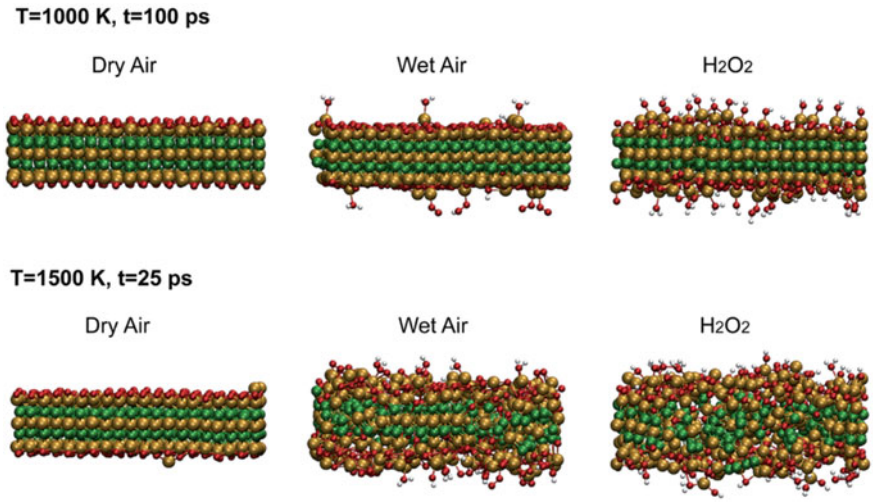

Fig. 1 The Ti_3C_2 MXene oxidation rates were compared in three different environments, including dry air, wet air, and hydrogen peroxide. It is clear that controlling the temperature would make the oxidation rate and formation of titania–carbon hybrid structure (carbon-Ti_3O_2) feasible. Color-coding: Ti (tan), O (red), H (white), and C (green)

treatment of MXene in dry and wet air in the presence of inert gas. Consequently, their simulations provide significant insights into the chemical stability of MXenes and introduce titania–carbon hybrids as a promising material in electrochemical storage, catalysis, and sensing.

It was found that MXenes can be applied as an efficient material for electrodes where their energy storage capacity is strongly correlated with the surface functional groups. Meng et al. [37] designed S-functionalized Ti_3C_2 MXenes employing DFT calculations and compared the electronic, geometric, dynamic stability, and sodium storage capacity of $Ti_3C_2S_2$ MXene. Based on their results, $Ti_3C_2S_2$, as the anode of Na-ion batteries, exhibits superior properties such as low open-circuit voltage (OCV), metallic behavior, low diffusion barrier, high storage capability, fast charge–discharge rates, and stable structure (both dynamically and thermally).

Zhang et al. [38] also employed a combination of DFT computations (with PBE functional) and experimented with tailoring adequate surface functionalization in MXene. Their study aimed to tailor the intrinsic electrical properties of $Ti_3C_2T_x$ MXene (T stands for F, OH, and O) and increase its lithium storage potential. They controlled the annealing process to achieve flexible $Ti_3C_2T_x$ films with few –F and –OH functional groups, few impurities, and high conductivity. DFT calculations indicated that the ion-diffusion barrier and Li adsorption energy of the $Ti_3C_2T_x$ MXene with low –F and –OH functional groups significantly decreased and increased, respectively, compared to $Ti_3C_2T_x$ MXene with high–F and OH–containing. Hence, $Ti_3C_2T_x$ MXenes with low–F and OH content have more potential for application in Li-ion storage and transfer devices.

For comparison purposes, in Table 1, we listed the capacities of various MXenes that have been used as the anode/cathode of metal-ion batteries (i.e., Li-ion, Na-ion and K-ion).

In order to tailor the surface of the electrodes, the charge extraction and optoelectronic properties of these electrodes, one can be engineered in perovskite solar cells. Agresti et al. [70] tuned the work function of (W_F) MXene ($Ti_3C_2T_x$) perovskite. This can be controlled with the surface functional group of MXene, to improve the properties of perovskite electrodes and TiO_2 electron transport layer (ETL). Using the induced dipole of $Ti_3C_2T_x$, they optimized the band alignments between perovskite/ETL interfaces to increase the charge transfer. The results of DFT further confirmed that the density of states and W_F of $Ti_3C_2T_x$ significantly depends on the type of surface functional groups, and the W_F for –OH and –O functional groups varies between 1.6 to 6.25 eV [71, 72].

$Ti_3C_2T_x$ ($T_x = -F, -O$, and –OH) MXenes are one of the pseudocapacitive electrode materials that have some unique properties such as high volumetric capacitance [73] (800 F cm^{-3}), high ionic conductivity, high intrinsic electronic, the presence of redox-active sites, and highly accessible surface area. Several groups have attempted to explain the charge storage mechanism of MXenes in various electrolytes using these features.

Shao et al. [74] investigated the charge storage mechanism of this MXene in an acidic electrolyte (H_2SO_4), both theoretically and experimentally. Their results demonstrated that Ti atoms undergo a redox reaction in the presence of confined water in the MXene layers. In addition, water molecules make fast charge compensation possible through a high proton diffusion rate. They also suggested that optimizing the MXene surface termination groups (−F, −O, and –OH) can improve the rate performance of MXenes electrodes. Consequently, the hydroxyl functional group (–OH) plays an important role in promoting the intercalation between water molecules and the MXene layers. As the number of −OH groups increases, proton transfer decreases due to the disruption of the water molecules organization. Moreover, the performance of the $Ti_3C_2T_x$ electrode decreases in the presence of a large number of −OH groups. MD simulations were used to obtain more insight into the charge storage mechanism in $Ti_3C_2O_{0.9}F_{0.8}(OH)_{0.3}$ and $Ti_3C_2O_{1.185}F_{0.8}(OH)_{0.015}$ MXenes, named P-MXene and 500-MXene, respectively.

Accordingly, water molecules can't be present within the MXene layers, and the electrochemical cycle leads to water intercalation into MXene layers. They perform MD simulations on the P-MXene and 500-MXene samples with a large initial value of *c* lattice parameter (c-LP) and a small amount of pre-intercalated water molecules. After reaching the equilibrium state of MD simulations, a single layer of water molecules was presented between the layers of both MXene samples. For 500-MXene, hydronium ions (H_3O^+) and water molecules form a well-organized layer with a network of waters linked by hydrogen-bond (H-bond). As shown in Fig. 2, during the electrochemical process, the formed H-bond networks cause a rapid proton transfer and increase the efficiency of the 500-MXene electrode.

In the case of P-MXene, the large number of −OH groups on the outermost surface of the sample disturb the H-bond networks and lower the proton transfer

Table 1 Various MXenes as active electrode material in metal-ion batteries

	MXene	References	Capacity ($mAhg^{-1}$)	Rate	Notes
Li-ion	Ti_2CT_X	[39]	110	1 C[a]	Retained after 80 cycles
	H_2O_2 treated Ti_2C	[40]	389	100 mAg^{-1}	Retained after 50 cycles
	Ti_3C_2 paper	[41]	410	1 C	Maintained 110 $mAhg^{-1}$ at 36 C after 700 cycle
	$Nb_4C_3T_X$	[42]	310	0.1 Ag^{-1}	380 $mAhg^{-1}$ after 100 cycles
	Nb_2AlC	[43]	170	1 C	Measured after 150 cycles
	V_2AlC	[43]	260	1 C	Measured after 150 cycles
	V_2CT_X	[43]	260	1 C	Measured after 150 cycles
	Hf_3C_2Tz	[44]	1567	200 mAg^{-1}	Measured after 200 cycles
	Ti_3CNT_X	[45]	300	0.4 Ag^{-1}	Measured after 1000 cycles
	MoS_2/Ti_3C_2-MXene@C	[46]	580	20 Ag^{-1}	95% retained after 1000 cycles
	$MoS_2/Ti_3C_2T_X$	[47]	656	50 mAg^{-1}	70% retained after 50 cycles
	$MoS_2/Mo_2TiC_2T_X$	[48]	90	5 Ag^{-1}	92% retained after 100 cycles
	$TiO_2/Ti_3C_2T_X$	[49]	124	50 mAg^{-1}	Retained after 400 cycles
	TiO_2/Ti_2CT_X	[50]	389	0.1 Ag^{-1}	Retained after 70 cycles
	$Ti_3C_2T_X/Co_3O_4$	[51]	50	20 C	Retained after 100 cycles
	Fe_3O_4@$Ti_3C_2T_X$	[52]	278	5 C	Measured after 800 cycles
	CNTs@Ti_3C_2	[53]	430	1 Ag^{-1}	Measured after 300 cycles
	Mo_2C/CNT	[54]	560	0.4 Ag^{-1}	Measured after 70 cycles
	Ti_3C_2/CNF	[55]	320	1 C	Retained after 2900 cycles at 100 C
	$Ti_3C_2T_X$/CNTs "paper"	[56]	100	0.1 C	80 $mAhg^{-1}$ after 500 cycles at 1 C

(continued)

Table 1 (continued)

	MXene	References	Capacity ($mAhg^{-1}$)	Rate	Notes
	$Ti_XTa_{(4-X)}C_3$	[57]	459	0.5 C	97% Retained after 200 cycles
	$Si@Ti_3C_2T_X$	[58]	1672	1.0 Ag^{-1}	Measured after 200 cycles
Na-ion	$Ti_3C_2T_X$	[59]	79	0.2 Ag^{-1}	Retained after 500 cycles
	Ti_3C_2TX spheres	[60]	330	50 mAg^{-1}	Increased 40% after 1000 cycles at 0.5 Ag^{-1}
	$TiO_2/Ti_3C_2T_X$	[56]	101	0.2 Ag^{-1}	Retained after 2000 cycles
	$Hf_3C_2T_X$	[61]	68	50 mAg^{-1}	Retained after 200 cycles
	$TiO_2@Ti_3C_2T_X$	[62]	220	30 mAg^{-1}	Retained after 5000 cycles
	$CoNiO_2/Ti_3C_2T_X$	[63]	188	0.3 Ag^{-1}	80% Retained after 140 cycles
	$SnS/Ti3C2T_X$	[64]	256	0.1 Ag^{-1}	Retained after 50 cycles
	$Sb_2O_3/Ti_3C_2T_X$	[65]	295	2 Ag^{-1}	97% Retained after 100 cycles
	Alkalized $Ti_3C_2T_X$ nanoribbons	[66]	85	0.3 Ag^{-1}	25% lost between 25 and 500th cycles
	Mo_2CT_X spheres	[60]	370	50 mAg^{-1}	Increased 38% after 1000 cycles at 0.5 Ag^{-1}
	V_2CT_X spheres	[60]	340	50 mAg^{-1}	Increased 20% after 1000 cycles at 0.5 Ag^{-1}
	V_2C	[68]	50	0.5 mVs^{-1}	
K-ion	V_2C	[69]	98	50 mAg^{-1}	At 6th cycle
	$K–V_2C$	[69]	195	50 mAg^{-1}	At 6th cycle
	Ti_3CNT_X	[70]	154	20 mAg^{-1}	75 mAg^{-1} after 100 cycles
	$K_2Ti_4O_9$ nanoribbons	[71]	88	0.3 Ag^{-1}	51% Retained after 900 cycles
	Alkalized $Ti_3C_2T_X$ nanoribbons	[66]	60	0.3 Ag^{-1}	60% Retained after 500 cycles

[a] 1 C = 100 mAg^{-1}

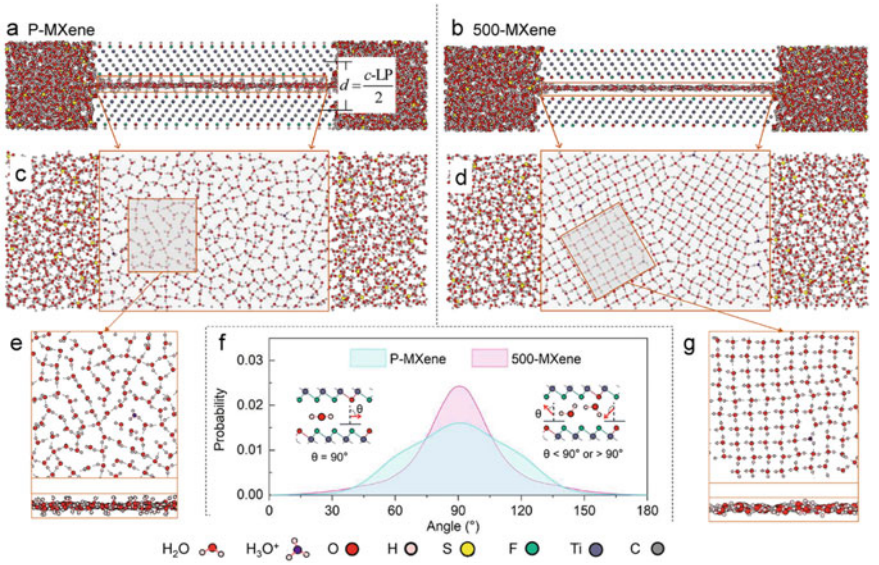

Fig. 2 **a** and **b** side views of the P-MXene and 500-MXene layers with surrounding electrolytes, respectively. **c** and **d** top views of the distribution confinrd water molecules between the layers of P-MXene and 500-MXenes, respectively. **e** and **g** the zoomed top and side views of water molecules confined between the P-MXene and 500-MXene layers. **f** The probability profiles of the dipole orientation of water molecules within the P-MXene and 500-MXene layers. The θ is the angle between the water molecule dipole moment of water and the normal surface of the electrode [74]

rate. Figure 2f displays the probability profiles, P(θ), for P-MXene and 500-MXene samples for the dipole orientation of the water molecules between layers. Accordingly, the water molecules were oriented almost parallel to the 500-MXene surface, where the orientation of the dipole was mainly concentrated around 90°, which favors proton transport.

4.2 Gas Sensing Properties

2D-Mxene are potentially useful for designing gas sensors at ambient temperature due to their high surface-aria-to-volume ratio. In fact, the transfer of charge between MXene and gas molecules causes gas adsorption. The latter leads to modulation of the MXenes conductivity [75]. Despite these attractive characteristics, constructing functional MXenes with interesting gas sensing potential at room temperature is a great challenge. For example, the interaction between gases and the MXenes surface is quantum in nature. Thus, the sensing behavior of MXene should be studied using DFT calculations which is computationally expensive. However, MD can be applied to investigate the gas flow rate (see Sect. 2.1) in the simulation system at different temperatures to analyze the sensing behavior of MXenes.

Zhao et al. [76] utilized an integration of DFT (with PBE functional) and bulk electrosensitive measurements to investigate the high electrocatalytic sensitivity of flexible gas sensor-based polyaniline/MXene nanocomposites (was named PANI/$Ti_3C_2T_x$). The $Ti_3C_2T_x$ MXene surface was decorated with PANI nanoparticles through in situ polymerization at low temperature to persuade significant mechanical stability, detection sensitivity, and rapid response rate. They attributed these excellent sensing activities to the presence of numerous high catalytic/absorption of functional groups (–OH, –O–, and –F) at the edge of Ti_3C_2 MXene and the synergetic effect of the composites.

Khakbaz et al. [77], using AIMD, found that the functionalized $Ti_3C_2T_x$ is thermodynamically stable. They investigated the sensing behavior of this MXene upon different gas molecules (CO, NO, CO_2, NO_2, N_2O, H_2S, and CH_4). $Ti_3C_2T_x$ MXene was found to be more sensitive to NH_3 compared to the other gases when the number of fluorine was lower than that of the other functional groups on the surface.

It is known that Mxenes have low stability in humid environments due to their hydration and oxidation in the presence of water molecules. Through surface treatment, Chen et al. [78] synthesized a $Ti_3C_2T_x$ –F superhydrophobic surface. Their DFT study suggested that ethanol can strongly interact with $Ti_3C_2T_x$ –F, which can be used as an ethanol sensor even in presence of water.

4.3 Mechanical Property

Beyond the high volumetric capacity of MXenes, they are predicted to possess high mechanical properties in two bulk and single-atom thick two-dimensional (2D) forms. Although MXenes are one of the hardest materials, the mechanical characteristics of MXenes, such as bending rigidity, have not been completely studied compared to the other ultrathin materials. Borysiuk et al. [79] simulated the bending deformation of the three different MXene nanoribbons (Ti_2C, Ti_3C_2, and Ti_4C_3) with a length and width of 12.0 and 1.1 nm, respectively, in which the atoms at both edges were fixed during the simulation.

As shown in Fig. 3, the Ti atoms in the central area of the top Ti_2C layer were subjected to the external bending force. First, the simulation was performed at 1 K using parametrized reactive bond-order FF. Then, the bending rigidity and central deflection of the 2D titanium carbides were calculated as a function of external force. For the Ti_2C nanoribbon at small deflections, the calculated bending rigidity (D) was 5.21 eV and increased nonlinearly to a maximum of 12.79 eV for larger deflections and before disintegration. With minimal deflection, D values were reported to be 49.55 and 47.43 for Ti_3C_2 and Ti_4C_3 nanoribbons, respectively, larger than D of MoS_2 (9.61, [80]). The obtained D and the effective spring constant (k_{eff}) for graphene with similar size and method were reported ~ 2.3 eV and 0.36 N/m, respectively [81]. The k_{eff} for Ti_2C MXene was ~ 0.82 N/m because Ti_2C MXene is more resistant to bending than graphene.

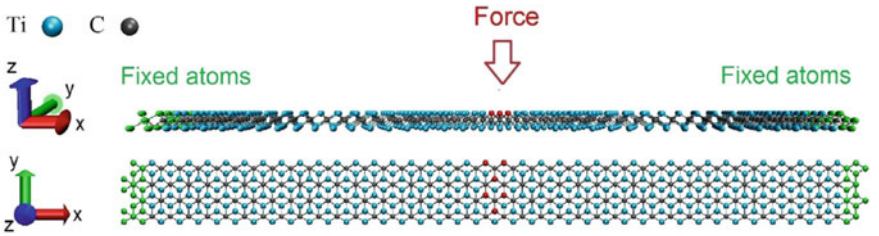

Fig. 3 The configuration of the simulation setup of the external force field applied on Ti_2C nanoribbon. Fixed atoms at the edges are represented in green. The red color refers to the external force applied to the central Ti atoms [79]

4.4 Colloidal and Photochemical Stability

In addition to the above-mentioned characteristics of MXenes, the colloidal and photochemical stability of 2D MXene flakes in the environment are important features and should be considered before practical use. Shen et al. [82] experimentally and theoretically. studied these two features for delaminated $Ti_3C_2T_x$ MXene flakes modified ith hydrazine (HMH), KOH, and water labelled as HMH-Ti_3C_2, KOH-Ti_3C_2, and H_2O-Ti_3C_2, respectively. It was concluded that the modification could adequately increase the dispersibility of the MXene flakes. They demonstrated that HMH-Ti_3C_2 and KOH-Ti_3C_2 have greater photochemical and colloidal stability with greater resistance to oxidation in the presence of UV and visible light irradiation and their surface electronegativity increased. DFT calculations and MD simulations were used to describe the mechanisms behind the differences in photochemical stability of the $Ti_3C_2T_x$ MXene flakes. It was revealed that K^+ ions protect the flakes by inhibiting the coupling between Ti^{3+} and ROS, while HMH through photoelectrons absorbing and direct reacting with ROS leads to stronger protection. This study shows that MXenes structures are stable under colloidal and photochemical aquatic environments and can be used in such environmental conditions.

4.5 Hybrid of MXenes Structures with Other Materials

In addition, one can apply the unique feature of MXene structure in conjunction with other materials to improve their characteristics. For example, reduced graphene oxide sheets (rGO) are used in many applications, including flexible energy storage systems and portable electrical devices. However, some factors, such as low electrical conductivities and mechanical properties, limit the development of this type of device.

Various solutions have been offered to improve the efficiency of rGO sheets devices. Zhou et al. [83] used Ti–O-C covalent bonds to join functionalized graphene oxide platelets with exfoliated MXene (M) nanosheets, resulting in MrGO sheets. In addition, a conjugated molecule AD was cross-linked with MrGO sheets. The

incorporation of M and AD molecules into the rGO sheets reduces the porosity of the graphene sheets and increases the alignment of the rGO sheets.

Therefore, MrGOAD sheets have high compactness, electrical conductivity, and toughness. To investigate the fracture process of the MrGOAD sheet, molecular dynamics (MD) simulations were performed at 300 K, and 1 bar using all-atom optimized potentials suitable for liquid simulations (AA-OPLS). In addition, to consider the long-range coulombic and the non-bonded van der Waals interactions, the particle–particle-particle mesh method (PPPM) and the 12–6 Lennard–Jones potential were used. The width and length of a single rGO (MXene) were 2.74 nm and 22.30 (~3.51 nm), respectively.

The epoxy (-O-) and hydroxyl (OH) functional groups were assumed to have a ratio of 0.03 to the carbon atoms in the rGO sheet, which was in good accord with the experimental sample. Also, First-principles calculations based on DFT calculations and plane-wave basis set were used to explore the interfacial energy of MXene/MXene, MXene/rGO, and rGO/rGO. The MD simulation demonstrated that these superior properties resulted from the synergistic interfacial interaction effect in Ti–O-C covalent bond, sliding of MXene nanosheets, and π-π bridge. The obtained MrGOAD sheets can be considered as flexible supercapacitors containing high volumetric power generation and energy storage.

Furthermore, the interplay between confinement, electrolyte ions, solvent, and electrolyte has a major influence on 2D-layered materials to increase energy storage, power delivery, and water desalination efficiency. Gao et al. [84] reported a multiscale theory/modelling and experiments to study the interaction, capacitive energy storage, and mechanical properties of Ti_3C_2 MXene in aqueous ions (Li^+, Na^+, K^+, Cs^+, and Mg^{2+}). Their study highlighted not only the importance of the position and dynamics of cations located between MXene sheets in energy storage but also revealed that by understanding the rational hydration coordination number of protons and cations, one can explain its energetic behavior under confinement.

Ab initio MD and *operando* calorimetry measurements revealed that H^+ rehydration and cation dehydration play a critical role in heat variations between experiments and theory. They show a *1/d* relationship between the average distance of cation and the surface of MXene. Moreover, they modified the Helmholtz model to clearly explain the EDL mechanism for different layered materials in various aqueous electrolytes.

In another work, Jalali et al. [3] investigated the effects of titanium carbide MXene to confine water molecules. Their study is a theoretical confirmation of the measured capacitance of nano-confined water in MXenes [85]. Using extensive MD simulation obtained an abnormal polarization of the confined water molecules near the MXene walls when cations (Li^+, Na^+, K^+, Rb^+) were present between MXene layers. Then, they built a capacitance-based model for the electric double-layer capacitor to illustrate the dielectric properties of nano-confined water in MXene. Consequently, it was shown that the ionic radius and the hydration shell of the cations could notably alter the dielectric response of nano-confined water in the studied system. The capacitance increases nonlinearly with increasing the hydration shell in the order of $Li^+ > Na^+ > K^+ > Rb^+$.

Designing a new membrane based on MXene and other 2D materials that can be applied as a sieving membrane for molecules and ions is also important in clean water production. Layer spacing and its role in water flow primarily impact such sieving materials. Zeng et al. [86] studied the role of interlayer spacing in the case of dopamine-functionalized graphene oxide (DGO) intercalated nanosheets into the $Ti_3C_2T_x$ MXene. They investigated this composite (DGO/MXene) for sieving dyes from wastewater. The interlayer spacing (d) of MXene/DGO bilayer was simulated by considering the composite material as a parallel surface in the xy direction using UFF. In DGO/MXene composite, DGO nanosheets can increase mechanical stability and reduce interlayer spacing.

The MD simulation revealed that the permeation rate of water molecules into the MXene layers was controlled directly by d of nanosheets. The water was permeated through the nanochannels present in the interlayer of DGO and MXene nanosheets. They explained that electrostatic interaction and physical sieving could influence the removal of dyes in composite membranes.

4.6 Intrinsic Characteristics of MXene

One of the excellent characteristics of MXenes is their layered structure that can be intercalated and de-intercalated with organic and inorganic molecules (formaldehyde, urea, cations, water, etc.). There are many studies on $Ti_3C_2T_x$ MXene (T_x = –OH, –O–, and –F) in aqueous solution and its interaction with urea (application in discarded spent dialysate). For instance, Meng et al. [87] found that $Ti_3C_2T_x$ can adsorb urea and remove it from aqueous solution dialysate at an initial urea concentration of 30 mg/dL by the efficiency of urea removal of 99% and 94%, respectively, without any cytotoxicity. Furthermore, they studied the urea molecules' spatial orientation and adsorption energy on $Ti_3C_2T_x$ MXene using DFT. According to their calculations, urea adsorption on $Ti_3C_2T_x$ MXene is stable along with parallel and vertical directions, where the parallel orientation is the most stable.

Overexposure to formaldehyde (HCHO) can cause a destructive impact on human health and the environment, which must be removed from indoor air. Zhang et al. [88] represented that $Ti_3C_2O_2$ MXene can efficiently capture the HCHO molecule. The adsorption energy was estimated to be 0.45 eV, using DFT calculations with the PAW method and PBE exchange–correlation functional. The HCHO adsorption capacity was approximately 6 mmol/g, calculated via AIMD and a simulation time of 7 ps. The MD simulation revealed that the HCHO remains stable on $Ti_3C_2O_2$ MXene surface up to 450 K, and its desorption was observed when the temperature exceeds 500 K.

MXenes with various chemical composition ranges and functionalization gained tremendous attention from many experimental and theoretical groups because of their tunable thermal and electronic features. Hence, MXenes can be used to design new energy storage and conversion devices. For example, Sarikurt et al. [89] used DFT, density-functional perturbation theory (DFPT), and the Boltzmann Transport

Theory, to calculate the values of lattice thermal conductivity(κ_l), thermoelectric figure-of-merit (zT), and Seebeck coefficients for two different functionalization configurations of oxygen terminated MXene monolayer (M_2CO_2, M = Ti, Zr, Hf, Sc). They carried out the calculation employing the generalized gradient approximation (GGA) within the PBE functional. These values vary by 40%, depending on the structural model. In addition, they discovered the adsorption site of the oxygen atom on the M_2CO_2 surface could remarkably change the thermoelectric and electronic features of M_2CO_2 MXene that can be designed to change the thermoelectric properties.

Zhang et al. [90] systematically studied the electronic, elastic, and structural properties of pure and functionalized 2D carbide/nitride MXenes ($Ti_{n+1}C_n/Ti_{n+1}N_n$ and $Ti_{n+1}C_nT_2/Ti_{n+1}N_nT_2$, n = 1, 2, 3, T: –F, –O and –OH) using DFT calculations. $Ti_{n+1}C_n$ MXenes exhibited large monolayer thicknesses, small electrical conductivity, large lattice constant, large stability, and small in-plane Young's moduli compared to $Ti_{n+1}N_n$ MXenes. Structural stability was improved for thicker MXenes monolayer. According to the E_{ad} results, MXenes nitrides have a stronger preference to be functionalized with F, –O, and –OH terminal groups, especially –O, due to the more active surface of nitride-based MXenes. The existence of free electron states in $Ti_{n+1}C_n$ and $Ti_{n+1}N_n$ functionalized MXenes with hydroxyl functional groups provides excellent transmission channels.

Also, the design of MXenes that have unique features compared to their own structures can be artificially accessible.

The elastic strain limits of 2D materials are more significant than their bulk counterparts, which can be adjusted by strain engineering. One more application of MXenes is found in spintronic devices due to the high electron mobility and conductivity of MXenes. $Hf_2MnC_2O_2$ MXene was observed to have a high magnetic moment per formula unit (3 μB) and a high Curie temperature (T_C > 800 K). By applying uniaxial strain on $Hf_2MnC_2O_2$ monolayer, Siriwardane et al. [91] modified its electronic, magnetic, and structural properties. They carried out their DFT calculations using PBE functional. In the absence of strain, $Hf_2MnC_2O_2$ is a ferromagnetic semiconductor hiving indirect band-gap. Whit a 1–3% tensile strain in the armchair direction, the band-gap transition from indirect to direct was observed.

A transition from semiconductor to metal was predicted under 4% strain in both zigzag and armchair directions. This MXene became a half-metal and favorable material for spintronic applications when strains of 7% and 9% were applied in the zigzag and armchair directions, respectively. Therefore, by applying tensile strain, the T_C of materials can be improved. The Curie temperature of $Hf_2MnC_2O_2$ MXene at 4% strain in both directions was about 706 K, increasing to 1200 K under 8% strain. Based on effective mass calculations, they reported that the desirable direction for electron transport is armchair ($\Gamma - X$ direction) due to the small effective masses.

There are several limits to the practical use of MXene and other 2D materials. For instance, preventing from swelling in water is one of the challenging problems in using 2D-material as a membrane for seawater desalination due to the tendency of these materials to swell in water and their instability in water and other aqueous solutions. Ding et al. [92] theoretically/experimentally reported a non-swelling behavior of $Ti_3C_2T_x$ MXene membranes in the presence of intercalated Al^{3+} cations.

DFT calculations were performed to predict the Al^{3+}adsorption position between $Ti_3C_2T_x$ MXene layers. They considered four models of Ti_3C_2, $Ti_3C_2O_2$, $Ti_3C_2(OH)_2$ and $Ti_3C_2F_2$ that the binding energies of Al^{3+} on them was +0.17 eV, −0.89 eV, + 1.92 eV and +1.82 eV, respectively. Therefore, they concluded a strong interaction between oxygen functional groups of the $Ti_3C_2T_x$ and Al^{3+} cations that can inhibit MXene swelling. Furthermore, molecular orbital analysis and charge transfer results indicated that the formation of the Al–O ionic bond could stabilize the *d*-spacing of the $Ti_3C_2T_x$ MXene nanosheets.

Chemical modification of 2D materials can improve their electronic harmony along with other materials. Gao et al. [93] studied the substitution and adsorption of a large number of single transition metal atoms (M = Fe, Co, Ni, Cu, Zn, Ru, Rh, Pd, Ag, Cd, Os, Ir, Pt, Au, Hg) on Ti_3C_2 MXene using DFT and PBE functional. Accordingly, single metal atoms were adsorbed on Ti_3C_2 MXene stronger than graphene and graphyne with adsorption energy (E_{ad}) in the range of −1.05 to −7.98 eV.

They found the E_{ad} and the substitution energy (E_{sub}) correlate almost linear with chemical properties, including Bader charge and bond length of Ti_3C_2 MXenes due to the electronic and geometric impact of doping metals on the electronic harmonic. In the case of an atom substitution on Ti_3C_2, the volcano curve between the E_{sub} and Bader charges was observed, and there was a discrepancy in the charge transfers process. Suggest that the E_{sub} cannot explain solely through charge transfer, and other chemical properties should be considered further.

4.7 Heterostructures of MXene

As mentioned in the previous section, the heterostructures of 2D-materials, generally joined through van der Waals (vdW) interactions, can exhibit new electronic properties different from the individual electronic properties of the dissimilar 2D materials. Thus, these 2D materials may have the potential for use in various applications, such as catalysis, electric energy storage, and electronics. MXenes, in conjunction with the other 2D materials, is a great conducting reinforcement. The charge transfer and the interfacial coupling of 2D materials become stronger and faster when they are fused with Mxenes, which improves the electrochemical properties of 2D materials [94].

Li et al. [95] studied different prototypical heterostructures of MXene $Ti_3C_2T_2$ (T = O, OH, F; terminal groups) and graphene using DFT and PBE functional. To account for vdW interactions, they used Grimme's (DFT-D3) scheme in their calculations. Their results demonstrated that the stacking order and the functional groups on the surface of these heterostructures could alter band structure, adhesion energy, and charge transfer.

Based on the significant difference in the work function of the graphene with the MXenes, the interaction between heterostructures of MXene and graphene follows the order: $Ti_3C_2(OH)_2$ > $Ti_3C_2O_2$ > $Ti_3C_2F_2$. The Dirac point of the graphene shifted as a result of charge transfer between the graphene monolayer and the $Ti_3C_2T_2$ MXene monolayer. The interface in the bilayer graphene/monolayer MXene

heterostructures broke the symmetry of AB-stacking bilayer graphene, and a gap was opened up at the K point of the graphene band structures.

In another work, Li et al. [96] simulated the interfacial built-in electric field of the MXene/monolayer transition metal dichalcogenide asymmetric heterostructures (aMXene/mTMDC). The MXene structure that the bottom or top electronegative atom plane was removed was named aMXene. In their work, spin-polarized DFT calculations were performed with PAW potential and two PBE and HSE functionals. By designing the asymmetric structure of MXene, a high dipole moment was observed that was perpendicular to the 2D-MXene plane. It was clear that in the aMXene structure, the unpassivated metal atoms were unstable and electropositive. However, in the aMXene/mTMDC bilayer, the aMXene was coupled with the electronegative chalcogenide atoms, breaking this instability and making tunable band structures possible. The engineered aMXene/mTMDC bilayers can possibly be used in several applications such as catalysis/photocatalysis, spintronics, and optoelectronics.

Also, Obodo et al. [97] investigated a DFT study of the application of Ti_3C_2 MXene monolayer as platinum support (Ti_3C_2-nPt, n = the number of the platinum layer) towards the catalytic dehydrogenation of methylcyclohexane (MCH). Their calculations were performed through PBE functional and Tkatcheno–Scheffler method to account for the vdW interaction. They found that this reaction would be possible on both pristine and supported platinum surfaces. Their results demonstrated that the application of Ti_3C_2 MXene monolayer as support leads to an increase in the catalytic activity of the surface toward dehydrogenation of MCH. The total dehydrogenation energies per H_2 molecule for the studied surfaces were –20.7, 19.8, 15.10, 11.80, and 12.40 kcal/mol for the Ti_3C_2, Ti_3C_2-1Pt, Ti_3C_2-2Pt, Ti_3C_2-3Pt, and Pt (111) structures, respectively.

Ganeshan et al. [98] used MD simulation with ReaxFF and DFT calculations to study the various physical properties of confined electrolyte between the interlayer space of the 2D-TiO_2/$Ti_3C_2T_2$ (T = O, OH) heterostructures. Their results show that the mobility of water molecules confined between 2D-TiO_2 improved where their localized jump rate was faster on the 2D-TiO_2 surface. In addition, they investigated that the oxygen ridges on the surface limit the self-diffusion of water in 2D-TiO_2. For the aqueous electrolytes containing Li^+, Na^+, and K^+ ions, the 2D-TiO_2 heterostructures had more favorable sites for the adsorption of these cations as well as protons. The latter demonstrated that the 2D-TiO_2 has the potential to accommodate the protons in contrast to the MXene homostructures. They found that in the aqueous electrolytes with Na^+, a planar layer can be formed between water molecules. Hence, the water dynamics decrease significantly in these electrolytes. Also, Li^+ mainly adsorbed on the surface of 2D-TiO_2 as compared to the $Ti_3C_2T_2$ MXene. Moreover, it was revealed that the 2D-TiO_2/$Ti_3C_2(OH)_2$ heterostructure has excellent proton storage capacity, where protons were transferred from $Ti_3C_2(OH)_2$ to the 2D-TiO_2.

4.8 Catalytic Purposes

Many MXene and its functionalized, structure engineered, and metal-doped counterparts have been used for catalytic purposes and to tailor their intrinsic properties. The design of a photo-induced catalyst for hydrogen production from water-splitting attracted a great deal of attention from researchers. Li et al. [99], aiming at the in-situ construction strategy together with one-step calcination, synthesized 2D/3D g-C_3N_4/Ti_3C_2 heterojunction in which lamellar g-C_3N_4 was uniformly distributed on the surface of Ti_3C_2.

Under visible light irradiation, the photocatalytic hydrogen production rate of g-C_3N_4/Ti_3C_2 composites was estimated to be significantly larger than that of pure g-C_3N_4. The DFT calculations and Kelvin probe measurements indicated that Schottky junction occurs between g-C_3N_4 and Ti_3C_2, controlling the photo-induced carriers' electron–hole recombination. In addition, the collaboration of the high conductivity of Ti_3C_2 and the intimate interface of g-C_3N_4/Ti_3C_2 heterojunction can simplify the electron transfer.

Metal-support interactions (MSIs) can improve the catalytic properties of supported nanoparticles. This cooperation provides an opportunity to design a wide range of heterogeneous catalysis for electrochemical and gas-phase reactions. Li et al. [100] used carbide-based MXene to support platinum and studied its application in the catalytic dehydration of light alkane. Atomic resolution HAADF-STEM was used to demonstrate the intermetallic surface, and DFT calculations were performed to explain the high catalytic activity of the intermetallic surface. They concluded that MXene support could vary the nature of active sites and enhance their selectivity toward activating the C–H bond.

Luo et al. [101] studied the electrocatalytic reaction of nitrogen (N_2) to produce ammonia (NH_3) through $Ti_3C_2O_2$ MXene under ambient conditions. Their experimental and theoretical evidence revealed that the basal plane of MXene was almost inert, and the exposed edge sites were the active sites of $Ti_3C_2O_2$ MXene. Based on their results, the adjustment of the active sites is an efficient strategy to improve the electrosynthesis of NH_3. From their experimental point of view, tailoring the MXene nanosheet to a smaller size can increase faradic efficiency. An indication that small MXenes have many active edge sites that can be a metal host active site in ammonia electrosynthesis.

As demonstrated in Fig. 4a, they proposed five possible mechanisms for the electrocatalytic reaction of N_2 to NH_3 using DFT calculations with PBE functional. Based on these DFT results, the low-energy path of the edge plane compared to the basal plane feasible the electrocatalytic reaction occurs at the edge active sites (see Fig. 4). According to the reaction energies demonstrated in pathways in Fig. 4, the most active site on the edge plane was the middle titanium atom.

The hydrogen evolution reaction (HER) studies have attracted tremendous attraction as a source of green energy production. Bai et al. [102] investigated a theoretical study based on the DFT calculations (with PBE functional) and a Fermi-abundance model. This discloses the origin of electrocatalysts for hydrogen HER on Mxenes

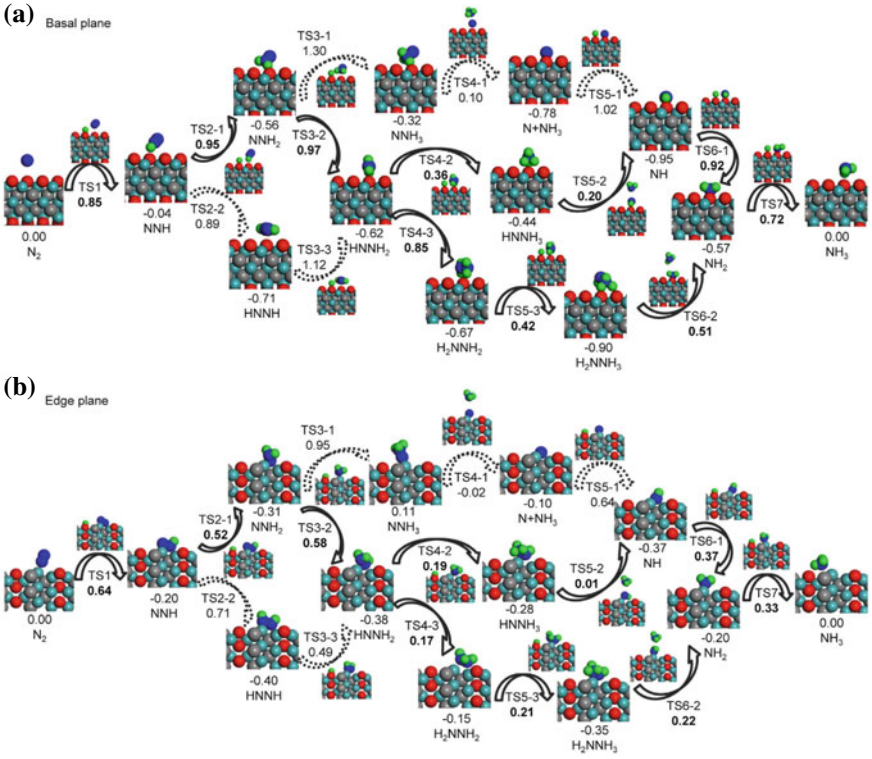

Fig. 4 The reaction profile is displaced on the basal plane and at the edge plane (**a** and **b**) of $Ti_3C_2O_2$ MXene. The structures and energies (in eV) of the intermediates and transition states (TSs) presented in various pathways of N_2 reduction reaction catalyzed on the basal plane (**a**) and the edge plane (**b**) are also demonstrated. (solid and dotted arrows refer to the low-energy and unfavorable routes, respectively). Color-coding: Ti (sky blue), O (red), H (green), N(blue), and C (gray) [101]

(M_2NO_2 and M_2CO_2, M = Sc, Ti, V, Cr, Zr, Nb, Mo, Hf, Ta, and W). According to the Fermi-abundance model, it was found that the O atoms at the Mxenes surface, especially their occupied *p* electronic states, play a crucial role in HER. Moreover, the free energy of hydrogen adsorption for Nb_2NO_2 and Ti_2NO_2 Mxenes was nearly zero, suggesting that they can be promising HER electrocatalysts.

Zhang et al. [103] synthesized $Mo_2TiC_2T_x$ MXene containing Mo vacancies in its outer layer by an electrochemical exfoliation process. Their experimental/theoretical (DFT with PBE functional) results revealed the abundant Mo vacancies in the basal plane of the synthesized MXene play as an active site to trap a single Pt atom. Furthermore, they demonstrated that the $Mo_2TiC_2T_x$–Pt structure has more catalytic efficiency than the pristine $Mo_2TiC_2T_x$ MXene. The strong covalent bond between the single platinum cations and the other atoms in the synthesized MXene makes the structure of $Mo_2TiC_2T_x$–Pt stable against HER.

Le et al. [104] improved the catalytic activity of $Ti_3C_2T_x$ MXenes for HER using ammonia heat treatment and doping with nitrogen atoms. They found that N-doping alters the electronic configuration of MXene electrocatalysts that have improved catalytic reactivity, structure stability, and electrical conductivity. They also optimized the annealing temperature of the N-doped $Ti_3C_2T_x$ MXenes to achieve several properties, including low overpotential, long-term durability, and the ideal value (0 eV) for the Gibbs free energy of the hydrogen adsorption, which the annealing temperature was estimated to be 600 °C. This temperature was also confirmed by DFT calculations using PBE functional.

Also, renewable fuels and chemical feedstock can be produced by the electrocatalytic carbon dioxide reduction reaction (CO_2RR). Handoko et al. [105] experimentally/theoretically studied the electrocatalytic CO_2RR through the mediation of Ti_2CT_x and Mo_2CT_x MXenes as a catalyst. It was found that the main CO_2RR product on the studied MXenes was formic acid. In addition, their DFT results demonstrated that a lower overpotential was achieved when the amounts of –F was low (more –O).

5 Challenges and Prospects

Although extensive studies have been conducted to explore MXene's properties and find novel applications of MXenes, research is still in the incipient stage. The latter causes that the actual practical applications face several challenges. Some of the challenges in both synthesizing and simulation of MXenes are listed below:

(i) Lack of direct 3D precursor of MXenes production.

(ii) Delamination of MAX phases by intercalation agents such as HF, LiF, HCl, and DMSO leads to the formation of few-layer MXene. These agents are hazardous to the environment. The eco-friendly intercalation agents rather than the conventional fluoride containing etchants are highly demanded.

(iii) It was demonstrated that the energy storage capacity and the electrochemical properties of MXenes depend mainly on their surface functional groups, porosity, and curved geometry. Therefore, much effort must be devoted to simulating/fabricating the thermodynamically stable porous MXene with, e.g. new functional groups and MXene's curved counterparts is required. In fact, a stable structure of MXenes that contains novel functional groups (beyond O, OH, F and different metals) are necessary.

(iv) On the one hand, the structure of MXenes contains several transition metals, which limit their investigation by the DFT method due to computational complexity. On the other hand, the introduced force fields, such as ReaxFF, do not adequately predict the electrical, optic, sensing, and thermodynamic properties of MXenes. Consequently, the development of a new force field and quantum computers are required to study the various feature of the MXenes.

Furthermore, simulation of new MXene nanocomposite and heterostructures with various 0D/2D, 1D/2D, 2D/2D, and 3D/2D layered structures might shed insight on future MXenes synthesizing techniques and applications.

6 Conclusion

This chapter showed that a wide range of MXenes properties could be characterized by using both DFT and MD simulations and their application in the simulation of MXene structures. We demonstrated that both methods are useful to simulate different physical and chemical properties of these 2D materials. Based on the intrinsic feature of the studied systems, MD and/or DFT technics have been employed by several groups to model the MXene structures. They were used to model MXene structures for various applications, including intercalation, exfoliation, energy storage, photocatalytic water splitting, and water catalysis. In some instances, MD and DFT were used to verify the experiment results. It is necessary to develop more precise large-scale systems that are more equivalent to experimental circumstances.

References

1. Naguib, M., Kurtoglu, M., Presser, V., Lu, J., Niu, J., Heon, M., Hultman, L., Gogotsi, Y., Barsoum, M.W.: Two-dimensional nanocrystals produced by exfoliation of Ti_3AlC_2. Adv. Mater. **23**, 4248–4253 (2011)
2. Naguib, M., Mochalin, V.N., Barsoum, M.W., Gogotsi, Y.: 25^{th} anniversary article: MXenes: a new family of two-dimensional materials. Adv. Mater. **26**, 992–1005 (2014)
3. Jalali, H., Khoeini, F., Peeters, F.M., Neek-Amal, M.: Hydration effects and negative dielectric constant of nano-confined water between cation intercalated MXenes. Nanoscale **13**, 922–929 (2021)
4. Lee, E., VahidMohammadi, A., Prorok, B.C., Yoon, Y.S., Beidaghi, M., Kim, D.J.: Room temperature gas sensing of two-dimensional titanium carbide (MXene). ACS Appl. Mater. Interfaces **9**, 37184–37190 (2017)
5. Vahid Mohammadi, A., Moncada, J., Chen, H., Kayali, E., Orangi, J., Carrero, C.A., Beidaghi, M.: Thick and freestanding MXene/PANI pseudocapacitive electrodes with ultrahigh specific capacitance. J. Mater. Chem. A **6**, 22123–22133 (2018)
6. Anasori, B., Lukatskaya, M.R., Gogotsi, Y.: 2D metal carbides and nitrides (MXenes) for energy storage. Nat. Rev. Mater. **2**, 1–17 (2017)
7. Anasori, B.: Gogotsi ÛG 2D Metal Carbides and Nitrides (MXenes) (1). Springer, Berlin (2019)
8. MacKerell, A.D., Jr., Bashford, D., Bellott, M.L.D.R., Dunbrack, R.L., Jr., Evanseck, J.D., Field, M.J., Fischer, S., Gao, J., Guo, H., Ha, S., Joseph-McCarthy, D.: All-atom empirical potential for molecular modeling and dynamics studies of proteins. J. Phys. Chem. B **102**, 3586–3616 (1998)
9. Rappé, A.K., Casewit, C.J., Colwell, K.S., Goddard, W.A., III., Skiff, W.M.: UFF, a fullperiodic table force field for molecular mechanics and molecular dynamics simulations. J. Am. Chem. Soc. **114**, 10024–10035 (1992)

10. Sun, H.: COMPASS: An ab initio force field optimized for condensed-phase application–Overview with details on alkane and benzene compounds. J. Phys. Chem. **102**, 7338–7364 (1998)
11. Jorgensen, W.L., Maxwell, D.S., Tirado-Rives, J.: Development and testing of the OPLSall-atom force field on conformational energetics and properties of organic liquids. J. Am. Chem. Soc. **118**, 11225–11236 (1996)
12. van Duin, A.C.T., Dasgupta, S., Lorant, F., Goddard, W.A.: III. ReaxFF: a reactive force field for hydrocarbons. J. Phys. Chem. A **105**, 9396–9409 (2001)
13. Gibbs, J.W.: Elementary principles in statistical mechanics. Courier Corporation (2014)
14. Marx, D., Hutter, J.: Ab initio molecular dynamics: theory and implementation. Modern Methods Algorithms Quantum Chem **1**(301–449), 141 (2000)
15. Le, T.D., Murad, M.A.: A new multiscale model for flow and transport in unconventional shale oil reservoirs. Appl. Math. Model. **64**, 453–479 (2018)
16. Chambre, P.A., Samuel, A.S.: Flow of rarefied gases. Princeton University Press (2017)
17. Hui, X., Chao, L.: Molecular dynamics simulations of gas flow in nanochannel with a Janus interface. AIP Adv. **2**, 042126 (2012)
18. Firestein, K.L., von Treifeldt, J.E., Kvashnin, D.G., Fernando, J.F., Zhang, C., Kvashnin, A.G., Podryabinkin, E.V., Shapeev, A.V., Siriwardena, D.P., Sorokin, P.B., Golberg, D.: Young's modulus and tensile strength of Ti_3C_2 MXene nanosheets as revealed by in situ TEM probing, AFM nanomechanical mapping, and theoretical calculations. Nano Lett. **20**, 5900–5908 (2020)
19. Jarzynski, C.: Nonequilibrium equality for free energy differences. Phys. Rev. Lett. **78**, 2690 (1997)
20. Perdew, J.P., Burke, K., Ernzerhof, M.: Generalized gradient approximation made simple. Phys. Rev. Lett. **77**, 3865 (1996)
21. Ernzerhof, M., Perdew, J.P., Burke, K.: Coupling-constant dependence of atomization energies. Int. J. Quantum Chem. **64**, 285–295 (1997)
22. Heyd, J., Scuseria, G.E.: Efficient hybrid density functional calculations in solids: assessment of the Heyd–Scuseria–Ernzerhof screened Coulomb hybrid functional. J. Chem. Phys. **121**, 1187–1192 (2004)
23. Heyd, J., Scuseria, G.E.: Assessment and validation of a screened Coulomb hybrid density functional. J. Chem. Phys. **120**, 7274–7280 (2004)
24. Heyd, J., Peralta, J.E., Scuseria, G.E., Martin, R.L.: Energy band gaps and lattice parameters evaluated with the Heyd-Scuseria-Ernzerhof screened hybrid functional. J. Chem. Phys. **123**, 174101 (2005)
25. Heyd, J., Scuseria, G.E., Ernzerhof, M.: Hybrid functionals based on a screened Coulomb potential. J. Chem. Phys. **118**, 8207–8215 (2003)
26. Henderson, T.M., Izmaylov, A.F., Scalmani, G., Scuseria, G.E.: Can short-range hybrids describe long-range-dependent properties? J. Chem. Phys. **131**, 044108 (2009)
27. Izmaylov, A.F., Scuseria, G.E., Frisch, M.J.: Efficient evaluation of short-range Hartree-Fock exchange in large molecules and periodic systems. J. Chem. Phys. **125**, 104103 (2006)
28. Krukau, A.V., Vydrov, O.A., Izmaylov, A.F., Scuseria, G.E.: Influence of the exchange screening parameter on the performance of screened hybrid functionals. J. Chem. Phys. **125**, 224106 (2006)
29. Kohn, W., Sham, L.J.: Self-consistent equations including exchange and correlation effects. Phys. Rev. **140**, A1133 (1965)
30. Parr, R.G.: Density Functional Theory of Atoms and Molecules. In: Horizons of Quantum Chemistry, pp. 5–15. Springer, Dordrecht (1980)
31. Hohenberg, P., Kohn, W.: Inhomogeneous electron gas. Phys. Rev. **136**, B864 (1964)
32. Grimme, S., Antony, J., Ehrlich, S., Krieg, H.A.: consistent and accurate ab initio parametrization of density functional dispersion correction (DFT-D) for the 94 elements H-Pu. J. Chem. Phys. **132**, 154104 (2010)
33. Grimme, S., Ehrlich, S., Goerigk, L.: Effect of the damping function in dispersion corrected density functional theory. J. Chem. Phys. **32**, 1456–1465 (2011)

34. Tkatchenko, A., Scheffler, M.: Accurate molecular van der Waals interactions from ground-state electron density and free-atom reference data. Phys. Rev. Lett. **102**, 073005 (2009)
35. Lotfi, R., Naguib, M., Yilmaz, D.E., Nanda, J., Van Duin, A.C.: A comparative study on the oxidation of two-dimensional Ti_3C_2 MXene structures in different environments. J. Mater. Chem. A **6**, 12733–12743 (2018)
36. Osti, N.C., Naguib, M., Ostadhossein, A., Xie, Y., Kent, P.R., Dyatkin, B., Rother, G., Heller, W.T., Van Duin, A.C., Gogotsi, Y., Mamontov, E.: Effect of metal ion intercalation on the structure of MXene and water dynamics on its internal surfaces. ACS Appl. Mater. Interfaces **8**, 8859–8863 (2016)
37. Meng, Q., Ma, J., Zhang, Y., Li, Z., Zhi, C., Hu, A., Fan, J.: The S-functionalized Ti_3 C_2 Mxene as a high capacity electrode material for Na-ion batteries: a DFT study. Nanoscale **10**, 3385–3392 (2018)
38. Zhang, H., Xin, X., Liu, H., Huang, H., Chen, N., Xie, Y., Deng, W., Guo, C., Yang, W.: Enhancing lithium adsorption and diffusion toward extraordinary lithium storage capability of freestanding $Ti_3C_2T_x$ MXene. J. Phys. Chem. C **123**, 2792–2800 (2019)
39. Naguib, M., Come, J., Dyatkin, B., Presser, V., Taberna, P.L., Simon, P., Barsoum, M.W., Gogotsi, Y.: MXene: a promising transition metal carbide anode for lithium-ion batteries. Electrochem. Commun. **16**, 61–64 (2012)
40. Ahmed, B., Anjum, D.H., Hedhili, M.N., Gogotsi, Y., Alshareef, H.N.: H_2O_2 assisted room temperature oxidation of Ti_2C MXene for Li-ion battery anodes. Nanoscale **8**, 7580–7587 (2016)
41. Mashtalir, O., Naguib, M., Mochalin, V.N., Dall'Agnese Y, Heon M, Barsoum MW, Gogotsi Y,: Intercalation and delamination of layered carbides and carbonitrides. Nat. Commun. **4**, 1–7 (2013)
42. Zhao, S., Meng, X., Zhu, K., Du, F., Chen, G., Wei, Y., Gogotsi, Y., Gao, Y.: Li-ion uptake and increase in interlayer spacing of Nb_4C_3 MXene. Energy Storage Mater. **8**, 42–48 (2017)
43. Naguib, M., Halim, J., Lu, J., Cook, K.M., Hultman, L., Gogotsi, Y., Barsoum, M.W.: New two-dimensional niobium and vanadium carbides as promising materials for Li-ion batteries. J. Am. Chem. Soc. **135**, 15966–15969 (2013)
44. Zhou, J., Zha, X., Zhou, X., Chen, F., Gao, G., Wang, S., Shen, C., Chen, T., Zhi, C., Eklund, P., Du, S.: Synthesis and electrochemical properties of two-dimensional hafnium carbide. ACS Nano **11**, 3841–3850 (2017)
45. Du, F., Tang, H., Pan, L., Zhang, T., Lu, H., Xiong, J., Yang, J., Zhang, C.J.: Environmental friendly scalable production of colloidal 2D titanium carbonitride MXene with minimized nanosheets restacking for excellent cycle life lithium-ion batteries. Electrochim. Acta **235**, 690–699 (2017)
46. Wu, X., Wang, Z., Yu, M., Xiu, L., Qiu, J.: Stabilizing the MXenes by carbon nanoplating for developing hierarchical nanohybrids with efficient lithium storage and hydrogen evolution capability. Adv. Mater. **29**, 1607017 (2017)
47. Zheng, M., Guo, R., Liu, Z., Wang, B., Meng, L., Li, F., Li, T., Luo, Y.: MoS_2 intercalated p-Ti3C2 anode materials with sandwich-like three dimensional conductive networks for lithium-ion batteries. J. Alloys Compd. **735**, 1262–1270 (2018)
48. Chen, C., Xie, X., Anasori, B., Sarycheva, A., Makaryan, T., Zhao, M., Urbankowski, P., Miao, L., Jiang, J., Gogotsi, Y.: MoS_2-on-MXene heterostructures as highly reversible anode materials for lithium-ion batteries. Angew. Chem. Int. Ed. **57**, 1846–1850 (2018)
49. Zhang, C., Kim, S.J., Ghidiu, M., Zhao, M.Q., Barsoum, M.W., Nicolosi, V., Gogotsi, Y.: Layered orthorhombic $Nb_2O_5@Nb_4C_3T_x$ and $TiO_2@Ti_3C_2T_x$ hierarchical composites for high performance Li-ion batteries. Adv. Funct. Mater. **26**, 4143–4151 (2016)
50. Ahmed, B., Anjum, D.H., Hedhili, M.N., Gogotsi, Y., Alshareef, H.N.: H_2O_2 assisted room temperature oxidation of Ti 2 C MXene for Li-ion battery anodes. Nanoscale **8**, 7580–7587 (2016)
51. Zhao, M.Q., Torelli, M., Ren, C.E., Ghidiu, M., Ling, Z., Anasori, B., Barsoum, M.W., Gogotsi, Y.: 2D titanium carbide and transition metal oxides hybrid electrodes for Li-ion storage. Nano Energy **30**, 603–613 (2016)

52. Wang, Y., Li, Y., Qiu, Z., Wu, X., Zhou, P., Zhou, T., Zhao, J., Miao, Z., Zhou, J., Zhuo, S.: Fe_3O_4@ Ti_3C_2 MXene hybrids with ultrahigh volumetric capacity as an anode material for lithium-ion batteries. J. Mater. Chem. A **6**, 11189–11197 (2018)
53. Zheng, W., Zhang, P., Chen, J., Tian, W.B., Zhang, Y.M., Sun, Z.M.: In situ synthesis of CNTs@ Ti 3 C 2 hybrid structures by microwave irradiation for high-performance anodes in lithium ion batteries. J. Mater. Chem. A **6**, 3543–3551 (2018)
54. Halim, J., Kota, S., Lukatskaya, M.R., Naguib, M., Zhao, M.Q., Moon, E.J., Pitock, J., Nanda, J., May, S.J., Gogotsi, Y., Barsoum, M.W.: Synthesis and characterization of 2D molybdenum carbide (MXene). Adv. Funct. Mater. **26**, 3118–3127 (2016)
55. Lin, Z., Sun, D., Huang, Q., Yang, J., Barsoum, M.W., Yan, X.: Carbon nanofiber bridged two-dimensional titanium carbide as a superior anode for lithium-ion batteries. J. Mater. Chem. A **3**, 14096–14100 (2015)
56. Byeon, A., Zhao, M.Q., Ren, C.E., Halim, J., Kota, S., Urbankowski, P., Anasori, B., Barsoum, M.W., Gogotsi, Y.: Two-dimensional titanium carbide MXene as a cathode material for hybrid magnesium/lithium-ion batteries. ACS Appl. Mater. Interfaces **9**, 4296–4300 (2017)
57. Syamsai, R., Rodriguez, J.R., Pol, V.G., Van Le, Q., Batoo, K.M., Adil, S.F., Pandiaraj, S., Muthumareeswaran, M.R., Raslan, E.H., Grace, A.N.: Double transition metal MXene ($Ti_xTa_{4-x}C_3$) 2D materials as anodes for Li-ion batteries. Sci. Rep. **11**, 1–13 (2021)
58. Tian, Y., An, Y., Feng, J.: Flexible and freestanding silicon/MXene composite papers for high-performance lithium-ion batteries. ACS Appl. Mater. Interfaces **11**, 10004–10011 (2019)
59. Yang, C., Liu, Y., Sun, X., Zhang, Y., Hou, L., Zhang, Q., Yuan, C.: In-situ construction of hierarchical accordion-like TiO_2/Ti_3C_2 nanohybrid as anode material for lithium and sodium ion batteries. Electrochim. Acta **271**, 165–172 (2018)
60. Zhao, M.Q., Xie, X., Ren, C.E., Makaryan, T., Anasori, B., Wang, G., Gogotsi, Y.: Hollow MXene spheres and 3D macroporous MXene frameworks for Na-ion storage. Adv. Mater. **29**, 1702410 (2017)
61. Guo, X., Zhang, J., Song, J., Wu, W., Liu, H., Wang, G.: MXene encapsulated titanium oxide nanospheres for ultra-stable and fast sodium storage. Energy Storage Mater. **14**, 306–313 (2018)
62. Tao, M., Zhang, Y., Zhan, R., Guo, B., Xu, Q., Xu, M.: A chemically bonded CoNiO2 nanoparticles/MXene composite as anode for sodium-ion batteries. Mater. Lett. **230**, 173–176 (2018)
63. Zhang, Y., Guo, B., Hu, L., Xu, Q., Li, Y., Liu, D., Xu, M.: Synthesis of SnS nanoparticle-modified MXene ($Ti_3C_2T_x$) composites for enhanced sodium storage. J. Alloys Compd. **732**, 448–453 (2018)
64. Guo, X., Xie, X., Choi, S., Zhao, Y., Liu, H., Wang, C., Chang, S., Wang, G.: Sb_2O_3/MXene ($Ti_3C_2T_x$) hybrid anode materials with enhanced performance for sodium-ion batteries. J. Mater. Chem. A **5**, 12445–12452 (2017)
65. Lian, P., Dong, Y., Wu, Z.S., Zheng, S., Wang, X., Wang, S., Sun, C., Qin, J., Shi, X., Bao, X.: Alkalized Ti_3C_2 MXene nanoribbons with expanded interlayer spacing for high-capacity sodium and potassium ion batteries. Nano Energy **40**, 1–8 (2017)
66. Dall'Agnese Y, Taberna PL, Gogotsi Y, Simon P,: Two-dimensional vanadium carbide (MXene) as positive electrode for sodium-ion capacitors. J. Phys. Chem. Lett. **6**, 2305–2309 (2015)
67. Ming, F., Liang, H., Zhang, W., Ming, J., Lei, Y., Emwas, A.H., Alshareef, H.N.: Porous MXenes enable high performance potassium ion capacitors. Nano Energy **62**, 853–860 (2019)
68. Naguib, M., Adams, R.A., Zhao, Y., Zemlyanov, D., Varma, A., Nanda, J., Pol, V.G.: Electrochemical performance of MXenes as K-ion battery anodes. Chem. Commun. **53**, 6883–6886 (2017)
69. Dong, Y., Wu, Z.S., Zheng, S., Wang, X., Qin, J., Wang, S., Shi, X., Bao, X.: Ti_3C_2 MXene-derived sodium/potassium titanate nanoribbons for high-performance sodium/potassium ion batteries with enhanced capacities. ACS Nano **11**, 4792–4800 (2017)
70. Agresti, A., Pazniak, A., Pescetelli, S., Di Vito, A., Rossi, D., Pecchia, A., der Maur, M.A., Liedl, A., Larciprete, R., Kuznetsov, D.V., Saranin, D.: Titanium-carbide MXenes for work function and interface engineering in perovskite solar cells. Nat. Mater. **18**, 1228–1234 (2019)

71. Liu, Y., Xiao, H., Goddard, W.A., III.: Schottky-barrier-free contacts with two-dimensional semiconductors by surface-engineered MXenes. J. Am. Chem. Soc. **138**, 15853–15856 (2016)
72. Chenot, C., Robiette, R., Collin, S.: First evidence of the cysteine and glutathione conjugates of 3-sulfanylpentan-1-ol in hop (Humulus lupulus L.). J. Agric. Food Chem. **67**, 4002–4010 (2019)
73. Lukatskaya, M.R., Kota, S., Lin, Z., Zhao, M.Q., Shpigel, N., Levi, M.D., Halim, J., Taberna, P.L., Barsoum, M.W., Simon, P., Gogotsi, Y.: Ultra-high-rate pseudocapacitive energy storage in two-dimensional transition metal carbides. Nat. Energy **2**, 1–6 (2017)
74. Shao, H., Xu, K., Wu, Y.C., Iadecola, A., Liu, L., Ma, H., Qu, L., Raymundo-Piñero, E., Zhu, J., LinZ, T.P.L.: Unraveling the charge storage mechanism of $Ti_3C_2T_x$ MXene electrode in acidic electrolyte. ACS Energy Lett. **5**, 2873–2880 (2020)
75. Huang, K., Li, Z., Lin, J., Han, G., Huang, P.: Correction: Two-dimensional transition metal carbides and nitrides (MXenes) for biomedical applications. Chem. Soc. Rev. **47**, 6889–6889 (2018)
76. Zhao, L., Wang, K., Wei, W., Wang, L., Han, W.: High-performance flexible sensing devices based on polyaniline/MXene nanocomposites. InfoMat **1**, 407–416 (2019)
77. Khakbaz, P., Moshayedi, M., Hajian, S., Soleimani, M., Narakathu, B.B., Bazuin, B.J., Pourfath, M., Atashbar, M.Z.: Titanium carbide MXene as NH_3 sensor: realistic first-principles study. J. Phys. Chem. C **123**, 29794–29803 (2019)
78. Chen, W.Y., Lai, S.N., Yen, C.C., Jiang, X., Peroulis, D., Stanciu, L.A.: Surface functionalization of Ti3C2T x MXene with highly reliable superhydrophobic protection for volatile organic compounds sensing. ACS Nano **14**, 11490–11501 (2020)
79. Borysiuk, V.N., Mochalin, V.N., Gogotsi, Y.: Bending rigidity of two-dimensional titanium carbide (MXene) nanoribbons: a molecular dynamics study. Comput. Mater. Sci. **143**, 418–424 (2018)
80. Castellanos-Gomez, A., Poot, M., Steele, G.A., van der Zant, H.S.J., Agraït, N., Rubio-Bollinger, G.: Elastic properties of freely suspended MoS_2 nanosheets. Adv. Mater. **24**, 772–775 (2012)
81. Wang, Q.: Simulations of the bending rigidity of graphene. Phys. Lett. A **374**, 1180–1183 (2010)
82. Shen, S., Ke, T., Rajavel, K., Yang, K., Lin, D.: Dispersibility and hotochemical stability of delaminated MXene flakes in water. Small **16**, 2002433 (2020)
83. Zhou, T., Wu, C., Wang, Y., Tomsia, A.P., Li, M., Saiz, E., Fang, S., Baughman, R.H., Jiang, L., Cheng, Q.: Super-tough MXene-functionalized graphene sheets. Nat. Commun. **11**, 1–11 (2020)
84. Gao, Q., Sun, W., Ilani-Kashkouli, P., Tselev, A., Kent, P.R., Kabengi, N., Naguib, M., Alhabeb, M., Tsa, W.Y., Baddorf, A.P., Huang, J.: Tracking ion intercalation into layered Ti_3C_2 MXene films across length scales. Energy Environ. Sci. **13**, 2549–2558 (2020)
85. Kim, K., Ando, Y., Sugahara, A., Ko, S., Yamada, Y., Otani, M., Okubo, M., Yamada,: A Dense charge accumulation in MXene with a hydrate-melt electrolyte. Chem. Mater. **31**, 5190–5196 (2019)
86. Zeng, G., Lin, Q., Wei, K., Liu, Y., Zheng, S., Zhan, Y., He, S., Patra, T., Chiao, Y.H.: High-performing composite membrane based on dopamine-functionalized graphene oxide incorporated two-dimensional MXene nanosheets for water purification. J. Mater. Sci. **56**, 6814–6829 (2021)
87. Meng, F., Seredych, M., Chen, C., Gura, V., Mikhalovsky, S., Sandeman, S., Ingavle, G., Ozulumba, T., Miao, L., Anasori, B., Gogotsi, Y.: MXene sorbents for removal of urea from dialysate: a step toward the wearable artificial kidney. ACS Nano **12**, 10518–10528 (2018)
88. Zhang, Y., Zhou, Z., Lan, J., Zhang, P.: Prediction of $Ti_3C_2O_2$ MXene as an effective capturer of formaldehyde. Appl. Surf. Sci. **469**, 770–774 (2019)
89. Sarikurt, S., Çakır, D., Keçeli, M., Sevik, C.: Influence of surface functionalization on thermal transport and thermoelectric properties of MXene monolayers. Nanoscale **10**, 8859–8868 (2018)

90. Zhang, N., Hong, Y., Yazdanparast, S., Zaeem, M.A.: Superior structural, elastic and electronic properties of 2D titanium nitride MXenes over carbide MXenes: a comprehensive first principles study. 2D Mater. 5:045004 (2018)
91. Siriwardane, E.M., Karki, P., Loh, Y.L., Çakır, D.: Strain–spintronics: modulating electronic and magnetic properties of $Hf_2MnC_2O_2$ MXene by uniaxial strain. J. Phys. Chem. C **123**, 2451–12459 (2019)
92. Ding, L., Li, L., Liu, Y., Wu, Y., Lu, Z., Deng, J., Wei, Y., Caro, J., Wang, H.: Effective ion sieving with $Ti_3C_2T_x$ MXene membranes for production of drinking water from seawater. Nat. Sustain. **3**, 296–302 (2020)
93. Gao, Y., Cao, Y., Gu, Y., Zhuo, H., Zhuang, G., Deng, S., Zhong, X., Wei, Z., Chen, J., Pan, X., Wang, J.G.: Functionalization Ti_3C_2 MXene by the adsorption or substitution of single metal atom. Appl. Surf. Sci. **465**, 911–918 (2019)
94. Zhou, S., Yang, X., Pei, W., Liu, N., Zhao, J.: Heterostructures of MXenes and N-doped graphene as highly active bifunctional electrocatalysts. Nanoscale **10**, 10876–10883 (2018)
95. Li, R., Sun, W., Zhan, C., Kent, P.R., Jiang, D.E.: Interfacial and electronic properties of heterostructures of MXene and graphene. Phys. Rev. B **99**, 085429 (2019)
96. Li, B., Guo, H., Wang, Y., Zhang, W., Zhang, Q., Chen, L., Fan, X., Zhang, W., Li, Y., Lau, W.M.: Asymmetric MXene/monolayer transition metal dichalcogenide heterostructures for functional applications. Npj Comput. Mater. **5**, 1–8 (2019)
97. Obodo, K.O., Ouma, C.N.M., Modisha, P.M., Bessarabov, D.: Density functional theory calculation of Ti_3C_2 MXene monolayer as a catalyst and catalyst support for platinum towards the dehydrogenation of methylcyclohexane to toluene. Appl. Surf. Sci. **529**, 147186 (2020)
98. Ganeshan, K., Shin, Y.K., Osti, N.C., Sun, Y., Prenger, K., Naguib, M., Tyagi, M., Mamontov, E., Jiang, D.E., Van Duin, A.C.: Structure and dynamics of aqueous electrolytes confined in 2D-TiO_2/$Ti_3C_2T_2$ MXene heterostructures. ACS Appl. Mater. Interfaces **12**, 58378–58389 (2020)
99. Li, J., Zhao, L., Wang, S., Li, J., Wang, G., Wang, J.: In situ fabrication of 2D/3D g-C_3N_4/Ti_3C_2 (MXene) heterojunction for efficient visible-light photocatalytic hydrogen evolution. Appl. Surf. Sci. **515**, 145922 (2020)
100. Li, Z., Yu, L., Milligan, C., Ma, T., Zhou, L., Cui, Y., Qi, Z., Libretto, N., Xu, B., Luo, J., Shi, E.: Two-dimensional transition metal carbides as supports for tuning the chemistry of catalytic nanoparticles. Nat. Commun. **9**, 1–8 (2018)
101. Luo, Y., Chen, G.F., Ding, L., Chen, X., Ding, L.X., Wang, H.: Efficient electrocatalytic N_2 fixation with MXene under ambient conditions. Joule **3**, 279–289 (2019)
102. Bai, X., Ling, C., Shi, L., Ouyang, Y., Li, Q., Wang, J.: Insight into the catalytic activity of MXenes for hydrogen evolution reaction. Sci. Bull. **63**, 1397–1403 (2018)
103. Zhang, J., Zhao, Y., Guo, X., Chen, C., Dong, C.L., Liu, R.S., Han, C.P., Li, Y., Gogotsi, Y., Wang, G.: Single platinum atoms immobilized on an MXene as an efficient catalyst for the hydrogen evolution reaction. Nat. Catal. **1**, 985–992 (2018)
104. Le, T.A., Bui, Q.V., Tran, N.Q., Cho, Y., Hong, Y., Kawazoe, Y., Lee, H.: Synergistic effects of nitrogen doping on MXene for enhancement of hydrogen evolution reaction. ACS Sustain. Chem. Eng. **7**, 16879–16888 (2019)
105. Handoko, A.D., Chen, H., Lum, Y., Zhang, Q., Anasori, B., Seh, Z.W.: Two-dimensional titanium and molybdenum carbide MXenes as electrocatalysts for CO_2 reduction. Iscience **23**, 101181 (2020)

Energy Storage Applications of MXene

Jensheer Shamsudeen Seenath

Abstract The excellent electronic conductivity, mechanical properties, superior chemistries, and unique morphologies enable MXene to be a potential candidate for a plethora of applications ranging from sensors and electronic devices to biomedical and electrochemical energy storage. The surfaces functional groups in MXenes lead to high hydrophilicity and are able to react with various species to generate stable colloidal solutions in water. MXenes are widely employed for energy storage applications, including metal ion batteries and electrochemical capacitors (supercapacitors). In this chapter, the application of MXenes in metal-ion batteries and supercapacitors is provided with detailed examples.

1 MXenes for Supercapacitors

Supercapacitors (SCs) are also called electrochemical capacitors, are potential energy storage devices that possess high power density, quick charge/discharge ability, and ultra-long lifetime [1]. According to their charge storage mechanism, SCs can be divided into electric double-layer capacitors (EDLCs) or pseudocapacitors. The EDLCs store charge via the electrical double layer formed at the interface between electrode and the electrolyte. As charge storage is mainly through adsorption and desorption of ions without any charge transfer, EDLCs render high-power density performance. On the other hand, pseudocapacitors rely on the redox reaction to store energy, hence exhibiting a high energy density but short cycling performance [2]. A hybrid supercapacitor combines the key characteristics of an EDLC and the pseudocapacitor with energy density between EDLCs and pseudocapacitors and power density comparable to EDLCs. Because supercapacitors have a low energy density,

J. Shamsudeen Seenath (✉)
LAAS-CNRS, Universite de Toulouse, Toulouse, France
e-mail: jshamsudee@laas.fr; jensheer.shamsudeen.seenath@umontreal.ca

Faculty of Arts and Sciences, Department of Chemistry, University of Montréal, Montréal, Québec, Canada

M. Khalid et al. (eds.), *Fundamental Aspects and Perspectives of MXenes*,
Engineering Materials, https://doi.org/10.1007/978-3-031-05006-0_7

there is a lot of interest in developing cost-effective and high-performance electrode materials. The supercapacitor electrodes derived from 2D materials have been enticing due to atomic-scale thickness, numerous active surface sites, and excellent mechanical properties. MXene is a rising star among all 2D materials with good conductivity, hydrophilic surface functional groups and tunable surface chemistry, along with key characteristics of fast charge–discharge and long cycling stability. MXene electrode has shown excellent supercapacitor performance, including high volumetric capacitance and energy density values, by eliminating the need for any metallic current collectors. However, like any other 2D material, MXene is prone to stacking and losing the electrochemically active surface, affecting the performance [3]. MXene needs to be engineered through strategies such as intercalation, doping, or composites or hybrids with other materials to overcome this challenge. Importantly, for practical application of SCs, volumetric capacitance, energy, and power density are very important, and for most SCs achieving high volumetric performance is a major challenge. The high bulk density of MXene reduces the volume of SCs and widens the application range. The energy density of a capacitor can be expressed as $E = 1/2\ CV^2$, where C denotes the capacitance and V means the working voltage window. Therefore, it is understood that a high energy density can be achieved either by enlarging the working voltage window or by increasing the capacitance.

(a) **As SC electrodes**

There have been several reports on MXene-based SCs with excellent performance characteristics. In the traditional electrode preparation route using 2D nanomaterials, the electrochemical performance greatly relies on the electrode thickness. Hence, it's challenging to realize both high energy and power density concomitantly. Although increasing the electrode film thickness could be an option, but is often followed by sluggish ion transport kinetics with long and tortuous channels [3]. Several strategies have been put forward to resolve the ion transport issue in thicker films, such as enlarging the inert layer spacing through intercalation and introducing defects to improve electronic properties, etc. Even though these approaches improve performance, the key challenges are not fully addressed. Recently, Xia et al. reported the assembly of 2D MXene electrodes from parallel to a vertical mode of arrangement (Fig. 1a) [4]. They adopted a process towards constructing vertically aligned nanofilms by utilizing the liquid crystal characteristics of 2D materials by controlling their orientation and arrangement in the dispersion. The electrochemical behavior of both the vertical and parallelly assembled films of MXene were then compared. It was observed that the pseudocapacitance remained almost the same when the thickness of MXene lamellar liquid crystal (MXLLC) films increased from 40 to 200 μm. In contrast, the capacitance decreases drastically by increasing the thickness from 6 to 35 μm for suction filtrated films (Fig. 1c). CVs show the superior rate performance of MXLLC film at different scan rates using a film thickness of 200 μm (Fig. 1b). Furthermore, excellent cycling performance is demonstrated at a current density of 20 A g^{-1}, with nearly 100% capacitance retention after 20,000 cycles (Fig. 1d). Moreover, for a film of 200 μm thickness, at a scan rate below 2000 mV $s^{-1}$the

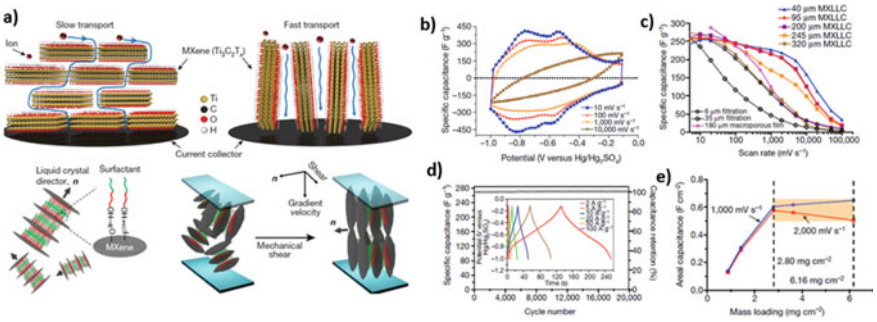

Fig. 1 **a** Ion transport mechanism of horizontally and vertically stacked $Ti_3C_2T_x$ MXene films with a depiction of shear plates arrangement process of surfactant ($C_{12}E_6$) enhanced MXLLC (MXene layered liquid crystal). **b–f** Electrochemical performance of MXLLC electrode. **b** CV curves at different scan rates (electrode thickness:200 μm). **c** Comparison of the rate performance of MXLLC film and vacuum filtered MXene at scan rate between 10 and 100 000 mV s^{-1}, the specific capacitance of microporous MXene film ((thickness: 180 μm)) is shown for comparison. **d** Cycling stability study of 200 μm thick MXLLC film at 20 A g^{-1} with inset showing the charge–discharge curves at various current densities. **e** Areal capacitance as a function of the mass loading with marked yellow region showing the mass-dependent capacitance [4]

areal capacitance value has surpassed the standard of supercapacitor electrode (0.6 F cm^{-2}) (Fig. 1e) [4].

Lukatskaya et al. proposed a strategy to enhance the capacitance of Ti_3C_2 MXene through the intercalation method. The intercalation of various cations yielded a "Ti_3C_2 paper" (p-Ti_3C_2) and then investigated their electrochemical performance in detail (Fig. 2a–c) [5]. An increase in the interlayer space is observed as a result of the pre-intercalation of different ions between MXene layers, which resulted in high electrochemical performance (Fig. 2d–g). For example, a free-standing paper electrode with a thickness under 20 μm in KOH electrolyte showed volumetric capacitance of 450 F cm^{-3} at 2 mV s^{-1}, and when the scan rate increased to 100 mV s^{-1}, the performance still retained at 280 F cm^{-3}. The intercalation of ions between MXene layers is researched using various acid and alkali salts, and changes in lattice space are studied using the X-ray diffraction method. The interlayer spacing varies significantly with the concentrated solution. In contrast, the change in the lattice is very minimal with neutral solution, and with acetic acid or sulfuric acid, there is no change at all. A performance comparison between multilayer $Ti_3C_2T_x$ and p-$Ti_3C_2T_x$ is presented in Fig. 2f, g.

MXene-derived organic material hybrids are promising electrodes for energy storage. In a recent report, Seenath et al. developed an MXene-coupled nitrogen-doped porous carbon (MX-MC-N) hybrid electrode with the help of conjugated microporous polymer (Fig. 3a) [6]. The strong coupling and interfacial interaction between nitrogen-doped porous carbon and MXene layers in MX-MC-N boosted the electrochemical charge storage by delivering a high capacitance up to 245 F g^{-1} at 0.6 A g^{-1} and an excellent cycling stability performance in 1 M H_2SO_4 (Fig. 3b,c).

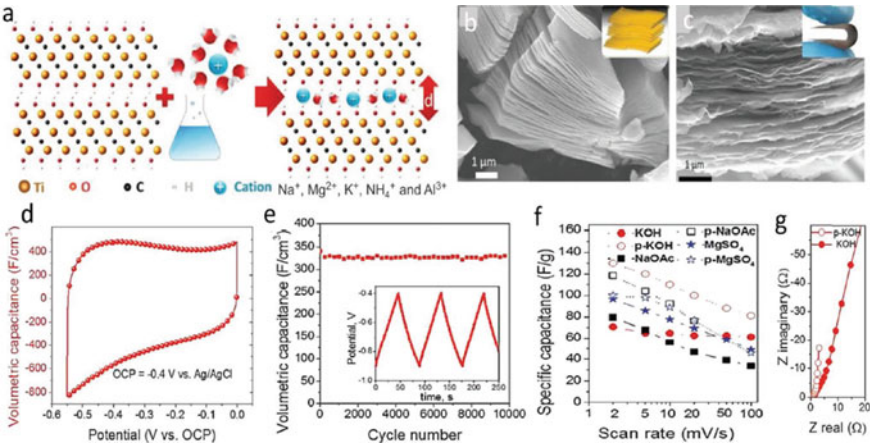

Fig. 2 **a** Schematic representation of different sized cation intercalation between MXene layers. **b** FESEM image of $Ti_3C_2T_x$, the inset shows schematic of layered MXene. **c** FESEM image of the paper electrode with inset is a photograph showing the flexibility. **d** CV curve of $Ti_3C_2T_x$ paper electrode in KOH electrolyte. **e** Cycling performance of the paper electrode, the inset shows the charge–discharge curves at 1 A g^{-1}. **f** Rate performance of $Ti_3C_2T_x$ and paper electrode. g) EIS of $Ti_3C_2T_x$ and paper $Ti_3C_2T_x$ electrodes in KOH electrolyte [5]

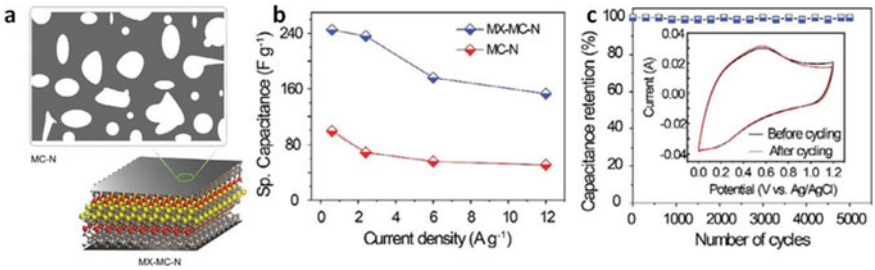

Fig. 3 **a** Schematic of the MXene-coupled nitrogen-doped porous carbon (MX-MC-N) electrode. **b** Specific capacitance comparison of MX-MC-N and MC-N electrodes at different current densities. **c** Cycling performance of MX-MC-N with CV curves before and after long cycling [6]

Moreover, symmetric supercapacitors based on MXene are extensively studied. MXene-based electrodes are first tested in a three-electrode set-up to understand the electrochemical stability window and then fabricate symmetric supercapacitors in a sandwiched configuration using solid-state electrolytes. In most of the reports, a flexible substrate is employed to load the active material to develop all-solid-state flexible supercapacitors [7–13].

(b) Asymmetric SCs

Along with achieving high capacitance, the potential window of expansion is imperative to enhance the energy density performance in SCs. Using MXene electrode material in aqueous electrolytes, the symmetric supercapacitors show a narrow potential window, hence lower energy density. Therefore, it is convenient to fabricate asymmetric supercapacitors using MXene as negative electrode material to overcome this issue. Most of the EDLC materials are of the ideal choice for positive electrodes (e.g., reduced graphene oxide) [14–16] in combination with $Ti_3C_2T_x$ for the construction of asymmetric supercapacitors. However, the performance is limited mainly by the lower capacitance of the EDLC electrode. Hence, alternate materials exhibiting pseudocapacitive and battery-type charge storage were investigated. For example, Jiang et al. reported an asymmetric MXene SC with a voltage window of 1.5 V, the highest among other MXene-based aqueous SCs [17]. To fabricate the SC, they employed $Ti_3C_2T_x$ ink on carbon fibers (CF) and RuO_2 grown on CF as the negative and positive electrodes, respectively and tested the performance in 1 M H_2SO_4 electrolyte and PVA/H_2SO_4 gel electrolyte (Fig. 4). Interestingly, the $Ti_3C_2T_x$/CF in 1 M H_2SO_4 displayed a high capacitance of 350 F g^{-1} at 100 mV s^{-1} along with excellent capacitance retention, owing to high conductivity, stability window, and proton-coupled pseudocapacitive charge storage. The asymmetric SC (RuO_2//$Ti_3C_2T_x$ full device) showed a capacitance of 78 F g^{-1} with high energy density and power density values (45 mW h cm^{-2} at 6 mW cm^{-2}). Moreover, the asymmetric device displayed excellent cycling stability after 20,000 cycles. This report suggests using MXene as the negative electrode material for constructing asymmetric supercapacitors. There

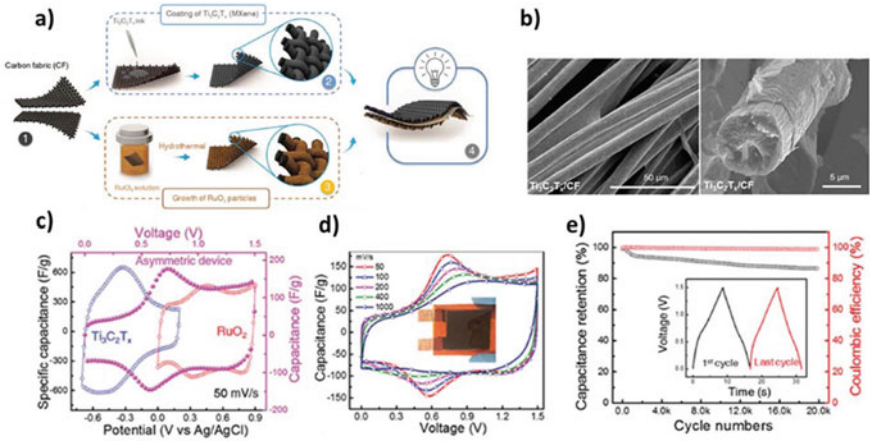

Fig. 4 **a** Schematic depiction of the assembling of an asymmetric supercapacitor based on MXene as negative electrode. **b** SEM images (at low and high magnification) revealing uniform coverage of $Ti_3C_2T_x$ on carbon fibers. **c** Comparison of CV curves of $Ti_3C_2T_x$/CF, RuO_2/CF, and asymmetric device at 50 mV s^{-1}. **d** CV curves of the asymmetric device ($Ti_3C_2T_x$/CF//RuO_2/CF) at different scan rates. **e** Cycling stability study and coulombic efficiency of the asymmetric device at 20 A g^{-1} [17]

are already few studies based on positive electrodes ofredox-active rGO– polymer (PPy, PEDOT, PANI, 2,5-dihydroxy-1,4-benzoquinone (DBQ) in combination with MXene in acidic electrolyte [18, 19].

In another report, an asymmetric SC was developed from a redox-active molecule (hydroquinone) reaction on a CNT as a positive electrode and a negative electrode based on $Ti_3C_2T_x$ in combination with proton-conducting Nafion film separator in H_2SO_4 electrolyte (Fig. 5) [20]. The active potential windows based on the complementary proton-coupled redox reactions at both electrodes showed a voltage window of up to 1.6 V. The hybrid supercapacitor delivered a high specific capacitance (176 F g^{-1} at 2 mV s^{-1}) and an energy density of 62 W h kg^{-1}, outperforming other state-of-the-art aqueous asymmetric supercapacitors. In addition, there are other several reports on MXene-based asymmetric supercapacitors (e.g., $Ti_3C_2T_x$//CoAl-layered double hydroxides (LDHs) [21], activated carbon (AC)//$Ti_3C_2T_x$/NiCoAl-LDHs, [22] and $Ti_3C_2T_x$/CuS//$Ti_3C_2T_x$).

The applicability of MXenes as negative electrodes for asymmetric SCs, including hybrid metal-ion capacitors, employing non-aqueous electrolytes is a potential strategy to expand the stability window of the device. However, keeping the high capacity without losing the rate performance remains challenging. In addition, the key characteristic of an SC is its excellent cyclability, and the poor cycling stability issue must be addressed in these systems through further understanding of the underlying charge storage mechanism [23].

(c) Metal-ion hybrid SCs

It is known that batteries' high energy density comes with a lower power density (low charge/discharge rates) challenge. On the contrary, the high-power SCs manifest lower energy density performance. To mitigate this issue, new types of potentially emerging energy storage devices, known as hybrid SCs have shown great promise as they fill the gap between metal-ion (lithium or sodium) batteries and SCs [23–25].

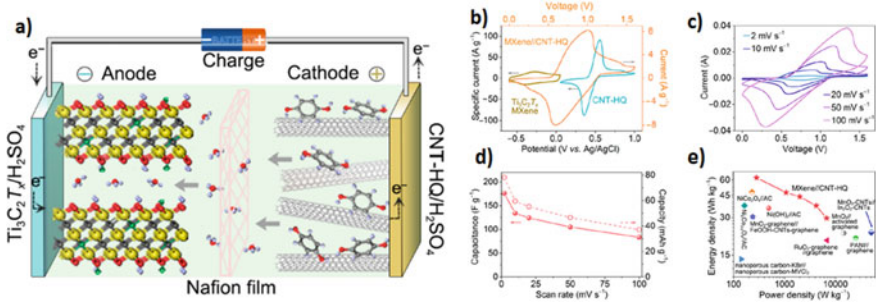

Fig. 5 **a** Graphical representation of the hydrogen-ion-rocking-chair MXene//CNT-HQ asymmetric supercapacitors. **b** Comparison of the CV curves of CNT-HQ, MXene, and the asymmetric device at 20 mV s^{-1}. **c** CV curves of the asymmetric device at different scan rates. **d** Rate performance of the device (specific capacitance and capacity at scan rates up to 100 mV s^{-1}). **e** Ragone plot (specific energy vs. specific power) comparison of MXene//CNT-HQ with other reported state-of-the-art asymmetric supercapacitors [20]

A hybrid SC can be of a composite hybrid or comprised of a battery-type electrode (metal-ion intercalation/de-intercalation) and a capacitor-type electrode (ion adsorption/desorption) or even in an asymmetric hybrid configuration [23, 26, 27]. Owing to high capacitance values of MXenes in aqueous electrolytes, several MXene compositions, including $Ti_3C_2T_x$, Ti_2C, Nb_2CT_x, and V_2C, have been studied and explored as electrode materials for Li-ion and Na-ion capacitors [28–33]. In comparison to aqueous electrolytes, supercapacitors using organic electrolytes containing metal ions (Li^+, Na^+, K^+) manifest a wider stability window with reversible intercalation de-intercalation between the MXene layers. For example, an asymmetric lithium-ion SC employing Ti_2CT_x and AC in combination with $LiPF_6$/EC/DMC electrolyte showed a voltage of 3.5 V with cyclability up to 10C for 1000 galvanostatic charge/discharge cycles [34].

In a typical example of a hybrid SC, CTAB-Sn(IV)@Ti_3C_2 was constructed using a simple liquid-phase cetyltrimethylammonium bromide (CTAB) prepillaring and Sn^{4+} pillaring method (Fig. 6a) [29]. The elemental mapping data confirmed the intercalation of Sn ion in the interlayer of the CTAB@Ti_3C_2 (Fig. 6b–e). The pillaring effect helped in the intercalation of more Li^+ ions into the interlayer space of $Ti_3C_2T_x$, resulting in the good rate performance and cycling stability of CTAB-Sn(IV)@Ti_3C_2 anode. In addition, the LIC using CTAB-Sn(IV)@Ti_3C_2 as anode

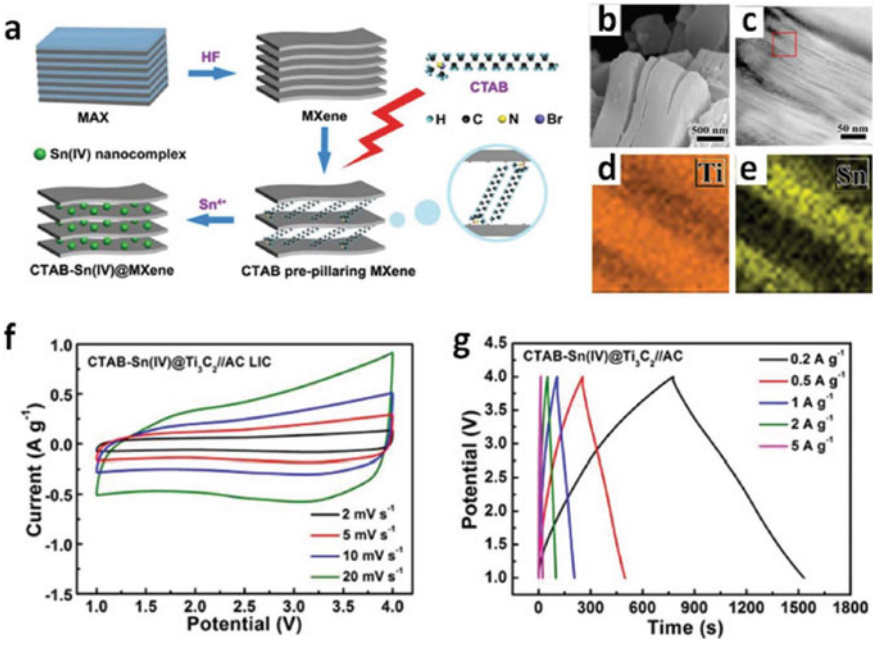

Fig. 6 MXene-based Li-ion hybrid SC. **a** Schematic showing the preparation of CTAB-Sn(IV)@Ti_3C_2. **b** SEM image of CTAB-Sn(IV)@Ti_3C_2. **c–e** STEM image and corresponding elemental mapping of Ti and Sn in CTAB-Sn(IV)@Ti_3C_2. **f** CV curves at different scan rates and **g** Charge/discharge curves at different current densities of CTAB-Sn(IV)@Ti_3C_2//AC LIC [29]

rendered a superior energy density and higher power density performance (45.31 Wh kg^{-1} and 10.8 kW kg^{-1}). Moreover, a deviation from the ideal rectangular shape in the CV of CTAB-Sn(IV)@Ti_3C_2//AC LIC is due to the difference in the charge storage mechanisms at the positive and negative electrodes (Fig. 6f). The GCD curves showed nearly symmetrical lines, showing the reversibility of the ion-storage mechanism (Fig. 6g). Other reported lithium-ion SC electrodes, including Nb_2CT_x–CNT/$LiFePO_4$, lithiated Nb_2CT_x–CNT/Nb_2CT_x–CNT, were all displayed windows up to 3 V with capacities of 24 and 36 mA h g^{-1}, respectively [35].

Moreover, MXenes were also employed in the fabrication of sodium-ion capacitors. For instance, a sodium ion SC using alluaudite $Na_2Fe_2(SO_4)_3$ positive electrode coupled with MXene negative electrode showed a cell voltage of 2.4 V and delivered capacities of 90 and 40 mA h g^{-1} at 1.0 and 5.0 A g^{-1}, respectively [30]. Sodium-ion SCs were assembled from a composite $Ti_3C_2T_x$/CNTs anode and $Na_{0.44}MnO_2$ cathode [36]. MXene having vanadium as M layer, V_2CT_x, demonstrated potential for Na^+ intercalation combined with hard carbon as the cathode [32]. Besides, acid/alkali-treated V_2CT_x showed remarkable K^+ ion storage capacity for a potassium-ion capacitor with ($K_xMnFe(CN)_6$) cathode, a Prussian blue analog. The as assembled full cell showed a superior voltage of 3.3 V within 0.01–4.6 V range, delivering a high energy density of 145 W h kg^{-1} at a power density of 112.6 W kg^{-1} [37]. In another example, an asymmetric K^+-ion SC consisting $Ti_3C_2T_x$ coupled with MnO_2 electrode in a water-in-salt electrolyte rendered a high voltage of 2.2 V [38].

The unique properties of the $Ti_3C_2T_x$ electrode were investigated in aqueous Li-ion and Na-ion SCs. The devices displayed excellent charge storage characteristics compared to aqueous full cell batteries. This reveals that $Ti_3C_2T_x$ is an excellent capacitor-type electrode for developing future hybrid SCs [28].

(2) **Micro-supercapacitors**

The development and implementation of the Internet of Things (IoT) put heavy thrust on portable, flexible, wearable self-powered electronic systems, which foster the development of micro-electrochemical energy storage devices (MEESDs), such as micro-supercapacitors (MSCs) and micro-batteries (MBs) [39]. Although MSC can be integrated and power microelectronic components and distributed sensor networks, achieving high-volumetric and areal capacitance is still a bottleneck. The micro-supercapacitors (MSCs) designed in either symmetric or asymmetric configurations can power various key components such as microsensors or wearable electronic devices. The operations of these systems require less power consumption, and the use of solution processing of MXenes is desirable owing to higher pseudocapacitance contribution. Until now, several approaches have been reported to fabricate MXene-based MSCs [40].

Recently, Nicolosi's group reported a low-cost expanded flexible MSCs using conductive hydrophilic 2D MXene ink with efficient rapid printing production method without the need of any extra additives or polymers [40] (Fig. 7). The flexible MXene MSCs with a tailored structure are appealing to use as an efficient power system for the next generation of microelectronics. With rapid growth production,

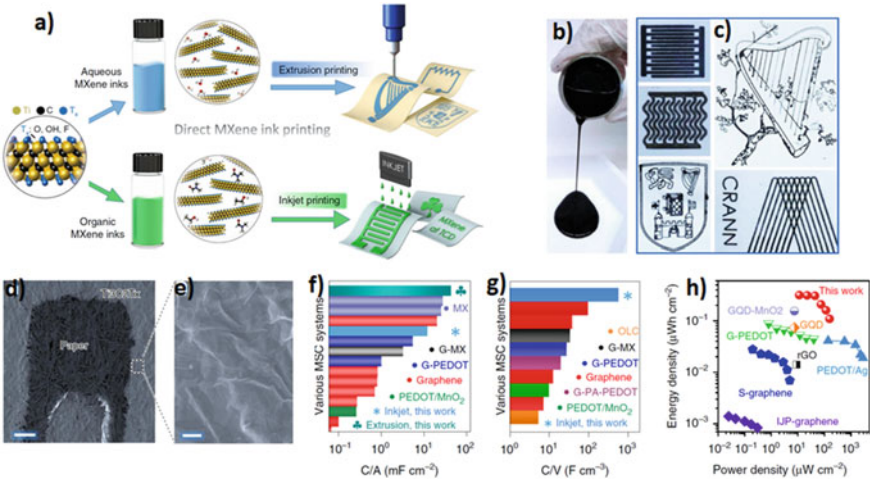

Fig. 7 **a** Schematic illustration of inkjet printing and extrusion printing process to generate various patterns, such as MSCs, MXene letters, ohmic resistors, etc. **b** Photograph of viscous MXene aqueous ink. **c** Optical images of printed patterns of MXene MSCs and other configurations on paper. **d** SEM image of printed MXene MSC (scale bar = 200 μm). **e** High-resolution SEM image showing a continuous film of stacked, interconnected MXene nanosheets (scale bar = 500 nm). **f** Comparison of areal volumetric capacitance with other reported MSC devices. **h** Areal energy vs. power density performance of MXene MSC with other reported MSCs [40]

minimal material waste, and scalability, the inkjet MSC displayed a remarkable volumetric capacitance of 512 F cm^{-3}, superior to other 2D material (e.g., graphene)-based MSCs (≤100). Moreover, at a power density of 11.4 μW cm^{-2}, the extrusion printing-based MSC delivered an energy density of 0.32 μW h cm^{-2}. Apparently, both MSCs (extrusion and inkjet printed) showed excellent capacitance retention after long cycling).

The same year, Zhang et al. [41] reported low-cost and efficient expandable flexible MSCs using a rapid 3D printing stamping production route with the help of a novel viscous hydrophilic conductive MXenes ink (Fig. 8). The width and the finger gap of the interdigitated $Ti_3C_2T_x$ MSC (I-$Ti_3C_2T_x$) on the paper electrode were examined using SEM (ca. 415 μm and ca. 550 μm for width and gap, respectively) (Fig. 8e). However, it requires further improvement on the uniformity of finger electrodes (Fig. 8f). It is also possible to generate other intricate geometries for MSCs, including spiral $Ti_3C_2T_x$ MSCs, by following a similar approach (Fig. 8d). Interestingly, these flexible MSCs on paper substrates exhibit a conductive network with low charge resistance (<15%) even under repetitive cycles of bending and release cycles and remained stable over long exposure periods. The interdigitated $Ti_3C_2T_x$ MSC showed a high areal capacitance value of 61 mF cm^{-2} at 25 μA cm^{-2}, and it still shows 50 mF cm^{-2} when the current density increases 32 times with characteristics of capacitive charge storage, excellent cycle life, high energy and power densities (Fig. 8h). The production of $Ti_3C_2T_x$ MSCs can be further enlarged by designing

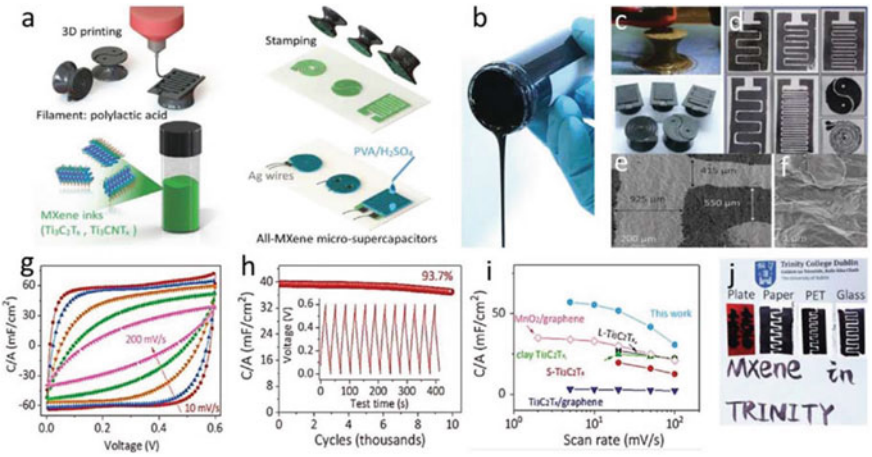

Fig. 8 **a** Construction of MXene MSCs using the stamping method. **b** Photograph showing thick and viscous MXene ink. **c**, **d** Various stamps with specific patterns and corresponding stamped MXene MSCs having various architectures. **e**, **f** Low and high-resolution SEM image of the interdigitated $Ti_3C_2T_x$ MSC (I-$Ti_3C_2T_x$) on a paper substrate showing the width and gap between the finger electrodes. **g** CV curves at different scan rates & **h** cycling study of I-$Ti_3C_2T_x$ MSC (the inset shows GCD curves at 200 μA cm^{-2}). **i** Rate performance of I-$Ti_3C_2T_x$ MSCs with other state-of-the-art MSCs. **j** Printed and handwritten MXene ink on different substrates [41]

pads or cylindrical seals along with a cold rolling process, and in a few seconds, a dozen of such MSCs with high areal capacitance (as high as 56.8 mV cm^{-2} at 10 mV s^{-1}) can be manufactured.

Compared to previously reported MSCs, the stamping technique enabled MSCs to display superior areal capacitance and rate performance (Fig. 8i). Through further optimization (synthesis process, MXene surface chemistry, and stamping design), high areal and volumetric performance can be accomplished to enable efficient powering for the next generation of microelectronic systems.

Another interesting report of MXene-based MSCs, where Chen et al. demonstrated a flexible interdigitated MSC by printing thixotropic ink composed of $RuO_2.xH_2O$@$Ti_3C_2T_x$ MXene nanosheets and silver nanowires. The MSC showed the highest volumetric capacitance of 864.2 F cm^{-3} at 1 mV s^{-1} with excellent long-term cyclability [42]. A screen-printed asymmetric MSC using $Ti_3C_2T_x$//CoAl-LDHs showed the highest energy density of 8.84 mW h cm^{-2} along with excellent flexibility performance [21]. An on-chip MXene MSC assembled through photolithographic lift-off process on a SiO_2/Si substrate and spray-coating delivered a volumetric performance of 30 F cm^{-3} with excellent rate handling up to 300 V s^{-1} along with ultra-low relaxation time constant [43]. In another approach using laser scribing, Peng et al. demonstrated a CO_2 laser scribed current collector-free flexible all-solid-state MXene MSC showing excellent charge storage performance [44]. In an interesting report using freestanding and lightweight MXene/bacterial cellulose composite paper, an all-solid-state stretchable MSCs is fabricated through a direct

laser-cutting Kirigami patterning method [45]. In addition, a 3D MSC is developed using the laser cutting method by employing MXene–graphene composite aerogel rendering self-healing ability [46]. Other than the aforementioned fabrication techniques, several other alternative techniques have been investigated for MXene MSCs, including direct writing, [47], mask-assisted deposition, [48] and automated scalpel patterning, [49–51].

In summary, various strategies can realize MSCs using MXenes due to their facile processing and excellent robustness of MXene nanosheets. The assembled MSC devices show excellent performance due to the high conductivity and volumetric capacitance of MXenes. Nonetheless, the development of MXene MSCs is still in its infancy, and further material development, use of novel electrolytes, and device optimization need to be carefully examined [40].

(3) **MXene-engineered electrodes for batteries**

Developing advanced battery materials (cathode and anode) is imperative to boost the ion storage capacity or voltage window to accomplish a higher energy density of EVs with longevity and longer driving distance. However, poor conductivity of electrodes, large volume expansion, and unstable solid electrolyte interphase (SEI) films are among the key challenges preventing their practical application. The discovery of MXenes in the recent past has helped mitigate a few of the issues by acting as both electrochemical active material and conductive 2D substrates towards the developing advanced functional electrodes. The reversible insertion/extraction of alkali metal ions, including Li^+, Na^+, K^+, and Mg^{2+}, are undoubtedly the key to understanding rechargeable batteries [52, 53]. The unique characteristics, including excellent electrical conductivity, high hydrophilicity, and the ability to host various cations, make 2D $Ti_3C_2T_x$ a potential candidate as a high-performance electrode in rechargeable batteries. Interestingly, a larger interlayer space in 2D material confers a lower intercalation barrier for ions with minimal volume changes during the charge–discharge cycles [30, 54, 55]. Since it's possible to tune MXene's interlayer spacing and make surface functional group modification, several studies have been reported using $Ti_3C_2T_x$ and $Ti_3C_2T_x$-based composites for Li-ion batteries (LIBs), Na-ion batteries (SIBs), Li–S batteries (LSBs), among others [56–59]. The common strategies employed to achieve good performance were structural engineering of $Ti_3C_2T_x$, modification of chemical composition, and making composites with other materials. The following sections summarize some of the key advances of Ti3C2Tx-based electrodes reported in LIBs, SIBs, and LSBs.

(a) **Lithium-ion Batteries**

LIBs are considered as a potential candidate for future energy storage owing to their high specific energy, superior cyclability, no memory effect, etc. LIBs are currently a key player in portable electronics with huge application potential with successful implementation in electric vehicles [60, 61]. Since electrode materials play a vital role in LIB performance, substantial research has been carried out to engineer the electrode materials manifesting superior charge storage with excellent electron and ion conductivity toward more powerful LIBs [62, 63]. 2D materials (e.g.,

graphene, [64] transition metal dichalcogenides, [52] and transition metal carbides [65]) in comparison with other electrode materials is shown to have key merits (high surface-to-volume, channels for fast ion-migration, and excellent interfacial interaction) to act as promising candidates for LIBs.

The DFT calculation studies on 2D $Ti_3C_2T_x$ predicted its ability to host Li-ions through the formation of $Ti_3C_2Li_2$, and the intercalated Li^+ occupied the space previously filled with Al atoms [66]. In this case, the theoretical Li-ion capacity is 320 mA h g^{-1} that is on par with the Li-ion capacity of graphite (LiC_6, 372 mA h g^{-1}). Following DFT studies to understand the Li storage ability and electronic properties of Ti_3C_2, $Ti_3C_2F_2$, and $Ti_3C_2(OH)_2$ indicate that Ti_3C_2, devoid of the surface functional group, has immense potential to be LIB anode owing to metallic conductivity, low ion diffusion barrier, and high theoretical capacity [56]. In $Ti_3C_2F_2$ and $Ti_3C_2(OH)_2$, the surface functional groups likely affect the ion diffusion, lowering the Li storage capacity. In later studies, the delaminated Ti_3C_2 paper obtained from f-Ti_3C_2 flakes showed excellent Li storage performance with a superior specific capacity value of 410 mA h g^{-1} after 100 cycles, which is fourfold higher as compared to f-Ti_3C_2 (Fig. 9a) [67]. In the case of f-Ti_3C_2, the capacity reported

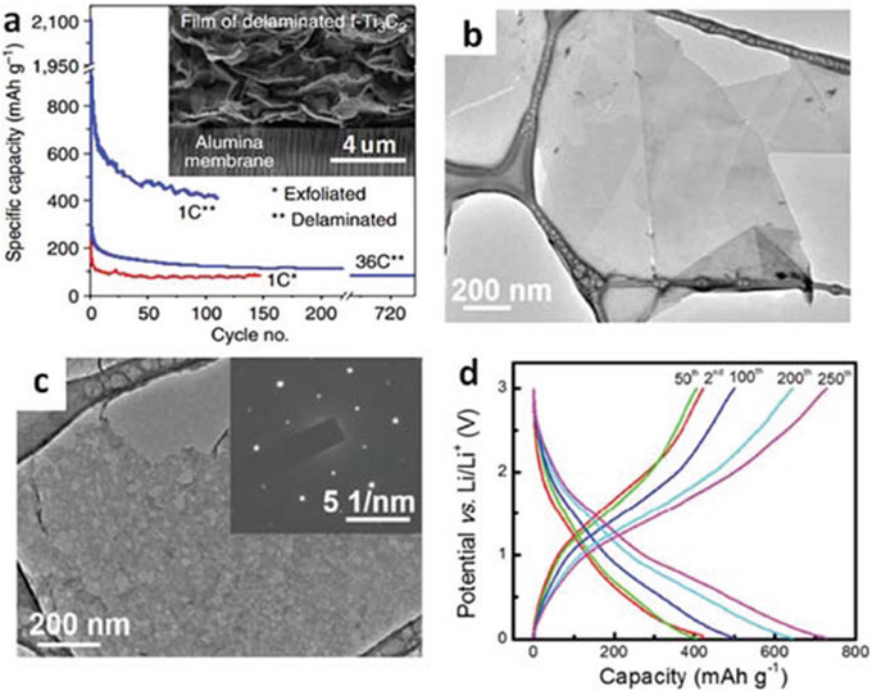

Fig. 9 **a** LIB performance of exfoliated and delaminated f-Ti_3C_2-based anode (the inset shows SEM image of the delaminated f-Ti_3C_2 film) [67] **b** TEM image of $Ti_3C_2T_x$ flakes & **c** TEM image and SAED pattern of p-$Ti_3C_2T_x$ flakes after chemical etching. **d** GCPL curves of a p-$Ti_3C_2T_x$/CNT film during cycling [71]

at 1 C surpassed the predicted theoretical capacity value [56]. To address the key challenges of MXenes such as decreased ion accessibility due to stacking/restacking of $Ti_3C_2T_x$ flakes, poor diffusion of charge carriers along the perpendicular-to layer direction, and the inefficient active site utilization, interlayer spacers such as carbon nanotubes and conducting polymers have been incorporated between the $Ti_3C_2T_x$ layers. The $Ti_3C_2T_x$/CNT films constructed using CNTs spacers manifested an excellent capacity of 1250 mA h g^{-1}. Apparently, the GCPL charge–discharge curves showed no lithiation/de-lithiation plateaus, indicating capacitive charge storage of p-$Ti_3C_2T_x$/CNT electrode (Fig. 9d). In another example, conductive carbon nanofibers (CNFs) bridges were introduced inside and outside the gaps of $Ti_3C_2T_x$ particles [68]. The as-synthesized $Ti_3C_2T_x$/CNF particles manifested an enhanced reversible capacity and excellent rate characteristics compared to pure $Ti_3C_2T_x$ particles. A few-layered $Ti_3C_2T_x$ obtained by the DMSO intercalation between multi-layered $Ti_3C_2T_x$ exhibited a capacity of 123.6 mA h g^{-1} at 1 C superior to the $Ti_3C_2T_x$ without intercalation [69]. Another report produced a freestanding disc of $Ti_3C_2T_x$ by simple room temperature cold pressing of multi-layered $Ti_3C_2T_x$ powders. It is then employed as LIB anode, which displayed an areal capacity of 15 mA h cm^{-2} [70]. Engineering porous architectures of MXene is another explored strategy to enhance ion diffusion and kinetics, and there have been several reports on MXene-based porous nanoarchitecture. In a typical example, mesoporous MXene flakes were synthesized from partially oxidized MXene through a chemical acid etching process. The TEM image comparing the morphology of $Ti_3C_2T_x$ flakes and porous $Ti_3C_2T_x$ flakes with selected area electron diffraction (SAED) pattern revealed a hexagonal crystal symmetry with no change in MXene phase (Fig. 9b,c). The mesoporous MXene electrode showed better performance owing to the enhanced electrolyte ion accessibility [71]. In addition, a MXene-based freestanding macroporous foam was produced using filtration technique and with the help of sulfur templates. An excellent capacity value of 455.5 mAh g^{-1} at 50 mA g^{-1} with high rate capability (101 mAh g^{-1} at 18 A g^{-1}) is assigned to the creation of more active sites and facilitated ionic movement [72]. Importantly, MXene-based LIB electrodes produced via pore engineering explicitly eliminate the need for metal current collectors, conductive additives, and any polymer binder, thus enhancing the energy density of LIBs.

Compared to heavier members of the MXene family (e.g., M_3X_2 and M_4X_3), lighter formula weight compositions (e.g., M_2X) manifest higher gravimetric capacities [73]. For instance, Ti_2C has a theoretical charge storage capacity of 320 mAh g^{-1}, which is two times higher in comparison to the value of Ti_3C_2 [66]. The experimental results suggest a capacity of 160 mAh g^{-1} for Ti_2C versus 110 mAh g^{-1} for Ti_3C_2 and the difference stem from the inactive TiC layer inTi_3C_2 [67]. Moreover, the metal element in MXene plays a crucial role in determining the actual capacity. For example, compared to Ti_2C, the Nb_2C has a higher molecular weight, but the gravimetric capacity is 180 mAh g^{-1}, while V_2C showed a higher capacity of 280 mAh g^{-1} under similar electrochemical characterization conditions (Fig. 10a) [74]. Such discrepancy in the capacities could be attributed to the variations in material processing and electrode preparation routes or due to the difference in the fundamental electronic structure, which demand further in-depth study. Besides, surface

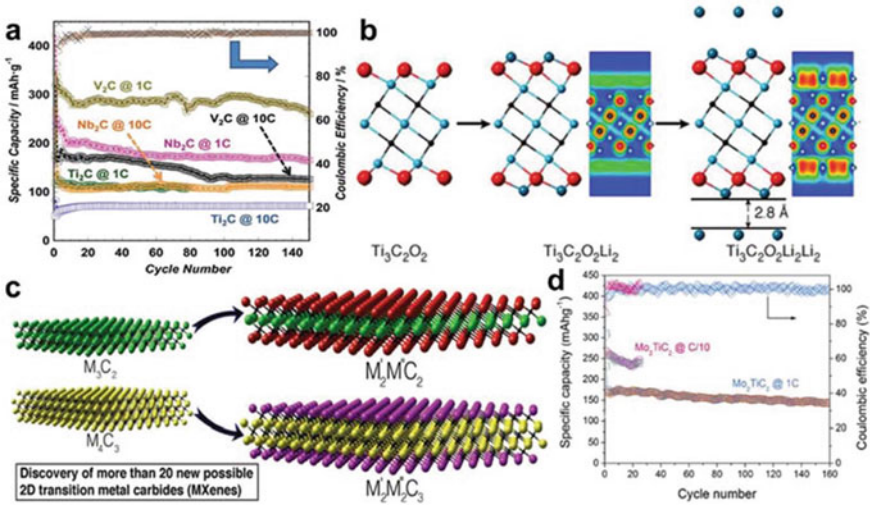

Fig. 10 **a** Specific capacity and cycling stability studies for Nb_2C, V_2C, and Ti_2C (at 1 C and 10 C rates) [74] **b** Valence electron localization function of $Ti_3C_2O_2Li_2$ with or without an extra Li layer [76] **c** Schematic of the preparation of $M'_2\ M''C_2/M'_2\ M''_2C_3$ MXenes. **d** Cycling study of Mo_2TiC_2 obtained at 0.1 C and 1 C rates [77]

functional groups in MXene also influence ion storage and kinetics. According to some theoretical and experimental results, the -F and -OH groups hinder the Li^+ transport and storage in both Ti_3C_2 and V_2C [56, 75]. But the lithiated O-functionalized MXene may be the reason behind the additional Li^+ storage (Fig. 10b) [76], where extra Li layers are adsorbed above already lithiated O-terminated MXene, which could explain the high capacity of d-Ti_3C_2. This suggests that performance enhancement is possible by introducing suitable functional groups and rational MXene composition.

Another important method to adjust the bandgap and surface chemistry of MXenes is by introducing heteroatoms or doping. In a typical example, Mo doped Ti_2CT_x ($Mo_2TiC_2T_x$) delivered a capacity of 269 mAh g^{-1} at 0.1 C (Fig. 10c,d) [77]. In another report, Co^{2+} ions were intercalated into multi-layered V_2C MXene, which expanded the interlayer spacing through stronger V–O-Co bonding and delivered a capacity of 1117.3 mAh g^{-1} at 0.1 A g^{-1} with excellent cyclability [78]. Though there are many reports based on heteroatom doping of MXene, the heteroatoms content is remarkably lower. Hence, novel controlled doping strategies have to be developed to enhance the charge storage performance of MXenes further.

In an intriguing approach ofmPVP-assisted liquid-phase immersion, Sn^{4+}-modified Ti_3C_2 (polyvinylpyrrolidone(PVP)–Sn(IV)@Ti_3C_2), were synthesized. The 2D alk-$Ti_3C_2T_x$ network helped to boost the electronic conductivity with facilitated ion migration and alleviate the volume expansion/contraction issue of Sn during cycling [79]. Moreover, a superior reversible specific capacity of 635 mA h g^{-1} at 100 mA g^{-1} is obtained due to the synergistic interaction between the alk-$Ti_3C_2T_x$

matrix and Sn by forming a pillar between alk-$Ti_3C_2T_x$ layers. Another major route to maximize the performance of MXenes for LIBs is their composites with other potential anode materials. Transition metal oxides (TMOs) are promising in this regard due to their low cost, nontoxicity, and high theoretical capacity. There's a report based on SnO_2 and Ti_3C_2 hybrid (SnO_2–Ti_3C_2) employed as an anode for LIBs exhibiting a discharge capacity of 1030 mA h g^{-1} at 100 mA g^{-1} [80]. Importantly, hydrothermal strategy is the most common route for metal oxide synthesis, which may often lead to oxidation and structural degradation of MXenes. Therefore, this issue should be carefully addressed while preparing MXene-based composites [81]. As an alternative to this, atomic layer deposition (ALD) was adopted to generate a SnO_2/MXene anode for LIBs [82]. As a bottom-up technique of nanomaterial fabrication, ALD yielded conformal coating of SnO_2 films on the MXene surface, exhibiting a high specific capacity where the MXene sheets act as a conductive network able to afford large volume changes during cycling (Fig. 11a,b). The alloying/dealloying of SnO_2 was a significant contribution to the observed capacity, as evident from the distinct CVs of $SnO_2/Ti_3C_2T_x$ electrodes having different SnO_2 loading (Fig. 12a). The performance of SnO_2/MXene is further enhanced through the deposition of a thin HfO_2 passivation layer over SnO_2 using ALD, which then exhibited capacity retention of 843 mA h g^{-1} after 50 cycles (Fig. 12b). However, maintaining a high energy density at high rates is still a challenge in most composites. This is because of the use of $Ti_3C_2T_x$ particles with limited interface utilization, which can be overcome by using delaminated $Ti_3C_2T_x$ for fabricating MXene-based composites. In another report, a

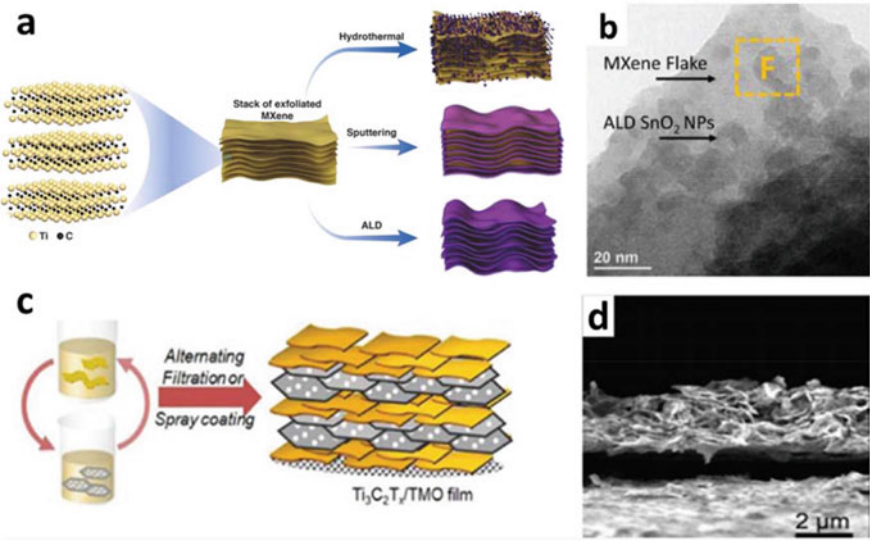

Fig. 11 $Ti_3C_2T_x$-based composite electrodes for LIBs. **a** Schematic of different techniquesutilized for the deposition ofSnO_2 on $Ti_3C_2T_x$. **b** TEM image of SnO_2-coated $Ti_3C_2T_x$. [82] **c** Schematic of the method used to generate $Ti_3C_2T_x$/TMO hybrid film. **d** SEM image of $Ti_3C_2T_x/NiCo_2O_4$ hybrid (cross-sectional view of the film) [84].

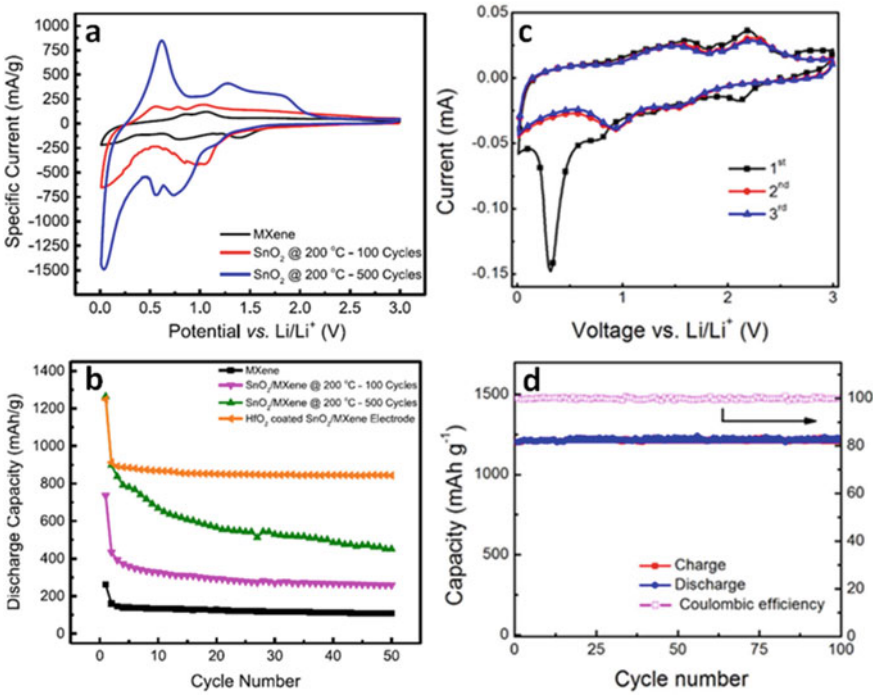

Fig. 12 $Ti_3C_2T_x$-based composite electrodes for LIBs. **a** CVs of $Ti_3C_2T_x$ electrodes at 0.2 mV/s with different cycles and temperatures. **b** Cycling study of $Ti_3C_2T_x$ electrode, $SnO_2/Ti_3C_2T_x$ electrodes, and HfO_2-coated $SnO_2/Ti_3C_2T_x$ electrode over 50 cycles at 500 mA/g [82]. **c** CVs of spray-coated $Ti_3C_2T_x/NiCo_2O_4$ films at 0.1 mV s^{-1}. d) Cycling performance of the $Ti_3C_2T_x/NiCo_2O_4$ hybrid film at 1 C [84]

two-stage oxidation of $Ti_3C_2T_x$ was carried out to generate a new core–shell layered structure, where TiO_2 acts as a shell formed by the oxidation of the $Ti_3C_2T_x$ with-residual $Ti_3C_2T_x$ at the core [83]. Compared to pristine $Ti_3C_2T_x$, the partial oxidation strategy normally leads to an better energy-storage performance owing to the high capacities of TiO_2 with conductive carbide core layer structure.

Moreover, MXene-TMO hybrid films exhibiting high conductivity, good flexibility, and superior electrochemical performance were prepared using alternating filtration, spray coating, and in situ growth strategy. Some of the examples include hybrid films of $Ti_3C_2T_x$ with Co_3O_4 or $NiCo_2O_4$ [84]. For instance, a layer-by-layer spray coating technique produced a Ti3C2Tx/NiCo2O4 hybrid film electrode (Fig. 11c,d). The CVs of the $Ti_3C_2T_x/NiCo_2O_4$ displayed multiple redox peaks corresponding to the redox transition of $NiCo_2O_4$ with a high ability for Li storage (Fig. 12c). The $Ti_3C_2T_x/NiCo_2O_4$ retained a high capacity of ca. 1200 mA h g^{-1} for more than 100 cycles at a 1 C rate with excellent coulombic efficiency (Fig. 12d). All of the reported MXene-based flexible freestanding hybrid films manifested an

excellent performance for LIBs as $Ti_3C_2T_x$ primarily acts as conductive matrix along with the high charge storage capacity contribution of TMOs.

To further expand the potential of MXene and generate MXene-based micro/nanomaterials, post-synthetic treatment of MXene is necessary. The common approaches followed, including hydrothermal or solvothermal synthesis, refluxing, and calcination may often lead to the surface oxidation of the MXene and can impact the electrical conductivity and passivate MXene's reactive surface. Therefore, to overcome the thermodynamic metastability issue and keep MXene against structural degradation, a simple carbon nano plating strategy was successfully executed [85]. As a result, 2D hierarchical nanocomposites were successfully prepared by assembling carbon-coated few-layered MoS_2 nanoplates on carbon-stabilized Ti_3C_2 MXene. The as-produced MoS_2/Ti_3C_2-MXene@C nanohybrids showed an excellent Li storage capacity with 95% retention after 3000 cycles. Other than $Ti_3C_2T_x$, various other compositions of MXene (Nb_2C, [31, 86] V_2C, [87] Ti_3CNT_x, [88] Nb_4C_3, [89] Hf_3C_2 Tz, [90] and Mn_2C, [91]) have been explored for LIBs. These results may open room for developing various other types of MXene and their applications as electrode materials for LIBs with superior capacity and cycling stability performance.

In addition, the excellent electrical conductivity (8000 S cm^{-1}), high flexibility, and robustness of MXene nanosheets present opportunities as current collectors for LIBs as an alternative to traditional metal-based current collectors. For example, a full LIB battery was assembled using multi-layered $Ti_3C_2T_x$ loaded on a 5 μm $Ti_3C_2T_x$ thin film current collector as anode with $LiFePO_4$ cathode, which has characteristics of low device weight, thickness, and electrochemical performance comparable to LIBs assembled using conventional Cu and Al current collectors [92]. This strategy will undoubtedly be beneficial for developing flexible and high-energy–density LIBs with a vast choice of active materials.

Other Metal-ion Batteries

Due to the continuous consumption of lithium resources for LIBs and the depletion of lithium, there is constant pressure to develop batteries using naturally abundant metal resources. Alternative alkali metals such as Na, K, Mg, and Al are particularly appealing for use in rechargeable batteries and will be the developing low-cost solutions for renewable energy-storage applications due to their environmental friendliness and natural availability [93]. The alkali metal ions, including sodium, potassium, magnesium, etc., have already demonstrated the ability to intercalate between the 2D MXene layers and will be the potential host for other types of emerging novel metal-ion batteries [94, 95]. The first principle simulation studies were performed to unveil the Na, K, Mg, Ca, and Al storage mechanisms in MXenes [96]. The studies have shown that both O-terminated and pristine MXenes are promising to be used as electrode materials, with the latter showing superior charge storage behavior. Moreover, DFT calculations were carried out to understand the intercalation behavior of various ions with MXenes. The study showed a high capacity for M_2C-type MXenes, potentially used in rechargeable batteries [73]. In addition, the first-principles density

functional calculations corroborated a linear dependency between the storage capacities and effective ion radius and maximum adatom content with calculated capacity values of 447.8, 351.8, 191.8, and 319.8 mA h g^{-1} for Li, Na, K, and Ca, respectively with Ti_3C_2 host material [97].

(b) **Sodium-ion Batteries**

The rich source, cost-effectiveness, and low redox potential of sodium make rechargeable sodium-ion batteries (SIBs) an attractive alternative to LIBs [98, 99]. Because Li and Na have common alkali metal properties, the approach used to generate LIBs might also be used to develop SIBs. However, the larger ion radius of Na^+ (1.06 Å) vs Li^+ (0.76 Å) imposes a mass transport challenge during the electrochemical charge storage, as it is in the case of graphite, which is a commercial LIB anode material. Because of the insufficient sodium-ion storage performance, graphite is inappropriate to be used in SIB [54]. Therefore, researchers meticulously put effort into developing high performance anode materials for SIBs.

It is evident that layered 2D nanomaterials with open morphologies including graphene and TMDs have the potential to act as Na host materials rendering high capacities [100]. The ab initio DFT was carried out to understand the effect of $Ti_3C_2T_x$ interlayer space on Na-ion storage and ion diffusion [101]. The studies demonstrated that the interlayer-expanded $Ti_3C_2T_x$ significantly reduces the diffusion barrier for Na^+ and makes Na ions move swiftly over MXenes, hence boosting the sodium storage capacity. Although the facilitated ionic movement is favored with the increased interlayer distance, it might lower the redox potential of $Ti_3C_2T_x$ to a small extent. MXene materials, on the other hand, are promising for SIBs, especially for high-rate SIB applications, because of their high electronic conductivity and rapid ionic diffusion.

The discharge capacity first reported for $Ti_3C_2T_x$ nanosheets is 370 mA h g^{-1}, corresponding to 2.79 Na per formula unit. This indicates the potential of MXene for accommodating ions of a larger radius [96]. The Na-ion intercalation mechanism in $Ti_3C_2T_x$ nanosheets was probed using solid-state Na magic angle spinning nuclear magnetic resonance spectroscopy and DFT calculation data [102]. The study using a non-aqueous Na^+ electrolyte showed a reversible Na^+ intercalation/de-intercalation into the interlayer space. During the initial sodiation process, desolvation of Na^+ with intercalation happens, along with the solvent molecule insertion leading to the expansion of interlayer space. Also, sodiation/desodiation processes doesn't cause any major change in the $Ti_3C_2T_x$ electrode strucure, resulting in a high cycling stability with faster kinetics (Figs. 13a,b). The experimental study showed an initial discharge capacity of 270 mA h g^{-1}, correlating to ≈2.0 Na^+ intercalation/per $Ti_3C_2T_x$ unit (Fig. 13c). Besides, the first observed irreversible capacity is ascribed to the stable solid electrolyte interphase due to the electrolyte decomposition. After about 100 cycles, $Ti_3C_2T_x$ showed good cycling stability along with a specific capacity value of ca. 100 mA h g^{-1}.

The restacking and aggregation issues of MXenes layers due to week van der Waals interactions and hydrogen bonds are one of the major challenges preventing

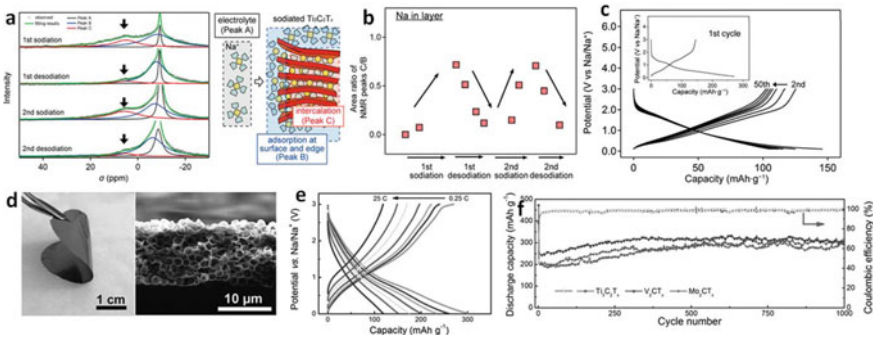

Fig. 13 **a** Investigation of the Na insertion mechanism into $Ti_3C_2T_x$ MXene using ^{23}Na MAS NMR spectra. The NMR signals during the first two cycles can be deconvoluted into three peaks (black, blue, and red lines), originating from different Na^+ species. **b** Estimated amount of intercalated Na in the layer based on the NMR peak ratio, C/B. **c** The sodiation/desodiation potential curves for $Ti_3C_2T_x$ [102]. **d** Digital i and a cross-sectional SEM image of the flexible 3 macroporous $Ti_3C_2T_x$ film. **e** GCPL charge/discharge curves of 3D $Ti_3C_2T_x$ at different C rates. **f** Cycling stability of the 3D macroporous MXene electrodes [105]

their application in liquid media [3, 103, 104]. Recent studies have focused on overcoming the stacking tendency of the exfoliated MXenes, and in one of the reports, 2D $Ti_3C_2T_x$ were engineered to 3D hollow architectures (Figs. 13d) [105]. The 3D macroporous MXene networks showed superior stability, high conductivity, and excellent performance. As Na-ion battery anodes, the flexible $Ti_3C_2T_x$ macroporous film showed remarkable storage capacity, rate performance, and cycling stability compared to multilayer films (Fig. 13e,f). Similarly, 3D films of V_2CT_x and Mo_2CT_x were constructed, which showed capacities of 295, 310, and 290 mA h g^{-1} for 3D $Ti_3C_2T_x$, V_2CT_x, and Mo_2CT_x respectively at 2.5 C for up to 1000 cycles (Fig. 13f). Among them, 3D films of V_2CT_x displayed the best cycling performance owing to its large interlayer spacing. The development of macroporous 3D MXene films open new avenues for constructing other MXene-based materials for applications including energy storage, environmental, and biomedical fields, catalysis etc.

Constructing composites with electrochemically active materials is a major strategy to boost charge storage performance. The interlayer spacer materials can mostly enhance the Na storage capacity by preventing the restacking between MXene sheets. A freestanding $Ti_3C_2T_x$/CNT porous film was constructed using self-assembly between negatively charged $Ti_3C_2T_x$ and positively charged CNTs spacers [36]. The $Ti_3C_2T_x$/CNT electrode exhibited a high volumetric Na storage capacity of 421 mA h cm^{-3} at 20 mA g^{-1}. In another report, $MoS_2/Ti_3C_2T_x$ composite was assembled using a simple hydrothermal route with in situ intercalations of MoS_2 nanosheets between $Ti_3C_2T_x$ layers (Fig. 14a) [106]. Compared to pristine $Ti_3C_2T_x$, The $MoS_2/Ti_3C_2T_x$ electrode rendered a reversible capacity of 250.9 mA h g^{-1} at 100 mA g^{-1} after 100 cycles and 88% retention of capacity, revealing the effectiveness of synergistic interaction. (Fig. 14b) It's noteworthy that multilayer $Ti_3C_2T_x$ is used to fabricate $MoS_2/Ti_3C_2T_x$ composite, leading to low utilization of MXene's

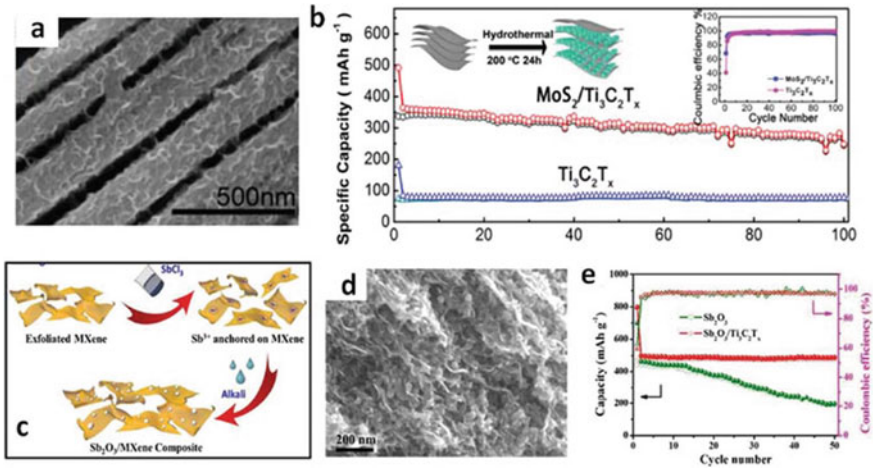

Fig. 14 MXene-based nano composites for SIBs. **a** SEM image of $MoS_2/Ti_3C_2T_x$. **b** Cycling and coulombic efficiency study of pure $Ti_3C_2T_x$ and $MoS_2/Ti_3C_2T_x$ (inset shows a depiction of the hydrothermal synthesis of the $MoS_2/Ti_3C_2T_x$) [106]. **c** A schematic showing the route towards$Sb_2O_3/Ti_3C_2T_x$. **d** SEM image of $Sb_2O_3/Ti_3C_2T_x$ composite. **e** Cycling study of the $Sb_2O_3/Ti_3C_2T_x$ and Sb_2O_3 electrodes [107].

active sites. To mitigate this issue, a solution-phase method that doesn't require any thermal processing was adopted to construct $Sb_2O_3/Ti_3C_2T_x$ composites using pre-exfoliated $Ti_3C_2T_x$ [107]. The hydrolysis treatment led to the homogeneous deposition of Sb_2O_3 on the $Ti_3C_2T_x$ sheets, and the missing heating step protected $Ti_3C_2T_x$ from getting oxidized (Fig. 14c). The SEM image of $Sb_2O_3/Ti_3C_2T_x$ displayed a hierarchical architecture with uniform coverage of Sb_2O_3 nanoparticles on $Ti_3C_2T_x$ networks (Fig. 14d). After about 100 cycles, the $Sb_2O_3/Ti_3C_2T_x$ composite electrode manifested an excellent capacity of 472 mA h g^{-1} at 100 mA g^{-1}, much higher than bare Sb_2O_3 nanoparticles (Fig. 14e).

Besides, other types of MXenes, including V_2CT_x, Y_2N, and Mo_2C, have also found interest as anodes for SIBs along with $Ti_3C_2T_x$-based electrodes [108–110].

(c) Potassium-ion Batteries

A few of the MXenes compositions recently explored for potassium-ion batteries (PIBs) are Ti_3CNT_z, $Ti_3C_2T_z$, and Nb_2CT_z. They are employed primarily as anode materials for PIBs, along with a detailed investigation on the intercalation mechanism [94]. It is well-known that rational architecting of MXene-based nanostructures is imperative to enhance capacity performance. For instance, a 3D porous framework of $Ti_3C_2T_x$ nanoribbons (a-Ti_3C_2 MNRs) was assembled by shaking pristine $Ti_3C_2T_x$ in an alkaline solution of KOH (Fig. 15a) [57]. Owing to the interconnected porous frameworks, the narrow width of nanoribbons along with the larger interlayer spacing attributed to the excellent ion reaction kinetics and enhanced structural stability of a-Ti_3C_2. As anode materials, a-Ti_3C_2 presented an excellent K-ion storage performance with a superior capacity of 42 mA h g^{-1} at 200 mA g^{-1} after 500 cycles (Fig. 15c).

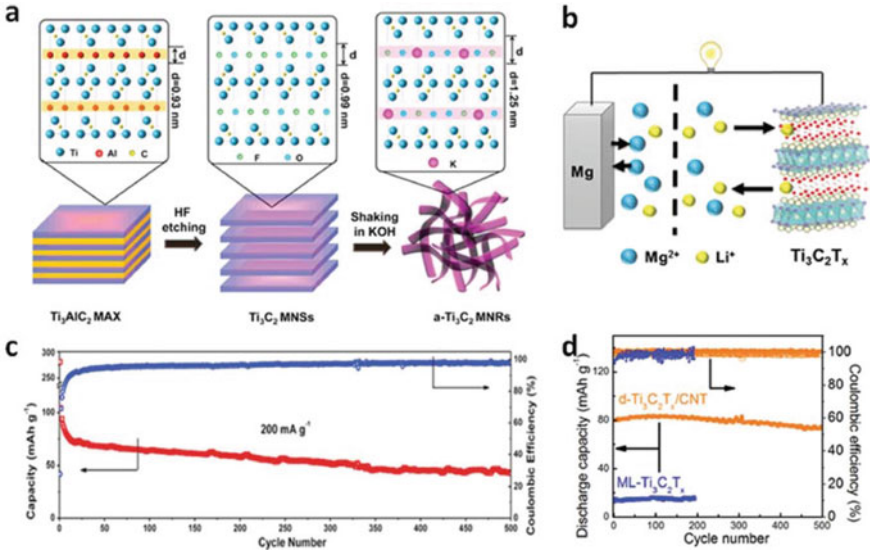

Fig. 15 PIBs and hybrid batteries based on $Ti_3C_2T_x$ MXene. **a** Scheme of the synthesis of a-Ti_3C_2 MNRs. **b** Depiction of a hybrid Mg^{2+}/Li^+ battery employing $Ti_3C_2T_x$ as the cathode material. **c** Cycling and coulombic efficiency performance of a-Ti_3C_2 MNRs. **d** Cycling stability and coulombic efficiency of ML-$Ti_3C_2T_x$ and pre-cycled d-$Ti_3C_2T_x$/CNT cathodes at 100 mA g^{-1} [57, 113]

In addition, by performing a concurrent oxidation and alkalization treatment under hydrothermal conditions, $Ti_3C_2T_x$ can be converted to ultrathin potassium titanate (M-KTO, $K_2Ti_4O_9$) nanoribbons [111]. The M-KTO electrode showed excellent capacity, rate capability, and outstanding cyclability performance for PIBs. This clearly shows the potential of rationally designed MXene-based anodes for PIBs to achieve superior electrochemical performance.

Furthermore, it's important to note that multivalent ions (e.g., Mg, Ca, and Al) compared to monovalent ions may grant a higher energy density output due to multi-electron redox chemistry [112]. However, finding the right host materials and suitable electrolyte combinations is a significant challenge for realizing nonconventional metal-ion batteries [97]. Recently, $Ti_3C_2T_x$ has been employed as a cathode in a hybrid Mg^{2+}/Li^+ battery, highlighting the practicability of using MXenes for unconventional metal-ion batteries (Fig. 15b,d) [113].

(d) Lithium-Sulfur Batteries

LSBs are emerging solutions to future energy-storage devices due to the natural abundance of sulfur and the potential redox reaction between elemental sulfur and Li, leading to a high theoretical capacity and energy density performance [114, 115]. LSBs suffer from capacity drop and cyclability issues despite having these merits. This can be ascribed to the low electrical conductivity of sulfur and its discharge products (Li_2S_2/Li_2S). Moreover, the large volume change during cycling and the shuttling effect of soluble long-chain lithium-sulfur compounds (Li_2S_{4-8}) between the

cathode and anode hinder the practical application of LSBs. Therefore, to overcome this shortcoming, various strategies have been recently demonstrated [116, 117]. The most common method for lithium polysulfides (LiPSs) confinement in the cathode is carefully selecting materials with high conductivity and surface area as hosts [115, 118]. To date, materials such as porous carbons, hollow carbon spheres, graphene, and TiO_2 hollow spheres were reported as cathode hosts [119–121].

MXene-derived materials can operate as S hosts because of their strong electrical conductivity and distinctive 2D layered structure. A reported S/Ti_2CT_x composite with 70% S displayed a specific capacity of ca. 1200 mA h g^{-1} at 0.2 C along with stable long-term cycling performance [122]. Stronger interactions of the polysulfide compounds with Ti and hydroxy surface groups led to the chemisorption of LiPSs, which was elucidated using X-ray photoelectron spectroscopy (XPS) studies. Similarly, the S/layered $Ti_3C_2T_x$ composite was employed as an LSB cathode (Fig. 16a) [123]. The SEM images revealed that the diffusion process helped fill sulfur between $Ti_3C_2T_x$ interlayer space (Fig. 16b,c). The S/L-$Ti_3C_2T_x$ electrode showed an excellent rate performance with good capacity retention (970 mA h g^{-1} after 100 cycles) (Fig. 16d,e). Recent findings with the help of XPS and DFT calculations provide

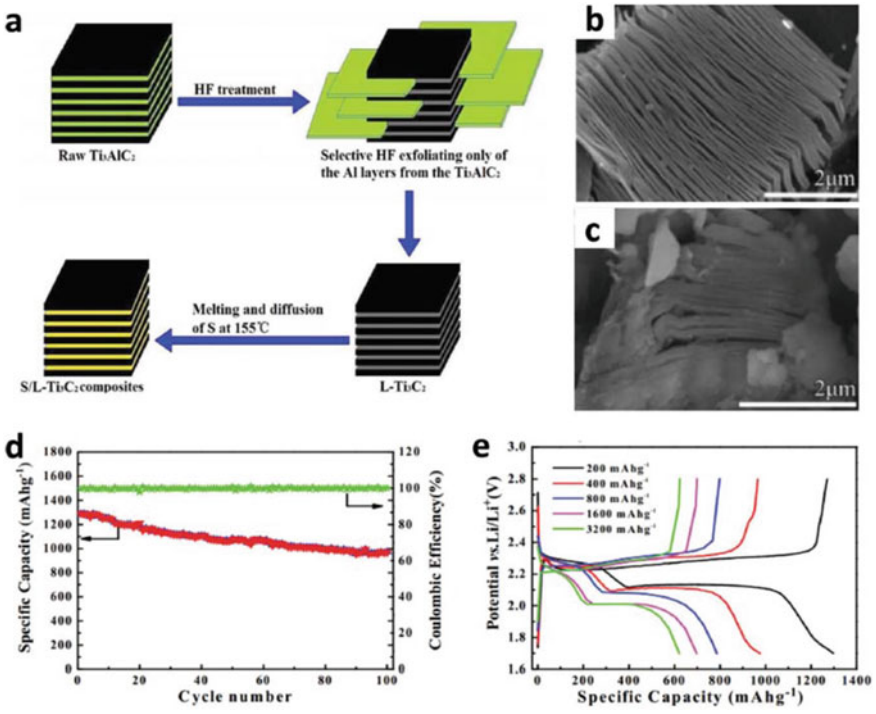

Fig. 16 **a** $Ti_3C_2T_x$ MXene as a cathode in LSB. **b** Schematic of the preparation of S/$Ti_3C_2T_x$. **b**, **c** SEM images of the bare $Ti_3C_2T_x$ and S/$Ti_3C_2T_x$ composite. **d** Cycling stability study of the S/$Ti_3C_2T_x$ electrode. **e** GCPL curves of the S/$Ti_3C_2T_x$ at different current densities [123]

insights into improved cycling performance, primarily because the Ti-S bond interaction followed by thiosulfate/polythionate conversion bestow a distinct pathway to entrap polysulfides [58]. It's imperative to further research $Ti_3C_2T_x$-based materials to understand the interactions of LiPSs on bare and surface-functionalized $Ti_3C_2T_x$ with -F, -O, and -OH groups before employing in LSBs as either S host or as additive materials.s.

Another key strategy to block the free movement of LiPSs between the electrodes is through the polymeric separator modification [124]. 2D materials such as graphene and graphene oxide (GO) are widely employed as functional interlayers as they can be efficiently packed on the separator with excellent interfacial affinity with the S cathode [125, 126]. In an interesting report, a commercially available celgard separator is modified using $Ti_3C_2T_x$ nanosheets, which showcased enhanced performance for LSBs due to the high electrical conductivity and trapping of polysulfides effectively (Fig. 17a-c) [127]. In another report, $Ti_3C_2T_x$ nanosheet-covered glass fiber was assembled to fabricate LSB (Fig. 17d) [128]. Notably, using $Ti_3C_2T_x$ nanosheets, it is possible to significantly tackle the dissolution of LiPSs and improve the utilization of S. Later, with the support of ab initio calculations, it was shown that Ti_3C_2 allow the adsorption of S_8 and LiPSs (Li_2S, Li_2S_4, Li_2S_6, and Li_2S_8) via stronger ionic interaction between Ti and S cations (Fig. 17e). The removal of OH- and F- functional groups of $Ti_3C_2T_x$ can further boost the Li–S battery performance through the weakening of the S–Ti interaction (Fig. 17f).

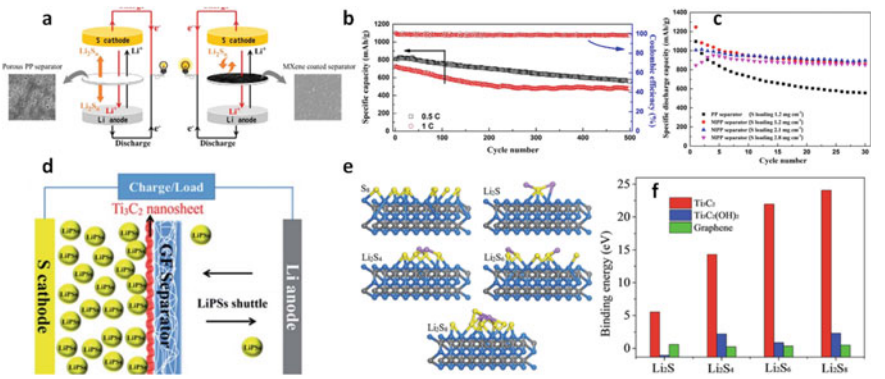

Fig. 17 $Ti_3C_2T_x$ MXene-based separator for LSBs. **a** Schematic illustration of the Li−S cells employing PP and MPP separators. **b** Long-term cycling study of Li−S batteries with MPP separators at rates of 0.5 C and 1 C. **c** Cycling data of the cells utilizing PP separators and MPP separators with different sulfur loadings [127]. **d** Schematic depiction of the electrodes with the separator($Ti_3C_2T_x$-modified GF membrane). **e** Ab initio calculated structures of S_8, Li_2S, Li_2S_4, Li_2S_6, and Li_2S_8 adsorbed on Ti_3C_2. **f** Comparison of ab initio calculated binding energies of Li_2S, Li_2S_4, Li_2S_6, and Li_2S_8 with Ti_3C_2, $Ti_3C_2(OH)_2$, and graphene [128]

Conclusion and Future Perspectives

2D MXenes have aroused greater interest due to their excellent metallic conductivity, hydrophilicity, structural versatility as well as for their potential applications. This chapter focuses on the research developments of MXenes and their composites their structural and functional synergies for energy-storage applications such as SCs and rechargeable batteries. The intercalation of cations between MXene layers leads to electric double-layer capacitance, while pseudocapacitance arises from the change in the transition metal oxidation state. The intercalated materials or incorporation of electrochemically active materials (e.g., CNT, conducting polymers, TMDs) into MXene can act as an interlayer spacer, effectively inhibiting the restacking issue can improve electrochemical behavior by contributing to the energy storage performance. MXenes are potential host materials for hybrid SCs and rechargeable metal-ion batteries, which has also been confirmed theoretically. In addition to high metallic conductivity, MXenes show low ion intercalation/diffusion barrier, tunable interlayer spacing, and the presence of numerous active sites, which are characteristics highly sought for battery electrodes. Importantly, MXenes can afford large volume expansions during electrochemical cycling while maintaining conductivity and structural integrity. In addition, MXene can act as a potential electrode material for the next generation of batteries such as Al-ion and hybrid batteries as it is possible to intercalate multivalent ions between the MXene layers. MXenes can be used as prospective host materials or functional separators for high-performance LSBs due to their 2D morphology and excellent adsorption of polysulfides. A summary of MXene-based materials in terms of morphology, synthesis route, and electrochemical performance is presented in Table 1.

Although MXenes have shown great potential for energy storage, many challenges prevent their commercial applications. First and foremost, developing cost-efficient, safe, and high yield synthesis routes while preserving the inherent properties of MXenes is paramount to realizing their practical application. Another issue with MXene is its chemical stability and ease of oxidizing under harsh environments, affecting the structural integrity and loss of metallic conductivity. Therefore, it is imperative to develop effective strategies to safeguard MXenes from oxidation while processing. Besides, it's necessary to have a comprehensive knowledge of MXenes' structural architectures such as surface chemistry, interlayer spacing, and layer by layer stacking and their influence on the charge storage properties. Efforts towards tuning the interlayer spacing of MXenes should be further researched to promote facilitated ion diffusion/intercalation kinetics. This may also be beneficial for incorporating electrochemically active guest species such as S and transition metal oxides, contributing to higher charge storage.

Another important point is the rational understanding of the ion dynamics and charge storage mechanism between MXene sheets and the development of effective strategies to realize MXene-based hybrid structures. It's noteworthy that delaminated MXenes offer a higher surface area than undelaminated stacked MXene for better active site utilization by the electrolyte. The introduction of defects via heteroatom doping and their influence on electrochemical performance is an enticing approach.

Table 1 Comparison of MXene-based materials for supercapacitors and rechargeable battery applications

Material	Synthesis method	Morphology	Application	Performance, cycle number	References
$Ti_3C_2T_x$	Intercalation followed by filtration	Paper, layered	Supercapacitor	442 F cm^{-3} @ 2 mV s^{-1}, 10,000 cycles	[5]
$Ti_3C_2T_x$	MILD etching	paper clay	Supercapacitor	900 F cm^{-3} @ 2 mV s^{-1}, 10,000 cycles	[129]
$Ti_3C_2T_x$	Intercalation and surface modification	Powder, layered	Supercapacitor	517 F g^{-1} @ 1 A g^{-1}, 10,000 cycles	[130]
$Ti_3C_2T_x$	Filtration followed by immersion in electrolyte	Hydrogel film	Supercapacitor	1500 F cm^{-3} @ 2 mV s^{-1}, 10,000 cycles	[131]
Ti_2CT_x	Postetch Annealing under N_2/H_2	Nanosheets	Supercapacitor (Symmetric)	51 F g^{-1} @ 1 A g^{-1}, 6000 cycles	[132]
$Ti_3C_2T_x$/CNT	Alternative filtration	Paper, Sandwiched	Supercapacitor	390 F cm^{-3} @ 2 mV s^{-1}, 10,000 cycles	[133]
$Ti_3C_2T_x$/graphene	Electrostatic self-assembly	Flexible film	Supercapacitor	1040 F cm^{-3} @ 2 mV s^{-1}, 20,000 cycles	[134]
$Ti_3C_2T_x$/LDH	Liquid deposition	3D Porous	Supercapacitor	1061 F g^{-1} @ 1 A g^{-1}, 4000 cycles	[135]
$Ti_3C_2T_x$/PC	Polymerisation and carbonisation	Layered Porous	Supercapacitor	245 F g^{-1} @ 0.6 A g^{-1}, 5000 cycles	[6]
$(Mo_{2/3}Y_{1/3})_2$c/CNT	Selective etching	Layered sheet	Supercapacitor	1500 F cm^{-3} @ 2 mV s^{-1}, 10,000 cycles	[136]
$Ti_3C_2T_x$/PANI	In-situ Polymerisation	Layered, Sandwiched	Supercapacitor	461 F g^{-1} @ 0.2 A g^{-1}, 5000 cycles	[9]
1 T-MoS_2/Ti_3C_2	Magneto-hydrothermal synthesis	Heterostructures with 3D interconnected network	Supercapacitor (Symmetric)	347 mF cm^{-2} @ 2 mA cm^{-2}, 20,000 cycles	[137]

(continued)

Table 1 (continued)

Material	Synthesis method	Morphology	Application	Performance, cycle number	References
$Ti_3C_2T_x$/PVA	Filtration	Flexible, Free-Standing	Supercapacitor	530 F cm^{-3} @ 2 mV s^{-1}, 10,000 cycles	[138]
$Ti_3C_2T_x$	3D printing	Layered flakes	Micro supercapacitor	1035 mF cm^{-2} @ 2 mV s^{-1}	[139]
$Ti_3C_2T_x$	Femtosecond laser etching	Layered film	Micro supercapacitor	308 mF cm^{-3} @ 5 mV s^{-1}, 10,000 cycles	[140]
$Ti_3C_2T_x$/CNT	Filtration	Free standing film	LIBs	12,500 mA h g^{-1} @ 0.1 C, 100 cycles	[71]
$Ti_3C_2T_x$	HF etching	Powder, layered	LIBs	200 mA h g^{-1} @ 50 mA g^{-1}, 200 cycles	[141]
$SnO_2/Ti_3C_2T_x$	Hydrothermal treatment	Powder, layered	LIBs	1030.1 mA h g^{-1} @ 100 mA g^{-1}, 2300 cycles	[80]
Nb_2CT_x/CNT	Filtration	Flexible paper	LIBs	420 mA h g^{-1} @ 0.5C	[31]
RGO/Ti_2CT_r	Vacuum filtration	Wrinkled sheets	LIBs	700 mA h g^{-1} @ 0.1 A g^{-1}, 100 cycles	[143]
$MoS_2/Ti_3C_2T_x$	In-situ intercalation	Nanosheet-on-layer	SIBs	250.9 mA h g^{-1} @ 100 mA g^{-1}, 100 cycles	[106]
$Sb_2O_3/Ti_3C_2T_x$	Solution-phase synthesis	Crumpled layers	SIBs	472 mA h g^{-1} @ 100 mA g^{-1}, 100 cycles	[107]
$Sb_2O_3/Ti_3C_2T_x$	Post-etch melt diffusion	Layered	LSBs	1291 mA h g^{-1} @ 200 mA g^{-1}, 100 cycles	[123]
S/CNT-$Ti_3C_2T_x$	Melt-diffusion	Nanosheet	LSBs	1263 mA h g^{-1} @ C/20, 1200 cycles	[58]

However, further research should be focused along this direction to enhance the charge storage performance of MXene for SCs and batteries. Besides, to achieve long-term cycling stability, constituting strong interfacial interactions between the components in MXene hybrid consisting of various bonding such as covalent bonds, hydrogen bonds, and electrostatic interactions as well as controlling the morphology has of great importance. Lastly, the surface functionalities on MXene play a vital role in determining the battery performance as it may affect ion transport behavior. Since there are no reports on MXenes without surface functional groups, it will be interesting to develop synthesis methods to realize and evaluate the performances of non-functionalized vs functionalized MXene as electrode materials. The constant research interest in MXenes and future advancements are expected to mitigate the challenges to cater to the application of MXene-based materials for efficient electrochemical energy storage systems.

References

1. Simon, P., Gogotsi, Y.: Nat. Mater **19**, 1151 (2020)
2. Simon, P., Gogotsi, Y.: Nat. Mater **7**, 845 (2008)
3. Orangi, J., Beidaghi, M.: Adv. Funct. Mater. n/a, 2005305
4. Xia, Y., Mathis, T.S., Zhao, M.Q., Anasori, B., Dang, A., Zhou, Z., Cho, H., Gogotsi, Y., Yang, S.: Nature **557**, 409 (2018)
5. Lukatskaya, M.R., Mashtalir, O., Ren, C.E., Dall'Agnese, Y., Rozier, P., Taberna, P.L., Naguib, M., Simon, P., Barsoum, M.W., Gogotsi, Y.: Science **341**, 1502 (2013)
6. Seenath, J.S., Biswal, B.P.: Adv. Energy Sustain. Res. **2**, 2000052 (2021)
7. Guo, M., Liu, C.B., Zhang, Z.Z., Zhou, J., Tang, Y.H., Luo, S.L.: Adv. Func. Mater. **28**, 1803196 (2018)
8. Zhang, C.J., Anasori, B., Seral-Ascaso, A., Park, S.H., McEvoy, N., Shmeliov, A., Duesberg, G.S., Coleman, J.N., Gogotsi, Y., Nicolosi, V.: Adv Mater **29**, 1702678 (2017); Hu, M.M., Li, Z.J., Li, G.X., Hu, T., Zhang, C., Wang, X.H.: Adv. Mater. Technol. **2**, 1700143 (2017)
9. Seenath, J.S., Biswal, B.P.: Adv. Mater. Interf. n/a, 2101263
10. Zhu, M.S., Huang, Y., Deng, Q.H., Zhou, J., Pei, Z.X., Xue, Q., Huang, Y., Wang, Z.F., Li, H.F., Huang, Q., Zhi, C.Y.: Adv. Energy Mater. **6**, 1600969 (2016)
11. Vaghasiya, J.V., Mayorga-Martinez, C.C., Sofer, Z., Pumera, M.: ACS Appl. Mater. Interfaces. (2020). https://doi.org/10.1021/acsami.0c12879
12. Gund, G.S., Park, J.H., Harpalsinh, R., Kota, M., Shin, J.H., Kim, T.-I., Gogotsi, Y., Park, H.S.: Joule **3**, 164 (2019)
13. Yu, C., Gong, Y., Chen, R., Zhang, M., Zhou, J., An, J., Lv, F., Guo, S., Sun, G.: Small e1801203 (2018)
14. Couly, C., Alhabeb, M., Van Aken, K.L., Kurra, N., Gomes, L., Navarro-Suárez, A.M., Anasori, B., Alshareef, H.N., Gogotsi, Y.: Adv. Electron. Mater. **4**, 1700339 (2018)
15. Navarro-Suárez, A.M., Van Aken, K.L., Mathis, T., Makaryan, T., Yan, J., Carretero-González, J., Rojo, T., Gogotsi, Y.: Electrochim. Acta **259**, 752 (2018)
16. Yang, X., Wang, Q., Zhu, K., Ye, K. Wang, G., Cao, D., Yan, J.: Adv. Funct. Mater. n/a, 2101087
17. Jiang, Q., Kurra, N., Alhabeb, M., Gogotsi, Y., Alshareef, H.N.: Adv. Energy Mater. **8**, 1703043 (2018)
18. Boota, M., Gogotsi, Y.: Adv. Energy Mater. **9**, 1802917 (2019)
19. Boota, M., Chen, C., Van Aken, K.L., Jiang, J., Gogotsi, Y.: Nano Energy **65**, 104022 (2019)

20. Hu, M., Cui, C., Shi, C., Wu, Z.-S., Yang, J., Cheng, R., Guang, T., Wang, H., Lu, H., Wang, X.: ACS Nano **13**, 6899 (2019)
21. Xu, S., Dall'Agnese, Y., Wei, G., Zhang, C., Gogotsi, Y., Han, W.: Nano Energy **50**, 479 (2018)
22. Zhao, R., Wang, M., Zhao, D., Li, H., Wang, C., Yin, L.: ACS Energy Lett. **3**, 132 (2017)
23. Ding, J., Hu, W., Paek, E., Mitlin, D.: Chem. Rev. **118**, 6457 (2018)
24. Dong, S., Lv, N., Wu, Y. Zhu, G., Dong, X.: Adv. Funct. Mater. n/a, 2100455
25. Liu, H., Liu, X., Wang, S., Liu, H.-K., Li, L.: Energy Storage Mater. (2020). https://doi.org/10.1016/j.ensm.2020.03.003
26. Wang, H., Zhu, C., Chao, D., Yan, Q., Fan, H.J.: Adv. Mater **29**, 1702093 (2017)
27. Lim, E., Jo, C., Kim, M.S., Kim, M.-H., Chun, J., Kim, H., Park, J., Roh, K.C., Kang, K., Yoon, S., Lee, J.: Adv. Func. Mater. **26**, 3711 (2016)
28. Zhu, K., Zhang, H., Ye, K., Zhao, W., Yan, J., Cheng, K., Wang, G., Yang, B., Cao, D.: ChemElectroChem **4**, 3018 (2017)
29. Luo, J., Zhang, W., Yuan, H., Jin, C., Zhang, L., Huang, H., Liang, C., Xia, Y., Zhang, J., Gan, Y., Tao, X.: ACS Nano **11**, 2459 (2017)
30. Wang, X., Kajiyama, S., Iinuma, H., Hosono, E., Oro, S., Moriguchi, I., Okubo, M., Yamada, A.: Nat. Commun. **6**, 6544 (2015)
31. Mashtalir, O., Lukatskaya, M.R., Zhao, M.-Q., Barsoum, M.W., Gogotsi, Y.: Adv. Mater. **27**, 3501 (2015)
32. Dall'Agnese, Y., Taberna, P.-L., Gogotsi, Y., Simon, P.: J. Phys. Chem. Lett. **6**, 2305 (2015)
33. Kajiyama, S., Szabova, L., Iinuma, H., Sugahara, A., Gotoh, K., Sodeyama, K., Tateyama, Y., Okubo, M., Yamada, A.: Adv. Energy Mater. **7**, 1601873 (2017)
34. Come, J., Naguib, M., Rozier, P., Barsoum, M.W., Gogotsi, Y., Taberna, P.L., Morcrette, M., Simon, P.: J. Electrochem. Soc. **159**, A1368 (2012)
35. Byeon, A., Glushenkov, A.M., Anasori, B., Urbankowski, P., Li, J., Byles, B.W., Blake, B., Van Aken, K.L., Kota, S., Pomerantseva, E., Lee, J.W., Chen, Y., Gogotsi, Y.: J. Power Sources **326**, 686 (2016)
36. Xie, X.Q., Zhao, M.Q., Anasori, B., Maleski, K., Ren, C.E., Li, J.W., Byles, B.W., Pomerantseva, E., Wang, G.X., Gogotsi, Y.: Nano Energy **26**, 513 (2016)
37. Ming, F., Liang, H., Zhang, W., Ming, J., Lei, Y., Emwas, A.-H., Alshareef, H.N.: Nano Energy **62**, 853 (2019)
38. Avireddy, H., Byles, B.W., Pinto, D., Delgado Galindo, J.M., Biendicho, J.J., Wang, X., Flox, C., Crosnier, O., Brousse, T., Pomerantseva, E., Morante, J.R., Gogotsi, Y.: Nano Energy **64**, 103961 (2019)
39. Kyerematen, N.A., Brousse, T., Pech, D.: Nat. Nanotechnol. **12**, 7 (2017)
40. Jiang, Q., Lei, Y., Liang, H., Xi, K., Xia, C., Alshareef, H.N.: Energy Storage Mater. https://doi.org/10.1016/j.ensm.2020.01.018
41. Zhang, C., McKeon, L., Kremer, M.P., Park, S.-H., Ronan, O., Seral-Ascaso, A., Barwich, S., Coileáin, C.Ó., McEvoy, N., Nerl, H.C., Anasori, B., Coleman, J.N., Gogotsi, Y., Nicolosi, V.: Nat. Commun. **10**, 1795 (2019)
42. Zhang, C.F., Kremer, M.P., Seral-Ascaso, A., Park, S.H., McEvoy, N., Anasori, B., Gogotsi, Y., Nicolosi, V.: Adv. Func. Mater. **28**, 1705506 (2018)
43. Li, H.P., Li, X.R., Liang, J.J., Chen, Y.S.: Adv. Energy Mater. **9**, 1803987 (2019)
44. Jiang, Q., Kurra, N., Maleski, K., Lei, Y., Liang, H., Zhang, Y., Gogotsi, Y., Alshareef, H.N.: Adv. Energy Mater. **9**, 1901061 (2019)
45. Peng, Y.Y., Akuzum, B., Kurra, N., Zhao, M.Q., Alhabe, M., Anasori, B., Kumbur, E.C., Alshareef, H.N., Ger, M.D., Gogotsi, Y.: Energy Environ. Sci. **9**, 2847 (2016)
46. Jiao, S., Zhou, A., Wu, M., Hu, H.: Adv. Sci. **6**, 1900529 (2019)
47. Yue, Y., Liu, N., Ma, Y., Wang, S., Liu, W., Luo, C., Zhang, H., Cheng, F., Rao, J., Hu, X., Su, J., Gao, Y.: ACS Nano **12**, 4224 (2018)
48. Quain, E., Mathis, T.S., Kurra, N., Maleski, K., Van Aken, K.L., Alhabeb, M., Alshareef, H.N., Gogotsi, Y.: Adv. Mater. Technol. **4**, 1800256 (2019)
49. Hu, H., Hua, T.: J. Mater. Chem. A **5**, 19639 (2017)

50. Salles, P., Quain, E., Kurra, N., Sarycheva, A., Gogotsi, Y.: Small **14**, 1802864 (2018)
51. Li, P., Shi, W., Liu, W., Chen, Y., Xu, X., Ye, S., Yin, R., Zhang, L., Xu, L., Cao, X.: Nanotechnology **29**, 445401 (2018)
52. Li, J., Levitt, A., Kurra, N., Juan, K., Noriega, N., Xiao, X., Wang, X., Wang, H., Alshareef, H.N., Gogotsi, Y.: Energy Storage Mater. **20**, 455 (2019)
53. Wang, H., Feng, H., Li, J.: Small **10**, 2165 (2014)
54. Tian, H., Gao, T., Li, X., Wang, X., Luo, C., Fan, X., Yang, C., Suo, L., Ma, Z., Han, W., Wang, C.: Nat. Commun. **8**, 14083 (2017)
55. Wen, Y., He, K., Zhu, Y., Han, F., Xu, Y., Matsuda, I., Ishii, Y., Cumings, J., Wang, C.: Nat. Commun. **5**, 4033 (2014)
56. Peng, L., Zhu, Y., Chen, D., Ruoff, R.S., Yu, G.: Adv. Energy Mater. **6**, 1600025 (2016)
57. Tang, Q., Zhou, Z., Shen, P.: J. Am. Chem. Soc. **134**, 16909 (2012)
58. Lian, P., Dong, Y., Wu, Z.-S., Zheng, S., Wang, X., Sen, W., Sun, C., Qin, J., Shi, X., Bao, X.: Nano Energy **40**, 1 (2017)
59. Liang, X., Rangom, Y., Kwok, C.Y., Pang, Q., Nazar, L.F.: Adv. Mater. **29**, 1603040 (2017)
60. Ghidiu, M., Kota, S., Halim, J., Sherwood, A.W., Nedfors, N., Rosen, J., Mochalin, V.N., Barsoum, M.W.: Chem. Mater. **29**, 1099 (2017)
61. Nitta, N., Wu, F., Lee, J.T., Yushin, G.: Mater. Today **18**, 252 (2015)
62. Ji, L., Lin, Z., Alcoutlabi, M., Zhang, X.: Energy Environ. Sci. **4**, 2682 (2011)
63. Goodenough, J.B., Kim, Y.: Chem. Mater. **22**, 587 (2010)
64. Chen, D., Chen, W., Ma, L., Ji, G., Chang, K., Lee, J.Y.: Mater. Today **17**, 184 (2014)
65. Sun, Y., Wu, Q., Shi, G.: Energy Environ. Sci. **4**, 1113 (2011)
66. Anasori, B., Lukatskaya, M.R., Gogotsi, Y.: Nat. Rev. Mater. **2**, 16098 (2017)
67. Naguib, M., Kurtoglu, M., Presser, V., Lu, J., Niu, J., Heon, M., Hultman, L., Gogotsi, Y., Barsoum, M.W.: Adv. Mater. **23**, 4248 (2011)
68. Mashtalir, O., Naguib, M., Mochalin, V.N., Dall'Agnese, Y., Heon, M., Barsoum, M.W., Gogotsi, Y.: Nat. Commun. **4**, 1716 (2013)
69. Lin, Z., Sun, D., Huang, Q., Yang, J., Barsoum, M.W., Yan, X.: J. Mater. Chem. A **3**, 14096 (2015)
70. Sun, D., Wang, M., Li, Z., Fan, G., Fan, L.-Z., Zhou, A.: Electrochem. Commun. **47**, 80 (2014)
71. Kim, S.J., Naguib, M., Zhao, M., Zhang, C., Jung, H.-T., Barsoum, M.W., Gogotsi, Y.: Electrochim. Acta **163**, 246 (2015)
72. Ren, C.E., Zhao, M.-Q., Makaryan, T., Halim, J., Boota, M., Kota, S., Anasori, B., Barsoum, M.W., Gogotsi, Y.: ChemElectroChem. **3**, 689 (2016)
73. Zhao, Q., Zhu, Q., Miao, J., Zhang, P., Wan, P., He, L., Xu, B.: Small **15**, 1904293 (2019)
74. Eames, C., Islam, M.S.: J. Am. Chem. Soc. **136**, 16270 (2014)
75. Naguib, M., Halim, J., Lu, J., Cook, K.M., Hultman, L., Gogotsi, Y., Barsoum, M.W.: J. Am. Chem. Soc. **135**, 15966 (2013)
76. Hu, J., Xu, B., Ouyang, C., Yang, S.A., Yao, Y.: J. Phys. Chem. C **118**, 24274 (2014)
77. Xie, Y., Naguib, M., Mochalin, V.N., Barsoum, M.W., Gogotsi, Y., Yu, X., Nam, K.-W., Yang, X.-Q., Kolesnikov, A.I., Kent, P.R.C.: J. Am. Chem. Soc. **136**, 6385 (2014)
78. Anasori, B., Xie, Y., Beidaghi, M., Lu, J., Hosler, B.C., Hultman, L., Kent, P.R.C., Gogotsi, Y., Barsoum, M.W.: ACS Nano **9**, 9507 (2015)
79. Wang, C., Xie, H., Chen, S., Ge, B., Liu, D., Wu, C., Xu, W., Chu, W., Babu, G., Ajayan, P.M., Song, L.: Adv. Mater. **30**, 1802525 (2018)
80. Luo, J., Tao, X., Zhang, J., Xia, Y., Huang, H., Zhang, L., Gan, Y., Liang, C., Zhang, W.: ACS Nano **10**, 2491 (2016)
81. Wang, F., Wang, Z., Zhu, J., Yang, H., Chen, X., Wang, L., Yang, C.: J. Mater. Sci. **52**, 3556 (2017)
82. Gao, Y., Wang, L., Zhou, A., Li, Z., Chen, J., Bala, H., Hu, Q., Cao, X.: Mater. Lett. **150**, 62 (2015)
83. Ahmed, B., Anjum, D.H., Gogotsi, Y., Alshareef, H.N.: Nano Energy **34**, 249 (2017)
84. Tang, H., Zhuang, S., Bao, Z., Lao, C., Mei, Y.: ChemElectroChem. **3**, 871 (2016)

85. Zhao, M.-Q., Torelli, M., Ren, C.E., Ghidiu, M., Ling, Z., Anasori, B., Barsoum, M.W., Gogotsi, Y.: Nano Energy **30**, 603 (2016)
86. Wu, X., Wang, Z., Yu, M., Xiu, L., Qiu, J.: Adv. Mater. **29**, 1607017 (2017)
87. Zhu, J., Chroneos, A., Schwingenschlögl, U.: Physica Status Solidi (RRL) Rapid Res. Lett. **9**, 726 (2015)
88. Liu, F., Zhou, J., Wang, S., Wang, B., Shen, C., Wang, L., Hu, Q., Huang, Q., Zhou, A.: J. Electrochem. Soc. **164**, A709 (2017)
89. Du, F., Tang, H., Pan, L., Zhang, T., Lu, H., Xiong, J., Yang, J., Zhang, C.: Electrochim. Acta **235**, 690 (2017)
90. Zhao, S., Meng, X., Zhu, K., Du, F., Chen, G., Wei, Y., Gogotsi, Y., Gao, Y.: Energy Storage Mater. **8**, 42 (2017)
91. Zhou, J., Zha, X., Zhou, X., Chen, F., Gao, G., Wang, S., Shen, C., Chen, T., Zhi, C., Eklund, P., Du, S., Xue, J., Shi, W., Chai, Z., Huang, Q.: ACS Nano **11**, 3841 (2017)
92. Zhou, Y., Zu, X.: Electrochim. Acta **235**, 167 (2017)
93. Wang, C.-H., Kurra, N., Alhabeb, M., Chang, J.-K., Alshareef, H.N., Gogotsi, Y.: ACS Omega **3**, 12489 (2018)
94. Wang, Y., Chen, R., Chen, T., Lv, H., Zhu, G., Ma, L., Wang, C., Jin, Z., Liu, J.: Energy Storage Mater. **4**, 103 (2016)
95. Khazaei, M., Ranjbar, A., Arai, M., Sasaki, T., Yunoki, S.: J. Mater. Chem. C **5**, 2488 (2017)
96. Ming, F., Liang, H. Huang, G., Bayhan, Z., Alshareef, H.N.: Adv. Mater. n/a, 2004039
97. Xie, Y., Dall'Agnese, Y., Naguib, M., Gogotsi, Y., Barsoum, M.W., Zhuang, H.L., Kent, P.R.C.: ACS Nano **8**, 9606 (2014)
98. Er, D., Li, J., Naguib, M., Gogotsi, Y., Shenoy, V.B.: ACS Appl. Mater. Interfaces. **6**, 11173 (2014)
99. Palomares, V., Serras, P., Villaluenga, I., Hueso, K.B., Carretero-González, J., Rojo, T.: Energy Environ. Sci. **5**, 5884 (2012)
100. Kim, S.-W., Seo, D.-H., Ma, X., Ceder, G., Kang, K.: Adv. Energy Mater. **2**, 710 (2012)
101. Xue, Y., Zhang, Q., Wang, W., Cao, H., Yang, Q., Fu, L.: Adv. Energy Mater. **7**, 1602684 (2017)
102. Yu, Y.-X.: J. Phys. Chem. C **120**, 5288 (2016)
103. Kajiyama, S., Szabova, L., Sodeyama, K., Iinuma, H., Morita, R., Gotoh, K., Tateyama, Y., Okubo, M., Yamada, A.: ACS Nano **10**, 3334 (2016)
104. Xiong, D., Shi, Y., Yang, H.Y.: Mater. Today (2021). https://doi.org/10.1016/j.mattod.2020.12.004
105. Wang, C., Chen, S., Song, L.: Adv. Funct. Mater. n/a, 2000869
106. Zhao, M.-Q., Xie, X., Ren, C.E., Makaryan, T., Anasori, B., Wang, G., Gogotsi, Y.: Adv. Mater. **29**, 1702410 (2017)
107. Wu, Y., Nie, P., Jiang, J., Ding, B., Dou, H., Zhang, X.: ChemElectroChem. **4**, 1560 (2017)
108. Guo, X., Xie, X., Choi, S., Zhao, Y., Liu, H., Wang, C., Chang, S., Wang, G.: J. Mater. Chem. A **5**, 12445 (2017)
109. Bak, S.-M., Qiao, R., Yang, W., Lee, S., Yu, X., Anasori, B., Lee, H., Gogotsi, Y., Yang, X.-Q.: Adv. Energy Mater. **7**, 1700959 (2017)
110. Hou, J., Tu, K., Chen, Z.: J. Phys. Chem. C **120**, 18473 (2016)
111. Lv, X., Song, J., Lai, Y., Fang, J., Li, J., Zhang, Z.: J. Energy Storage **8**, 205 (2016)
112. Dong, Y., Wu, Z.-S., Zheng, S., Wang, X., Qin, J., Wang, S., Shi, X., Bao, X.: ACS Nano **11**, 4792 (2017)
113. Come, J., Black, J.M., Lukatskaya, M.R., Naguib, M., Beidaghi, M., Rondinone, A.J., Kalinin, S.V., Wesolowski, D.J., Gogotsi, Y., Balke, N.: Nano Energy **17**, 27 (2015)
114. Byeon, A., Zhao, M.-Q., Ren, C.E., Halim, J., Kota, S., Urbankowski, P., Anasori, B., Barsoum, M.W., Gogotsi, Y.: ACS Appl. Mater. Interfaces. **9**, 4296 (2017)
115. Bruce, P.G., Freunberger, S.A., Hardwick, L.J., Tarascon, J.-M.: Nat. Mater. **11**, 19 (2012)
116. Manthiram, A., Chung, S.-H., Zu, C.: Adv. Mater. **2015**, 27 (1980)
117. Fang, X., Peng, H.: Small **11**, 1488 (2015)
118. Manthiram, A., Fu, Y., Chung, S.-H., Zu, C., Su, Y.-S.: Chem. Rev. **114**, 11751 (2014)

119. Su, D., Cortie, M., Fan, H., Wang, G.: Adv. Mater. **29**, 1700587 (2017)
120. Zhou, W., Xiao, X., Cai, M., Yang, L.: Nano Lett. **14**, 5250 (2014)
121. Song, J., Yu, Z., Gordin, M.L., Wang, D.: Nano Lett. **16**, 864 (2016)
122. Wei Seh, Z., Li, W., Cha, J.J., Zheng, G., Yang, Y., McDowell, M.T., Hsu, P.-C., Cui, Y.: Nature Commun. 4, 1331 (2013)
123. Liang, X., Garsuch, A., Nazar, L.F.: Angew. Chem. Int. Ed. **54**, 3907 (2015)
124. Zhao, X., Liu, M., Chen, Y., Hou, B., Zhang, N., Chen, B., Yang, N., Chen, K., Li, J., An, L.: J. Mater. Chem. A **3**, 7870 (2015)
125. Hao, Y., Xiong, D., Liu, W., Fan, L., Li, D., Li, X.: ACS Appl. Mater. Interfaces. **9**, 40273 (2017)
126. Rosenman, A., Markevich, E., Salitra, G., Aurbach, D., Garsuch, A., Chesneau, F.F.: Adv. Energy Mater. **5**, 1500212 (2015)
127. Huang, J.-Q., Xu, Z.-L., Abouali, S., Akbari, M., Garakani, Kim, J.-K.: Carbon 99, 624 (2016)
128. Song, J., Su, D., Xie, X., Guo, X., Bao, W., Shao, G., Wang, G.: ACS Appl. Mater. Interfaces. **8**, 29427 (2016)
129. Lin, C., Zhang, W., Wang, L., Wang, Z., Zhao, W., Duan, W., Zhao, Z., Liu, B., Jin, J.: J. Mater. Chem. A **4**, 5993 (2016)
130. Ghidiu, M., Lukatskaya, M.R., Zhao, M.-Q., Gogotsi, Y., Barsoum, M.W.: Nature **516**, 78 (2014)
131. Li, J., Yuan, X., Lin, C., Yang, Y., Xu, L., Du, X., Xie, J., Lin, J., Sun, J.: Adv. Energy Mater. **7**, 1602725 (2017)
132. Lukatskaya, M.R., Kota, S., Lin, Z., Zhao, M.-Q., Shpigel, N., Levi, M.D., Halim, J., Taberna, P.-L., Barsoum, M.W., Simon, P., Gogotsi, Y.: Nat. Energy **2**, 17105 (2017)
133. Rakhi, R.B., Ahmed, B., Hedhili, M.N., Anjum, D.H., Alshareef, H.N.: Chem. Mater. **27**, 5314 (2015)
134. Zhao, M.-Q., Ren, C.E., Ling, Z., Lukatskaya, M.R., Zhang, C., Van Aken, K.L., Barsoum, M.W., Gogotsi, Y.: Adv. Mater. **27**, 339 (2015)
135. Yan, J., Ren, C.E., Maleski, K., Hatter, C.B., Anasori, B., Urbankowski, P., Sarycheva, A., Gogotsi, Y.: Adv. Func. Mater. **27**, 1701264 (2017)
136. Wang, Y., Dou, H., Wang, J., Ding, B., Xu, Y.L., Chang, Z., Hao, X.D.: J. Power Sources **327**, 221 (2016)
137. Persson, I., El Ghazaly, A., Tao, Q., Halim, J., Kota, S., Darakchieva, V., Palisaitis, J., Barsoum, M.W., Rosen, J., Persson, P.O.A.: Small **14**, e1703676 (2018)
138. Wang, X., Li, H., Li, H., Lin, S., Ding, W., Zhu, X., Sheng, Z., Wang, H., Zhu, X., Sun, Y.: Adv. Funct. Mater. n/a, 0190302
139. Ling, Z., Ren, C.E., Zhao, M.-Q., Yang, J., Giammarco, J.M., Qiu, J., Barsoum, M.W., Gogotsi, Y.: Proc. Natl. Acad. Sci. **111**, 16676 (2014)
140. Orangi, J., Hamade, F., Davis, V.A., Beidaghi, M.: ACS Nano (2019). https://doi.org/10.1021/acsnano.9b07325
141. Li, Q., Wang, Q., Li, L., Yang, L., Wang, Y., Wang, X., Fang, H.-T.: Adv. Energy Mater. n/a, 2000470
142. Wang, X., Shen, X., Gao, Y., Wang, Z., Yu, R., Chen, L.: J. Am. Chem. Soc. **137**, 2715 (2015)
143. Xu, S., Dall'Agnese, Y., Li, J., Gogotsi, Y., Han, W.: Chem. Europ. J. **24**, 18556 (2018)

Environmental Applications of MXenes

Syed Asad Raza Kazmi, Faisal Shahzad, Syed Muhammad Husnain, Muhammad Taqi Mehran, and Nadir Abbas

Abstract MXenes have emerged as a strong candidate to address several environmental concerns owing to their excellent hydrophilicity, tunable surface chemistry, good surface area and catalytic activity. MXenes possess significant sorption selectivity and excellent reduction capability for different pollutants present in water. This chapter summarizes the recent development for environmental applications using MXenes and/or their composites. The role of inherent surface functional groups, interlayer spacing, synthesis methods, and surface functionalization of MXene for the adsorptive removal of different pollutants is discussed. The sequestration of target pollutants, including heavy metal ions, radionuclides, anions, organic and inorganic compounds, dyes, have been discussed in detail, along with their removal mechanisms and regeneration ability. The MXene adsorbents for removing gaseous pollutants are also discussed along with associated mechanisms. The disposal of radionuclide waste using MXene and its composites is also presented. Lastly, the strategies to enhance the environmental applications of MXenes and an insight into the future research has been documented.

S. A. R. Kazmi
Department of Chemistry, Pakistan Institute of Engineering and Applied Sciences (PIEAS), Islamabad 45650, Pakistan

F. Shahzad (✉)
Department of Metallurgy and Materials Engineering, National Center for Nanotechnology, Pakistan Institute of Engineering and Applied Sciences (PIEAS), Islamabad 45650, Pakistan
e-mail: faisal@pieas.edu.pk

S. M. Husnain
Chemistry Division, Directorate of Science, Pakistan Institute of Nuclear Science and Technology (PINSTECH), Islamabad 45650, Pakistan

M. T. Mehran
School of Chemical and Materials Engineering, National University of Sciences and Technology (NUST), H-12, Islamabad, Pakistan

N. Abbas
Department of Chemical Engineering, College of Engineering, University of Hail, Hail 81441, Saudi Arabia

M. Khalid et al. (eds.), *Fundamental Aspects and Perspectives of MXenes*,
Engineering Materials, https://doi.org/10.1007/978-3-031-05006-0_8

Keywords MXene · Heavy metal ions · Radionuclide · Water treatment · Organic and inorganic pollutants

1 Introduction

As a result of rapid industrialization and urbanization in recent decades, untreated waste discharges have been causing significant environmental contamination and damage to human health. Heavy metals, industrial effluents, particulate matter, herbicides, pesticides, fertilizers, and volatile organic compounds (VOCs) are only a few of the many pollutants contributing to environmental pollution [1, 2]. It is undoubtedly one of the most serious issues confronted by society today. The remediation of toxins in the air, water, and soil, demands the development of new technologies and materials. Researchers have employed a variety of biological and physiochemical approaches to eliminate various environmental contaminants, including aerobic digestion [3], biochar therapy [4], membrane filtration [5] and adsorption [6]. Adsorption is the simplest, cheapest and most efficient method widely adapted. Adsorption can be employed to remove organic, inorganic (soluble or insoluble), and biological pollutants [7]. Since it is a surface phenomenon directly related to the number of available active sites on the surface, materials with a large specific surface area and abundant active sites are preferred for effective and high capacity contaminant adsorption [8]. Graphene [9], graphene oxide [10], two-dimensional metal organic framework (2D-MOF) [11], nano zerovalent iron (nZVI) [12], clays [13] and other 2D nanomaterials [14] have been widely researched for their impressive remediation properties owing to their large specific surface area, environmental flexibility and outstanding biocompatibility.

With the synthesis of T_3C_2 in 2011, Gogotsi and Barsum unveiled a novel class of 2D nanomaterials by selectively etching the Al atoms in the stacked hexagonal ternary carbide, Ti_3AlC_2, with aqueous HF at room temperature. The typical formula for MXenes is $M_{n+1}X_nT_x$ (n = 1–3), where M is an early transition metal group, X is carbon and/or nitrogen, and T_x is surface terminal groups (–OH, –O–, and/or –F). MXenes have outstanding mechanical, electrical, optical, chemical and physical properties [15], making them a potential choice for a wide range of applications such as energy storage[16], catalysis [17], optoelectronics [18], EMI shielding [19], batteries [20–22], plasmonic [23, 24], sensing [25] and other applications [26]. Because of their excellent hydrophilicity [27–29], tunable surface chemistry [30–32], large surface area [33], and catalytic activity [34], MXenes have emerged as a strong candidate for addressing a variety of environmental concerns. These materials have high adsorption capacity [35] and excellent reduction capability for various pollutants found in water [36–40].

The recent developments in MXene environmental applications and their composites are summarized in this chapter. The role of MXene's inherent surface functional groups, interlayer spacing, synthesis methods, and surface functionalization in the adsorptive removal of various pollutants is discussed. The removal of a variety of

hazardous contaminants such as heavy metal ions, radionuclides, anions, organic and inorganic compounds, and dyes, as well as their removal mechanisms and regeneration ability, has been thoroughly discussed. MXenes adsorbents for the removal of gaseous pollutants are also discussed with their associated removal mechanisms. The use of MXenes and their composites for radionuclide waste disposal has also been summarized. Finally, we have also provided suitable strategies for improving the environmental applications of MXenes and an insight into future guidelines for research.

2 Adsorptive Environmental Applications of MXenes for Wastewater Treatment

After their discovery in 2011 [41], researchers have attempted to investigate the mechanism of interaction of different pollutants with the surface of MXenes [29, 42]. Researchers have therefore studied various MXenes and their hybrids for the removal of heavy metal ions [14], radionuclides [43], organic dyes [44] and gaseous molecules [45]. The presence of functional groups have been shown to improve their removal efficiencies, and the remediation mechanisms involved electrostatic interaction, ion exchange, coordination, inner sphere complex formation, intermolecular attractions, photocatalytic degradation and reductive adsorption [46, 47].

MXenes has a charged surface because of their different polar functionalities. According to several studies, the point zero charge (PZC) of pristine MXene is around 2 and 3 [39, 46]. MXene has a negative zeta potential for pH above PZC and positive zeta potential at pH below PZC. As a result, the MXene surface is negative above PZC (at higher pH values) and positive below PZC (at lower pH values). At pH values greater than 3, researchers have attempted to remove metal cations and cationic dyes (via electrostatic interaction), whereas anions have been removed at pH values less than 2. There is a broad pH working range for cation removal, but highly acidic conditions are needed to remove anions from water. To achieve a positive surface charge over a wide pH range, researchers have synthesized various MXene-based composites [48] or functionalized the MXene surface [49].

Treatment of MXene with alkali hydroxides (KOH, NaOH, and LiOH) improved adsorption efficiency [50]. This is believed to be due to an increased interlayer spacing and an ion-exchange mechanism. The functionality responsible for metal cation adsorption is [M–O]-H^+, which is converted to [M–O]-A^+ (where A = alkali metal) by treating MXene with alkali. The effect of interlayer spacing on ion-adsorption on the surface has also been studied, and the results show that increased interlayer spacing increases ion-adsorption with the surface [32, 51]. The pillaring of the MXene nanosheets has also verified this via reduced-graphene oxide (rGO) [32] and terephthalic acid [51]. MXenes performance has also been compared with other adsorbents like activated carbon [52] and MOFs [46], which have far larger surface area than

MXenes. MXenes have emerged as a promising candidate for removing different environmental pollutants due to their rich surface chemistry.

2.1 Removal of Metal Ions

Water contamination has become a global problem as a result of the discharge of untreated industrial and domestic wastewater directly into water bodies. According to the United States Environmental Protection Agency (US EPA), 300–400 million tons of heavy metals, solvents, and other waste are released into the world's water supplies each year as a harmful byproduct of industrial production [53]. One of the most dangerous and predominant contaminants are heavy metals. They are non-degradable and tend to accumulate in the food chain.

2.1.1 Lead Removal

The toxic effects of lead (Pb) on plants, animals, and humans have stimulated the interest of environmental scientists. The usage of Pb-containing chemicals such as anti-knocking agents, oil, agrochemicals, paint etc., are the primary source of Pb pollution in the environment [54]. It is one of the most harmful heavy metals, and its ingestion through the food chain has been shown to pose a health risk to both plants and humans. In industrialized economies, the proper disposal of lead is still a problem to protect human health. However, many developed countries do not properly dispose-off the industrial waste. Furthermore, waste solutions are dumped directly into water sources, posing a health risk to humans. Pb enters the food chain due to agricultural practices and creates significant problems by interfering with a variety of functions in human systems and other living organisms. The World Health Organization (WHO), the European Union, the (US EPA) and the Guidelines for Canadian Drinking Water Quality defined the acceptable levels of Pb in drinking water at 0.01, 0.01, 0.015 and 0.01 mg L^{-1}, respectively [55].

Several researchers have investigated lead removal using MXenes. For example, Peng et al. reported the synthesis of alk-MXene via chemical exfoliation followed by alkalization intercalation [29]. The successful intercalation of Na ions is verified by a 002 peak shift towards a lower angle in XRD (Fig. 1a). It was discovered that surface hydroxyl groups are important sites for Pb (II) ions that have been activated by alkali treatment. The ion exchange mechanism was used to describe the increased adsorption capacities of Pb (II). Furthermore, pH impacted Pb (II) uptake, with an optimum pH range of 5 to 7 and minimal removal at pH 1 (Fig. 1b). As a result, the adsorbent was regenerated by lowering the pH, i.e., acid treatment. Density functional theory (DFT) findings demonstrated that the vertical hydroxyl group to titanium atom was essential for heavy metal ion removal. In contrast, fluoride functionality reduced the adsorption performance of 2D layered MXene ($Ti_3C_2(OH)_xF_{2-x}$) [42]. Another DFT study revealed that variations in adsorption capabilities and binding energies are

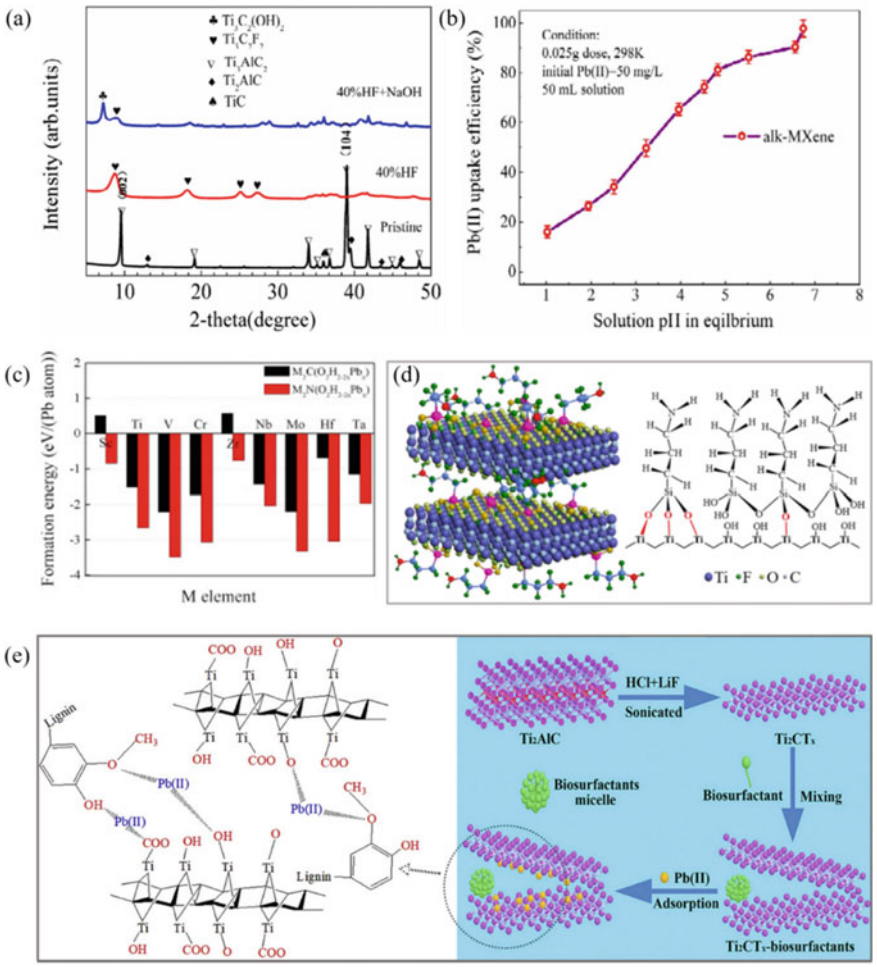

Fig. 1 **a** Comparison of XRD spectra of alkali treated MXene with MAX phase and pristine MXene, **b** Adsorption behavior of alk-MXene at various pH values for Pb (II) removal (Reprinted with permission from Ref. [29]) **c** Formation energies of various M_2X type MXenes covered with Pb (II) (1/9 ml) (Reprinted with permission from Ref. [56]) **d** Schematic illustration of amino-silane functionalized MXene (Reprinted with permission from Ref. [49]) **e** Scheme for the synthesis of biosurfactant-functionalized Ti_2CT_X and mechanism of interaction of adsorbent with Pb (II) ions (Reprinted with permission from ref [57])

mainly influenced by functional groups [56], where high Pb (II) adsorption capacity of Ti_2C, i.e. 2560 mg g^{-1}, compared to Cu (II) was observed. The findings of Guo et al. have shown that high Pb (II) affinity, excellent thermal stability, potential capacity control, and preferential adsorption ability make MXenes, in particular V_2C, a good candidate for cleaning or ion-separating materials in heavy metal contamination situations. According to systematic first principle studies, bond formation of lead

with metal nitrides has low formation energies as compared to metal carbides [56]. Furthermore, $Ti_2C(OH)_2$ was found to be a promising candidate for Pb removal in terms of uptake kinetics and adsorption capability per unit mass. $Zr_2C\ (OH)_2$ and $Sc_2C\ (OH)_2$ are the only $M_2C\ (OH)_2$ type MXenes that cannot adsorb Pb due to their positive formation energies, as shown in (Fig. 1c).

In another work, Gu et al. reported the synthesis of 2D MAX@titanate nanocomposites by simple oxidation and alkali treatment method [58]. Using KOH (T-KTO) and NaOH (T-NTO) treatment of the MAX phase, he produced a variety of morphologies with outstanding adsorption performance. The new procedure boosted their specific surface areas while improving the availability of active surface functionalities. Among T-NTO and T-KTO, T-KTO showed a maximum adsorption capacity of 328.9 mg g^{-1} at pH 5. Furthermore, investigations indicated that the pH of the solution had a significant impact on the Pb (II) adsorption process. Zhang et al. reported the synthesis of the amino-functionalized $Ti_3C_2T_x$ MXene (alk-MXene-NH_2) nanosheets by alkalization-grafting modification using a silane coupling agent (Fig. 1 d) [49]. Alk-MXene-NH_2 has the highest BET-specific surface area (up to 129.21 $m^2\ g^{-1}$) among other MXene-based adsorbents. It also showed a high removal capacity of 384.63 mg g^{-1} for Pb (II) compared to other 2D-adsorbents. Wang et al. used three bio-surfactants, lignosulfonate (anionic surfactant), chitosan (cationic surfactant), and enzymatic hydrolysis lignin (EHL, non-ionic surfactant) for the functionalization of MXene nanosheets to improve the adsorption activity of MXene for Pb (II) (Fig. 1e) [57]. EHL-functionalized Ti_2CT_X demonstrated a maximum adsorption potential of 232.9 mg g^{-1} for Pb (II). It was thought that EHL has increased the availability of active sites and facilitated the exchange and chelation of Pb (II) ions with surface functional groups of MXene. Jun et al. compared the adsorption behavior of MXene with activated carbon powder. They stated that the activated carbon powder had a large surface area relative to MXene, but later had a high adsorption efficiency due to its more negative surface area [52]. Four separate heavy metals Cu (II), Zn (II), Pb (II), and Cd (II) was efficiently absorbed from a single electrolyte solution using MXene as an adsorbent. FTIR and XPS studies have shown that the main mechanisms of Pb (II) ion adsorption are due to electrostatic interaction, ion exchange and inner-sphere complex formation.

2.1.2 Mercury Removal

Mercury (Hg) is one of the most critical toxins in the world. It exists in the ecosystem as a result of natural and anthropogenic causes, and both animals and humans are exposed to the adverse effects of this toxic heavy metal and its compounds. The key contributors to rising Hg levels worldwide are anthropogenic Hg emissions from a variety of processes, including coal combustion, metal mining and manufacturing, cement processing, and waste incineration [59]. In addition, mercury is globally dispersed through the atmosphere, with atmospheric deposition being the largest source of Hg in the oceans [60].

Shahzad et al. employed a hydrothermal method to synthesize MXene magnetic nanocomposite (MGMX nanocomposite), which demonstrated high stability and outstanding Hg (II) removal capability [61]. Figure 2a shows the excellent Hg (II) removal in a wider pH range with maximal Hg (II) adsorption of 1128.41 mg^{-1} g^{-1}. The MGMX nanocomposite showed great potential to be reused via regeneration. The hydrophilicity, stability, large number of surface functional groups, and facile separation after the reaction make the MGMX nanocomposite an effective adsorbent for removing toxic Hg (II). In another work, MXene core ($Ti_3C_2T_x$) shell aerogel spheres with an exceptional adsorption potential of 932.84 mg g^{-1} for mercuric ions

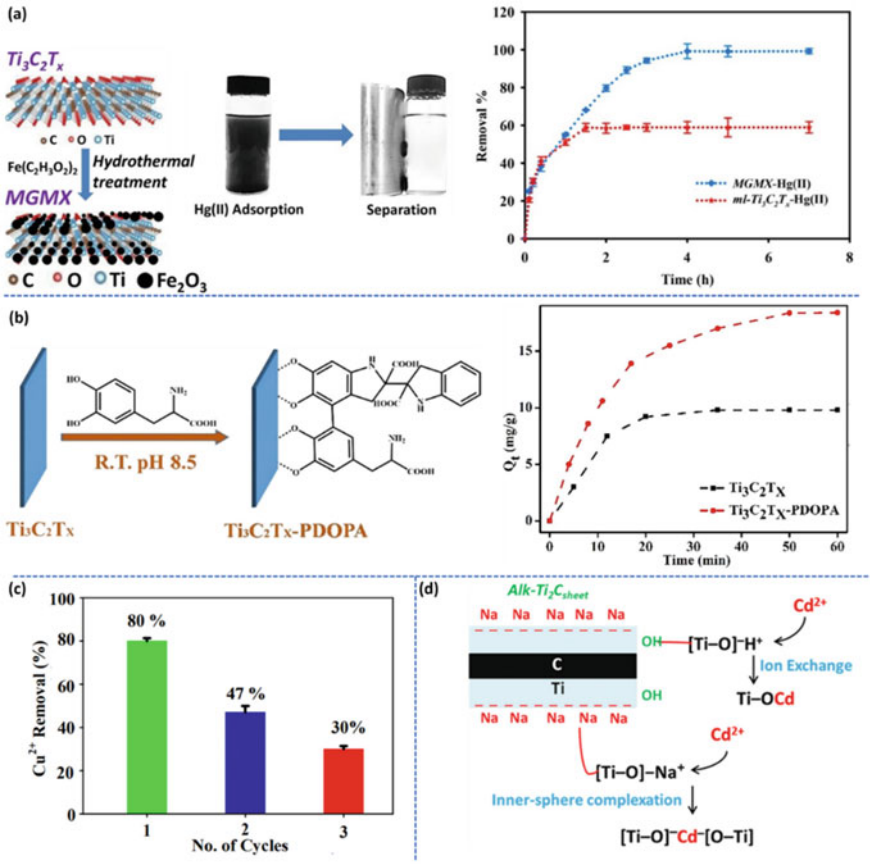

Fig. 2 **a** Schematic illustration of Synthesis of Magnetic MXene and Hg (II) sequestration and graph showing Hg (II) adsorption efficiency of $Ti_3C_2T_x$ and the *MGMX* nanocomposite (Reprinted with permission from Ref. [61]) **b** Cu adsorption capability by regenerated DL-Ti3C2Tx for three cycles. (Reprinted with permission from Ref. [39]) **c** Scheme for the synthesis of $Ti_3C_2T_X$-PDOPA through mussel-inspired chemistry and the Cu^{2+} adsorption comparison (Reprinted with permission from Ref. [63]) **d** Schematic diagram showing the mechanisms involved in Cd^{2+} removal via Alk-Ti_2Csheet (Reprinted with permission from Ref. [64])

were prepared [62]. The aerogel sphere demonstrated 100% removal efficiency for mercuric ions and >90% for the five heavy metals (Cd^{2+}, Cr^{3+}, Pb^{2+}, Cu^{2+} besides Hg^{2+}). The composite aerogel was effective at extreme pH levels, and its micro size spherical shapes enable it to be used in packed columns.

2.1.3 Copper and Cadmium Removal

Copper and cadmium are widely used metals in various industrial applications, such as electroplating, metal finishing, and etching [12]. Like other toxic heavy metals, Cd (II) and Cu (II) do not degrade in the environment and accumulate over time. Because of their high solubility in water, they can be easily transferred to bio-systems raising several health concerns. As a result, contaminated effluent must be treated prior to its discharge into the environment [65–67].

Shahzad et al. investigated the effectiveness of 2D $Ti_3C_2T_x$ MXene for aqueous medium adsorption. Delaminated (DL)–$Ti_3C_2T_x$ nanosheets showed good Cu^{2+} removal efficiency owing to the hydrophilic nature of surface functionalities and large specific surface area. Cu^{2+} reductive adsorption was facilitated by oxygenated moieties in MXene's layered structure, resulting in Cu_2O and CuO species [39]. Compared to multilayer (ML)-$Ti_3C_2T_x$, DL–$Ti_3C_2T_x$ showed rapid uptake kinetics. Delaminated nanosheets removed 80% of the contaminant within 1 min and demonstrated a removal capacity of 78.45 mg g^{-1}, 2.7 times higher than activated carbon. Despite its high adsorption capacity, Fig. 2b revealed that the adsorbent deteriorates as the number of cycles is increased, showing its poor capability for regeneration. This behavior might be explained by inadequate desorption of chemically bound Cu^{2+} and the production of TiO_2 nanoparticles due to MXene's partial oxidation. Since Cu^{2+} tends to reduce to Cu^{1+} and oxidize the nanosheets irreversibly, regeneration of $Ti_3C_2T_x$ adsorbent appears difficult. In another report, the fabrication of MXene-based polymeric composites ($Ti_3C_2T_X$-PDOPA) was documented by Gan et al. using amino acid (Levo-DOPA) functionalization of MXene [63]. The composite showed pH-dependent, efficient Cu^{2+} adsorption. The kinetics plot of Cu^{2+} (Fig. 2c) adsorption shows a rapid increase in the adsorption capacities with the increasing contact time (0–12 min). After that, the increment rate slowed down, and the adsorption curves remained stable for the next 60 min before equilibrium was reached. $Ti_3C_2T_x$-PDOPA, on the other hand, has a far higher Cu^{2+} adsorption potential than $Ti_3C_2T_x$, which may be attributed to the dopamine functional groups. Therefore, the approach makes $Ti_3C_2T_x$-PDOPA a favorable candidate for Cu^{2+} removal from wastewater via electrostatic attraction. It may provide a facile route to prepare various derivatives by exploiting the functional groups present on dopamine and MXenes.

Elumalai et al. reported the formation of the TiO_2-rutile phase on DL-MXene by aqueous phase reaction of amino acids (AAs) with MXene [68]. $Ti_3C_2T_x$'s surface functionalities facilitated the spontaneous intercalation of AAs, allowing the interlayer spacing to widen and accommodate the AA molecules. Furthermore, only

aromatic AAs produced the rutile phase, while aliphatic AAs had no oxidative reaction. Cu^{2+} ions were adsorbed from an aqueous solution using histidine functionalized rutile TiO_2@d-$Ti_3C_2T_x$ hybrid with a maximum uptake of 95 mg g^{-1}. In another approach, Shahzad et al. reported the successful green synthesis of Alk-Ti_2C nanofibers and Alk-Ti_2C sheets to remove Cd^{2+}. Exfoliated nanostructures (Alk-Ti_2C sheet and Alk-Ti_2C fiber) exhibited high thermal, chemical and mechanical stability as well as have abundant oxygenated functionalities that serve as active sites [64]. The maximum adsorption capacity of Cd^{2+} ion sequestration nanostructures was determined to be 325.89 mg g^{-1}, one of the highest reported values for comparable materials such as graphene oxide. In a comprehensive quantitative study, adsorption-coupled oxidation, electrostatic interactions, and complex formation confirmed the interaction of hydroxyl groups with Cd^{2+} ions (Fig. 2d).

2.2 Radionuclide Removal

Nuclear energy has received a great deal of attention because of its advantages over rapidly depleting conventional fuel supplies, i.e., its fuel has a high energy density and emits no greenhouse gases. However, despite these benefits, the nuclear industry generates radioactive pollutants having a half-life from months to millions of years and a high potential to disperse into the environment. These radionuclides are a serious threat to terrestrial and subterranean ecosystems and pose substantial health implications such as developmental anomalies, birth malformations, miscarriage, and tumors in different organs. As a result, their complete elimination and disposal are critical in nuclear waste management. This section discussed various radionuclide removal by using MXenes or their variants.

2.2.1 Uranium Removal

Wang et al. published the first study that used multilayer V_2CT_x MXene to extract U (VI) from wastewater [69]. DFT and EXAFS studies revealed that the U (VI) is adsorbed on V_2CT_x via bidentate coordination bond formation by hydroxyl functionalities connected to V atoms. The deprotonation of the hydroxyl group following the attachment of U (VI) demonstrates that the adsorption mechanism is ion exchange-based. Zhang et al. performed DFT calculations to investigate uranyl ion adsorption on hydroxylated titanium carbide nanosheets [70]. The development of both inner- and outer-sphere adsorption configurations, as well as the binding energies associated with them, were investigated. The interaction of uranyl ions with the H_2O, other anionic ligands (Cl, OH, and NO_3), and $Ti_3C_2(OH)_2$ nanosheets were strong enough to develop strong chemical linkages. In a similar approach, Zhang et al. used DFT-based electronic structure methods to investigate the adsorption behaviors of uranyl ions on hydroxylated V_2C nanosheets [71]. Uranyl adsorbates with various ligands CO_3^{2-}, H_2O, and OH have been explored and concluded that

aquouranyl binds strongly to the hydroxylated V_2C nanosheets among all the uranyl species tested. The strong association between uranyl ions and OH or CO_3^{2-} ligands causes the U–O linkage at the adsorption site to weaken. Furthermore, they discovered that U-F bonds are weaker on the adsorption platform as compared to U–O bonds, implying that F terminations are less favorable. Wang et al. demonstrated an unprecedented increase in the adsorption potential of $Ti_3C_2T_x$ for radionuclide sequestration via a hydrated intercalation method [72]. The possibility of imprisoning the representative actinide U (VI) within multilayered $Ti_3C_2T_x$ was also verified by logical control of the interlayer space.

On the other hand, Wang et al. demonstrated that a two-dimensional transition metal carbide, Ti_2CT_x, can effectively extract uranium using a sorption-reduction technique (Fig. 3a) [37]. Batch experiments showed effective U (VI) sequestration over a wide pH range, with a maximum removal capacity of 470 mg g^{-1} at pH 3.0. Wang et al. designed a unique composite of n-ZVI mounted on alkalized $Ti_3C_2T_x$ nanosheets (nZVI/Alk- $Ti_3C_2T_x$). Using an in-situ growth process for reductive capture/removal of U (VI) from aqueous solution in anaerobic conditions (Fig. 3b) [73]. Because of the uniform dispersion of nZVI on MXene substrates, nZVI/Alk- $Ti_3C_2T_x$ demonstrated rapid uptake kinetics with good selectivity (q_{max} = 1315 mg g^{-1}). The composite showed removal efficiency of 69.5% in 10 ppm humic acid solution, 88.9% in 1.0 mM $NaHCO_3$ and 95.1% removal efficiency in simulated groundwater. The sequestration mechanism may include reductive immobilization, hydrolysis precipitation, and inner-sphere complexation, which depends on nZVI consumption and solution's pH. In another report, Zhang et al. successfully functionalized MXene with carboxyl terminated aryl diazonium salt (Fig. 3c) and increased its radionuclide chelating ability as well as its water stability [74]. The carboxyl terminated $Ti_3C_2T_x$ MXene (TCCH) exhibited significant adsorption capacities (97.1 mg g^{-1} for Eu and 344.8 mg g^{-1} for U) as well as a remarkable radionuclide removal efficiency (>90%) from simulated water. The findings indicate that U (VI) adsorption on TCCH is inner-sphere coordination, whereas EU (III) adsorption is affected by electrostatic interaction and inner-sphere complexation. In another approach, Zhang et al. used diazonium salt grafting to successfully position amidoxime chelating groups on $Ti_3C_2T_x$ MXene surfaces [35]. The addition of amidoxime functional groups to $Ti_3C_2T_x$ nanosheets increased their selectivity for uranyl species and also enhanced their chemical stability in water. To exploit the outstanding electrical conductivity of MXene, the functionalized adsorbent was coated on carbon cloth to fabricate a self-standing electrode. When an electrical field was applied, the removal capacity of U (VI) increased from 294 to 626 mg g^{-1}, surpassing all the previously reported electro-sorptive adsorbents (Fig. 3d).

2.2.2 Barium Removal

Barium, an alkaline earth metal, is found in the Earth's crust as oxide, sulfide, and halide. Its water solubility allows it to travel massive distances in aquatic systems. Therefore, it is also utilized in "produced water" in the oil and gas sector [75].

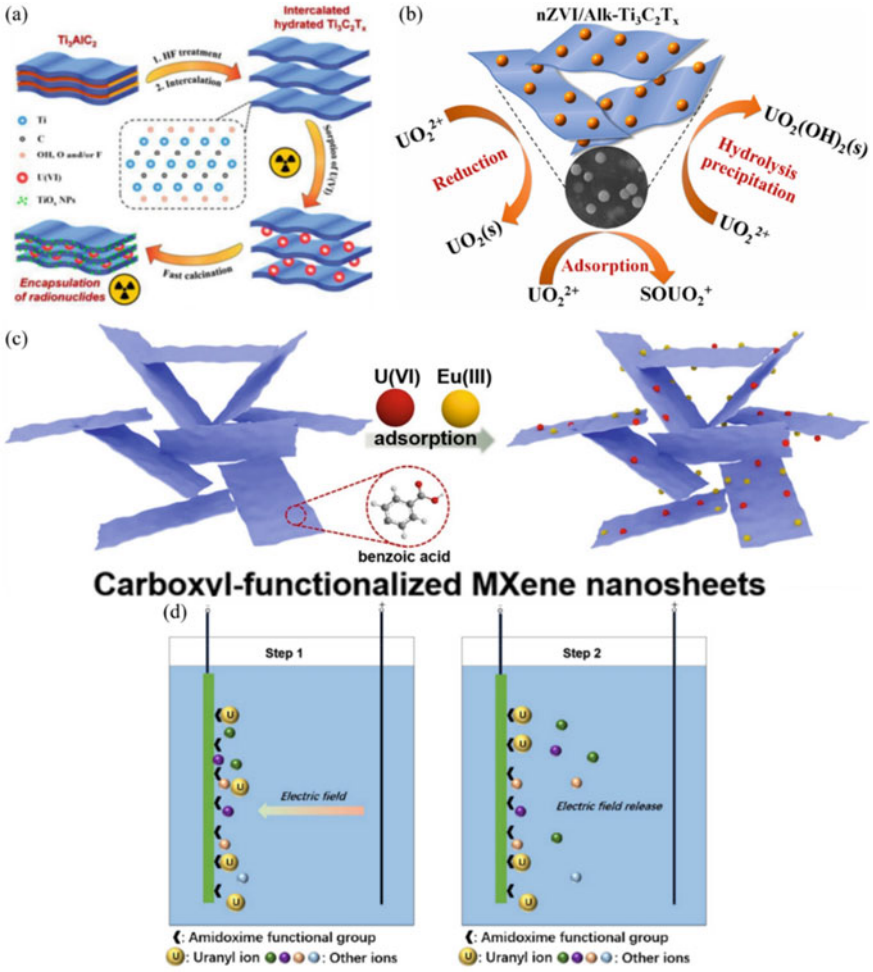

Fig. 3 **a** Hydrated intercalation of $Ti_3C_2T_x$ MXene for efficient U (VI) removal and immobilization (Reprinted with permission from Ref. [72]) **b** Schematic diagram showing that the elimination of U (VI) can be accomplished through a variety of routes (Reprinted with permission from Ref. [73]) **c** Figure depicting the adsorption of Eu (III) and U (VI) on carboxyl-functionalized $Ti_3C_2T_x$ (Reprinted with permission from ref[74]) **d** Schematic diagram of electrosorption process at pulse potential (Reprinted with permission from Ref. [35])

Unfortunately, barium in the water is not only hazardous to the living creatures that consume it, but it may also cause pipe blockage and the collapse of the whole production process if used untreated in the industry [76]. That is why barium removal from water is critical, and researchers have explored MXenes for barium removal to solve this issue.

Fard et al. reported the synthesis of $Ti_3C_2T_x$ nanosheets and conducted experiments to investigate Barium adsorption [76]. $Ti_3C_2T_x$ nanosheets showed high preferential adsorption in the presence of other competitive metal ions with a maximum removal capacity of 9.3 mg g^{-1} under optimized conditions. It was reported that the surface of MXene is largely terminated by electronegative functionalities that act as adsorption sites for Ba (II) ions. The D-R model showed that the adsorption process is chemisorption and has physisorption character as well (Fig. 4a). Mu et al. conclusively demonstrated that alkalization of MXene nanosheets for Ba^{2+} sequestration with an adsorption capacity of 46.46 mg g^{-1}, which is approximately three times that of pristine $Ti_3C_2T_x$ [77]. Jun et al. studied $Ti_3C_2T_x$ for Sr^{2+} and Ba^{2+} removal from simulated wastewater, and the results showed high adsorption capacities of 225 and 180 mg g^{-1}, respectively [78]. Negatively charged MXene adsorbed Sr^{2+} and Ba^{2+} through electrostatic attraction, as verified by the pH effect and ionic strength study. FTIR and XPS analysis revealed that MXene adsorbed Sr^{2+} and Ba^{2+}, respectively, via inner-sphere coordination and ion exchange mechanism (Fig. 4b). MXene showed excellent reusability for at least four cycles.

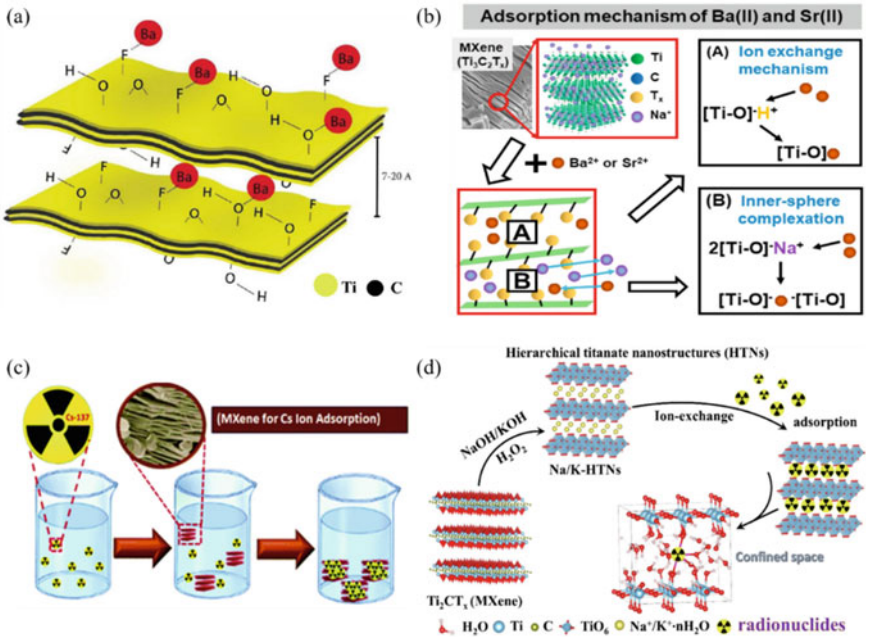

Fig. 4 **a** Interaction mechanism of Ba^{2+} ions with MXene Surface (Reprinted with permission from Ref. [76]) **b** Removal mechanism of Ba^{2+}/Sr^{2+} by MXene. (Reprinted with permission from Ref. [78]) **c** MXene nanosheets for Cs ion adsorption (Reprinted with permission from Ref. [79]) **d** Removal mechanism of radionuclides by MXene-derived HTNs. (Reprinted with permission from Ref. [80])

2.2.3 Thorium Removal

Alongside uranium, thorium is acknowledged as one of the alternative energy sources for power plant operation in the nuclear energy sector. Thorium is much less hazardous than uranium when used in a fuel cycle. Mining, industrial boilers, rare-earth extraction, phosphate fertilizer production, and coal-fired utilities all led to a significant increase in thorium levels in the atmosphere as a result of wastewater generated by those processes. Internal thorium poisoning may not cause immediate radiation harm, but long-term harmful effects may develop after prolonged exposure due to its weak but long-lived radioactivity [81].

Li et al. examine the efficiency of a Ti_2CT_x MXene for removing thorium, Th (IV) [47]. Ti_2CT_x-hydrated has a substantially larger adsorption potential than Ti_2CT_x-dried due to the increased separation of nanosheets and facile intercalation of Th (IV) ions. The maximum removal capacity of Ti_2CT_x-hydrated was 213.2 mg g^{-1}. The SEM results showed that the Ti_2CT_x hydrated layer structures are well preserved after adsorption. The increase in Ti_2CT_x-hydrate interlayer space elucidated by XRD indicated that a considerable quantity of Th (IV) has been intercalated between MXene nanosheets. According to XPS results, the binding energies of the Th (IV)-loaded Ti_2CT_x sample were lower than those of Th $(NO_3)_4$, suggesting that the sorption mechanism involves Th (IV) complexation. In addition, the solution pH was also monitored before and after adsorption. A higher concentration of protons was observed after adsorption, which supports a proton exchange mechanism. Therefore, a Ti–O–Th linkage is expected to develop during adsorption process.

2.2.4 Palladium Removal

Palladium, which possesses versatile physicochemical properties, has been widely employed in a wide range of applications, including electronic and electrical devices, medicine, catalysis, and jewelry. It is mostly produced from mineral ores and scrapped electrical items. Some palladium isotopes, such as ^{107}Pd and ^{105}Pd, are found in spent nuclear effluent generated from uranium fission and are typically non-radioactive or only weakly radioactive. As a result, it is important to recover more palladium from polluted wastewater in order to protect the environment and conserve resources [82].

Mu et al. produced a series of MXene samples at varied etching temperatures (25, 35, and 45 °C) to demonstrate its effect on MXene's Pd-removal performance [82]. Adsorption experiments indicated that the adsorption statistics MXene-45, MXene-35, and MXene-25 were more compatible with the Langmuir model, with maximum Pd (II) adsorption capacities 184.56, 163.82, and 118.86 mg g^{-1}, respectively. The high adsorption capacities were ascribed to the large surface area and high interlayer d-spacing. Alkalization of MXene does not affect Pd (II) adsorption, according to ICP-AES reports; therefore, no ion exchange process is involved in Pd (II) adsorption. XRD analysis after the adsorption experiment showed the shift of (002) peak towards a lower angle, i.e., increasing the interlayer spacing. XPS studies confirmed that Pd (II) adsorption was expected to be chemisorption.

2.2.5 Cesium Removal

The Fukushima incident was one of the worst nuclear disasters in nuclear history after the Chernobyl accident, resulting in the release of many nuclides, especially cesium (^{137}Cs, ^{134}Cs), into the atmosphere. Cesium can easily enter human organs through food channels, competing with potassium, which is the root cause of many diseases. Aside from that, the long half-life of radioactive cesium (2 years for ^{137}Cs and 30 years for ^{134}Cs) and high solubility in water are the main reasons why cesium nuclides are the most problematic [83].

Khan et al. reported that MXene has a Cs^+ removal capacity of 25.4 mg g^{-1} and an equilibrium time of 1 min at room temperature (Fig. 4c) [79]. The high adsorption capacity was attributed to abundant negative surface functionalities and increased surface area. The pseudo-second-order model best fits the kinetics of Cs^+ adsorption, whereas the Freundlich model best fits the adsorption equilibrium data. According to the thermodynamic parameters, the adsorption process is endothermic. The adsorbent demonstrated good Cs^+ removal capability in neutral to slightly alkaline conditions. Furthermore, Cs^+ may be preferentially adsorbed even in the presence of significant levels of competitive cations (Li^+, Na^+, K^+, Mg^{+2}, and Sr^{2+}). After 5 adsorption–desorption cycles, the adsorbent retained 91% of its adsorption performance when regenerated with 0.2 M HCl. Jun et al. presented outstanding adsorption capacity of $Ti_3C_2T_x$ (i.e., 148 mg g^{-1}) for radioactive Cs^+ [84]. The effect of four different ions (NaCl, KCl, $CaCl_2$, and $MgCl_2$) as well as three different organic acids (sodium oleate, oxalic acid, and citric acid) on Cs^+ adsorption by MXene was investigated. The effects of various inorganic ions on distribution coefficient (K_d) reduction were as follows: $K^+ > Ca^{2+} > Mg^{2+} > Na^+$. The effects of organic acids were in the order citric acid > oxalic acid > sodium oleate, which corresponded to the order of acid surface charge. As a result, Cs^+ binds strongly to highly negatively charged organic acids (such as citric acid) rather than MXene, lowering the K_d. Furthermore, XPS and FTIR studies supported the ion exchange mechanism in the removal of Cs^+ from wastewater.

2.2.6 Europium Removal

Europium, one of the 15 lanthanides, is the costliest and essential rare earth element, with applications in various fields. For example, Europium salts are used to produce newer phosphorescent paints and powders. In addition, Eu (III) is a critical raw material in the audio, film, and computer industries. Nonetheless, Eu (III) is known to be moderately toxic by ingestion, which can contaminate body fluids and cause various diseases, resulting in unnecessary damage to the human body [85]. Furthermore, Eu (III) is present in spent nuclear fuel. Nuclear disasters such as Fukushima and Chernobyl poisoned the atmosphere with long-lived isotopes [86], and therefore it is essential to remove these contaminants from the atmosphere.

Zhang et al. developed hierarchical titanate nanostructures derived from MXenes (HTNs) that can efficiently extract EU (III) in the aqueous phase using an in-situ

oxidation conversion method [80]. The confined region across the layers of HTNs was intercalated with a significant quantity of water and numerous surface hydroxyl functionalities, allowing $Na^+/K^+/H^+$ to be readily mixed or introduced, resulting in more effective ion-exchange sites (Fig. 4d). The active sites are exchanged with Eu (III) hydrated ions due to stronger electrostatic attraction and hydrogen bonding, resulting in substantial sorption (Table 1).

2.3 Anion Removal

Bromate (BrO_3^-) ions are found in drinking water as a disinfectant by-product. WHO has recommended up to 10 $\mu g\ L^{-1}$ as an acceptable limit of BrO_3^-. BrO_3^- may cause severe diarrhea, abdominal pain, lung edema and nervous breakdown. Pandey et al. reported that using lamellar 2D titanium carbide, it is possible to remove toxic bromate anions in a reductive manner (Fig. 5a) [36]. At pH 7, an excellent reduction potential of toxic bromate (321.8 mg g^{-1}) was obtained in just 50 min. Since titanium carbide was oxidized, the regeneration was poor. However, its products (TiO_2/C) can be used in other catalytic applications.

Technetium-99 is a β-emitter and by-product of nuclear fission of ^{235}U and is widely used in radiopharmacy as a tumor locating agent. Its discharge into water bodies is hazardous. Wang et al. demonstrated the synthesis of a novel 3D-crosslinked MXene-polyelectrolyte nanocomposite with superior perrhenate removal capacity (simulant of pertechnetate) [40]. The incorporation of poly (diallyldimethylammonium chloride) (PDDA) to the Ti_2CT_x nanosheets controls the surface charge and improves the stability, resulting in a Re removal capacity of 363 mg g^{-1} and rapid adsorption kinetics. Modulation of surface charge resulted in widening the working range up to pH 10. (Fig. 5b) Surprisingly, even at 1800 times higher concentrations of competing ions (such as SO_4^{2-} and Cl^-), the Ti_2CT_x/PDDA nanocomposite displayed excellent selectivity for ReO_4^- ions. Batch sorption experiments and XPS verified the immobilization mechanism as a sorption-reduction method.

Chromium solutions are commonly used in many manufacturing processes such as chromium plating, textile dyeing, wood preservation, pulp and paper industries, pigmentation, and tanning. Cr (VI) is a potent oxidizing agent, and as a result, Cr (VI) bioaccumulation can lead to acute, sub-acute or chronic poisoning, mutagenesis, and carcinogenesis. Cr (VI) is typically very mobile and soluble in aqueous solutions, but Cr (III) lacks these features. Because Cr (III) is more stable and less toxic as compared to Cr (VI), the remediation strategies are generally intended to reduce Cr (VI) to Cr (III).

Ying et al. developed $Ti_3C_2T_x$ nanosheets with a capacity of 250 mg g^{-1} for reductive removal of Cr (VI) from water. The adsorbent not only reduced the Cr (VI) to Cr (III) but also adsorbed the Cr (III) (Fig. 6a) [93]. The reductive behavior of $Ti_3C_2T_x$ was further investigated with other oxidizing agents, such as $K_3[Fe(CN)_6]$, $KMnO_4$, and $NaAuCl_4$. Zou et al. reported the synthesis of self-assembled urchin-like rutile TiO_2–C (u-RTC), having a high percentage of (001)

Table 1 MXene based adsorbents for the removal of various heavy metal cations

MXene based Adsorbent	Heavy metal	Adsorption conditions			Removal capacity (mg g^{-1})	Major finding	References
		pH	Time	Temp (K)			
$Ti_3C_2(OH/ONa)_x\ F_{2-x}$	Pb (II)	6	2 min	323	140.1	OH and ONa groups are responsible for removal	[29]
$Ti_3C_2T_x$	Pb (II)	6	2 h	293	36.6	Ion-exchange and inner sphere coordination were the chief mechanism	[87]
Biosurfactant-functionalized Ti_2CT_XMXene nanosheets	Pb (II)	5	24 h	303	232.9	EHL (non-ionic surfactant) showed superior performance than cationic and anionic surfactants	[57]
KH570 silane functionalized $Ti_3C_2T_x$	Pb (II)	1–6	2 h	303	147.97	Optimized amount of coupling agent expose abundant OH groups of MXene nanosheets	[88]
$Ti_3C_2T_X$-PDOPA	Cu (II)	7	60 min	298	65.12	Self-polymerization of dopamine which was functionalized on MXene nanosheets	[63]
$Ti_3C_2T_x$	Cu (II)	5	3 min	298	78.45	Reductive sequestration of heavy metal ions	[89]
$Ti_3C_2T_x$ core–shell spheres containing sodium alginate	Hg (II)	4.5	24 h 298 K 932.84	298	932.84	The composite beads can be used in packed columns, it showed outstanding performance even at highly acidic conditions	[62]

(continued)

Table 1 (continued)

MXene based Adsorbent	Heavy metal	Adsorption conditions			Removal capacity (mg g^{-1})	Major finding	References
		pH	Time	Temp (K)			
Magnetic $Ti_3C_2T_x$ nanocomposite	Hg (II)	6	24 h	298	1128.41	In-situ functionalization of magnetic nanoparticles was carried out	[61]
$Ti_3C_2T_x$ MXene-based films	Cr (VI)	4	0–3000 min	Ambient temperature	84	MXene surface was modified with HCl treatment and films were fabricated with rGO intercalation	[32]
$Ti_3C_2(OH)_{0.8}F_{1.2}$ Transformed to urchin like rutile titania carbon	Cr (VI)	5.8–6.5	10–20 h	298	62	High concentration of 001 facets were responsible for removal	[90]
$Ti_3C_2T_x$	Cr (VI)	2–12	40 min	303	103.56	Electrostatic interactions were responsible for removal	[91]
Ti_3C_2	Cr (VI)		14 h	298	80	High specific surface area and electrostatic interactions were responsible for adsorption	[92]
$Ti_3C_2T_x$	Ba (II)	7	2 h	298	9.3	OH groups prefer to interact with divalent cations	[76]
V_2CT_x	U (VI)	5	4.5	RT	174	Abundant OH and F groups served as active functionalities	[69]

(continued)

Table 1 (continued)

MXene based Adsorbent	Heavy metal	Adsorption conditions			Removal capacity (mg g^{-1})	Major finding	References
		pH	Time	Temp (K)			
Ti_2CT_x	U (VI)	3	0–100 h		470	Reductive sequestration influenced by pH was observed	[37]
nZVI/Alk- $Ti_3C_2T_x$	U (VI)	3.5	24 h	298 K	1315	Removal mechanism involved surface complexation, reductive immobilization and hydrolysis precipitation	[73]
$Ti_3C_2T_x$	Pd (II)		0–3000	293 K	184.56	Increasing the etching temperature, increases the active functionalities	[82]
Ti_2CT_x hydrated	Th (IV)	3	720 min	282–312	213.2	Removal mechanism involved Inner-sphere complexation	[47]
Ti_2CT_x MXene-derived hierarchical titanate nanostructures Na-HTNs	Eu (III)	4.0	0–300 min	298	221.7	Effect of alkali treatment on Nano-confinement and inter-layer spacing	[80]

(continued)

Table 1 (continued)

MXene based Adsorbent	Heavy metal	Adsorption conditions			Removal capacity (mg g^{-1})	Major finding	References
		pH	Time	Temp (K)			
K-HTNs	Eu (III)	4.0	0–300 min	298	202.8	-do-	[80]
$Ti_3C_2T_x$	Cs (I)	6	30 min	298	25.42	Electrostatic interaction and ion-exchange were principal removal mechanisms	[79]
$Ti_3C_2T_x$	Cs (I)	7	1 h	293–313	148	Ion-exchange mechanism was followed	[84]

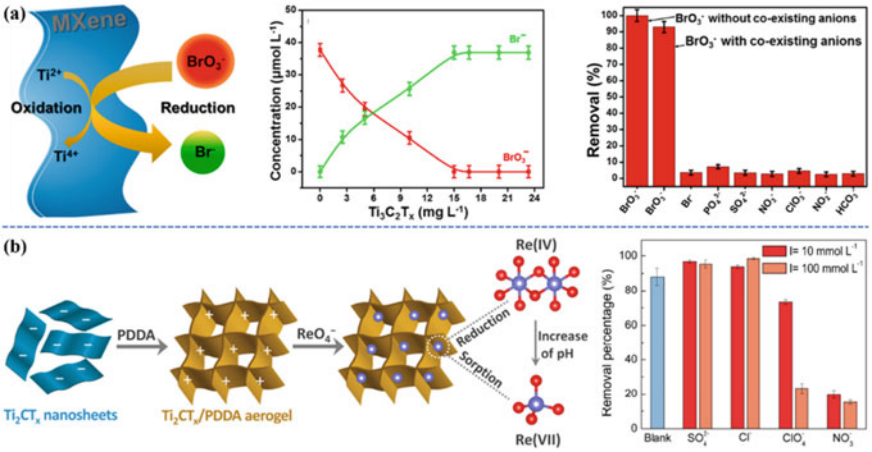

Fig. 5 **a** (left to right) Mechanism of Reductive removal of bromate ions, dependence on the concentration of adsorbent, selectivity among various competitive anions (Reprinted with permission from Ref. [36]) **b** Removal of Rhenate ions using positively charged Ti_2CT_x/PDDA aerogel and effect of competitive anions on removal efficiency (Reprinted with permission from Ref. [40])

facets, by in-situ phase transformation of MXene [90]. Previously, pristine MXene had a 62 mg g^{-1} adsorption capacity, and layered anatase TiO_2–C (l-ATC) had an 11 mg g^{-1} adsorption capacity, whereas u-RTC exhibited a 225 mg g^{-1} Cr (VI) adsorption capacity. Tang et al. synthesized an accordion-like layered Ti_3C_2 MXene that had a high Cr (VI) removal efficiency of 80 mg g^{-1} in the form of chromate at extremely acidic conditions [92]. The synthesis of a novel nZVI@MXene composite using a simple two-step wet chemical process was reported by He et al. [94]. The OH functionalities facilitated the incorporation of nZVI onto the MXene surface, resulting in a large interlayer distance between MXene nanosheets (Fig. 6b). Both (MXene and nZVI) function together to reductively adsorb Cr (VI) from water, with 194.87 mg g^{-1} adsorption capacity at pH = 2. The findings indicated that this composite could be useful for potential water purification needs. Since $Ti_3C_2T_x$ has a negative surface charge, it cannot be used to remove anionic contaminants due to electrostatic repulsion. To address this issue, Jin et al. functionalized MXene nanosheets with poly(m-phenylenediamine) and achieved a positive surface charge under acidic conditions (Fig. 6c) [48] and increased the specific surface area (55.93 m^2 g^{-1}). In comparison to PmPD (384.73 mg g^{-1}) and $Ti_3C_2T_x$ MXene (137.45 mg g^{-1}), the composite had a high Cr (VI) removal capacity of 540.47 mg g^{-1}. In another finding, Wang et al. reported a facile and simple synthesis of 2D/0D heterojunction MXene/TiO_2, which had a Cr (VI) removal efficiency of 99.35%, three times higher than that pristine Ti_3C_2 [95]. The high conductivity Ti_3C_2 MXene with its distinct lamellar nanostructure significantly boosts the photo-electrocatalytic potential of the composite as a cocatalyst. Zhang et al. used one-step hydrothermal synthesis to develop magnetic α-Fe_2O_3/$ZnFe_2O_4$ heterojunctions, and they used an ultrasonic

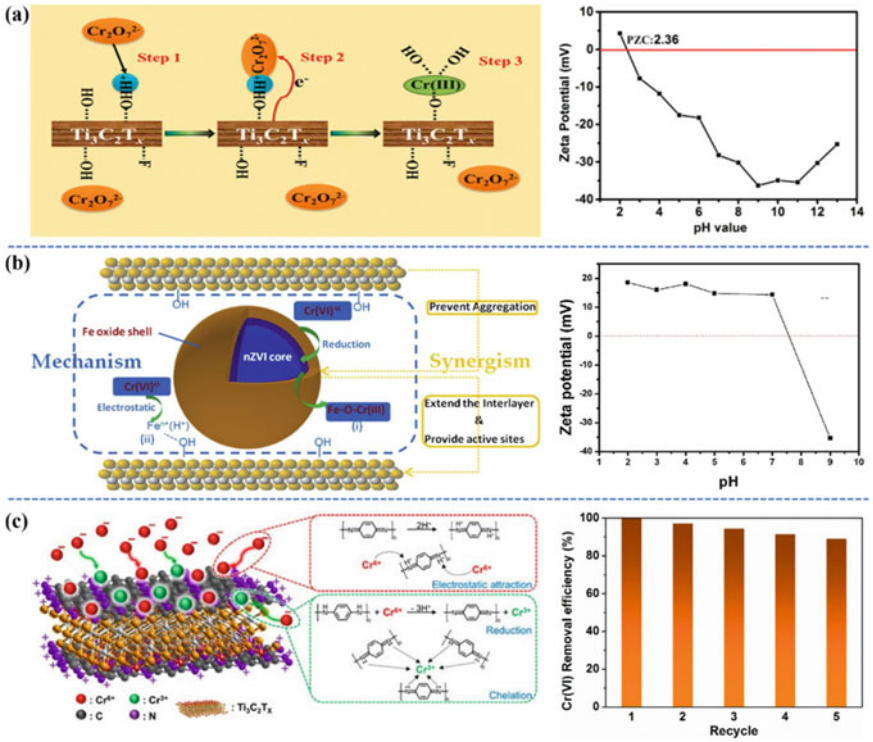

Fig. 6 **a** Schematic diagram for reductive removal of Chromate ions and Zeta Potential of prepared MXene (Reprinted with permission from Ref. [93]) **b** Schematic diagram for reductive removal of Chromate ions and Zeta Potential of prepared MXene (Reprinted with permission from Ref. [94]) **c** Schematic diagram for reductive removal of Chromate ions and Removal efficiency after five consecutive cycles (Reprinted with permission from Ref. [48])

assisted self-assembly approach to synthesize α-$Fe_2O_3/ZnFe_2O_4@Ti_3C_2$ MXene photocatalyst for dispersing magnetic α-$Fe_2O_3/ZnFe_2O_4$ heterojunctions on Ti_3C_2 [96]. The α-$Fe_2O_3/ZnFe_2O_4@Ti_3C_2$ MXene was found to have a higher photocatalytic capacity than the α-$Fe_2O_3/ZnFe_2O_4$ heterojunctions in removing Rhodamine B (RhB) pollutant and Cr (VI) in water due to the improving photoelectron ability.

It is well established that amino groups are readily protonated below neutral pH. When these amino groups are present on a material surface, high positive zeta potential values can be achieved. Kong et al. optimized the quantity of amino-silane coupling agent for chemical functionalization of MXene nanosheets and tested for Cr (VI) removal at acidic pH [97]. The findings were compelling, as the adsorbent beat pristine MXene with a removal capacity of 107.5 mg g^{-1}. Regeneration investigations up to six adsorption–desorption cycles revealed that the functionalized MXene was more stable than pristine MXene. Yang et al. recently published a paper on the chemical functionalization of MXene nanosheets with chitosan and imidazole rings [98]. The authors performed amino silane functionalization followed

by the Radziszewski process to synthesize polyimidazole rings functionalized with chitosan. The synthesized material was evaluated as adsorbent for Cr (VI) ions. The functionalized material exhibited a better elimination capacity of 119.5 mg g^{-1} within 80 min as compared to pristine MXene, which was 39 mg g^{-1}. The data analysis revealed that electrostatic interaction and physisorption are the mechanisms of metal elimination. Due to the oxidation during reductive removal of Cr (VI), the composite cannot be regenerated to its full capacity. In another report, Rehman et al. reported the synthesis of in-situ hybrid δ-MnO_2/MXene nanocomposite for Cr (VI) removal [99]. The ion removal efficiency and adsorption capacity were compared among pristine MXene, pristine MnO_2 and the in-situ hybrid δ-MnO_2/MXene. The in-situ hybrid δ-MnO_2/MXene outperformed others with an adsorption capacity of 353 mg g^{-1}. Further studies and optimizations revealed that electrostatic attractions are the principal interactions governing the adsorption process.

2.4 Organic Dye Removal

Organic dyes are the most frequently used chemicals in textile, printing, tanning, and paper industries, with some applications in the pharmaceutical, cosmetics, and food processing industries. In addition, some synthetic organic dyes are applied in both human and veterinary medicine as pharmacologically active substances (PASs). However, the discharge of organic dyes poses an environmental problem due to their toxic effects on aquatic ecosystems and life on land [100].

Mashtalir et al. investigated the adsorptive and photocatalytic properties of multilayered $Ti_3C_2T_x$ [101]. It was shown to be a very effective adsorbent for the cationic dye MB whereas the anionic dye AB was not removed, following the electrostatic interaction mechanism. When $Ti_3C_2T_x$ was mixed with dyes in their respective solutions and irradiated with UV light, both the dyes were degraded (Fig. 7a). Wei et al. reported a simple method for widening the nanosheets spacing of $Ti_3C_2T_x$ and tuning its surface functionalities via alkaline treatment at elevated temperatures to adjust the adsorption efficiency of $Ti_3C_2T_x$ [50]. LiOH increased the interlayer separation of $Ti_3C_2T_x$ up to 29% and changed -F functionalities to -OH ones. NaOH- $Ti_3C_2T_x$ and LiOH- $Ti_3C_2T_x$ exhibited fast MB adsorption compared to other MXene adsorbents. Moreover, NaOH- $Ti_3C_2T_x$ had a maximum removal capacity of 189 mg g^{-1} for MB (Fig. 7b), which was attributed to surface adsorption and intercalation adsorption. According to the experimental results, the Langmuir isotherm best reflected the improved removal efficiency for cationic dyes.

Zhu et al. fabricated a magnetic 2D-MXene (2D-MX@Fe_3O_4) nanocomposite and studied its adsorption properties against MB at different temperatures [104]. In neutral solution, the nanocomposite exhibited a negatively charged surface, which aided electrostatic interaction between cationic MB and 2D-MX@Fe_3O_4. Furthermore, the removal mechanism revealed that at 55 °C, hydrogen bonding in combination with electrostatic attractions dictated the MB adsorption process, but at 25 °C, surface adsorption through electrostatic attractions was the primary mechanism.

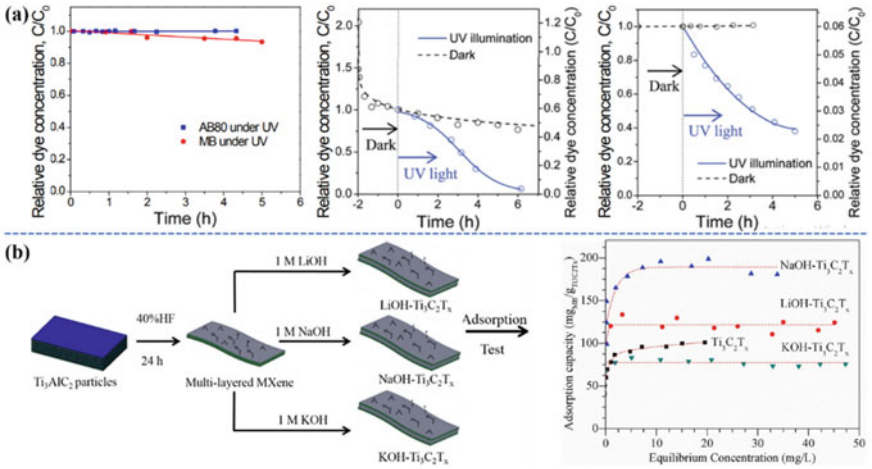

Fig. 7 **a** Relative dye concentration under UV in the absence of $Ti_3C_2T_x$ (left), Relative dye concentration of Methylene Blue in the dark and under UV exposure in the presence of $Ti_3C_2T_x$ (center), Relative dye concentration of Acid Blue in the dark and under UV exposure in the presence of $Ti_3C_2T_x$ (right) (Reprinted with permission from Ref. [101]) **b** Schematic diagram for the synthesis of alk-MXene and application for MB adsorption (left), Adsorption capacity (mg g^{-1}) of $Ti_3C_2T_x$, KOH- $Ti_3C_2T_x$, NaOH- $Ti_3C_2T_x$ and LiOH- $Ti_3C_2T_x$ (Reprinted with permission from Ref. [50])

Zhang et al. also fabricated a magnetic MXene (MXene@Fe_3O_4) nanocomposite using a simple two-step exfoliation method followed by in situ growth of magnetic nanoparticles, demonstrating high MB removal efficiency from aqueous solution (Fig. 8a) [102]. The Langmuir isotherm is followed by the MB removal mechanism, with a maximum adsorbed quantity of 11.68 mg g^{-1}. The impact of pH on adsorption was also investigated, and it was shown that adsorption is pH sensitive, with optimum adsorption occurring at pH = 3 or 11. When the pH is greater than 5.12, electrostatic interaction becomes more significant (zeta potential of 5.12). The adsorbent possesses a negative surface charge above point zero charge (PZC, 5.12) which can electrostatically interact with cationic dye. Lei et al. synthesized the green and efficient adsorbent $Ti_3C_2T_x$ –SO_3H by coupling-diazotization of $Ti_3C_2T_x$ with sulfanilic acid to remove cationic dye MB [103]. Empirical evidence has shown that the adsorption potential of $Ti_3C_2T_x$–SO_3H is 111.11 mg g^{-1} while that of raw material is only 21.10 mg g^{-1} (Fig. 8b). The electrostatic interaction between cationic dye and adsorbent in the alkaline environment is responsible for the removal efficiency of MB.

In another study, Peng et al. observed that MXenes synthesized through hydrothermal etching (h-Ti_3C_2) had a larger BET specific surface area than those synthesized via standard HF etching, leading to improved cationic dye adsorption, MB [105]. The HF etching method was compared to the hydrothermal synthesis. The peaks at 9.8° and 39.1° that originated from the Ti_3AlC_2 (002) and (104) planes disappeared after 24 h of HF etching, whereas a series of bigger peaks emerged after

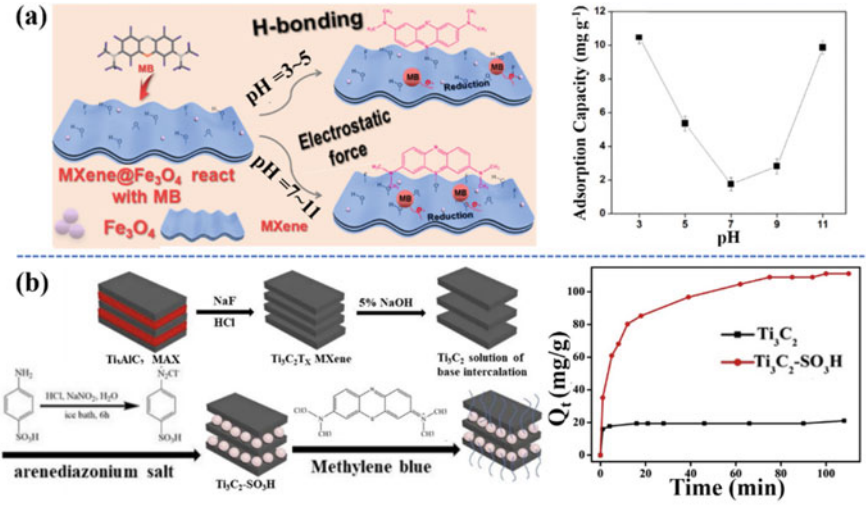

Fig. 8 **a** Schematic diagram showing effect of pH on Methylene Blue adsorption (Reprinted with permission from Ref. [102]) **b** Schematic illustration of the synthesis of adsorbent and application for MB removal (Reprinted with permission from Ref. [103])

4 h of etching that is attributed to the Ti_3C_2 (002), (004), and (006) planes (Fig. 9a). In contrast, the (002) reflection of h- Ti_3C_2 is at 7°, which is much lower than the (9°) reflection of t- Ti_3C_2. This research shows that h-Ti_3C_2 has an increased interlayer separation than t-Ti_3C_2, implying that the hydrothermal technique is more efficient for MXene synthesis. An increase in interlayer spacing has increased the available surface area, which enhanced the adsorption capacity (Fig. 9b) of the adsorbent by exposing a large number of active sites. Vakili et al. developed $Ti_3C_2T_x$ MXene pillared with terephthalate via a green and simple mechanochemical approach to sequestration of organic contaminants in wastewater [51]. Adsorbent demonstrated a high specific surface area of 135.7 $m^2\ g^{-1}$ and a maximum removal capacity of 209 mg g^{-1} for MB due to the increased interlayer separation between the MXene nanosheets. A mechanochemical method was used to recycle the spent adsorbent and generate the MAX phase, which involves the addition of aluminum and the carbonization of terephthalate and pollutants into carbide. Tran et al. revealed that $Ti_3C_2T_x$ MXene, largely F-terminated, is a viable option for MB removal in wastewater [107]. The MXene was discovered to be largely terminated with flouride functionalities synthesized via standard etching procedure. Within 5 min, the F-terminated MXene adsorbed 92% of the MB in a 20 μM MB solution. Surface terminations were shown to be transformed by increasing adsorption–desorption cycles. In this example, the -F groups were substituted with -OH groups, which reduced the removal effectiveness for dyes but suggested its application for metal cation removal. For the other organic dyes, the MXene adsorption capacity was found to be lower.

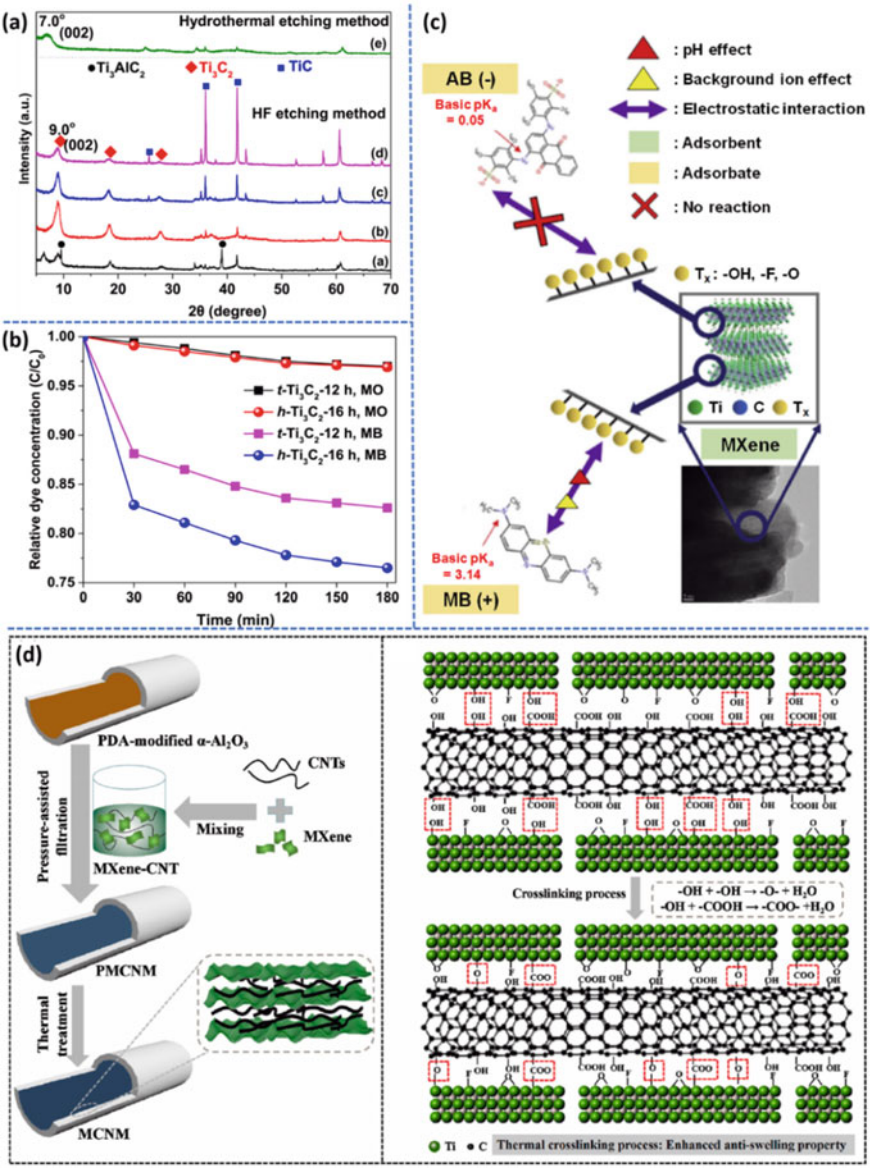

Fig. 9 **a** XRD spectra of t-Ti_3C_2 prepared at different etching times (4–36 h) and hydrothermally synthesized MXene h-Ti_3C_2 (from a to e) **b** Dye removal efficiency of t-Ti_3C_2 and h- Ti_3C_2 (Reprinted with permission from Ref. [105]) **c** Plausible mechanism of dye removal (Reprinted with permission from Ref. [46]) **d** Schematic illustration of synthesis of MXene-CNT membranes via Pressure assisted filtration and thermal treatment (left) and Thermal crosslinking process (right) (Reprinted with permission from Ref. [106])

Jun et al. used MXene, and Al based metal organic frame (MOF) to eliminate synthetic dyes (MB, AB) from the wastewater model (Fig. 9c) [46]. The zeta potential and BET findings indicated that MXene PZC was at pH 3. It had a surface area of 9 m^2 g^{-1}, with a removal capacity of 140 mg g^{-1} for MB attributed to electrostatic interactions. On the other hand, MOF had PZC at pH 9 and a surface area of 630 m^2 g^{-1} when tested for AB (anionic dye), indicating a removal capacity of 200 mg g^{-1}. When the two adsorbents were compared, it was obvious that MXene had higher selectivity and a faster absorption rate, whereas MOF had high MB and AB removal capabilities but low selectivity.

Pressurized membrane-based separation technology has sparked great interest in green energy and water purification due to its decreased CO_2 footprints, improved scalability and energy & cost-effectiveness. Although 2D membranes have high water permeability, the majority of previously developed 2D membranes are constrained by the highly stacked nanosheets, i.e., low interlayer spacing. Sun et al. used a novel thermal crosslinking technique to develop a multidimensional MXene@CNT membrane with higher efficiency and anti-swelling features (Fig. 9d) [106]. Negative surface charge on CNTs was responsible for their uniform dispersion in MXene ink due to electrostatic repulsion. Following that, pressure-assisted filtration was performed, followed by thermal treatment to create a 3D cross-linked structure of MXene@CNT with high water separation efficiency. The process of crosslinking can be attributed to the loss of water by condensation of MXene's -OH functionalities and -COOH or/and -OH functionalities, resulting in new chemical bonds. Chemical connections hampered the material's swelling property, as proven by 50-h operational experiments. The adsorption behavior of the membranes was investigated for inorganic content and dye removal (Rhodamine B, Congo red, and methyl orange). In a similar approach, Yao et al. reported a facile method for producing porous MXene/single-walled carbon nanotubes films (p-MX/SWCNTs) that were utilized as a freestanding electrode for electrosorption of organic contaminants [108]. When the applied voltage was 1.2 V, the as-prepared film (p-MX/SWCNTs) had a phenomenal adsorption potential for MB of 1068.8 mg g^{-1}, which is far higher than the open circuit value of 55.8 mg g^{-1}. The as-prepared electrode has a maximum adsorption potential of 28,403.7 mg g^{-1} and excellent reusability without secondary contamination. Furthermore, to investigate the selectivity of the electrode for cationic dyes over anionic dyes experiments were carried out at various pH values. Results demonstrated that there was superior adsorption of MO at pH 3 and 6 while at pH 9, MB was preferentially removed from the solution. This trend can be explained by electrostatic interactions of contaminant dyes with the adsorbent electrode having a pH-sensitive charged surface. Therefore, by changing the pH values, selective adsorption of dyes can be achieved.

Karthikeyan et al. explored MXenes as an adsorbent for removing methyl orange (MO), from wastewater [91]. MXenes demonstrated a better MO uptake rate and a high removal capacity of 94.8 mg g^{-1}. Calculations demonstrated that pseudo-second order kinetics and the Langmuir isotherm best match the data, revealing that MO was chemisorbed on the MXene surface. Zhang et al. found that in order to enhance the removal efficiency of $Ti_3C_2T_x$ for MB and allow its reuse, sodium alginate (SA) was

used to immobilize $Ti_3C_2T_x$ to shape $Ti_3C_2T_x$ /SA beads [109]. Ionic crosslinking was used to make the beads out of $Ti_3C_2T_x$ powder and SA. According to the findings, $Ti_3C_2T_x$ /SA-30% was selected as the optimal mass ratio, with a maximum removal capacity of 92.17 mg g^{-1} at neutral pH. By coating the membrane surface with tannic acid (TA)-metal complex film, Tong et al. improved the selectivity of the 2D MXene membrane [110]. Membranes with reduced mean pore size and surface zeta potential, as well as increased surface hydrophilicity, resulted from the surface alteration. High water permeability, low salt ion rejection, and improved contaminant removal are all features of the modified membrane. The water permeability and $MgSO_4$ rejection of the MXene-Fe membrane are 261.6 LMH-bar and 13.1%, respectively. The resistance of the membrane to 4-hydroxybenzoic acid, cinnamic acid and RhB increased by 35-, 64- and 108-fold after surface modification, respectively. The modified membranes could be used for drinking water treatment as well as water reuse.

Quyen et al. developed and applied advanced synthesis of nanoflower structures consisting of TiO_2@Ti_3C_2 nanoflowers with three-dimensional (3D) porous frameworks from 2D Ti_3C_2 MXene for organic pollutant degradation (Fig. 10a) [111]. In terms of application, the heterojunction of TiO_2@Ti_3C_2 showed extraordinary photocatalytic efficiency towards Rhodamine B (RhB) compared to the performance of pristine Ti_3C_2 and commercial TiO_2. Furthermore, even after 5 degradation cycles, the TiO_2@Ti_3C_2 composite demonstrates good recyclability. Luo et al. successfully prepared a cube-like Co_3O_4 particle-modified self-assembled MXene (Ti_3C_2) nanocomposite using a simple solvothermal process [113]. In batch model experiments, the performance of the obtained samples was evaluated as a new nanocatalyst for degrading methylene blue and Rhodamine B. The prepared Mxene-Co_3O_4 nanocomposites can be regenerated and reused for eight consecutive cycles. Yin et al. prepared sandwich-like composite catalyst $Cu_2O/TiO_2/Ti_3C_2$ for highly efficient catalytic conversion of nitro compounds using a readily available solvent reduction method [113]. The catalyst exhibited promising catalytic rates for 4-nitrophenol (4-NP) and 2-nitroaniline (2-NA), with pseudo-first-order reaction rate constants (k) of 0.114 and 0.163 min^{-1}, respectively. Surprisingly, even after eight catalytic cycles, catalytic conversion remains 92 and 95% respectively, showing that catalytic converters have a high re-use capacity. Ti_3C_2 offers numerous sites for Cu_2O production and minimizes MXene nanosheets aggregation during in-situ Cu_2O synthesis, which is responsible for excellent catalytic performance. Vigneshwaran et al. reported the synthesis of sulphide rich MXene based photocatalyst intercalated with LDH, via hydrothermal method, for degradation of RhB (RhB) (Fig. 9b) [112]. Under visible light radiation, the designed photocatalyst $NiCo_2S_4$ on MXene (NCS@MX) demonstrated increased catalytic efficiency and decomposed RhB to almost 100% within 20 min. By boosting the optical responsiveness and recombination rate, NCS@MX enhanced the separation efficiency of photoinduced e^{-1} and h^+, therefore improving the photocatalytic decomposition of RhB. Furthermore, in five repeated RhB degradation tests, NCS@MX demonstrated excellent photo-stability with only a minor decline in catalytic performance. NCS@MX is likely to be used in wastewater treatment because to its low cost, environmental friendliness, and generation of non-toxic side products. Zheng et al. used an in situ solvothermal approach with F^{-1} ($NaBF_4$)

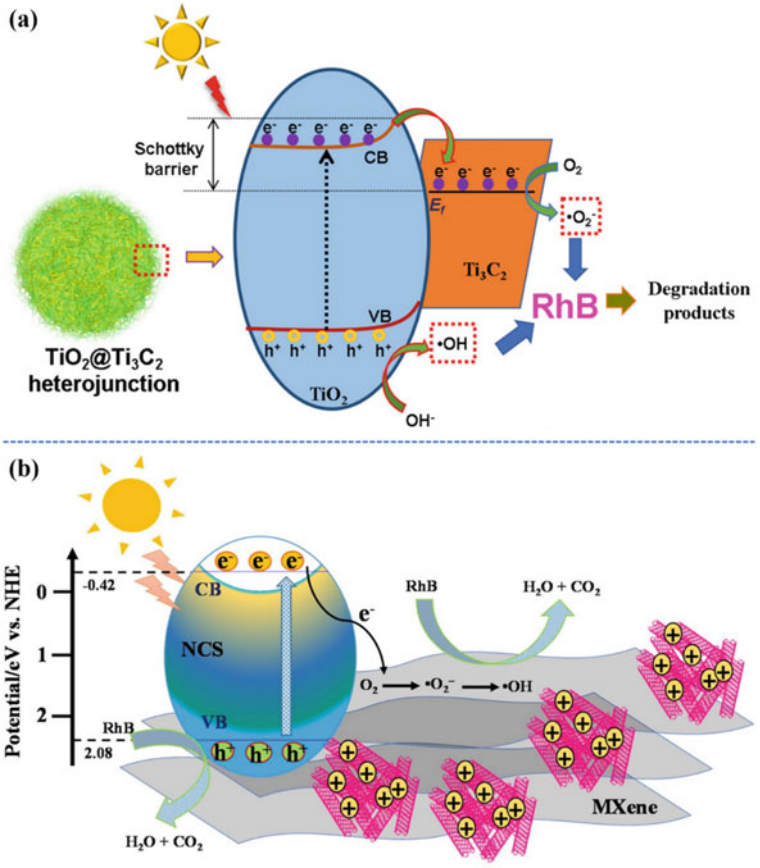

Fig. 10 **a** Photocatalytic degradation of RhB in the presence of TiO_2@Ti_3C_2 catalyst (Reprinted with permission from Ref. [111]) **b** A sketch of possible charge transfer and separation of e^--h^+ pairs in the Vis/NCS@MX system for the catalytic RhB degradation (Reprinted with permission from Ref. [112])

as a co-surfactant to regulate the oxidation of $Ti_3C_2T_x$, where the concentration of F^{-1} will change the percentages of (101) and (001) TiO_2 embedded in the layers of $Ti_3C_2T_x$. This leads to adsorb and photo-catalytically degrade organic dyes when the co-surfactant is 1.5 mmol F^{-1} [114]. The TT-15 heterojunction has a particular surface area of 108.37 $m^2\ g^{-1}$, which helped to increase the interfacial area between the organic dyes and the photocatalyst. Under 500 W mercury light, the photocatalytic degradation efficiencies of MB and MO of TT-15 were greater than 97.5% and 79.5%, respectively, and the kinetic constants of MB and MO degradation were 0.10711 min^{-1} and 0.04537 min^{-1}, respectively.

In another work, Kim et al. fabricated $Ti_3C_2T_x$ MXenes ultrafiltration (UF) membrane (MXene-UF) to eliminate MB and MO from polluted water [115].

MXene-UF (0.92 for MO and 0.90 for MB) had a higher normalized flux as compared to UF (0.90 for MO and 0.86 for MB) and PAC-UF (0.75 for MO and 0.72 for MB). The addition of MXene and PAC to the UF membrane improved its bio-fouling resistance. The analysis showed that PAC-UF has a good adsorption efficiency while MXene-UF has high selectivity. At high ionic strength and in the presence of other competitive cations, lower normalized flux and retention were observed for MB (Table 2).

3 Adsorptive Environmental Applications of MXenes for Gaseous Contaminants Removal

Increased urbanization and industrialization have increased energy demand, which is mostly met by burning fossil fuels, resulting in the release of large amounts of toxic greenhouse gases such as CO_2, CO, CH_4, SO_x, NO_x, and others [118]. Their increased concentration in the environment is causing anthropogenic global warming. Researchers have investigated and implemented a wide range of materials for the adsorptive elimination of these gases [9, 119, 120]. The intriguing properties of a novel family of 2D MXenes have prompted researchers to investigate their gaseous adsorption capability. On this topic, Sun et al. has summarized the reduction of N_2 and CO_2 in a review article [44].

3.1 CO_2 Gas Removal

Adsorptive removal of Carbon dioxide (CO_2) and conversion into value-added products or fuels is a critical pathway for mitigating the greenhouse effect. Therefore, the research and development of new materials with high CO_2 capture and conversion rates have drawn much attention. Chen et al. reviewed the MXene-based materials for effective CO_2 capture and conversion to value-added products [45]. Persson et al. demonstrated a novel method for terminating MXene nanosheets with non-inherent groups and then explored MXene for carbon capture applications [121]. Following the termination of surface functionalities, the $Ti_3C_2T_x$ was then evaluated for CO_2 adsorption. Even at low pressures, 12 mol kg^{-1} CO_2 was adsorbed on MXene nanosheets. It has been suggested that even higher loadings can be achieved after H_2 and CO_2 exposure at higher pressures. The depleted MXene exhibited a little affinity for N_2, indicating that the sheets were extremely selective for CO_2. Furthermore, the MXene demonstrated great stability during the trials, indicating that it might be a viable commercial choice for carbon capture.

Garcia et al. explored CO_2 capture and storage on MXene (M2C) surfaces (M 14 Ti, V, Hf, Zr, Nb, W, Ta, M) using DFT PBE simulations with D3 Grimme correction dispersion [122]. The results reveal adsorption energy of 3.69 eV with

Table 2 Removal Efficiency of different dyes by MXene based adsorbents

MXene based Adsorbent	Dye	Adsorption Conditions			Removal Capacity (mg g^{-1})	Major Finding	References
		pH	Time	Temp (K)			
$Ti_3C_2T_x$	MB	>3	20 h		39	Electrostatic attractions between MXene Surface and cationic dye	[101]
Alk- $Ti_3C_2T_x$	MB	6.5		298	189- NaOH 177- LiOH 121- KOH	Increased separation between MXene nanosheets due to intercalation of alkali cations	[50]
2D-MX@Fe_3O_4	MB		24 h	298 and 328	11.68 (at 328 K)	At 298 K, electrostatic attractions were dominating, while at 328 K hydrogen bonding was dominant	[104]
MXene@Fe_3O_4	MB	3, 11	24 h		11.68	Effect of pH was studied, at pH 3 electrostatic attractions were dominant while at pH 11 hydrogen bonding was dominant	[102]
Phytic acid@MXene	MB	3			42	Surface charge was tailored via pH adjustment to selectively adsorb the dye on the basis of charge	[116]
	RhB	11			22	-do-	[116]
Ultrasonication (US)-assisted $Ti_3C_2T_x$ MXene	MB	4,7and10			87	Surface charge engineering via pH control and delamination of MXene sheet via ultrasonication was carried out	[52]

(continued)

Table 2 (continued)

MXene based Adsorbent	Dye	Adsorption Conditions			Removal Capacity (mg g^{-1})	Major Finding	References
		pH	Time	Temp (K)			
V_2CT_x MXene	MB	5–11		288–318	111.11 at 288	Hydrogen bonding and electrostatic interaction were dominant mechanisms	[117]
Ti_3C_2-SO_3H	MB	7		298	111	Diazonium functionalized MXene showed superior adsorption due to delamination of MXene nanosheets and availability of sulfonic groups	[103]
h-MXene Nb_2C Ti_3C_2	MB		2 h		24	It was showed that hydrothermal etching had outperformed the traditional etching method for MXene synthesis in Dye removal applications	[105]
$Ti_3C_2T_x$	MB	2	5 min		91.9%	F terminations were shown to be more responsible for dye removal than other terminations	[107]

(continued)

Table 2 (continued)

MXene based Adsorbent	Dye	Adsorption Conditions			Removal Capacity (mg g^{-1})	Major Finding	References
		pH	Time	Temp (K)			
p-MXene@SWCNT Films	MB				28,403.7	The as-prepared films showed exceptional removal efficiency via electro-sorption. Furthermore, by tuning the applied voltage we can further improve the selectivity on the basis of charge and size	[108]
2D- $Ti_3C_2T_x$	MO	2–12	40 min		94.8	Electrostatic interactions was principal removal mechanism	[91]
MXene@SA (sodium alginate) beads	MB	7	8 h	298	92.17	The main mechanism of removal was internal and external diffusion through pores of beads	[109]

strong activation of CO_2 (i.e., the creation of anionic $CO_2^{-\delta}$ species converted into elongated δ (CO) bonds with bent structures, and a charge transfer from M_2C to CO_2 higher than 2e for Hf_2C). Theoretically, CO_2 could be adsorbed even at elevated temperatures and low partial pressures. MXenes were also found to adsorb up to 8.25 mol CO_2 kg^{-1} of substrates.

Guo et al. investigated the M_2C-type MXenes for their potential use as CO_2 capture and converter using DFT [123]. The study included 9 metal carbides, Ti, Zr, Hf, V, Nb, Ta, Cr, Mo, and W. Calculations suggested that all the M_2C MXenes spontaneously demonstrated capture and activation of carbon dioxide (with Mo and W showing superior performance), that can be attributed to the lone pair electrons of the surface and can easily be explained by specific M atom charges in M_2C M type. Wang et al. studied the effect of specific surface area on the CO_2 adsorption capacity of $Ti_3C_2T_x$ [124]. The adsorption capacity of $Ti_3C_2T_x$ with a surface area of 21 m^2 g^{-1} was 5.79 mmol g^{-1} whereas, it could reach 44.2 mmol g^{-1} at a higher specific area when calculated theoretically. Studies by Morales-Garcia et al. suggested that MXenes atomic layers have a little but noticeable effect on CO_2 adsorption [125]. Results showed that MXene compounds containing transition metals with d^2 configuration have the highest CO_2 adsorption energy, followed by those containing transition metals with d^3 and d^4 configurations. CO_2 adsorption energies and geometries of selected MXenes were compared to the surfaces of parent transition metal carbides (TMC, 111). TMC's (111) surface is unstable and difficult to grow experimentally. The results show that the thickest structure of M_2C (0001) surfaces offer a route to the limiting TMC (111) surface. In another study, According to Khalediali dusti et al., the inherent defects of $Mo_2TiC_2T_x$ MXene promote CO_2 capture due to the distinctive electronegative surface functionalities [126]. CO_2 made strong bonding at defective sites as compared to perfect sites on MXene. Therefore, increasing the defect content in MXene nanosheets may increase the adsorption capacity.

CO_2 is the primary cause of global warming. Therefore, to remove CO_2 from the atmosphere, researchers have developed several materials; however, most of them had selectivity concerns. Park et al. developed a 3D porous MXene aerogel with a uniform pore size of 11.4 nm and 2.5 nm [130]. Despite a relatively low specific surface area, the aerogel exhibited substantial selectivity for CO_2 over N_2. Soroush et al. reported the fabrication of Pebax@MXene composite for CO_2 removal [127]. The $Ti_3C_2T_x$/Pebax combination reduces crystallinity while promoting polymer phase separation, which enhances CO_2 diffusion. The mechanism depicted schematically in (Fig. 11a) is most likely responsible for regulating the diffusion of N_2 and CO_2 gas molecules through the membrane. CO_2 may be more easily adsorbed on the $Ti_3C_2T_x$ surface because it has a greater quadrupole moment as compared to N_2. The diameter of the interlayer channels between $Ti_3C_2T_x$ nanosheets is about 0.35 nm, which is wider than the kinetic diameter of CO_2 but lower than that of N_2. $Ti_3C_2T_x$ nanosheets' ultra-microporous framework serves as a molecular sieve, which improves CO_2 diffusion selectivity. Moreover, the designed material showed a highly reduced cost for per ton CO_2 production, i.e., $29 compared to $40 of pristine Pebax membrane. Lin et al. reported the exploitation of MXene to trap a deep eutectic solvent in its nanoslits [131]. With CO_2 permeance of 26.35 GPU, the combination of

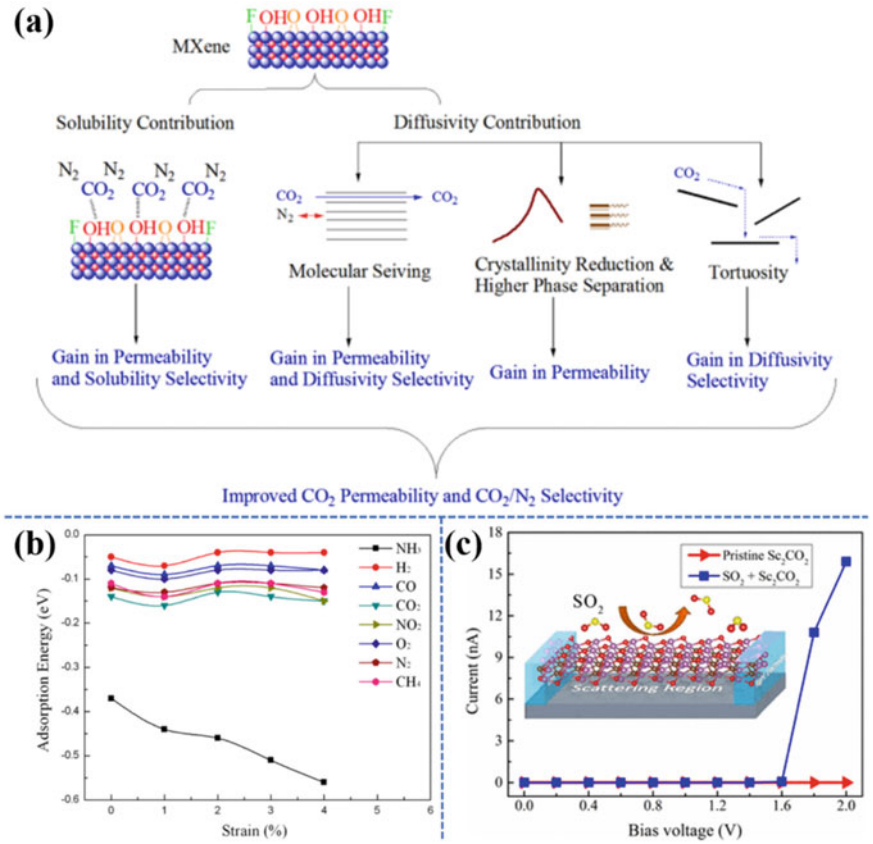

Fig. 11 **a** Plausible mechanism for diffusion of N_2 and CO_2 molecules through $Ti_3C_2T_x$ − Pebax membranes (Reprinted with permission from Ref. [127]) **b** Adsorption energies of H_2, CO_2, O_2, CO, NH_3, N_2, and NO_2 molecules on Ti_2CO_2 surface (Reprinted with permission from Ref. [128]) **c** Plot of current vs voltage along the zigzag orientation of pristine Sc_2CO_2 and SO_2-adsorbed monolayers (Reprinted with permission from Ref. [129])

MXene and new ionic liquid equivalent exhibited a higher affinity for CO_2 over other light gases. The impact of hydrogen bonding and nanoconfinement was confirmed by molecular dynamic simulations. Furthermore, the unique hybrid was thermally and chemically stable.

3.2 Other Gases (NO_x, SO_x, H_2S, NH_3, and CO) Removal

Aside from CO_2, industrial gaseous discharge contains a significant number of SO_x, NO_x, NH_3, H_2S, CH_4, and volatile organic compounds (VOC). When these gases

are inhaled, they cause extreme respiratory infections. Furthermore, their release into the atmosphere causes acid rain, which drastically impacts land and aquatic environments; thus, their removal is important. Therefore, some studies have been conducted to investigate the properties of MXenes for the elimination of these toxic pollutants.

Yu et al. performed the first-principles simulations to explore the potential of MXene towards removing different gases. They investigated the adsorption of NH_3, H_2, CH_4, CO, CO_2, N_2, NO_2, and O_2 on monolayer Ti_2CO_2 for its use as an adsorbent or gas sensor (Fig. 11b) [128]. Only NH_3 was found to be chemisorbed with a charge transfer of 0.174 e. Furthermore, even at high applied strain, the monolayer adsorbent demonstrated high selectivity and sensitivity for NH_3. Lee et al. reported using a scalable wet-spinning process to create metal binder-free $Ti_3C_2T_x$ MXene/graphene hybrid fibers [132]. The hybrid fibers demonstrated excellent mechanical and electrical properties, making them ideal for flexible wearable gas sensors. Because of the synergistic effects of MXene/graphene electronic properties and gas-adsorption capabilities, the created fibers have a high NH_3 gas sensitivity at room temperature. The hybrid fibers also demonstrated excellent mechanical flexibility with a $\pm$ 0.2% fluctuation in resistance and low noise resistance even after 2000 cycles of bending, allowing gas sensing during deformation. MXenes have also been extensively used and studied for N_2 reduction into NH_3 [133–137]. To use as effective electrocatalytic nitrogen fixation catalysts with high selectivity, Xu et al. developed 1 T-MoS_2 nanospots assembled on conductive Ti_3C_2 MXene (1 T-MoS_2@Ti_3C_2) [138]. The composite 1 T-MoS_2@Ti_3C_2 demonstrated good NRR activity with 10.94% faradic efficiency (FE) and 30.33 $\mu g\ h^{-1}\ mg^{-1}$. NH_3 yield rate with $-$ 0.3 V vs. RHE (Reference Hydrogen Electrode). The effect of varied loading concentrations of 1 T-MoS_2 nanospot on catalytic efficiency was evaluated. When loading was increased, the NH_3 yield rate and related FEs were increased initially, then progressively dropped. When the load is 10%, both hit their limit simultaneously. Ti_3C_2 MXene's NH_3 yield rates and FEs are 3.25 $g\ h^{-1}\ mg^{-1}$ and 2.65%, respectively, which are lower than yield rates of 30.33 $g\ h^{-1}\ mg^{-1}$ and FEs of 10.94% with 10 wt% loading of 1 T-MoS_2. The significant difference in catalytic performance among two samples indicates that 1 T-MoS_2 nanospots play a substantial role in boosting Ti_3C_2 MXene's nitrogen fixation efficiency.

VOC detection at the parts per billion (ppb) stage is important for early disease diagnosis. High sensitivity necessitates a high signal-to-noise ratio. Kim et al. demonstrated that MXenes have high metallic conductivity, resulting in low noise and a completely functionalized surface, resulting in a strong signal [139]. At room temperature, $Ti_3C_2T_x$ MXene gas sensors had a very low limit of detection of 50–100 ppb for VOC gases. Furthermore, the signal-to-noise ratio was two orders of magnitude higher than that of other 2D materials because of the exceptionally low noise. These findings provide insight into the use of highly functionalized metallic sensing channels to develop highly sensitive sensors.

Liu et al. investigated the influence of various flouride salts on the etching of MAX on the surface structure of MXene. According to computational models and XPS results, the cations of flouride salts (NH_4^+, K^+, Na^+, and Li^+) impact the surface

morphology of synthesised MXene, which affects their methane adsorption efficiency. The maximum methane adsorption potential was 8.5 $cm^3\ g^{-1}$, whereas the lowest was 11.6 $cm^3\ g^{-1}$ for Ti_3C_2. MXenes derived from NH_4F and LiF can adsorb methane at high pressures and retain it at low pressures, indicating that they might be used in hazardous gas trapping and methane storage. MXenes prepared from KF and NaF, on the other hand, can adsorb methane at high pressures but were unable to hold it at low pressures. Ma et al. investigated the adsorption of SO_2 on O-terminated M_2CO_2 (M = Sc, Hf, Zr, and Ti) monolayers using first-principles calculations [129]. The results predicted that Sc_2CO_2 would have superior sensing properties against toxic SO_2 gas, such as high selectivity and sensitivity, controllable capture, or reversible release when external tensile strains or E-fields were applied. Furthermore, SO_2 adsorption on Sc_2CO_2 resulted in significant changes in electronic band structures as well as significant charge transfer (Fig. 11c). Hu et al. recently published a study on synthesising a ternary composite of g-C_3N_4, TiO_2, and $Ti_3C_2T_x$ [140]. Melamine was used to make g-C_3N_4, which was subsequently coated on partially oxidized metal carbide sheets. The ternary composite was used as a Z-scheme photocatalyst for NOx sequestration. Superior light absorption and increased interaction between adsorbate gas and adsorbent have been demonstrated in a highly interconnected heterogeneous composite. The composite exhibited a removal efficiency of 66.3% for NO with no formation of NO_2. Apart from CO_2 and N_2 fixation, MXene based materials have also been used as sensors [25, 141–143], catalysts for production of valuable products [144], and syngas separation [145].

4 Waste Disposal Using MXene and Their Composites

The fission radionuclides products such as uranium ($^{235,238}U$), strontium (^{90}Sr), cesium (^{137}Cs), barium ($^{133,\ 140}Ba$), and thorium (^{232}Th) pose a severe threat to the environment due to their prolonged half-lives and mobility [146]. Therefore, nuclear waste storage and management are significant problems that must be resolved immediately to avoid environmental and health risks. These radionuclides pose a severe threat to the terranean and subterranean ecosystems, as well as negative health consequences such as developmental abnormalities, birth malformations, miscarriage, and different malignancies in various organs [147, 148]. The use of adsorbents that selectively absorb undesirable ions will purify water polluted by radionuclides of the fission products.

Due to the high specific surface, hydrophobic nature, and a large number of active sites, the 2D layered MXenes have emerged as ideal adsorbents for radionuclides produced during the fission reactions. Khan et al. investigated the uptake capacity of ^{137}Cs by $Ti_3C_2T_x$ MXene from radioactive wastewater, where the adsorbent showed the maximum removal capacity of 25.4 mg g^{-1} [79]. The adsorptive removal of other environmental contaminants such as Pb^{2+}, Hg^{2+}, U^{6+}, Cu^{2+}, and Ba^{2+} has also been investigated, and the effectiveness of MXene has been established [29, 61, 69, 76, 89, 149]. Zhang et al. reviewed the adsorptive environmental applications

of MXenes and identified the main properties of MXenes, which are responsible for the outstanding adsorption behavior of MXenes [150]. Rasool et al. found that encapsulating the radionuclides in suitable intercalants can change the interlayer spacing of MXene nanosheets, potentially increasing the availability of active surface functionalities to develop inner-sphere coordination complexes. Similarly, Wang et al. used a hydrated intercalation technique to achieve an unprecedented high adsorption capability enhancement of $Ti_3C_2T_x$ for U^{6+} radionuclide elimination [72].

However, spent adsorbents pose a substantial challenge due to storage and handling issues. Traditionally, exhausted adsorbents are contained in mortar and concrete, which may hold the material for many years. These structures, however, subsequently leached out in harsh environmental conditions [151]. Ultimate immobilization of the radionuclide containing adsorbents through high-temperature processes, such as in a glass, is also considered one of the safe ways [152–154]. In one such effort, Hassan et al. investigated the MXene post-decontamination treatment with improved thermal stability after adsorbing Cs from radioactive wastewater to produce a stable matrix for ultimate disposal [155]. The authors used the cold sintering technique to solidify the MXene matrix, as shown in Fig. 12a. Due to the cold sintering technique, a fully dense matrix was achieved below 200 °C, and the highly-dense sintered matrix showed very low leaching rates of 10^{-4} $gm^{-2}d^{-1}$. In this study, the introduction of hydroxyapatite (HAp) ceramic as a host matrix provides the green strategy for the immobilisation of cesium-adsorbed MXene nanosheets. Results showed that MXene-HAp (MX-HAp) composite has slightly greater thermal stability than pure Cs-adsorbed MXene. Both HAp and MXene were integrated through a cold sintering process to remove any chances of later leaching of the radionuclide (Fig. 12b, c). It was reported that the leaching rates by using MXene-HAp cold sintered matrix were order of magnitude lower as compared to conventional immobilization techniques. Lower leaching rates were reported in the cold-sintered MX-HAp composite due to effective encapsulation of the exhausted adsorbent (MXene) by HAp and enhanced stability of MXene towards oxidation in the HAp matrix. Figure 12d, e, f shows the EDS mapping with backscattered electron (BSE) image of the cold-sintered Cs-adsorbing composite indicating a homogeneous distribution of MXene (Ti atoms) and adsorbed Cs within the matrix.

The MXenes and their composites show very high potential for nuclear [43] and environmental waste disposal [44]. There is a strong need to investigate further different possibilities, including large-scale contaminated water treatment and safe ultimate disposal through immobilization.

5 Challenges and Future Prospects

MXenes, a nearly decade-old family, have presented a wide array of potential applications such as electrochemistry [156, 157], environmental remediation [158], and EMI shielding [159]. However, technological limitations must be removed to broaden

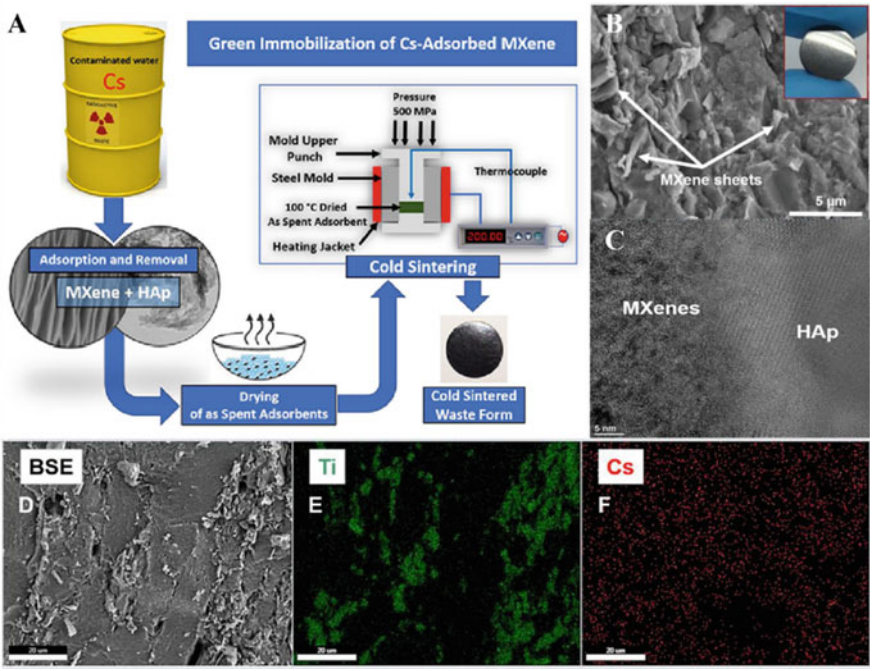

Fig. 12 **a** Process for green immobilization of Cs adsorbed MXene **b** The SEM image of fractured surface (obtained by cold sintering) indicates that the exhausted adsorbent has been effectively cemented. **c** The presence of incoherent grain boundaries in the HRTEM image indicates that the matrix components have been well integrated **d**, **e**, **f** BSE image and EDS mapping confirm the presence of Ti in the MXene phase as well as the successful loading of Cs (F) into the MX-HAp composite. Reproduced with permission from Ref. [155] Copyright 2021, Elsevier

its application spectrum and exploit its potential in daily life [160]. In this part, we shall look at the challenges MXenes faces in environmental remediation applications.

The MXene synthesis procedure/route involves using highly toxic HF acid [161]. Therefore, it is important to develop ecologically benign methods for the production of MXene, involving green chemicals instead of HF. In this direction, molten salt etching methods have been developed with tunable MXene surface chemistry. Although many other approaches have been studied, there is still a pressing need for an efficient and green synthetic method that not only involves the use of environmentally benign reagents but can also be employed for mass production of MXene. Until now, the bottom-up route to MXene production has received little attention [160]. A focus on this area of study might lead to major advancements in the production of MXenes with the finest attributes. Like other nanomaterials, MXenes are in the form of finely divided powder which could easily clog the filter pores resulting in the reduced flow rate during the continuous water treatment. In order to overcome this issue, attention should be given on MXene based composites in which MXene could

be loaded and/or coated on the economical porous substrate, including Polyurethane foams or sand, etc.

MXene nanosheets are thermally unstable in aerobic conditions at temperatures over 200 °C and can be degraded to TiO_2, CO_2, and carbon at elevated temperatures [162]. Engineering of surface functionalities of MXenes may have a substantial impact on MXene's long-term stability, which must be extensively explored further to get deep insights. MXenes oxidize readily in aqueous and oxygenated conditions, thus restricting their use in various environmental applications and long-term storage [71]. Several efforts have been made to improve MXene stability in diverse environments. However, there is still a dire need for a comprehensive methodology to limit MXenes' structural deterioration due to oxidation. Surface functionalization via silane coupling agents or diazonium salts could be a viable approach. The studies to tailor the properties of MXenes have to be studied further, and integrative efforts from experimental trials and theoretical modellings are required to increase our insight into MXenes' capabilities. Nevertheless, the inherent features of MXenes may be tuned by modulating the surface terminations and interlayer spacing, which are intimately linked to MXenes' environmental endurance [160].

MXenes have excellent removal capacities for a wide range of species, but their limited selectivity for targeted species restricts their use in real-world applications. Highly selective functionalities, such as crown ethers, when grafted onto the MXene surface may potentially resolve the problem. MXenes have the highest electrical conductivity than any other nanomaterial; however, their surface functional groups and multilayered structure reduce their conductivity [163]. To address this issue, one has to extensively investigate certain functional groups that do not compromise conductivity and offer large-scale delaminated structures.

Similarly, the majority of documented studies measured the maximum adsorption capacity of MXene towards various pollutants. However, adsorption capacity alone is not a judgement criterion for the performance of the MXene adsorbent because the maximum adsorption capacity is sensitively affected by the initial concentration of the target contaminant. Therefore, proper evaluation should be made by the partition coefficient (PC) concept, which is the ratio of adsorption capacity to its corresponding final contaminant concentration. So far, the reported adsorption experiments have been done on laboratory-scale systems that do not properly represent real-world contaminated sites. Furthermore, these investigations include higher pollutants concentrations that are not environmentally realistic. The majority of the documented investigations studied the adsorption behavior of the adsorbents while employing batch adsorption mode; however, for future research, column-based dynamic operation is required for commercial applications.

Another significant difficulty is analyzing the life cycle of MXenes in the environment and assessing their potentially harmful consequences [160]. MXenes and their derivatives have the potential to harm humans and other living creatures. The principal exposure routes for nanomaterials, like other nanomaterials, might be

through the gastrointestinal system, skin, and respiratory system. Although research on the possible hazardous implications of MXenes is insufficient, recent studies have highlighted concerns about MXenes' potential detrimental effects on the aquatic ecosystem and human beings.

6 Summary

In summary, MXenes have revealed remarkable environmental clean-up applications, especially for the adsorptive sequestration of heavy metal ions, radionuclides metalloids, anions, organic dyes, pharmaceuticals, and gaseous contaminants. More than 30 members of the MXene family have been synthesized to date, with $Ti_3C_2T_x$ being the most intensively studied for water remediation applications. However, over a dozen MXenes are still unexplored for environmental applications and therefore must be explored to understand the adsorptive removal process in different MXenes. The stability of MXene in the presence of water is a critical factor that limits its long-term use of water treatment. Therefore, proper surface modifications are essential to enhance its stability and efficacy for an extended period of application. Similarly, the toxicity and reusability of MXene need to address in detail for viable, practical applications. The adsorption efficiency of MXenes is proven to be highly dependent on their surface functionalities and etching conditions. It can easily bind with numerous pollutants due to the abundance of hydrophilic groups, and hence it is not target selective in its pristine form. However, adequate surface functionalization is necessary for the selective uptake of the contaminant in environmental samples. Furthermore, multifunctional composites of MXenes with various matrices are shown to possess good adsorptive removal of contaminants.

References

1. Vrijheid, M., Casas, M., Gascon, M., Valvi, D., Nieuwenhuijsen, M.: Environmental pollutants and child health—a review of recent concerns. Int. J. Hyg. Environ. Health **219**(4–5), 331–342 (2016)
2. Khin, M.M., Nair, A.S., Babu, V.J., Murugan, R., Ramakrishna, S.: A review on nanomaterials for environmental remediation. Energy Environ. Sci. **5**(8), 8075–8109 (2012)
3. Mahat, S.B., Omar, R., Idris, A., Kamal, S.M.M., Idris, A.I.M.: Dynamic membrane applications in anaerobic and aerobic digestion for industrial wastewater: a mini review. Food Bioprod. Process. **112**, 150–168 (2018)
4. Saleem, M., Bachmann, R.T.: A contemporary review on plant-based coagulants for applications in water treatment. J. Ind. Eng. Chem. **72**, 281–297 (2019)
5. Pendergast, M.M., Hoek, E.M.: A review of water treatment membrane nanotechnologies. Energy Environ. Sci. **4**(6), 1946–1971 (2011)
6. Santhosh, C., Velmurugan, V., Jacob, G., Jeong, S.K., Grace, A.N., Bhatnagar, A.: Role of nanomaterials in water treatment applications: a review. Chem. Eng. J. **306**, 1116–1137 (2016)
7. Jiuhui, Q.: Research progress of novel adsorption processes in water purification: a review. J. Environ. Sci. **20**(1), 1–13 (2008)

8. Spagnoli, A.A., Giannakoudakis, D.A., Bashkova, S.: Adsorption of methylene blue on cashew nut shell based carbons activated with zinc chloride: the role of surface and structural parameters. J. Mol. Liq. **229**, 465–471 (2017)
9. Kemp, K.C., Seema, H., Saleh, M., Le, N.H., Mahesh, K., Chandra, V., et al.: Environmental applications using graphene composites: water remediation and gas adsorption. Nanoscale **5**(8), 3149–3171 (2013)
10. Pendolino, F., Armata, N.: Graphene oxide in environmental remediation process. Springer (2017)
11. Xu, R., Jian, M., Ji, Q., Hu, C., Tang, C., Liu, R., et al.: 2D water-stable zinc-benzimidazole framework nanosheets for ultrafast and selective removal of heavy metals. Chem. Eng. J. **382**, 122658 (2020)
12. Zou, Y., Wang, X., Khan, A., Wang, P., Liu, Y., Alsaedi, A., et al.: Environmental remediation and application of nanoscale zero-valent iron and its composites for the removal of heavy metal ions: a review. Environ. Sci. Technol. **50**(14), 7290–7304 (2016)
13. Biswas, B., Warr, L.N., Hilder, E.F., Goswami, N., Rahman, M.M., Churchman, J.G., et al.: Biocompatible functionalisation of nanoclays for improved environmental remediation. Chem. Soc. Rev. **48**(14), 3740–3770 (2019)
14. Wu, Y., Pang, H., Liu, Y., Wang, X., Yu, S., Fu, D., et al.: Environmental remediation of heavy metal ions by novel-nanomaterials: a review. Environ. Pollut. **246**, 608–620 (2019)
15. Lei, J.-C., Zhang, X., Zhou, Z.: Recent advances in MXene: preparation, properties, and applications. Front. Phys. **10**(3), 276–286 (2015)
16. Xiong, D., Li, X., Bai, Z., Lu, S.: Recent advances in layered Ti3C2Tx MXene for electrochemical energy storage. Small **14**(17), 1703419 (2018)
17. Morales-García, A., Calle-Vallejo, F., Illas, F.: MXenes: new horizons in catalysis. ACS Catal. **10**(22), 13487–13503
18. Jiang, X., Kuklin, A.V., Baev, A., Ge, Y., Ågren, H., Zhang, H., et al.: Two-dimensional MXenes: from morphological to optical, electric, and magnetic properties and applications. Phys. Rep. **848**, 1–58 (2020)
19. Shahzad, F., Alhabeb, M., Hatter, C.B., Anasori, B., Hong, S.M., Koo, C.M., et al.: Electromagnetic interference shielding with 2D transition metal carbides (MXenes). Science **353**(6304), 1137–1140 (2016)
20. Naguib, M., Come, J., Dyatkin, B., Presser, V., Taberna, P.-L., Simon, P., et al.: MXene: a promising transition metal carbide anode for lithium-ion batteries. Electrochem. Commun. **16**(1), 61–64 (2012)
21. Er, D., Li, J., Naguib, M., Gogotsi, Y., Shenoy, V.B.: Ti3C2 MXene as a high capacity electrode material for metal (Li, Na, K, Ca) ion batteries. ACS Appl. Mater. Interfaces. **6**(14), 11173–11179 (2014)
22. Liang, X., Garsuch, A., Nazar, L.F.: Sulfur cathodes based on conductive MXene nanosheets for high-performance lithium–sulfur batteries. Angew. Chem. **127**(13), 3979–3983 (2015)
23. Xu, H., Ren, A., Wu, J., Wang, Z.: Recent advances in 2D MXenes for photodetection. Adv. Func. Mater. **30**(24), 2000907 (2020)
24. Velusamy, D.B., El-Demellawi, J.K., El-Zohry, A.M., Giugni, A., Lopatin, S., Hedhili, M.N., et al.: MXenes for plasmonic photodetection. Adv. Mater. **31**(32), 1807658 (2019)
25. Sinha, A., Zhao, H., Huang, Y., Lu, X., Chen, J., Jain, R.: MXene: an emerging material for sensing and biosensing. TrAC Trends Anal. Chem. **105**, 424–435 (2018)
26. Zhang, Y., Wang, L., Zhang, N., Zhou, Z.: Adsorptive environmental applications of MXene nanomaterials: a review. RSC Adv. **8**(36), 19895–19905 (2018)
27. Naguib, M., Mochalin, V.N., Barsoum, M.W., Gogotsi, Y.: 25th anniversary article: MXenes: a new family of two-dimensional materials. Adv. Mater. **26**(7), 992–1005 (2014)
28. Hu, M., Hu, T., Li, Z., Yang, Y., Cheng, R., Yang, J., et al.: Surface functional groups and interlayer water determine the electrochemical capacitance of Ti3C2 T x MXene. ACS Nano **12**(4), 3578–3586 (2018)
29. Peng, Q., Guo, J., Zhang, Q., Xiang, J., Liu, B., Zhou, A., et al.: Unique lead adsorption behavior of activated hydroxyl group in two-dimensional titanium carbide. J. Am. Chem. Soc. **136**(11), 4113–4116 (2014)

30. Sarycheva, A., Gogotsi, Y.: Raman spectroscopy analysis of the structure and surface chemistry of Ti3C2T x MXene. Chem. Mater. **32**(8), 3480–3488 (2020)
31. Ihsanullah, I.: MXenes (two-dimensional metal carbides) as emerging nanomaterials for water purification: progress, challenges and prospects. Chem. Eng. J. **388**, 124340 (2020)
32. Xie, X., Chen, C., Zhang, N., Tang, Z.-R., Jiang, J., Xu, Y.-J.: Microstructure and surface control of MXene films for water purification. Nat. Sustain. **2**(9), 856–862 (2019)
33. Naguib, M., Mashtalir, O., Carle, J., Presser, V., Lu, J., Hultman, L., et al.: Two-dimensional transition metal carbides. ACS Nano **6**(2), 1322–1331 (2012)
34. Luo, Y., Chen, G.-F., Ding, L., Chen, X., Ding, L.-X., Wang, H.: Efficient electrocatalytic N2 fixation with MXene under ambient conditions. Joule **3**(1), 279–289 (2019)
35. Zhang, P., Wang, L., Huang, Z., Yu, J., Li, Z., Deng, H., et al.: Aryl diazonium-assisted amidoximation of MXene for boosting water stability and uranyl sequestration via electrochemical sorption. ACS Appl. Mater. Interfaces **12**(13), 15579–15587 (2020)
36. Pandey, R.P., Rasool, K., Abdul Rasheed, P., Mahmoud, K.A.: Reductive sequestration of toxic bromate from drinking water using lamellar two-dimensional Ti3C2TX (MXene). ACS Sustain. Chem. Eng. **6**(6), 7910–7917 (2018)
37. Wang, L., Song, H., Yuan, L., Li, Z., Zhang, Y., Gibson, J.K., et al.: Efficient U (VI) reduction and sequestration by Ti2CT x MXene. Environ. Sci. Technol. **52**(18), 10748–10756 (2018)
38. He, F., Zhu, B., Cheng, B., Yu, J., Ho, W., Macyk, W.: 2D/2D/0D TiO2/C3N4/Ti3C2 MXene composite S-scheme photocatalyst with enhanced CO2 reduction activity. Appl. Catal. B **272**, 119006 (2020)
39. Shahzad, A., Rasool, K., Miran, W., Nawaz, M., Jang, J., Mahmoud, K.A., et al.: Two-dimensional Ti3C2T x MXene nanosheets for efficient copper removal from water. ACS Sustain. Chem. Eng. **5**(12), 11481–11488 (2017)
40. Wang, L., Song, H., Yuan, L., Li, Z., Zhang, P., Gibson, J.K., et al.: Effective removal of anionic Re (VII) by surface-modified Ti2CT x MXene nanocomposites: implications for Tc (VII) sequestration. Environ. Sci. Technol. **53**(7), 3739–3747 (2019)
41. Naguib, M., Kurtoglu, M., Presser, V., Lu, J., Niu, J., Heon, M., et al.: Two-dimensional nanocrystals produced by exfoliation of Ti3AlC2. Adv. Mater. **23**(37), 4248–4253 (2011)
42. Guo, J., Peng, Q., Fu, H., Zou, G., Zhang, Q.: Heavy-metal adsorption behavior of two-dimensional alkalization-intercalated MXene by first-principles calculations. J. Phys. Chem. C **119**(36), 20923–20930 (2015)
43. Hwang, S.K., Kang, S.-M., Rethinasabapathy, M., Roh, C., Huh, Y.S.: MXene: an emerging two-dimensional layered material for removal of radioactive pollutants. Chem. Eng. J. 125428 (2020)
44. Sun, Y., Li, Y.: Potential environmental applications of MXenes: a critical review. Chemosphere 129578 (2021)
45. Chen, Y., Liu, C., Guo, S., Mu, T., Wei, L., Lu, Y.: CO2 capture and conversion to value-added products promoted by MXene-based materials. Green Energy Environ. (2020)
46. Jun, B.-M., Heo, J., Taheri-Qazvini, N., Park, C.M., Yoon, Y.: Adsorption of selected dyes on Ti3C2Tx MXene and Al-based metal-organic framework. Ceram. Int. **46**(3), 2960–2968 (2020)
47. Li, S., Wang, L., Peng, J., Zhai, M., Shi, W.: Efficient thorium (IV) removal by two-dimensional Ti2CTx MXene from aqueous solution. Chem. Eng. J. **366**, 192–199 (2019)
48. Jin, L., Chai, L., Yang, W., Wang, H., Zhang, L.: Two-dimensional titanium carbides (Ti3C2Tx) functionalized by poly (m-phenylenediamine) for efficient adsorption and reduction of hexavalent chromium. Int. J. Environ. Res. Public Health **17**(1), 167 (2020)
49. Zhang, G., Wang, T., Xu, Z., Liu, M., Shen, C., Meng, Q.: Synthesis of amino-functionalized Ti 3 C 2 T x MXene by alkalization-grafting modification for efficient lead adsorption. Chem. Commun. **56**(76), 11283–11286 (2020)
50. Wei, Z., Peigen, Z., Wubian, T., Xia, Q., Yamei, Z., ZhengMing, S.: Alkali treated Ti3C2Tx MXenes and their dye adsorption performance. Mater. Chem. Phys. **206**, 270–276 (2018)
51. Vakili, M., Cagnetta, G., Huang, J., Yu, G., Yuan, J.: Synthesis and regeneration of a MXene-based pollutant adsorbent by mechanochemical methods. Molecules **24**(13), 2478 (2019)

52. Jun, B.-M., Kim, S., Rho, H., Park, C.M., Yoon, Y.: Ultrasound-assisted Ti3C2Tx MXene adsorption of dyes: Removal performance and mechanism analyses via dynamic light scattering. Chemosphere **254**, 126827 (2020)
53. Shaheen, S.M., Niazi, N.K., Hassan, N.E., Bibi, I., Wang, H., Tsang, D.C., et al.: Wood-based biochar for the removal of potentially toxic elements in water and wastewater: a critical review. Int. Mater. Rev. **64**(4), 216–247 (2019)
54. Kumar, A., MMS, C.-P., Chaturvedi, A.K., Shabnam, A.A., Subrahmanyam, G., Mondal, R. et al.: Lead toxicity: health hazards, influence on food chain, and sustainable remediation approaches. Int. J. Environ. Res. Public Health **17**(7), 2179 (2020)
55. Duruibe, J.O., Ogwuegbu, M., Egwurugwu, J.: Heavy metal pollution and human biotoxic effects. Int. J. Phys. Sci. **2**(5), 112–118 (2007)
56. Guo, J., Fu, H., Zou, G., Zhang, Q., Zhang, Z., Peng, Q.: Theoretical interpretation on lead adsorption behavior of new two-dimensional transition metal carbides and nitrides. J. Alloy. Compd. **684**, 504–509 (2016)
57. Wang, S., Liu, Y., Lü, Q.-F., Zhuang, H.: Facile preparation of biosurfactant-functionalized Ti2CTX MXene nanosheets with an enhanced adsorption performance for Pb (II) ions. J. Mol. Liq. **297**, 111810 (2020)
58. Gu, P., Zhang, S., Zhang, C., Wang, X., Khan, A., Wen, T., et al.: Two-dimensional MAX-derived titanate nanostructures for efficient removal of Pb (II). Dalton Trans. **48**(6), 2100–2107 (2019)
59. Pirrone, N., Cinnirella, S., Feng, X., Finkelman, R.B., Friedli, H.R., Leaner, J., et al.: Global mercury emissions to the atmosphere from anthropogenic and natural sources. Atmos. Chem. Phys. **10**(13), 5951–5964 (2010)
60. Outridge, P.M., Mason, R., Wang, F., Guerrero, S., Heimburger-Boavida, L.: Updated global and oceanic mercury budgets for the United Nations Global Mercury Assessment 2018. Environ. Sci. Technol. **52**(20), 11466–11477 (2018)
61. Shahzad, A., Rasool, K., Miran, W., Nawaz, M., Jang, J., Mahmoud, K.A., et al.: Mercuric ion capturing by recoverable titanium carbide magnetic nanocomposite. J. Hazard. Mater. **344**, 811–818 (2018)
62. Shahzad, A., Nawaz, M., Moztahida, M., Jang, J., Tahir, K., Kim, J., et al.: Ti3C2Tx MXene core-shell spheres for ultrahigh removal of mercuric ions. Chem. Eng. J. **368**, 400–408 (2019)
63. Gan, D., Huang, Q., Dou, J., Huang, H., Chen, J., Liu, M., et al.: Bioinspired functionalization of MXenes (Ti3C2TX) with amino acids for efficient removal of heavy metal ions. Appl. Surf. Sci. **504**, 144603 (2020)
64. Shahzad, A., Nawaz, M., Moztahida, M., Tahir, K., Kim, J., Lim, Y., et al.: Exfoliation of titanium aluminum carbide (211 MAX phase) to form nanofibers and two-dimensional nanosheets and their application in aqueous-phase cadmium sequestration. ACS Appl. Mater. Interfaces **11**(21), 19156–19166 (2019)
65. Al-Saydeh, S.A., El-Naas, M.H., Zaidi, S.J.: Copper removal from industrial wastewater: a comprehensive review. J. Ind. Eng. Chem. **56**, 35–44 (2017)
66. Godt, J., Scheidig, F., Grosse-Siestrup, C., Esche, V., Brandenburg, P., Reich, A., et al.: The toxicity of cadmium and resulting hazards for human health. J. Occup. Med. Toxicol. **1**(1), 1–6 (2006)
67. Awual, M.R.: A facile composite material for enhanced cadmium (II) ion capturing from wastewater. J. Environ. Chem. Eng. **7**(5), 103378 (2019)
68. Elumalai, S., Yoshimura, M., Ogawa, M.: Simultaneous delamination and rutile formation on the surface of Ti3C2Tx MXene for copper adsorption. Chem. Asian J. **15**(7), 1044–1051 (2020)
69. Wang, L., Yuan, L., Chen, K., Zhang, Y., Deng, Q., Du, S., et al.: Loading actinides in multilayered structures for nuclear waste treatment: the first case study of uranium capture with vanadium carbide MXene. ACS Appl. Mater. Interfaces **8**(25), 16396–16403 (2016)
70. Zhang, Y.-J., Lan, J.-H., Wang, L., Wu, Q.-Y., Wang, C.-Z., Bo, T., et al.: Adsorption of uranyl species on hydroxylated titanium carbide nanosheet: a first-principles study. J. Hazard. Mater. **308**, 402–410 (2016)

71. Zhang, C.J., Pinilla, S., McEvoy, N., Cullen, C.P., Anasori, B., Long, E. et al.: Oxidation stability of colloidal two-dimensional titanium carbides (MXenes) **29**(11), 4848–4856 (2017)
72. Wang, L., Tao, W., Yuan, L., Liu, Z., Huang, Q., Chai, Z., et al.: Rational control of the interlayer space inside two-dimensional titanium carbides for highly efficient uranium removal and imprisonment. Chem. Commun. **53**(89), 12084–12087 (2017)
73. Wang, S., Wang, L., Li, Z., Zhang, P., Du, K., Yuan, L., et al.: Highly efficient adsorption and immobilization of U (VI) from aqueous solution by alkalized MXene-supported nanoscale zero-valent iron. J. Hazard. Mater. **408**, 124949 (2021)
74. Zhang, P., Wang, L., Du, K., Wang, S., Huang, Z., Yuan, L., et al.: Effective removal of U (VI) and Eu (III) by carboxyl functionalized MXene nanosheets. J. Hazard. Mater. **396**, 122731 (2020)
75. Fakhru'l-Razi, A., Pendashteh, A., Abdullah, L.C., Biak, D.R.A., Madaeni, S.S., Abidin, Z.Z.: Review of technologies for oil and gas produced water treatment. J. Hazard. Mater. **170**(2–3), 530–551 (2009)
76. Fard, A.K., Mckay, G., Chamoun, R., Rhadfi, T., Preud'Homme, H., Atieh, M.A.: Barium removal from synthetic natural and produced water using MXene as two dimensional (2-D) nanosheet adsorbent. Chem. Eng. J. **317**, 331–342 (2017)
77. Mu, W., Du, S., Yu, Q., Li, X., Wei, H., Yang, Y.: Improving barium ion adsorption on two-dimensional titanium carbide by surface modification. Dalton Trans. **47**(25), 8375–8381 (2018)
78. Jun, B.-M., Park, C.M., Heo, J., Yoon, Y.: Adsorption of Ba2+ and Sr2+ on Ti3C2Tx MXene in model fracking wastewater. J. Environ. Manag. **256**, 109940 (2020)
79. Khan, A.R., Husnain, S.M., Shahzad, F., Mujtaba-ul-Hassan, S., Mehmood, M., Ahmad, J., et al.: Two-dimensional transition metal carbide (Ti 3 C 2 T x) as an efficient adsorbent to remove cesium (Cs+). Dalton Trans. **48**(31), 11803–11812 (2019)
80. Zhang, P., Wang, L., Yuan, L.-Y., Lan, J.-H., Chai, Z.-F., Shi, W.-Q.: Sorption of Eu (III) on MXene-derived titanate structures: The effect of nano-confined space. Chem. Eng. J. **370**, 1200–1209 (2019)
81. Aziman, E.S., Mohd Salehuddin, A.H.J., Ismail, A.F.: Remediation of thorium (IV) from wastewater: Current status and way forward. Sep. Purif. Rev. **50**(2), 177–202 (2021)
82. Mu, W., Du, S., Li, X., Yu, Q., Wei, H., Yang, Y., et al.: Removal of radioactive palladium based on novel 2D titanium carbides. Chem. Eng. J. **358**, 283–290 (2019)
83. Khandaker, S., Chowdhury, M.F., Awual, M.R., Islam, A., Kuba, T.: Efficient cesium encapsulation from contaminated water by cellulosic biomass based activated wood charcoal. Chemosphere **262**, 127801 (2021)
84. Jun, B.-M., Jang, M., Park, C.M., Han, J., Yoon, Y.: Selective adsorption of Cs+ by MXene (Ti3C2Tx) from model low-level radioactive wastewater. Nucl. Eng. Technol. **52**(6), 1201–1207 (2020)
85. Laguel, S., Samar, M.H.: Removal of Europium (III) from water by emulsion liquid membrane using Cyanex 302 as a carrier. Desalin Water Treat. **165**, 269–280 (2019)
86. Tang, N., Liang, J., Niu, C., Wang, H., Luo, Y., Xing, W. et al. Amidoxime-based materials for uranium recovery and removal. **8**(16) 7588–7625 (2020)
87. Jun, B.-M., Her, N., Park, C.M., Yoon, Y.: Effective removal of Pb (ii) from synthetic wastewater using Ti 3 C 2 T x MXene. Environ. Sci. Water Res. Technol. **6**(1), 173–180 (2020)
88. Du, Y., Yu, B., Wei, L., Wang, Y., Zhang, X., Ye, S.: Efficient removal of Pb (II) by Ti 3 C 2 T x powder modified with a silane coupling agent. J. Mater. Sci. **54**(20), 13283–13297 (2019)
89. Shahzad, A., Rasool, K., Miran, W., Nawaz, M., Jang, J., Mahmoud, K. et al.: ACS Sustain. Chem. Eng. **5**, 11481–11488 (2017)
90. Zou, G., Guo, J., Peng, Q., Zhou, A., Zhang, Q., Liu, B.: Synthesis of urchin-like rutile titania carbon nanocomposites by iron-facilitated phase transformation of MXene for environmental remediation. J. Mater. Chem. A **4**(2), 489–499 (2016)
91. Karthikeyan, P., Ramkumar, K., Pandi, K., Fayyaz, A., Meenakshi, S., Park, C.M.: Effective removal of Cr (VI) and methyl orange from the aqueous environment using two-dimensional (2D) Ti3C2Tx MXene nanosheets. Ceram. Int. **47**(3), 3692–3698 (2021)

92. Tang, Y., Yang, C., Que, W.: A novel two-dimensional accordion-like titanium carbide (MXene) for adsorption of Cr (VI) from aqueous solution. J. Adv. Dielectr. **8**(05), 1850035 (2018)
93. Ying, Y., Liu, Y., Wang, X., Mao, Y., Cao, W., Hu, P., et al.: Two-dimensional titanium carbide for efficiently reductive removal of highly toxic chromium (VI) from water. ACS Appl. Mater. Interfaces **7**(3), 1795–1803 (2015)
94. He, L., Huang, D., He, Z., Yang, X., Yue, G., Zhu, J., et al.: Nanoscale zero-valent iron intercalated 2D titanium carbides for removal of Cr (VI) in aqueous solution and the mechanistic aspect. J. Hazard. Mater. **388**, 121761 (2020)
95. Wang, H., Cui, H., Song, X., Xu, R., Wei, N., Tian, J., et al.: Facile synthesis of heterojunction of MXenes/TiO2 nanoparticles towards enhanced hexavalent chromium removal. J. Colloid Interface Sci. **561**, 46–57 (2020)
96. Zhang, H., Li, M., Zhu, C., Tang, Q., Kang, P., Cao, J.: Preparation of magnetic α-Fe2O3/ZnFe2O4@ Ti3C2 MXene with excellent photocatalytic performance. Ceram. Int. **46**(1), 81–88 (2020)
97. Kong, A., Sun, Y., Peng, M., Gu, H., Fu, Y., Zhang, J., et al.: Amino-functionalized MXenes for efficient removal of Cr (VI). Colloids Surf. A **617**, 126388 (2021)
98. Yang, G., Hu, X., Liang, J., Huang, Q., Dou, J., Tian, J., et al.: Surface functionalization of MXene with chitosan through in-situ formation of polyimidazoles and its adsorption properties. J. Hazard. Mater. 126220 (2021)
99. Khan, A.R., Awan, S.K., Husnain, S.M., Abbas, N., Anjum, D.H., Abbas, N., et al.: 3D Flower like δ-MnO2/MXene Nano-Hybrids for the Removal of Hexavalent Cr from Wastewater. Ceramics International (2021)
100. Tkaczyk, A., Mitrowska, K., Posyniak, A.: Synthetic organic dyes as contaminants of the aquatic environment and their implications for ecosystems: a review. Sci. Total Environ. **717**, 137222 (2020)
101. Mashtalir, O., Cook, K.M., Mochalin, V.N., Crowe, M., Barsoum, M.W., Gogotsi, Y.: Dye adsorption and decomposition on two-dimensional titanium carbide in aqueous media. J. Mater. Chem. A **2**(35), 14334–14338 (2014)
102. Zhang, P., Xiang, M., Liu, H., Yang, C., Deng, S.: Novel two-dimensional magnetic titanium carbide for methylene blue removal over a wide pH range: insight into removal performance and mechanism. ACS Appl. Mater. Interfaces. **11**(27), 24027–24036 (2019)
103. Lei, Y., Cui, Y., Huang, Q., Dou, J., Gan, D., Deng, F., et al.: Facile preparation of sulfonic groups functionalized Mxenes for efficient removal of methylene blue. Ceram. Int. **45**(14), 17653–17661 (2019)
104. Zhu, Z., Xiang, M., Shan, L., He, T., Zhang, P.: Effect of temperature on methylene blue removal with novel 2D-Magnetism titanium carbide. J. Solid State Chem. **280**, 120989 (2019)
105. Peng, C., Wei, P., Chen, X., Zhang, Y., Zhu, F., Cao, Y., et al.: A hydrothermal etching route to synthesis of 2D MXene (Ti3C2, Nb2C): enhanced exfoliation and improved adsorption performance. Ceram. Int. **44**(15), 18886–18893 (2018)
106. Sun, Y., Xu, D., Li, S., Cui, L., Zhuang, Y., Xing, W., et al.: Assembly of multidimensional MXene-carbon nanotube ultrathin membranes with an enhanced anti-swelling property for water purification. J. Membr. Sci. **623**, 119075 (2021)
107. Tran, N.M., Ta, Q.T.H., Sreedhar, A., Noh, J.-S.: Ti3C2Tx MXene playing as a strong methylene blue adsorbent in wastewater. Appl. Surf. Sci. **537**, 148006 (2021)
108. Yao, C., Zhang, W., Xu, L., Cheng, M., Su, Y., Xue, J., et al.: A facile synthesis of porous MXene-based freestanding film and its spectacular electrosorption performance for organic dyes. Sep. Purif. Technol. **263**, 118365 (2021)
109. Zhang, Z.-H., Xu, J.-Y., Yang, X.-L.: MXene/sodium alginate gel beads for adsorption of methylene blue. Mater. Chem. Phys. **260**, 124123 (2021)
110. Tong, X., Liu, S., Qu, D., Gao, H., Yan, L., Chen, Y., et al.: Tannic acid-metal complex modified MXene membrane for contaminants removal from water. J. Membr. Sci. **622**, 119042 (2021)
111. Quyen, V.T., Thanh, D.M., Van Le, Q., Viet, N.M., Nham, N.T., Thang, P.Q.: Advanced synthesis of MXene-derived nanoflower-shaped TiO2@ Ti3C2 heterojunction to enhance photocatalytic degradation of Rhodamine B. Environ. Technol. Innov. **21**, 101286 (2021)

112. Vigneshwaran, S., Park, C.M., Meenakshi, S.: Designed fabrication of sulfide-rich bi-metallic-assembled MXene layered sheets with dramatically enhanced photocatalytic performance for Rhodamine B removal. Sep. Purif. Technol. **258**, 118003 (2021)
113. Luo, S., Wang, R., Yin, J., Jiao, T., Chen, K., Zou, G., et al.: Preparation and dye degradation performances of self-assembled MXene-Co3O4 nanocomposites synthesized via solvothermal approach. ACS Omega **4**(2), 3946–3953 (2019)
114. Zheng, H., Meng, X., Chen, J., Que, M., Wang, W., Liu, X., et al.: In situ phase evolution of TiO2/Ti3C2Tx heterojunction for enhancing adsorption and photocatalytic degradation. Appl. Surf. Sci. **545**, 149031 (2021)
115. Kim, S., Yu, M., Yoon, Y.: Fouling and retention mechanisms of selected cationic and anionic dyes in a Ti3C2T x MXene-ultrafiltration hybrid system. ACS Appl. Mater. Interfaces. **12**(14), 16557–16565 (2020)
116. Cai, C., Wang, R., Liu, S., Yan, X., Zhang, L., Wang, M., et al.: Synthesis of self-assembled phytic acid-MXene nanocomposites via a facile hydrothermal approach with elevated dye adsorption capacities. Colloids Surf. A **589**, 124468 (2020)
117. Lei, H., Hao, Z., Chen, K., Chen, Y., Zhang, J., Hu, Z., et al.: Insight into adsorption performance and mechanism on efficient removal of methylene blue by accordion-like V2CT x MXene. J. Phys. Chem. Lett. **11**(11), 4253–4260 (2020)
118. Stone, V.: Environmental air pollution. Am. J. Respir. Crit. care Med. **162**(supplement_1), S44-S7 (2000)
119. Khan, N.A., Hasan, Z., Jhung, S.H.: Adsorptive removal of hazardous materials using metal-organic frameworks (MOFs): a review. J. Hazard. Mater. **244**, 444–456 (2013)
120. Gopinath, K.P., Vo, D.-V.N., Prakash, D.G., Joseph, A.A., Viswanathan, S., Arun, J.: Environmental applications of carbon-based materials: a review. Environ. Chem. Lett. 1–26 (2020)
121. Persson, I., Halim, J., Lind, H., Hansen, T.W., Wagner, J.B., Näslund, L.Å., et al.: 2D transition metal carbides (MXenes) for carbon capture. Adv. Mater. **31**(2), 1805472 (2019)
122. Morales-García, Á., Fernández-Fernández, A., Viñes, F., Illas, F.: CO 2 abatement using two-dimensional MXene carbides. J. Mater. Chem. A **6**(8), 3381–3385 (2018)
123. Guo, Z., Li, Y., Sa, B., Fang, Y., Lin, J., Huang, Y., et al.: M2C-type MXenes: promising catalysts for CO2 capture and reduction. Appl. Surf. Sci. **521**, 146436 (2020)
124. Wang, B., Zhou, A., Liu, F., Cao, J., Wang, L., Hu, Q.: Carbon dioxide adsorption of two-dimensional carbide MXenes. J. Adv. Ceram. **7**(3), 237–245 (2018)
125. Morales-García, Á., Mayans-Llorach, M., Viñes, F., Illas, F.: Thickness biased capture of CO2 on carbide MXenes. Phys. Chem. Chem. Phys. **21**(41), 23136–23142 (2019)
126. Khaledialidusti, R., Mishra, A.K., Barnoush, A.: Atomic defects in monolayer ordered double transition metal carbide (Mo 2 TiC 2 T x) MXene and CO 2 adsorption. J. Mater. Chem. C **8**(14), 4771–4779 (2020)
127. Shamsabadi, A.A., Isfahani, A.P., Salestan, S.K., Rahimpour, A., Ghalei, B., Sivaniah, E., et al.: Pushing rubbery polymer membranes to be economic for CO2 separation: embedment with Ti3C2T x MXene nanosheets. ACS Appl. Mater. Interfaces **12**(3), 3984–3992 (2019)
128. Yu, X.-f, Li, Y.-c, Cheng, J.-b, Liu, Z.-b, Li, Q.-z, Li, W.-z, et al.: Monolayer Ti2CO2: a promising candidate for NH3 sensor or capturer with high sensitivity and selectivity. ACS Appl. Mater. Interfaces **7**(24), 13707–13713 (2015)
129. Ma, S., Yuan, D., Jiao, Z., Wang, T., Dai, X.: Monolayer Sc2CO2: a promising candidate as a SO2 gas sensor or capturer. J. Phys. Chem. C **121**(43), 24077–24084 (2017)
130. Park, K.H., Kim, S., Hwang, H., Hwang, M.-J., Song, S.H., Shim, W.-G., et al.: Ti3C2T x MXene-based three-dimensional architecture for carbon dioxide capture. J. Nanosci. Nanotechnol. **21**(9), 4902–4907 (2021)
131. Lin, H., Gong, K., Hykys, P., Chen, D., Ying, W., Sofer, Z., et al.: Nanoconfined deep eutectic solvent in laminated MXene for efficient CO2 separation. Chem. Eng. J. **405**, 126961 (2021)
132. Lee, S.H., Eom, W., Shin, H., Ambade, R.B., Bang, J.H., Kim, H.W., et al.: Room-temperature, highly durable Ti3C2T x MXene/graphene hybrid fibers for NH3 gas sensing. ACS Appl. Mater. Interfaces **12**(9), 10434–10442 (2020)

133. Jin, Z., Liu, C., Liu, Z., Han, J., Fang, Y., Han, Y., et al.: Rational design of hydroxyl-rich Ti3C2Tx MXene quantum dots for high-performance electrochemical N2 reduction. Adv. Energy Mater. **10**(22), 2000797 (2020)
134. Zheng, S., Li, S., Mei, Z., Hu, Z., Chu, M., Liu, J., et al.: Electrochemical nitrogen reduction reaction performance of single-boron catalysts tuned by MXene substrates. J. Phys. Chem. Lett. **10**(22), 6984–6989 (2019)
135. Qin, J., Hu, X., Li, X., Yin, Z., Liu, B., Lam, K.-H.: 0D/2D AgInS2/MXene Z-scheme heterojunction nanosheets for improved ammonia photosynthesis of N2. Nano Energy **61**, 27–35 (2019).
136. Liu, D., Zhang, G., Ji, Q., Zhang, Y., Li, J.: Synergistic electrocatalytic nitrogen reduction enabled by confinement of nanosized Au particles onto a two-dimensional Ti3C2 substrate. ACS Appl. Mater. Interfaces **11**(29), 25758–25765 (2019)
137. Cheng, Y., Dai, J., Song, Y., Zhang, Y.: Single molybdenum atom anchored on 2D Ti 2 NO 2 MXene as a promising electrocatalyst for N 2 fixation. Nanoscale **11**(39), 18132–18141 (2019)
138. Xu, X., Sun, B., Liang, Z., Cui, H., Tian, J.: High-performance electrocatalytic conversion of N2 to NH3 using 1T-MoS2 anchored on Ti3C2 MXene under ambient conditions. ACS Appl. Mater. Interfaces **12**(23), 26060–26067 (2020)
139. Kim, S.J., Koh, H.-J., Ren, C.E., Kwon, O., Maleski, K., Cho, S.-Y., et al.: Metallic Ti3C2T x MXene gas sensors with ultrahigh signal-to-noise ratio. ACS Nano **12**(2), 986–993 (2018)
140. Hu, X., Wang, Y., Ling, Z., Song, H., Cai, Y., Li, Z., et al.: Ternary g-C3N4/TiO2/Ti3C2 MXene S-scheme heterojunction photocatalysts for NOx removal under visible light. Appl. Surf. Sci. **556**, 149817 (2021)
141. Lee, E., VahidMohammadi, A., Prorok, B.C., Yoon, Y.S., Beidaghi, M., Kim, D.-J.: Room temperature gas sensing of two-dimensional titanium carbide (MXene). ACS Appl. Mater. Interfaces **9**(42), 37184–37190 (2017)
142. Lee, E., VahidMohammadi, A., Yoon, Y.S., Beidaghi, M., Kim, D.-J.: Two-dimensional vanadium carbide MXene for gas sensors with ultrahigh sensitivity toward nonpolar gases. ACS Sens. **4**(6), 1603–1611 (2019)
143. Mehdi Aghaei, S., Aasi, A., Panchapakesan, B.: Experimental and theoretical advances in MXene-based gas sensors. ACS Omega **6**(4), 2450–2461 (2021)
144. Zhao, D., Chen, Z., Yang, W., Liu, S., Zhang, X., Yu, Y., et al.: MXene (Ti3C2) vacancy-confined single-atom catalyst for efficient functionalization of CO2. J. Am. Chem. Soc. **141**(9), 4086–4093 (2019)
145. Khan, A.A., Tahir, M.: Well-designed 2D/2D Ti3C2TA/R MXene coupled g-C3N4 heterojunction with in-situ growth of anatase/rutile TiO2 nucleates to boost photocatalytic dry-reforming of methane (DRM) for syngas production under visible light. Appl. Catal. B **285**, 119777 (2021)
146. Ojovan, M., Lee, W.: Nuclear waste disposal. An introduction to nuclear waste immobilisation, 2nd edn. Elsevier, Amsterdam, Netherlands (2014)
147. Koťátková, J., Zatloukal, J., Reiterman, P., Kolář, K.: Concrete and cement composites used for radioactive waste deposition. J. Environ. Radioact. **178**, 147–155 (2017)
148. Ojovan, M., Lee, W., Kalmykov, S.: Immobilisation of radioactive waste in cement. In: An Introduction to Nuclear Waste Immobilisation, pp. 179–200 (2005)
149. Prasad, M., Saxena, S.: Sorption mechanism of some divalent metal ions onto low-cost mineral adsorbent. Ind. Eng. Chem. Res. **43**(6), 1512–1522 (2004)
150. Zhang, Y., Wang. A.L., Zhanga, B.N., Zhoua, Z.: Adsorptive environmental applications of MXene nanomaterials: a review. Rsc Adv. **8**(36):19895–19905 (2018)
151. Zamorani, E.: Deeds and misdeeds of cement composites in waste management. Cem. Concr. Res. **22**(2–3), 359–367 (1992)
152. ul Hassan, M., Iqbal, S., Yun, J.-I., Ryu, H.J.: Immobilization of radioactive corrosion products by cold sintering of pure hydroxyapatite. J. Hazard. Mater. **374**, 228–237 (2019)
153. ul Hassan, M., Venkatesan, S., Ryu, H.J.: Non-volatile immobilization of iodine by the cold-sintering of iodosodalite. J. Hazard. Mater. **386**, 121646 (2020)

154. Venkatesan, S., ul Hassan, M.., Ryu, H.J.: Adsorption and immobilization of radioactive ionic-corrosion-products using magnetic hydroxyapatite and cold-sintering for nuclear waste management applications. J. Nucl. Mater. **514**, 40–49 (2019).
155. ul Hassan, M., Lee, S., Mehran, M.T., Shahzad, F., Husnain, S.M., Ryu, H.J.: Post-decontamination treatment of MXene after adsorbing Cs from contaminated water with the enhanced thermal stability to form a stable radioactive waste matrix. J. Nucl. Mater. **543**, 152566 (2021)
156. Xiong, D., Li, X., Bai, Z., Lu, S.J.S.: Recent advances in layered Ti3C2Tx MXene for electrochemical energy storage. **14**(17), 1703419 (2018)
157. Pang, J., Mendes, R.G., Bachmatiuk, A., Zhao, L., Ta, H.Q., Gemming, T., et al. : Applications of 2D MXenes in energy conversion and storage systems. **48**(1), 72–133 (2019)
158. Tunesi, M.M., Soomro, R.A., Han, X., Zhu, Q., Wei, Y., Xu, B.J.N.C.: Application of MXenes in environmental remediation technologies **8**(1), 1–19 (2021)
159. Iqbal, A., Sambyal, P., Koo, C.M.J.A.F.M.: 2D MXenes for electromagnetic shielding: a review. **30**(47), 2000883 (2020)
160. Ihsanullah, I., Ali HJC SiC, Engineering E Technological challenges in the environmental applications of MXenes and future outlook. 2 100034 (2020)
161. Naguib, M., Barsoum, M.W., Gogotsi, Y.J.A.M.: Ten years of progress in the synthesis and development of MXenes **33**(39), 2103393 (2021)
162. Seredych, M., Shuck, C.E., Pinto, D., Alhabeb, M., Precetti, E., Deysher, G. et al.: High-temperature behavior and surface chemistry of carbide MXenes studied by thermal analysis **31**(9), 3324–3332 (2019)
163. Zhang, Z., He, Y., Lv, Y., Zhang, L., Chen, X., Wu, Z., et al.: Effect of surface structure and composition on the electromagnetic properties of Ti3C2T x MXenes for highly efficient electromagnetic wave absorption **124**(36), 19666–19674 (2020).

MXenes for Electromagnetic Interference (EMI) Shielding

Chang Ma, Qi Yuan, and Ming-Guo Ma

Abstract With the rapid advancement of science and technology, mobile devices are becoming increasingly popular among people, accompanied by an increase in the severity of electromagnetic (EM) radiation pollution. Recently, MXene, as a new-born family of two-dimensional nanomaterials, has been applied in energy conversion, energy storage, sensors, catalysis, medical therapy, and electromagnetic interference (EMI) shielding and other fields due to its outstanding conductivity, hydrophilicity, tunable surface chemistry, large specific area, and high photothermal effect. Since the first report on EMI shielding of $Ti_3C_2T_x$ in 2016, numerous works have been devoted to designing MXene-based EMI shielding materials. This chapter aims at highlighting the recent trends and advancements in this area. In the chapter, we introduce the EMI, discuss the mechanism of EMI shielding, present the characteristics of MXene-based EMI shielding materials, review the role of carbides and nitrides in EMI shielding and finally provide an insight into future works. In addition, this chapter provides an overview of different advanced materials, devices, and futuristic applications of MXenes for EMI shielding.

Keywords MXenes · Carbides · Nitrides · Electromagnetic interference · EMI shielding

1 Introduction

In recent years, the development and innovation of technology and large-scale implementations of electronic equipment enable electromagnetic (EM) pollution to become a universal and severe problem [1, 2]. Researchers have even found that excessive exposure to EM waves may lead to many serious sequences for the human body, such as adverse effects on brain development and cancerization [3–5]. An EM wave contains both electric and magnetic fields [1]. Based on Maxwell's EM field

C. Ma · Q. Yuan · M.-G. Ma (✉)
Research Center of Biomass Clean Utilization, Engineering Research Center of Forestry Biomass Materials and Bioenergy, Beijing Key Laboratory of Lignocellulosic Chemistry, College of Materials Science and Technology, Beijing Forestry University, Beijing 100083, PR, China
e-mail: mg_ma@bjfu.edu.cn

M. Khalid et al. (eds.), *Fundamental Aspects and Perspectives of MXenes*, Engineering Materials, https://doi.org/10.1007/978-3-031-05006-0_9

theory, they are closely related. The electric field, magnetic field, and the propagation direction of EM waves are perpendicular to each other [6]. EM waves can be classified according to their frequency as gamma rays, X-rays, visible light, microwave (MW), radio waves, etc., [4]. EMI is a form of EM pollution that results either from the natural environment (like cosmic noise, atmospheric noise, solar flare, and thunder) or artificial devices (like radar, radio, navigation) [7, 8]. Another worrisome electromagnetic interference (EMI) is from the nuclear device [9]. EMI is no longer a new concept, which significantly influences almost all sorts of domains, including military instrument operation, electrommunications, medical devices, and so on [7]. Therefore, to avoid these serious problems, a phenomenon called EMI shielding involves the process of reflection and/or absorption causing. The EMI shielding materials with conductivity can play a role of a shield to protect the organisms or devices from harmful EM radiations to a certain extent. Thus, EMI shielding materials are significant to the environment, human body, and industry [8, 10]. The shielding effectiveness (SE) depends on the conductivity, thickness, and structure of materials [1, 4, 7]. In view of the outstanding conductivity, first-generation EMI shielding materials are pure metals (like copper, aluminum or nickel, stainless steel, etc.), possessing outstanding EMI SE. However, they are restricted by high cost, large density, poor flexibility, and susceptibility to corrosion [4].

MXenes (denoted as $M_{n+1}X_nT_x$, where M is an early transition metal, X is C and/or N, and T_x is terminating groups), as a newly blooming nanomaterial family, have drawn much attention lately thanks to their 2D layered structure, outstanding conductivity, and gifted hydrophily [11, 12]. Since Gogotsi and his co-workers developed the few-layered $Ti_3C_2T_x$ in 2012 [13], MXenes have been applied to such fields as supercapacitors [14–16], batteries [17–19], sensors [20–22], actuators [23, 24], nanogenerators [25–27], heaters [28] and so on [29]. In 2016, Shahzad et al. [30] published that MXene membrane was used for EMI shielding firstly with desirable EMI SE of 92 dB, which is a huge breakthrough for EMI shielding of MXenes. Therefore, MXene-based EMI shielding materials have become a new research hotspot, and the progress brings EMI shielding materials a new developing chance [31].

This chapter will introduce the EMI, discuss the EMI shielding mechanism, present the performances of MXene-based EMI shielding materials, review the role of carbides and nitrides in EMI shielding, and finally provide an insight into future works.

2 Electromagnetic Interference

Nowadays, the EM pollution produced by different electronic devices has spread all over the lives of modern people, as shown in Fig. 1. The pollution caused by EM radiation everywhere is difficult to detect and extremely hidden but far-reaching, so it must be strictly controlled [1, 32, 33]. EMI generated by EM waves can degrade or hinder the effective operation of nearby electronic equipment (and/or components). Under the current development trend, more complex electronic systems lead to a sharp

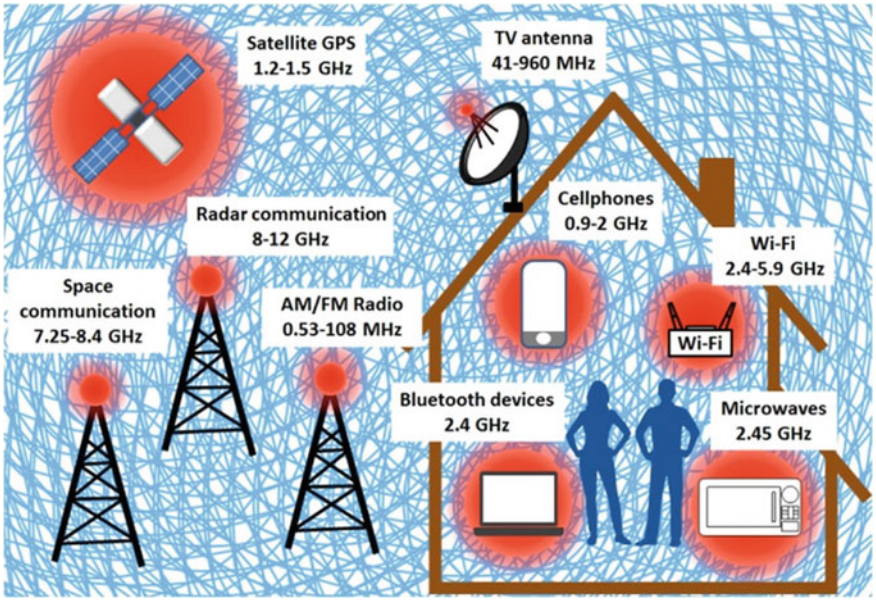

Fig. 1 Diagram of the modern people surrounded by EM pollution. Adapted with permission [40]. Copyright 2019, Elsevier Ltd

increase in EMI pollution. For example, in order to achieve rapid response and miniaturization, the packaging density of electronic devices is getting higher and higher. As a result, electronic equipment with high power, fast operation, small size, and easy to carry will emit diversified EM waves to the surrounding environment, affecting the electronic system in the precision electronic equipment, thereby reducing the efficiency and utilization of the equipment, and even causing system crashes, equipment damage, and failure [34]. The failure of electronic and electrical equipment caused by EMI occurs every year globally and causes severe economic losses. In addition, EM radiation pollution has a significant impact on the national defense industry, and countermeasures based on EM radiation have played an important role in modern warfare.

EM radiation pollution can also cause various diseases and threaten human health by disrupting the normal function of the human life system [35]. For example, after prolonged exposure to excessive EM radiation, the human body usually exhibits the nervous system's problems such as headaches, memory loss, difficulty sleeping, serious brain tumors, and other brain disorders [36, 37]. Furthermore, long-term exposure to high-dose microwave radiation can disrupt the body's immune system. EM wave pollution will also affect the normal physiological functions of higher organisms, triggering gene mutations and causing offspring deformation [38]. Therefore, even if someone is exposed to low-power or low-frequency high-energy EM waves for a long time, they should be aware of the potential danger.

Since all kinds of information are mainly transmitted in the form of EM waves, EM wave leakage is a significant problem for computers and their network systems. Once the EM waves carrying important information are leaked out, they can be captured and interpreted by highly sensitive instruments. Whether it is a country, an enterprise, or an individual, all face the potential danger of information leakage. Therefore, preventing EMI and ensuring the safe transmission of information is an important issue that needs to be solved urgently today [39].

3 EMI Shielding

3.1 EMI Shielding Mechanism

When a beam of incoming EM wave strikes the EMI shielding material, it interacts with the surface, mainly reflection, absorption, and multiple reflections (Fig. 2) [38]. The original interaction is the reflection of EM waves. The intrinsic impedance of shielding material is significantly different from that of the medium in which EM waves are propagated, and conductive materials with mobile charge carriers (electrons and holes) are good reflectors of EM waves [7]. Therefore, the conductivity (σ) of material is one of the significant indexes to evaluate its reflection performance for shielding. As a result, the discontinuity at the interface is essential rather

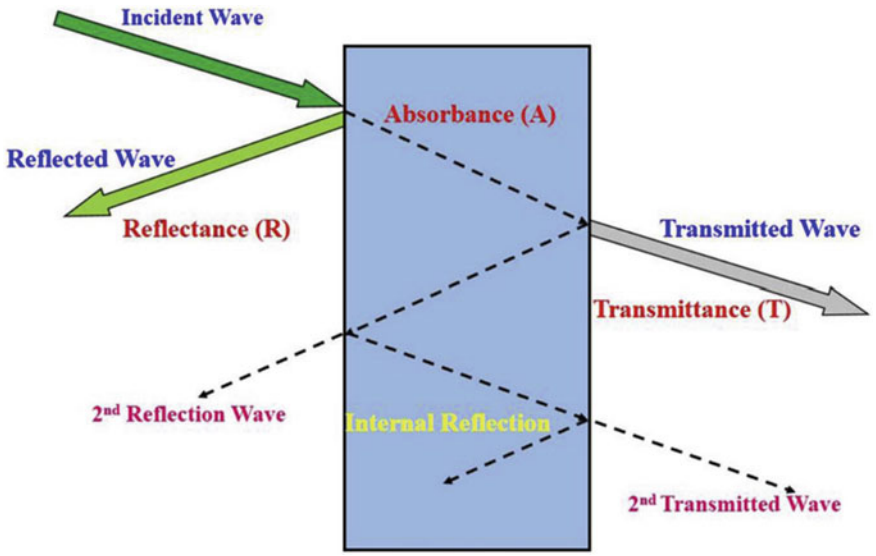

Fig. 2 Diagram of various mechanisms of EMI shielding. Adapted with permission [2]. Copyright 2018, Elsevier Ltd

than the thickness in reflection for shielding material [41, 42]. The remaining EM waves enter the materials, undergoing another important interaction process, absorption. The absorption occurs if electric and/or magnetic dipoles are present in the shielding materials. Furthermore, the absorption loss was found to be proportional to the thickness. When the EM waves encounter another surface or interface within the shielding material, some will undergo multiple internal reflections. Therefore, shielding materials with larger surface or interface areas like foam and aerogel are preferable for internal reflection. EM waves that travel through the EMI shielding material and cannot be sufficiently attenuated from any of the above mechanisms are called transmitted waves. According to the shielding mechanism mentioned earlier, EMI shielding materials are generally grouped into reflection-predominant and absorption-predominant.

The SE represents the ability to attenuate EM waves, which are expressed in decibel (dB). It could also be understood as the intensity difference between the original and residual EM waves. Therefore, SE can be calculated by the relative parameters of the incident (subscript In) and transmitted (subscript Trans) EM waves as the following Eq. (1):

$$SE = 20\log_{10}\frac{E_{Trans}}{E_{In}} = 20\log_{10}\frac{H_{Trans}}{H_{In}} = 10\log_{10}\frac{P_{Trans}}{P_{In}} \tag{1}$$

where, E, H, and P represent the strength of electric field, magnetic field, and plane wave, respectively.

The shielding theory of Schelkunoffs states the relation of the total SE (SE_T). The reflection loss (SE_R), the absorption loss (SE_A), and the multiple reflections loss (SE_M) satisfied the following Eq. (2) [43]:

$$SE_T = SE_R + SE_A + SE_M \tag{2}$$

The SE_R, SE_A, and SE_M can be calculated respectively by Eqs. (3–5) [4]:

$$SE_R = -10\log_{10}\left(\frac{\sigma_T}{16f\varepsilon\mu_r}\right) \tag{3}$$

$$SE_A = -3.34t\sqrt{f\sigma_T\mu_r} \tag{4}$$

$$SE_M = 20\log_{10}\left(1 - 10^{\frac{SE_A}{10}}\right) \tag{5}$$

where σ_T is the electrical conductivity of shielding material (S cm^{-1}), f refers to the frequency of EM waves, ε refers to electric permittivity, μ_r represents magnetic permittivity of the medium, and t refers to the thickness. It could be observed the SE_R decreases while SE_A increases with the increase in f for fixed shielding material.

From Eq. (5), it is clear that SE_M is relevant to SE_A. The role of SE_M is necessary only in the thin metals and under the circumstance of low EM band frequencies. Multiple reflections can be ignored when the absorption loss is higher than 10 dB or in the thick shields. If the SE is less than 10 dB for all shielding materials, this material would be considered inefficient. When SE is greater than 20 dB, it can attenuate 99% of the incoming waves. EMI shielding efficiency (%) could be calculated from SE by Eq. (6):

$$\text{Shielding efficiency}(\%) = 100 - \left(\frac{1}{10^{\frac{SE}{10}}}\right) \times 100 \tag{6}$$

Generally, SE ≥ 20 dB is the minimum standard to meet the industrial and commercial protections requirements [30].

3.2 EMI Shielding Measurement

The three techniques are commonly conducted for measuring EMI SE, which are introduced below [44, 45]:

(1) Waveguide method: As the name implies, different waveguides were used in the waveguide method. Waveguide is the module wherein the shielding material was introduced. The type of chosen waveguide was dependent on the frequency range of the test. Generally, the higher the frequency, the smaller the waveguide. Therefore, the waveguide method is suitable for analyses of composite materials based on aligned nanostructures [4].
(2) Coaxial transmission line method: The material is made into the rectangular toroid shape inserted between the inner and outer conductors [4, 7].
(3) Free space method: It is a non-contact method. The major shortcoming of the free space method is that the required thickness for the tested sample is larger than the aforementioned methods. However, the main advantage is that the incidence angle of EM radiations can be adjusted [4].

3.3 Types of EMI Shielding Materials

3.3.1 Metal-Based Materials

Metallic materials are applied in EMI shielding because of their excellent electrical and thermal conductivity. Because metallic materials have a large number of free electrons and a very small skin depth, EM waves are mainly reflected off the surface [4]. Metallic conductors can also be used to eliminate static charges accumulated in electronic equipment or to dissipate heat generated by a high-speed machine.

Conventional metal materials for EMI shielding include copper, iron, silver, nickel, aluminum, etc. Moreover, alloys with high magnetic permeability are often employed for EMI shielding [7]. However, metallic materials also have some limiting factors. For example, the price of copper is relatively expensive, iron materials are easy to rust, and the density of steel is too high [46]. Moreover, EMI shielding materials composed of two different metals are susceptible to electrochemical corrosion, resulting in a serious decline in EMI shielding performance [47].

Although there are some deficiencies in lightweight and rapid preparation, metallic materials are still one of the conventional EMI shielding materials in many scenarios because they have better conductivity and mechanical strength than many polymer materials.

3.3.2 Conductive Polymer-Based Materials

There is no doubt that lightweight and high efficiency will become the critical requirements of EMI shielding materials for electronic devices in the future. In the EMI shielding application of traditional metal materials, negative factors such as high specific gravity, susceptibility to corrosion, and complex processing have seriously hindered its applications. The polymer material is a promising alternative material because of its advantages of low density, low cost, anti-corrosion, and easy processing. Therefore, it is widely used in electronics, transportation, aerospace, energy, defense, and infrastructure [47–49].

Conductive polymers like polyaniline (PANI) [50] and polypyrrole (PPy) [51] have drawn attention because of their unique electronic property. However, their processing abilities have been limited by the extensive delocalization of π-electrons and the inherent rigidity of the chains of these conductive polymers [1]. Moreover, the conductive polymers will swell, contract, or soften, which will weaken their mechanical strength and electrical characteristics. Therefore, researchers usually solve the above problems by introducing other materials in order to make EMI shielding composite materials.

3.3.3 Nanocomposite-Based Materials

Traditional composites are mainly filled with micron filler. With the development of nanoscience and technology, the unique physical and chemical properties and the relationship between filler size and nanomaterials' performance have gradually turned into a focus of attention. Generally, nanotechnology refers to manipulating matter on the atomic or molecular scale and the use of nanoscale materials and structures. Nanoparticles often have a larger surface area-to-volume ratio, higher interfacial reactivity, and unique nano-enhancing effects based on the nano-size effect. Therefore, nanocomposite-based EMI shielding materials have caught more and more concern [52]. Metal nanowires [53], graphene [54–56], carbon nanotubes

(CNTs) [57–59], carbon fibers [60–63], graphite [64, 65], carbon black [66], and MXenes [67] have been widely used.

4 Role of Carbides in EMI Shielding

MXene is a class of two-dimensional materials and consists of transition metal carbides or nitrides. Due to the excellent conductivity of MXene, they are seen as a promising candidate for EMI shielding materials.

4.1 MXene Films

At first, vacuum filtered freestanding films assembled from MXene have exhibited great potential in EMI shielding because of their unique layered structure and outstanding conductivity. In 2016, pure MXene films prepared by vacuum-assisted filtration were first applied to the EMI shielding field. Shahzad et al. [30] measured the EMI shielding performances of three different types of laminar MXene films and MXene-polymer hybrids with varying contents of MXene. The results demonstrated that a pure $Ti_3C_2T_x$ film with 45 μm thickness displayed an exceptional conductivity of 4665.1 S cm^{-1} and an excellent EMI shielding SE of 92 dB, which is the highest level in the same thickness processing materials at that time. Moreover, a potential mechanism of EMI shielding was suggested. When EM waves hit the surface of the MXene nanosheets, some of them were immediately reflected. The remaining waves travel through the MXene film and interact with the high electron density of MXene, leading to an ohmic loss of EM waves. The surviving EM waves can be reflected and forth between the layers (I, II, III, and so on) until they are fully absorbed (Fig. 3).

Although the pristine MXene film shows prominent EMI shielding performance, it undergoes poor mechanical performance (tensile strength of 22 MPa), limiting their practical applications. Fortunately, there are abundant functional groups (like -F and -OH) on the surface of MXene sheets, which are beneficial to interact with polymers by hydrogen bonding. Therefore, some researchers took advantage of this, and numerous MXene-based composites films were fabricated for solving the mechanical strength problem. Cao et al. [68] designed MXene/CNFs composites with a nacre-like lamellar structure via filtrating (Fig. 4a). 1D CNFs with abundant hydroxyl groups (-OH) played a role in strengthening the composite materials, which both connect the adjacent MXene sheets and improve the stress transfer (Fig. 4b). By adjusting the proportion of MXene to CNFs, the tensile strength and strain of composite membrane reached 135.4 MPa and 16.7%, respectively, which were better for pure MXene and pure CNFs membrane. With 20 wt% of CNFs, the MXene/CNFs hybrid film exhibited ~ 25.8 dB in X-band at a thickness of 74 μm.

In addition to CNFs, other materials such as aramid nanofibers (ANFs or Kevlar) are utilized to reinforce MXene-based hybrid films. Wei et al. [69]

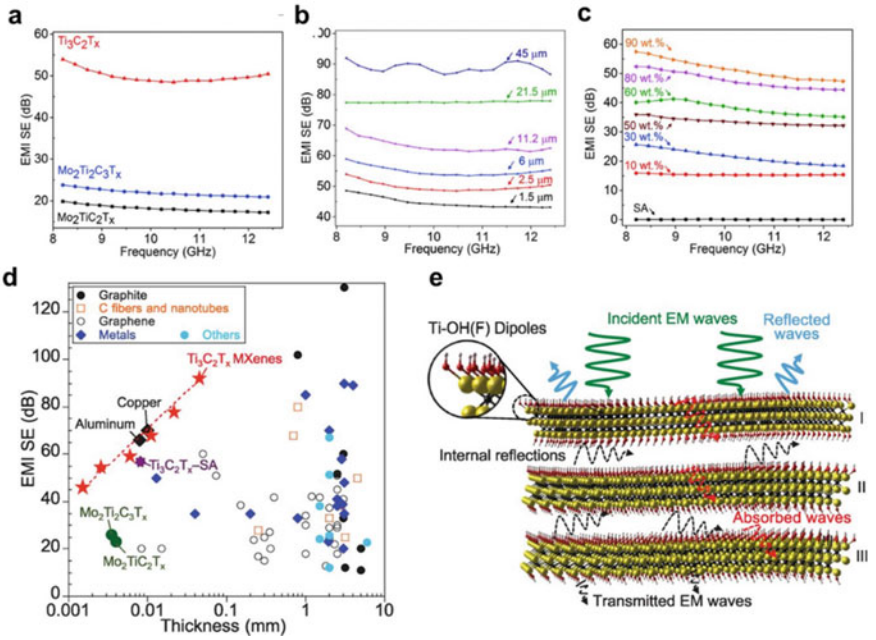

Fig. 3 **a** EMI shielding performances of $Mo_2TiC_2T_x$, $Mo_2Ti_2C_3T_x$, and $Ti_3C_2T_x$. **b** EMI shielding performances of $Ti_3C_2T_x$. **c** EMI shielding performances of $Ti_3C_2T_x$-SA. **d** EMI shielding performances versus thickness of different materials. **e** Representation of EMI shielding mechanism. **a–e** Adapted with permission [30]. Copyright 2016, AAAS

reported an MXene/ANFs hybrid films with "bricks and cement" structure via the filtration method. MXene layers acted as "bricks", and ANFs were used for "cement" between "MXene bricks" for connection and stabilization. The as-obtained composite enhanced mechanical property (116.71 MPa) and EMI shielding performance (34.71 dB at 12.4 GHz). Liu et al. [70] developed vacuum filtered ultrathin MXene-GO hybrid films for EMI shielding. MXene nanosheets were bridged with GO sheets with hydrogen bonds for reinforcing the pure films, forming a densely packed layered structure. The obtained composites demonstrated outstanding fracture strength (209 MPa) and toughness (1.09 MJ m^{-3}) under the premise of maintaining a satisfactory electrical conductivity (4.62×10^4 to 2.62×10^5 S m^{-1}). A composite film at only 7 μm thick had an outstanding EMI shielding performance up to 50 dB.

It is a disadvantage to maintain the original conductivity and EMI shielding property for the homogeneous hybrid films prepared by directly mixing MXene and nonconducting reinforcements [71]. Therefore, it is desired to design a novel strategy that can strengthen MXene-based composite films but not affect the electrical conductivity and the EMI SE. Alternating vacuum filtration (AVF) was chosen to mold a gradient and sandwich structure to meet this target. Zhou et al. [72] prepared a kind of multilayered films with alternating CNF layers and MXene layers with a tensile

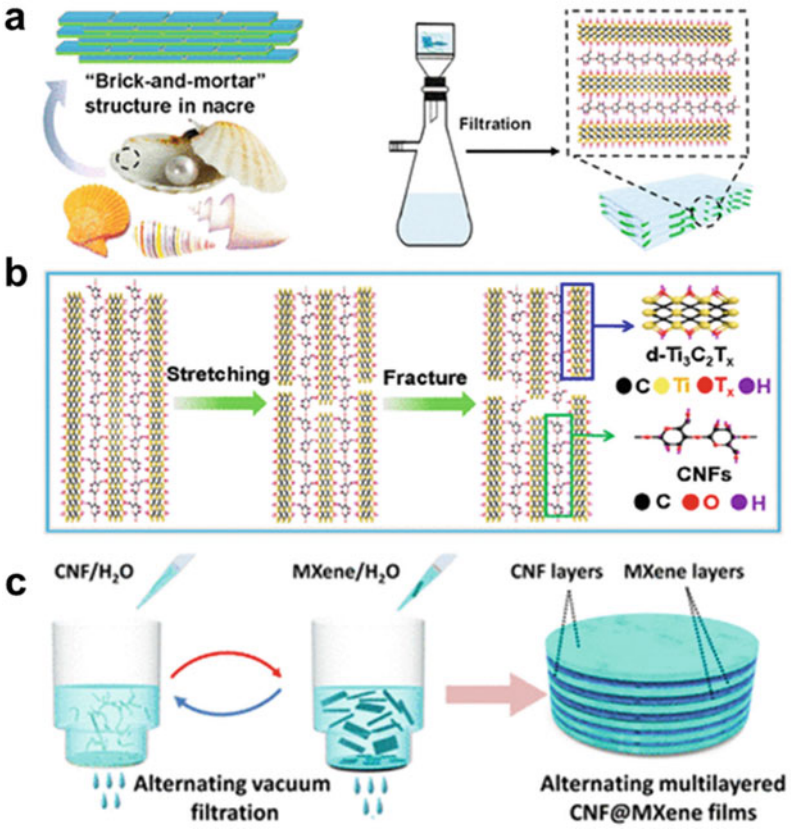

Fig. 4 **a** Schematic illustration of nacre-like lamellar structure and the vacuum filtration preparation process. **b** Schematic diagram of the fracture mechanism. Adapted with permission [68]. Copyright 2018, American Chemical Society. **c** AVF process to prepare alternating CNF@MXene films. Adapted with permission [72]. Copyright 2020, American Chemical Society

strength of 112.5 MPa, which improved the electrical conductivity (621–82 S m^{-1}) and EMI SE (~40 dB), compared to the aforementioned homogeneous MXene/CNF hybrid film (Fig. 4c). Furthermore, given the high conductivity, this alternating multilayered CNF@MXene film shows a significant electrothermal-conversion performance under a low safe voltage, making the alternating multilayered CNF@MXene possible to be applied in various real scenarios for wearable electronics and personal heating systems.

Another method uses a conductive material as reinforcement, such as silver nanowires (AgNWs) [73]. AgNWs were introduced into MXene layers to fabricate a hybrid membrane with a "brick-and-mortar" structure. When the thickness is 16.9 μm, the tensile strength and shielding performance of the thin membrane prepared by low load nanocellulose as binder can reach 63.80 MPa and 42.7 dB.

Moreover, conducting polymers were also employed to retain intrinsic electrical conductivity [74]. Polymeric chains intercalated in MXene nanosheets create conductive paths that help the electrons flow. MXene and PEDOT:PSS nanocomposites were investigated [75]. Conductive polymeric chains between the MXene nanosheets improved the conductivity (340.5 S cm^{-1}), and the EMI SE at 11.1 μm thickness was 42 dB.

In addition to vacuum filtrated film, designing hybrid films with a layer-by-layer (LBL) structure is another way to build MXene EMI shielding materials. LBL stands for alternate layer structure. LBL structures could be assembled by a variety of solution-processing methods such as spin-coating [76], spray-coating [77], dip-coating [78], and so on [72].

Weng et al. [77] prepared an MXene-CNTs LBL film by spin-spraying method, which integrated numerous advantages of thin, transparency, excellent conductivity, good stability, and high flexibility in one. The pre-prepared semi-transparent MXene-CNT LBL hybrid film exhibited good conductivity over 130 S cm^{-1} and exceptional specific EMI SE up to 58,187 dB cm^2 g^{-1}, due to the excellent conductivity of MXene and CNTs and the special LBL structure (Fig. 5a–c). As shown in Fig. 5d, Jin et al. [79] developed a poly (vinyl alcohol) (PVA)/MXene membrane with alternating multilayered structure by multilayered casting. The resultant PVA/MXene multilayered film (19.5 wt% MXene) at 27 μm thickness showed a satisfied conductivity of 716 S m^{-1}, a predominant EMI SE of 44.4 dB, and specific shielding effectiveness of 9343 dB cm^2 g^{-1}. This superb EMI shielding property is because of the impedance mismatch between conducting layers and non-conducting layers of the multilayered

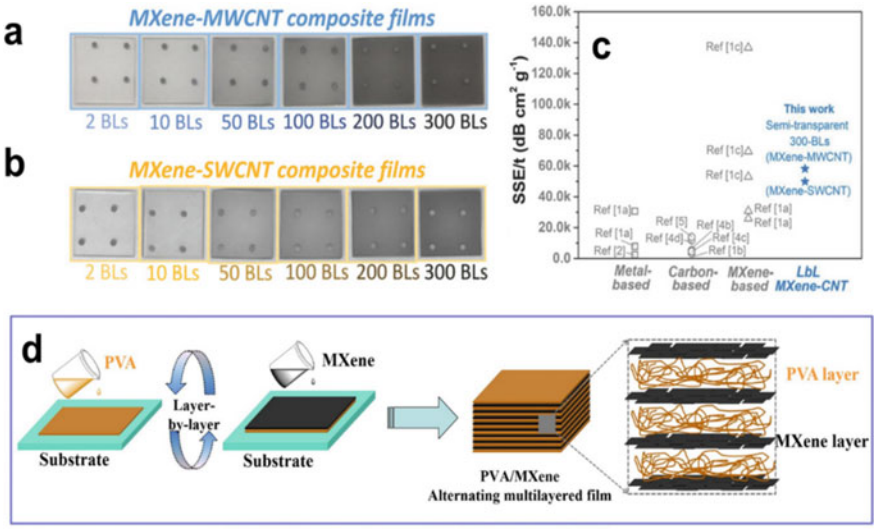

Fig. 5 **a–b** MXene/CNT LBL hybrid films of multi-layers. **c** Comparison of the specific EMI SE. Adapted with permission [77]. Copyright 2018, Wiley–VCH. **d** The fabrication pf MXene/PVA multilayered hybrid films. Adapted with permission [79]. Copyright 2020, Elsevier Ltd

LBL structure, which enhances the internal scattering and absorption of EM waves. In addition, the plane thermal conductivity of the obtained film is 4.57 W/mK.

In addition, MXene hybrid films are also employed to further enhance the EMI SE by introducing other conductive or magnetic materials. Wang et al. [80] designed a flexible and ultrathin poly (vinylidene fluoride) (PVDF)/MXene/ Ni chain hybrid films and discussed the synergistic effect of 2D MXene and quasi-1D Ni chains. The conductivity of 892 S m-1 and the EMI SE of 34.4 dB was obtained for the PVDF/MXene/Ni chain film with 0.36 mm thick hybrid film. Furthermore, the tensile strength, Young's modulus, and toughness of composite film were 41.9 ± 1.6 MPa, 1.18 ± 0.007 GPa, and 2.9 ± 0.08 MJ m^{-3}, all of which were better than when MXene or Ni chains were used alone.

4.2 MXene-Coating Textiles and Fabrics

MXene-coating textiles and fabrics are considered promising candidates for wearable EMI shielding materials owing to their breathability, durability, and washability. Ma et al. [81] designed an MXene-decorated air-laid paper by dipping-drying. As a flexible substrate, the air-laid paper consists of polyester and cellulose without any binder or additive, making air-laid paper hydrophilic and durable. The as-prepared paper exhibits a conductivity of 173.0 S m^{-1} and EMI SE of 16.36 dB. In addition, it is worth noting that the composite demonstrated outstanding durability after folding and sweat-treating.

Another recent work investigates a multifunctional and water-resistant MXene-wrapped polyester textile [82]. Figure 6a demonstrates the fabrication and functions of this textile. The MXene nanosheets are decorated with polymerized PPy without any initiator like $FeCl_3$. Still, because of van der Waals force and hydrogen bonding, the polyester textile fibers are tightly wrapped PPy/MXene nanosheets. Finally, the composite textiles were coated with a water-resistant layer of silicone, which improved this multifunctional textile's stability and working life (Fig. 6b). The as-obtained PPy/MXene-textile revealed a superb conductivity of 1000 S m^{-1} and an EMI shielding SE of 42 dB. In addition, the composite textile shows a good Joule heating performance with excellent stability, which broadens the application field of this textile in wearable intelligent garments.

Liu et al. [83] demonstrated a leaf-like MXene/silver nanowire (AgNW) textile for EMI shielding and moisture monitoring (Fig. 6c). A scalable vacuum-assisted LBL assembly method was employed to fabricate this multifunctional textile. After oxygen plasma and polyethyleneimine treatment, the textile was alternately coated with MXene and AgNWs, which was like a leaf. Finally, after 5 months of aging, the hydrophilic composite silk textile converted to hydrophobicity. In this unique nanostructure, 2D MXene nanosheets and 1D AgNWs constructed a good conductive network, giving the obtained fabric interesting properties, including low sheet

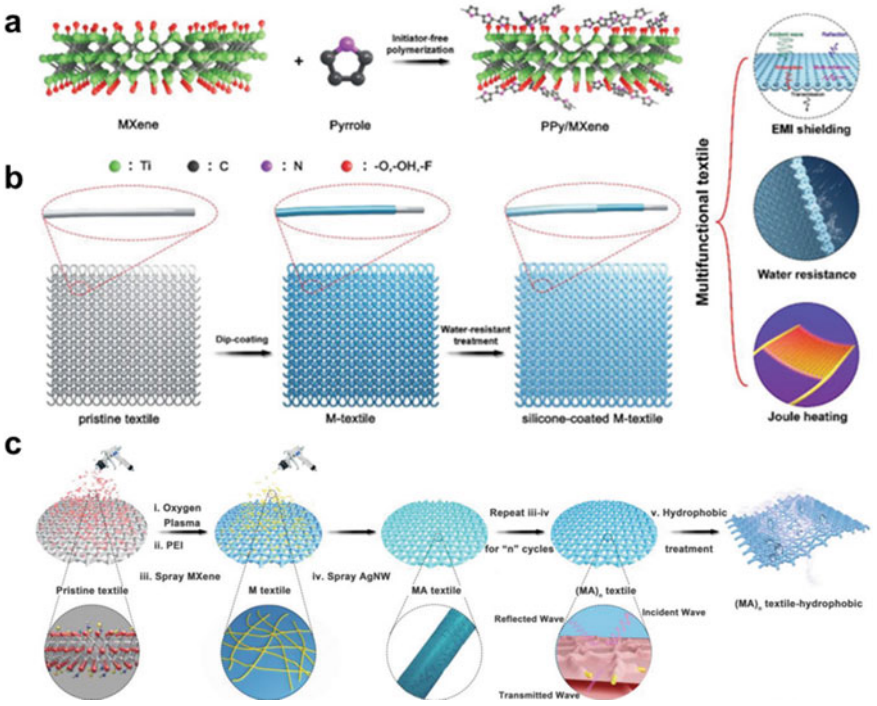

Fig. 6 Schematic diagram of **a** decoration of MXene with polymerized PPy, and **b** preparation and functions of this composite textile. Adapted with permission [82]. Copyright 2019, Wiley–VCH. **c** Fabrication of MXene/AgNWs-decorated silk textile. Adapted with permission [83]. Copyright 2019, Wiley–VCH

resistance and superb EMI SE over 90 dB. Besides, the obtained textile shows sensitivity to moisture response and self-derived hydrophobicity. Therefore, this textile is a promising candidate for wearable devices thanks to its stability and functions.

4.3 MXene-Based Foams and Aerogels

Porous MXene foams and aerogels are well suited to modern EMI shielding materials due to their exceptionally low density. Liu et al. [84] demonstrated lightweight and flexible $Ti_3C_2T_x$ MXene foams for EMI shielding. Figure 7 shows the preparation process. First, single-layered MXene nanosheets were obtained via etching and sonication, and then vacuum-assisted filtration was developed to assemble these MXene nanosheets into a freestanding film. Finally, the pre-prepared MXene film was sandwiched between two ceramic wafers, treated with hydrazine, and heated at 90 °C. In this foaming process, pores were introduced into the parallelly ordered and layered structure of MXene freestanding film, which facilitated a higher EMI

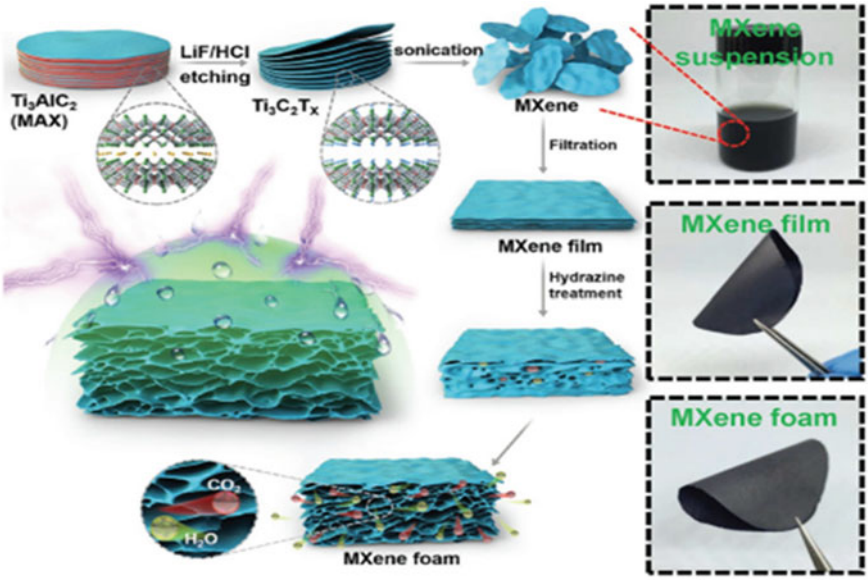

Fig. 7 Preparation of the hydrophobic MXene foam. Adapted with permission [84]. Copyright 2018, Wiley–VCH

wave attenuation to 70 dB. Furthermore, due to the removal of oxygen terminations during the foaming process, the surface wettability of the MXene film was changed to hydrophobic, increasing the stability and endurance of smart wearable electronics, particularly in humid settings.

Freeze-drying is one of the common conventional methods to establish a porous structure. However, Freezing-casting, as a specific kind of freezing-drying, is employed to build robust, compressible, and lightweight aerogels, which suit wearable devices. Bidirectional freeze-casting was used by Han et al. [85] to create anisotropic flexible MXene aerogels with long-range order of aligned lamellar structures, which differs from standard freezing-drying to make random aerogels. This study uses three types of MXene family to build conductive MXene aerogels, and their EMI SE (SE_T) reaches 70.5, 69.2, and 54.1 dB, respectively. In addition, the $Ti_3C_2T_x$ has a high absolute shielding efficacy (SSE/t) of 88,182 dB cm g^{-1} thanks to its ultralow density (0.0055 g cm^{-3}).

Wu et al. [86] designed a compressible and durable PDMS-coated MXene composite foam for EMI shielding and detecting EM leakage. This MXene/sodium alginate (SA) aerogel was prepared via a directional freezing-casting method, followed by a coating of a thin PDMS layer to improve the stability. As a result, the MXene/SA composite foam shows a high electric conductivity of 2211 S m^{-1} in a density of $\approx$ 20 mg cm^{-3} and a satisfied average SE of 70.5 dB. In addition, the hybrid aerogel with directional porous architecture reserves its high EMI shielding SE after up to 500 compression cycles, making it a candidate for wearable sensors or

Table 1 EMI shielding performances of carbides MXene and its hybrid materials

Materials	Thickness (mm)	SE (dB)	SSE/t (dB cm^2 g^{-1})	Ref
$Ti_3C_2T_x$/CNF/CNT	0.038	38.4	8020	[71]
$Ti_3C_2T_x$/epoxy	2	41	/	[87]
$Ti_3C_2T_x$/Ni	1.3	33.8	/	[88]
$Ti_3C_2T_x$/wax	0.8	70	1776	[89]
$Ti_3C_2T_x$/polystyrene	2	62	/	[90]
$Ti_3C_2T_x$/natural rubber	0.25	53.6	/	[91]
$Ti_3C_2T_x$/carbon	2	46	/	[92]
$Ti_3C_2T_x$/calcium alginate	0.026	54.3	17,586	[93]
$Ti_3C_2T_x$/CNT textiles	/	32.6	/	[94]
$Ti_3C_2T_x$/Ni/wax	/	74.14	/	[95]
$Ti_3C_2T_x$/wood	8	29.3	/	[96]
Silicone-coated $Ti_3C_2T_x$/cellulose	0.54	39.4	/	[97]
$Ti_3C_2T_x$/aramid nanofibers	1.9	56.8	3558	[98]

other electronics. Table 1 shows the EMI shielding performances of representative carbides composite materials.

5 Role of Nitrides in EMI Shielding

Few studies have looked into the role of nitrides MXene in EMI shielding compared to carbides ($Ti_3C_2T_x$). For example, the EMI shielding capability of vacuum filtered Ti_3CNT_x films was investigated by Han et al. [99]. The as-obtained Ti_3CNT_x film with a thickness of ~ 5 μm had a conductivity of 2712 S cm^{-1} and an EMI SE of around 50 dB. In 2020, a breakthrough of nitrides for EMI shielding materials was reported by Iqbal and coworkers [100]. Compared to higher conductive $Ti_3C_2T_x$ or foils, Ti_3CNT_x-based materials at the same thickness have moderate electrical conductivity and provide a higher SE (up to 116 dB). This exceptional shielding property of Ti_3CNT_x was obtained by thermal annealing. As a result, slit pores were developed in the annealed films with a broad size distribution ranging from tens of nanometers to micrometers. Moreover, heat treatment of Ti_3CNT_x removed the adsorbed molecular species between MXene sheets. However, these factors alone cannot fully explain the observed increase within the framework of existing shielding theories. Therefore, further exploration is needed to explain the mechanisms.

6 Challenges and Prespective

Although MXene-based EMI shielding materials have been widely investigated, some outstanding challenges still need to be addressed.

(1) The mechanical properties of MXene-based EMI shielding materials need to be further improved. There are some previous works that reported attempts for mechanical enhancement. For example, cellulose nanofiber reinforced MXene films, ANFs strengthened MXene films, etc. However, the increase of mechanical strength of most materials is usually at the cost of loss of EMI SE at present. Therefore, balancing the mechanical properties and EMI SE performances is vital. Designing special structures or using conductive reinforcements may be the way to solve this problem.

(2) The long-term durability and stability of EMI shielding material is significant for practical wearable applications under different circumstances. Although MXene-based EMI shielding materials have excellent conductivities and high SE values, current studies have fewer tests of durability and stability during use. Therefore, testing and improving durability and stability are critical for wearable EMI shielding materials. In particular, the properties of wearable EMI shielding materials should keep after folding or sweat and stains treatments.

(3) Furthermore, proper breathability is another critical factor that evaluates whether the material is suitable for wearing. Although most fabric-based MXene-based EMI shielding materials inherit the good breathability of fabric substrates, more research has not focused on the breathability of flexible materials.

(4) The MXene-based EMI shielding material with a single function is difficult to meet the trend. Therefore, it is imperative to develop versatile materials. Materials with thermal management, sensing, EMI shielding, and other functions could broaden the range of possible scenarios, especially in harsh environments.

7 Conclusion

As discussed above, MXene materials have shown great attractive features, making them good candidates for EMI shielding. Various strategies have been used to construct MXene-based EMI shielding materials, including dipping-drying, freeze-casting, vacuum-assistant filtration, and so on. MXene-based composites give state-of-the-art EMI shielding performances due to their excellent conductivities and unique structures. However, the research of MXene-based EMI shielding materials is in its infancy, and there are still vast prospects to explore. We hope that this chapter could provide an insight into the progress and challenges of MXene-based EMI shielding materials.

Acknowledgements The financial support from the National Key R&D Program of China (2019YFC1905901), the Beijing Forestry University Outstanding Young Talent Cultivation Project (2019JQ03014), and the Key Production Innovative Development Plan of the Southern Bingtuan (2019DB007) is gratefully acknowledged.

References

1. Jiang, D., Murugadoss, V., Wang, Y., et al.: Electromagnetic interference shielding polymers and nanocomposites-a review. Polym. Rev. **59**, 280–337 (2019)
2. Singh, A.K., Shishkin, A., Koppel, T., Gupta, N.: A review of porous lightweight composite materials for electromagnetic interference shielding. Comp. Part B-Eng. **149**, 188–197 (2018)
3. Wan, Y.J., Zhu, P.L., Yu, S.H., et al.: Graphene paper for exceptional EMI shielding performance using large-sized graphene oxide sheets and doping strategy. Carbon **122**, 74–81 (2017)
4. Sankaran, S., Deshmukh, K., Ahamed, M.B., Pasha, S.K.K.: Recent advances in electromagnetic interference shielding properties of metal and carbon filler reinforced flexible polymer composites: a review. Comp. Part A-Appl. Sci. Manuf. **114**, 49–71 (2018)
5. Christ, A., Douglas, M., Nadakuduti, J., Kuster, N.: Assessing human exposure to electromagnetic fields from wireless power transmission systems. Proc. IEEE **101**, 1482–1493 (2013)
6. Shi, Y.D., Yu, H.O., Li, J., et al.: Low magnetic field-induced alignment of nickel particles in segregated poly (L-Lactide)/Poly(Epsilon-Caprolactone)/multi-walled carbon nanotube nanocomposites: towards remarkable and tunable conductive anisotropy. Chem. Eng. J. **347**, 472–482 (2018)
7. Wanasinghe, D., Aslani, F.: A review on recent advancement of electromagnetic interference shielding novel metallic materials and processes. Comp. Part B-Eng. **176**, 107207 (2019)
8. Li, Y., Feng, Z., Huang, L., et al.: Additive manufacturing high performance graphene-based composites: a review. Comp. Part A-Appl. Sci. Manuf. **124**, 105483 (2019)
9. Prather, W.D., Baum, C.E., Torres, R.J., et al.: Survey of worldwide high-power wideband capabilities. IEEE Trans. Electromagn. Compat. **46**, 335–344 (2004)
10. Iqbal, A., Sambyal, P., Koo, C.M.: 2D MXenes for electromagnetic shielding: a review. Adv. Func. Mater. **30**, 2000883 (2020)
11. Lin, B., Yuen, A.C.Y., Li, A., et al.: MXene/chitosan nanocoating for flexible polyurethane foam towards remarkable fire hazards reductions. J. Hazard. Mater. **381**, 120952 (2020)
12. Li, H., Liang, J.: Recent development of printed micro-supercapacitors: printable materials, printing technologies, and perspectives. Adv. Mater. **32**, 1805864 (2020)
13. Naguib, M., Mashtalir, O., Carle, J., et al.: Two-dimensional transition metal carbides. ACS Nano **6**, 1322–1331 (2012)
14. Zang, X., Wang, J., Qin, Y., et al.: Enhancing capacitance performance of $Ti_3C_2T_x$ MXene as electrode materials of supercapacitor: from controlled preparation to composite structure construction. Nano-Micro Lett. **12**, 77 (2020)
15. Wang, Y., Wang, X., Li, X., et al.: Intercalating ultrathin MoO_3 nanobelts into mxene film with ultrahigh volumetric capacitance and excellent deformation for high-energy-density devices. Nano-Micro Lett. **12**, 115 (2020)
16. Ran, F., Wang, T., Chen, S., et al.: Constructing expanded ion transport channels in flexible mxene film for pseudocapacitive energy storage. Appl. Surf. Sci. **511**, 145627 (2020)
17. Bu, F., Zagho, M.M., Ibrahim, Y., et al.: Porous MXenes: synthesis, structures, and applications. Nano Today **30**, 100803 (2020)
18. Zhao, Q., Zhu, Q., Miao, J., et al.: 2D MXene nanosheets enable small-sulfur electrodes to be flexible for lithium-sulfur batteries. Nanoscale **11**, 8442–8448 (2019)

19. Jiao, L., Zhang, C., Geng, C., et al.: Capture and catalytic conversion of polysulfides by in situ built TiO_2-MXene heterostructures for lithium-sulfur batteries. Adv. Energy Mater. **9**, 1900219 (2019)
20. Zhan, X., Si, C., Zhou, J., Sun, Z.: MXene and MXene-based composites: synthesis. Prop. Environ. Relat. Appl. Nanoscale Horizons **5**, 235–258 (2020)
21. Shi, X., Wang, H., Xie, X., et al.: Bioinspired ultrasensitive and stretchable MXene-based strain sensor via nacre-mimetic microscale "brick-and-mortar" architecture. ACS Nano **13**, 649–659 (2019)
22. Liu, J., Jiang, X., Zhang, R., et al.: MXene-enabled electrochemical microfluidic biosensor: applications toward multicomponent continuous monitoring in whole blood. Adv. Func. Mater. **29**, 1807326 (2019)
23. Nguyen, V.H., Tabassian, R., Oh, S., et al.: Stimuli-responsive MXene-based actuators. Adv. Func. Mater. **30**, 1909504 (2020)
24. Wang, J., Liu, Y., Cheng, Z., et al.: Highly conductive MXene film actuator based on moisture gradients. Angewandte Chem. Int. Edit. **59**, 14029–14033 (2020)
25. Lao, J., Wu, S., Gao, J., et al.: Electricity generation based on a photothermally driven $Ti_3C_2T_x$ MXene nanofluidic water pump. Nano Energy **70**, 104481 (2020)
26. Tu, S., Jiang, Q., Zhang, J., et al.: Enhancement of dielectric permittivity of $Ti_3C_2T_x$, MXene/polymer composites by controlling flake size and surface termination. ACS Appl. Mater. Interf. **11**, 27358–27362 (2019)
27. Jiang, Q., Wu, C., Wang, Z., et al.: MXene electrochemical microsupercapacitor integrated with triboelectric nanogenerator as a wearable self-charging power unit. Nano Energy **45**, 266–272 (2018)
28. Ma, C., Yuan, Q., Du, H., et al.: Multiresponsive MXene ($Ti_3C_2T_x$)-decorated textiles for wearable thermal management and human motion monitoring. ACS Appl. Mater. Interf. **12**, 34226–34234 (2020)
29. Naguib, M., Mochalin, V.N., Barsoum, M.W., Gogotsi, Y.: 25th anniversary article: mxenes: a new family of two-dimensional materials. Adv. Mater. **26**, 992–1005 (2014)
30. Shahzad, F., Alhabeb, M., Hatter, C.B., et al.: Electromagnetic interference shielding with 2D transition metal carbides (MXenes). Science **353**, 1137–1140 (2016)
31. Ma, C., Cao, W.T., Zhang, W., et al.: Wearable, ultrathin and transparent bacterial celluloses/MXene film with janus structure and excellent mechanical property for electromagnetic interference shielding. Chem. Eng. J. **403**, 126438 (2021)
32. Gong, S., Zhu, Z.H., Arjmand, M., et al.: Effect of carbon nanotubes on electromagnetic interference shielding of carbon fiber reinforced polymer composites. Polym. Compos. **39**, E655–E663 (2018)
33. Sawai, P., Chattopadhaya, P.P., Banerjee, S.: Synthesized reduce graphene oxide (rGO) filled polyetherimide based nanocomposites for EMI shielding applications. Mater. Today-Proc. **5**, 9989–9999 (2018)
34. Wang, X.X., Shu, J.C., Cao, W.Q., et al.: Eco-mimetic nanoarchitecture for green EMI shielding. Chem. Eng. J. **369**, 1068–1077 (2019)
35. Jagatheesan, K., Ramasamy, A., Das, A., Basu, A.: Electromagnetic absorption behaviour of ferrite loaded three phase carbon fabric composites. Smart Mater. Struct. **27**, 025004 (2018)
36. Lai, H., Singh, N.P.: Single- and double-strand DNA breaks in rat brain cells after acute exposure to radiofrequency electromagnetic radiation. Int. J. Radiat. Biol. **69**, 513–521 (1996)
37. Zhang, J., Sumich, A., Wang, G.Y.: Acute effects of radiofrequency electromagnetic field emitted by mobile phone on brain function. Bioelectromagnetics **38**, 329–338 (2017)
38. Joshi, A., Datar, S.: Carbon nanostructure composite for electromagnetic interference shielding. Pramana J. Phys. **84**, 1099–1116 (2015)
39. Nam, Y.W., Kumar, S.K.S., Ankem, V.A., Kim, C.G.: Multi-functional aramid/epoxy composite for stealth space hypervelocity impact shielding system. Compos. Struct. **193**, 113–120 (2018)
40. Gupta, S., Tai, N.H.: Carbon materials and their composites for electromagnetic interference shielding effectiveness in X-band. Carbon **152**, 159–187 (2019)

41. Fano, U.: Atomic theory of electromagnetic interactions in dense materials. Phys. Rev. **103**, 1202–1218 (1956)
42. Liehr, A.D.: Interaction of electromagnetic radiation with matter .I. Theory of optical rotatory power-topic B. Digonal dihedral compounds compounds of lower symmetry. J. Phys. Chem. **68**, 3629 (1964)
43. Erdogan, M.K., Karakisla, M., Sacak, M.: Polypyrrole and silver particles coated poly(Ethylene Terephthalate) nonwoven composite for electromagnetic interference shielding. J. Compos Mater. **52**, 1353–1362 (2018)
44. Al-Saleh, M.H., Saadeh, W.H., Sundararaj, U.: EMI shielding effectiveness of carbon based nanostructured polymeric materials: a comparative study. Carbon **60**, 146–156 (2013)
45. Song, Q., Ye, F., Yin, X., et al.: Carbon nanotube-multilayered graphene edge plane core-shell hybrid foams for ultrahigh-performance electromagnetic-interference shielding. Adv. Mater. **29**, 1701583 (2017)
46. Zeng, Z., Jiang, F., Yue, Y., et al.: Flexible and ultrathin waterproof cellular membranes based on high-conjunction metal-wrapped polymer nanofibers for electromagnetic interference shielding. Adv. Mater. **32**, 1908496 (2020)
47. Kumar, P., Maiti, U.N., Sikdar, A., et al.: Recent advances in polymer and polymer composites for electromagnetic interference shielding: review and future prospects. Polym. Rev. **59**, 687–738 (2019)
48. Dhawan, R., Kumar, R., Chaudhary, A., et al.: Investigation on pitch derived mesocarbon spheres based metal composites for highly efficient electromagnetic interference shielding. Comp. Part B-Eng. **175**, 107168 (2019)
49. Lim, G.H., Woo, S., Lee, H., et al.: Mechanically robust magnetic carbon nanotube papers prepared with $CoFe_2O_4$ nanoparticles for electromagnetic interference shielding and magnetomechanical actuation. ACS Appl. Mater. Interf. **9**, 40628–40637 (2017)
50. Pan, T., Zhang, Y., Wang, C., et al.: Mulberry-like polyaniline-based flexible composite fabrics with effective electromagnetic shielding capability. Compos. Sci. Technol. **188**, 107991 (2020)
51. Gahlout, P., Choudhary, V.: Microwave shielding behaviour of polypyrrole impregnated fabrics. Comp. Part B-Eng. **175**, 107093 (2019)
52. Zhao, X., Lv, L., Pan, B., et al.: Polymer-supported nanocomposites for environmental application: a review. Chem. Eng. J. **170**, 381–394 (2011)
53. Lin, S., Liu, J., Wang, Q., et al.: Highly robust, flexible, and large-scale 3d-metallized sponge for high-performance electromagnetic interference shielding. Adv. Mater. Technol. **5**, 1900761 (2020)
54. Gupta, S., Sharma, S.K., Pradhan, D., Tai, N.H.: Ultra-light 3D reduced graphene oxide aerogels decorated with cobalt ferrite and zinc oxide perform excellent electromagnetic interference shielding effectiveness. Comp. Part A-Appl. Sci. Manuf. **123**, 232–241 (2019)
55. Wang, L., Wu, Y., Wang, Y., et al.: Laterally compressed graphene foam/acrylonitrile butadiene styrene composites for electromagnetic interference shielding. Comp. Part A-Appl. Sci. Manuf. **133**, 105887 (2020)
56. Chen, Y., Poetschke, P., Pionteck, J., et al.: Multifunctional cellulose/rGO/Fe_3O_4 composite aerogels for electromagnetic interference shielding. ACS Appl. Mater. Interf. **12**, 22088–22098 (2020)
57. Lecocq, H., Garois, N., Lhost, O., et al.: Polypropylene/carbon nanotubes composite materials with enhanced electromagnetic interference shielding performance: properties and modeling. Comp. Part B-Eng. **189**, 107866 (2020)
58. Wang, T., Yu, W.C., Zhou, C.G., et al.: Self-healing and flexible carbon nanotube/polyurethane composite for efficient electromagnetic interference shielding. Comp. Part B-Eng. **193**, 108015 (2020)
59. Feng, D., Liu, P., Wang, Q.: Selective microwave sintering to prepare multifunctional Poly(Ether Imide) bead foams based on segregated carbon nanotube conductive network. Ind. Eng. Chem. Res. **59**, 5838–5847 (2020)
60. He, M., Xu, P., Zhang, Y., et al.: Phthalocyanine nanowires@GO/carbon fiber composites with enhanced interfacial properties and electromagnetic interference shielding performance. Chem. Eng. J. **388**, 124255 (2020)

61. Lee, J., Liu, Y., Liu, Y., et al.: Ultrahigh electromagnetic interference shielding performance of lightweight, flexible, and highly conductive copper-clad carbon fiber nonwoven fabrics. J. Mater. Chem. C **5**, 7853–7861 (2017)
62. Li, Y.M., Deng, C., Zhao, Z.Y., et al.: Carbon fiber-based polymer composite via ceramization toward excellent electromagnetic interference shielding performance and high temperature resistance. Comp. Part A-Appl. Sci. Manuf. **131**, 105769 (2020)
63. Jung, S., Cho, D.: Effect of fiber feeding route upon extrusion process on the electromagnetic, mechanical, and thermal properties of nickel-coated carbon fiber/polypropylene composites. Comp. Part B-Eng. **187**, 107861 (2020)
64. Zhou, T., Xu, C., Liu, H., et al.: Second time-scale synthesis of high-quality graphite films by quenching for effective electromagnetic interference shielding. ACS Nano **14**, 3121–3128 (2020)
65. Guan, H., Chung, D.D.L.: Radio-wave electrical conductivity and absorption-dominant interaction with radio wave of exfoliated-graphite-based flexible graphite, with relevance to electromagnetic shielding and antennas. Carbon **157**, 549–562 (2020)
66. Ju, J., Kuang, T., Ke, X., et al.: Lightweight multifunctional polypropylene/carbon nanotubes/carbon black nanocomposite foams with segregated structure, ultralow percolation threshold and enhanced electromagnetic interference shielding performance. Compos. Sci. Technol. **193**, 108116 (2020)
67. Yang, R., Gui, X., Yao, L., et al.: Ultrathin, lightweight, and flexible cnt buckypaper enhanced using mxenes for electromagnetic interference shielding. Nano-Micro Lett. **13**, 66 (2021)
68. Cao, W.T., Chen, F.F., Zhu, Y.J., et al.: Binary strengthening and toughening of MXene/cellulose nanofiber composite paper with nacre-inspired structure and superior electromagnetic interference shielding properties. ACS Nano **12**, 4583–4593 (2018)
69. Wei, H., Wang, M., Zheng, W., et al.: 2D $Ti_3C_2T_x$ MXene/aramid nanofibers composite films prepared via a simple filtration method with excellent mechanical and electromagnetic interference shielding properties. Ceram. Int. **46**, 6199–6204 (2020)
70. Liu, J., Liu, Z., Zhang, H.B., et al.: Ultrastrong and highly conductive MXene-based films for high-performance electromagnetic interference shielding. Adv. Electron. Mater. **6**, 1901094 (2020)
71. Cao, W., Ma, C., Tan, S., et al.: Ultrathin and Flexible CNTs/MXene/cellulose nanofibrils composite paper for electromagnetic interference shielding. Nano-Micro Lett. **11**, 72 (2019)
72. Zhou, B., Zhang, Z., Li, Y., et al.: Flexible, robust, and multifunctional electromagnetic interference shielding film with alternating cellulose nanofiber and mxene layers. ACS Appl. Mater. Interf. **12**, 4895–4905 (2020)
73. Miao, M., Liu, R., Thaiboonrod, S., et al.: Silver nanowires intercalating $Ti_3C_2T_x$ MXene composite films with excellent flexibility for electromagnetic interference shielding. J. Mater. Chem. C **8**, 3120–3126 (2020)
74. Zhang, Y., Wang, L., Zhang, J., et al.: Fabrication and investigation on the ultra-thin and flexible $Ti_3C_2T_x$/Co-doped polyaniline electromagnetic interference shielding composite films. Compos. Sci. Technol. **183**, 107833 (2019)
75. Liu, R., Miao, M., Li, Y., et al.: Ultrathin biomimetic polymeric $Ti_3C_2T_x$ MXene composite films for electromagnetic interference shielding. ACS Appl. Mater. Interf. **10**, 44787–44795 (2018)
76. De, S., Lyons, P.E., Sorel, S., et al.: Transparent, flexible, and highly conductive thin films based on polymer–nanotube composites. ACS Nano **3**, 714–720 (2009)
77. Weng, G.M., Li, J., Alhabeb, M., et al.: Layer-by-layer assembly of cross-functional semitransparent MXene-carbon nanotubes composite films for next-generation electromagnetic interference shielding. Adv. Func. Mater. **28**, 1803360 (2018)
78. Sundaram, H.S., Han, X., Nowinski, A.K., et al.: One-step dip coating of zwitterionic sulfobetaine polymers on hydrophobic and hydrophilic surfaces. ACS Appl. Mater. Interf. **6**, 6664–6671 (2014)
79. Jin, X.X., Wang, J.F., Dai, L.Z., et al.: Flame-retardant Poly(Vinyl Alcohol)/MXene multilayered films with outstanding electromagnetic interference shielding and thermal conductive performances. Chem. Eng. J. **380**(9), 122475 (2020)

80. Wang, S.J., Li, D.S., Jiang, L.: Synergistic effects between MXenes and Ni chains in flexible and ultrathin electromagnetic interference shielding films. Adv. Mater. Interf. **6**, 1900961 (2019)
81. Ma, C., Liu, T., Xin, W., et al.: Breathable and wearable mxene-decorated air-laid paper with superior folding endurance and electromagnetic interference-shielding performances. Front. Mater. **6**, 308 (2019)
82. Wang, Q.W., Zhang, H.B., Liu, J., et al.: Multifunctional and water-resistant Mxene-decorated polyester textiles with outstanding electromagnetic interference shielding and joule heating performances. Adv. Func. Mater. **29**, 1806819 (2019)
83. Liu, L.X., Chen, W., Zhang, H.B., et al.: Flexible and multifunctional silk textiles with biomimetic leaf-like MXene/silver nanowire nanostructures for electromagnetic interference shielding, humidity monitoring, and self-derived hydrophobicity. Adv. Func. Mater. **29**, 1905197 (2019)
84. Liu, J., Zhang, H.B., Sun, R., et al.: Hydrophobic, flexible, and lightweight Mxene foams for high-performance electromagnetic-interference shielding. Adv. Mater. **29**, 1702367 (2017)
85. Han, M., Yin, X., Hantanasirisakul, K., et al.: Anisotropic MXene aerogels with a mechanically tunable ratio of electromagnetic wave reflection to absorption. Adv. Optic. Mater. **7**, 1900267 (2019)
86. Wu, X., Han, B., Zhang, H.-B., et al.: Compressible, durable and conductive polydimethylsiloxane-coated MXene foams for high-performance electromagnetic interference shielding. Chem. Eng. J. **381**, 122622 (2020)
87. Wang, L., Chen, L., Song, P., et al.: Fabrication on the annealed $Ti_3C_2T_x$ MXene/epoxy nanocomposites for electromagnetic interference shielding application. Comp. Part B-Eng. **171**, 111–118 (2019)
88. Liang, L., Han, G., Li, Y., et al.: Promising $Ti_3C_2T_x$ MXene/Ni chain hybrid with excellent electromagnetic wave absorption and shielding capacity. ACS Appl. Mater. Interf. **11**, 25399–25409 (2019)
89. Li, X., Yin, X., Liang, S., et al.: 2D Carbide MXene Ti_2CT_x as a novel high-performance electromagnetic interference shielding material. Carbon **146**, 210–217 (2019)
90. Sun, R., Zhang, H.-B., Liu, J., et al.: Highly conductive transition metal carbide/carbonitride(Mxene)@polystyrene nanocomposites fabricated by electrostatic assembly for highly efficient electromagnetic interference shielding. Adv. Func. Mater. **27**, 1702807 (2017)
91. Luo, J.Q., Zhao, S., Zhang, H.B., et al.: Flexible, stretchable and electrically conductive Mxene/natural rubber nanocomposite films for efficient electromagnetic interference shielding. Compos. Sci. Technol. **182**, 107754 (2019)
92. Wang, L., Qiu, H., Song, P., et al.: 3D $Ti_3C_2T_x$ MXene/C hybrid foam/epoxy nanocomposites with superior electromagnetic interference shielding performances and robust mechanical properties. Comp. Part A-Appl. Sci. Manuf. **123**, 293–300 (2019)
93. Zhou, Z., Liu, J., Zhang, X., et al.: Ultrathin MXene/calcium alginate aerogel film for high-performance electromagnetic interference shielding. Adv. Mater. Interf. **6**, 1802040 (2019)
94. Zheng, X., Hu, Q., Wang, Z., et al.: Roll-to-roll layer-by-layer assembly bark-shaped carbon nanotube/$Ti_3C_2T_x$ MXene textiles for wearable electronics. J. Colloid Interf. Sci. **602**, 680 (2021)
95. Hu, S., Li, S., Xu, W., et al.: Core@shell and sandwich-like $Ti_3C_2T_x$@Ni particles with enhanced electromagnetic interference shielding performance. Ceram. Int. **47**(21), 29995 (2021)
96. Wang, Z., Han, X., Zhou, Z., et al.: Lightweight and elastic wood-derived composites for pressure sensing and electromagnetic interference shielding. Comp. Sci. Techol. **213**(8), 108931 (2021)
97. Wei, X., Ma, M.G., Chen, F.: Silicone-coated MXene/cellulose nanofiber aerogel films with photothermal and joule heating performances for electromagnetic interference shielding. ACS Appl. Nano Mater. **4**, 7234–7243 (2021)

98. Lu, Z., Jia, F., Zhuo, L., et al.: Micro-porous MXene/aramid nanofibers hybrid aerogel with reversible compression and efficient EMI shielding performance. Comp. Part B-Eng. **217**(15), 108853 (2021)
99. Han, M.K., Shuck, C.E., Rakhmanov, R., et al.: Beyond $Ti_3C_2T_x$: MXenes for electromagnetic interference shielding. ACS Nano **14**, 5008–5016 (2020)
100. Iqbal, A., Shahzad, F., Hantanasirisakul, K., et al.: Anomalous absorption of electromagnetic waves by 2D transition metal carbonitride Ti_3CNT_x (MXene). Science **369**, 446 (2020)

MXene as Catalyst

Wai Yin Wong and Raja Rafidah Raja Sulaiman

Abstract Two-dimensional (2D) MXenes have been intensively studied as photo- and electrocatalysts for environmental and energy applications, including water splitting, carbon dioxide reduction, nitrogen reduction, organic pollutant degradation and oxygen reduction. This chapter discusses the photocatalytic and electrocatalytic properties of various types of MXenes/MXene composite materials for the targeted applications. Photocatalysts with MXene composites exhibited significant improvement in photocatalytic activity owing to the role of MXene as an electron sink in the heterostructure. The presence of the Schottky barrier with MXene composites effectively delayed the electron–hole pair recombination and thus improved both activity and stability. MXene exhibited some inherent activity towards photodegradation of several types of organic pollutants. For electrocatalysis, some improvement in catalytic activity with MXenes/MXene composites was revealed, with its role as the catalyst support to enable uniform distribution of electrocatalyst nanoparticles onto its surface. The synergistic effect in the metal–metal support interaction has altered the electronic structure and properties, leading to a change in the energy barrier for the electrocatalysis reactions. Nonetheless, challenges such as MXene oxidation and the synthesis of MXenes/MXene composites must be overcome to develop MXene applications on a commercial scale. This chapter also concluded with the future perspectives on using MXene as catalysts.

1 Introduction

Since the introduction of 2D MXene over the past decade, tremendous works have focused on a wide range of its applications. Among all, MXene as catalysts presents a wide window for materials exploration and performance improvement. The discovery of MXene for catalysis began in 2016, focusing on photocatalysis in hydrogen evolution reaction, oxygen evolution reaction, carbon dioxide conversion and nitrogen reduction reaction. With the rising concern on sustainable energy and water supply

W. Y. Wong (✉) · R. R. R. Sulaiman
Fuel Cell Institute, Universiti Kebangsaan Malaysia, UKM, 43600 Bangi, Selangor, Malaysia
e-mail: waiyin.wong@ukm.edu.my

M. Khalid et al. (eds.), *Fundamental Aspects and Perspectives of MXenes*,
Engineering Materials, https://doi.org/10.1007/978-3-031-05006-0_10

worldwide, various environmental benign technologies developments are on the move. These include photocatalytic water splitting for green hydrogen production as a next-generation energy carrier, photodegradation for water treatment and conversion of greenhouse gas of carbon dioxide (CO_2) to green fuels. The rapid development of MXene-based composite materials as photocatalysts has generally received positive outcomes, with tremendous improvement in the performance of the various photocatalytic processes mentioned. The unique features in MXene suiting its application as photocatalyst include its high active surface area as 2D materials, outstanding electrical conductivity, and the potential for band gap engineering via modification on termination groups and composite with photocatalytic materials.

Meanwhile, the development of MXene as the electrocatalysts are still in infancy. Several areas, not limited to these, which are receiving some attention, include electrocatalytic water splitting for hydrogen generation, oxygen reduction reaction used for energy generation through fuel cells and Li-ion batteries devices, and nitrogen reduction reaction for environmental pollution mitigation. MXene-based electrocatalysts adopt high electron conductivity, large surface area and tunable surface functional groups to provide more catalytic active sites, significantly enhancing electrocatalytic activity. MXene and MXene-supported electrocatalysts have been widely investigated for hydrogen (H_2) evolution reactions, in which MXenes contribute to lowering the energy barriers for the formation of hydrogen. Other electrocatalytic reactions, including oxygen evolution and nitrogen reduction, have shown positive outcomes to catalytic performance while still requiring in-depth studies on the reaction mechanism and their long-term durability under real operating conditions.

2 Photocatalytic Effect of MXenes/MXene Composites

Photocatalysis is regarded as the most sustainable method of converting solar energy into chemical energy for various applications. More focus is paid on environmentally related applications such as water splitting, carbon dioxide reduction, and photocatalytic degradation of water contaminants. Photocatalysis involves the absorption of light on semiconductor photocatalyst and subsequently induce the excitation of electrons (e^-) from the valance band (VB) to the conduction band (CB), forming a hole (h^+) in the initial position for a nanosecond. This allows the electrons and holes to migrate to the photocatalyst surface and serve as the active sites for the photocatalytic oxidation or reduction reaction with the adsorbed species [68]. Most often, 2D nanostructured materials have been investigated as the photocatalysts owing to the ability to construct a heterojunction structure which shortens the charge transfer path with good contact area, thus accelerating the electron–hole (e^--h^+) separation and simultaneously reducing the tendency of e^--h^+ recombination, beneficial for a stable photocatalytic reaction [89]. MXenes, which emerge as the next generation 2D materials, have been studied extensively in the past decade, produced through the etching of MAX phase with the general formula of $M_{n+1}AX_n$ (M = early *d*-group transition metal, A = Aluminium (Al) or Silicone (Si), X = C or N). The successful etching of

A layers led to the formation of MXene with the general formula of $M_{n+1}X_nT_x$ (T_x = surface termination groups of fluoride (-F), oxide (-O), or/and hydroxide (-OH)) [61]. Compared to other semiconductor photocatalysts, MXenes possess a lower Fermi level due to the hybridization between the *d* orbitals of M and the *p* orbitals of T_x [25, 35], favoring its role as co-catalysts to mediate the electron transfer. On the most commonly studied Ti_3C_2 Mxene, the -F and -OH termination groups were found to change the metallic character of pristine Ti_3C_2 MXene to semiconductor with the band gap values of 0.1 eV and 0.05 eV, respectively [61]. By engineering the band gap in MXenes, the desired photocatalytic performance can be realised when suitably composite with semiconductor materials [66].

2.1 Photocatalytic Water Splitting

To date, there are two main approaches to the use of MXenes for photocatalytic water splitting, (1) MXenes as the co-catalyst and (2) MXene derivatives as the photocatalysts or new derivate with other semiconductors [8]. The conventional water-splitting photocatalysts such as titanium dioxide (TiO_2) [37, 79, 113], molybdenum disulfide (MoS_2) [49, 101], Cadmium sulfide (CdS) [97], ZnS [84] and metal-free graphitic-carbon nitride (g-C_3N_4) [18, 43], despite possessing suitable band gap for photon absorption in the visible light region, the rapid photoinduced electron–hole (e^--h^+) recombination has limited the hydrogen production. To overcome the issue, co-catalyst is commonly used to construct the Schottky junction on the photocatalyst to delay the process. Graphene [60] and MoS_2 [72] are often selected as co-catalysts owing to their 2D morphology and high electrical conductivity. 2D MXenes with high specific surface area (SSA) and excellent electrical conductivity possess the advantage of providing enormous adsorption sites for H_3O^+ as the intermediate species in the H_2 evolution reaction [5]. For example, the heterojunction of g-C_3N_4/ Ti_3C_2 demonstrated a wider photo-absorption window than g-C_3N_4, which favors more photoinduced carriers [43]. Notably, pristine Ti_3C_2 MXene itself does not possess any photocatalytic activity [78]. Upon visible light irradiation, photoinduced e^--h^+ pairs are generated on g-C_3N_4. Ti_3C_2 acts as the receptor of electrons immigrate from g-C_3N_4 through the Schottky junction, leading to effective charge separation [70]. Figure 1 illustrates the H_2 evolution on the Ti_3C_2 MXene/photocatalyst composites with visible light irradiation.

The co-catalytic effect of Ti_3C_2 takes place with the -O termination group surface as the adsorption sites [70] and facilitate the H_2 evolution on this surface. Different heterojunction engineering leads to different H_2 evolution mechanisms that take place at different surfaces. When platinum (Pt) nanoclusters were photo-deposited onto the g-C_3N_4/ Ti_3C_2 with -F termination, the lower work function of MXene [54] compared to Pt facilitates the further electrons transfer from Ti_3C_2 to Pt [2]. The two-step electron immigration has effectively delayed the charge recombination [9], improving the H_2 evolution reaction.

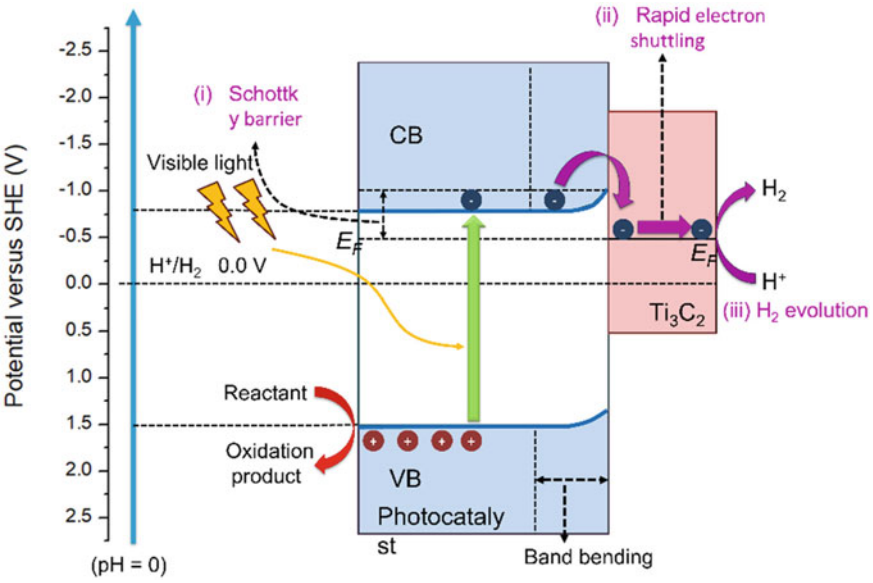

Fig. 1 Mechanism for H_2 evolution at Ti_3C_2 MXene/photocatalyst composites with visible light irradiation. Redrawn and modified from [70]

Tremendous works have focused on density functional theory (DFT) calculation and experiments to identify how the types of MXenes, compositions [78], heterojunctions [14, 71, 97, 101] and surface termination groups [25] affect the work function, which can be tuned to align with the semiconductor's band edge [25]. However, this chapter will only focus on the MXenes that have been successfully synthesised experimentally for the abovementioned photocatalytic applications. Su et al. [78] reported 2D/2D heterojunction of Ti_3C_2/g-C_3N_4 with varying amounts of Ti_3C_2 monolayers (range from 1.0 to 5.0 wt%) composite with g-C_3N_4 3.0 wt% Ti_3C_2 was revealed as the optimum amount in the composite, with the maximum H_2 evolution rate at 72.3 μmol h^{-1} g^{-1}, exceeding 10 times than that the pristine g-C_3N_4. Photoluminescence (PL) spectroscopy analysis on the O-terminated Ti_3C_2/g-C_3N_4 sample revealed the elimination of the peak at 550 nm, commonly assigned to the sub-gap defects in the photocatalyst, which would lead to the undesired charge recombination. This correlate to the ability of the 2D/2D O-terminated Ti_3C_2/g-C_3N_4 interfaces with Schottky junction to delay the e^- - h^+ recombination, and results in the improvement in the hydrogen yield as well as its photochemical stability. The effect of electron trapping on the MXene surface towards the improvement on the H_2 evolution performance is displayed in Fig. 2. Further improvement was observed on properly engineered 2D/2D/2D heterojunction of $Ti3C_2$/MoS_2/TiO_2 nanosheets [49]. The in situ growth of TiO_2 on Ti_3C_2 with subsequent deposition of MoS_2 layer onto TiO_2 (001) facet yielded an extremely high H_2 evolution rate of 6425.297 μmol h^{-1} g^{-1}, on the composition optimized sample. It is known that the (001) and (101) facets of TiO_2

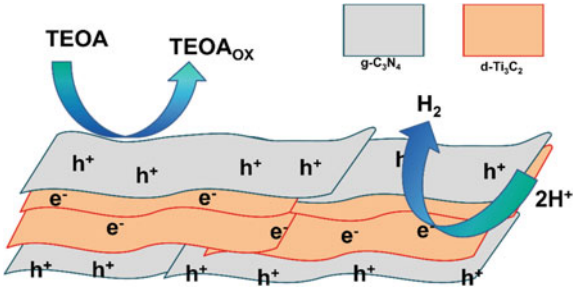

Fig. 2 Illustration of electron trapping at Mxene surface serving as the active sites for H_2 evolution. Redrawn from [5]

have a high electron affinity which is among the crucial factor for enhancing the photocatalytic H_2 evolution. Meanwhile, the improper facet pairs matching could lead to rapid charge recombination, which impedes the water splitting efficiency [67]. In this work, the close proximity between TiO_2 and Ti_3C_2 nanolayers enhanced the role of Ti_3C_2 as electrons sink during the photoexcitation on TiO_2 facets. The deposition of MoS_2 onto the TiO_2 has also assist in capturing the electrons generated from TiO_2 simultaneously, thereby providing two active sites on the co-catalysts for further enhancement in photocatalytic H_2 evolution rate and photochemical stability, as shown in Fig. 3.

Aside from H_2 evolution, O-terminate Ti_3C_2 MXene has also demonstrated a co-catalytic effect for photoinduced oxygen evolution reaction (OER). An exemplary study on 2D-Bi_2MoO_6@2D-MXene by Zuo et al. [122] revealed a similar Schottky junction effect which enhances the e^- - h^+ separation efficiency through the electron transfer to MXene, enabling the OER occurs on the Bi_2MoO_6 surface with h^+ as the active sites. Similar to Su et al. [78], the MXene composition plays a significant

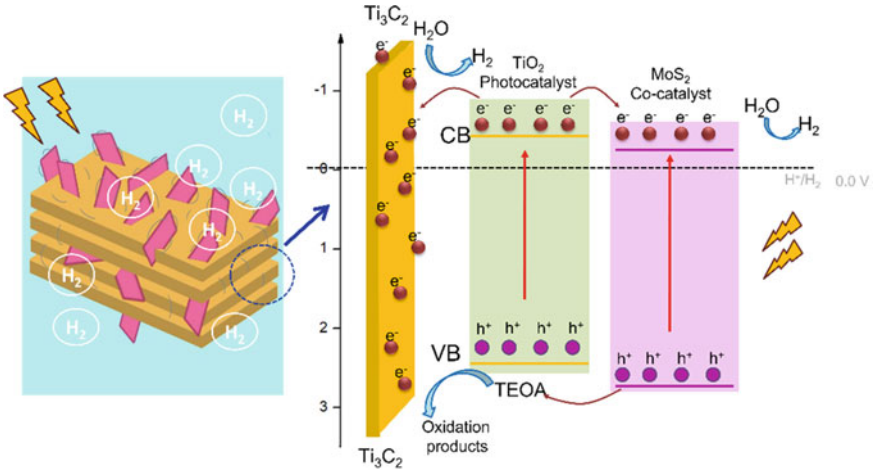

Fig. 3 Mechanism for photocatalytic H_2 evolution on 2D/2D/2D $Ti_3C_2/TiO_2/MoS_2$ heterojunctions with abundant active sites. Redrawn and modified from [49]

role in optimizing the oxygen evolution rate; In this work, the optimized composition demonstrated the highest OER rate of 734.0 μmol h^{-1} g^{-1}, near to eightfold improvement over pristine Bi_2MoO_6. X-ray photoelectron spectroscopy (XPS) revealed the role of O atoms as the medium for electrons transfer from Bi_2MoO_6 to MXene. The electrons transfer occurs when the Fermi level of Bi_2MoO_6 (−4.31 eV) > O-terminated Ti_3C_2 (−5.04 eV), as well as the higher work function of O-terminated Ti_3C_2 (6.13 eV) than Bi_2MoO_6 (4.59 eV).

Su et al. [44] have also demonstrated that the intimacy of the 2D-2D heterojunction plays a critical role in the performance enhancement compared to other heterostructures such as 2D/0D and 0D/2D when similar photocatalysts are used. Yet, it is worth noting that superior performance could be obtained on all types of heterostructures such as 0D/2D [14, 71], 1D/2D [97, 118] and 2D/2D with MXenes as nanocomposites, with illustrations shown in Fig. 4. For instance, 0D/2D MoS_2/Ti_3C_2 heterostructure prepared from the hydrothermal method has shown the successful MoS_2 nanospheres intercalation and deposition through the MXene layers [71]. Moreover, a wider light absorption band was observed on this composite material with the optimized content of the MoS_2/Ti_3C_2, achieving the H_2 evolution rate of 6144.7 μmol h^{-1} g^{-1}, compared to only 2626 μmol h^{-1} g^{-1} obtained on pristine MoS_2. Other examples of 0D semiconductor materials include TiO_2 [79] and $CdLa_2S_4$ [14] nanoparticles, which have demonstrated the H_2 evolution rate with the order of 10^0 – 10^1 mmol h^{-1} g^{-1} when monolayer Ti_3C_2 is used as co-catalyst. This is because Ti_3C_2 has enhanced the light absorption on the TiO_2 in the visible light

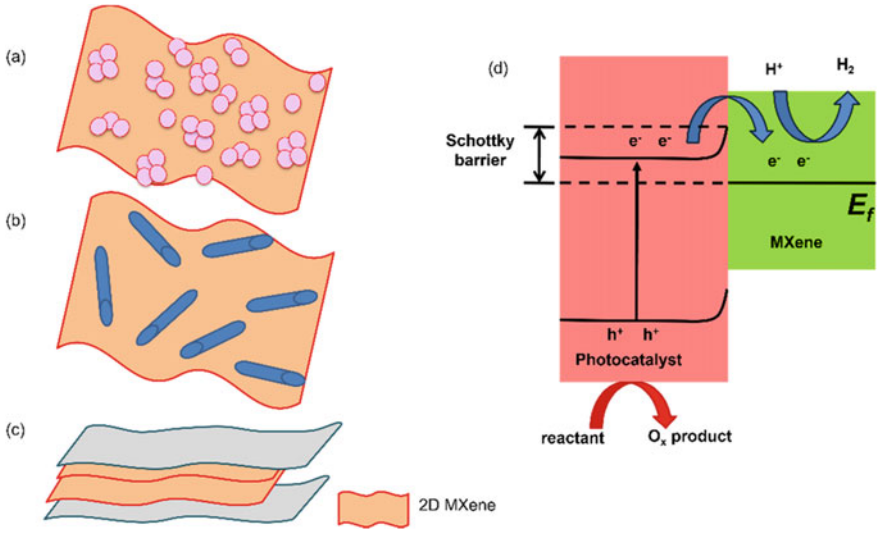

Fig. 4 Mxene as co-catalyst with the **a** 0D/2D, **b** 1D/2D and **c** 2D/2D heterostructures of photocatalyst composite for **d** improved photocatalytic H_2 evolution performance through Schottky barrier

region. More interestingly, cadmium lanthanum sulfide ($CdLa_2S_4$)/ Ti_3C_2 nanocomposite achieved more superior H_2 evolution rate of 11.18 mmol h^{-1} g^{-1} than on the noble Pt/$CdLa_2S_4$ (1.73 mmol h^{-1} g^{-1}), implying the vital role of MXene as the breakthrough co-catalyst for photocatalytic water splitting application.

Meanwhile, 1D/2D heterojunction structures such as TiO_2 nanofibers/Ti_3C_2 [121] and CdS nanorod/Ti_3C_2 [97] have both reported with significant enhancement in H_2 evolution rates than the pristine counterparts. Notably, most of the 1D/2D or 2D/2D are prepared via the electrostatic self-assembly method to achieve the desired orientation of the heterojunction. It was highlighted from the literature works on the important use of MXene monolayer as the electron mediator. Studies on the compositions variation [78, 49, 122] and use of monolayer/ multilayer [79] MXene for this application have indicated that the larger SSA of the MXene available for interfacial contact with the photocatalyst has enhanced the photocatalytic efficiency. Sufficiently large SSA of MXene leads to an increase in the light absorption on the composites and thus demonstrate lower photoluminescence (PL) effect, favoring the suppression of e^--h^+ recombination [71]. In contrast, multilayer MXene possesses lower SSA and is bulkier in structure, which results in less homogenous particle distribution [79]. Su et al. [79] reported a 5 wt. % multilayer Ti_3C_2 with TiO_2 nanoparticles demonstrated a lower H_2 evolution rate than that with 2 wt. % monolayer Ti_3C_2.

Inspired by the graphene/TiO_2 structure with excellent photocatalytic activity, the accordion-like multilayer Ti_3C_2 MXene was first attempted to be used as the precursor for one-pot synthesis of 2D carbon/TiO_2 with high SSA [23]. The ease of oxidation in delaminated MXene under an oxidative environment has sparked the light in the structural transformation on MXene. Under controlled oxidation at a suitable temperature, the layered MXene structure could be retained in the form of carbon, with the oxidized species of TiO_2 adhering/intercalating between the layers [23]. Later, various oxidation techniques were introduced to tune the desired morphology of the photocatalysts for enhancing the water splitting efficiencies. Li et al. [47] employed a series of processes, including concurrent oxidation and alkalization of delaminated Ti_3C_2, ion exchange and calcination at temperatures varied from 300–500 °C to produce a hybrid Ti_3C_2-TiO_2 nanoflowers. High-resolution transmission electron microscopy analysis (HRTEM) revealed the co-existence of Ti_3C_2 and TiO_2 in the nanoflowers with large SSA. This novel structure calcined at 500 °C displayed more superior H_2 evolution rate (783.11 μmol h^{-1} g^{-1}) than the Pt/SiO_2 calcined at the same temperature. More interestingly, this novel photocatalyst also demonstrated a bifunctional catalytic reaction with an excellent O_2 evolution rate, accounting for 501.98 μmol h^{-1} g^{-1}, compared to only 22.07 μmol h^{-1} g^{-1}on the TiO_2 nanobelt. However, the presence of the Schottky junction still accounted for the high performance of water splitting. Another approach on Ti_3C_2 oxidation was attempted via thermal treatment with carbon dioxide (CO_2) at a temperature range from 700 to 800 °C [106] to produce 2D carbon/TiO_2. Heat treatment at 700 °C with CO_2 flux at 150 sccm led to distinctive thin carbon layers with TiO_2 nanosheets formed uniformly between the layers. These 2D carbon layers were claimed to be the key driver for the e^--h^+ separation, with H_2 evolution rate of 24.0 μmol h^{-1} g^{-1}

obtained, comparable to graphene/C-TiO_2 (21.67 μmol h^{-1} g^{-1}) tested using the same sacrificial reagent of triethanolamine (TEOA) [39].

The partially oxidised Ti_3C_2 MXene into TiO_2 to composite with other photocatalysts such as MoS_2 [48] and g-C_3N_4 [18] to form heterojunctions were reported with very promising outcomes. For instance, the hydrothermally oxidized Ti_3C_2 was used to synthesized vacancy defected $Mo_xS@TiO_2@Ti_3C_2$ through further modification. This work demonstrated the H_2 evolution rate of the nanocomposite photocatalysts of as much as 193 times of that on pristine TiO_2 nanosheets. Meanwhile, C-TiO_2/g-C_3N_4, using oxidized Ti_3C_2 MXene as C-TiO_2 precursor, also displayed more superior photocatalytic H_2 evolution rate than the g-C_3N_4 counterpart. These works have collectively demonstrated the feasibility of creating higher oxidative stability MXene derivate to play a role as the photocatalyst or co-catalyst for photocatalytic water splitting applications, with very promising H_2 yield.

2.2 *Photocatalytic Carbon Dioxide (CO_2) Reduction*

Photocatalytic CO_2 reduction is one benign environmental approach to convert the CO_2 into renewable fuels such as carbon monoxide (CO), methanol (CH_3OH), formic acid (HCOOH), methane (CH_4) and formaldehyde (HCHO) [21]. Like photocatalytic water splitting, photoinduced carbon dioxide reduction reaction (CO_2RR) proceeds via the sequential process of light absorption, e^--h^+ separation, CO_2 species adsorption on the active sites, reduction reaction and finally, product desorption from the catalyst surface. The final products are determined by the different binding modes of $CO2^{\delta-}$ on the photocatalyst surfaces. Viewing the successful employment of MXenes for photocatalytic water splitting, some works have been devoted to the use of MXenes, for photocatalytic CO_2RR. However, only Ti_3C_2 MXenes have been employed as the new photocatalyst composite for this application. It is worth noting that the material instability of MXenes has led to limited works reported compared to photocatalytic water splitting. Among the few reported works, the CO_2RR products generated reported with the use of the MXenes or MXene nanocomposites are CO [12, 26, 45, 62, 76, 90, 96, 100], CH_4 [6, 26, 28, 45, 62, 90, 96] and CH_3OH [6]. Figure 5 illustrates the process of photocatalytic CO_2RR to green fuels.

TiO_2 and g-C_3N_4 nanosheets were attempted to construct the 2D/2D heterojunctions with Ti_3C_2 MXene for photocatalytic CO_2RR through mechanical mixing [96]. A comparison of the CO and CH_4 production, as well as selectivity, was made. The superior photocatalytic CO_2RR activities in the TiO_2/Ti_3C_2 and g-C_3N_4/Ti_3C_2 than TiO_2 or g-C_3N_4 were convinced through the higher yield of the products. Much higher CO selectivity was found compared to CH_4, agreeing with many prior works. More interestingly, TiO_2/Ti_3C_2 demonstrated an exceptionally high CH_4 yield of 6.34 ppm compared to the others, which recorded values below 2 ppm. Meanwhile, the ternary heterojunction of $Ti_3C_2T_x/TiO_2$/g-C_3N_4 has led to a lower yield of CH_4

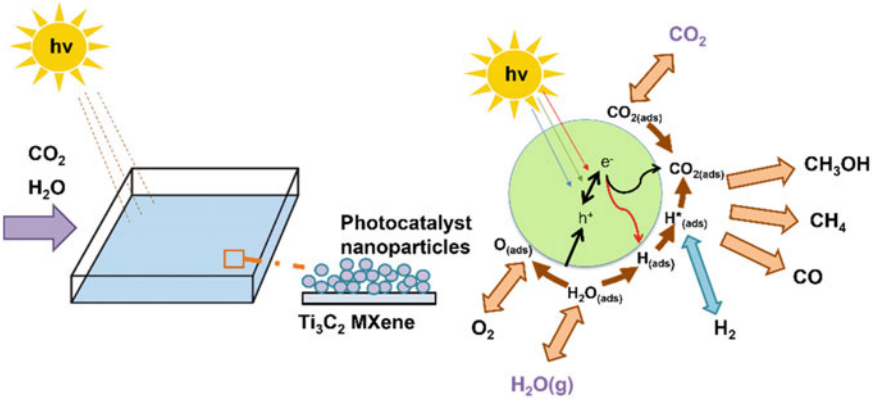

Fig. 5 Illustration for the photocatalytic CO_2RR on MXene composite to produce green fuels. Redrawn and modified from [85]

despite improvement of CO yield being reported. Notably, this ternary heterojunction further enhanced the H_2 evolution compared to the binary heterojunction, as explained in the previous section.

In situ growth of TiO_2 under various calcination temperatures on Ti_3C_2 to produce TiO_2/Ti_3C_2 photocatalyst was reported. TiO_2/Ti_3C_2 calcined at 550 °C was found to exhibit the highest photocurrent and CH_4 production rate (0.22 μmol h^{-1}), with no loss in activity after 5 cycles and was 3.7 times higher than the commercial TiO_2. This work claimed to achieve the highest CH_4 production rate with only half of the amount of photocatalyst used compared to other works [103, 120]. Partial oxidation of Ti_3C_2 into TiO_2, which was directly grown on top of Ti_3C_2 sheets, created an intimate pathway for electron transfer from TiO_2 to Ti_3C_2, which has led to spatial separation for e^- - h^+. Applicable to all photocatalytic applications, such a design provides a heterojunction that increases the photocatalytic stability and enhances the CO_2RR herein. A similar approach of in situ growth of g-C_3N_4 nanosheets over Ti_3C_2 was attempted with urea as a precursor through simple calcination (Yang et al. 2020). The work demonstrated the optimized sample yield of CO (5.19 μmol h^{-1} g^{-1}), which was 8.1 times higher than the pristine g-C_3N_4, with lower selectivity of CH_4. The heterojunction was believed to have improved the CO_2 adsorption and thus activation for the CO_2RR. Another ternary junction with different configurations of 2D/2D/0D $TiO_2/C_3N_4/Ti_3C_2$ MXene reported a novel S-scheme junction for accelerating spatial charge separation with a suitable band gap for CO_2 reduction to both CO and CH_4. This ternary junction had the highest CO_2RR rate as well as the highest yields of CO (4.39 $\mu molg^{-1}$ h^{-1}) and CH_4 (1.20 $\mu molg^{-1}$ h^{-1}). These values were three- and eight-fold higher than those on TiO_2 nanosheets. Mechanistically, the higher Fermi level in the sandwiched C_3N_4 layer is prone to transfer the electrons to the TiO_2 and Ti_3C_2. This charge redistribution leads to band bending and an internal electric field (IEF) formation at the interfaces [71]. The electrons on both TiO_2 and C_3N_4 layers were excited to the conduction bands upon solar irradiation. Under the influence of

band bending, IEF and Coulombic force, the photoinduced electrons in TiO_2 tend to recombine with h^+ on the C_3N_4. Parallelly, the photoinduced electrons in C_3N_4 were transported to T_3C_2, creating the electron sink to facilitate the CO_2 reduction [21, 46].

Ti_3C_2 MXenes have also been used to form a heterojunction with other well-known CO_2RR photocatalysts, including nickel-aluminium layered double hydroxide (NiAl-LDH) [76], single atom cobalt (Co) [12], formamidinium lead bromide quantum dots [69], cesium lead bromide ($CsPbBr_3$) perovskite nanocrystal [62], Zinc indium sulfide ($ZnIn_2S_4$) [90], bismuth tungstate (Bi_2WO_6) [6, 120] etc. The electrostatic assembly of Ti_3C_2 layer on TiO_2@$ZnIn_2S_4$ has shown remarkable improvement on CH_4 selectivity (52.7%) with the production of 34.0 μmol g^{-1} over 3 h irradiation time. This value recorded 28 times higher than the meso-TiO_2 nanosphere. It also demonstrated 6.6-fold improvement for CO production (30.5 μmol g^{-1}). With most works reported on enhancement for CO and CH_4 production using Ti_3C_2 MXene as co-catalyst, only one work reported with appreciable amount of CH_3OH, i.e. on using the ultrathin Ti_3C_2/Bi_2WO_6 photocatalyst [6] synthesised through hydrothermal growth of Bi_2WO_6 nanosheets on the Ti_3C_2 layer. Notably, the need for six electrons transfer for the synthesis of CH_3OH from CO_2 and water is the main challenge whereby most photocatalysts do not possess suitable band energy to overcome the kinetic and thermodynamic criteria to proceed to CH_3OH production, leading to a higher yield of CO, CH_4 and others [85]. One typical type of photocatalyst which could achieve 0.45 μmolg^{-1} h^{-1} under UV irradiation was Cu@TiO_2 (anatase) coated with fibre optic for enhanced light concentration transmission [95]. On Bi_2WO_6, the bulk photocatalyst did not possess the suitable band gap (2.7 eV) for the photocatalytic CO_2RR [42], while the quantum effect on the ultrathin Bi_2WO_6 nanosheets has widened the band gap to 2.98 eV [6]. Interestingly, based on a recent review paper [11], this is the first time that Bi_2WO_6 demonstrated the successful conversion of CO_2 into CH_3OH (0.44 μmol g^{-1} h^{-1}), along with the main product of CH_4 ((1.78 μmol g^{-1} h^{-1})). The total conversion was recorded 4.6 times higher than Bi_2WO_6 nanosheets. The author attributed this high photocatalytic performance to the 2D/2D heterojunction with quantum effect whereby the presence of Ti_3C_2 could activate the catalyst through the electrons sink effect, as well as the large SSA of Ti_3C_2, which provides more active sites for effective CO_2 adsorption. Nonetheless, the mechanisms involved in the photocatalytic CO_2RR to different fuel types remained elusive.

2.3 Photocatalytic Degradation

Photocatalytic degradation of water contaminants such as dyes, pharmaceutically active substances and others is one promising low-cost method for water treatment. This process involves the non-selective oxidation of organic pollutants using the hydroxyl radicals (•OH) and superoxide anions ($\bullet O_2^-$) generated in the aqueous solution through the redox reaction involving h^+ (oxidation of OH^-) and e^- (reduction

of O_2) [12]. There are intensive focuses on employing Ti_3C_2 MXenes as composites with TiO_2 or other materials with good reports on removal efficiencies. Photocatalytic degradation of dyes such as Rhodamine B (RhB) [75, 109], Congo Red (CR) [31, 32]; [83] and methyl orange (MO) [19] have been reported with the removal efficiencies of 90 to 100%. The mechanism involved is distinctive from that for water splitting and CO_2RR despite the preliminary step of the same photoinduced e–h + separation. The main intermediate species required during the photocatalytic degradation process are h^+, $\bullet O_2^-$ and/or •OH [12]. Although many photocatalysts have been identified with a narrow band gap suitable for its function under visible light irradiation, the fast e^--h^+ recombination on the catalyst has hindered their actual application for photo-degradation of pollutants. A wide range of photocatalyst materials have thus been investigated to form a composite with Ti_3C_2 experimentally and have successfully demonstrated significant improvement in photodegradation efficiency owing to (1) increased electrical conductivity, and (2) prolong the e^-h^+ recombination. In most works, delaminated multilayers Ti_3C_2 was used to composite with the photocatalysts for this application.

$Ti_3C_2/In_2S_3/CdS$ prepared via hydrothermal method demonstrated 99.1% removal of RhB in 10 min and 96% removal of MO in 30 min under visible light irradiation [19]. The role of MXene as co-catalyst to CdS, In_2S_3, and In_2S_3/CdS in this process is evitable, with a significant improvement in the photodegradation rate. More interestingly, the work demonstrated via the radical trapping experiments with the presence of radical scavengers that h^+ and $\bullet O_2^-$ are the reactive species in the photo-degradation on this catalyst. The OH- terminated Ti_3C_2 acts as the electron trap site prolonging the e^- lifetime for generation of $\bullet O_2^-$ and allowing photodegradation of RhB and MO to occur on the Ti_3C_2 surface. Meanwhile, more works demonstrated on compositing doped or undoped bismuth-based photocatalyst with Ti_3C_2 with promising results [50, 75, 82, 83]. $BiFeO_3$ nanoparticles deposited on Ti_3C_2 demonstrated complete removal of CR after visible light irradiation for 42 min with a dose of 200 mg L^{-1}, compared to only near to 30% removal using $BiFeO_3$ nanoparticles [32]. The photocatalyst remained stable with no significant performance lost after four cycles of photostability test and no change in the crystal phase structures. The slight reduction in the band gap of the nanohybrid from 2.01 eV on pure $BiFeO_3$ nanoparticles, to 1.96 eV, larger specific surface area (147 m^2 g^{-1}) owing to the presence of MXene, reduced crystallite size, have collectively contributed to the excellent performance of the nanohybrid with the delayed mechanism in the charge recombination. Meanwhile, La-Mn-co-doped $BiFeO_3/Ti_3C_2$ in their other work [31] demonstrated a lower dose of 100 mgL^{-1} and shorter photodegradation duration of 30 min required for the total removal of CR, indicating the importance of narrowing the band gap through doping of photocatalyst, towards the overall synergistic effect with MXene in the photocatalytic reactions. Li et al. [50] also demonstrated that $BiOBr/Ti_3C_2$ could completely photodegrade RhB in 75 min under the same irradiation environment.

Interestingly, Ti_3C_2 displayed inherent photodegradation activity under visible light in a few reported works [50, 83, 109], although the mechanism was not discussed. Notably, the black sheet of Ti_3C_2 was promising in harvesting visible light over a wide wavelength region (400–700 nm) under UV–vis analysis. Tariq

et al. [83] reported that the pure Ti_3C_2 MXene was capable of degrading 80% of CR in 120 min [83]. It is possible that the MXene could partially be oxidized to form $Ti_3C_2O_2$ or TiO_2, which are photoactive towards organic pollutants in wastewater. This was reported in several works using MXene derived TiO_2-based composites such as $In_2S_3/TiO_2@Ti_3C_2$ [86], $TiO_2/BiVO_4$ [75] derived from Ti_3C_2 [75], Ti_3C_2-TiO_2 nanodots [15] etc., as the photodegradation catalysts. The exceptional role of MXene as derivative for TiO_2 was demonstrated by Wang et al. [86], whereby the photodegradation of MO on $In_2S_3/TiO_2@Ti_3C_2$ was found higher than In_2S_3/TiO_2 by 1.5 times. Moreover, this composite also displayed better MO removal efficiency than In_2S_3/MoS_2, In_2S_3/CNT, and In_2S_3/reduced graphene oxide. The lower work function of Ti_3C_2 MXene and the excellent anisotropic carrier mobility and electrical conductivity has significantly improved the charge separation at the heterojunction with the photocatalysts. Unlike the functional group decoration on carbon nanostructure surfaces that would impede the electron transfer, surface termination group of MXene was found to act the bridge with the photocatalyst interface and facilitate the electron transfer. Finally, similar to other photocatalysts, the performance of the organic pollutant removal of the MXene based photocatalysts are also dependent on the precursor ratio [86], active surface area [32], and crystal phase [15].

3 Electrocatalytic Effect of MXenes/MXene Composites

Electrocatalysis is a process that involves heterogeneous catalysis on an electrode–electrolyte interface, where electrochemical reactions occur. The adsorbed species on the electrode surface may undergo oxidation or reduction with the exchange of electrons and ions and eventually form a final product. Electrocatalysis has been widely used, especially at the laboratory scale, for applications such as water splitting, oxygen reduction reaction, fuel electrooxidation, nitrogen reduction reactions, etc. Electrocatalysts facilitate the electrocatalytic reaction through several steps in the reaction mechanisms with different thermodynamic potentials for different reactions. The desired electrocatalyst should be able to catalyse a reaction with the lowest possible overpotential at the greatest efficiency [41]. Typical electrocatalysts are based on noble or transition metals in the form of pure metals, alloys, and oxides. Others include phosphides, nitrides, carbides, layered double hydroxides (LDHs), metal organic framework (MOFs), and carbon-based materials such as carbon nanotubes (CNTs) are also regarded as potential electrocatalysts [34, 52, 53, 102]. Among 2D nanomaterials, MXene has also been actively studied as an electrocatalytic material in recent years. The metal-like, high electron conductivity of MXene lowers the charge transfer resistance, which in turn accelerates the kinetics in electrocatalytic reactions. Moreover, the electrocatalytic activity of MXene is tunable by varying the "M" (M = Ti, Mo, Cr) and surface termination groups (T = -O, -OH, -F) [69, 92]. Owing to these characteristics, the MXene are generally being utilized as supports to improve the properties and performance of electrocatalysts [69, 92,

93]. This section will discuss the application of Mxenes for electrocatalytic water splitting, oxygen reduction, and nitrogen reduction reactions.

3.1 Electrocatalytic Water Splitting

Electrocatalytic water splitting involves the cathodic hydrogen evolution reaction HER and anodic OER process for green hydrogen generation [7, 73, 92]. HER mechanism involves three steps, namely the Volmer, Heyrovsky, and Tafel steps. This reaction can occur in either acid or alkaline electrolytes. Furthermore, HER is also more catalytically active in acidic conditions. Conventional cathodic electrocatalyst for hydrogen production is based on the noble metal Pt/C, which has superior catalytic activity towards HER owing to its near optimum Gibbs free energy for hydrogen adsorption (ΔG_H), where hydrogen adsorption is neither too weak nor too strong [58]. However, the high cost of Pt/C limits its usage for large-scale fabrication of electrocatalytic water splitting electrodes. Transition metal-based electrocatalysts offer a lower cost advantage, where among these catalysts materials, nickel (Ni)-based catalysts, including pure Ni and Ni alloys, are commonly used [59]. Alternatively, cobalt (Co)-based catalysts have also been investigated, such as CoP and CoS [102]. Despite their active kinetics, the overall catalytic activity of transition metal-based HER electrocatalysts are still inferior to Pt/C to date [114, 116]. The introduction of 2D nanomaterials, particularly graphene, can enhance the dispersibility of catalyst nanoparticles (NPs) and electron conductivity [30, 91]. Among Mxenes, $Ti_3C_2T_x$ MXene is commonly selected in applications to HER [93]. However, pristine Mxenes have limited HER activity. Ti-based Mxenes such as Ti_2CT_x can display an overpotential of 609 mV. Mo-based catalysts are more catalytically active with a lower overpotential of 283 mV at 10 mA/cm^2 under acid conditions [74]. Moreover, -O terminated MXenes display are more favourable for HER than non-terminated MXenes [24, 33]. Several MXenes, including the Ti_3C_2, displayed ΔG_H closer to the optimum value when terminated with oxygen, for instance, the $Ti_3C_2O_2$, as shown in the volcano plot in Fig. 6 [22]. This is due to the –O groups functioning as active sites for H adsorption. In Fig. 6, Ti_3C_2 has a more negative value that indicates stronger H bonding. The O groups on $Ti_3C_2O_2$ weaken the bonding with H, increasing the exchange current density and promoting hydrogen desorption; therefore, favouring HER [22, 92].

Various studies have addressed that the different synthesis methods, precursor's concentration and MXene termination groups have affected the overall performance and mechanism [92, 93, 112]. Given their active electrocatalytic activity towards HER, high electron conductivity, large surface area and structural stability, MXenes function as effective supports/substrates for water splitting electrocatalysts. Selective etching of MXene can produce metal vacancy defects with the ability to adsorb and reduce metal ions to form single metal atoms [111, 112]. This is one of the methods to produce MXene-single atom catalysts (SACs) hybrids which demonstrates excellent HER catalytic activity. Interaction between MXene and SACs altered the ΔG_H

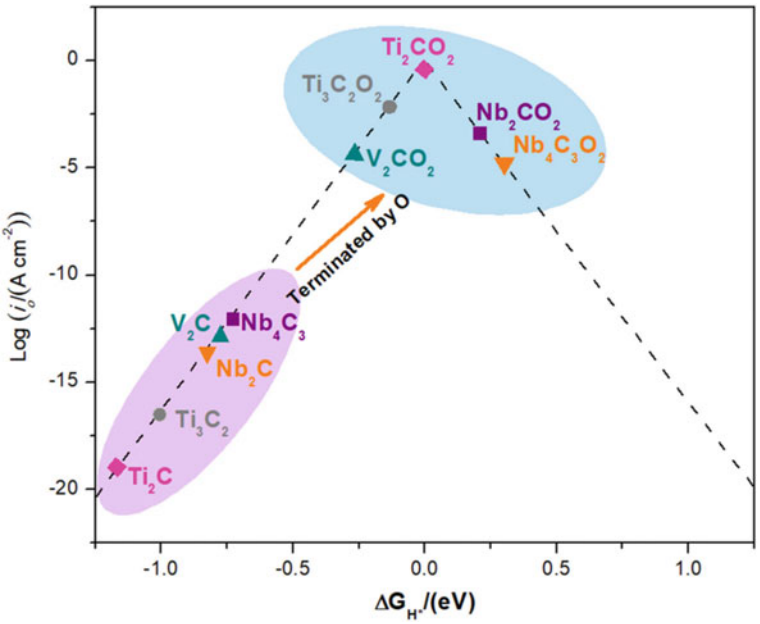

Fig. 6 Volcano plot of the exchange current density (i_o) versus the average hydrogen adsorption Gibbs free energy, ΔG_H. Redrawn and modified from [22]

closer to the optimum value through alteration of electron configuration and accelerated charge transfer. MXene-SACs also exhibit abundant active sites for H adsorption [112]. Immobilizing noble metal SAC such as Pt provides the advantage of reducing the Pt loading in the cathode. For example, Zhang et al. [111] immobilized single Pt atoms in the lattice defects of MXene $Mo_2TiC_2T_x$ for electrocatalytic HER in acids. Overpotential for the $Mo_2TiC_2T_x$-Pt_{SA} with around 1.2 wt.% immobilized Pt was revealed at 77 mV for the mass activity of 8.3 A/mg, which was about 39.5 times better than 40 wt.% of the state-of-the-art Pt/C. $Mo_2TiC_2T_x$-Pt_{SA} showed optimum ΔG_H because of lower charge density from replacing Mo atoms with Pt single atoms. Furthermore, $Mo_2TiC_2T_x$-Pt_{SA} exhibited lower charge transfer resistance, no aggregation of Pt single atoms, minimization of Pt loading, and excellent catalytic stability for 100 h. Besides noble metals, introducing transition metal single atoms in MXenes significantly enhances HER. Co single atoms present in Mo_2CT_x resulted in the replacement of Mo by Co atoms that tune the surface adsorption energy, making it more favourable to bind with hydrogen. Co provided more active sites and increased the electrochemically active surface area, enhancing intrinsic activity [40]. Besides SACs, interactions between HER catalyst nanoparticles and MXene prevent aggregation and enhance hydrogen adsorption. Nickel cobalt (NiCo) alloys are regarded as promising HER catalysts for alkaline conditions [99, 102]. HER is especially more sluggish in alkaline than in acids; thus, accelerating its kinetics is crucial for developing low-cost electrocatalysts for alkaline water electrolysers.

Du et al. [17] reported that a composite of NiCo with Ti_3C_2 MXene leads to a more optimum ΔG_H for favourable hydrogen adsorption and desorption. Further doping with niobium (Nb) increases the electronic conductivity by shifting the Fermi energy level closer to the conductive band, lowering the Nb-doped $Ti_3C_2T_x$/NiCo overpotential to 43.4 mV at 10 mA/cm^2 in alkaline, which was close to the value for Pt/C with 34.4 mV overpotential.

Heterostructures consisting of MXene have been synthesised with materials such as MoS_2, where such heterostructures offer structural stability and high electron conductivity [93]. Liang et al. [51] revealed that strong coupling between MoS_2 with Mo_2CT_x help improve the electron conductivity, electrochemical active surface area and durability. Doping with Co into MoS_2/Mo_2CT_x further enhanced these properties, leading to a lower overpotential of 112 mV at 10 mA/cm^2 in alkaline compared to 345 mV and 280 mV for pristine MoS_2 and Mo_2CT_x, respectively. In addition, carbon-coating of $Ti_3C_2T_x$ can protect the MXene from spontaneous oxidation under oxygen-containing catalytic environment. Interactions between carbon-coated $Ti_3C_2T_x$ with MoS_2 further improved structural stability, electron conductivity and lowered the overpotential in acid, where $Ti_3C_2T_x$ contributes to the fast electron transfer rate while MoS_2 provide good catalytic activity towards HER [106].

Similar to HER, MXenes have been applied as supports and hybridized with OER electrocatalysts for water splitting. Transition metal-based catalysts consisting of Nickel (Ni) alloys such as NiFe and NiCo, as well Co-based catalysts, are promising with excellent intrinsic activity towards OER [115, 88]. Generally, $Ti_3C_2T_x$ MXene is applied in OER among other MXenes; however, they are inefficient [92]. Therefore, producing hybrids through MXene-SACs and MXene-supported OER catalysts exhibit enhanced properties and intrinsic activity. Furthermore, DFT calculations have revealed that the presence of single atoms such as Cu [13] and Co [38] on MXene could alter the adsorption energies for intermediates, facilitating adsorption and desorption of OH* and facilitating OH* deprotonation to OOH*. For instance, Chen et al. [13] anchored Cu atoms on Ti_2NO_2 MXene, where bonding energies of the oxygen intermediates on Cu-Ti_2NO_2 are found to be moderate, leading to more favourable OER.

Co and Ni-based layered double hydroxides (LDHs) are among the efficient OER electrocatalysts for alkaline water splitting. MXene-supported LDHs display enhanced OER primarily due to better electron transfer [92]. Benchakar et al. [4] reported the synergistic effect between Co-LDH and $Ti_3C_2T_x$, which prevents surface oxidation on the MXene, maintaining its surface chemistry and the high electron conductivity in the hybrid catalyst. OER electrode potential was improved to around 1.57 V vs RHE at 10 mA/cm^2 for the Co-LDH/$Ti_3C_2T_x$, compared to 1.62 V vs RHE and 1.64 V vs RHE for bare Co-LDH and IrO_2, respectively. Additionally, NiFe-LDH paired with Ti_3C_2 MXene exhibited improvement in stability and electron conductivity, with 2D hierarchical structures giving large electrochemically active surface area [105]. Further doping with P groups also provides the nickel–iron (NiFe)-LDH/Ti_3C_2 with additional active sites [10]. Aside from LDHs, MXene also efficiently supports OER catalyst nanoparticles. Lu et al. [55] successfully synthesised Ti_3C_2 MXene anchored with cobalt oxide (Co_3O_4) nanocubes, where the cubes are

uniformly distributed on the MXene's surface. The 0D/2D heterostructure and high electron conductivity of MXene help accelerate the charge transfer in the hybrid catalyst, lowering the OER overpotential to 300 mV at 10 mA/cm^2, while unsupported Co_3O_4 had an overpotential of 390 mV.

In recent years, the application of MXenes in bifunctional electrocatalysts for overall water splitting has been investigated with positive outcomes. These bifunctional catalysts display the capability to catalyse both HER and OER under acid or alkaline conditions with satisfactory performance despite the challenge of the sluggish HER kinetics in alkaline and OER kinetics in acids. MXene-SACs were found to exhibit bifunctional characteristics. Peng et al. [65] showed that Ru single atoms on ultrathin $Ti_3C_2T_x$ improved HER/OER performance than bare $Ti_3C_2T_x$. Overpotentials for Ru_{SA}-$Ti_3C_2T_x$ were 70 and 290 mV at 10 mA/cm^2 for HER and OER in acid, respectively. Moreover, the Ru_{SA}-$Ti_3C_2T_x$ also displayed enhanced catalytic activity for ORR attributed to the lower adsorption energies for the intermediates. On the other hand, Ni single atoms displayed strong binding to MXene such as Cr_2CO_2, contributing to fast electron transfer and improved HER/OER activity [16].

Ni and Co-based electrocatalysts have been extensively studied for their bifunctional properties, including several well-known materials such as alloys NiFe, NiCo, and CoFe, as well as their phosphide and sulphide derivatives [88]. MXene-supported bifunctional electrocatalysts show retention and enhanced kinetics for HER/OER. Wang et al. [87] reported the lower overpotentials for HER and OER of $Mo_2TiC_2T_x$-supported NiFe nanoparticles. NiFe provides the active sites for OER while Mo on the MXene catalyses HER. Furthermore, interfacial interactions between NiFe and $Mo_2TiC_2T_x$ lead to electron transfer at the NiFe-MXene interface, facilitating intermediate NiOOH formation and lowering the energy required for hydrogen adsorption and *OOH formation (in the OER limiting step). In other studies, the successful growth of mesoporous NiCoP on Ti_3C_2 MXene results in a synergistic effect where MXene facilitates electron transfer to promote the HER/OER catalytic activity of nickel cobalt phosphide (NiCoP) while enlarging the active surface area [107]. Similarly, the growth of Co_2P on $Ti_3C_2T_x$ MXene also promotes HER/OER activity through its numerous active sites, moderate binding energies towards intermediate species, smaller overpotentials and better catalytic durability [57].

3.2 Electrocatalytic Nitrogen Reduction Reaction (N_2RR)

Electrocatalytic N_2RR offers an efficient and clean production of ammonia through the adsorption and protonation of N_2. However, electrocatalytic N_2RR faces challenges in (1) high energy required to break the N_2 triple bond (~941 kJ/mol), (2) strong interactions between N with the active sites, competing HER, leading to a poor ammonia (NH_3) yield [104]. MXenes, based on Ti and Mo, have demonstrated the properties to adsorb and induce N_2 activation with high selectivity towards N_2RR. N_2 adsorption and catalytic reaction can occur on the basal and edge sites of the MXene [92]. $Ti_3C_2T_x$ are commonly selected MXene for N_2RR, where those with -F and

-OH terminations exhibit selectivity towards N_2RR. Several different pathways are possible on the electroreduction of N_2 to NH_3, as shown in Fig. 7a [3]. On $Ti_3C_2O_2$, the active sites can present on the O- terminal groups on basal planes or Ti atoms in the edge planes, where theoretical calculations have shown that the MXene with the O-terminals at the basal plane must overcome higher activation energies, as shown in Fig. 7b [56]. This indicates that the presence of termination groups can also cause difficulties in N_2 adsorption and exhibit very limited Faradaic efficiency (FE) of less than 10% [52, 56, 92, 119]. Several MXenes are modified in terms of their composition and termination groups to overcome this limitation. The utilization of MXene

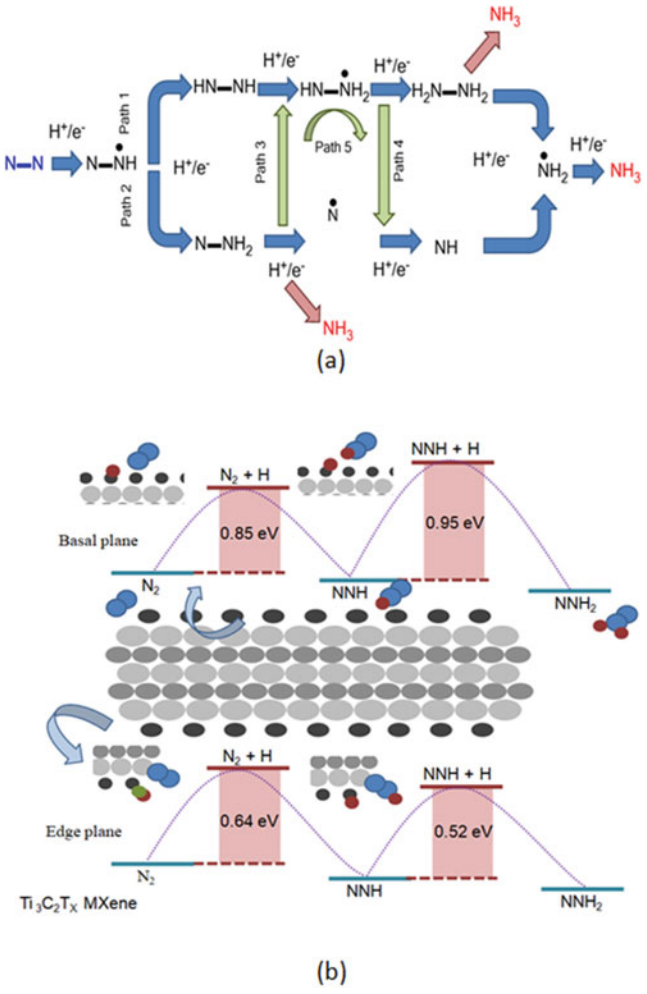

Fig. 7 **a** Proposed pathways for the formation of NH_3 from N_2, redrawn and modified from [3]. **b** Difference between the activation energies on the basal planes and edge planes of $Ti_3C_2T_x$MXene, redrawn and modified from [56]

as supports for N_2RR electrocatalysts was found to enhance the activity, structural stability and yield of NH_3 compared to bare MXenes and unsupported catalysts [52].

MXene-SAC hybrids have been investigated for electrocatalytic N_2RR, with single-atom catalysts such as Ru [29, 64], Mo [29], and Zr [44] confined on the defected MXene surface. MXene plays a role in enhancing the electron transfer between the single atoms and MXene, elongating and weakening the N≡N triple bond and lowering the hydrogenation thermodynamic energy barrier to promote electrocatalytic N_2RR activity while improving selectivity towards N_2RR. Huang et al. [29] revealed the rapid N_2 reduction on Mo@Mo_2CO_2MXene following a distal or hybrid mechanism. Furthermore, the presence of Mo, or Ru on the Mo_2CO_2, was able to suppress H adsorption, where Mo@Mo_2CO_2 showed better selectivity due to stabilized adsorbed NNH on the catalyst with multi-dinitrogen. Furthermore, Ru single atom supported on Mo_2CT_x have enhanced FE of 25.77%, with the ammonia yield around 40.57 μg/h mg_{cat} [64].

MXene-supported TiO_2 catalysts are typically studied for photocatalytic N_2RR; however, TiO_2 also exhibits potential for electrocatalytic N_2RR. Synergistic effects between TiO_2 and $Ti_3C_2T_x$ have good selectivity towards N_2RR and produce stable NH_3 generation [20, 110]. Fang et al. [20] successfully grew TiO_2 nanoparticles on $Ti_3C_2T_x$ through one-step ethanol-thermal treatment. Rich oxygen vacancies on TiO_2 function as active sites for catalyzing N_2 into NH_3, while the MXene increases the electron conductivity and specific surface area as well as minimizing TiO_2 aggregation. Efficient electron transfer helped weaken the N≡N bond. FE was achieved at 16.07% with a good NH_3 yield of 32.17 μg/h mg_{cat} in 0.1 M HCl at −045 and −0.55 V vs RHE, respectively. Aside from TiO_2, $Ti_3C_2T_x$ MXene is also able to prevent aggregation of MnO_2 [36]. Surface manganese (Mn) atoms contribute as active sites to activate the N_2 molecules. MnO_4/$Ti_3C_2T_x$ hybrid displayed NH_3 yield around 34.12 μg/h mg_{cat} and 11.39% FE at −0.55 V versus RHE in 0.1 M HCl, thus N_2 reduction capability of the MnO_4/$Ti_3C_2T_x$ can be regarded as active as the hybrid with TiO_2.

3.3 Electrocatalytic Oxygen Reduction Reaction (ORR)

Electrochemical ORR involves two different pathways in aqueous solution: (1) direct four-electron pathway for the conversion of O_2 to H_2O, and (2) two-electron pathway to convert O_2 to H_2O_2. ORR is an important reaction in fuel cells and metal-air battery systems. It is a cathodic reaction in proton exchange membrane fuel cell (PEMFC) that is limited by its sluggish kinetics and the use expensive of Pt-based catalysts [1, 77, 80, 81]. MXenes also function as excellent support for ORR catalysts, given their high electron conductivity and surface area. $Ti_3C_2T_x$ MXenes are commonly utilized, and these MXene-based catalysts significantly improved their electrocatalytic activity and durability [1]. MXene-SACs have been investigated for their application to ORR, which shows enhanced electron transfer and promotes the breaking of O_2 bonds. Different SACs would show different selectivity, where Cu is

found favourable for H_2O, and noble metals such as Pt and gold (Au) favours H_2O_2 formation [112]. Peng et al. [63] determined the lower overpotential of Cu SAC supported on Ti_2CO_2 (0.25 V) compared to Pt/C (0.4 V) for ORR in PEMFC. The presence of Cu improved the electron transfer to the active sites in the MXene-SAC, providing moderate activation energy for the rate-determining step, which was the *OOH hydrogenation. The Cu-Ti_2CO_2 exhibited high selectivity for H_2O formation and was found thermally stable at room temperature. Additionally, Ruthenium single atom catalysts (Ru-SACs) also show the ability to enlarge the electrochemically active surface area and lower the energy barriers for the formation of the intermediates during ORR on the surface of $Ti_3C_2T_x$, as shown in Fig. 8. Ru, therefore, facilitates the ORR activity on the MXene, aside from also speeding up the kinetics for HER and OER as previously mentioned in Sect. 2.1 [65].

MXene effectively supports other noble metal or transition metal-based nanoparticles, which not only improved ORR but also durability. Zhang et al. [108] showed that the Pt-supported $Ti_3C_2T_x$ exhibit higher ORR current density than Pt/C as a result of modified electronic structure and good electron conductivity, with selectivity to the four-electron pathway. Furthermore, Pt-$Ti_3C_2T_x$ also showed improvement in carbon corrosion resistance than Pt/C and showed minimal agglomeration of Pt, thus indicating its improved stability. Another noble metal, palladium (Pd), supported on $Ti_3C_2T_x$, also exhibit lesser agglomeration. A combination of $Ti_3C_2T_x$ with CNT, alongside the supported Pd, facilitates the electron conductivity, bifunctional catalytic activity of both ORR and HER in alkaline, and the stability of the catalyst [113].

Besides noble metals, MXene-supported transition metal ORR catalysts are also promising for lower-cost catalysts with excellent electrocatalytic activity. These transition metals include Co [117], Iron-based such as Fe–N-C [94], and manganese oxide (Mn_3O_4) [98]. Zhang et al. [117] successfully synthesised Co nanoparticles

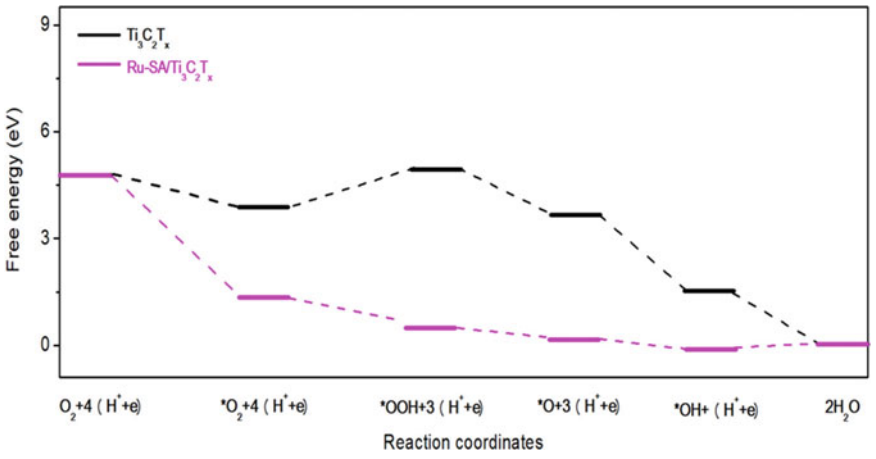

Fig. 8 Free energy for intermediate adsorption and formation on $Ti_3C_2T_x$ and Ru-SA/$Ti_3C_2T_x$, redrawn and modified from [65]

encapsulated in N-doped CNTs grown in-situ on $Ti_3C_2T_x$ MXene. Strong interfacial interactions between N-doped CNTs and $Ti_3C_2T_x$ helped enhance the charge transfer. Combination with Co further improved the bifunctional OER/ORR of the Co/N-CNT@$Ti_3C_2T_x$. In terms of ORR, Co/N-CNTs@$Ti_3C_2T_x$ had lower overpotential than Pt/C in 0.1 M KOH, while the reaction favours a four-electron pathway with hydrogen peroxide (H_2O_2) yield of less than 15%. Further, Xue et al. [98] reported the improved stability of Mn_3O_4 with Ti_3C_2 MXene. The current retention of Mn_3O_4/Ti_3C_2 was 40% after 40 h, indicating some extent of ORR stability with catalytic performance close to that of Pt/C, attributed to good distribution of Mn_3O_4 on MXene and high electron transfer in the hybrid structure [98]. In another study, the Fe–N-C/MXene hybrid structure exhibited stable ORR short-term durability with 2.6% degradation compared to 15.8% for Pt/C [94]. Besides, $Ti_3C_2T_x$ can be utilize to derive TiO_2-encapsulated carbon nitride (CN_x) when calcinated in presence of melamine-cyanuric acid [27]. The $TiO_2C@CN_x$ demonstrated excellent ORR contributed by the good hydrophilicity, presence of oxygen-vacancies from the carbon-coating layer, and minimized contact resistance. Moreover, the $TiO_2C@CN_x$ also exhibited the ability to catalyse HER and OER.

4 Challenges and Future Perspectives

MXene has inevitably led to significant improvement in both photocatalytic and electrocatalytic activity of the catalysts. Nonetheless, several areas still require specific attention for long-term and real-life applications. Although more than 100 types of MXenes have been identified, $Ti_3C_2T_x$ remains the focused type for various studies. Notably, this type of MXene possesses superior electrical conductivity and high stability under a reductive environment, yet, in most studies, no inherent catalytic activity was found. Density function theory analysis has revealed the potential of several other MXene compounds with catalytic activity, including Mo-, V-, Nb-based, etc. These materials should be further explored experimentally to understand the catalytic properties and materials stability, to suit the specific catalytic applications.

On the stability aspects, MXenes employed as photocatalysts demonstrated promising photocatalytic stability. Nonetheless, long-term stability tests were still limited. Meanwhile, when used as electrocatalysts, most studies conducted stability tests under a limited duration of less than 1000 h. Long-term durability under varying reaction conditions is crucial for large-scale, real-world applications. MXenes with different compositions and termination groups may exhibit variations in their stability under changing conditions. It is also known that MXene can easily degrade through oxidation in an aqueous solution. Several measures can be considered in improving the stability of the catalyst, including incorporating antioxidation agents and carbon, as well as optimising the preparation conditions. Multilayer MXenes demonstrated better stability than a few layers MXenes despite the more superior catalytic effects in the latter due to larger surface area and thus better electronic conductivity. Therefore, optimising the MXene layers and compositions remains crucial to balance catalytic

activity and stability. Hence, the long-term stability of the catalysts is vital to be investigated for actual operations.

In-depth studies of MXene-based catalysts, including the employment of different termination groups, at the atomic scale, such as the change in the structure and electronic state of the MXene during the photocatalytic and electrocatalytic reaction, still requires in-depth investigation. Identification of the actual active sites involved in the reactions steps is higher sought after. *In-situ* techniques and computational studies should be adopted to explore the actual mechanisms in MXene and MXene hybrids under various catalytic conditions. Moreover, large-scale production of MXene and MXene-supported catalysts should be explored with different synthesis methods, including systematic surface termination groups decoration on MXenes for different applications, to ensure that the means of production are feasible and cost-effective. Lastly, the life cycle and the environmental impact analysis should be studied prior to the large-scale production.

5 Conclusion

This chapter discussed the employment of MXenes/ MXene composites as photo- and electrocatalysts for various environmental and energy-related applications. In addition, the properties and performance improvement of the catalysts were discussed for various applications, including water splitting, CO_2RR, N_2RR, and ORR. Finally, the challenges and future perspectives towards using MXene materials for catalytic applications were concluded.

Acknowledgements The authors acknowledge the Ministry of Higher Education Malaysia through the Fundamental Research Grant Scheme with project code FRGS/1/2019/STG01/UKM/02/2 to support this work.

References

1. Ahmad Junaidi, N.H., Wong, W.Y., Loh, K.S., Rahman, S., Daud, W.R.W.: A comprehensive review of MXenes as catalyst supports for the oxygen reduction reaction in fuel cells. Int. J. Energy Res. **45**(11), 15760–15782 (2021). https://doi.org/10.1002/er.6899
2. An, X., Wang, W., Wang, J., Duan, H., Shi, J., Yu, X.: The synergetic effects of Ti3C2 MXene and Pt as co-catalysts for highly efficient photocatalytic hydrogen evolution over g-C3N4. Phys. Chem. Chem. Phys. **20**(16), 11405–11411 (2018). https://doi.org/10.1039/C8CP01123K
3. Azofra, L.M., Li, N., MacFarlane, D.R., Sun, C.: Promising prospects for 2D d2–d4 M3C2 transition metal carbides (MXenes) in N2 capture and conversion into ammonia. Energy Environ. Sci. **9**(8), 2545–2549 (2016). https://doi.org/10.1039/C6EE01800A
4. Benchakar, M., Bilyk, T., Garnero, C., Loupias, L., Morais, C., Pacaud, J., et al.: MXene supported cobalt layered double hydroxide nanocrystals: facile synthesis route for a synergistic

oxygen evolution reaction electrocatalyst. Adv. Mater. Interfaces **6**(23), 1901328 (2019). https://doi.org/10.1002/admi.201901328
5. Biswal, L., Nayak, S., Parida, K.: Recent progress on strategies for the preparation of 2D/2D MXene/g-C3N4 nanocomposites for photocatalytic energy and environmental applications. Catal. Sci. Technol. **11**(4), 1222–1248 (2021). https://doi.org/10.1039/D0CY02156C
6. Cao, S., Shen, B., Tong, T., Fu, J., Yu, J.: 2D/2D Heterojunction of Ultrathin MXene/Bi2WO6 nanosheets for improved photocatalytic CO2 reduction. Adv. Func. Mater. **28**(21), 1800136 (2018). https://doi.org/10.1002/adfm.201800136
7. Chandrasekaran, S., Ma, D., Ge, Y., Deng, L., Bowen, C., Roscow, J., et al.: Electronic structure engineering on two-dimensional (2D) electrocatalytic materials for oxygen reduction, oxygen evolution, and hydrogen evolution reactions. Nano Energy **77**, 105080 (2020). https://doi.org/10.1016/j.nanoen.2020.105080
8. Chang, H., Li, X.Z., Shi, L.N., Zhu, Y.R., Yi, T.F.: Towards high-performance electrocatalysts and photocatalysts: design and construction of MXenes-based nanocomposites for water splitting. Chem. Eng. J. 421 (2021). https://doi.org/10.1016/j.cej.2021.129944
9. Chang, K., Mei, Z., Wang, T., Kang, Q., Ouyang, S., Ye, J.: MoS2/graphene cocatalyst for efficient photocatalytic H2 evolution under visible light irradiation. ACS Nano **8**(7), 7078–7087 (2014). https://doi.org/10.1021/nn5019945
10. Chen, J., Long, Q., Xiao, K., Ouyang, T., Li, N., Ye, S., et al.: Vertically-interlaced NiFeP/MXene electrocatalyst with tunable electronic structure for high-efficiency oxygen evolution reaction. Sci. Bulletin. **66**(11), 1063–1072 (2021). https://doi.org/10.1016/j.scib.2021.02.033
11. Chen, T., Liu, L.Z., Hu, C., Huang, H.W.: Recent advances on Bi2WO6-based photocatalysts for environmental and energy applications. Chin. J. Catal. **42**(9), 1413–1438 (2021). https://doi.org/10.1016/S1872-2067(20)63769-X
12. Chen, Y.H., Qi, M.Y., Li, Y.H., Tang, Z.R., Wang, T., Gong, J.L. et al.: Activating two-dimensional Ti3C2Tx-MXene with single-atom cobalt for efficient CO2 photoreduction. Cell Rep. Phys. Sci. **2**(3) (2021c). https://doi.org/10.1016/j.xcrp.2021.100371
13. Chen, Z., Fan, X., Shen, Z., Ruan, X., Wang, L., Zeng, H., et al.: Cu anchored Ti2NO2 as high performance electrocatalyst for oxygen evolution reaction: a density functional theory study. ChemCatChem **12**(16), 4059–4066 (2020). https://doi.org/10.1002/cctc.202000591
14. Cheng, L., Chen, Q., Li, J., Liu, H.: Boosting the photocatalytic activity of CdLa2S4 for hydrogen production using Ti3C2 MXene as a co-catalyst. Appl. Catal. B **267**, 118379 (2020). https://doi.org/10.1016/j.apcatb.2019.118379
15. Cheng, X., Zu, L., Jiang, Y., Shi, D., Cai, X., Ni, Y., et al.: A titanium-based photo-Fenton bifunctional catalyst of mp-MXene/TiO2−x nanodots for dramatic enhancement of catalytic efficiency in advanced oxidation processes. Chem. Commun. **54**(82), 11622–11625 (2018). https://doi.org/10.1039/C8CC05866K
16. Cheng, Y., Dai, J., Song, Y., Zhang, Y.: Nanostructure of Cr2CO2 MXene supported single metal atom as an efficient bifunctional electrocatalyst for overall water splitting. ACS Appl. Energy Mater. **2**(9), 6851–6859 (2019). https://doi.org/10.1021/acsaem.9b01329
17. Du, C.-F., Sun, X., Yu, H., Liang, Q., Dinh, K.N., Zheng, Y., et al.: Synergy of Nb doping and surface alloy enhanced on water-Alkali electrocatalytic hydrogen generation performance in Ti-based MXene. Adv. Sci. **6**(11), 1900116 (2019). https://doi.org/10.1002/advs.201900116
18. Esfahani, R.A.M., Fruehwald, H.M., Laschuk, N.O., Sullivan, M.T., Egan, J.G., Ebralidze, I.I., et al.: A highly durable N-enriched titanium nanotube suboxide fuel cell catalyst support. Appl. Catal. B **263**, 118272 (2020)
19. Fang, H., Pan, Y., Yin, M., Xu, L., Zhu, Y., Pan, C.: Facile synthesis of ternary Ti3C2–OH/ln2S3/CdS composite with efficient adsorption and photocatalytic performance towards organic dyes. J. Solid State Chem. **280**, 120981 (2019a). https://doi.org/10.1016/j.jssc.2019.120981
20. Fang, Y., Liu, Z., Han, J., Jin, Z., Han, Y., Wang, F., et al.: High-performance electrocatalytic conversion of N2 to NH3 using oxygen-vacancy-Rich TiO2 In situ grown on Ti3C2Tx MXene. Adv. Energy Mater. **9**(16), 1803406 (2019b). https://doi.org/10.1002/aenm.201803406

21. Fu, J., Jiang, K., Qiu, X., Yu, J., Liu, M.: Product selectivity of photocatalytic CO2 reduction reactions. Mater. Today **32**, 222–243 (2020). https://doi.org/10.1016/j.mattod.2019.06.009
22. Gao, G., O'Mullane, A.P., Du, A.: 2D MXenes: a new family of promising catalysts for the hydrogen evolution reaction. ACS Catal. **7**(1), 494–500 (2017). https://doi.org/10.1021/acscatal.6b02754
23. Gao, Y., Chen, H., Zhou, A., Li, Z., Liu, F., Hu, Q., et al.: Novel hierarchical TiO2/C nanocomposite with enhanced photocatalytic performance. NANO **10**(05), 1550064 (2015). https://doi.org/10.1142/S1793292015500642
24. Handoko, A.D., Fredrickson, K.D., Anasori, B., Convey, K.W., Johnson, L.R., Gogotsi, Y., et al.: Tuning the basal plane functionalization of two-dimensional metal carbides (MXenes) to control hydrogen evolution activity. ACS Appl. Energy Mater. **1**(1), 173–180 (2018). https://doi.org/10.1021/acsaem.7b00054
25. Hantanasirisakul, K., Gogotsi, Y.: Electronic and optical properties of 2D transition metal carbides and nitrides (MXenes). Adv. Mater. **30**(52), 1804779 (2018). https://doi.org/10.1002/adma.201804779
26. He, F., Zhu, B., Cheng, B., Yu, J., Ho, W., Macyk, W.: 2D/2D/0D TiO2/C3N4/Ti3C2 MXene composite S-scheme photocatalyst with enhanced CO2 reduction activity. Appl. Catal. B **272**, 119006 (2020). https://doi.org/10.1016/j.apcatb.2020.119006
27. He, L.H., Liu, J.M., Liu, Y.K., Cui, B.B., Hu, B., Wang, M.H., et al.: Titanium dioxide encapsulated carbon-nitride nanosheets derived from MXene and melamine-cyanuric acid composite as a multifunctional electrocatalyst for hydrogen and oxygen evolution reaction and oxygen reduction reaction. Appl. Catalysis B-Environ. **248**, 366–379 (2019). https://doi.org/10.1016/j.apcatb.2019.02.033
28. Hu, J.M., Ding, J., Zhong, Q.: Ultrathin 2D Ti3C2 MXene Co-catalyst anchored on porous g-C3N4 for enhanced photocatalytic CO2 reduction under visible-light irradiation. J. Colloid Interface Science. **582**, 647–657 (2021). https://doi.org/10.1016/j.jcis.2020.08.047
29. Huang, B., Li, N., Ong, W.-J., Zhou, N.: Single atom-supported MXene: how single-atomic-site catalysts tune the high activity and selectivity of electrochemical nitrogen fixation. J. Mater. Chem. A. **7**(48), 27620–27631 (2019). https://doi.org/10.1039/C9TA09776G
30. Hughes, J.P., Clipsham, J., Chavushoglu, H., Rowley-Neale, S.J., Banks, C.E.: Polymer electrolyte electrolysis: a review of the activity and stability of non-precious metal hydrogen evolution reaction and oxygen evolution reaction catalysts. Renew. Sustain. Energy Rev. **139**, 110709 (2021). https://doi.org/10.1016/j.rser.2021.110709
31. Iqbal, M.A., Ali, S.I., Amin, F., Tariq, A., Iqbal, M.Z., Rizwan, S.: La- and Mn-Codoped Bismuth Ferrite/Ti3C2 MXene composites for efficient photocatalytic degradation of congo red dye. ACS Omega **4**(5), 8661–8668 (2019). https://doi.org/10.1021/acsomega.9b00493
32. Iqbal, M.A., Tariq, A., Zaheer, A., Gul, S., Ali, S.I., Iqbal, M.Z., et al.: Ti3C2-MXene/Bismuth ferrite nanohybrids for efficient degradation of organic dyes and colorless pollutants. ACS Omega **4**(24), 20530–20539 (2019). https://doi.org/10.1021/acsomega.9b02359
33. Jiang, Y., Sun, T., Xie, X., Jiang, W., Li, J., Tian, B., et al.: Oxygen-functionalized ultrathin Ti3C2Tx MXene for enhanced electrocatalytic hydrogen evolution. Chemsuschem **12**(7), 1368–1373 (2019). https://doi.org/10.1002/cssc.201803032
34. Khan, M.A., Zhao, H., Zou, W., Chen, Z., Cao, W., Fang, J., et al.: Recent progresses in electrocatalysts for water electrolysis. Electrochem. Energy Rev. **1**(4), 483–530 (2018). https://doi.org/10.1007/s41918-018-0014-z
35. Khazaei, M., Ranjbar, A., Ghorbani-Asl, M., Arai, M., Sasaki, T., Liang, Y., et al.: Nearly free electron states in MXenes. Phys. Rev. B **93**(20), 205125 (2016). https://doi.org/10.1103/PhysRevB.93.205125
36. Kong, W., Gong, F., Zhou, Q., Yu, G., Ji, L., Sun, X., et al.: An MnO2–Ti3C2Tx MXene nanohybrid: an efficient and durable electrocatalyst toward artificial N2 fixation to NH3 under ambient conditions. J. Mater. Chem. A. **7**(32), 18823–18827 (2019). https://doi.org/10.1039/C9TA04902A
37. Kong, X., Gao, P., Jiang, R., Feng, J., Yang, P., Gai, S., et al.: Orderly layer-by-layered TiO2/carbon superstructures based on MXene's defect engineeringfor efficient hydrogen evolution. Appl. Catal. A **590**, 117341 (2020). https://doi.org/10.1016/j.apcata.2019.117341

38. Kou, Z., Zang, W., Pei, W., Zheng, L., Zhou, S., Zhang, S., et al.: A sacrificial Zn strategy enables anchoring of metal single atoms on the exposed surface of holey 2D molybdenum carbide nanosheets for efficient electrocatalysis. J. Mater. Chem. A. **8**(6), 3071–3082 (2020). https://doi.org/10.1039/C9TA12838G
39. Kuang, L., Zhang, W.: Enhanced hydrogen production by carbon-doped TiO2 decorated with reduced graphene oxide (rGO) under visible light irradiation. RSC Adv. **6**(3), 2479–2488 (2016). https://doi.org/10.1039/C5RA26096E
40. Kuznetsov, D.A., Chen, Z., Kumar, P.V., Tsoukalou, A., Kierzkowska, A., Abdala, P.M., et al.: Single site cobalt substitution in 2D molybdenum carbide (MXene) enhances catalytic activity in the hydrogen evolution reaction. J. Am. Chem. Soc. **141**(44), 17809–17816 (2019). https://doi.org/10.1021/jacs.9b08897
41. Lasia, A.: Impedance Spectroscopy Applied to the Study of Electrocatalytic Processes. In: Wandelt, K. (ed.) Encyclopedia of Interfacial Chemistry, pp. 241–263. Elsevier, Oxford (2018)
42. Li, C., Xu, Y., Tu, W., Chen, G., Xu, R.: Metal-free photocatalysts for various applications in energy conversion and environmental purification. Green Chem. **19**(4), 882–899 (2017). https://doi.org/10.1039/C6GC02856J
43. Li, J., Zhao, L., Wang, S., Li, J., Wang, G., Wang, J.: In situ fabrication of 2D/3D g-C3N4/Ti3C2 (MXene) heterojunction for efficient visible-light photocatalytic hydrogen evolution. Appl. Surf. Sci. **515**, 145922 (2020). https://doi.org/10.1016/j.apsusc.2020.145922
44. Li, L., Wang, X., Guo, H., Yao, G., Yu, H., Tian, Z., et al.: Theoretical screening of single transition metal atoms embedded in MXene defects as superior electrocatalyst of nitrogen reduction reaction. Small Methods. **3**(11), 1900337 (2019). https://doi.org/10.1002/smtd.201900337
45. Li, X., Bai, Y., Shi, X., Huang, J.D., Zhang, K., Wang, R. et al.: Mesoporous g-C3N4 /MXene (Ti3C2Tx) heterojunction as a 2D electronic charge transfer for efficient photocatalytic CO2 reduction. Appl. Surface Sci. 546 (2021). https://doi.org/10.1016/j.apsusc.2021.149111
46. Li, X., Liu, C., Wu, D., Li, J., Huo, P., Wang, H.: Improved charge transfer by size-dependent plasmonic Au on C3N4 for efficient photocatalytic oxidation of RhB and CO2 reduction. Chin. J. Catal. **40**(6), 928–939 (2019). https://doi.org/10.1016/S1872-2067(19)63347-4
47. Li, Y., Deng, X., Tian, J., Liang, Z., Cui, H.: Ti3C2 MXene-derived Ti3C2/TiO2 nanoflowers for noble-metal-free photocatalytic overall water splitting. Appl. Mater. Today **13**, 217–227 (2018). https://doi.org/10.1016/j.apmt.2018.09.004
48. Li, Y., Ding, L., Liang, Z., Xue, Y., Cui, H., Tian, J.: Synergetic effect of defects rich MoS2 and Ti3C2 MXene as cocatalysts for enhanced photocatalytic H2 production activity of TiO2. Chem. Eng. J. **383**, 123178 (2020). https://doi.org/10.1016/j.cej.2019.123178
49. Li, Y., Yin, Z., Ji, G., Liang, Z., Xue, Y., Guo, Y., et al.: 2D/2D/2D heterojunction of Ti3C2 MXene/MoS2 nanosheets/TiO2 nanosheets with exposed (001) facets toward enhanced photocatalytic hydrogen production activity. Appl. Catal. B **246**, 12–20 (2019). https://doi.org/10.1016/j.apcatb.2019.01.051
50. Li, Z., Zhang, H., Wang, L., Meng, X., Shi, J., Qi, C., et al.: 2D/2D BiOBr/Ti3C2 heterojunction with dual applications in both water detoxification and water splitting. J. Photochem. Photobiol. A **386**, 112099 (2020). https://doi.org/10.1016/j.jphotochem.2019.112099
51. Liang, J., Ding, C., Liu, J., Chen, T., Peng, W., Li, Y., et al.: Heterostructure engineering of Co-doped MoS2 coupled with Mo2CTx MXene for enhanced hydrogen evolution in alkaline media. Nanoscale **11**(22), 10992–11000 (2019). https://doi.org/10.1039/C9NR02085C
52. Lim, K.R.G., Handoko, A.D., Nemani, S.K., Wyatt, B., Jiang, H.-Y., Tang, J., et al.: Rational design of two-dimensional transition metal carbide/nitride (MXene) hybrids and nanocomposites for catalytic energy storage and conversion. ACS Nano **14**(9), 10834–10864 (2020). https://doi.org/10.1021/acsnano.0c05482
53. Liu, Q., Wang, E., Sun, G.: Layered transition-metal hydroxides for alkaline hydrogen evolution reaction. Chin. J. Catal. **41**(4), 574–591 (2020). https://doi.org/10.1016/s1872-2067(19)63458-3
54. Liu, Y., Xiao, H., Goddard, W.A.: Schottky-barrier-free contacts with two-dimensional semiconductors by surface-engineered MXenes. J. Am. Chem. Soc. **138**(49), 15853–15856 (2016). https://doi.org/10.1021/jacs.6b10834

55. Lu, Y., Fan, D., Chen, Z., Xiao, W., Cao, C., Yang, X.: Anchoring Co3O4 nanoparticles on MXene for efficient electrocatalytic oxygen evolution. Sci. Bulletin. **65**(6), 460–466 (2020). https://doi.org/10.1016/j.scib.2019.12.020
56. Luo, Y., Chen, G.-F., Ding, L., Chen, X., Ding, L.-X., Wang, H.: Efficient electrocatalytic N2 fixation with MXene under ambient conditions. Joule. **3**(1), 279–289 (2019). https://doi.org/10.1016/j.joule.2018.09.011
57. Lv, Z., Ma, W., Dang, J., Wang, M., Jian, K., Liu, D., et al.: Induction of Co2P growth on a MXene (Ti3C2Tx)-modified self-supporting electrode for efficient overall water splitting. J. Phys. Chem. Lett. **12**(20), 4841–4848 (2021). https://doi.org/10.1021/acs.jpclett.1c01345
58. Mahmood, N., Yao, Y., Zhang, J.-W., Pan, L., Zhang, X., Zou, J.-J.: Electrocatalysts for hydrogen evolution in alkaline electrolytes: mechanisms, challenges, and prospective solutions. Adv. Sci. **5**(2), 1700464 (2018). https://doi.org/10.1002/advs.201700464
59. Miller, H.A., Bouzek, K., Hnat, J., Loos, S., Bernäcker, C.I., Weißgärber, T., et al.: Green hydrogen from anion exchange membrane water electrolysis: a review of recent developments in critical materials and operating conditions. Sustain. Energy Fuels **4**(5), 2114–2133 (2020). https://doi.org/10.1039/C9SE01240K
60. Mohd Shah, N.R.A., Mohamad Yunus, R., Rosman, N.N., Wong, W.Y., Arifin, K., Jeffery, M.L.: Current progress on 3D graphene-based photocatalysts: from synthesis to photocatalytic hydrogen production. Int. J. Hydrogen Energy **46**(14), 9324–9340 (2021). https://doi.org/10.1016/j.ijhydene.2020.12.089
61. Naguib, M., Kurtoglu, M., Presser, V., Lu, J., Niu, J., Heon, M., et al.: Two-dimensional nanocrystals produced by exfoliation of Ti3AlC2. Adv. Mater. **23**(37), 4248–4253 (2011). https://doi.org/10.1002/adma.201102306
62. Pan, A.Z., Ma, X.Q., Huang, S.Y., Wu, Y.S., Jia, M.J., Shi, Y.M., et al.: CsPbBr 3 perovskite nanocrystal grown on MXene nanosheets for enhanced photoelectric detection and photocatalytic CO2 reduction. J. Phys. Chem. Lett. **10**(21), 6590–6597 (2019). https://doi.org/10.1021/acs.jpclett.9b02605
63. Peng, Q., Zhou, J., Chen, J., Zhang, T., Sun, Z.: Cu single atoms on Ti2CO2 as a highly efficient oxygen reduction catalyst in a proton exchange membrane fuel cell. J. Mater. Chem. A. **7**(45), 26062–26070 (2019). https://doi.org/10.1039/C9TA08297B
64. Peng, W., Luo, M., Xu, X., Jiang, K., Peng, M., Chen, D., et al.: Spontaneous atomic ruthenium doping in Mo2CTX MXene defects enhances electrocatalytic activity for the nitrogen reduction reaction. Adv. Energy Mater. **10**(25), 2001364 (2020). https://doi.org/10.1002/aenm.202001364
65. Peng, X., Zhao, S., Mi, Y., Han, L., Liu, X., Qi, D., et al.: Trifunctional single-atomic Ru sites enable efficient overall water splitting and oxygen reduction in acidic media. Small **16**(33), 2002888 (2020). https://doi.org/10.1002/smll.202002888
66. Persson, P.O.Å., Rosen, J.: Current state of the art on tailoring the MXene composition, structure, and surface chemistry. Curr. Opin. Solid State Mater. Sci. **23**(6), 100774 (2019). https://doi.org/10.1016/j.cossms.2019.100774
67. Phawa, C., Prayoonpokarach, S., Sinthiptharakoon, K., Chakthranont, P., Sangkhun, W., Faungnawakij, K., et al.: Effects of matching facet Pairs of TiO2 on photoelectrochemical water splitting behaviors. ChemCatChem **12**(7), 2116–2124 (2020). https://doi.org/10.1002/cctc.201901857
68. Qu, Y., Duan, X.: Progress, challenge and perspective of heterogeneous photocatalysts. Chem. Soc. Rev. **42**(7), 2568–2580 (2013). https://doi.org/10.1039/C2CS35355E
69. Que, M.D., Zhao, Y., Yang, Y.W., Pan, L.K., Lei, W.Y., Cai, W.H., et al.: Anchoring of formamidinium lead bromide quantum dots on Ti3C2 nanosheets for efficient photocatalytic reduction of CO2. ACS Appl. Mater. Interfaces. **13**(5), 6180–6187 (2021). https://doi.org/10.1021/acsami.0c18391
70. Ran, J., Gao, G., Li, F.-T., Ma, T.-Y., Du, A., Qiao, S.-Z.: Ti3C2 MXene co-catalyst on metal sulfide photo-absorbers for enhanced visible-light photocatalytic hydrogen production. Nat. Commun. **8**(1), 13907 (2017). https://doi.org/10.1038/ncomms13907

71. Ren, D., Zhang, W., Ding, Y., Shen, R., Jiang, Z., Lu, X., et al.: In situ fabrication of robust cocatalyst-free CdS/g-C3N4 2D–2D Step-Scheme heterojunctions for highly active H2 evolution. Solar RRL. **4**(8), 1900423 (2020). https://doi.org/10.1002/solr.201900423
72. Rosman, N.N., Mohamad Yunus, R., Jeffery Minggu, L., Arifin, K., Salehmin, M.N.I., Mohamed, M.A., et al.: Photocatalytic properties of two-dimensional graphene and layered transition-metal dichalcogenides based photocatalyst for photoelectrochemical hydrogen generation: an overview. Int. J. Hydrogen Energy **43**(41), 18925–18945 (2018). https://doi.org/10.1016/j.ijhydene.2018.08.126
73. Sahoo, P.K., Bisoi, S.R., Huang, Y.-J., Tsai, D.-S., Lee, C.-P.: 2D-layered non-precious electrocatalysts for hydrogen evolution reaction: fundamentals to applications. Catalysts **11**(6), 689 (2021)
74. Seh, Z.W., Fredrickson, K.D., Anasori, B., Kibsgaard, J., Strickler, A.L., Lukatskaya, M.R., et al.: Two-dimensional molybdenum carbide (MXene) as an efficient electrocatalyst for hydrogen evolution. ACS Energy Lett. **1**(3), 589–594 (2016). https://doi.org/10.1021/acsenergylett.6b00247
75. Shi, L., Xu, C., Jiang, D., Sun, X., Wang, X., Wang, Q., et al.: Enhanced interaction in TiO2/BiVO4 heterostructures via MXene Ti3C2-derived 2D-carbon for highly efficient visible-light photocatalysis. Nanotechnology **30**(7), 075601 (2018). https://doi.org/10.1088/1361-6528/aaf313
76. Shi, Q.R., Zhang, X.Y., Yang, Y., Huang, J.J., Fu, X.L., Wang, T.Y., et al.: 3D hierarchical architecture collaborating with 2D/2D interface interaction in NiAl-LDH/Ti3C2 nanocomposite for efficient and selective photoconversion of CO2. J. Energy Chem. **59**, 9–18 (2021). https://doi.org/10.1016/j.jechem.2020.10.038
77. Si, F., Zhang, Y., Yan, L., Zhu, J., Xiao, M., Liu, C., et al.: 4 - Electrochemical Oxygen Reduction Reaction. In: Xing, W., Yin, G., Zhang, J. (eds.) Rotating Electrode Methods and Oxygen Reduction Electrocatalysts, pp. 133–170. Elsevier, Amsterdam (2014)
78. Su, T., Hood, Z.D., Naguib, M., Bai, L., Luo, S., Rouleau, C.M., et al.: 2D/2D heterojunction of Ti3C2/g-C3N4 nanosheets for enhanced photocatalytic hydrogen evolution. Nanoscale **11**(17), 8138–8149 (2019). https://doi.org/10.1039/C9NR00168A
79. Su, T., Hood, Z.D., Naguib, M., Bai, L., Luo, S., Rouleau, C.M., et al.: Monolayer Ti3C2Tx as an effective Co-catalyst for enhanced photocatalytic hydrogen production over TiO2. ACS Appl Energy Mater. **2**(7), 4640–4651 (2019). https://doi.org/10.1021/acsaem.8b02268
80. Sudarsono, W., Wong, W.Y., Loh, K.S., Kok, K.-Y., Syarif, N., Abidin, A.F.Z., et al.: Elucidating the roles of the Fe-Nx active sites and pore characteristics on Fe-Pani-biomass-derived RGO as oxygen reduction catalysts in PEMFCs. Mater. Res. Bull. **145**, 111526 (2022). https://doi.org/10.1016/j.materresbull.2021.111526
81. Sudarsono, W., Wong, W.Y., Loh, K.S., Majlan, E.H., Syarif, N., Kok, K.-Y. et al.: Noble-free oxygen reduction reaction catalyst supported on Sengon wood (Paraserianthes falcataria L.) derived reduced graphene oxide for fuel cell application. Int. J. Energy Res. **44**(3), 1761–74 (2020). https://doi.org/10.1002/er.5015
82. Sun, C., Wang, R.: Enhanced photocatalytic activity of Bi2WO6 for the degradation of TC by synergistic effects between amorphous Ti and Ni as hole–electron cocatalysts. New J. Chem. **44**(26), 10833–10839 (2020). https://doi.org/10.1039/D0NJ00015A
83. Tariq, A., Ali, S.I., Akinwande, D., Rizwan, S.: Efficient visible-light photocatalysis of 2D-MXene nanohybrids with Gd3+- and Sn4+-codoped bismuth ferrite. ACS Omega **3**(10), 13828–13836 (2018). https://doi.org/10.1021/acsomega.8b01951
84. Tie, L., Yang, S., Yu, C., Chen, H., Liu, Y., Dong, S., et al.: In situ decoration of ZnS nanoparticles with Ti(3)C(2) MXene nanosheets for efficient photocatalytic hydrogen evolution. J. Colloid Interface Sci. **545**, 63–70 (2019). https://doi.org/10.1016/j.jcis.2019.03.014
85. Tountas, A.A., Peng, X., Tavasoli, A.V., Duchesne, P.N., Dingle, T.L., Dong, Y., et al.: Towards solar methanol: past, present, and future. Adv. Sci. **6**(8), 1801903 (2019). https://doi.org/10.1002/advs.201801903
86. Wang, H., Wu, Y., Xiao, T., Yuan, X., Zeng, G., Tu, W., et al.: Formation of quasi-core-shell In2S3/anatase TiO2@metallic Ti3C2Tx hybrids with favorable charge transfer channels

for excellent visible-light-photocatalytic performance. Appl. Catal. B **233**, 213–225 (2018). https://doi.org/10.1016/j.apcatb.2018.04.012
87. Wang, J., He, P., Shen, Y., Dai, L., Li, Z., Wu, Y., et al.: FeNi nanoparticles on Mo2TiC2Tx MXene@nickel foam as robust electrocatalysts for overall water splitting. Nano Res. **14**(10), 3474–3481 (2021). https://doi.org/10.1007/s12274-021-3660-0
88. Wang, J., Yue, X., Yang, Y., Sirisomboonchai, S., Wang, P., Ma, X., et al.: Earth-abundant transition-metal-based bifunctional catalysts for overall electrochemical water splitting: a review. J Alloys Compd. **819**, 153346 (2020). https://doi.org/10.1016/j.jallcom.2019.153346
89. Wang, K., Li, J., Zhang, G.: Ag-Bridged Z-Scheme 2D/2D Bi5FeTi3O15/g-C3N4 heterojunction for enhanced photocatalysis: mediator-induced interfacial charge transfer and mechanism insights. ACS Appl. Mater. Interfaces. **11**(31), 27686–27696 (2019). https://doi.org/10.1021/acsami.9b05074
90. Wang, K., Li, X.H., Wang, N., Shen, Q.H., Liu, M.C., Zhou, J.C., et al.: Z-Scheme core-shell meso-TiO2@ZnIn2S4/Ti3C2 MXene enhances visible light-driven CO2-to-CH4 selectivity. Ind. Eng. Chem. Res. **60**(24), 8720–8732 (2021). https://doi.org/10.1021/acs.iecr.1c00713
91. Wang, L., Li, Y., Xia, M., Li, Z., Chen, Z., Ma, Z., et al.: Ni nanoparticles supported on graphene layers: an excellent 3D electrode for hydrogen evolution reaction in alkaline solution. J. Power Sources. **347**, 220–228 (2017). https://doi.org/10.1016/j.jpowsour.2017.02.017
92. Wang, Y., Nian, Y., Biswas, A.N., Li, W., Han, Y., Chen, J.G.: Challenges and opportunities in utilizing MXenes of carbides and nitrides as electrocatalysts. Adv. Energy Mater. **11**(3), 2002967 (2021). https://doi.org/10.1002/aenm.202002967
93. Wei, Y., Soomro, R.A., Xie, X., Xu, B.: Design of efficient electrocatalysts for hydrogen evolution reaction based on 2D MXenes. J. Energy Chem. **55**, 244–255 (2021). https://doi.org/10.1016/j.jechem.2020.06.069
94. Wen, Y.Y., Ma, C., Wei, Z.T., Zhu, X.X., Li, Z.X.: FeNC/MXene hybrid nanosheet as an efficient electrocatalyst for oxygen reduction reaction. RSC Adv. **9**(24), 13424–13430 (2019). https://doi.org/10.1039/c9ra01330j
95. Wu, J.C.S.: Photocatalytic reduction of greenhouse gas CO2 to fuel. Catal. Surv. Asia **13**(1), 30–40 (2009). https://doi.org/10.1007/s10563-009-9065-9
96. Wu, J.L., Zhang, Y., Lu, P., Fang, G.Q., Li, X., Yu, W.W. et al.: Engineering 2D multi-hetero-interface in the well-designed nanosheet composite photocatalyst with broad electron-transfer channels for highly-efficient solar-to-fuels conversion. Appl. Catalysis B-Environl. 286 (2021). https://doi.org/10.1016/j.apcatb.2021.119944
97. Xiao, R., Zhao, C., Zou, Z., Chen, Z., Tian, L., Xu, H., et al.: In situ fabrication of 1D CdS nanorod/2D Ti3C2 MXene nanosheet Schottky heterojunction toward enhanced photocatalytic hydrogen evolution. Appl. Catal. B **268**, 118382 (2020). https://doi.org/10.1016/j.apcatb.2019.118382
98. Xue, Q., Pei, Z.X., Huang, Y., Zhu, M.S., Tang, Z.J., Li, H.F., et al.: Mn3O4 nanoparticles on layer-structured Ti3C2 MXene towards the oxygen reduction reaction and zinc-air batteries. J. Mater. Chem. A. **5**(39), 20818–20823 (2017). https://doi.org/10.1039/c7ta04532h
99. Yan, Y., Xia, B.Y., Zhao, B., Wang, X.: A review on noble-metal-free bifunctional heterogeneous catalysts for overall electrochemical water splitting. J. Mater. Chem. A. **4**(45), 17587–17603 (2016). https://doi.org/10.1039/c6ta08075h
100. Yang, C., Tan, Q.Y., Li, Q., Zhou, J., Fan, J.J., Li, B. et al.: 2D/2D Ti3C2 MXene/g-C3N4 nanosheets heterojunction for high efficient CO2 reduction photocatalyst: dual effects of urea. Appl. Catalysis B-Environ. 268 (2020). https://doi.org/10.1016/j.apcatb.2020.118738
101. Yao, Z., Sun, H., Sui, H., Liu, X.: 2D/2D Heterojunction of R-scheme Ti3C2 MXene/MoS2 nanosheets for enhanced photocatalytic performance. Nanoscale Res. Lett. **15**(1), 78 (2020). https://doi.org/10.1186/s11671-020-03314-z
102. Yu, F., Yu, L., Mishra, I.K., Yu, Y., Ren, Z.F., Zhou, H.Q.: Recent developments in earth-abundant and non-noble electrocatalysts for water electrolysis. Mater. Today Phys. **7**, 121–138 (2018). https://doi.org/10.1016/j.mtphys.2018.11.007
103. Yu, J., Low, J., Xiao, W., Zhou, P., Jaroniec, M.: Enhanced photocatalytic CO2-reduction activity of anatase TiO2 by coexposed 001 and 101 facets. J. Am. Chem. Soc. **136**(25), 8839–8842 (2014). https://doi.org/10.1021/ja5044787

104. Yu, L.-l., Qin, J.-z., Zhao, W.-j., Zhang, Z.-g., Ke, J., Liu, B.-j.: Advances in two-dimensional MXenes for Nitrogen electrocatalytic reduction to ammonia. Int. J. Photoenergy. 2020, 5251431 (2020). https://doi.org/10.1155/2020/5251431
105. Yu, M., Zhou, S., Wang, Z., Zhao, J., Qiu, J.: Boosting electrocatalytic oxygen evolution by synergistically coupling layered double hydroxide with MXene. Nano Energy **44**, 181–190 (2018). https://doi.org/10.1016/j.nanoen.2017.12.003
106. Yuan, W., Cheng, L., Zhang, Y., Wu, H., Lv, S., Chai, L., et al.: 2D-Layered Carbon/TiO2 hybrids derived from Ti3C2MXenes for photocatalytic hydrogen evolution under visible light irradiation. Adv. Mater. Interfaces **4**(20), 1700577 (2017). https://doi.org/10.1002/admi.201700577
107. Yue, Q., Sun, J., Chen, S., Zhou, Y., Li, H., Chen, Y., et al.: Hierarchical mesoporous MXene–NiCoP electrocatalyst for water-splitting. ACS Appl. Mater. Interfaces. **12**(16), 18570–18577 (2020). https://doi.org/10.1021/acsami.0c01303
108. Zhang, C., Ma, B., Zhou, Y.K., Wang, C.: Highly active and durable Pt/MXene nanocatalysts for ORR in both alkaline and acidic conditions. J. Electroanalyt. Chem. 865 (2020a). https://doi.org/10.1016/j.jelechem.2020.114142
109. Zhang, H., Li, M., Cao, J., Tang, Q., Kang, P., Zhu, C., et al.: 2D a-Fe2O3 doped Ti3C2 MXene composite with enhanced visible light photocatalytic activity for degradation of Rhodamine B. Ceram. Int. **44**(16), 19958–19962 (2018). https://doi.org/10.1016/j.ceramint.2018.07.262
110. Zhang, J., Yang, L., Wang, H., Zhu, G., Wen, H., Feng, H., et al.: In situ hydrothermal growth of TiO2 nanoparticles on a conductive Ti3C2Tx MXene nanosheet: a synergistically active Ti-Based nanohybrid electrocatalyst for enhanced N2 reduction to NH3 at ambient conditions. Inorg. Chem. **58**(9), 5414–5418 (2019). https://doi.org/10.1021/acs.inorgchem.9b00606
111. Zhang, J., Zhao, Y., Guo, X., Chen, C., Dong, C.-L., Liu, R.-S., et al.: Single platinum atoms immobilized on an MXene as an efficient catalyst for the hydrogen evolution reaction. Nat. Catal. **1**(12), 985–992 (2018). https://doi.org/10.1038/s41929-018-0195-1
112. Zhang, M., Lai, C., Li, B., Liu, S., Huang, D., Xu, F., et al.: MXenes as superexcellent support for confining single atom: properties, synthesis, and electrocatalytic applications. Small **17**(29), 2007113 (2021). https://doi.org/10.1002/smll.202007113
113. Zhang. P., Wang, R.R., Xiao, T., Chang, Z., Fang, Z.W., Zhu, Z.L. et al.: The high-performance bifunctional catalyst Pd/Ti3C2Tx-carbon nanotube for oxygen reduction reaction and hydrogen evolution reaction in alkaline medium. Energy Technol **8**(7) (2020b). https://doi.org/10.1002/ente.202000306
114. Zhang, S., Zhang, X., Rui, Y., Wang, R., Li, X.: Recent advances in non-precious metal electrocatalysts for pH-universal hydrogen evolution reaction. Green Energy Environment. (2020). https://doi.org/10.1016/j.gee.2020.10.013
115. Zhang, W., Li, D., Zhang, L., She, X., Yang, D.: NiFe-based nanostructures on nickel foam as highly efficiently electrocatalysts for oxygen and hydrogen evolution reactions. J. Energy Chem. **39**, 39–53 (2019). https://doi.org/10.1016/j.jechem.2019.01.017
116. Zhang, X.-Y., Yu, W.-L., Zhao, J., Dong, B., Liu, C.-G., Chai, Y.-M.: Recent development on self-supported transition metal-based catalysts for water electrolysis at large current density. Appl. Mater. Today **22**, 100913 (2021). https://doi.org/10.1016/j.apmt.2020.100913
117. Zhang, Y.K., Jiang, H.L., Lin, Y.X., Liu, H.J., He, Q., Wu, C.Q. et al.: In Situ growth of cobalt nanoparticles encapsulated nitrogen-doped carbon nanotubes among Ti3C2Tx (MXene) matrix for oxygen reduction and evolution. Adv. Mater. Interfaces **5**(16) (2018c). https://doi.org/10.1002/admi.201800392
118. Zhang, Z.T., Yi, G.Y., Li, P., Zhang, X.X., Fan, H.Y., Wang, X.D., et al.: Engineering approach toward catalyst design for solar photocatalytic CO2 reduction: a critical review. Int. J. Energy Res. **45**(7), 9895–9913 (2021). https://doi.org/10.1002/er.6603
119. Zhao, J., Zhang, L., Xie, X.-Y., Li, X., Ma, Y., Liu, Q., et al.: Ti3C2Tx (T = F, OH) MXene nanosheets: conductive 2D catalysts for ambient electrohydrogenation of N2 to NH3. J. Mater. Chem. A. **6**(47), 24031–24035 (2018). https://doi.org/10.1039/C8TA09840A
120. Zhou, Y., Tian, Z., Zhao, Z., Liu, Q., Kou, J., Chen, X., et al.: High-yield synthesis of ultrathin and uniform Bi_2WO_6 square nanoplates benefitting from photocatalytic reduction of CO_2 into

renewable hydrocarbon fuel under visible light. ACS Appl. Mater. Interfaces. **3**(9), 3594–3601 (2011). https://doi.org/10.1021/am2008147

121. Zhuang, Y., Liu, Y., Meng, X.: Fabrication of TiO2 nanofibers/MXene Ti3C2 nanocomposites for photocatalytic H2 evolution by electrostatic self-assembly. Appl. Surf. Sci. **496**, 143647 (2019). https://doi.org/10.1016/j.apsusc.2019.143647
122. Zuo, G., Wang, Y., Teo, W.L., Xie, A., Guo, Y., Dai, Y., et al.: Enhanced photocatalytic water oxidation by hierarchical 2D-Bi2MoO6@2D-MXene Schottky junction nanohybrid. Chem. Eng. J. **403**, 126328 (2021). https://doi.org/10.1016/j.cej.2020.126328

Biomedical Applications of MXenes

Selvaganapathy Ganesan, K. R. Ethiraj, Mohan Kumar Kesarla, and Arunkumar Palaniappan

Abstract This chapter deals with various biomedical applications of MXenes, from biosensing, photothermal and photodynamic anticancer therapy, combination anticancer therapy with other treatment modalities, theranostics, antimicrobial treatment platforms to more recent tissue engineering applications. The chapter throws light on the mechanistic understanding of the role of MXenes in various types of biosensors fabrication, with an emphasis on wearable sensors. The chapter also gives a detailed understanding of MXenes' role as photothermal, photodynamic, and theranostic agents. The chapter also explicates the importance of MXenes in antimicrobial treatment and their relevance in treating antimicrobial resistance. Finally, the chapter also discusses the biocompatibility studies on MXene, which are an important aspect for MXene to have continued usage in biomedical applications. Overall, this chapter gives an overview of various biomedical applications and the relevance of MXenes in each of these applications.

Keywords Biosensors · Theranostics · Tissue engineering · Antimicrobials · Wearable sensors

1 Introduction

Recent advancements in the biomedical sciences and nanotechnology significantly impacted the diagnosis, treatment, and management of various diseases. As a result, novel nanomaterials are being developed for a wide range of biomedical applications.

S. Ganesan · A. Palaniappan (✉)
Centre for Biomaterials, Cellular and Molecular Theranostics (CBCMT), Vellore Institute of Technology, Vellore, India
e-mail: arunkumar.p@vit.ac.in

S. Ganesan · K. R. Ethiraj
School of Advanced Sciences, Vellore Institute of Technology, Vellore, India

M. K. Kesarla
Instituto de Ciencias Físicas, Universidad Nacional Autónoma de Mexico, 62210 Cuernavaca, Morelos, Mexico

M. Khalid et al. (eds.), *Fundamental Aspects and Perspectives of MXenes*, Engineering Materials, https://doi.org/10.1007/978-3-031-05006-0_11

The main determinants for the success of these nanomaterials are their composition, structure, morphology, physicochemical properties, and efficient interaction with the biological systems. Moreover, the issues of biocompatibility, biodistribution, excretion and cellular uptake of these bionanomaterials are significant. Therefore, they must be taken into account to ensure the feasibility of the clinical translation of these nanomaterials.

In recent times, several classes of nanomaterials with a wide range of morphologies such as nanotubes, nanosheets, nanospheres, nanowires, nanoribbons, nano flowers, and nanocages have been successfully synthesized and engineered for application in biosensing, drug delivery (especially targeted drug delivery), tissue engineering, antimicrobial, immunomodulation, neuromodulation, and cancer treatment platforms. These include nanomaterials from carbon allotropes (graphene; carbon nanotubes; carbon quantum dots), graphitic carbon nitride, gold nanostructures, copper sulfide nanoparticles (NPs), molybdenum NPs, and various other biopolymeric nanomaterials. On this line, a new class of 2D nanomaterials system called MXenes has emerged as a potential biomaterial candidate to interface with biological systems and to serve as building blocks in the fabrication of nano-biomaterial device platforms.

MXenes are two-dimensional (2D) inorganic compounds with a thickness of a few atomic layers and are composed of transition metal carbides, nitrides, or carbonitrides such as titanium carbide (Ti_3C_2) and titanium carbonitride (Ti_2CN). MXenes have an exclusive combination of properties, like high electrical conductivity, good biocompatibility, hydrophilic surface behavior, good mechanical stability, excellent optical, plasmonic, and physiochemical properties. MXenes also possess good biological properties, with high surface area for improved drug loading/delivery, good hydrophilic surface for better biocompatibility, good conductivity, and electromagnetic field, especially near-infrared light absorption property for imaging purposes like computed tomography (CT) scans and magnetic resonance imaging (MRI). Because of these suitable properties, there is an uprising research interest in MXenes for biomedical applications, which started around 2016. This chapter will give an overview of the various biomedical applications of MXenes, starting from biosensing, cancer therapy to the latest works on tissue engineering applications, which is summarized in Fig. 1.

2 MXenes for Biosensing Applications

Biosensing involves the detection of biomolecules using an analytical device, which converts a biological response into electrical, optical, or other quantifiable signals/parameters. It has wide applications in medical diagnosis, environmental monitoring, biology, agriculture, defence, and food safety. The first biosensor discovered in 1962 by Clark and Lyons determined glucose in biological samples [2]. Following this, biosensors advanced rapidly, thanks to innovative research in electrochemistry and nanotechnology, which led to bioelectronics. In the past few decades,

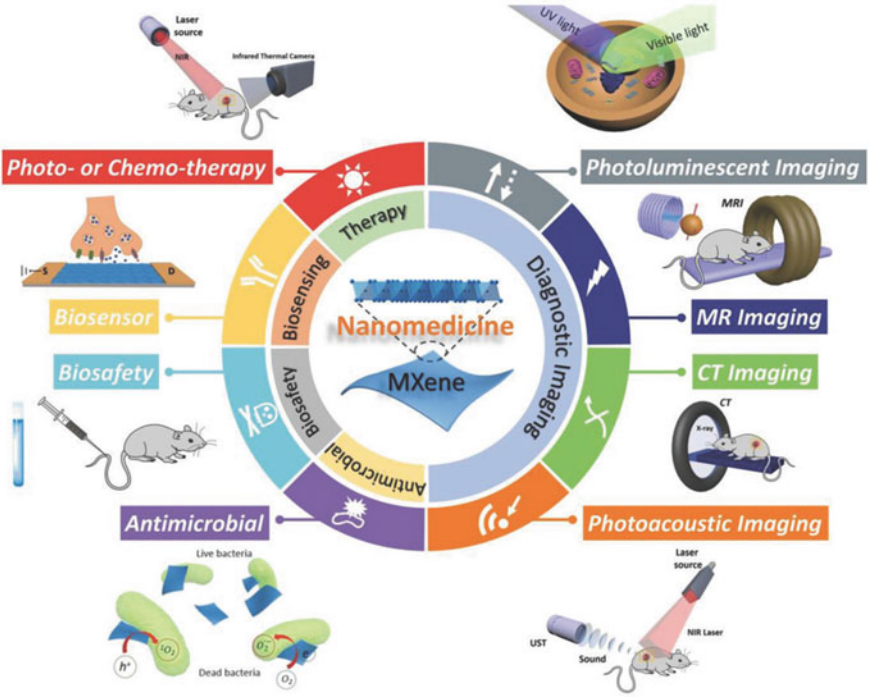

Fig. 1 Schematic overview of the MXene-based biomedical applications (figure reproduced with permission from [1])

two-dimensional nanomaterials have been explored much in the area of biosensors development because of their high surface area, unique geometries, biocompatibility, and, more importantly, their more relevant physicochemical properties. Since the introduction of MXene in 2011, it has gained extensive attention for its excellent physicochemical properties, mechanical characteristics, very high surface sensitivity, and selectivity detection. Figure 2a gives an overview of the working principle of biosensors, and Fig. 2b provides an overview of relevant properties of MXene for biosensing applications. Moreover, MXene nanosheets have a large surface area, rich in surface functional groups such as –O, –OH, and –F, making them easier to be modulated to absorb a variety of biomolecules and alter the conductive properties [3–5]. Moreover, MXenes, with their semi-conductive metallic properties with a proper bandgap, exhibit fewer current leakages in an off-state than graphene, which favors a higher detection sensitivity [6].

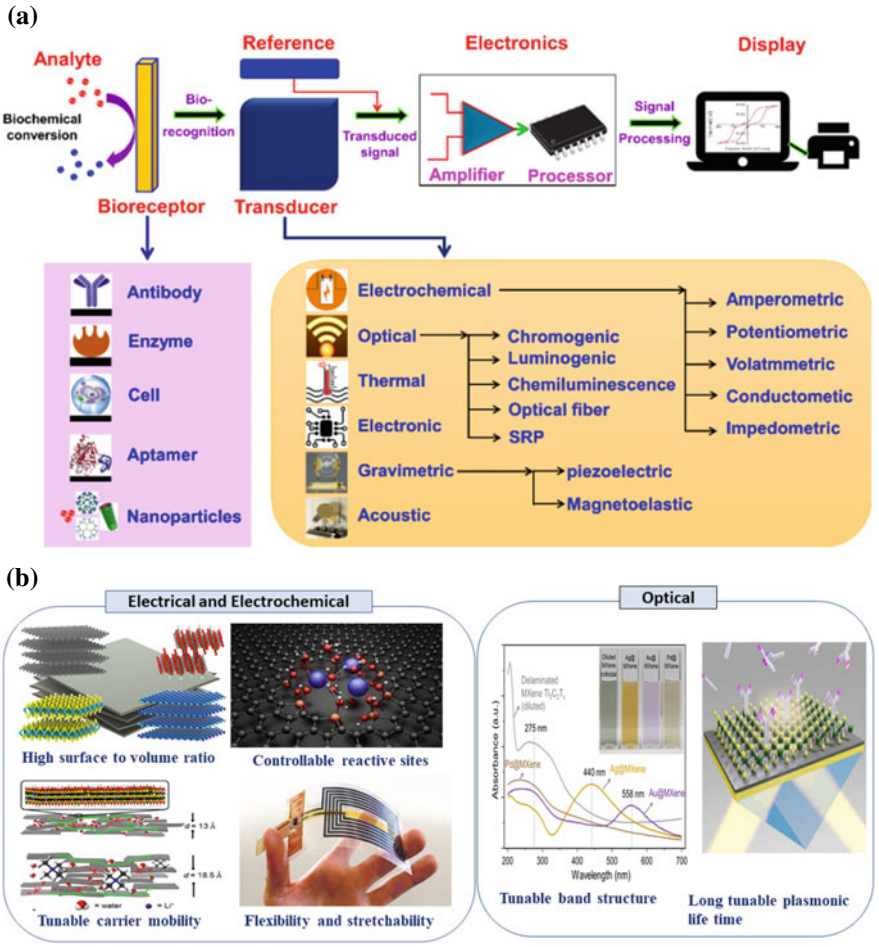

Fig. 2 **a** Schematic overview of the working principle of the biosensor (figure reproduced with permission from [7]). **b** Beneficial properties of MXene as they relate to sensing mechanisms (figure reproduced with permission from [8–13])

2.1 MXene in Electrochemical Biosensors

2.1.1 Enzyme-Based Electrochemical Sensors

The properties like excellent conductivity, optical and plasmonic properties, exceptional surface chemistry, and biocompatibility attract MXene as an interesting matrix material for the fabrication of biosensors [14]. Based on the recognition element type, biosensors can be categorized as enzymatic, non-enzymatic, whole-cell, and immunosensors [15]. Among these, enzymatic biosensors are extremely sensitive, selective, and reversible [16]. The study of direct electron transfer (DET) of redox

enzymes or proteins helps understand proteins' fundamental thermodynamics and their kinetic properties, which allows a foundation for the fabrication of mediator-free biosensors [3, 17]. Furthermore, the enzymes can be easily trapped on the MXene surface, and due to the excellent charge mobility of MXene, better electrical communication can be accomplished between the enzyme and the electrode [18]. Therefore, MXene is an ideal matrix candidate to enable DET with improved electrode kinetics, better sensitivity, high selectivity, and lower LOD with the potential to retain the bioactivity of immobilized enzymes or proteins. Furthermore, incorporation of metal or metal oxide nanoparticles on the protein/enzyme immobilized MXene interface leads to improvement of the overall surface area of the working electrode and reduction in the overpotential during electroanalysis, which improves the efficiency of MXene sensors [19].

This section discusses the electrochemical and biochemical sensors utilizing MXene and its hybrids as direct or indirect redox transducers and catalysts. An electrochemical phenol biosensor based on MXene and tyrosinase is designed to detect phenol. The devised MXene-based tyrosinase biosensors displayed satisfactory analytical performance over a wide range from 0.05 to 15.5 μmol L^{-1}, with a detection limit of 12 nmol L^{-1} and sensitivity of 414.4 mA M^{-1} [21]. An enzymatic biosensor is designed based on beta-hydroxybutyrate incorporated on MXene nanosheets. The $Ti_3C_2T_x$ MXene sheets are used as a matrix to immobilize beta-hydroxybutyrate dehydrogenase (beta-HBD), a sensing probe. MXene was combined with beta-HBD by sonication, and bovine serum albumin (BSA) and glutaraldehyde (GA) were added to enhance beta-HBD stability. The prepared MXene-beta-HBD composite was immobilized on the ruthenium hexamine-modified gold (Au)-printed circuit board electrode. The prepared biosensor detected beta-hydroxybutyrate with high sensitivity and with a wide linear response range [22]. The Ti_3C_2 MXene nanosheet functionalized with amino-silane is used to detect cancer biomarkers like carcinoembryonic antigen (CEA). Here the detection of CEA by the covalently bound anti-CEA bio receptor, the sensing probe on the Ti_3C_2 MXene nanosheet, the redox signals from the ([Ru (NH3)6]3+) decreased due to the formation of the immune complex on the Ti_3C_2 MXene nanosheets. This was used to evaluate the detection of the CEA in a highly sensitive way [23].

Hybridization of MXene with other nanomaterials can be used to design electrochemical biosensors. A hybrid film of MXene with graphene (MG) is evaluated for the electrochemical detection of glucose. A three-dimensional porous film was prepared by combining MXene and graphene on the glassy carbon electrode, which improved the enzyme loading and reduced the unwanted aggregation of the graphene. The enzyme, Glucose oxidase (GOx) is the sensing probe for glucose detection, which could react with glucose through a redox reaction. The biosensor fabrication process is elucidated in Fig. 3. The prepared MG hybrid film has excellent loading capacity due to its large, activated surface area, abundant pores, and enough surface hydrophilicity. The fabricated biosensor exhibited an outstanding glucose sensing performance better than the other types of 3D porous material based biosensors [24] (Table 1).

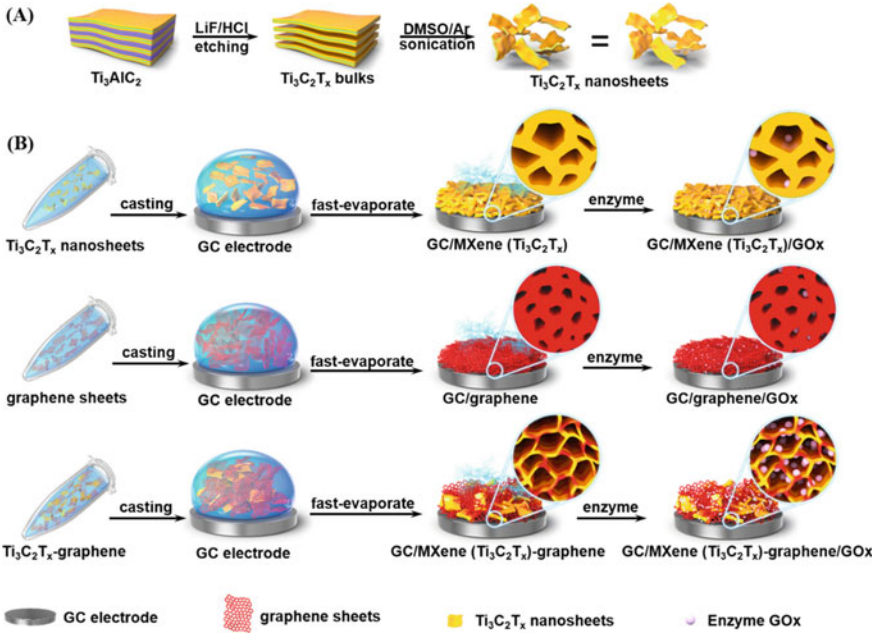

Fig. 3 Schematic representation of the preparation strategies of **a** $Ti_3C_2T_x$ nanosheets; **b** Pure $Ti_3C_2T_x$ Film, Pure Graphene Film, and MG Hybrid Film for enzyme Immobilization (reproduced with permission from [20])

2.1.2 Nucleic Acid-Based Electrochemical Biosensors

A label-free MXene based electrochemical gliotoxin biosensor was developed by combining MXene nanosheet with tetrahedral DNA nanostructure (TDN) and horseradish peroxidase (HRP). To determine the gliotoxin detection performance of this biosensor, gliotoxin mixed with gliotoxin aptamer/signal probe was injected into this biosensor. Upon addition, the gliotoxin is strongly bound to the gliotoxin aptamer of the gliotoxin aptamer/signal probe. As a result, the signal probe was detached from the gliotoxin aptamer and attached to the TDN's capture probe in the TDN/MXene complex. The gliotoxin detection ability of this biosensor is determined by the quantification of the signal from the signal probe bound to the TDN/MXene complex. Due to the MXene nanosheets' high conductivity and flexibility, this fabricated biosensor showed a highly sensitive limit of detection of 1.63 pg/mL and a detection range of 1.63 to 3260 pg/mL for gliotoxin [35].

In another study, gold (Au) nanoparticles and MXenes were used as multiple micro RNAs (miRNAs) electrochemical biosensors. In this biosensor, the role of MXene was an electrocatalyst for the effective electrochemical signal enhancement, while gold nanoparticle was used to immobilize two different single-strand DNA (ssDNA) molecules modified with redox molecules (methylene blue and ferrocene). These were used as the sensing probes for multiple miRNA (miR-21 and miR-141)

Table 1 Summary of MXene based materials for detection of various analytes and their detection limits

No	Electrode material	Target Analyte	Technique	Detection Limit	References
1	$Ti_3C_2T_x$	Carbendazim	Differential pulse voltammetry	0.0103	[25]
2	Pd@$Ti_3C_2T_x$	L-cysteine	Amperometry	0.14	[26]
3	Hb/Ti_3C_2-GO	H_2O_2	Differential pulse voltammetry	1.95	[27]
4	Nafion/Hb/Ti_3C_2	H_2O_2	Amperometry	0.02	[5]
5	MB-$Ti_3C_2T_x$	Urea Uric acid Creatinine	Square wave voltammetry	0.02 5 1.2	[28]
6	MXene-MWCNT	Catechol (CT) Hydroquinone (HQ)	Cyclic voltammetry	6.6×10^{-3} for CT 3.9×10^{-3} for HQ	[29]
7	Nafion stabilized $Ti_3C_2T_x$	Dopamine	Amperometry	0.003	[30]
8	MXene/DNA/Pd/Pt	Dopamine	Amperometry	0.003	[31]
9	AChE/Ag@$Ti_3C_2T_x$/GCE	Malathion	Amperometry	3.27×10^{-15}	[32]
10	MXene/Prussian blue wearable sensor	Glucose Lactase	Chronoamperometry	0.33	[33]
11	MXene/Au/GCE	Glucose	Amperometry	3.9	[34]

detection. The assay time was reduced to 80 min with a four-fold higher electrochemical signal than biosensors prepared without the MXene (detection sensitivity of 204 aM and 138 aM for miR-21 and miR-141 detection, respectively) [36]. In addition, an electrochemical biosensor of a similar type was developed to detect miRNA-155 [37].

Kheyrabadi et al. developed an electrochemical aptasensor to detect thyroxine using nanohybrid material composed of MoS_2 and MXene ($Ti_3C_2T_X$). For this biosensor design, MoS_2 and MXene nanosheets were hybridized on the screen-printed carbon electrode on which gold nanostructures were electrochemically synthesized. These gold nanostructures help in the amplification of the electrochemical signal derived from the detection of thyroxine. The detection was made possible by binding thyroxine-specific RNA aptamer modified with ferrocene onto the gold surface through thiol bindings. In the absence of thyroxine, the RNA aptamer existed as a folded structure, with the ferrocene located near the metallic surface. Upon thyroxine addition, the structure of the RNA aptamer unfolds, which induced the faraway position of the ferrocene from the metallic surface and reduced the redox signal from the ferrocene. The biosensor thus developed showed an ultralow limit

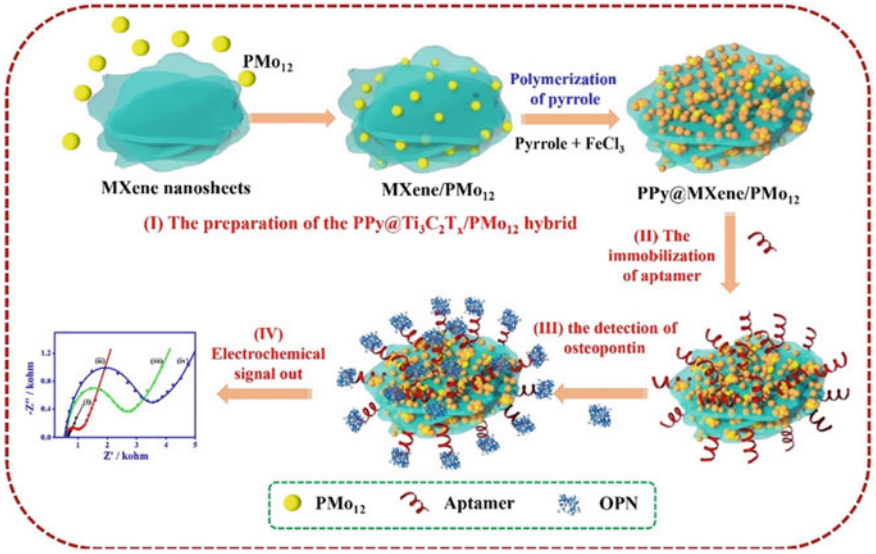

Fig. 4 Schematic representation of the biosensor fabrication based on PPy@$Ti_3C_2T_x$/PMO_{12} for OPN detection. The sequential steps include (I) the preparation of the PPy@$Ti_3C_2T_x$/PMo_{12} hybrid, (II) the aptamer immobilization, (III) the OPN detection, and (IV) the electrochemical signal out (reproduced with permission from [40])

of detection (0.39 pg/mL) and a wide linear response range (7.8×10^{-1} to 7.8×10^6 pg/mL) [38]. Another ultrasensitive miRNA-182 biosensor was also explored with a similar combination of materials with MXene [39].

MXene-based nanohybrids are also evaluated as a biosensor for detecting Osteopontin (OPN), an important protein that could be used to diagnose cancer progression. The nanohybrid comprises of polypyrrole embedded in $Ti_3C_2T_x$ MXene and phosphomolybdic acid (PMo_{12}) surface (denoted as PPy@$Ti_3C_2T_x$/PMo_{12}). The biosensor fabrication process is elucidated in Fig. 4. The Osteopontin aptamers are immobilized on the nanohybrid surface, which helps capture the analyte. This aptasensor showed a very low detection limit of 0.98 fg mL^{-1}, as well as high selectivity and stability, good reproducibility, acceptable regenerability, and applicability in human serum samples [40].

2.2 MXene Based Optical Biosensors

In addition to electrochemical biosensors, MXenes are widely being explored as an optical biosensor due to their chemical stability, easy surface functionalization, ability to synthesize fluorescent Mxene-based quantum dots (MQDs) with high water solubility, dispersibility, and biocompatibility due to their high hydrophilicity.

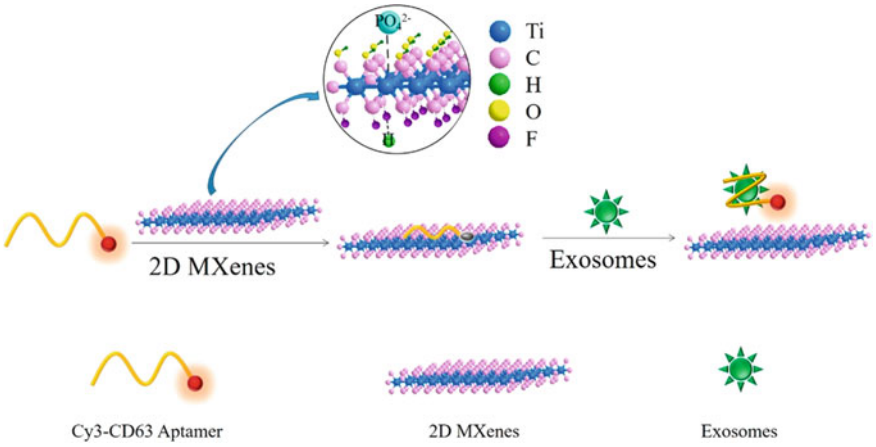

Fig. 5 Schematic representation of fluorescence resonance energy transfer (FRET)-based biosensing systems for the detection of exosomes using Ti_3C_2 MXene nanosheets combined with the Cy3-labeled CD63 (exosome transmembrane protein) aptamer (reproduced with permission from [41])

Novel fabrication techniques and surface functionalization of MXenes and MQDs to achieve high hydrophilicity and enable better fluorescent quantification efficiency make MXenes an attractive candidate for optical biosensors.

In most cases, the MXene nanosheets play the role of quenching molecules which blocks the emitted fluorescent signals from the fluorescent sensing probes before detecting the target molecules for the operation of the fluorescent biosensors. Zhang et al. developed a fluorescence resonance energy transfer (FRET)-based biosensing system to detect exosomes using Ti_3C_2 MXene nanosheets combined with the Cy3-labeled CD63 (exosome transmembrane protein) aptamer, which is shown in Fig. 5. The sensing probe, Cy3 labeled-CD63 aptamer, was bound to MXene nanosheet. In the absence of the exosome, the fluorescence signal of the Cy3 was quenched by the MXene nanosheets due to the proximity between the Cy3 and the MXene nanosheet. However, upon exosome addition, the Cy3-labeled CD63 aptamer detached from the MXene nanosheets and then bound with the added exosomes. This resulted in restoring the quenched signal of the Cy3, which allowed fluorescent detection of the exosome. This biosensor system exhibited high sensitivity towards exosome sensing in a wide range from 104 to 109 exosomes/mL, with a low detection limit of 1.4×10^3 exosomes/mL. This detection limit was 1000 times lower than that obtained from typical enzyme-linked immunosorbent assay (ELISA) methods [41].

MXene can be an ideal material for ECL applications because of its surface properties and negative functionalization. The high negative charge density paired with a large surface area permits adequate immobilization of the ECL probing agent, while Mxene's high conductivity allows the charge transportation, enhancing the ECL signal [42]. Fang and coworkers designed an ECL sensor to detect single nucleotide mismatching. A single nucleotide mismatching is very common, and the distinction

of such single nucleotide mutation is beneficial in diagnosing certain diseases [43]. $Ti_3C_2T_x$ can be used as a highly conductive substrate to immobilize $(Ru(bpy)_3)^{2+}$, producing ECL signals upon interaction with adenine and guanine. This ECL sensor displayed outstanding viability when tested for single-nucleotide mismatch using a model of oligonucleotides containing p53 gene segment. This ECL sensor could distinguish a single nucleotide mismatch at a low concentration of 1.0 nmol/L. The $Ti_3C_2T_x$ nanosheets are used to immobilize the aptamer to detect exosomes using the ECL method. Upon interaction with exosomes, these aptamer molecules resulted in an enhanced ECL signal of the probing agent, luminol. This technique enabled to detection of the exosomes of MCF-7. The detection sensitivity of this ECL-based sensor was 125 particles/μL, which was 100 times lesser than that of the commonly used ELISA technique [44].

In another study, Ti_3C_2 MXene nanosheets and fluorescein-labeled ssDNA (FAM-ssDNA) were used to develop a fluorescent DNA biosensor to diagnose the human papillomavirus (HPV). Briefly, without the analyte, the fluorescence signal from the FAM was quenched when the FAM-ssDNA was immobilized on the MXene. However, upon exposure to an analyte (the target DNA, which was the partial sequence of the HPV gene), FAM-ssDNA formed double-stranded DNA (dsDNA) by hybridization with the analyte and was released from the MXene. Upon release from the MXene, the fluorescence signal of the FAM was restored, and this fluorescent intensity was measured to analyze the concentration of the added target DNA [45].

MXene, in the form of nanosheets, played the role of quenching agents in biosensors, while MQDs are used in biosensing applications due to their fluorescent emission property. In one instance, researchers developed a fluorescent biosensor for Fe^{3+} detection using MQDs with a size of 1.75 nm, having excitation and emission wavelength of 320 nm and 410 nm, respectively. Upon exposure to Fe^{3+}, there occurs quenching of MQDs' fluorescence due to the synergistic effect of the internal filtering effect (IFE) of the Fe^{3+} (which hinders MQDs from receiving the excitation wavelength) and electrostatic interactions of the Fe^{2+} (obtained through the reduction of the by MQDs Fe^{3+} by MQDs). It was found that the Fe^{3+} detection method using the fabricated Ti_3C_2 MQD-based biosensor had excellent reproducibility [46]. Another biosensor with a similar principle was developed using polylysine-coated Ti_3C_2 MQDs (PL-MQDs) to detect cytochrome c (Cyt c) and trypsin. Further, PL-MQDs had an excitation wavelength of 330 nm and an emission wavelength of 415 nm [47].

MXenes have also been used in a colorimetric optical biosensor because of their rapid usage, low cost, and sensitive detection by naked eyes, making them a potential candidate for point-of-care testing. In one example, researchers developed a heterostructure made of the $Ti_3C_2T_x$ MXene nanosheet and the Ni, Fe layered double hydroxide (NiFe-LDH) (MXene/NiFe-LDH) for the detection of glutathione (GSH). Here, the combination MXene/NiFe-LDH showed a higher catalytic property than the catalytic properties of the MXene nanosheets or NiFe-LDH alone. The colorimetric change in the [MXene/NiFe-LDH, 3,3',5,5'-tetramethylbenzidine (TMB),

and H_2O_2] system upon addition of GSH was used in the biosensing application [48].

2.3 MXene as Wearable Sensor

Flexible, wearable electronics for personalized health monitoring, human motion detection, prosthetic devices, and robotics have attracted tremendous biomedical technology in the past few decades. Wearable devices should possess good mechanical compliance and unique sensitivity. Flexible, wearable electronics require highly surface-mounted materials to fit the complex structure of different objects with good electrical behavior in daily movements. This is very difficult with silicon (Si) based electronics because Si is a rigid material. Because of MXene's unique physiochemical properties, electrical and biological characteristics, MXene-based wearable devices for sensing are much explored in recent times. Variation in the intracellular pH is an important factor in detecting diseases like cancer or Alzheimer's disease. Chen et al. reported pH-responsive Ti_3C_2 MXene quantum dots. They monitored the intercellular pH by developing a ratio-metric photoluminescence probe. Because of good biocompatibility, stability, high water dispersibility, and low toxicity, MXenes make a good platform for developing wearable practical fluorescent nano-sensors. MXene based wearable sensors are also developed for detecting other small molecules like glucose and phenols [49]. Rakhi and colleagues developed Ti_3C_2/Au composites for sensitive enzymatic glucose detection, which resulted in good electrocatalytic activity by a wide linear range detection limit of 0 to 18 mM and a low detection limit of 5.9 μM [34]. Cai et al. revealed Ti_3C_2/CNT composite with very high sensitivity and tunable sensing range. Using a spray coating technique, they fabricated a sandwich layer of Ti_3C_2 nanoflakes and single wall CNT. This wearable strain sensor reliably detected and differentiated the small deformations in the throat during speaking and the deformations in the knee associated with different movements like walking, running, and jumping. The sensitivity of this flexible strain sensor has a gauge factor (GF) of 64.6 and 772.60 in the range strain between 0–30% and 40–70%, respectively [50]. Biomimetic strain sensors based on a hierarchical architecture nacre-inspired design reported by Shi and coworkers for human motion detection. It is fabricated by $Ti_3C_2T_x$-AgNW and polydopamine (PDA) /Ni^{2+}, and it exhibits a large GF value of 8767.4 in the strain range of 77–83%, the lowest of 256.1 GF in 0–15% of strain [51]. MXene coated Airlaid paper (AP) fabric-based pressure sensors are fabricated using a dip-coating method by Yao et al. It shows a unique hierarchal network structure and reversible electrical contact of the MXene. MXene AP pressure sensor shows excellent mechanical-sensing performance. The sensor results in high sensitivity of (7.65 kPa1 at 0–3.3 kPa), a broad sensing range (0–300 kPa), and excellent reproducibility over 1000 cycles, which satisfies the requirements for a high-performance pressure sensor [52]. Luo et al. prepared superhydrophobic, breathable and multifunctional MXene based textile through dip coating assembly. Here the MXene NSs were coated on the polydopamine (PDA) fiber surface by van der Waals force and

hydrogen bondingPDA/MXene Ns has a large working temperature range of (25–100 °C), highest temperature coefficient resistance of −1.8% $°C^{-1}$ and Contact angle (CA) of ~151° gives satisfactory breathability with good recyclability and durability [53].

CNT/MXene/ polydimethylsiloxane (PDMS) composite based strain sensor was developed by Xiaowen Xu and his coworkers for real time human healthcare monitoring. It shows reliable responses at different frequencies and with long-term durability (over 1,000 cycles). The sensor provides the advantages of superior anti-interference to temperature changes and water washing. This result demonstrates a less than 10% resistance change as the temperature rises from −20 to 80 °C or after sonication in the water for 120 min [54]. Zhang et al. reported polyvinyl alcohol (PVA) based Ti_3C_2 MXene hydrogels, with high sensing capabilities, excellent stretchability, and good self-heal ability. This sensor's gauge factor (GF) was 25, which is 10 times higher than a pristine hydrogel. The unique sensing performance of these MXene hydrogels makes it a promising material for wearable electronics and artificial skin to sense the 3D motions, including bio signaling and touch sensing [55]. Wang et al. reported a skin-inspired Ti_3C_2 MXene/natural microcapsule composite film with an interlocked structure, which mimics the structure and function of human skin. This sensor amplifies the weak pressure signal and shows excellent stability.

Figure 6 summarizes the concept of the interlocking structure of MXene composite and the high mechanical deformability of interlocking composite material [56].

3 MXene's Role in Cancer Theranostics

3.1 Photothermal Therapy

Cancer is one of the leading causes of death globally in the current times. As of 2020, there were 19.3 million cancer cases worldwide, and the death rates are about 47%. By 2040, the number of cancer cases is expected to rise to 29.5 million, and the number of cancer-related deaths is projected to increase by more than 60% [57]. Researchers across the globe are working towards developing new strategies in cancer research for early diagnosis and treatments. One such approach is to use light waves to kill cancer cells. The photothermal Conversion agent (PTA) are the ones that convert light waves to heat because of their inherent photothermal effect. As a result, they raise the local temperature of the tumor region, thereby killing the tumor cells. This technique is called Photothermal therapy (PTT).

Photothermal therapy (PTT) is a promising alternative to conventional cancer treatments due to its high site-specificity, minimal damage to normal tissue, and high ablation efficiency. The Photothermal therapy (PTT) platforms promise the passive/active targeting of photothermal conversion agents (PTAs) inside tumor cells that can be activated via NIR irradiation at low intensity and power density. Two

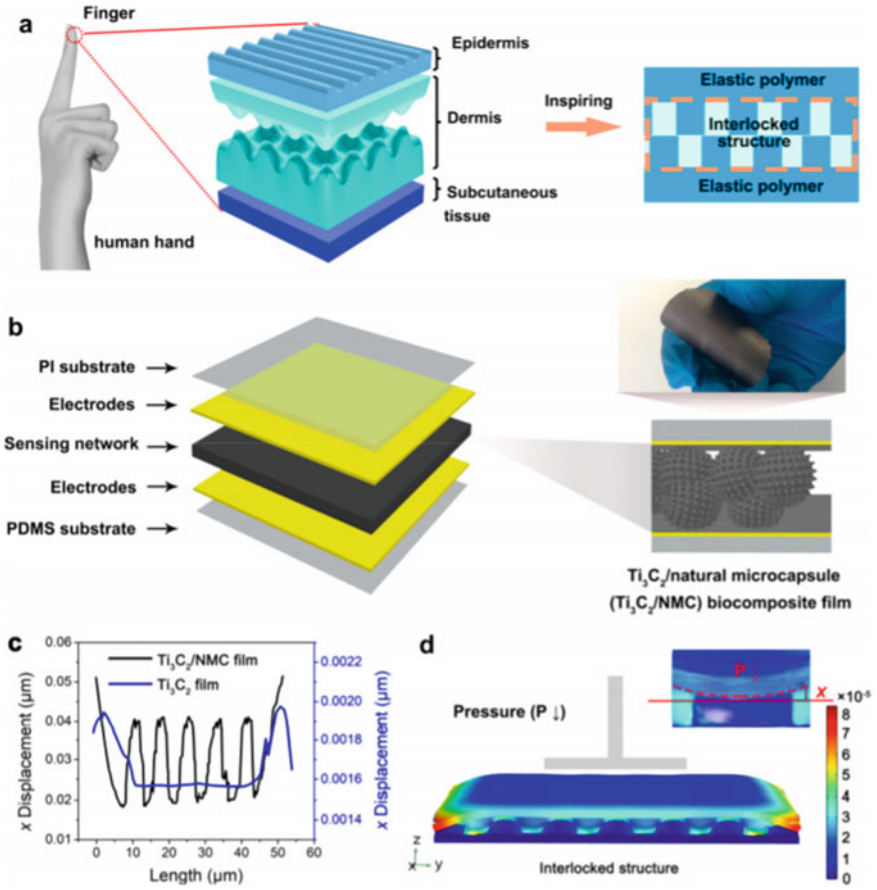

Fig. 6 **a** schematic illustration of the structure of the human skin and fabrication of material in interlocking structure **b** schematic illustration of flexible sensor **c** Finite element method FEM analysis **d** Cross-sectional view of FEM bio-composite films deformation and distribution in the interlocking structure (reproduced with permission from [56])

biological transparency windows are located between 650 to 950 nm as (first NIR window) and 1000 nm to 1350 nm as (second NIR window), where the optimal tissue transmission has been obtained with low scattering and energy absorption. This provides maximum radiation penetration through tissues and minimizes autofluorescence [1, 58]. In a very short period, several nanomaterials with different morphologies have been explored as PTAs, which are as follows: gold nanoparticles with different morphologies because of their optical property as results of localized surface plasma resonance (LSPR) [59, 60], nanoscale carbon allotropes especially CNTs [61, 62], polypyrrole(PPY), poly(3,4-ethylenedioxythiophene) polystyrene sulfonate PEDOT:PSS [63, 64], CuS nanoparticles [65, 66], iron oxide nanoparticles [67, 68] and some other 2D layered nanomaterials like MXenes, WS_2 [69]and MoS_2

[70]. Among all these, MXenes are a recent addition because of their unique planar structure, exceptional transformable 2D inlayer nanostructure, convenient chemical composition, chemical diversity, and superior physiochemical features, strong optical absorption in second NIR window of 1000 nm to 1350 nm [71].

MXene's versatile properties make it a perfect material for biomedical applications in recent times. 2D multifunctional MXene and its composites have been extended for theranostics applications comprising photothermal therapy (PTT), photothermal/photodynamic/chemo synergistic therapy, diagnostic imaging, biosensing, and antibacterial [1, 72, 73].

3.2 MXene in Photothermal Therapy (PTT)

Xuan et al. synthesized and studied the photothermal therapeutic efficiency of aluminum oxoanion-functionalized titanium carbide sheets. These 2D materials exhibited strong absorption in the NIR region with a high mass extinction coefficient of 29.1 Lg^{-1} cm^{-1} at 808 nm. This material was superior to the recently identified photo absorption materials, including gold nanoparticles, carbon allotropes, and transition-metal dichalcogenides. Strong and broad absorption in the NIR region of these 2D functionalized titanium carbide sheets is mainly because they behave as photothermal agents for anticancer therapy [74]. Dai and coworkers prepared MnO_x /Ti_3C_2 for photothermal and bioimaging applications. It shows a photothermal conversion efficiency of 30.6% to 22.9%. The presence of the MnO_x component on MnO_x/Ti_3C_2 helps identify the tumor site and thus eventually killing them. The Mn–O bonds are easily broken up under the mild acidic conditions of tumor micro environments, which releases Mn^{2+} ions. This maximizes the interaction between paramagnetic Mn centers and water molecules, enhancing the T1-weighted MRI performances. Here MnO_x acts as a contrast agent for tumor diagnosis [75]. Yu and colleagues identified a fluorine-free synthetic method to prepare Ti_3C_2 QDs for PTT application.

The prepared MXene QDs displayed an extinction coefficient of 52.8 Lg^{-1} cm^{-1} at 808 nm. The photothermal conversion efficiency of the synthesized MXene QDs was 52.2% which was significantly higher than the previously reported MXene QDs. The photostability of these QDs also was evaluated and found to be stable even after five cycles [76]. A study by Szuplewska and colleagues [77] revealed the PTT potential of superficially modified Ti_2C MXene using PEG. These PEG-Ti_2C flakes exhibited better biocompatibility—the in vitro cell studies of these PEG-Ti_2C exhibited distinguished NIR-induced death of cancerous cells. The study also discussed the cytocompatibility of MXenes towards normal healthy cells. In addition to the titanium-containing MXenes, other MXene compounds were also effective in anticancer therapy. For example, compounds like tantalum carbide (Ta_4C_3) have better photothermal conversion efficiency than Ti_3C_2. This novel Ta_4C_3 MXene exhibited good photothermal stability and good colloidal stability in physiological media. Moreover, these Ta_4C_3 possess a longer half-life in blood circulation and increased

accumulation in the tumor cell. This is due to the difference in the NP size and enhanced permeability and retention (EPR) effect [78]. Generally, the PTT agents, including MXenes, have an absorption peak in the first biological window (NIR-I). Still, the maximum permissible exposure (MPE), which matches the maximum safe laser power density for human skin exposure, is higher for NIR-II than for NIR-I. The Niobium carbide (Nb_2C) can be used as a PTT agent in the first and second biological window regions. A surface modification of Nb_2C sheets was performed using PVP to improve the stability and biocompatibility in physiological conditions [79]. Good photothermal conversion efficiencies at both 808 nm and 1064 nm were observed with this Nb_2C. Selective and enhanced accumulation of Nb_2C-PVP MXenes in cancerous cells were confirmed by inductively coupled plasma atomic emission spectroscopy (ICPAES) and confocal microscopy.

3.3 MXene's Role in Synergistic Treatments: Drug Delivery and Photothermal Therapy

A combination of PTT with other anticancer treatment strategies like chemotherapy and photodynamic therapy (PDT) was currently being explored by researchers worldwide. A beneficial synergistic effect was observed with this combination treatment strategy [80]. This is helpful to reduce the dose of the chemotherapeutic agent, lowering the amount of photothermal agents and photosensitizers. In addition to this, this effect helps to reduce the laser powers for PTT and PDT, which leads to fewer side effects and good treatment results [81, 82]. Like other photothermal agents, MXenes also exhibited agreeable results when combined with other antitumor agents. The rich surface chemistry of MXene provides promising anchoring sites for therapeutic drug molecules and targeting moieties. The OH groups present on the surface of the MXene can electrostatically adsorb cationic molecules such as doxorubicin (Dox), a chemotherapeutic drug commonly used to treat cancer. A synergistic PTT, PDT, and chemotherapy were evaluated for the Ti_3C_2 [83, 84]. A study by Yun Xiu Liu and colleagues revealed the structure, drug loading, release, magnetic controlling behavior, photothermal performance, and synergistic therapeutic efficiency of MXene-cobalt-nanowires Ti_3C_2-CoNWs, the heterojunction nanocarrier. This functionalization resulted in a drug loading ability of 225.05% and exhibited drug-releasing behavior by inducing pH/ NIR stimulation. This also shows improved control on carriers for synergistic anticancer treatment with higher photothermal conversion efficiency (PCE) of 34.42%. The schematic illustration in Fig. 7a summarizes the synthesis procedure of Ti_3C_2 CoNWs heterojunction, and Fig. 7b represents the combination of nanocarriers and their dual stimuli-responsive drug release [83]. A study by Gongyuan Liu and coworkers revealed the chemotherapy using doxorubicin-loaded MXene, and active tumor accumulation was achieved by coating the MXene with Hyaluronic acid (HA), which has a high affinity to cancer cells that overexpress CD44. A synergistic effect after *in vi*vo PTT using Ti_3C_2-DOX was observed, as

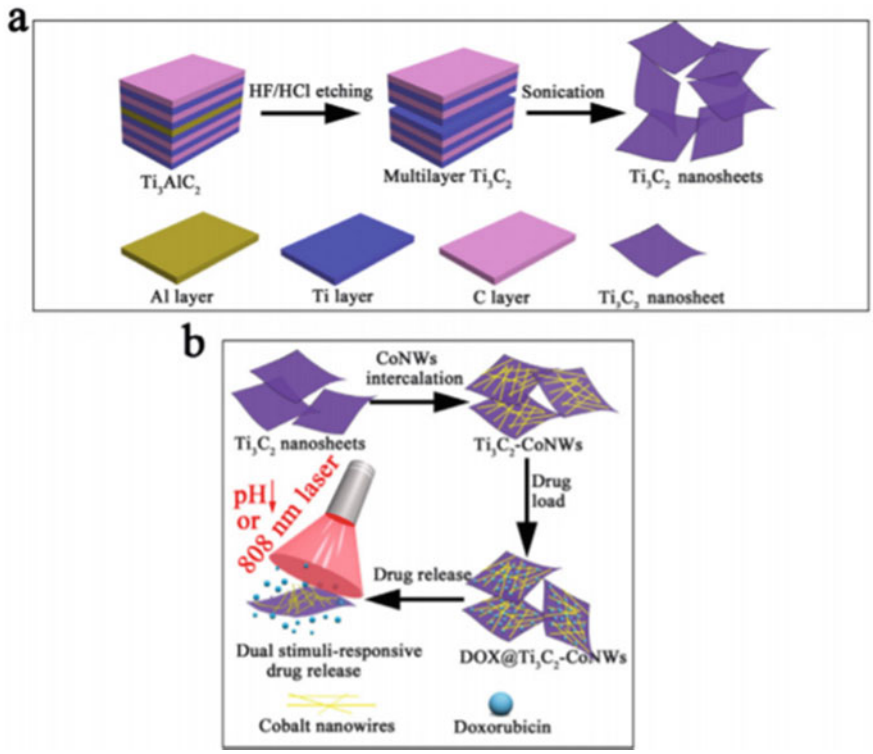

Fig. 7 **a** Schematic of the synthesis protocol of Ti_3C_2 nanosheet and **b** Schematic representation of the synthesis of Ti_3C_2 CoNWs heterojunction and subsequent Doxorubicin loading, followed by their dual stimuli-responsive drug release (reproduced with permission from [83])

DOX alone or Ti_3C_2-DOX without laser irradiation led to only partial tumor growth inhibition [84].

3.4 MXene Based Theranostics Systems

Theranostics systems impart both diagnostic (imaging) and therapeutic (treatment) modalities in one go. These systems may constitute a combination of diagnostic and therapeutic modalities in a single platform using nanomaterials.

Typically, the images employed in cancer diagnostics are magnetic resonance imaging (MRI), X-ray computed tomography (CT), and photoacoustic imaging (PA). Among these, MRI is characterized by high sensitivity and soft-tissue contrast; CT gives very high spatial resolution, while PA offers higher penetration depths than the others by detecting the ultrasound waves generated by the laser-irradiated tissue. The

synthesis of novel contrast agents with concurrent multimodal imaging and therapeutic capabilities allows the development of theranostics platforms for synergistic imaging and treatment. Gadolinium (Gd^{2+}), despite its recognition as contrast agents for MRI and its long retention time in the body, suffers from potentially toxic side effects [85, 86]. Liu and colleagues revealed superparamagnetic iron oxide nanoparticles (INOP) functionalized MXene composite(Ta_4C_3-IONP-SPs) for efficient breast cancer theranostics [87]. Here, the Ta component of the Ta_4C_3-IONP-SPs composite exhibits CT contrast property because of its higher X-ray attenuation coefficient and higher atomic number (Z = 73). The superparamagnetic INOP act as an MRI imaging contrast agent. Ta_4C_3-IONP-SPs have a PCE of 32.5%. Zong and coworkers revealed polyoxometalates functionalized Ti_3C_2 with the integration of Gadolinium (Gd), Tungstan (W) GdW_{10} as a contrast agent [88]. Tantalum carbide MXene was used to synthesize MnO_x/Ta_4C_3 composites using an *in-situ* reaction. These composites exhibited high photothermal conversion efficiency compared to MnO_x/Ti_3C_2. Figure 8 gives a schematic overview of the synthetic procedure of MnO_x/Ta_4C_3 composite nanosheets and PTT mechanism [89] (Table 2).

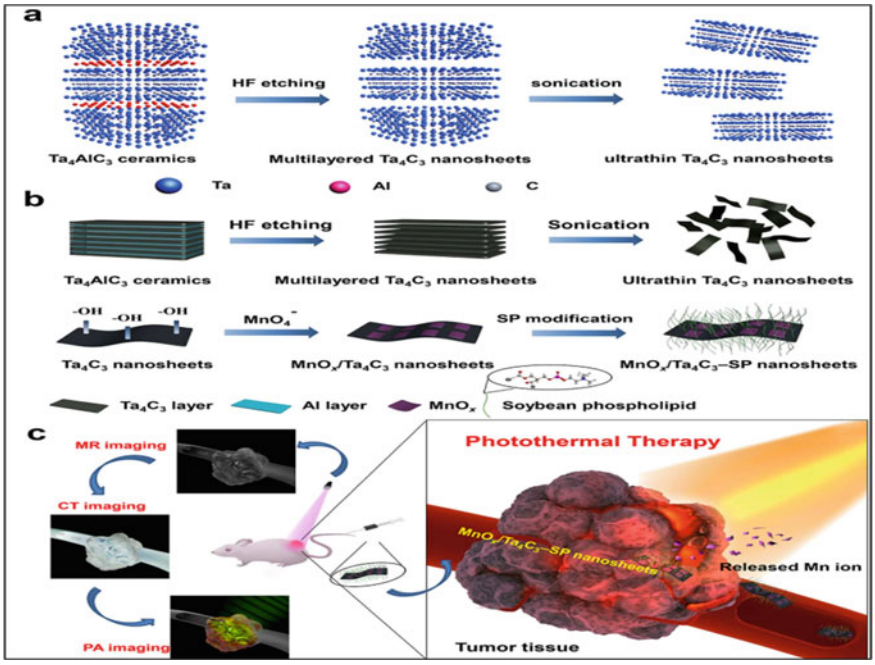

Fig. 8 **a** Schematic illustration of the synthesis of MXene nanosheets. **b** scheme of the synthetic procedure for MnOx/Ta_4C_3−SP MXene composite nanosheet. **c** Schematic illustration of theranostic functions of MnOx/Ta_4C_3−SP composite nanosheets and MRI/CT/PA imaging-guided efficient PTT ablation of cancer (Fig. 8 is reproduced with permission from [89])

Table 2 List of various MXene and its composites with essential parameters used in PTT

No	MXene	Photothermal conversion efficiency (%)	Extinction Coefficient ($l.g^{-1}$ cm^{-1})	In vivo administered dose (for PTT) ($mg.kg^{-1}$)	Half Life (systemic) (h)
1	Ta_4C_3-SP	44.7	4.06	20 (iv)	1.59
2	Ti_3C_2-SP	30.6	25.2	20	0.76
3	MnOx/Ti_3C_2-SP	22.9	5.0	2.5	–
4	Ti_3C_2 QDs	52.2	52.8	0.5	–
5	MnO_x/Ta_4C_3-SP	34.9	8.67	20	–
6	Ta_4C_3-IONP-SP	32.5	4	20	0.5
7	GdW_{10}/Ti_3C_2	21.9	22.5	20	0.83

4 Versatile Biomedical Applications

4.1 Tissue Engineering

MXene is currently thriving as a novel inorganic nanomaterial for biologic and biomedical applications. The metallic conductivity, hydrophilicity, and other unique physiochemical performances makes it an attractive material in tissue engineering [90], especially in bone tissue engineering [91, 92], neural tissue engineering [93], and cardiac tissue engineering [94, 95].

4.1.1 Cardiac Tissue Engineering

According to World Health Organization (WHO), cardiovascular diseases (CVD) are among the major causes of death worldwide. About 17.9 million people get affected by CVD, which leads to death in most cases. The death rate of CVD worldwide is 32% [96]. The regeneration capacity of cardiomyocytes is limited, which results in clinicians giving only symptomatic reliefs to the patients. However, with the advent of the cardiac tissue engineering arena, researchers are working towards regenerating cardiac tissue using various innovative strategies. Some of them include the development of biomaterials that assist in delivering various cells for cellular therapy, biomaterials for the delivery of various drugs/ growth factors that helps in the neo-vascularization, immune modulation, and finally, the development of conducting engineered cardiac patches (ECP), which helps in the remission of conduction through the damaged cardiac tissue, thus restoring the functionality of the damaged heart.

To develop conducting cardiac patches, various nanomaterials are being explored as conducting moieties within the patch. Some of them include gold-based nanostructures, graphene oxide-based nanostructures, and other conducting polymeric nanostructures. The recent addition to this list is MXenes. MXenes, due to their exceptional conducting property, is one of the best materials to be used in the conducting cardiac patch.

MXene based bio-inks show promising potential in cardiac tissue engineering. Ye and colleagues reported Ti_2C-cryogel ECP for MI. Ti_2C-cryogel exhibited suitable elasticity and good electrical conductivity matching the natural heart. Furthermore, upon implantation of Ti_2C cryogel ECP on the infarcted myocardium of MI rats for 4 weeks, they found a marked decrease in inflammatory reactions, improved formation of dense microvessels, and finally, improvement in the heart function. The authors concluded that the Ti_2C-cryogel ECP provided a suitable 3D microenvironment and thus showed a promising cardiac repair efficacy [94]. Figure 9 summarizes the fabrication process of Ti_2C-cryogel and its application in a rat MI model [94]. Basara and coworkers reported $Ti_3C_2T_x$ MXene-PEG composite 3D printed cardiac patch. It demonstrated the patterning capability of MXene/ PEG composite, where the cells on the cardiac patch are made to align in the same orientation with the rest

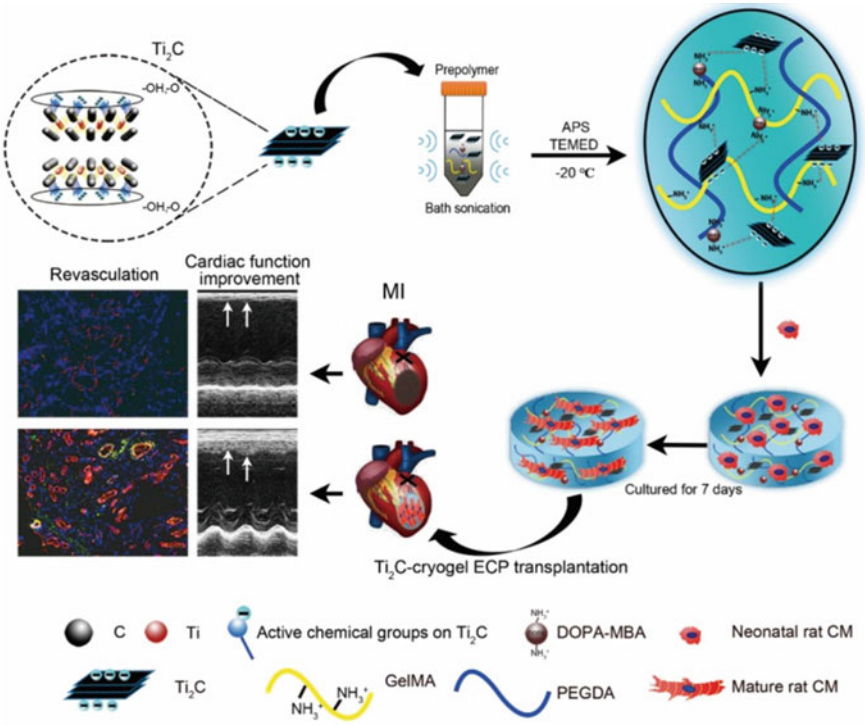

Fig. 9 Schematic illustration of the fabrication of ECP made with Ti_2C-cryogel and its application in a rat MI model (figure reproduced with permission of [94])

of the heart using the aerosol jet printing. This resulted in greater improvements in the signal transduction from healthy heart tissue through the cardiac patch [95].

4.2 Biocompatibility of MXene

The biocompatibility of nanomaterials cannot be determined directly by viewing the constituting elements' size, shape, aqueous dispersion, surface charge, and hydrophilicity behavior. The primary mechanisms of nanoscale material-inducing toxicity are (1) oxidative damage to the cells, (2) slower clearance in the renal pathway and accumulation in the organs, (3) damage to blood cells, (4) specific toxicity to the reproductive, neural, or embryonic system and (5) genotoxicity. Thus, a broad biosafety evaluation is required to investigate all the possible interactions between the nanoscale material and the living system, taking into account various mechanisms of toxicity, the effects of shape, size, and physicochemical properties. Some preliminary data on the cytocompatibility and biocompatibility of MXenes are already out there in the literature. Ti_3C_2 is the most commonly investigated MXene in biomedical applications [83, 84, 93–95]. Ye and colleagues studied the biocompatibility properties of Ti_3C_2 cryogel using cell viability studies like live/dead cell staining assay and CCK-8 assay on cardiomyocytes (CM). They found increased cell survival (90%) on Ti_3C_2 based cryogel than Ti_3C_2 free cryogel (74%) [94]. Zong and colleagues reported good in vivo biocompatibility properties of GdW10@Ti_3C_2 composite MXene NSs [88]. Gongyuan Liu et al. revealed that Ti_3C_2 nanosheets passed in the bloodstream are excreted through urine via physiological renal clearance pathway or are retained in the tumor tissue through enhanced permeability and retention (EPR) effect without getting accumulated in the major organs. MXene's biodistribution and biosafety are confirmed by the absence of any significant body weight loss and an absence of necrotic process in the major organ levels at acute (1-day), subacute (7-day), and chronic (30-days) of different time intervals after injection of high doses of MXenes [84]. Similar results have been reported for the systemic biocompatibility and cytocompatibility of tantalum carbide MXene Ta_4C_3 [78, 89] and niobium carbide MXene Nb_2C [28].

4.3 MXenes for Antimicrobial Treatment

Antibiotic resistance is a serious concern in the current scenario, and new antibiotics or antibiotic treatment strategies are required to combat antibiotic-resistant or biofilm-forming bacteria. A rapid, effective, and broad-spectrum antibacterial strategy is developed with MXene and light. This study revealed an effective strategy against fifteen different bacterial strains, including methicillin-resistant *Staphylococcus aureus* (MRSA) and vancomycin-resistant *Enterococci* (VRE). In this case,

the combination of Ti_3C_2 MXene with light (808 nm) exhibited an antimicrobial effect within 20 min. These Ti_3C_2 MXenes, upon exposure to light, kill the bacteria residing within biofilm by destructing the biofilm structures [97]. The antibacterial effect of natural polymeric bandages can be enhanced by incorporating 2D nanomaterials. Encapsulation of delaminated Ti_3C_2Tz MXene (Tz-termination species) flakes within chitosan nanofibers was prepared for passive antibacterial wound dressing applications. The antibacterial potential of these crosslinked $Ti_3C_2T_z$-chitosan composite fibers was evaluated against gram-positive and gram-negative organisms [98]. The antibacterial properties of single and multi-layered $Ti_3C_2T_x$ MXene flakes in colloidal solution were evaluated against *E. coli* and *Bacillus subtilis*. It was found to have a concentration dependent antibacterial effect, and also more than 98% of the cells lost their viability at 200 μg/mL $Ti_3C_2T_x$. This study also revealed that the antibacterial nature of Ti_3C_2Tx MXene flakes was superior to the antibacterial nature of graphene oxide [99]. A heterojunction structure of MXene is prepared by anchoring Cu_2O on MXene nanosheets by electrostatic effect. These Cu_2O/MXene exhibited significant antibacterial activity against *S. aureus and P. aeruginosa* [100]. A study by Zhou et al. utilized the highly conducting $Ti_3C_2T_x$ MXenes to develop multifunctional scaffolds for the methicillin-resistant Staphylococcus aureus (MRSA)-infected wound healing. These multifunctional scaffolds were prepared by reaction between poly(glycerol- ethylenimine), $Ti_3C_2T_x$ MXene@polydopamine nanosheets, and oxidized hyaluronic acid. These multifunctional scaffolds possess the properties like self-healing nature, high electrical conductivity, tissue-adhesive feature, antibacterial activity, particularly to MRSA [101]. A multifunctional hydrogen scaffold is designed by incorporating 2D antibacterial conductive $Ti_3C_2T_x$ MXenes and antioxidant CeO_2 for the tissue reconstruction associated with MDR infections. Zheng et al. fabricated the multifunctional scaffold by integrating the MXene@CeO_2 nanocomposites in Schiff-based chemical crosslinked hydrogel of polyethylenimine embedded Pluronic F127 (F127-PEI) and oxidized sodium alginate (OSA). These scaffolds possess multifunctional properties like antiinflammatory, antibacterial, and antioxidative potentials, conductive bioactivities, tissue-adhesive ability and fast hemostatic capacity [102]. The light conversion capacity of the Ti_3C_2TX nano-sheets gained a momentum in the treatment of infectious diseases and control of bacterial resistance. Rosenkranz et al. designed a photothermal antibacterial system using multi-layer (MX) $Ti_3C_2T_x$ nano-sheets using the heat conversion property of these MXenes. The study reveals, MX inhibiting growth of *S. aureus* and *E. coli* in a better way due to MXenes' reversible bacteria trapping [103]. Zheng and coworkers reported synergistic MXene based membrane for bacterial resistance by conjugating Ti_3C_2 MXene NSs with gold nanoclusters. This antimicrobial mechanism suppressed both gram-positive and gram-negative bacteria, with low IC 50 values of 11.7 μg mL^{-1} of Ti_3C_2 and 0.04 μm of AuNCs [104]. Rasool and colleagues showed an efficient antifouling property of Ti_3C_2 MXene membrane, facilitating a sustainable water treatment process. Polyvinylidene fluoride (PVDF) membrane with Ti_3C_2 MXene coating showed excellent antibacterial activity on different bacteria. Moreover, the aged MXene membrane showed higher growth inhibition of 99%, while the fresh ones showed only 73% [105]. Figure 10a summa-

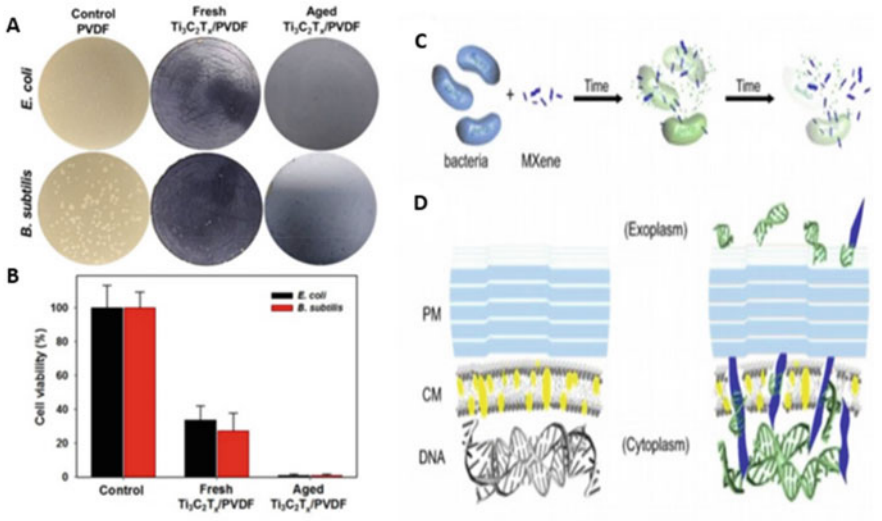

Fig. 10 **a** Antibacterial studies (growth inhibitation and cell viability measurements) of E.coli, **b** subtilis with fresh and aged MXene membrane(figure reproduced with permission from [105]. **c** interaction of MXene NSs with the bacterial cell wall and depression of bacterial cells. **d** Schematic representation of the mechanism of Ti_3C_2 sharp nanosheets cutting bacterial cell wall and getting on to bacterial cytoplasmic region (reproduced with permission from [106])

rizes the growth inhibition of different bacteria by aged and fresh Ti_3C_2 MXene membrane, and Fig. 10b represents the cell viability measurements of bacteria against the MXene membrane [105]. Shamsabadi et al. revealed the antimicrobial effect of colloidal MXene NSs [106]. The study showed that the direct physical interactions between the NSs sharp edges and bacteria membrane surfaces play a significant part in the antibacterial activity of the NSs. Figure 10c represents the interactions of the NSs with bacteria cells, the release of bacteria DNA, and depression of bacteria cells. Figure 10d shows the mechanism of Ti_3C_2 sharp nanosheets cutting bacterial cells and getting on to bacteria cytoplasmic region [106].

Challenges and future prospects

The rise of new nanomaterials in biomedical applications requires a thorough evaluation of their biosafety and toxicity. These are of the utmost importance in determining the accurate capability for clinical translation. The recent discoveries and the mass of data regarding the biocompatibility of MXenes are still very limited. However, some preliminary evaluation suggests that MXenes are compatible with cellular viability and growth and do not cause any hemolytic damage to red blood cells in vitro. Moreover, when engineered in ultrathin NSs, they can be excreted through the physiological renal clearance pathway and do not appear to cause any toxic effects in the major organs. These results are encouraging and assist the promising potential of MXenes as novel biomaterials. Nevertheless, to establish the biocompatibility of

MXene, future extensive exploration must be conducted to take into account all the probable mechanisms of contact between MXenes and living systems at long standing time scales. MXenes, with their exceptional optical properties, have been employed for bioimaging and biosensing. The excellent light to heat transition competence makes MXene an absolute biocompatible and proficient nanoscale material for PTT appliances. But problems like stability in the physiological environment/controlled release of drugs and biodegradability need to be explored. Even though MXene loaded hydrogel can be NIR-responsive for drug release, they still have limitations like low photothermal conversion, poor photothermal stability, and improper temperature range in biomedical applications [107]. Material innovation and technological advancement can help develop high-performance and sensitive diagnostic devices, efficient antimicrobial compounds/personal protection equipment such as face masks and shields, and many other components for medical equipment. 2D materials like MXenes are an emerging solution for biomedical applications due to the outstanding functional properties and feasibility of integrating with any system. In addition, MXene composites such as MXene–graphene display many remarkable properties such as high electrical conductivity, surface functionalization feasibility, excellent photocatalytic and photo-heat conversion properties, outstanding antimicrobial behavior, and many other flexible properties [108]. In the condition of biosensing, MXene shows magnificent performance as an electrode material for enzymatic, mediator-free biosensing of Reactive nitrogen species (RNS) and Reactive oxygen species (ROS), also for high-sensitivity glucose monitoring systems, which can help to find relevant applications in diabetes diagnosis and monitoring. In addition, MXene can be processed into field-effect transistors (FETs) for monitoring the electrical and chemical activities of cultured neurons at high resolution. The transition of the optoelectronic properties of the MXene films provides the possibility of performing simultaneous optical imaging, which could permit a wide range of applications in neuroscience studies. Finally, MXene shows promising capability for stretchable strain and pressure sensors, which opens new applications in human healthcare monitoring. The rise of MXenes in biomedical applications is just started, and a long way to go. The surprising physicochemical properties and species mass are available now in the library of MXenes, which opens up unprecedented possibilities to optimize the material properties matching distinct applications and cellular targets, many of which yet to be explored.

5 Conclusion

This chapter discusses emerging biomedical applications of MXenes, from biosensing, photothermal cancer therapy, antimicrobial therapy, and more recent tissue engineering applications. MXenes, due to their hydrophilicity, excellent plasmonic properties, electrical conductivity, and ease of their surface modifications, have excelled in biosensing applications. This chapter covered various types of biosensors like enzyme and non-enzyme based electrochemical biosensors, fluorescent

biosensors, colorimetric biosensors, and a few others. In the case of cancer therapy, MXene and their nanohybrids-based photodynamic and photothermal therapy were discussed. This chapter also focuses on synergistic anticancer therapy of MXenes with other forms of therapy and theranostic systems. MXene's role as an antibacterial agent is also discussed in this chapter. Overall, MXene is a potential bionanomaterial with excellent physicochemical properties and is currently being extensively researched in the biomedical arena. However, its successful translation towards clinics is still a long way to go. It depends immensely on further understanding of its biocompatibility properties, for which more extensive and intense biocompatibility studies both in vitro as well as in vivo are warranted.

References

1. Lin, H., Chen, Y., Shi, J.: Insights into 2D MXenes for versatile biomedical applications: current advances and challenges ahead. Adv. Sci., 5 (2018).https://doi.org/10.1002/advs.201800518
2. Clark, L.C., Lyons, C.: Electrode systems for continuous monitoring in cardiovascular surgery. Ann. N Y Acad. Sci. **102**, 29–45 (1962). https://doi.org/10.1111/j.1749-6632.1962.tb13623.x
3. Liu, H., Duan, C., Yang, C. et al.: A novel nitrite biosensor based on the direct electrochemistry of hemoglobin immobilized on MXene-Ti3C2. Elsevier B.V (2015)
4. Santander, J., Fonseca, L., Udina, S., Marco, S.: Ac ce pte d M us p (2007). https://doi.org/10.1016/j.snb.2007.07.003
5. Wang, F., Yang, C., Duan, C., et al.: An Organ-like titanium carbide material (MXene) with multilayer structure encapsulating hemoglobin for a mediator-free biosensor. J. Electrochem. Soc. **162**, B16–B21 (2015). https://doi.org/10.1149/2.0371501jes
6. Xu, B., Zhu, M., Zhang, W., et al.: Ultrathin MXene-Micropattern-based field-effect transistor for probing neural activity. Adv. Mater **28**, 3333–3339 (2016). https://doi.org/10.1002/adma.201504657
7. Patel, S., Nanda, R., Sahoo, S., Mohapatra, E.: Biosensors in health care: The milestones achieved in their development towards lab-on-chip-analysis. Biochem. Res. Int. (2016). https://doi.org/10.1155/2016/3130469
8. Hantanasirisakul, K., Alhabeb, M., Lipatov, A., et al.: Effects of synthesis and processing on optoelectronic properties of titanium Carbonitride MXene. Chem Mater **31**, 2941–2951 (2019). https://doi.org/10.1021/acs.chemmater.9b00401
9. Scidà, A., Haque, S., Treossi, E., et al.: Application of graphene-based flexible antennas in consumer electronic devices. Mater Today **21**, 223–230 (2018). https://doi.org/10.1016/j.mattod.2018.01.007
10. Ouyang, Q., Zeng, S., Jiang, L., et al.: Two-dimensional transition metal dichalcogenide enhanced phase-sensitive plasmonic biosensors: theoretical insight. J. Phys. Chem. C **121**, 6282–6289 (2017). https://doi.org/10.1021/acs.jpcc.6b12858
11. Qiu, Y., Schwegler, B.R., Wang, L.P.: Polarizable molecular simulations reveal how silicon-containing functional groups govern the desalination mechanism in Nanoporous graphene. J. Chem. Theory Comput. **14**, 4279–4290 (2018). https://doi.org/10.1021/acs.jctc.8b00226
12. Spear, J.C., Ewers, B.W., Batteas, J.D.: 2D-nanomaterials for controlling friction and wear at interfaces. Nano Today **10**, 301–314 (2015). https://doi.org/10.1016/j.nantod.2015.04.003
13. Satheeshkumar, E., Makaryan, T., Melikyan, A., et al.: One-step solution processing of Ag, Au and Pd@MXene hybrids for SERS. Sci Rep **6**, 1–9 (2016). https://doi.org/10.1038/srep32049

14. Deshmukh, K., Kovářík, T., Khadheer Pasha, S.K.: State of the art recent progress in two dimensional MXenes based gas sensors and biosensors: a comprehensive review. Coord. Chem. Rev., 424 (2020).https://doi.org/10.1016/j.ccr.2020.213514
15. Ramanavicius, S., Ramanavicius, A.: Progress and insights in the application of mxenes as new 2d nanomaterials suitable for biosensors and biofuel cell design. Int. J. Mol. Sci. **21**, 1–17 (2020). https://doi.org/10.3390/ijms21239224
16. Devasenathipathy, R., Mani, V., Chen, S.M., et al.: Glucose biosensor based on glucose oxidase immobilized at gold nanoparticles decorated graphene-carbon nanotubes. Enzyme Microb. Technol. **78**, 40–45 (2015). https://doi.org/10.1016/j.enzmictec.2015.06.006
17. Zhu, J., Ha, E., Zhao, G., et al.: Recent advance in MXenes: a promising 2D material for catalysis, sensor and chemical adsorption. Coord. Chem. Rev. **352**, 306–327 (2017). https://doi.org/10.1016/j.ccr.2017.09.012
18. Yu, T., Breslin, C.B.: Review—two-dimensional titanium carbide MXenes and their emerging applications as electrochemical sensors. J. Electrochem. Soc. **167**, 037514 (2020). https://doi.org/10.1149/2.0142003jes
19. Sinha, A., Dhanjai, Z.H., et al.: MXene: An emerging material for sensing and biosensing. TrAC—Trends Anal. Chem. **105**, 424–435 (2018). https://doi.org/10.1016/j.trac.2018.05.021
20. Gu, H., Xing, Y., Xiong, P., et al.: Three-Dimensional porous Ti3C2Tx MXene-graphene hybrid films for glucose Biosensing. ACS Appl. Nano Mater **2**, 6537–6545 (2019). https://doi.org/10.1021/acsanm.9b01465
21. Wu, L., Lu, X., Dhanjai, et al.: 2D transition metal carbide MXene as a robust biosensing platform for enzyme immobilization and ultrasensitive detection of phenol. Biosens. Bioelectron. **107**, 69–75 (2018). https://doi.org/10.1016/j.bios.2018.02.021
22. Koyappayil, A., Chavan, S.G., Mohammadniaei, M. et al.: β-Hydroxybutyrate dehydrogenase decorated MXene nanosheets for the amperometric determination of β-hydroxybutyrate. Microchim Acta, 187 (2020).https://doi.org/10.1007/s00604-020-04258-y
23. Kumar, S., Lei, Y., Alshareef, N.H., et al.: Biofunctionalized two-dimensional $Ti3C_2$ MXenes for ultrasensitive detection of cancer biomarker. Biosens. Bioelectron. **121**, 243–249 (2018). https://doi.org/10.1016/j.bios.2018.08.076
24. Chen, J., Tong, P., Huang, L., et al.: Ti3C2 MXene nanosheet-based capacitance immunoassay with tyramine-enzyme repeats to detect prostate-specific antigen on interdigitated micro-comb electrode. Electrochim. Acta **319**, 375–381 (2019). https://doi.org/10.1016/j.electacta.2019.07.010
25. Wu, D., Wu, M., Yang, J., et al.: Delaminated Ti3C2Tx (MXene) for electrochemical carbendazim sensing. Mater Lett. **236**, 412–415 (2019). https://doi.org/10.1016/j.matlet.2018.10.150
26. Rasheed, P.A., Pandey, R.P., Jabbar, K.A., et al.: Sensitive electrochemical detection of l-cysteine based on a highly stable Pd@Ti3C2T:X(MXene) nanocomposite modified glassy carbon electrode. Anal. Methods **11**, 3851–3856 (2019). https://doi.org/10.1039/c9ay00912d
27. Zheng, J., Diao, J., Jin, Y., et al.: An inkjet printed Ti 3 C 2 -GO electrode for the electrochemical sensing of hydrogen peroxide. J. Electrochem. Soc. **165**, B227–B231 (2018). https://doi.org/10.1149/2.0051807jes
28. Liu, J., Jiang, X., Zhang, R., et al.: MXene-enabled electrochemical microfluidic biosensor: applications toward multicomponent continuous monitoring in whole blood. Adv. Funct. Mater **29**, 1–9 (2019). https://doi.org/10.1002/adfm.201807326
29. Huang, R., Chen, S., Yu, J., Jiang, X.: Self-assembled Ti3C2 /MWCNTs nanocomposites modified glassy carbon electrode for electrochemical simultaneous detection of hydroquinone and catechol. Ecotoxicol. Environ. Saf. **184**, 109619 (2019). https://doi.org/10.1016/j.ecoenv.2019.109619
30. Shahzad, F., Iqbal, A., Zaidi, S.A., et al.: Nafion-stabilized two-dimensional transition metal carbide (Ti3C2Tx MXene) as a high-performance electrochemical sensor for neurotransmitter. J. Ind. Eng. Chem. **79**, 338–344 (2019). https://doi.org/10.1016/j.jiec.2019.03.061
31. Zheng, J., Wang, B., Ding, A., et al.: Synthesis of MXene/DNA/Pd/Pt nanocomposite for sensitive detection of dopamine. J. Electroanal. Chem. **816**, 189–194 (2018). https://doi.org/10.1016/j.jelechem.2018.03.056

32. Jiang, Y., Zhang, X., Pei, L., et al.: Silver nanoparticles modified two-dimensional transition metal carbides as nanocarriers to fabricate acetycholinesterase-based electrochemical biosensor. Chem. Eng. J. **339**, 547–556 (2018). https://doi.org/10.1016/j.cej.2018.01.111
33. Lei, Y., Zhao, W., Zhang, Y., et al.: A MXene-Based Wearable biosensor system for high-performance in vitro perspiration analysis. Small **15**, 1–10 (2019). https://doi.org/10.1002/smll.201901190
34. Rakhi, R.B., Nayuk, P., Xia, C., Alshareef, H.N.: Novel amperometric glucose biosensor based on MXene nanocomposite. Sci. Rep. **6**, 1–9 (2016). https://doi.org/10.1038/srep36422
35. Wang, H., Li, H., Huang, Y., et al.: A label-free electrochemical biosensor for highly sensitive detection of gliotoxin based on DNA nanostructure/MXene nanocomplexes. Biosens. Bioelectron. **142**, 111531 (2019). https://doi.org/10.1016/j.bios.2019.111531
36. Mohammadniaei, M., Koyappayil, A., Sun, Y., et al.: Gold nanoparticle/MXene for multiple and sensitive detection of oncomiRs based on synergetic signal amplification. Biosens. Bioelectron. **159**, 112208 (2020). https://doi.org/10.1016/j.bios.2020.112208
37. Yang, X., Feng, M., Xia, J., et al.: An electrochemical biosensor based on AuNPs/Ti_3C_2 MXene three-dimensional nanocomposite for microRNA-155 detection by exonuclease III-aided cascade target recycling. J. Electroanal. Chem. **878**, 114669 (2020). https://doi.org/10.1016/j.jelechem.2020.114669
38. Kashefi-Kheyrabadi, L., Koyappayil, A., Kim, T., et al.: A MoS2@Ti3C2Tx MXene hybrid-based electrochemical aptasensor (MEA) for sensitive and rapid detection of Thyroxine. Bioelectrochemistry **137**, 107674 (2021). https://doi.org/10.1016/j.bioelechem.2020.107674
39. Liu, L., Wei, Y., Jiao, S., et al.: A novel label-free strategy for the ultrasensitive miRNA-182 detection based on MoS 2 /Ti 3 C 2 nanohybrids. Biosens. Bioelectron. **137**, 45–51 (2019). https://doi.org/10.1016/j.bios.2019.04.059
40. Zhou, S., Gu, C., Li, Z., et al.: $Ti_3C_2T_x$ MXene and polyoxometalate nanohybrid embedded with polypyrrole: ultra-sensitive platform for the detection of osteopontin. Appl. Surf. Sci. **498**, 143889 (2019). https://doi.org/10.1016/j.apsusc.2019.143889
41. Zhang, Q., Wang, F., Zhang, H., et al.: Universal Ti 3 C 2 MXenes Based Self-Standard Ratiometric fluorescence resonance energy transfer platform for highly sensitive detection of exosomes. Anal. Chem. **90**, 12737–12744 (2018). https://doi.org/10.1021/acs.analchem.8b03083
42. Soomro, R.A., Jawaid, S., Zhu, Q., et al.: A mini-review on MXenes as versatile substrate for advanced sensors. Chinese Chem. Lett. **31**, 922–930 (2020). https://doi.org/10.1016/j.cclet.2019.12.005
43. Fang, Y., Yang, X., Chen, T., et al.: Two-dimensional titanium carbide (MXene)-based solid-state electrochemiluminescent sensor for label-free single-nucleotide mismatch discrimination in human urine. Sens. Actuat. B Chem. **263**, 400–407 (2018). https://doi.org/10.1016/j.snb.2018.02.102
44. Zhang, H., Wang, Z., Zhang, Q., et al.: Ti 3 C 2 MXenes nanosheets catalyzed highly efficient electrogenerated chemiluminescence biosensor for the detection of exosomes. Biosens. Bioelectron. **124–125**, 184–190 (2019). https://doi.org/10.1016/j.bios.2018.10.016
45. Peng, X., Zhang, Y., Lu, D., et al.: Ultrathin Ti3C2 nanosheets based "off-on" fluorescent nanoprobe for rapid and sensitive detection of HPV infection. Sens. Actuat. B Chem. **286**, 222–229 (2019). https://doi.org/10.1016/j.snb.2019.01.158
46. Zhang, Q., Sun, Y., Liu, M., Liu, Y.: Selective detection of Fe3+ ions based on fluorescence MXene quantum dots via a mechanism integrating electron transfer and inner filter effect. Nanoscale **12**, 1826–1832 (2020). https://doi.org/10.1039/c9nr08794j
47. Liu, M., Zhou, J., He, Y., et al.: ε-Poly-L-lysine-protected Ti3C2 MXene quantum dots with high quantum yield for fluorometric determination of cytochrome c and trypsin. Microchim Acta, 186 (2019).https://doi.org/10.1007/s00604-019-3945-0
48. Li, H., Wen, Y., Zhu, X., et al.: Novel Heterostructure of a MXene@NiFe-LDH Nanohybrid with superior peroxidase-like activity for sensitive colorimetric detection of glutathione. ACS Sustain Chem. Eng. **8**, 520–526 (2020). https://doi.org/10.1021/acssuschemeng.9b05987

49. Chen, X., Sun, X., Xu, W., et al.: Ratiometric photoluminescence sensing based on Ti3C2 MXene quantum dots as an intracellular pH sensor. Nanoscale **10**, 1111–1118 (2018). https://doi.org/10.1039/c7nr06958h
50. Cai, Y., Shen, J., Ge, G., et al.: Stretchable Ti3C2Tx MXene/carbon nanotube composite based strain sensor with ultrahigh sensitivity and tunable sensing range. ACS Nano **12**, 56–62 (2018). https://doi.org/10.1021/acsnano.7b06251
51. Shi, X., Wang, H., Xie, X., et al.: Bioinspired Ultrasensitive and stretchable MXene-based strain sensor via nacre-mimetic microscale "brick-and-mortar" architecture. ACS Nano **13**, 649–659 (2019). https://doi.org/10.1021/acsnano.8b07805
52. Yao, D.-J., Tang, Z., Zhang, L., et al.: A highly sensitive, foldable and wearable pressure sensor based on MXene-coated airlaid paper for electronic skin. J. Mater Chem. C **9**, 12642–12649 (2021). https://doi.org/10.1039/d1tc02458b
53. Luo, J., Gao, S., Luo, H., et al.: Superhydrophobic and breathable smart MXene-based textile for multifunctional wearable sensing electronics. Chem. Eng. J. **406**, 126898 (2021). https://doi.org/10.1016/j.cej.2020.126898
54. Xu, X., Chen, Y., He, P., et al.: Wearable CNT/Ti3C2Tx MXene/PDMS composite strain sensor with enhanced stability for real-time human healthcare monitoring. Nano Res. **14**, 2875–2883 (2021). https://doi.org/10.1007/s12274-021-3536-3
55. Zhang, Y.Z., Lee, K.H., Anjum, D.H., et al.: MXenes stretch hydrogel sensor performance to new limits. Sci. Adv. **4**, 1–8 (2018). https://doi.org/10.1126/sciadv.aat0098
56. Wang, K., Lou, Z., Wang, L., et al.: Bioinspired interlocked structure-induced high deformability for two-dimensional titanium carbide (MXene)/natural microcapsule-based flexible pressure sensors. ACS Nano **13**, 9139–9147 (2019). https://doi.org/10.1021/acsnano.9b03454
57. https://gco.iarc.fr/today/ho The Global Cancer Observatory (GCO) 2020 cancer statistics. https://gco.iarc.fr/today/home
58. Hirsch, L.R., Stafford, R.J., Bankson, J.A., et al.: Nanoshell-mediated near-infrared thermal therapy of tumors under magnetic resonance guidance. Proc. Natl. Acad. Sci. USA **100**, 13549–13554 (2003). https://doi.org/10.1073/pnas.2232479100
59. Tsai, M.F., Chang, S.H.G., Cheng, F.Y., et al.: Au nanorod design as light-absorber in the first and second biological near-infrared windows for in vivo photothermal therapy. ACS Nano **7**, 5330–5342 (2013). https://doi.org/10.1021/nn401187c
60. El-Sayed, I.H., Huang, X., El-Sayed, M.A.: Selective laser photo-thermal therapy of epithelial carcinoma using anti-EGFR antibody conjugated gold nanoparticles. Cancer Lett. **239**, 129–135 (2006). https://doi.org/10.1016/j.canlet.2005.07.035
61. Moon, H.K., Lee, S.H., Choi, H.C.: In vivo near-infrared mediated tumor destruction by photothermal effect of carbon nanotubes. ACS Nano **3**, 3707–3713 (2009). https://doi.org/10.1021/nn900904h
62. Sobhani, Z., Behnam, M.A., Emami, F., et al.: Photothermal therapy of melanoma tumor using multiwalled carbon nanotubes. Int. J. Nanomed. **12**, 4509–4517 (2017). https://doi.org/10.2147/IJN.S134661
63. Zha, Z., Yue, X., Ren, Q., Dai, Z.: Uniform polypyrrole nanoparticles with high photothermal conversion efficiency for photothermal ablation of cancer cells. Adv. Mater **25**, 777–782 (2013). https://doi.org/10.1002/adma.201202211
64. Cheng, L., Yang, K., Chen, Q., Liu, Z.: Organic stealth nanoparticles for highly effective in vivo near-infrared photothermal therapy of cancer. ACS Nano **6**, 5605–5613 (2012). https://doi.org/10.1021/nn301539m
65. Zhou, M., Zhang, R., Huang, M., et al.: A chelator-free multifunctional [64Cu]CuS nanoparticle platform for simultaneous micro-PET/CT imaging and photothermal ablation therapy. J. Am. Chem. Soc. **132**, 15351–15358 (2010). https://doi.org/10.1021/ja106855m
66. Wu, X., Liu, K., Huang, Q., et al.: Photothermal Therapy Based on CuS nanoparticles for alleviating arterial restenosis induced by mechanical injury of endovascular treatment. Front Mater **7**, 1–10 (2021). https://doi.org/10.3389/fmats.2020.591281
67. Santra, S., Kaittanis, C., Grimm, J., Perez, J.M.: Drug/dye-loaded, multifunctional iron oxide nanoparticles for combined targeted cancer therapy and dual optical/magnetic resonance imaging. Small **5**, 1862–1868 (2009). https://doi.org/10.1002/smll.200900389

68. Ashkbar, A., Rezaei, F., Attari, F., Ashkevarian, S.: Treatment of breast cancer in vivo by dual photodynamic and photothermal approaches with the aid of curcumin photosensitizer and magnetic nanoparticles. Sci. Rep. **10**, 1–12 (2020). https://doi.org/10.1038/s41598-020-78241-1
69. Cheng, L., Liu, J., Gu, X., et al.: PEGylated WS2 nanosheets as a multifunctional theranostic agent for in vivo dual-modal CT/photoacoustic imaging guided photothermal therapy. Adv. Mater **26**, 1886–1893 (2014). https://doi.org/10.1002/adma.201304497
70. Shi, J., Li, J., Wang, Y., et al.: Recent advances in MoS2-based photothermal therapy for cancer and infectious disease treatment. J. Mater Chem. B **8**, 5793–5807 (2020). https://doi.org/10.1039/d0tb01018a
71. Xu, D., Li, Z., Li, L., Wang, J.: Insights into the Photothermal conversion of 2D MXene nanomaterials : synthesis , mechanism , and applications, 2000712 (2020).https://doi.org/10.1002/adfm.202000712
72. Szuplewska, A., Kulpińska, D., Dybko, A., et al.: Future applications of MXenes in biotechnology, nanomedicine, and sensors. Trends Biotechnol. **38**, 264–279 (2020). https://doi.org/10.1016/j.tibtech.2019.09.001
73. Dong, L.M., Ye, C., Zheng, L.L., et al.: Two-dimensional metal carbides and nitrides (MXenes): Preparation, property, and applications in cancer therapy. Nanophotonics **9**, 2125–2145 (2020). https://doi.org/10.1515/nanoph-2019-0550
74. Xuan, J., Wang, Z., Chen, Y., et al.: Organic-base-driven intercalation and delamination for the production of functionalized titanium carbide Nanosheets with superior Photothermal therapeutic performance. Angew. Chemie. Int. Ed. **55**, 14569–14574 (2016). https://doi.org/10.1002/anie.201606643
75. Dai, C., Lin, H., Xu, G., et al.: Biocompatible 2D titanium carbide (MXenes) composite nanosheets for pH-responsive MRI-guided tumor hyperthermia. Chem. Mater **29**, 8637–8652 (2017). https://doi.org/10.1021/acs.chemmater.7b02441
76. Yu, X., Cai, X., Cui, H., et al.: Fluorine-free preparation of titanium carbide MXene quantum dots with high near-infrared photothermal performances for cancer therapy. Nanoscale **9**, 17859–17864 (2017). https://doi.org/10.1039/c7nr05997c
77. Szuplewska, A., Kulpińska, D., Dybko, A., et al.: 2D Ti 2 C (MXene) as a novel highly efficient and selective agent for photothermal therapy. Mater Sci. Eng. C **98**, 874–886 (2019). https://doi.org/10.1016/j.msec.2019.01.021
78. Lin, H., Wang, Y., Gao, S., et al.: Theranostic 2D tantalum carbide (MXene). Adv. Mater **30**, 1–11 (2018). https://doi.org/10.1002/adma.201703284
79. Lin, H., Gao, S., Dai, C., et al.: A Two-dimensional biodegradable niobium carbide (MXene) for Photothermal tumor eradication in NIR-I and NIR-II Biowindows. J. Am. Chem. Soc. **139**, 16235–16247 (2017). https://doi.org/10.1021/jacs.7b07818
80. Wan, G., Chen, B., Li, L., et al.: Nanoscaled red blood cells facilitate breast cancer treatment by combining photothermal/photodynamic therapy and chemotherapy. Biomaterials **155**, 25–40 (2018). https://doi.org/10.1016/j.biomaterials.2017.11.002
81. Sheng, D., Liu, T., Deng, L., et al.: Perfluorooctyl bromide & indocyanine green co-loaded nanoliposomes for enhanced multimodal imaging-guided phototherapy. Biomaterials **165**, 1–13 (2018). https://doi.org/10.1016/j.biomaterials.2018.02.041
82. Shu, Y., Song, R., Zheng, A., et al.: Thermo/pH dual-stimuli-responsive drug delivery for chemo-/photothermal therapy monitored by cell imaging. Talanta **181**, 278–285 (2018). https://doi.org/10.1016/j.talanta.2018.01.018
83. Liu, Y., Han, Q., Yang, W., et al.: Two-dimensional MXene/cobalt nanowire heterojunction for controlled drug delivery and chemo-photothermal therapy. Mater Sci. Eng. C **116**, 111212 (2020). https://doi.org/10.1016/j.msec.2020.111212
84. Liu, G., Zou, J., Tang, Q., et al.: Surface Modified Ti3C2 MXene Nanosheets for tumor targeting Photothermal/Photodynamic/Chemo synergistic therapy. ACS Appl. Mater Interf. **9**, 40077–40086 (2017). https://doi.org/10.1021/acsami.7b13421
85. Fraum, T.J., Ludwig, D.R., Bashir, M.R., Fowler, K.J.: Gadolinium-based contrast agents: a comprehensive risk assessment. J. Magn. Reson. Imaging **46**, 338–353 (2017). https://doi.org/10.1002/jmri.25625

86. Lee, N., Choi, S.H., Hyeon, T.: Nano-sized CT contrast agents. Adv. Mater **25**, 2641–2660 (2013). https://doi.org/10.1002/adma.201300081
87. Liu, Z., Lin, H., Zhao, M., et al.: 2D superparamagnetic tantalum carbide composite MXenes for efficient breast-cancer theranostics. Theranostics **8**, 1648–1664 (2018). https://doi.org/10.7150/thno.23369
88. Zong, L., Wu, H., Lin, H., Chen, Y.: A polyoxometalate-functionalized two-dimensional titanium carbide composite MXene for effective cancer theranostics. Nano Res. **11**, 4149–4168 (2018). https://doi.org/10.1007/s12274-018-2002-3
89. Dai, C., Chen, Y., Jing, X., et al.: Two-Dimensional tantalum carbide (MXenes) composite Nanosheets for multiple imaging-guided photothermal tumor ablation. ACS Nano **11**, 12696–12712 (2017). https://doi.org/10.1021/acsnano.7b07241
90. Iravani, S., Varma, R.S.: MXenes and MXene-based materials for tissue engineering and regenerative medicine: recent advances. Mater Adv. (2021). https://doi.org/10.1039/d1ma00189b
91. Pan, S., Yin, J., Yu, L. et al.: 2D MXene-integrated 3D-printing scaffolds for augmented osteosarcoma phototherapy and accelerated tissue reconstruction. Adv. Sci. 7 (2020).https://doi.org/10.1002/advs.201901511
92. Huang, R., Chen, X., Dong, Y., et al.: MXene composite nanofibers for cell culture and tissue engineering. ACS Appl. Bio. Mater **3**, 2125–2131 (2020). https://doi.org/10.1021/acsabm.0c00007
93. Rastin, H., Zhang, B., Mazinani, A., et al.: 3D bioprinting of cell-laden electroconductive MXene nanocomposite bioinks. Nanoscale **12**, 16069–16080 (2020). https://doi.org/10.1039/d0nr02581j
94. Ye, G., Wen, Z., Wen, F., et al.: Mussel-inspired conductive Ti2C-cryogel promotes functional maturation of cardiomyocytes and enhances repair of myocardial infarction. Theranostics **10**, 2047–2066 (2020). https://doi.org/10.7150/thno.38876
95. Basara, G., Saeidi-Javash, M., Ren, X., et al.: Electrically conductive 3D printed Ti3C2Tx MXene-PEG composite constructs for cardiac tissue engineering. Acta Biomater (2020). https://doi.org/10.1016/j.actbio.2020.12.033
96. Cardiovascular, P.M.: Cardiovascular diseases (CVDs), 1–5 (2021)
97. Wu, F., Zheng, H., Wang, W., et al.: Rapid eradication of antibiotic-resistant bacteria and biofilms by MXene and near-infrared light through photothermal ablation. Sci. China Mater **64**, 748–758 (2021). https://doi.org/10.1007/s40843-020-1451-7
98. Mayerberger, E.A., Street, R.M., McDaniel, R.M., et al.: Antibacterial properties of electrospun Ti3C2Tz (MXene)/chitosan nanofibers. RSC Adv. **8**, 35386–35394 (2018). https://doi.org/10.1039/c8ra06274a
99. Rasool, K., Helal, M., Ali, A., et al.: Antibacterial activity of Ti3C2Tx MXene. ACS Nano **10**, 3674–3684 (2016). https://doi.org/10.1021/acsnano.6b00181
100. Wang, W., Feng, H., Liu, J., et al.: A photo catalyst of cuprous oxide anchored MXene nanosheet for dramatic enhancement of synergistic antibacterial ability. Chem. Eng. J. **386**, 124116 (2020). https://doi.org/10.1016/j.cej.2020.124116
101. Zhou, L., Zheng, H., Liu, Z., et al.: Conductive antibacterial hemostatic multifunctional scaffolds based on Ti3C2TxMXene Nanosheets for promoting multidrug-resistant bacteria-infected wound healing. ACS Nano **15**, 2468–2480 (2021). https://doi.org/10.1021/acsnano.0c06287
102. Zheng, H., Wang, S., Cheng, F., et al.: Bioactive antiinflammatory, antibacterial, conductive multifunctional scaffold based on MXene@CeO2 nanocomposites for infection-impaired skin multimodal therapy. Chem. Eng. J. **424**, 130148 (2021). https://doi.org/10.1016/j.cej.2021.130148
103. Rosenkranz, A., Perini, G., Aguilar-Hurtado, J.Y., et al.: Laser-mediated antibacterial effects of few- and multi-layer Ti3C2Tx MXenes. Appl. Surf. Sci. **567**, 150795 (2021). https://doi.org/10.1016/j.apsusc.2021.150795
104. Zheng, K., Li, S., Jing, L., et al.: Synergistic antimicrobial titanium carbide (MXene) conjugated with gold nanoclusters. Adv. Healthc Mater **9**, 1–9 (2020). https://doi.org/10.1002/adhm.202001007

105. Rasool, K., Mahmoud, K.A., Johnson, D.J., et al.: Efficient antibacterial membrane based on two-dimensional Ti3C2Tx (MXene) Nanosheets. Sci. Rep. **7**, 1–11 (2017). https://doi.org/10.1038/s41598-017-01714-3
106. Arabi Shamsabadi, A., Sharifian, M., Anasori, B., Soroush, M.: Antimicrobial mode-of-action of colloidal Ti3C2Tx MXene nanosheets. ACS Sustain. Chem. Eng. **6**, 16586–16596 (2018). https://doi.org/10.1021/acssuschemeng.8b03823
107. Dong, Y., Li, S., Li, X., Wang, X.: Smart MXene/agarose hydrogel with photothermal property for controlled drug release. Int. J. Biol. Macromol. **190**, 693–699 (2021). https://doi.org/10.1016/j.ijbiomac.2021.09.037
108. Dwivedi, N., Dhand, C., Kumar, P., Srivastava, A.K.: Emergent 2D materials for combating infectious diseases: the potential of MXenes and MXene-graphene composites to fight against pandemics. Mater Adv. **2**, 2892–2905 (2021). https://doi.org/10.1039/d1ma00003a

Advancements in MXenes

Vishal Chaudhary, Akash Sharma, Pradeep Bhadola, and Ajeet Kaushik

Abstract MXenes have gained an excessive interest in architecting new-generation wearable devices owing to their unique physicochemical characteristics and machine processability. Accordingly, different strategies for scalable manufacturing of MXenes are explored for its mass-level production. Using a large reactor with optimal control of reaction parameters, the chemical etching approach has emerged as a feasible, scalable strategy to synthesize MXenes. Moreover, alternative precursors like non-MAX phases and 'i-MAX' phases have advanced these synthesis strategies with a new prospect of scalable production. These developments have projected MXene as a promising candidate to design next-generation wearable electronics with advanced features like intelligent operation, portable, compact, self-powered, flexible, stretchable, bendable, and skin embedded nature. Due to these features, MXenes and their hybrids with materials such as macromolecules, graphene-based materials, and metals are the current choice of advanced nanomaterials to fabricate wearable physical, chemical, and biosensors with excellent performances. These materials have consistently excellent sensing performance in all wear and tear situations and possess biomedical, agriculture, workplace safety, and environmental monitoring applications. Besides excellent electric conductivity and the prospect of accommodating skin depth factors, MXene based materials are used to design wireless communication systems supporting Bluetooth, WiFi, and 5G requirements. It anticipates the

V. Chaudhary (✉)
Research Cell and Department of Physics, Bhagini Nivedita College, University of Delhi, New Delhi 110075, India
e-mail: chaudhary00vishal@gmail.com; drvishal@bn.du.ac.in

A. Sharma
School of Biological and Environmental Sciences, Shoolini University, Solan, Himachal Pradesh 173212, India

P. Bhadola
Centre for Theoretical Physics and Natural Philosophy, Nakhonsawan Studiorum for Advanced Studies, Mahidol University, Nakhonsawan 60130, Thailand

A. Kaushik
NanoBioTech Laboratory, Health System Engineering, Department of Environmental Engineering, Florida Polytechnic University, Lakeland, FL 33805, USA

M. Khalid et al. (eds.), *Fundamental Aspects and Perspectives of MXenes*, Engineering Materials, https://doi.org/10.1007/978-3-031-05006-0_12

enormous potential of MXene based materials to architect field-deployable compact sensors for personalized healthcare monitoring with intelligent wireless operation.

Keywords Wearable electronics · MXene · Wireless communication · Scalable production · Sensors

1 Advancement in Scalable Fabrication of MXenes

MXenes is a large class of 2-D metal carbides and nitrides showing tremendous potential to address diversified global challenges, including water scarcity, energy crisis, environmental redemption, and human health [1–3]. Unlike other 2-D materials, MXenes are generally hydrophilic with abundant surface functionalities with tunable capacity [1]. The desired application area can be easily targeted by optimizing these functionalities and tuning interlayer distance [4]. It has led to extensive dedicated research to find efficient fabrication strategies for high yield MXenes with the desired structural and chemical configuration. Many in-lab experimental strategies to architect MXenes have already been reported, including selective etching, exfoliation, chemical vapor deposition, atomic layer deposition, and green routes [1–3]. Due to low yield, high cost, and sophisticated instrumental requirements, these strategies are constrained for practical purposes [2, 3]. The main challenge associated with MXene mass-production is maintaining its excellent conductivity with mechanical strength simultaneously during machine processing. The bottom-up strategies, such as CVD or ALD, are limited due to issues relating to the requirement of using vacuum chambers and substrates for growth-limiting the final size of MXene [2, 5, 6]. However, these constraints are not present in top-down approaches.

Nevertheless, specific conditions required to be maintained in large reaction volumes are challenging [5]. It restricts the transfer of MXene technology from laboratories to industries, which indicates the need for scalable production. Nevertheless, MXenes do not possess any inherent limitation for synthesis batch size, and the scaling of MXene possibly is theoretically possible without any upper limit [5, 7]. The immediate attention to scalable production of MXenes is dedicated to tuning reaction parameters to optimize desired requirements.

1.1 Issues Related to Scalable Production

Controlling the size of reactor and uniform mixing simultaneously

The scaling of chemical reaction parameters is challenging due to critical factors such as technological and safety issues. For instance, to scale a reactor, non-linear effects like the surface-to-volume ratio of the reactor must be considered. In addition, the transfer of two reactants creates a significant issue when adding the desired relative quantities of precursors [5, 8, 9]. It indicates the importance of continuous uniform

stirring or mixing of precursors during the course of a reaction. Hence, the prime aspect of MXene machine processing is designing uniform mixing larger reactors. However, optimizing mixing parameters during the reaction in such a larger reactor is challenging and yet to be established.

Controlling heat transfer during reactions

There is a drastic change in heat transfer from the fluid to the reactor due to less relative reactor surface area available for cooling [5, 10]. It raises the concern of initiating runaway reactions and anticipates explosion. Hence, it results in an alteration in the reactor's internal temperature during production. It can affect the chemical kinetics of reactions and properties of the resultant product. Moreover, it can adversely affect the lattice arrangement, surface functionalities, interlayer distance, electrical conductivity, composition, and mechanical strength of produced MXenes.

Hence, there are numerous minor issues related to the large-scale production of MXenes, which depend upon various processing parameters. In other words, it is very challenging to transfer lab-scale technology to scalable industrial machine processing. However, few reports in the literature discuss the scalable production of MXenes and their prospects for industrial-scale fabrication.

1.2 Scalable Fabrication of MXene Through Chemical Route

The large-scale reactors for manufacturing MXenes at a massive scale are advantageous in tuning the properties, monitoring and optimizing the chemical reaction, reducing human resources, processing, safety, and low contamination. Moreover, the automated operation through a computer interface makes it easy to customize the reaction and its course and turns it into an intelligent synthesis strategy. For instance, Shuck et al. [5] reported the large-scale production of titanium carbide MXene using a custom-designed chemical reactor, as shown in Fig. 1. They prepared a large batch of MXene using an indigenous reactor and compared it with a small batch of MXene prepared through conventional lab-based chemical exfoliation.

The main parts of an indigenously designed reactor are a cooling jacket, gas inlet/outlet with screw feeder, mixer, thermocouple, and agitator. The cooling jacket is coupled with a cooling tank that allows the reaction temperature throughout the course of the reaction. The screw attached with the outlet/inlet allows the uniform addition of MAX precursor by applying downward pressure to the system. The internal reactor, including blades of mixer and thermocouple cascade, comprises Teflon to protect it from damage during HF reactions. The thermocouple allows monitoring the reaction temperature. Finally, the agitator is designed to achieve homogenous mixing of precursors during the reaction.

However, the designed reactor can be upgraded by considering advancements like replacing water with coolants in the cooling tank. In a typical synthesis, Shuck et al. [5], HF-based selective etching route is followed, resulting in $Ti_3C_2T_x$ multilayer

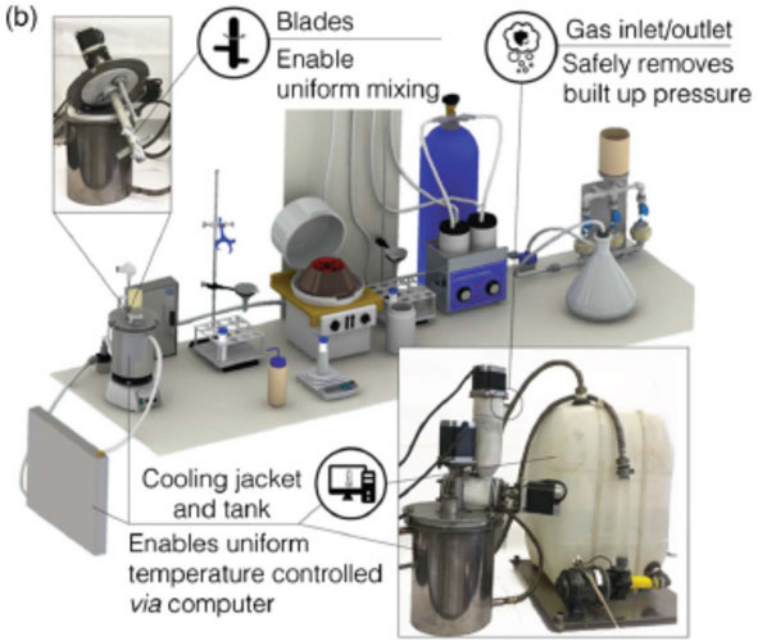

Fig. 1 Pictorial illustration of 3D model of MXene reactor for large-scale production; Reprinted with permission of [5]. Copyright 2020, Wiley

MXene and single-flake MXene for more extensive and smaller batches, respectively. Further, the synthesized MXenes were intercalated with water and vacuum dried subsequently. The yield of the larger batch was obtained be significant (52%) compared to that of the smaller batch indicating the success of the technique for mass production. XRD revealed similar structural characteristics of both the batches of MXene with all characteristic prominent peaks, as shown in Fig. 2.

Moreover, in the concerned study, XPS, UV–Visible, SEM, DLS, and Raman spectroscopies reveal that the products from both batches are identical in physicochemical characteristics [5]. Therefore, it indicates that this method can result in the mass production of MXenes without compromising their desired properties. Hence, the larger-reactor method has been proposed as a suitable technique for the scalable production of MXenes. However, the strategy has only been experimentally validated for $Ti_3C_2T_x$ -MXene and yet to be evaluated for other MXenes with similar configurations.

Furthermore, Zhang et al. [11] has reported an ammonium ion route to prevent aggregation and restacking of few-layered MXene nanosheets in large quantities. In a typical synthesis, a solution-phase flocculation method (NH^{4+} method and modified NH^{4+} method) has been adopted for large-scale production of MXenes with commercial requirements. The method is suitable for the large-scale production of various MXenes, including $Ti_3C_2T_x$, $Nb_4C_3T_x$, V_2CT_x, Nb_2CT_x, etc.

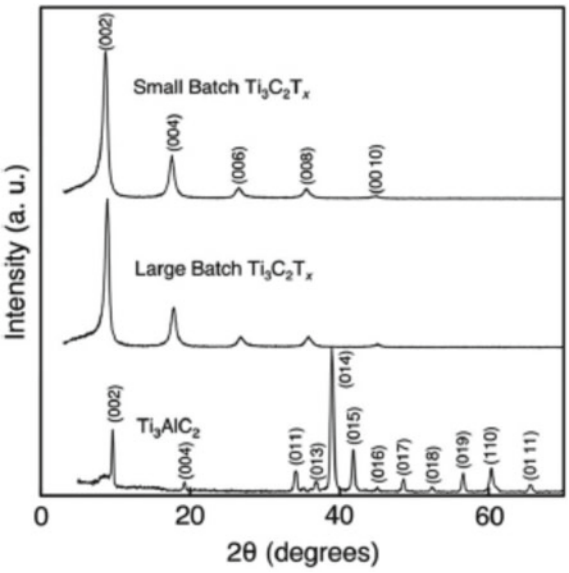

Fig. 2 Comparison of structural characteristics of the small and large batch produced $Ti_3C_2T_x$; Reproduced with permission [5]. Copyright 2020, Wiley

1.3 Scalable Synthesis of MXene Self-standing Films

There are other reports on scalable production of MXenes, their films, or hybrids with other materials aiming to meet industrial requirements both qualitatively and quantitatively [12–14]. In literature, the freestanding films of MXenes are reported to fabricate using vacuum-assisted filtration techniques [12, 15, 16]. MXene flakes are separated from their precursor solvent using a filtration membrane and vacuum pump in a typical process. However, its commercial use is limited due to several bottlenecks, including energy intensiveness, the dependence of area of film on filtration membrane, time-consuming requirements of the dedicated pump to fabricate each film, high cost, and low yield [12, 15, 16]. Other techniques used to fabricate freestanding films include natural sedimentation, spray-coating, blade-coating, and layer-by-layer assembly strategies [12, 16, 17]. However, these methods are constrained for commercial productions due to non-conductive fillers, which dramatically reduce their electrical conductivity and performance. The drop-casting technique is an attractive alternate technique to obtain MXenes films (owing to their hydrophilic nature) on the desired substrate [12, 18, 19]. However, the inverse methodology has been used to obtain self-standing MXene films on a hydrophobic surface [12]. Due to the hydrophobic nature of the substrate, the MXene interacts unfavorably with the substrate, and dried films can be easily delaminated from the substrate due to the prominent MXene-MXene interactions over MXene-substrate interactions.

Taylor et al. [12] reported the scalable fabrication of conductive freestanding $Ti_3C_2T_x$ film on a hydrophobic plastic substrate using the drop-casting technique. First, $Ti_3C_2T_x$ dispersion was prepared using the HF etching route in a typical

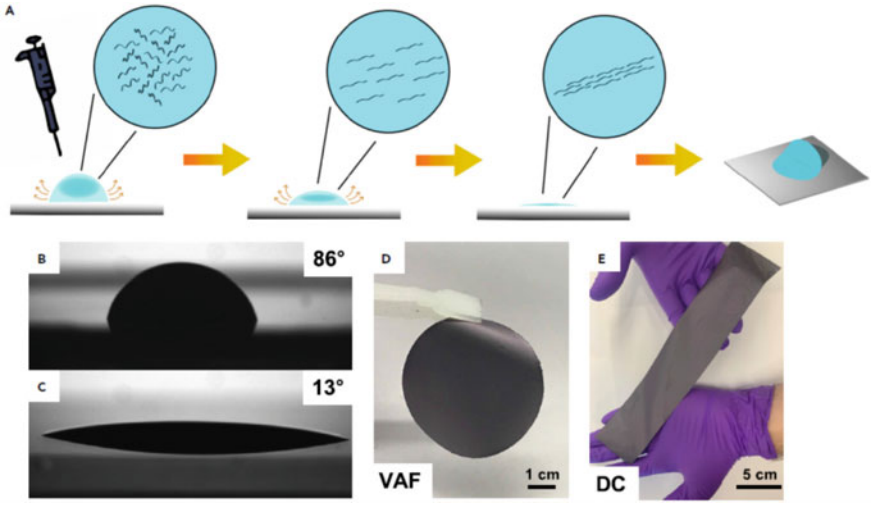

Fig. 3 Strategies to fabricate freestanding MXene films; Reproduced with permission [12]. Copyright 2020, Cell Press

synthesis. Then, the films were deposited by piping out $Ti_3C_2T_x$ dispersion over polyethylene film pulled tightly over a flat surface and subsequent drying, as shown in Fig. 3.

The physicochemical properties of obtained freestanding MXene film were significant with those prepared with the VAF route, which pints out the success of the adopted technique for scalable production. It is a cost-effective, time-saving, economical, high-yielding, and straightforward technique with commercial prospects to obtain freestanding films of MXene.

Moreover, an important fact related to MXene film scalable fabrication is prevention from the creation of voids during the synthesis. Wan et al. [14] reported a novel technique for scalable synthesis of MXene films through bridging-induced densification. The MXene layered structure was densified in a typical synthesis, and voids were removed using a sequential combination of covalent and hydrogen bonding agents. The obtained MXene films were reported to be scalable with enhanced mechanical strength and electrical conductivity with high performance in electromagnetic shielding.

1.4 Scalable Synthesis of MXene Hybrids

The scalable production of MXenes is not limited to its pristine form but has also been reported to the formation of its hybrids for diversified applications [20, 21]. For example, Levitt et al. [22] reported the synthesis of Continuous and Scalable Multifunctional MXene-Infiltrated Nanoyarns (nylon and polyurethane (PU) nanofiber

yarns) using one-step bath electrospinning technique. The fabricated MXene based nano yarns showed high-performance stain sensing with optimal stretchability and significant electrochemical properties.

For instance, Zhao et al. [23] reported the alternative stacking of MXene and reduced graphene oxide nanosheets using spray-assisted layer-by-layer assembly. The method is beneficial for fabricating significantly large, freestanding MXene/rGO heterostructured films with excellent electrochemical performance. Further, Wang et al. [24] reported the scalable synthesis of polyaniline nanodots intercalated into MXene film interlayers in the form of viscous functional inks with ultrahigh volumetric capacitance for supercapacitor applications. Similarly, various reports have reported the scalable synthesis of MXene and its nanocomposites for diversified applications, as listed in Table 1.

Hence, it is evident that the scalable synthesis strategies for MXenes are currently limited and only dedicated to $Ti_3C_2T_x$ MXene. Moreover, the scalable route to obtain pristine MXene is only achieved from the selective etching route [2, 3, 5]. However, this route results in environmental contamination due to the reactants' corrosive nature. As well, the other routes are limited in terms of yield. Hence, it is essential to design scalable routes to synthesize pristine MXene from MAX phases to meet the gap between technology and industries.

Furthermore, the fabrication of MXene films and hybrids from pre-synthesized MXene precursors has also been scaled for diversified applications. However, the studies are limited and only dedicated to specific applications. As a result, it has

Table 1 Scalable Synthesis of MXene and its hybrids

Material	Method	Application	References
$Ti_3C_2T_x$ membrane	Scalable brush-coating	Desalination and organic solvent recovery	[25]
$Ti_3C_2T_x$	Large reactor	Mass production	[5]
MXene films	Bridging induced densification	EMI shielding	[14]
$Na_{0.23}TiO_2/Ti_3C_2$ composites	In-situ transformation reaction	Lithium/sodium-ion batteries	[26]
$Ti_3C_2T_x$ MXene nanoyarns	Bath electrospinning	Strain sensor	[5]
Freestanding $Ti_3C_2T_x$ MXene films	Drop casting	EMI shielding	[12]
$Ti_3C_2T_x$ MXene inks	Extrusion printing and inkjet printing	Micro-supercapacitors	[13]
$Ti_3C_2T_x$ MXene-based on-chip	Cold laser-cutting followed by spin-coating	Energy storage	[27]
N-MXene/rGO (SNMG-40) hybrid film	Heteroatom doping strategy	Flexible energy storage device	[20]

created a large void between MXenes and their commercial use. Hence, dedicated research is essential to obtain scalable techniques for fabricating MXenes and hybrids for commercial applications.

2 Advanced Precursors for MXene Synthesis

2.1 Synthesis of MXene from Non-MAX Phases

The challenges in the scalable production of MXenes from MAX phases have led researchers to find alternative precursors for its production [2, 3, 28]. It has been reported in the literature that all the theoretically proposed MXene do not have MAX phases, especially for ternary metal carbides [2, 3, 28]. Hence, a quest to find new MAX phases and alternative precursors such as non-MAX phases has resulted in extensive research. Several transition metals such as Sc, Zr, and Hf are found in unique layered compound form $(MC)_n[Al(A)]_mC_{m-1}$ (with 'n' as same meaning discussed for MAX phases, 'm' id 3,4, and A is Si/Ge) instead of MAX phases [28]. Various Non-max precursors to synthesize MXenes have been listed in Table 2.

These Non-MAX phases are layered uniquely with Al (A)-C sublayers [28]. The non-MAX phase of $M_{n+1}AlC_n$ possesses Al layers intercalated by strong M-bonding layers, as shown in Fig. 4. However, other forms of non-MAX phase, i.e. $(MC)_n[Al(A)]_mC_{m-1}$ possess carbon shared with transition materials with AL (A) at their boundaries. It has been reported that the non-MAX phase $Zr_3Al_3C_5$ can be prepared by PES of Zr, Al, and graphite powders for the synthesis of the $Zr_3C_2T_x$ [28].

Table 2 List of reported Non-MAX phases based MXenes in literature

S. no.	Non-MAX precursors			Derived MXene
1	Zirconium-based [2, 28–30]	Al contained	$Zr_2Al_3C_4$ $Zr_3Al_3C_5$ $ZrAl_8C_7$ $ZrAl_4C_4$ $Zr_2Al_4C_5$ $Zr_3Al_4C_6$	Zr_2C_4 Zr_3C_5 ZrC_7 ZrC_4 Zr_2C_5, Zr_3C_6
		Al (A) contained	$Zr_2[Al\ (Si)]_4C_5$ $Zr_3[Al\ (Si)]_4C_6$ $[ZrY)]_2Al_4C_5$ $Zr_2[Al\ (Ge)]_4C_5$ $Zr_3[Al\ (Ge)]_4C_6$ $Zr[Al\ (Si)]_8C_7$	Zr_2C_5 Zr_3C_6 $[ZrY)]_2C_5$ Zr_2C_5 Zr_3C_6 ZrC_7
2	Hafnium-based [28]	Al contained	$Hf_2Al_4C_5$ $Hf_3Al_4C_6$ $HfAl_4$ $Hf_2Al_3C_4$	Hf_2C_5 Hf_3C_6 HfC_4 Hf_2C_4

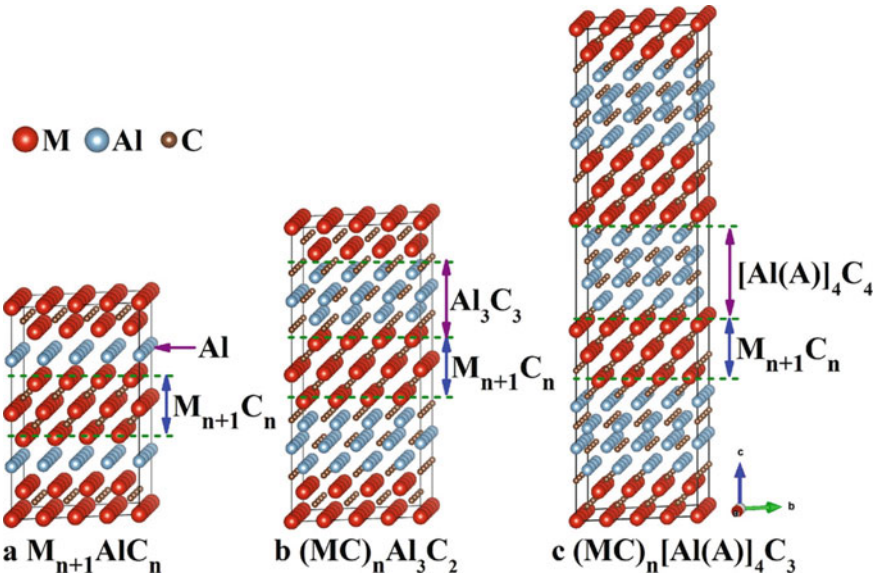

Fig. 4 Selective etching of a M_3AX_2 layered precursor to yield M_3X_2 MXene; Reproduced with permission [28]. Copyright 2019, Springer

Furthermore, the etching of '*A-C*' from the non-MAX phase is more conducive and convenient than the etching of 'A' element from MAX phases. It has also been shown the etching of 'A-C' to fabricate U_2CT_x MXene from $U_2Al_3C_4$ non-MAX phase is cost-effective and straightforward [28]. This etching strategy can be done through chemical reactions amongst HCl and molten LiF salt, which successfully remove the 'A' group more safely with very few defects. It results in large flake MXenes and develops large spacing amongst its layers due to intercalation with cations like Li^+. It has also been reported to modify and enhance its surface functionalities.

2.2 Fabrication from "i-MAX" Phases

Recently a new MAX phase termed "i-MAX" has been reported as a precursor for synthesizing MXenes [3, 31–34]. These are in-plane chemically ordered forms of MAX phases described by a general formula of "$(M^1_{2/3}M^2_{1/3})_2AX$" with M's as two different chemically ordered in-plane transition metals [32]. Since M^2 elements are present amongst the traditional 'A' elements and 'M' elements in the periodic table. They can be etched together with the 'A' layer by regulating the etching conditions during the formation of MXenes from 'i-MXenes'. It offers a way to comprehend 2-D materials with in-plane chemical order/ordered vacancies. Rosen et al. [32] reported the selective etching of Al and Sc atoms from in-plane chemically ordered "i-MXene" phase, i.e. $(Mo_{2/3}Sc_{1/3})_2AlC$ through 48 wt.% LiF/HCl or HF.

However, the etching time is different for the etchants (24 at room temperature and 48 h at 35 °C). It has resulted in the formation of 2-D $Mo_{1.33}CT_x$ nanosheets with ordered in-plane metal vacancies. However, the etching of MXene from 'i-MAX' is limited. For instance, $(V_{2/3}Sc_{1/3})_2AlC$ is soluble in numerous etchants such as 48 et% HF, HCl/NaF, and HCl/LiF at room temperature a MAX phase with less Sc content can be etched into $V_{2-x}C$ under the same circumstances [32]. Other "i-MAX" phases reported in the literature include $(Cr_{2/3}Sc_{1/3})_2AlC$, $(Cr_{2/3}Y_{1/3})_2AlC$, $(Mo_{2/3}Sc_{1/3})_2GaC$, $(Mo_{2/3}Y_{1/3})_2GaC$, and $(Cr_{2/3}Zr_{1/3})_2AlC$ [3, 32–34]. The structural design of MXenes can be realized at an atomic scale by exploring the etching of 'i-MAX' phases and bringing new prospects to develop scalable methods to develop MXenes.

3 MXenes in Wearable Electronics

Wearable electronics owing to excellent mechanical compliance and exceptional sensitivity, have attracted immense attention of the scientific community to design the next-generation devices for healthcare, automobiles, robotics, and prosthetics [35–38]. It requires flexible surface-mounted wearable devices with a compact design with consistent electrical characteristics under cyclic strain situations during regular movements [39, 40]. It has constrained the traditional use of silicon in manufacturing such surfaces and generated a quest to search for advanced nanomaterials with reliable physicochemical characteristics. MXenes have recently emerged as the material of interest to architect wearable devices like physical sensors, chemical sensors, and biosensors due to their unique physicochemical properties [38, 41–43]. MXenes have been reported to indulge in diversified applications, including health, environmental, and motion monitoring [38, 41, 43, 44]. The diversified range of applications of MXenes in wearable devices is due to their unique properties like layered 2-D morphology, tunable electrical and thermal conductivity, abundance of surface chemistries, variable interlayer distance, mechanical stability, and hydrophilicity [43, 45].

Furthermore, rich surface functionalities of MXenes allow appropriate surface modifications/functionalization and performs multi-interactions with target molecules [46]. It allows the tuning of MXene physicochemical nature as per desired targeted application with enhanced performance. Moreover, the high effective surface area and numerous functional groups on MXene surface catalysis their surface interaction with target signals resulting in superior surface phenomenon-based sensing performances [43, 47, 48]. Hence, MXenes have been extensively used in wearable electronics, especially in diversified sensors, including physical, chemical and biosensors.

3.1 Flexible Physical Sensors

MXenes synthesized using chemical etching usually exhibit several physicochemical properties superior or comparable to graphene, including hydrophilic nature, electronic properties, bendable strength, oxidation resistance, and electron irradiation resistance [39, 47]. As a result of its superior electrical properties, MXene is utilised in strain sensors to detect minor form variations. MXenes can also be machine processed swiftly due to their hydrophilic character. They can also be combined with other materials like polymers to attain the desired flexibility [41, 49]. Hence, MXenes have attracted the excessive interest of the scientific community towards physical sensors.

3.1.1 Flexible Strain Sensor

A flexible strain sensor works on the principle of transforming the tensile strength of the device into the resistance signal as output [50]. The applied external force cracks the sensor's internal conductive channel, resulting in a change in electrical properties [51]. MXenes are layered structures stacked together due to interaction forces like Vander Waal forces in a 2-D fashion [3]. The application of external stress on MXenes in the vicinity of effective sliding results in the formation of large cracks. It results in the breaking of conducting channels amongst MXene layers generating an output signal in the form of resistance variation. Generally, the sensitivity of the strain sensor is measured in terms of its gauge factor (G) given by [47]

$$G = \frac{\frac{\Delta r}{r_o}}{\frac{\Delta l}{l_o}}$$

with Δr/or representing variation in resistivity, where 'Δr' is the difference in resistivity after and before application of strain, 'or is the resistivity of the sensor at rest without applying strain, and 'Δl' is the absolute variation in length with 'l_o' as the original length without application of strain.

However, the common problem with designing wearable MXene based devices is the stacking of its layer and less flexibility [41]. It is often addressed by introducing a second phase material of different dimensions into the MXene layers. Various nanomaterials have been reported for use as intercalants to prevent stacking of MXene layers and provide flexibility. These nanomaterials include macromolecules, carbon nanostructures like carbon nanotubes (CNT), graphene and its derivatives, metal ions, and metal-based nanostructures [43, 46, 52, 53]. However, flexibility has been attained by using polymer substrates or fabricating their hybrid nanocomposites. For instance, Cai et al. [54] reported prevention of stacking of $Ti_3C_2T_x$ MXene layers by intercalating with hydrophilic single-walled carbon nanotubes (SWCNT) using a layer-by-layer spray coating strategy. The obtained structure is with disorderly

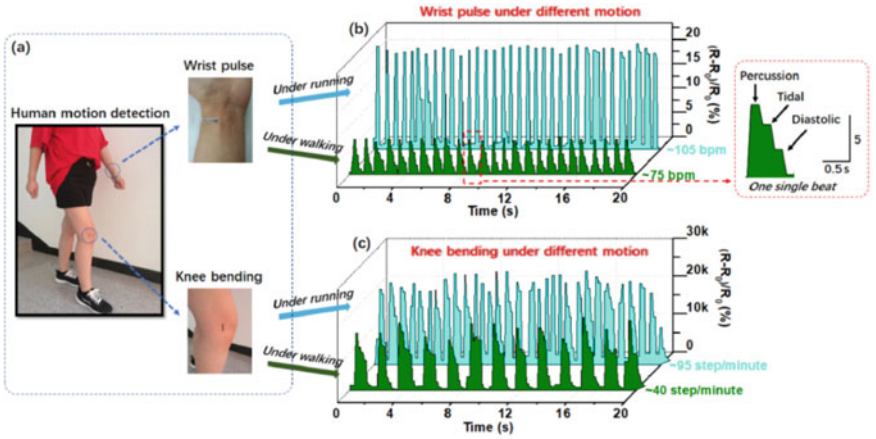

Fig. 5 Silver nanowire/$Ti_3C_2T_x$/Ni^{2+} based nacre-mimetic strain sensor; Reproduced with permission [44]. Copyright 2019, American Chemical Society

distributed SWCNT amongst the layers forming a conductive network. It has been evaluated as a strain sensor with sensitivity up to 64.6 in the range 0–30% of applied strain and 772.60 in 40–70% applied strain.

On the other hand, An et al. [55] achieved flexibility for $Ti_3C_2T_x$ nanosheets-based strain sensor through including poly (diallyl dimethylammonium chloride) (PDAC) using the LBL strategy. Further, the fabricated nanocomposites were loaded on different substrates, including polydimethylsiloxane (PDMS), indium tin oxide (ITO), silicon and polyethylene terephthalate (PET). As a result, the $Ti_3C_2T_x$/PDAC/PDMS-based strain sensor showed superior stretching performance up to 40%, whereas $Ti_3C_2T_x$/PDAC/PET sensor showed superior bending performance up to 35%. Furthermore, Shi et al. [44] fabricated silver nanowire/$Ti_3C_2T_x$ and introduced dopamine and nickel ions (Ni^{2+}) to architect a nacre-mimetic strain sensor, as shown in Fig. 5.

The reported sensitivity range is more than 200 for a whole applied strain range, which is superior to most of the reported flexible sensors in the literature. Hence, the addition of different dimensional amongst MXene sheets forms conducting network and prevents restacking, whereas polymer inclusion provides flexibility. Therefore, it endows the strain sensing performance of MXenes with optimal flexibility for wearable electronics.

Alternatively, Zhang et al. [56] reported using $Ti_3C_2T_x$ and polyvinylalcohol (PVA) hydrogel to achieve excellent stretchability, superior flexibility, and self-repair ability in fabricated strain sensors. The tensile strength of $Ti_3C_2T_x$/PVA hydrogel was 3400%, owing to cross-linking between surface end functionalities of $Ti_3C_2T_x$ and PVA hydrogel. Furthermore, the GF of the strain sensor in the range of 0–0.5 and 0.5–3.0% were reported to be 60–80 and 21, respectively. Similarly, Liao et al. reported evaluation of $Ti_3C_2T_x$/polyacrylamide/PVA hydrogel-based strain sensor with an excellent sensitivity of 44.85 with self-healing capabilities. Hence, the MXenes

possess the colossal potential to develop next-generation flexible strain sensors and enhance their sensing performances by fabricating nanocomposites and hydrogels.

3.1.2 Flexible Pressure Sensor

Flexible pressure sensors are generally piezoresistive in nature [57]. The application of external pressure on the sensor produces deformation in the material resulting in an output resistance signal [42, 56]. The sensitivity of pressure sensors is calculated similarly to the aforementioned for strain sensors [47]. Majorly the flexibility for pressure sensors is achieved by either using flexible polymer substrates such as PE, PET, PDMS or using aerogels [39]. For instance, Ma et al. [58] reported a flexible pressure sensor synthesized from multilayer $Ti_3C_2T_x$ on the polyimide (PI) integrated electrode substrate with the sensitivity of 180.1–94.8 and 94.8–45.9 in the range of 0.19–0.82 and 0.82–2.13%, respectively.

Furthermore, Yue et al. [59] reported piezoresistive pressure sensor based on MXene-sponge-PVA nanowires with ultrahigh sensitivity of 147 and 142 in the pressure range of 0–5.37 and 5.37–18.56 kPa, respectively. Guo et al. [60] fabricated a degradable transient pressure sensor based on polylactic acid (PLA)/MXene sandwiched structure. Alternatively, MXene based aerogels possessing high porosity and superelasticity are emerging for fabricating flexible pressure sensors. For instance, Ma et al. [61] reported $Ti_3C_2T_x$/rGO aerogel-based flexible pressure sensor with excellent sensing performance, as shown in Fig. 6. It is attributed to the synergistic effects of rGO providing high mechanical strength for the aerosol skeleton and $Ti_3C_2T_x$ providing high conductivity for a strong resistance output signal.

Furthermore, there are reports on the in-situ growth of MXenes in aerogels to fabricate pressure sensors. Wang et al. [62] reported skin-inspired $Ti_3C_2T_x$/natural microcapsule composite film with superior mechanical deformability, which mimics the structure and functionality of human skin. Hence, the main strategies to architect flexible pressure sensors using MXenes and their derivatives include aerogels and elastic substrates.

3.2 Wearable Biosensors

Wearable biosensors possess enormous potential in developing point-of-care advanced diagnostics and sensing strategies for rapid and economical detection [38]. Lately, MXenes have emerged as a potential candidate for developing wearable biosensors for various applications. For instance, Chen et al. [63] reported an intracellular pH detecting sensor based on $Ti_3C_2T_x$ quantum dots using a ratiometric photoluminescence probe. Lei et al. [64] reported an ultrasensitive enzymatic wearable sensor based on MXene/Prussian blue hybrid for glucose and lactate detection. They implemented a solid–liquid-air three-phase strategy to achieve a sufficient oxygen

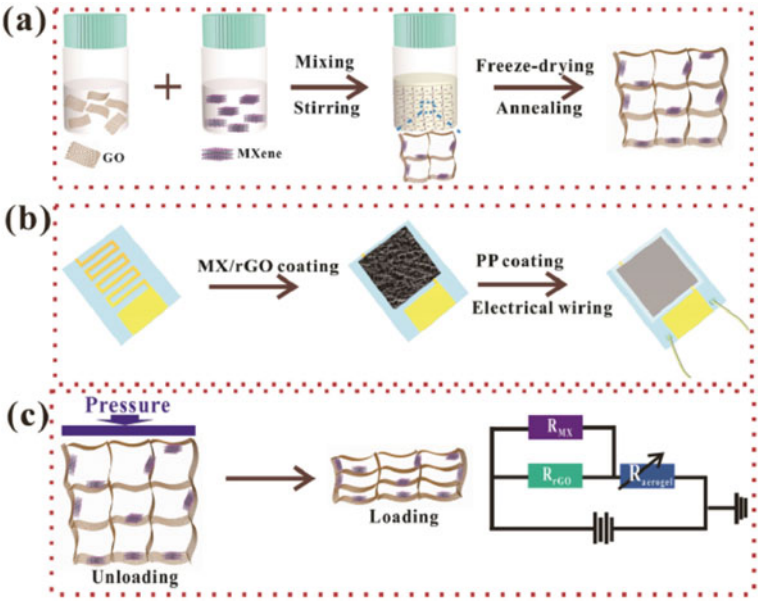

Fig. 6 Fabrication of $Ti_3C_2T_x$/rGO aerogel-based flexible pressure sensor; Reproduced with permission [61]. Copyright 2018, American Chemical Society

supply, increasing the biosensor's sensitivity. The achieved sensitivity using electrochemical techniques of 35.3 $\mu A\ mm^{-1}\ cm^{-2}$ for glucose and 11.4 $\mu A\ mm^{-1}\ cm^{-2}$ for lactate signify the strong prospect in personalized healthcare monitoring using wearable technology biosensors. Recently, Yang et al. [65] reported a hospital-on-chip system with multifunctional microneedle electrodes based on MXene nanosheets, as shown in Fig. 7. The reported biosensor was integrated on a single chip for enhanced diagnostics and therapies resembling a miniature hospital. The microneedles in this miniature system are used as a transdermal and painless patch to puncture dead skin, which acts as a barrier during drug delivery. In addition, it has been reported to sense the slight potential difference created in the body due to human arm muscle contraction and human eyes movement. Hence, the biosensor served two primary purposes required for medical treatment, including drug delivery and biosensing.

Furthermore, Zhang et al. [50] reported a hydrogel-based biosensor fabricated from polyvinyl alcohol, cellulose nanofibril, MXene nanosheets, and glycerol with significant electrical conductivity (2.58 mS cm^{-1}) and flexibility even at −18 °C. The biosensor exhibited high sensitivity (2.30), rapid response (0.165 s), inclusive working strain range (559%), good linearity (0.999), lower strain detecting range (1–5%), and varied operating temperature range (−18 to 60 °C). On the other hand, Soomro et al. [66] reported a biosensor based on TiO_2/MXene-$BiVO_4$ hybrid for robust detection of soluble CD44 proteins using photoelectrochemical strategy. The interfacial assembly was the epitome for stimulating fast charge carrier transfer from

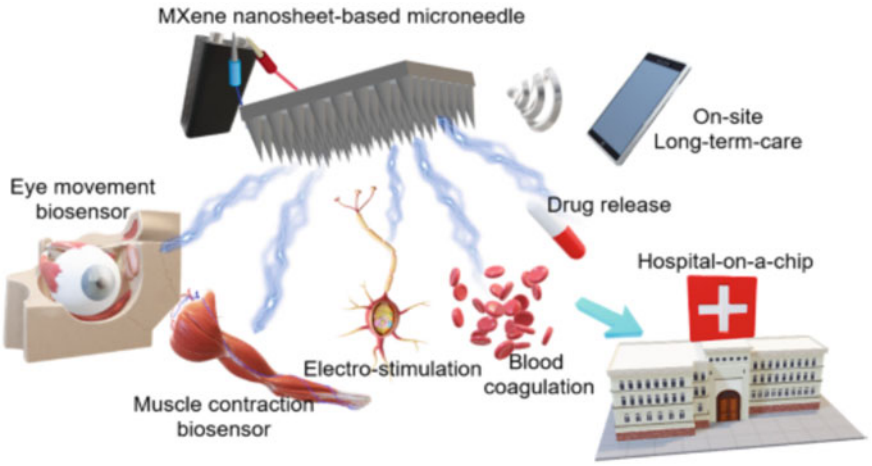

Fig. 7 Concept of hospital-on-chip using MXene nanosheets; Reproduced with permission [65]. Copyright 2021, American Chemical Society

photo-excited $BiVO_4$ and TiO_2 to $Ti_3C_2T_x$ Sheets, resulting in an energy level-cascade that allows negligible charge-carrier recombination besides strong photocatalytic redox reactions. The sensor detected a vast concentration CD44 window of $2.2 \times 10 - 4$ ng mL^{-1} to 3.2 ng mL^{-1} with a low detection limit of $1.4 \times 10 - 2$ pg mL^{-1} signifying its reliable clinical applicability. Hence, MXene and its hybrids possess tremendous potential in developing wearable biosensors for personalized healthcare monitoring and compact diagnostic techniques. However, the research is in its infancy, and it is required to be incorporated with advanced intelligent features and required dedicated clinical trials.

3.3 Wearable Chemical Sensors

MXene and its hybrids have been extensively reported for designing flexible gas/vapor/chemical species detecting sensors for diversified applications such as healthcare, environmental, safety, and agricultural monitoring [42, 43, 47]. This tremendous potential of MXene based materials for flexible chemical sensors has already been massively reviewed in numerous literature reports [43, 46, 47, 67]. However, their applicability for wearable devices is yet to be done for practical applications and at its infancy. The attainment of flexibility and stretchability is similar to that of physical and biosensors by using secondary materials like macromolecules or flexible substrates [52, 68]. Furthermore, the application of MXenes is not limited to gas/vapor sensing but also extended to water remediation application by removing heavy metal ions and radionuclides [69, 70]. Since the reports are extensive, they have been summarized in Table 3 for a broad outlook. Table 3 represents the compre-

Table 3 Flexible sensors based on MXene and its hybrids to detect gases and VOCs

Sensing material	VOC	Sensitivity (%)	Concentration	Recovery/response time
3TTP [71]	Methanol	2.7%	5 ppm	~1.5/1.7 min
	Ammonia	0.7	10 ppm	NR
	Nitrogen Dioxide	0.9	10 ppm	NR
	Acetone	0.08%	5 ppm	~1.5/1.7 min
$Ti_3C_2T_x$- PANI Sensor [72]	Ethanol	1.56%	1 ppm	0.4 s/0.5 s
	Ammonia	20	200 ppm	NR
PANI/$Ti_3C_2T_x$ [73]	Formaldehyde	0.2%	25 ppm	NR
	Hydrogen Sulfide	1	25 ppm	NR
PEDOT:PSS/$Ti_3C_2T_x$ [74]	Ammonia	0.05	25 ppb	~600 s/1400 s for 25 ppb
	Sulfur Dioxide	~0.02	25 ppm	NR
	Carbon Monoxide	~0.05	25 ppm	NR
	Carbon Dioxide	~0.01	10%	NR
Cationic polyacrylamide/$Ti_3C_2T_x$ [75]	Methanol	15%	2000 ppm	NR
	Ethanol	10%	2000 ppm	NR
	Acetone	10%	2000 ppm	NR
	Ammonia	1.5	50 ppm	~12–14 s for 150 ppm
Ti3C2Tx/ZnO spheres [76]	NO_2	41.93%	100 ppm	~34 s
Ti3C2Tx MXene/graphene hybrid fibers [20]	Ammonia	~600%	50 ppm	~20 min
Ti3C2Tx MXene@Pd [77]	Hydrogen	$(23.0 \pm 4.0)\%$	4% H_2	(32 ± 7) s
MXene/rGO/CuO hybrid aerogels [53]	Acetone	52.09%	100 ppm	~7.5 s

hensive outlook of flexible gas/vapor sensors reported experimentally for gas/volatile organic compound sensing using MXene based materials.

Although most of the reports mentioned in Table 3 have been anticipated for designing high-performance wearable gas/vapor sensors, the wearability of the device has not been explored. However, few reports address the MXene based sensors with wearable features. For instance, Tang et al. [6] reported wearable and stretchable VOC sensors based on MXene/polyurethane (PU) core-sheath fibers for efficient detection of acetone using the conductometric mode, as shown in Fig. 8.

The sensor exhibited excellent sensitivity (5–325 fold higher than planer MXene based sensor) towards a wide range of acetone (ppb level to saturated vapor) with

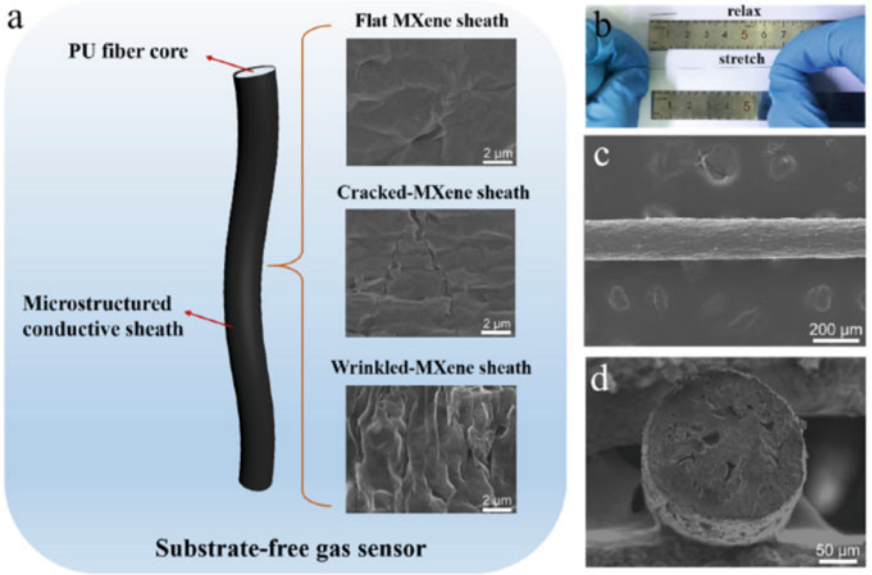

Fig. 8 MXene/polyurethane (PU) core-sheath fibers based conductometric sensor for detecting acetone; Reproduced with permission [6]. Copyright 2021, Elsevier

a high signal-to-noise ratio (SNR, 160% higher than planer MXene based sensor). Moreover, they introduced microcracks on the conductive fiber sheath, which can take deformation in human skin (30%) with a negligible sensing interference from generated tensile strain. Zhang et al. [78] reported ZnO/MXene nanowire (NW) arrays piezoelectric nanogenerator (PENG) driven formaldehyde sensor based on MXene/Co_3O_4 composite. The sensor exhibited excellent sensitivity of 52% towards 0.01 ppm of formaldehyde with rapid recovery (~5 s). The potential of the sensor for the self-driven and wearable feature was elaborately presented.

Furthermore, Zhang et al. [79] reported a latex/polytetrafluoroethylene-based triboelectric nanogenerators driven $Ti_3C_2T_x$ MXene/metal–organic framework-derived copper oxide (CuO) ammonia sensor. The self-driven NH3 sensor through TENG has an excellent response (V_g/V_a = 24.8 @ 100 ppm) at room temperature and shows an excessive potential in observing pork quality. On the other hand, Li et al. [80] reported a termination-modified $Ti_3C_2T_x$ VOC sensor for wearable ethanol monitoring in human exhaled breath. These reports demonstrate the potential of MXenes based sensing materials for architecting next-generation wearable medical electronics and intelligent healthcare. However, mass production and assessing performance with clinical data require extensive dedication for their practical applications.

4 MXenes in Wireless Communication

The developments of wearable devices are not limited to achieving flexibility and stretchability. It is essential to include internet-of-things (IoT) to design intelligent wearable devices, which use radio-frequency (RF) antennas [47, 81, 82]. Traditionally, metals like copper, silver, aluminum are used to design RF antennas owing to their excellent electrical conductivity. However, the intrinsic skin effect due to the thickness of these materials limits their commercial applicability. Due to the frequency dependence of skin depth, the thickness of metal-based antennas must be at least ~5 μm for these applications ensuring adequate space for the flow of charge carriers [81]. Recently, highly conducting 2-D nanomaterials such as MXenes possess the potential to develop next-generation compact, lightweight, portable, and flexible RF antennas [81–84]. It is attributed to their solution processability, excellent electrical conductivity, and rich surface functionalities. MXenes based negatively charged flakes possess ξ potential from −30 to −80 mV, which can be processed using various techniques such as spray coating, spin coating, drop-casting, and printing for RF applications [81, 83–85].

Sarychev et al. [81] reported the first dipole antenna based on MXenes of thickness in the range 62 nm–8 μm, operating in the Bluetooth and WiFi frequency bands at 2.4 GHz. They also fabricated a 1-μm-thick MXene RF identification device tag reaching a reading distance of 8 m at 860 MHz. They described a one-step spray approach for producing MXene-based antennas using MXene water-based colloidal ink. The fabricated antenna performed even at a considerably lower thickness (62 nm), reaching a gain of −7 dB, indicating that the MXene based antennas work at a shallow thickness than that of other reported materials possessing tremendous potential to develop next-generation ultrathin and transparent wireless devices. Li et al. [84] reported a stretchable SWCNT/MXene based dipole antenna with the uniaxial stretchability of 150% with unaffected reflected power <0.1%. Furthermore, they integrated this antenna with SWCNT/MXene electromagnetic shields (with shielding performance of 30–52 dB) to fabricate a mechanically stable wireless transmission system while attenuating the human body's EM absorption shown in Fig. 9.

On the other hand, Han et al. [83] reported $Ti_3C_2T_x$ MXene based microstrip transmission lines with less energy attenuation and patch antennas with high-power radiation in the frequency range of 5.6–16.4 GHz. The radiation efficiency of fabricated 5.5 μm thick MXene based patch antenna was comparable with standard 35 μm thick copper patch antenna at 16.4 GHz. They further demonstrated significant performance of MXene patch antenna array with integrated feeding circuits on a conformal surface at 28 GHz, which is required in practical 5G applications. Fu et al. [82] fabricated conductive fibers with MXene sheaths and alginate cores for developing wearable heaters and wireless communication systems using a cation-induced assembly strategy. Hence, MXenes, due to their excellent conductivity, tunable surface functionalities, and hydrophilic nature, possess the potential

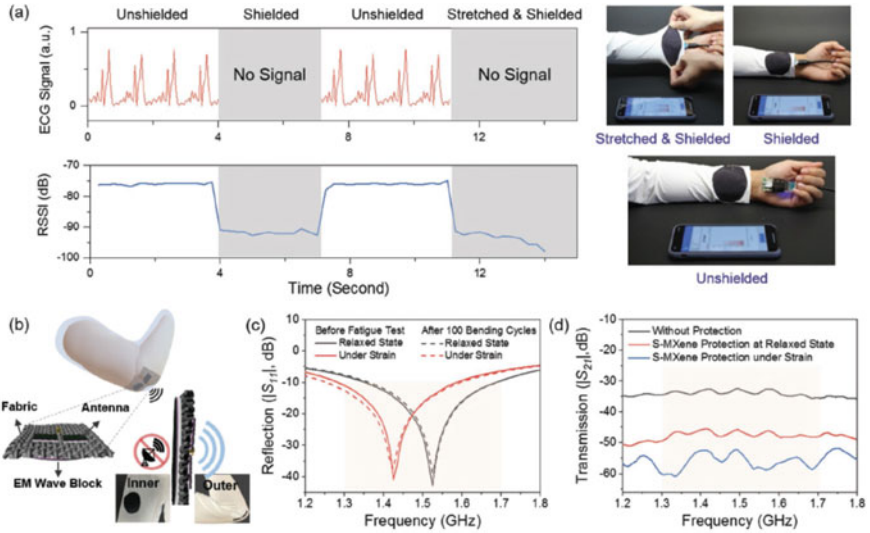

Fig. 9 Wearable Electronics using MXene based materials; Reproduced with permission [84]. Copyright 2020, Wiley

to be processed for architecting next-generation intelligent wireless communication systems.

5 Conclusions and Prospects

MXenes owing to their unique and tunable physicochemical characteristics like electrical conductivity, thermal stability, rich surface functionalities, good mechanical strength, and high effective surface area, have been used for developing next-generation wearable devices. Furthermore, their hydrophilic nature helps in machine processability and device fabrication. However, the first requirement is the scalable synthesis of MXene based materials, which is achieved using chemical etching strategies. These methods are limited by costing secondary contamination to the environment through byproducts, which raises safety concerns for manufacturers and users. It has raised a quest to explore alternative precursors like non-MAX and 'i-MAX' phases and advanced fabrication strategies like green synthesis and one-pot large reactor synthesis. Further, the requirement of flexibility and stretchability is achieved by either fabricating MXene-macromolecule hybrids or using flexible substrates. The optimum flexibility of these MXene-based materials is used to manufacture wearable electronic devices like physical, chemical, and biosensors. Owing to large effective surface area and rich surface chemistries, these materials exhibit excellent surface activities resulting in excellent sensing performances for strain, pressure, gas, volatile organic vapor, humidity, and biomolecule monitoring.

The advancement of these sensors is further done by including internet-of-things and designing wireless communication systems leading to developing intelligent wearable devices. Hence, MXene based materials with optimum flexibility open new prospects for commercially architecting next-generation intelligent field-deployable wearable devices with consistent performance in every harsh condition.

References

1. Chaudhary, V., Kaushik, A., Furukawa, H., Khosla, A.: Review—Towards 5th Generation AI and IoT Driven Sustainable Intelligent Sensors Based on 2D MXenes and Borophene. ECS Sens. Plus **1** (2022)
2. Naguib, M., Barsoum, M.W., Gogotsi, Y.: Ten years of progress in the synthesis and development of MXenes. Adv. Mater. **33**(39) (2021)
3. Wei, Y., Zhang, P., Soomro, R.A., Zhu, Q., Xu, B.: Advances in the synthesis of 2D MXenes. Adv. Mater. **33** (2021)
4. Seth, Y., Dharaskar, X., Chaudhary, V., Khalid, M., Walvekar, R.: Prospects of titanium carbide-based MXene in heavy metal ion and radionuclide adsorption for wastewater remediation: A review. Chemosphere **293** (2022)
5. Shuck, C.E., Sarycheva, A., Anayee, M., Levitt, A., Zhu, Y., Uzun, S., et al.: Scalable synthesis of $Ti_3C_2T_x$ MXene. Adv. Eng. Mater. **22**(3) (2020)
6. Tang, Y., Xu, Y., Yang, J., Song, Y., Yin, F., Yuan, W.: Stretchable and wearable conductometric VOC sensors based on microstructured MXene/polyurethane core-sheath fibers. Sens. Actuators B Chem. **1**, 346 (2021)
7. Hope, M.A., Forse, A.C., Griffith, K.J., Lukatskaya, M.R., Ghidiu, M., Gogotsi, Y., et al.: NMR reveals the surface functionalisation of Ti_3C_2 MXene. Phys. Chem. Chem. Phys. **18**(7) (2016)
8. Rao, K.S.M.S.R., Joshi, J.B.: Liquid phase mixing in mechanically agitated vessels. Chem. Eng. Commun. **74**(1) (1988)
9. Jaszczur, M., Młynarczykowska, A.: A general review of the current development of mechanically agitated vessels. Processes **8** (2020)
10. Gygax, R.: Chemical reaction engineering for safety. Chem. Eng. Sci. **43**(8) (1988)
11. Zhang, S., Huang, P., Wang, J., Zhuang, Z., Zhang, Z., Han, W.Q.: Fast and universal solution-phase flocculation strategy for scalable synthesis of various few-layered MXene powders. J. Phys. Chem. Lett. **11**(4) (2020)
12. Lipton, J., Röhr, J.A., Dang, V., Goad, A., Maleski, K., Lavini, F., et al.: Scalable, highly conductive, and micropatternable MXene films for enhanced electromagnetic interference shielding. Matter **3**(2) (2020)
13. Zhang, C. (John), McKeon, L., Kremer, M.P., Park, S.H., Ronan, O., Seral-Ascaso, A., et al.: Additive-free MXene inks and direct printing of micro-supercapacitors. Nat. Commun. **10**(1) (2019)
14. Wan, S., Li, X., Chen, Y., Liu, N., Du, Y., Dou, S., et al.: High-strength scalable MXene films through bridging-induced densification. Science **374**(6563) (2021)
15. Ding, L., Wei, Y., Wang, Y., Chen, H., Caro, J., Wang, H.: A two-dimensional lamellar membrane: MXene nanosheet stacks. Angew. Chemie Int. Ed. **56**(7) (2017)
16. Ling, Z., Ren, C.E., Zhao, M.Q., Yang, J., Giammarco, J.M., Qiu, J., et al.: Flexible and conductive MXene films and nanocomposites with high capacitance. Proc. Natl. Acad. Sci. USA **111**(47) (2014)
17. Li, C., Kota, S., Hu, C., Barsoum, M.W.: On the synthesis of low-cost, titanium-based mxenes. J. Ceram Sci. Technol. **7**(3) (2016)
18. Akuzum, B., Maleski, K., Anasori, B., Lelyukh, P., Alvarez, N.J., Kumbur, E.C., et al.: Rheological characteristics of 2D titanium carbide (MXene) dispersions: a guide for processing MXenes. ACS Nano. **12**(3) (2018)

19. Yu, M., Feng, X.: Scalable manufacturing of MXene films: moving toward industrialization. Matter **3**(2) (2020)
20. Liao, L., Jiang, D., Zheng, K., Zhang, M., Liu, J.: Industry-scale and environmentally stable $Ti_3C_2T_x$ MXene based film for flexible energy storage devices. Adv. Funct. Mater. **31**(35) (2021)
21. Lee, S.H., Eom, W., Shin, H., Ambade, R.B., Bang, J.H., Kim, H.W., et al.: Room-temperature, highly durable $Ti_3C_2T_x$ MXene/graphene hybrid fibers for NH3 gas sensing. ACS Appl Mater Interfaces **12**(9), 10434–10442 (2020)
22. Levitt, A., Seyedin, S., Zhang, J., Wang, X., Razal, J.M., Dion, G., et al.: Bath electrospinning of continuous and scalable multifunctional MXene-infiltrated nanoyarns. Small **16**(26) (2020)
23. Zhao, M.Q., Trainor, N., Ren, C.E., Torelli, M., Anasori, B., Gogotsi, Y.: Scalable manufacturing of large and flexible sheets of MXene/graphene heterostructures. Adv. Mater. Technol. **4**(5) (2019)
24. Wang, Y., Wang, X., Li, X., Bai, Y., Xiao, H., Liu, Y., et al.: Scalable fabrication of polyaniline nanodots decorated MXene film electrodes enabled by viscous functional inks for high-energy-density asymmetric supercapacitors. Chem. Eng. J. **405** (2021)
25. Wu, X., Ding, M., Xu, H., Yang, W., Zhang, K., Tian, H., et al.: Scalable $Ti_3C_2T_x$ MXene interlayered forward osmosis membranes for enhanced water purification and organic solvent recovery. ACS Nano. **14**(7) (2020)
26. Huang, J., Meng, R., Zu, L., Wang, Z., Feng, N., Yang, Z., et al.: Sandwich-like $Na_{0.23}TiO_2$ nanobelt/Ti_3C_2 MXene composites from a scalable in situ transformation reaction for long-life high-rate lithium/sodium-ion batteries. Nano Energy. **46** (2018)
27. Huang, H., He, J., Wang, Z., Zhang, H., Jin, L., Chen, N., et al.: Scalable, and low-cost treating-cutting-coating manufacture platform for MXene-based on-chip micro-supercapacitors. Nano Energy. **69** (2020).
28. Zha, X.H., Zhou, J., Eklund, P., Bai, X., Du, S., Huang, Q.: Non-MAX phase precursors for MXenes. In: 2D Metal Carbides and Nitrides (MXenes): Structure, Properties and Applications (2019)
29. Gao, G., , G., Li, J., Yao, K., Wu, M., Qian, M.: Monolayer MXenes: promising half-metals and spin gapless semiconductors. Nanoscale **8**(16) (2016)
30. Zhou, J., Zha, X., Chen, F.Y., Ye, Q., Eklund, P., Du, S., et al.: A two-dimensional zirconium carbide by selective etching of Al_3C_3 from nanolaminated $Zr_3Al_3C_5$. Angew. Chemie Int. Ed. **55**(16) (2016)
31. Sokol, M., Natu, V., Kota, S., Barsoum, M.W.: On the chemical diversity of the MAX phases. Trends Chem **1** (2019)
32. Ahmed, B., El Ghazaly, A., Rosen, J.: i-MXenes for energy storage and catalysis. Adv. Funct. Mater. **30** (2020)
33. Thörnberg, J., Halim, J., Lu, J., , R., Palisaitis, J., Hultman, L., et al.: Synthesis of $(V_{2/3}Sc_{1/3})_2AlC$ i-MAX phase and $V_{2-x}C$ MXene scrolls. Nanoscale **11**(31) (2019)
34. Meshkian, R., Dahlqvist, M., Lu, J., Wickman, B., Halim, J., Thörnberg, J., et al.: W-based atomic laminates and their 2D derivative $W_{1.33}C$ MXene with vacancy ordering. Adv. Mater. **30**(21) (2018)
35. Tan, P., Zou, Y., Fan, Y., Li, Z.: Self-powered wearable electronics. Wearable Technol. **1** (2020)
36. Gu, Y., Zhang, T., Chen, H., Wang, F., Pu, Y., Gao, C., et al.: Mini review on flexible and wearable electronics for monitoring human health information. Nanoscale Res. Lett. **14** (2019)
37. Neupane, G.P., Yildirim, T., Zhang, L., Lu, Y.: Emerging 2D MXene/organic heterostructures for future nanodevices. Adv. Funct. Mater. **30** (2020)
38. Khunger, A., Kaur, N., Mishra, Y.K., Ram Chaudhary, G., Kaushik, A.: Perspective and prospects of 2D MXenes for smart biosensing. Mater. Lett. **304** (2021)
39. Xin, M., Li, J., Ma, Z., Pan, L., Shi, Y.: MXenes and their applications in wearable sensors. Front. Chem. **8** (2020)
40. Hasan, M.M., Hossain, M.M., Chowdhury, H.K.: Two-dimensional MXene-based flexible nanostructures for functional nanodevices: a review. J. Mater. Chem A **9** (2021)

41. Ma, C., Ma, M.G., Si, C., Ji, X.X., Wan, P.: Flexible MXene-based composites for wearable devices. Adv. Funct. Mater. **31** (2021)
42. Riazi, H., Taghizadeh, G., Soroush, M.: MXene-based nanocomposite sensors. ACS Omega **6**(17) (2021)
43. Chaudhary, V., Gautam, A., Mishra, Y.K., Kaushik, A.: Emerging MXene–polymer hybrid nanocomposites for high-performance ammonia sensing and monitoring. Nanomaterials **11**(10) (2021 Sep. 24)
44. Shi, X., Wang, H., Xie, X., Xue, Q., Zhang, J., Kang, S., et al.: Bioinspired ultrasensitive and stretchable MXene-based strain sensor via nacre-mimetic microscale "brick-and-Mortar" architecture. ACS Nano **13**(1) (2019)
45. Kumar, J.A., Prakash, P., Krithiga, T., Amarnath, D.J., Premkumar, J., Rajamohan, N., et al.: Methods of synthesis, characteristics, and environmental applications of MXene: a comprehensive review. Chemosphere **286** (2022)
46. Mehdi Aghaei, S., Aasi, A., Panchapakesan, B.: Experimental and theoretical advances in MXene-based gas sensors. ACS Omega **6** (2021)
47. Ho, D.H., Choi, Y.Y., Jo, S.B., Myoung, J.M., Cho, J.H.: Sensing with MXenes: progress and prospects. Adv. Mater. (2021)
48. Li, D., Liu, G., Zhang, Q., Qu, M., Fu, Y.Q., Liu, Q., et al.: Virtual sensor array based on MXene for selective detections of VOCs. Sens. Actuators B Chem. **331** (2021)
49. Du, C.F., Zhao, X., Wang, Z., Yu, H., Ye, Q.: Recent advanced on the mxene–organic hybrids: Design, synthesis, and their applications. Nanomaterials **11** (2021)
50. Zhang, W., Ma, C., Huang, L.Z., Guo, W.Y., Li, D.D., Bian, J., et al.: Stretchable, antifreezing, non-drying, and fast-response sensors based on cellulose nanocomposite hydrogels for signal detection. Macromol. Mater. Eng. (2021)
51. Ma, Z., Li, S., Wang, H., Cheng, W., Li, Y., Pan, L., et al.: Advanced electronic skin devices for healthcare applications. J. Mater. Chem. B **7** (2019)
52. Li, Q., Li, Y., Zeng, W.: Preparation and application of 2D MXene-based gas sensors: a review. Chemosensors **9** (2021)
53. Liu, M., Wang, Z., Song, P., Yang, Z., Wang, Q.: Flexible MXene/rGO/CuO hybrid aerogels for high performance acetone sensing at room temperature. Sens. Actuators B Chem. **1**, 340 (2021)
54. Cai, Y., Shen, J., Ge, G., Zhang, Y., Jin, W., Huang, W., et al.: Stretchable $Ti_3C_2T_x$ MXene/carbon nanotube composite based strain sensor with ultrahigh sensitivity and tunable sensing range. ACS Nano **12**(1) (2018)
55. An, H., Habib, T., Shah, S., Gao, H., Radovic, M., Green, M.J., et al.: Surface-agnostic highly stretchable and bendable conductive MXene multilayers. Sci. Adv. **4**(3) (2018)
56. Zhang, Y.Z., Lee, K.H., Anjum, D.H., Sougrat, R., Jiang, Q., Kim, H., et al.: MXenes stretch hydrogel sensor performance to new limits. Sci. Adv. **4**(6) (2018)
57. Gasparini, A.: MXenes materials could be used in wearable pressure sensors. Scilight **2020**(45) (2020)
58. Ma, Y., Liu, N., Li, L., Hu, X., Zou, Z., Wang, J., et al.: A highly flexible and sensitive piezoresistive sensor based on MXene with greatly changed interlayer distances. Nat. Commun. **8**(1) (2017)
59. Yue, Y., Liu, N., Liu, W., Li, M., Ma, Y., Luo, C., et al.: 3D hybrid porous Mxene-sponge network and its application in piezoresistive sensor. Nano Energy **50** (2018)
60. Guo, Y., Zhong, M., Fang, Z., Wan, P., Yu, G.: A wearable transient pressure sensor made with MXene nanosheets for sensitive broad-range human-machine interfacing. Nano Lett. **19**(2) (2019)
61. Ma, Y., Yue, Y., Zhang, H., Cheng, F., Zhao, W., Rao, J., et al.: 3D synergistical MXene/reduced graphene oxide aerogel for a piezoresistive sensor. ACS Nano **12**(4) (2018)
62. Wang, K., Lou, Z., Wang, L., Zhao, L., Zhao, S., Wang, D., et al.: Bioinspired interlocked structure-induced high deformability for two-dimensional titanium carbide (MXene)/natural microcapsule-based flexible pressure sensors. ACS Nano **13**(8) (2019)

63. Chen, X., Sun, X., Xu, W., Pan, G., Zhou, D., Zhu, J., et al.: Ratiometric photoluminescence sensing based on Ti_3C_2 MXene quantum dots as an intracellular pH sensor. Nanoscale **10**(3) (2018)
64. Lei, Y., Zhao, W., Zhang, Y., Jiang, Q., He, J.H., Baeumner, A.J., et al.: A MXene-based wearable biosensor system for high-performance in vitro perspiration analysis. Small **15**(19) (2019)
65. Yang, Y.C., Lin, Y.T., Yu, J., Chang, H.T., Lu, T.Y., Huang, T.Y., et al.: MXene nanosheet-based microneedles for monitoring muscle contraction and electrostimulation treatment. ACS Appl Nano Mater. **4**(8), 7917–7924 (2021)
66. Soomro, R.A., Jawaid, S., Kalawar, N.H., Tunesi, M., Karakuş, S., Kilislioğlu, A., et al.: In-situ engineered MXene-TiO2/BiVO4 hybrid as an efficient photoelectrochemical platform for sensitive detection of soluble CD44 proteins. Biosens Bioelectron. **15**, 166 (2020)
67. Jian, Y., Qu, D., Guo, L., Zhu, Y., Su, C., Feng, H., et al.: The prior rules of designing $Ti_3C_2T_x$ MXene-based gas sensors. Front Chem. Sci. Eng. **15**(3), 505–517 (2021)
68. Dhall, S., Mehta, B.R., Tyagi, A.K., Sood, K.: A review on environmental gas sensors: materials and technologies. Sens. Int. **2** (2021)
69. Ihsanullah, I.: Potential of MXenes in water desalination: current status and perspectives. Nano-Micro Lett. **12** (2020)
70. Sun, Y., Li, Y.: Potential environmental applications of MXenes: a critical review. Chemosphere **271** (2021)
71. Yuan, W., Yang, K., Peng, H., Li, F., Yin, F.: A flexible VOCs sensor based on a 3D Mxene framework with a high sensing performance. J. Mater. Chem. A. **6**(37) (2018)
72. Zhao, L., Wang, K., Wei, W., Wang, L., Han, W.: High-performance flexible sensing devices based on polyaniline/MXene nanocomposites. InfoMat. **1**(3) (2019)
73. Li, X., Xu, J., Jiang, Y., He, Z., Liu, B., Xie, H., et al.: Toward agricultural ammonia volatilization monitoring: a flexible polyaniline/$Ti_3C_2T_x$ hybrid sensitive films based gas sensor. Sens. Actuators B Chem. **316** (2020)
74. Jin, L., Wu, C., Wei, K., He, L., Gao, H., Zhang, H., et al.: Polymeric $Ti_3C_2T_x$ MXene composites for room temperature ammonia sensing. ACS Appl. Nano Mater. **3**(12) (2020)
75. Zhao, L., Zheng, Y., Wang, K., Lv, C., Wei, W., Wang, L., et al.: Highly stable cross-linked cationic polyacrylamide/$Ti_3C_2T_x$ MXene nanocomposites for flexible ammonia-recognition devices. Adv. Mater. Technol. **5**(7) (2020)
76. Yang, Z., Jiang, L., Wang, J., Liu, F., He, J., Liu, A., et al.: Flexible resistive NO2 gas sensor of three-dimensional crumpled MXene $Ti_3C_2T_x$/ZnO spheres for room temperature application. Sens. Actuators B Chem. **326** (2021)
77. Zhu, Z., Liu, C., Jiang, F., Liu, J., Ma, X., Liu, P., et al.: Flexible and lightweight $Ti_3C_2T_x$ MXene@Pd colloidal nanoclusters paper film as novel H_2 sensor. J Hazard Mater. **15**, 399 (2020)
78. Zhang, D., Mi, Q., Wang, D., Li, T.: MXene/Co_3O_4 composite based formaldehyde sensor driven by ZnO/MXene nanowire arrays piezoelectric nanogenerator. Sens. Actuators B Chem. **15**, 339 (2021)
79. Zhang, D., Yu, L., Wang, D., Yang, Y., Mi, Q., Zhang, J.: Multifunctional latex/polytetrafluoroethylene-based triboelectric nanogenerator for self-powered organ-like mxene/metal-organic framework-derived cuo nanohybrid ammonia sensor. ACS Nano **15**(2), 2911–2919 (2021)
80. Li, X., An, Z., Lu, Y., Shan, J., Xing, H., Liu, G., et al.: Room temperature VOCs sensing with termination-modified $Ti_3C_2T_x$ MXene for wearable exhaled breath monitoring. Adv. Mater. Technol. (2021)
81. Sarycheva, A., Polemi, A., Liu, Y., Dandekar, K., Anasori, B., Gogotsi, Y.: 2D titanium carbide (MXene) for wireless communication. Sci. Adv. **4**(9) (2018)
82. Fu, X., Yang, H., Li, Z., Liu, N.C., Lee, P.S., Li, K., et al.: Cation-induced assembly of conductive MXene fibers for wearable heater, wireless communication, and stem cell differentiation. ACS Biomater. Sci. Eng. (2021)

83. Han, M., Liu, Y., Rakhmanov, R., Israel, C., Tajin, M.A.S., Friedman, G., et al.: Solution-processed $Ti_3C_2T_x$ MXene antennas for radio-frequency communication. Adv. Mater. **33**(1) (2021)
84. Li, Y., Tian, X., Gao, S.P., Jing, L., Li, K., Yang, H., et al.: Reversible crumpling of 2D titanium carbide (MXene) nanocoatings for stretchable electromagnetic shielding and wearable wireless communication. Adv. Funct. Mater. **30**(5) (2020)
85. Rasch, F., Postica, V., Schütt, F., Mishra, Y.K., Nia, A.S., Lohe, M.R., et al.: Highly selective and ultra-low power consumption metal oxide based hydrogen gas sensor employing graphene oxide as molecular sieve. Sens. Actuators B Chem. **320** (2020)

Novel MXenes—Advanced Synthesis and Tailored Material-Property Design

Agnieszka M. Jastrzębska, Philipp G. Grützmacher, and Andreas Rosenkranz

Abstract Since MXenes' discovery in 2011 (patent priority [1]), they have received tremendous attention in the scientific community [2, 3]. Numerous studies have shown that MXenes hold great potential in various applications, including supercapacitors, lithium-ion batteries, non-lithium-ion batteries, catalysis, photocatalysis, hydrogen production, methane absorption, metal-, ceramic- and polymer-based nanocomposites, field-effect transistors, transparent conductors, biomaterials, active agents for cancer treatment, and many more. In many of these applications, they also outperform other 2D layered materials. However, ongoing research and application of MXenes in different fields bring many challenges, which need to be tackled in the near future. This chapter aims to give an overview of challenges regarding MXenes' application in various fields and emphasize some potential solution strategies.

1 Development of Novel Types of MXenes and Beyond

1.1 Development of Novel MAX Phase Precursors

Novel MXenes may consider single M metal or various M metal elements (mono-M elements and solid solutions). Mono-M element MXenes correspond to simple compositions such as $Ti_3C_2T_x$, while more complex systems include the solid solution of two or more M elements such as $(Ti, V)_3C_2$.

A. M. Jastrzębska
Faculty of Materials Science and Engineering, Warsaw University of Technology, Wołoska 141, 02-507 Warsaw, Poland

P. G. Grützmacher
Department of Engineering Design and Product Development, TU Vienna, 1060 Wien, Austria

A. Rosenkranz (✉)
Department of Chemical Engineering, Biotechnology and Materials, University of Chile, Avenida Beauchef 851, Santiago, Chile
e-mail: arosenkranz@ing.uchile.cl

M. Khalid et al. (eds.), *Fundamental Aspects and Perspectives of MXenes*, Engineering Materials, https://doi.org/10.1007/978-3-031-05006-0_13

The search for novel types of MXenes is mainly connected to developing new starting materials since most of the synthesis approaches, irrespective of the used etchants and protocols, start with their parental MAX phase. Thereby, the composition of the MAX-phase will determine the composition of the resulting MXene. Consequently, selecting promising, novel MAX precursors for further processing is essential for MXenes' dynamic development. The increasing number of standard MAX compositions is expected to facilitate the emergence of many new MAX materials beyond the usage of Al as A-element. This, in turn, will enable the continuing exploration of more new types of MXenes beyond $Ti_3C_2T_x$. For instance, recent progress in this field includes describing interesting new non-Al phases such as Ti_2GaC, Nb_2GaC, Ti_2GaN, Ti_2CdC, Ti_2InN or Zr_2InN [4].

The history of MAX phases dates back to the 60 s when they were developed as Nowotny phases [5], ternary (T) or Hagg (H) phases [6]. This can be considered an important starting point for developing more than 100 carbides, and nitrides described today. Barsoum et al. accelerated the development of Nowotny's phases in the mid-90 s by describing the pure Ti_3SiC_2 phase with hexagonal symmetry (*P6*$_3$*/mmc* group) and the general formula $M_{n+1}AX_n$ (coining the term 'MAX phase') [7]. Regarding the $M_{n+1}AX_n$ formula, M stands for an early transition metal, A reflects a metal of group 13 or 14 (mostly Al), and X is carbon, nitrogen, or a mixture of both, while *n* takes integer values between 1 and 4. Therefore, MAX phases can be classified as 211 ($n = 1$), 312 ($n = 2$), 413 ($n = 3$), and 514 ($n = 4$). The recent extension of *n* to 4 allowed for the synthesis of 514 phases such as Mo_4VAlC_4 and the corresponding MXene (Mo_4VC_4) [8]. To this end, the corresponding MXenes can be divided into M_2X, M_3X_2, M_4X_3, and M_5X_4 (Fig. 1). The MXene formula also includes T_x ($M_{n+1}X_nT_x$), corresponding to all possible surfaces terminations, including –OH, =O, –F, –S, –Cl, –Se, –Br, –Te, and –I [9].

The rearrangement and ordering of the layered structure in MAX phases and their forming elements are additional prospective approaches for future MXenes' synthesis that may bring up new and interesting properties. Substituting the existing M' element atoms with other M" element atoms in quaternary MAX phases has significant consequences for their resulting phase stability and material properties [10–12]. The additional transition metal elements stabilize the obtained MAX solid solution by energetic (enthalpy-driven) forces. Next to a random distribution of the contained transition metal elements, alternating chains of M' and M" elements within the same M layer can be formed (in-plane ordering, *i*-MAX), or the different transition metal elements are located in separated atomic planes (out-of-plane ordering, *o*-MAX). Exploring the correct approaches to synthesize ordered systems in a controlled fashion by alloying is prospective for further improvement and future applications of MAX-based systems. For instance, changing the unstable ternary MAX phases such as Zr_2AlC or Bi_2AlC into quaternary $Zr_2(Al, Bi)C$ systems makes it possible to obtain thermodynamically stable compounds [13]. At this point, it becomes clear that the MXene family can be significantly enlarged by developing atomically ordered quaternary MAX phases with out-of-plane (*o*-MAX) and/or in-plane (*i*-MAX) ordering.

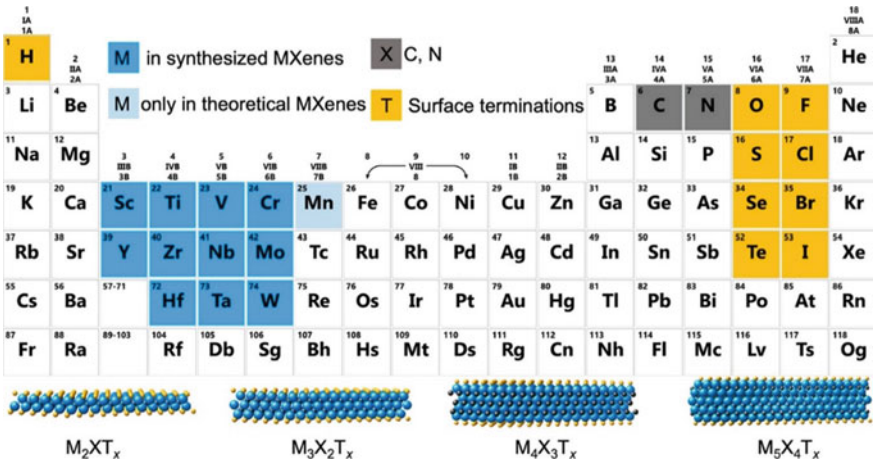

Fig. 1 Most recent benchmarking of MXene materials. The family of resulting $M_{n+1}X_n$ phases can be categorized by M_2X, M_3X_2, M_4X_3, and M_5X_4 formulas, where M stands for an early transition metal from groups 3–7 of the periodic table; X is C and/or N; $n = 1, 2, 3$ or 4; T_x resembles all possible surface terminations for a detailed formula $M_{n+1}X_nT_x$. It comprises –OH, =O, –F, –S, –Cl, –Se, –Br, –Te, –I [2, 8]. Reprinted (adapted) with permission from [9]. Copyright 2021 American Chemical Society

Successful etching of *o*-MAX will result in the formation of *o*-MXenes. For instance, MXenes' out-of-plane ordering is clearly visible for compositions such as $Mo_2TiC_2T_x$ (Fig. 2), where Mo atoms occupy the outer M layers, whereas Ti atoms occupy central M layers. Additional variations of the possible compositions come from the X-element. Carbonitrides are obtained when both carbon and nitrogen are present in the interleaving X layers (Ti_3CN). While there are many theoretical considerations of *o*-MAX phases [14], experimental approaches enabled the successful synthesis of Cr_2TiAlC_2 [15] and Mo_2TiAlC phases [16]. Recently, Meshkian et al. synthesized quaternary Mo_2ScAlC_2, verifying its superior stability compared to its ternary Mo_3AlC_2 and Sc_3AlC_2 counterparts [17]. Notably, HF etching of Mo_2ScAlC_2 delivered the first Sc-containing MXene—Mo_2ScC_2.

In addition to *o*-MAX phases, there is a possibility of in-plane ordering in quaternary MAX phases (*i*-MAX). The *i*-MAX phase structure can be written as $(M', M'')_2AlC$ with various interplay between M′ and M″ elements. For instance, the M′:M″ ratio for $(Mo_{2/3}Sc_{1/3})_2AlC$ structure is 2:1 [18, 19]. Further HF etching can remove the M″ element, thus producing *i*-MXenes with in-plane ordered vacancies, characterized by missing M″ element [20, 21]. Such produced $Mo_{1.33}C$ *i*-MXenes showed a remarkable volumetric capacitance of about 1200 F/cm^3. A fundamental understanding of these compounds and their formation principles will lead to new types of *o*-/*i*-MAX and their corresponding MXene phases. Therefore, exploring various M' and M" arrangements, selecting the involved elements with the right atomic sizes, and searching for the best molar combinations are essential for their synthesis at a larger scale.

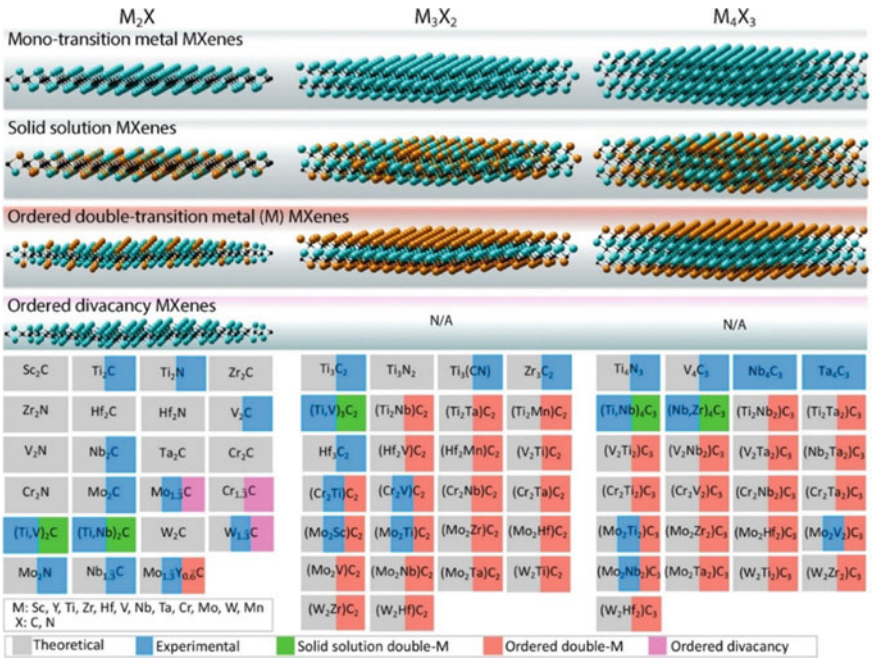

Fig. 2 The family of MXenes categorized by the number and ordering of M elements. The $M_{n+1}X_n$ phases can form mono-M elements, solid solution of M elements as well as ordered double-M elements. These can be subsequently grouped into M_2X, M_3X_2, and M_4X_3 formulas (where M = early transition metal; X=C and/or N). In addition, the solid solution of X combining C and N results in carbonitrides (coined C, N). Reprinted (adapted) with permission from [22]. Copyright 2019 American Chemical Society

1.2 Development of Non-MAX Phase Precursors

Non-MAX precursors are relatively uncharted territory, but a viable alternative. These precursors also possess layered structures and are considered promising MXene-related precursors due to their excellent stability, which holds especially true for elevated temperatures (for instance, 1200 °C [23]) as well as an excellent volumetric capacity in energy storage systems [24]. Most recent members of the non-MAX family include UAl_3C_3, $YbAl_3C_3$ [25], $Zr_2Al_3C_4$, $Zr_3Al_3C_5$ [26], and $YbAl_3C_3$ [27, 28]. Further works revealed the possibility of obtaining $ZrAl_4C_4$ [29], $ZrAl_8C_7$ [30], $Zr_2Al_4C_5$, $Zr_3Al_4C_6$ [31, 32], $[Zr_{1.97}Y_{0.03}]Al_4C_5$ [33], $Hf_3Al_4C_6$, and $Hf_2Al_4C_5$ [34] carbides. A recent study of Mocute et al. demonstrated Cr_2AlC and Cr_2GaC phases [35], whereas Ingason et al. further described a nano-laminated magnetic ternary Mn_2GaC phase [36].

Wang et al. also revealed the possibility of obtaining layered ternary non-MAX carbides with M elements chosen from Sc, Ti, V, Cr, Zr, Nb, Mo, Hf, W, and Ta [37]. It was verified that phases based upon Zr, Sc, and Hf adopt the $T_nAl_3C_{n+2}$ formula,

for which Al_4C_3-type layers separate TC slabs with a NaCl-type structure. Also, the $T_{n+1}AlC_n$ structure can be formed by neighboring Ti, V, Cr, Nb, Mo, W, and Ta elements. There are many possible combinations for these systems. The further development of non-MAX phases opens up the door for almost unlimited new MXenes.

Overall, the first principle studies were predominantly dedicated to exploring the physical properties of these new phases. Experimental approaches trail behind, together with the development of suitable etching routes. Nevertheless, some reports have shown plausibility of non-MAX phases as starting materials for MXenes' synthesis. Zhou et al. developed a method to selectively etch the Al_3C_3 slabs from $Zr_3Al_3C_5$ [23]. The obtained 2D $Zr_3C_2T_x$ MXenes showed thermal stability up to 1200 °C. Zha et al. utilized $Hf_3(Al, Si)_4C_6$ solid solutions to obtain $Hf_3C_2T_x$ [24]. Notably, the Si-supported etching process was based on weakening the bonding of Al in the starting phase. Meshikian et al. presented the synthesis of 2D Mo_2CT_x MXene by etching gallium layers from its parent Mo_2Ga_2C ternary carbide [17]. A similar approach has been pursued by Halim et al., who selectively etched gallium from the Mo_2Ga_2C ternary transition metal carbide ($M_{n+1}A_{n+1}X_n$), thus preparing 2D Mo_2CT_x [38]. An etching process based on a mild organic base was also employed to selectively etch out the $ScAl_3C_3$ layers to obtain 2D ScC_xT_x [39, 40].

Some more complex solid solutions also hold great promise to obtain new MXene types. They have a group formula of $(MC)_n[Al(A)]_mC_{m-1}$, in which n is 2–4, $m = 3$ or 4, and A stands for Si and/or Ge [41]. For instance, 2D hafnium carbide $Hf_3C_2T_x$ was obtained by selective etching of $Hf_3(Al, Si)_4C_6$ [42, 43]. In this case, the presence of Si atoms significantly weakened the adhesion of corresponding layers and, therefore, enabled the etching process.

1.3 *MXenes Beyond Ti_3C_2 and Demonstration of Novel X Elements*

We hypothesize that the X element of MXenes will find novel supplements such as B. Transition metal borides (MBenes) were first reported in 2015 by Ade and Hillebrecht and recently gained attention as promising 2D materials [44]. They are composed of X=B instead of C or N [44]. It is noted that MBenes possess different stoichiometries and variable modes of 2D layer sandwiching compared to the corresponding MXenes. MAB crystal structures can be divided into three major groups. The first group of structures is characterized by *Cmmm* (212 phases), *Immm* (414 phase), and *Cmcm* (222 phases) crystal symmetry. Other group members have *Pmmm* crystal symmetry (314 phases) and *Cmmm* symmetry (416 phases) [45]. Using etching approaches to remove the middle A layers makes it possible to obtain MBenes resembling their corresponding MAB phase symmetries, for instance, Ta_3B_4/Cr_3B_4-type MBenes with *Immm* symmetry or V_2B_3/Cr_4B_6-type MBenes with *Cmcm* symmetry [45].

Consequently, MBenes can be obtained from various starting phases, while predominantly orthorhombic structures of MAB, M_2AB_2, M_3AB_4, and M_4AB_6 phases are the most promising for MBenes synthesis. For instance, the MoAlB precursor powders with double Al layers [46], Mo_2AlB_2 [47] or Cr_2AlB_2 [48] can be used as starting materials [49]. MAB phases were so far only partially etched via mild inorganic acids or bases into 2D MoB or 2D CrB [48]. In other cases, the Ti_2InB_2 MAB phase was thermally dealloyed into 2D TiB [50]. While MAB precursors are the primary choice here, it is also possible to use bulk powders with a layered structure. In such a case, the MgB_2 [51], MnB [52], ZrB_2 [53] and GdB_6 [54] materials were used as parental phases for decomposition into 2D flakes. The disassembling process was based on an energetical input such as microwaves or ultrasounds as well as organic acids in the presence of hydrogen peroxide.

1.4 Large-Scale, Large-Area Single-Crystal MXene Films

While parental MAX and MXene phases are synthesized as bulk materials, obtaining them in other physical forms is highly desirable for various applications. Large-area thin films are highly prospective in electronics and high-tech applications. In this regard, the demonstration of vacuum-assisted bottom-up synthesis of MXenes via atomic layer deposition (ALD), physical vapor deposition (PVD), or metal organic chemical vapor deposition (MOCVD) techniques is equally important as compared to top-down assembly techniques. They offer unprecedented conditions for the MAX phase synthesis, such as low temperature and vacuum assistance. While the bottom-up optimization processes are more complex and time-consuming, this field is yet to be explored.

In 2014, Halim et al. developed transparent thin films composed of magnetron sputtered Ti_3AlC_2 with the size scale of 1×1 cm^2 [55]. The film was further reacted into MAX phase and etched into about 19 nm thick $Ti_3C_2T_x$ films using aqueous NH_4HF_2 or HF. These films exhibited ~90% transmittance to VIS–NIR light and a metallic conductivity down to 100 K. Upon crossing this temperature, they have shown a negative magnetoresistance, which is characteristic for many 2D solids with a weak localization phenomenon. Since the etching route was similar to top-down techniques, the obtained $Ti_3C_2T_x$ films were characterized with similar surface chemistry (–OH, –F, and –O surface terminations). In addition, Mo_2Ga_2C MAX was acquired by a similar approach and further etched into Mo_2CT_x thin films [17]. In this regard, crucial parameters for the successful synthesis by bottom-up methods include thin films preparation conditions on the most compatible substrates, low-temperature plasma optimization, further reaction into MAX phase, and thin-film etching conditions.

1.5 Controlling MXenes' Surface Chemistry

Tailoring MXenes' surface chemistry affects almost all physical properties of MXenes and holds great potential to unlock many practical applications. Among available terminations, oxygen is important for photocatalysis, hydrogen evolution reaction, electrochemical energy storage, etc. [56–59].

Due to the detailed knowledge about the surface chemistry of $Ti_3C_2T_x$, the extent to which standard functional groups (–OH, =O and –F) can saturate the surface seems to be well described. They appear from the basic preparation route of MXenes involving aqueous HF as an etchant and follow the order of $Ti_3C_2O_2$ > $Ti_3C_2F_2$ > $Ti_3C_2(OH)_2$ [60]. In these systems, O- and F-containing surface terminations of MXenes cannot be avoided.

While surface-grafting with other halogen terminations and their on-demand responsive adjustment is especially interesting, innovative surface tailoring routes are currently explored. The work of Chuang et al. allowed to obtain MXenes with –Cl surface terminations only ($Ti_3C_2Cl_2$ and Ti_2CCl_2) by using $ZnCl_2$ molten salt for etching the involved parental MAX phases [61]. Further etching approaches for obtaining –Br and/or –I terminated $Ti_3C_2T_x$ MXenes were based on water-free Lewis acids [62, 63]. Br-terminated MXenes were prepared by Kamysbayev et al. by using $CdBr_2$ melts for etching the MAX phase. Notably, the bromide groups were further changed to oxygen, sulfur, selenium, tellurium, and NH by performing substitution and elimination reactions with molten inorganic salts [64]. These MXenes showed interesting structural and electronic properties such as a giant in-plane lattice expansion (>18%) for $Ti_{n+1}C_n$ terminated with telluride (Te^{2-}) ligands or superconductivity for $Nb_{n+1}C_n$. Since it is possible to prepare Lewis acidic melts with other chemicals, it is reasonable to assume that novel etching routes are to be demonstrated soon.

The precise tailoring of MXenes' surface terminations is still a challenge due to the favored surface passivation and formation of metal oxides. Recently, Persson et al. defluorinated the MXenes' surface by vacuum-heating and subsequentially exposing it to O_2 at 450 °C, which led to oxygen supersaturation without breaking MXenes' structure. However, the extended O_2 exposure resulted in serve oxidation into TiO_2, with the reaction products H_2O and CO_2 desorbing from the surface [65].

The synthesis of bare MXenes without surface terminations is also a significant problem. So far, only molten salts-routes and interactions with Mg, Ca, and Al reduced the surface terminations [66]. However, it is known that any unterminated surface possesses a high energetical state. Consequently, bare MXenes are reported to be highly reactive in oxygen- or water-based environments as well as when exposed to light. Their surface further passivates by forming a thin metal oxide layer starting from the edge and continuing through the whole flake. To avoid irreversible transformation of bare MXene into the terminated/oxidized one, bare MXenes should be stored in the dark, oxygen-, and water-free conditions [67].

1.6 Theoretical Approaches for Reliably Predicting and Understanding the Properties of Novel MXenes

Theoretical calculations have been essential in understanding MXenes' structure [68]. Early predictions showed a hexagonal arrangement of the forming elements as well as the presence of surface terminations that are more likely located between three neighboring C atoms and above the hollow sites [69]. Subsequent studies verified the structure and revealed a more complicated arrangement of surface groups [70]. The exact locations and orientations of surface groups depend on both MXenes' constituent elements and the species of surface terminations. In terms of MXenes' properties, theoretical calculations so far shed light on (i) the structural and mechanical properties of MXenes, (ii) their electronic structure, pointing out the existence of topologically trivial or non-trivial metals and semiconductors, (iii) surface states, (iv) optical properties, (v) magnetic properties, (vi) transport properties (in quantum and semi-classical diffusive regimes) [71].

Based upon theoretical calculations [71], many possible applications have been identified for MXenes, including functional devices for (a) electronics, (b) magnetoelectronics, (c) optoelectronics, (d) sensorics, (e) thermoelectric power generators and coolers, as well as (f) plasmonics. Theoretical studies also indicate the possibility of employing MXenes as potential materials for hydrogen storage, catalytic and photocatalytic reactions due to nanoscale superconductivity, ultra-low work function, or Schottky barrier junctions. MXenes have been also predicted to be large band gap topological insulators that involve only *d* orbitals.

It is known that bare MXenes tend to be metallic. However, the metallic character diminishes with increasing *n* values, mostly owing to additional M–X bonds [72]. In contrast, terminated MXenes are narrow band-gap semiconductors or metals depending on the orientation of surface groups as well as the MXene type. For instance, surface terminated MXenes such as Ti_2CO_2, Zr_2CO_2, Hf_2CO_2, Sc_2CO_2, Sc_2CF_2, and $Sc_2C(OH)_2$ have indirect band gaps (0.45–1.8 eV), while direct band gaps appear in –OH terminated $Sc_2C(OH)_2$ [71]. This information allows for more rational engineering of surface-related properties of MXenes, which is crucial for optoelectronic or photocatalytic applications.

Theoretical predictions of many properties, particularly electronic properties, are based on first-principles calculations using the density functional theory (DFT) framework with various approximations for the exchange and correlation density functionals. Unfortunately, the obtained results considerably depend on the chosen approximation [73]. In this regard, better results are achieved by hybrid functionals, which are exchange–correlation energy functionals [74]. This strongly suggests that applying exact exchange and random phase approximation (RPA) for correlation would be advantageous together with the consideration of corrected, dispersive van der Waals forces. Relativistic effects need to be considered when performing theoretical calculations for MXenes since they constitute heavy transition metals with significant spin–orbit coupling (SOC). Therefore, the SOC in many cases should be

treated in a non-perturbative manner. Notably, MXenes' structure is frequently calculated with uniform surface termination—an idealistic view of the situation, which is far away from reality. In nearest future, more realistic modeling of MXenes will be necessary to consider the coexistence and random arrangement of various surface terminations. This will allow for a more accurate reflection of their complicated structure.

Although there are several experimental reports on the formation of heterostructures built from MXenes or a change in their shape into nanotubes and nanoribbons, it is expected that these systems will be investigated in more detail. Therefore, more theoretical studies of these systems are urgently needed. Ab-initio studies of bare and functionalized Ti_2CT_x, $Ti_3C_2T_x$, and V_2CT_x MXenes demonstrated the possibility of forming even zigzag, armchair nanoribbons [75] or nanotubes [76, 77]. It was shown that the band gap of armchair Ti_2CO_2 nanoribbons is ~1 eV, which is four times larger than the value of bare 2D MXene in flake form [76, 77]. Therefore, it appears to be possible to tailor the electron and hole carrier mobility within these nanoribbons via edge states engineering [78, 79].

Vertical or so-called van-der-Waals heterostructures of 2D materials have become a great opportunity for designing nanostructures with novel functionalities [80–82]. Stacking MXenes with transition metal dichalcogenides (TMDs), graphene, h-BN, or other 2D systems can open new doors for novel nanomaterials with exciting properties. Theoretical predictions of vertical heterostructures involving MXenes have been recently performed for MoS_2/Ti_2C and MoS_2/Ti_2CT_2 (with T = –F or –OH) [83], graphene/$Hf_2C(OH)_2$ [84], silicene/Sc_2CF_2 [85], Sc_2CF_2/Sc_2CO_2 [86] systems as well as various heterostructures involving TMDs such as TMDs/M_2CO_2 (M = Sc, Ti, Zr, and Hf) [87]. Results have shown interesting electronic properties of these systems. The most promising configurations are based on efficient stacking to achieve the most suitable band gap engineering. For instance, graphene/$Hf_2C(OH)_2$ heterostructures showed no chemical interactions between metallic $Hf_2C(OH)_2$ and semi-metallic graphene. Thereby, graphene is *n* doped by $Hf_2C(OH)_2$, which is mostly associated with electron transfer from the –OH surface terminations to graphene π^* states. Notably, the ~2.32 eV work function of $Hf_2C(OH)_2$ is ultralow compared to that of graphene (~4.26 eV). Therefore, while graphene receives electrons from MXenes, its energy dispersion is shifted to lower values of ~1.1 eV [84]. Moreover, studies on various transition metal dichalcogenides/Sc_2CO_2 heterostructures revealed the evolution of indirect band gaps ranging from ~0.13 to ~1.18 eV. These electronic properties enable the development of electronic devices [87].

2 New Synthesis Methods for MXenes

2.1 *Development of Novel and Scalable Techniques for MXenes' Synthesis*

In the pioneering work on the development of MXene [2], $Ti_3C_2T_x$ (T_x = –OH, −F, and =O) was obtained by extracting the Al layers from the parental Ti_3AlC_2 phase. The involved reactions included (i) $Ti_3AlC_2 + 3HF = AlF_3 + 3/2H_2 + Ti_3C_2$, (ii) $Ti_3C_2 + 2H_2O = Ti_3C_2(OH)_2 + H_2$, (iii) $Ti_3C_2 + 2HF = Ti_3C_2F_2 + H_2$. Reactions (ii) and (iii) led to the formation of –OH and –F terminations on a multilayered (ML) surface. Further intercalation with large organic cations (in some cases enhanced by an ultrasonication treatment) is proved to deliver few-layered (FL) or single-layered (SL) MXenes [67, 88]. This strategy was applied to etch almost all Al-containing MAX phases. Apart from HF concentration, crucial process parameters to control are temperature and time, which greatly vary depending on the particle size of the MAX phase.

Later, the use of ammonium bifluoride (NH_4HF_2) as an etchant was proposed to avoid hazardous HF [55]. Its milder nature and complementary cations serving as intercalants during etching made it a more suitable agent for MXenes' delamination. While etching and intercalation occur simultaneously, it is reasonable to derive the following reaction scheme: (i) $Ti_3AlC_2 + 3NH_4HF_2 = (NH_4)_3AlF_6 + 3/2H_2 + Ti_3C_2$; (ii) $Ti_3C_2 + NH_4HF_2 + H_2O = (NH_3)(NH_4)Ti_3C_2(OH)_xF_y$. However, the intercalation of both NH_3 and NH_4 between the MXene layers appeared to be slower and less vigorous. Consequently, the atomic layers in $Ti_3C_2T_x$ were rather restacked together than individually separated. Another possible etching route involves soaking Ti_3AlC_2 power in a solution of LiF and HCl. $Ti_3C_2T_x$ flakes produced this way showed larger lateral dimensions with a reduced number of structural defects, which characteristically occur frequently for HF-etched samples. The reduced defect density reflects the milder nature of the LiF + HCl etchant as compared with HF. Other combinations of fluoride salts such as NaF, KF, CsF, CaF_2, or tetrabutylammonium fluoride [$(C_4H9)_4NF$], with acids (e.g., HCl or H_2SO_4), showed similar etching behaviors.

In experimental practice, there are two methods suitable for obtaining multilayered $Ti_3C_2T_x$ MXene and their delamination to single flakes. The first one is called the 'clay method' and is based on mixing 5 M LiF with 6 M HCl and further sonication and/or heating, which reduces the resulting flake thickness [89]. Alternatively, a mixture of 7.5 M LiF and 9 M HCl can be utilized, which is subsequently not sonicated but only shaken vigorously [90, 91]. The second method is called minimally intensive layer delamination (MILD) because it allows obtaining less-defective single flakes [91]. The MILD method is flexible in terms of preparing the basic mixture, and reagents' concentrations can be adjusted from 7.5 M LiF/9 M HCl to 12 M LiF/9 M HCl at room temperature [92, 93].

The high-yield (50 g batch) MXene preparation was further reported by Shuck et al. [93]. In this method, $Ti_3C_2T_x$ was prepared by soaking Ti_3AlC_2 powder in

LiF and HCl solution (1 L reactor volume, 50 mL LiF, 150 mL H_2O, 300 mL of HCl with the 1:3:6 volume ratio), heating up to 35 °C for 24 h and washing the sediment to increase the pH and extract the supernatant. As a resulting product of this reaction, a clay-like paste was formed, which can be rolled to produce flexible, free-standing films with high volumetric capacitance. Moreover, the final mixture can be diluted prior to solution processing [94]. This proves that MXenes' synthesis can be up-scaled.

2.2 *Innovations Towards Environmentally Friendly Top-Down Approaches*

The development of safer, greener, and scalable top-down options is currently pursued. This includes rapid, high energy-supported fragmentation techniques, but also greener approaches for the synthesis of the involved MAX phases. While MXenes' selective etching is mainly based on harsh chemical reactions with dangerous or even explosive reagents and by-products, it is reasonable that scientists search for more human- and environmentally-friendly ways to obtain these promising compounds. In contrast to the MILD method, the latest approaches suggest using ultrarapid energy-induced techniques based on high-energetic fluidic or microfluidic devices supported with the energy of cavitation generated by ultrasound or acoustic waves. The localized application of mechanical energy for MXenes' defragmentation saves time and avoids the use of harsh chemicals.

Al-Antaki et al. reported a facile approach to synthesize $Ti_3C_2T_x$ MXenes, in which a vortex fluidic device (VFD) was used [95]. The equipment involved a millimeter-scale borosilicate glass inclined at an angle from −45° to 90° relative to the horizontal position that can rotate at speeds up to 9000 rpm. Two options for MXenes' defragmentation can be used: confined (with an exact amount of liquid in the tube) or continuous flow. The VFD seems a promising approach for MXene synthesis since the exfoliation of graphene from graphite, graphene oxide, or h-BN [84] has already been realized using this approach. In recent work, multilayered MXene sheets were obtained using VFD in dynamic and optimized conditions (nitrogen atmosphere, 0.5 mg/ml MXene, 1:1 mixture of isopropanol and water, VFD rotational speed of 4000 rpm, 45° tilt angle, and 0.5 ml/min flow rate). The VFD was further used by Al-Antaki et al. for the synthesis of nanocomposites made of MXene and TiO_2 anatase nanoparticles in aqueous H_2O_2 (30%) at a flow rate rate of 0.75 mL/min and a concentration of MXene of 0.5 mg/mL [95].

El Ghazaly et al. reported synthesizing $Ti_3C_2T_x$ MXene via an ultrafast, one-step technique based on surface acoustic waves (SAWs) [96]. By using LiF solution, the MAX phase was rapidly converted to MXene and further delaminated. Proton production through solution dissociation of water under acoustic excitation facilitated the underlying mechanism of the etching with fluorine ions by decreasing the pH and thus further enhancing the dissociation of LiF and providing more fluorine ions. The

high localization of mechanical vibrations with acceleration on the substrate surface of 10^8 m/s^2 increased ionic diffusion through the 2D MXene structures, accelerated the kinetics of the reaction, and assisted in further delaminating the sheets. Notably, energy-induced techniques based on high-energetic fluidic or microfluidic devices are sustainable due to low cost and safety aspects. These techniques tend to hold great potential regarding up-scaling, thus widely opening the door for MXenes' future applications.

At this point, it is worth mentioning that MAX phases and resulting MXenes can be also synthesized from low-cost precursors. The high environmental benefit of this approach, as well as lowering the production costs, are of unprecedented importance. A recent study of Jolly et al. proved that $Ti_3C_2T_x$ MXenes could be synthesized from recycled, waste tire-based carbon, recycled aluminum scrap, and titanium dioxide with molar ratios of 1.9C:6Al:3TiO_2 [97]. The process comprised heating the precursor mixtures up to 1350 °C for 1 h and MILD delamination under N_2 shielding. The final $Ti_3C_2T_x$ films demonstrated properties similar to traditionally obtained MXene, i.e., conductivity = 5857 ± 680 S/cm and capacitance = 285 F/g (1,012 F/cm^3) at 20 mV/s scan rates.

2.3 Understanding the Influence of MAX Structure and Properties on MXenes' Characteristics

MXenes can be model materials for testing the material-processing-properties-performance paradigm. However, the basic paradigm can be developed into a more complicated system that adapts to the unique properties of MXenes. The schematic representation of an adapted circular relationship, which takes structure, processing, chemistry, properties, performance, and transformation into consideration, is presented in Fig. 3. To achieve the desired structure, it is important to analyze the parental MAX phases, whose synthesis and properties have an impact on the resulting MXene structure. The structural purity of the final product is influenced by many processing factors. Every processing step, such as MAX phase synthesis, grinding, etching, and delamination, can leave its own trace in relation to the chemical and phase composition of the final product. In this context, the purity of the MAX phase is the most significant factor affecting MXenes' purity. The preparation of the bulk MAX phases can be achieved by various techniques. Researchers can choose between hot pressing (HP) [98, 99], hot isostatic pressing (HIP) [100], slip casting (SC) [101], self-propagating high-temperature synthesis (SHS) [7, 102], or pressure-assisted self-propagating high-temperature synthesis (PSHS) [103, 104]). Given the variety of methods and their specific synthesis conditions, the repeatability of MAX synthesis poses a challenge. Every single MAX batch may be composed of different phases with variable mass content. Also, the purity of used powders is a matter of concern since every additional element present is potentially transferrable to the final MXene product.

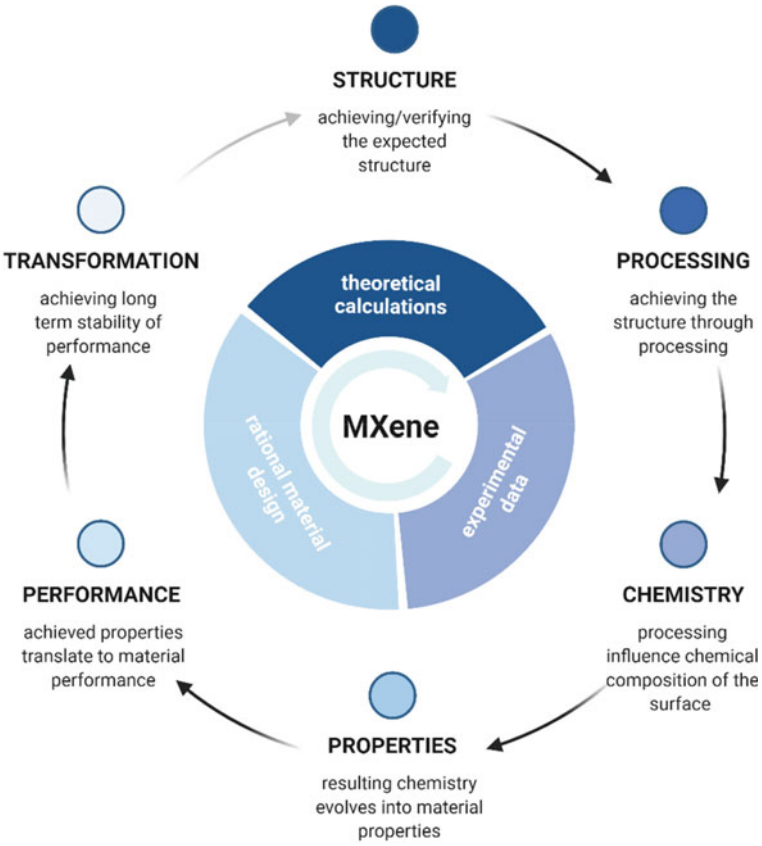

Fig. 3 Schematic representation of the circular relationship, adapted to MXenes as model materials for testing structure-processing-chemistry-properties-performance-transformation paradigm. The visible dependency of material-related elements is integrated with theoretical and experimental approaches to accelerate materials development through rational material design and further incorporation into final commercialized products that are processable and hold extraordinary and stable performance

While the final composition of the MAX phase relates to many factors [7], the abovementioned techniques have some similarities that can be used to control different MAX parameters. Considering SHS as an example, Ti_3AlC_2 is prepared by mixing elemental powders (Ti, Al, and graphite) or Ti_3Al with graphite powder, subsequent homogenization, and further pressing into a bulk material to enable better control over the SHS process evolution. The mixing step can therefore be optimized in terms of molar ratios and further processing with a standardized method. However, after ignition, the highly exothermal process propagates in an uncontrollable manner. The parameters of temperature and phase evolution (self-propagation) cannot be controlled and are unrepeatable [7]. Therefore, after SHS, the MAX product is a mixture of Ti_3AlC_2, Ti_2AlC, and TiC phases due to respective phase equilibria.

Zhou et al. revealed the reaction mechanism for which Ti_3AlC_2 is formed together with the presence of Ti_2AlC [105].

The energy for TiC formation is rather low. After the formation of octahedral Ti_6C, two different reaction pathways compete thermodynamically with each other. The first one leads to Ti_2AlC, which is thermodynamically more stable compared to Ti_3AlC_2. After the formation of Ti_2AlC, it can be further transformed into Ti_3AlC_2, which is an additional step in the reaction pathway. The second path leads from octahedral Ti_6C to cubic TiC, which, in turn, transforms into Ti_3AlC_2. Consequently, apart from Ti_3AlC_2, large amounts of Ti_2AlC and cubic TiC are present in the final MAX product.

Another reaction variant is based on the mixture of elemental powders (Ti, Al, and C). During the reaction to form the Ti–Al–C system, there is an exothermic reaction between Ti and Al at the beginning, thus increasing the temperature. When the conditions are favorable, another exothermic reaction in the Ti–C system is induced, which further proceeds until obtaining Ti–Al in liquid form, in which TiC dissolves. Ti_3AlC_2 is then formed between TiC and the molten Ti–Al. The final MAX product consists of Ti_3AlC_2, Al_3Ti, and TiC [11]. When unwanted reaction by-products are present in the final MAX phase, they are potentially transferable to MXene. For instance, minor amounts of cubic TiC can attach to flakes' edges. Nevertheless, the Al_3Ti by-product can be fully dissolved if harsh HF etching conditions are applied.

After product cooling, the next step of the process comprises wet-phase assisted grinding of the bulk product in a rotary-vibratory or planetary mill [106]. Grinding into several micrometer-sized power particles is important for the efficiency of the etching process. Since MAX phases are rather hard materials, WC balls are necessary to reduce particle size efficiently. A major disadvantage of these MAX post-processing steps is surface abrasion resulting in contamination originating from the grinding balls, which can be further minimized through process optimization.

The abovementioned problems come from experimental observations. However, they have true implications to the material-processing-property relationship. Therefore, to accelerate materials development through rational design, experimental approaches to obtain MXenes will be further backed up with theoretical approaches to achieve extraordinary and stable performance in a well-controlled environment.

2.4 Challenges in MXenes' Synthesis and Characterization

MXenes' quality greatly relates to the synthesis process used. In well-established processes, the MAX phase is the starting material, and its quality determines the final MXene [107]. Therefore, choosing the MAX phase with high purity without any side phases or unreacted substrates is crucial. In addition, the MAX phase needs to be prepared carefully with minimal impurities originating from mechanical milling [108]. Nevertheless, all these additives can be removed as sediment during etching and delamination. Furthermore, if these are solubilized in the acid, they can be washed out during the rinsing stage.

During the etching of $Ti_3C_2T_x$ MXenes, harsh conditions are applied to the MAX phase to solubilize and remove the interleaving aluminum layers. In early approaches, toxic and dangerous HF was used, and the most significant challenge was related to the safety of the researchers. Afterwards, the MILD process was developed based on optimized conditions and less harsh etchants. However, the process was still based on using in-situ formed HF from a mixture of HCl and LiF [92]. Further innovations using molten salts or ionic liquids enabled a safer and less toxic MXene synthesis [62]. However, their upscaling is highly limited due to expensive chemicals in contrast to primarily used water.

While MXenes' oxidation is critical, it is essential to adjust processing times and the properties of the initial MAX phase. In this sense, the most critical aspect is the grain size of the MAX phase. Larger grain sizes will result in unetched MXene grains, which will sediment from the colloidal solution. The collected sediment will thus need a second round of etching to completely remove Al. In contrast, smaller MAX grains tend to etch more easily. However, this requires longer milling times, thus resulting in more impurities coming from the milling balls and container. Additionally, smaller MAX grains result in smaller MXene flakes. Consequently, MXenes' quality (purity) can also be negatively affected when using smaller MAX grains.

A similar consideration needs to be made for the delamination process. Larger MXene grains will not fully delaminate, and longer delamination times may be required. The delamination may not even be completely realized. The delaminated flakes can also have larger dimensions if not reduced by sonication. From this point, the standardization of the material parameters became challenging as every single synthesis gives different results in terms of flake parameters [92]. In order to fully characterize the resulting MXene batches, parameters to carefully consider are conductivity, surface zeta potential, characteristic XRD pattern or Raman spectra. Various MXene batches may give similar XRD patterns, and Raman spectra as these techniques are specific to material composition and physical nature in bulk, but MXene nano-sheets may still differ in their physical properties [92]. Therefore, the challenge is to determine and track changes in flakes dimensions and chemistry (detailed arrangement of surface functional groups) by advanced and complementary material characterization.

The washing stage is also critical to fully remove all by-products of aluminum etching. This step is unspecific and finishes while the pH of the solution reaches about 6 or 7 [92]. In case of highly concentrated flakes dispersion, a significant amount of adsorbed Li^+ or Cl^- inorganic ions (for LiF/HCl etching and delamination) or TMA^+ organic ions (for HF etching and TMAOH delamination route) may be difficult to wash out. Consequently, multiple washing/centrifugation steps or filtration are needed and may take hours to achieve desired pH value.

Other challenges are related to different types of MXenes and their stoichiometries. For instance, $Ti_3C_2T_x$ can be easily etched and delaminated in LiF/HCl. In contrast, Nb_2CT_x or $Nb_4C_3T_x$ MXenes first need HF etching to be further delaminated with TBAOH or TMAOH. For these MXenes, the LiF/HCl approach is far less effective. Finally, the synthesis of $Ti_3C_2T_x$ can be up-scaled. Some MXenes

(V_2CT_x, Cr_2CT_x, or Ti_2NT_x) are difficult to etch or delaminate into single flakes at all due to their low stability and increased oxidation tendency. For these phases, only multi-layer MXenes may be synthesized.

The problem of preserving MXenes' structure is related to their oxidation stability [109]. This is another challenge related to decreased stability, an aspect that worsen at every stage of synthesis. MAX phases are highly stable because of the presence of interleaving A layers. Removing this layer via etching decreases the stability of the resulting multi-layer structure. However, multi-layers are still fairly stable to withstand sample preparation for various analyses and industrial applications. However, delamination to obtain few- and single-layers further destabilizes the structure. Under ambient conditions, few- and single-layers tend to oxidize after several hours while decomposing after several months. Consequently, the material needs to be kept in an oxygen-free and dark environment at low temperatures.

The mentioned issues also relate to the challenge to characterize the material [110]. Due to the rapid oxidation of the samples, proper characterization needs to be done immediately after synthesis. Therefore, to be successful in characterization, researchers need to act quickly to get the deserved results. Most characterization techniques perform measurements under ambient conditions, in air, or partially in the presence of water. Samples may oxidize during preparation in ambient conditions and while using specific equipment. These changes may be tracked by changing patterns/peak in XRD and Raman spectroscopy. The used laser intensity for the Raman measurements needs to be appropriately chosen to avoid MXenes' oxidation. Concerning surface chemistry, changes in surface chemistry can be detected by XPS or zeta potential. When the sample is measured immediately after synthesis, the zeta potential tends to be highly negative. XPS done after synthesis should detect metal bonding with hydroxide groups and fluorine and no metal oxide. If the material is oxidized, zeta potential will shift from a highly negative value closer to zero, and XPS will verify metal oxides [110].

3 Physical and Chemical Approaches to Tailor MXenes

As outlined in Sect. 2, the scientific research community continuously works on new synthesis approaches for MXenes with the overall goal of extending the field of available MXenes and reducing the use of toxic and hazardous HF synthesis strategies, thus increasing lab safety [22, 111, 112]. In this context, particular emphasis is laid on MXenes' quality (defect situation, purity) and x–y dimensions of the obtained sheets [111]. The surface terminations including $–O_2$, $–(OH)_2$, $–F_2$, $–Cl_2$, and their combinations can be intentionally utilized as anchoring points to chemically functionalize MXenes with the overall aim to change their physical and chemical properties [113]. The proper selection of the functional groups is considered to be the key to intentionally tune crucial properties of MXenes such as their thermal and oxidation stability, degree of hydrophobicity/hydrophilicity, dispersion stability, interfacial strength, and

surface chemistry, all of these being decisive for gas sensing or catalytic processes, among others.

When aiming at functionalizing MXenes, their interlayer spacing is essential since it can be used to tailor the access to active sites for functionalization [114]. MXenes' interlayer spacing can be manipulated by mechanical or chemical means, which can even lead to their delamination (few- or single-layer MXenes) [111, 112]. Ultrasonic treatments and shear mixing are well-explored mechanical delamination methods, while chemical delamination is realized by intercalating agents (ions and small molecules) or spacers (nanomaterials and polymers) [114, 115]. Intercalants help to expand MXenes' interlayer spacing and/or induce their delamination [114]. In the case of spacers, they are used to reduce the restacking tendency of MXene nano-sheets [114]. Irrespective of the used intercalation agent, this can be done either during or after etching. Cations (such as Li^+, Na^+, K^+, NH_4^+, Mg^{2+}, Al^{3+}) intercalated between the layers can increase the interlayer spacing [116]. The formation of pillared $Ti_3C_2T_x$ MXenes (spontaneous intercalation of cetyl trimethylammonium bromide (CTAB)) resulted in a tunable interlayer spacing [114]. It is also possible to simultaneously intercalate MXenes with several small molecules, and the addition of a co-intercalator can further expand MXenes' interlayer spacing. Regarding the use of nanomaterials as spacers, such as carbon nanotubes (CNTs), graphene, reduced graphene oxide (rGO), or MoS_2, their uniform distribution between the layers is the key aspect in preventing restacking, thus allowing the availability of many active sites [114]. Polymers can also be intercalated between layers, thus increasing MXenes' interlayer spacing [114, 117]. The usage of polymers to increase the interlayer spacing is beneficial due to enlarged distances compared to other intercalants, but it suffers from the polymers' long-term stability. To overcome this problem, in-situ polymerization on the outer MXene surface seems to be a promising approach [114].

Apart from using intercalating agents and spacers, MXenes can be covalently functionalized by a variety of molecules. In this regard, the covalent bonds typically act as connecting bridges between MXenes and an organic phase, thus enhancing their compatibility. This, in turn, helps to adjust the degree of hydrophilicity/hydrophobicity of the MXene nano-sheets as well as to improve the stability of suspensions in polar or apolar solvents and their resistance against oxidative degradation [118–120]. Moreover, incorporating pendant moieties with different chemical natures becomes possible, which enables multi-functionalization.

For MXenes' covalent functionalization, organosilanes, organophosphates, and aryldiazonium salts have been used as coupling agents. Organoalkoxysilanes have a general structure of $(RO)_3$–Si–R′–X, for which X is an organic functional group such as methyl, amine, epoxy, or vinyl, among others, R' stand for an aliphatic chain, and RO represents alkoxy group or silanol group that is removed by hydrolysis [121–123]. A critical aspect of this process connects with the presence of water, which is important for the first stage of the overall process (hydrolysis to form silanol groups (–SiOH)). Subsequently, the formation of oligomers is induced by a condensation process. Subsequently, they react with the available hydroxyl groups. Related to organosilanes, 3-(Aminopropyl)triethoxysilane (APTES) is the most used surface

modifying agent for MXenes' functionalization [124, 125]. Moreover, MXenes' functionalization with long alkylsilane chains is a strategy not only to improve their stability against oxidative degradation but also to enhance their stability in apolar solvents, since this approach helps to decrease the surface energy, thus increasing hydrophobicity [126]. In this context, it is important to point out that using long aliphatic chains (grafting onto MXenes) is tricky due to the different solubilities in polar and apolar solvents [126].

Regarding organophosphates, phosphonic acid (PA) ligands contain a central phosphorus atom, which is linked to two hydroxyl groups through single bonds, an oxygen atom through a double bond and an aliphatic chain [127, 128]. These ligands have been used as MXenes' surface modifying agent. This approach is interesting since the length and nature of functional groups in the aliphatic chain can be tailored, thus adjusting the resulting physical properties [129, 130]. Aryldiazonium salts being represented by $RN^{2+}X^{-}$ (R stands for an aromatic group and N^{2+} resembles the azo groups), are considerably new agents for bonding polymers and biomacromolecules (Fig. 4) [131]. These molecules start with a primary amine R–NH_2 that is capable of producing diazonium salts. Subsequently, the salt receives an electron, which promotes the cleavage of the C(aryl)–N bond, releasing N_2(g) and forms an aromatic free radical. This free radical interacts with the surface, establishing a new bond between the surface and the aryl group (substrate–O–C(Aryl)) [132, 133]. MXenes have also been functionalized using click chemistry, polymerization reactions, or catechol derivatives [134, 135]. In this regard, click chemistry is a simple approach and beneficial due to high achievable yields and little formation of by-products. An example is a reaction of isocyanates (R–N=C=O) with alcohols or thiols (XH, X=O; S) [136]. Different groups such as –OH and –SH can attack the

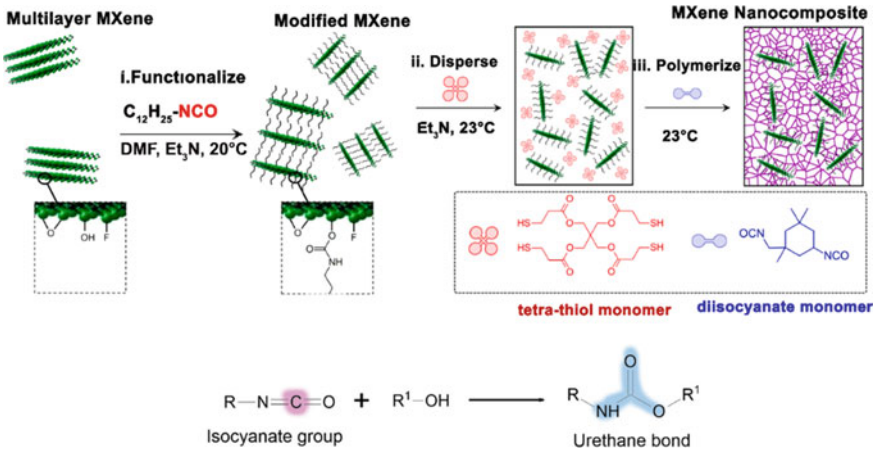

Fig. 4 Fabrication of nanocomposites based upon functionalized MXenes and thiourethane. The process begins by grafting dodecyl isocyanate onto the outer MXene surface, followed by in-situ polymerizations of tetra-thiol and diisocyanate at room temperature in a suspension of the functionalized MXenes [137]

carbon atom of the isocyanate group (R–N=C=O), thus establishing a new RNCO-O or RNCO-S bond. McDaniells et al. used dodecylisocyanate groups to functional multi-layer MXenes, potentially enabling up-scaling [137].

Based upon this short summary, it becomes evident that MXenes' functional groups are perfectly suited to induce functionalization. However, surface functionalization reactions can also oxidize the surface of MXenes. Therefore, new synthesis strategies for MXenes, which adjust the amount and nature of the respective surface termination as well as suppress oxidation, are urgently needed. As derived in this section, –OH surface terminations play a key role in MXenes' functionalization. If less –OH groups are available, less active sites are accessible for functionalization. Therefore, we hypothesize that the success of covalent modification relates to the degree of functionalization and concentration of –OH. We speculate that more work needs to be dedicated to generating MXenes with a high concentration of reactive groups (–OH or others) homogenously spread over the entire MXene surface. Most of the published research work has been published for $Ti_3C_2T_x$ since these nano-sheets are the most explored ones and the easiest to synthesize. However, MXenes based upon other early transition metals (M_2CT_x M=Sc, V, Cr, Zr, Nb, Mo, Hf, Ta, and so on) also holds exciting physical properties. To summarize, the combination of inherent metal center properties and chemical functionalization can synergistically improve the properties of MXenes. Consequently, MXenes' covalent manipulation/functionalization offers the opportunity to exploit new application areas.

New synthesis and functionalization approaches need to be connected with numerical simulations. This can help to predict the ongoing interfacial processes between MXene nano-sheets and the coupling agents. In this context, ab-initio DFT or MD simulation can help to explore the underlying processes. However, in case of DFT, it will be essential to consider van der Waals interactions. Regarding MD, the used potentials have to be selected in a careful manner. We envision that combining new synthesis methods and functionalization strategies together with numerical modelling and advanced high-resolution materials characterization can open the door for the development of MXenes with tailor-made properties.

The group of Anasori et al. has recently extended single- and double-early transition metal MXenes by high-entropy MXenes inspired by high-entropy alloys (Fig. 5) [90]. The synthesized high-entropy MXenes, consisting of four early transition metals, are based on high-entropy MAX-phases ($TiVNbMoAlC_3$ and $TiVCrMoAlC_3$), which were fabricated by reactive sintering. The first examples of experimentally realized high-entropy MXenes comprise $TiVNbMoC_3T_x$ and $TiVCrMoC_3T_x$, thus having the general formula of $M_4C_3T_x$.

HF-etching was used for the first successful synthesis of the high-entropy MXenes (48% HF for 4 days at 55 °C). By chemical delamination, the possibility to synthesize single-layer high-entropy MXenes was demonstrated [90]. During synthesis, the following chemical pathways were followed:

$TiVNbMoAlC_3$ to $TiVNbMoC_3$

$$TiVNbMoAlC3 + 3HF = TiVNbMoC_3 + AlF_3 + 3/2H_2$$

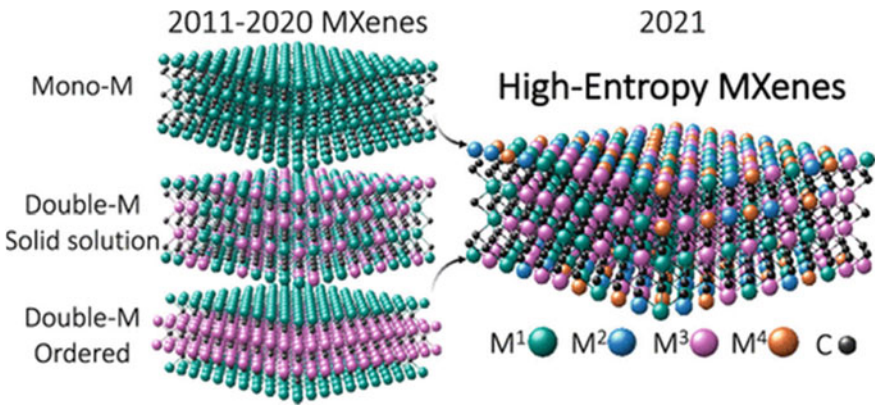

Fig. 5 Summary of the development of MXenes from mono-M over double-M MXenes as solid solution or ordered structure to high-entropy MXenes containing four different early transition metals [90]

$TiVNbMoC_3 + 2H_2O = TiVNbMoC_3(OH)_2 + H_2$

$TiVNbMoC_3 + 2HF = TiVNbMoC_3F_2 + H_2$

$TiVCrMoAlC_3$ to $TiVCrMoC_3$

$TiVCrMoAlC_3 + 3HF = TiVCrMoC_3 + AlF_3 + 3/2H_2$

$TiVCrMoAlC_3 + 2H_2O = TiVCrMoC_3(OH)_2 + H_2$

$TiVCrMoAlC_3 + 2HF = TiVCrMoC_3F_2 + H_2$

This initial study combining high-entropy alloys with 2D MXenes will pave the way for more numerical and experimental work on high-entropy alloys. Both approaches need to be pursued jointly to understand the underlying formation mechanisms and explore the respective property combination [90].

4 Material and Property Design

4.1 Assembly from 2D to 3D

Many applications such as energy storage and electromagnetic wave absorption require a large specific surface area, which is one of the main reasons for applying 2D materials in these fields. A prerequisite for the successful use of 2D materials in these applications is the existence of many individuals, high-quality flakes, resulting in a high surface-to-volume ratio. Additionally, MXenes' unique mechanical properties, such as their high flexibility, only fully emerge if there are many individual flakes or a specific sheet alignment/orientation [138]. However, similar to other 2D materials,

MXenes tend to demonstrate an increased tendency for restacking induced by strong van der Waals forces acting between the layers, thus greatly reducing the MXene surfaces' accessibility [114]. To boost MXenes' use in practical applications and to enhance their multifunctionality, approaches are investigated to prevent MXenes' restacking, thus preserving their 2D nature.

Several methods (illustrated in Fig. 6) are available to reduce MXenes' restacking tendency, including introducing intercalants or spacers as external components between the layers and their assembly into 3D materials [114]. The formation of 3D structures from 2D MXenes allows for the generation of materials with high porosity, large specific surface area, high electrical conductivity, and stable chemical and mechanical properties [139].

Ions, small molecules, other nanomaterials, or polymers are used as external components to introduce MXene layers [114]. The introduction of another material as intercalant or interlayer spacer leads to a change in the interlayer distance (i.e., c-lattice parameter), which is typically around 2 nm for $Ti_3C_2T_x$ MXenes. Mostly, the

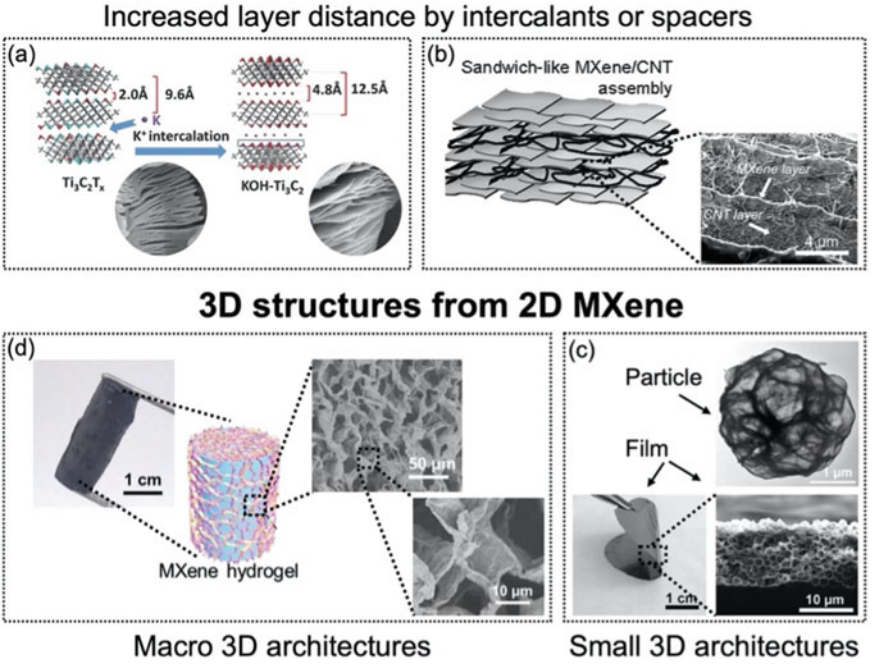

Fig. 6 Assembly of MXene nanosheets from 2 to 3D to preserve their 2D nature with a large specific surface area. Possibilities to achieve this comprise using **a** intercalants [140, 141] or **b** spacers [142]. Additionally, more complex structures such as **c** small 3D architectures in the form of particles [143] and **d** films [144] up to macro 3D architectures in the form of hydrogel or aerogels can be formed [145]. **a** Adapted with permission from [140, 141]. Copyright 2017 Wiley–VCH and [140, 141]. Copyright 2018 Elsevier. **b** adapted with permission from [142]. Copyright 2014 Wiley–VCH. **c** adapted with permission from [143]. Copyright 2018 American Chemical Society and [144]. Copyright 2017 Wiley–VCH. **d** adapted with permission from [145]. Copyright 2019 Wiley–VCH

interlayer distance is increased, depending on the used external component, whereby ions typically lead to the smallest change and polymers to the greatest, thus reaching interlayer distances of up to 4.8 nm [114]. The introduction of ions or molecules, such as Li^+-, Na^+-ions, water-, or urea-molecules helps to reduce interactions between individual layers and delaminates multi-layer stacks into few- or single-layers if the interlayer distance is sufficiently increased (Fig. 6a). Additionally, the stability of ion-intercalated MXenes is improved due to strong electrostatic interactions between intercalated cations and MXene flakes [146]. When using other nanomaterials or polymers, these are difficult to intercalate between stacked MXene layers but act mainly as spacers, thus preventing restacking of delaminated MXenes (Fig. 6b). Nanomaterials such as carbon nanotubes [147], graphene [148], or MoS_2 [149] have been used, and possible polymers comprise polyaniline [150] and polyvinyl alcohol [151]. The main challenge for these external components is achieving a homogenous distribution on MXenes' surface, thus effectively preventing restacking.

Even more effective to prevent MXenes' restacking and to increase interlayer distances is to change the architecture of the 2D MXene stacks to form 3D interconnected porous architectures (structures, films, or foams) as shown in Fig. 6c [114, 144, 152]. Small 3D architectures composed of 2D MXene sheets, which are interconnected, can be formed by filtration processes [152], template methods with sacrificial templates, which are later removed to form pores [144], or foaming processes, in which gaseous species are generated as reaction products [153]. Solution-based 3D assembly makes the formation of larger 3D network structures such as hydrogels or aerogels possible, where the solvent molecules prevent restacking (Fig. 6d). The assembly in 3D structures from solution requires a uniform nanosheets' dispersion to generate interconnected structures with strong connections. Since MXenes are highly hydrophilic, they can be well dispersed in aquatic solutions [154]. After achieving a good dispersion, adjacent MXene nanosheets have to be connected to form a 3D network via van der Waals forces, hydrogen bonds, or covalent bonding. In this regard, the high number of functional groups on the MXenes' outer surface causing their hydrophilicity has a negative impact due to the produced electrostatic repulsive forces hindering the connection of the sheets. By balancing MXenes' hydrophilicity and hydrophobicity, the interplane attraction and the electrostatic repulsion of the sheets can be controlled. In order to do so, crosslinkers are used, which can be reduced graphene oxide (rGO), cellulose, or divalent metal ions [114]. Additionally, the template method can be used to assemble 2D materials into 3D architectures, offering the advantage of reasonable control over pore size and shape [155]. Often emulsions such as oil and water are used as templates, and MXenes have to be modified to self-assemble at the interface, thus building a 3D network [156, 157]. Without modification of MXenes, they would remain dispersed in the aquatic phase owing to their high hydrophilicity. Bian et al. modified MXenes with cetyl trimethylammonium bromide, where the positively charged head attached to the negatively charged nanosheets and the hydrophobic carbon chain allowed for a modification of MXenes' hydrophilicity, resulting in a stable emulsion with MXenes distributed along the interface [156]. Subsequent polymerization of the continuous phase, i.e., the thin film of assembled MXenes, using a monomer and an initiator, generated

a 3D porous material. Additionally, solid materials such as polymer spheres from polystyrene can be used as templates [158]. Again, the interaction between MXenes and template have to be tuned. In a study presented by Sun et al., positively charged polystyrene spheres are used resulting in a strong electrostatic interaction with negatively charged MXenes [158]. Finally, freeze-casting is a possible technique to obtain 3D porous MXene architectures as aerogels, where a MXene colloidal solution is rapidly cooled down resulting in the formation of ice crystals. The boundary of the growing ice crystals rejects the MXene nanosheets, which are entrapped at the interface between the ice and the remaining liquid, thus forming a 3D network along the ice crystals' boundary. Removing the ice template generates the aerogel [159].

For all the aforementioned methods, it is still a matter of ongoing debate and research to create 3D structures with bigger sizes, good mechanical properties such as high flexibility, high oxidation resistance, high number of interconnections, and stable functional groups [114]. Additionally, the microstructure of these 3D assemblies in terms of pore size, shape, and distribution has to be carefully tuned to obtain favorable properties.

4.2 Tribological and Mechanical Properties

MXenes' tribological and mechanical properties are still underexplored and often overlooked, despite the fact that a fundamental understanding of these properties is crucial for optimizing their usage in many applications [111]. In this context, high mechanical strength is required to withstand volume changes during charging and discharging cycles in energy storage and catalysis or withstand bending in wearable devices [111]. Moreover, knowledge and enhancement of MXenes' tribological properties are vital for usage in nanogenerators or wearable electronics [160].

In the tribological community, 2D materials have found great interest as they often show low friction owing to their easy-to-shear ability between individual layers [111], as schematically depicted in Fig. 7. MXenes, with their great versatility in terms of chemical composition and stoichiometry, are excellent candidates representing model materials to study the effect of layer thickness, interlayer distance, and mechanical properties of individual layers. Despite this, the number of publications in this field of application is low, with about 15 papers published in 2020 [111]. These studies mainly assessed the suitability of MXenes as solid lubricants [161–163], lubricant additives [164], or reinforcement phase in composites [165, 166].

The interest of MXenes to be used as a lubricant can be traced back to their high mechanical stiffness, which is with an effective Young's modulus of 0.33 TPa among the highest for solution-processes 2D materials [167], as well as their low sliding energy barrier of 0.017 eV (Ti_2CO_2), being close to graphene's energy barrier of 0.002 eV [168]. Up to now, the results on the tribological properties are promising. When used as a lubricant additive, friction was reduced by up to 54% [169], and the greatest reduction in wear volume was over 90% when compared with a base oil [164]. Regarding solid lubrication, MXenes were able to reduce friction up to six

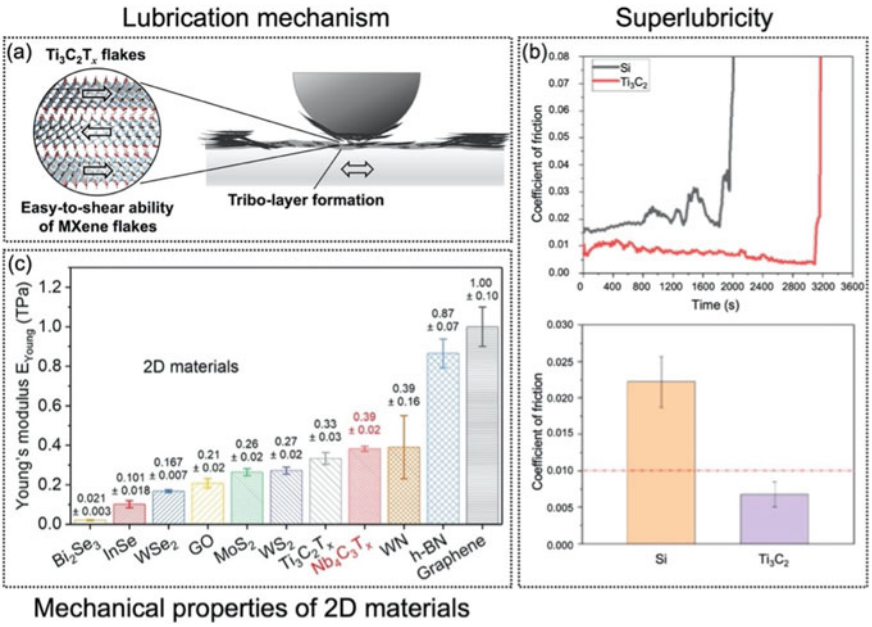

Fig. 7 **a** A schematic representation of the lubrication mechanism thought to be responsible for the outstanding lubrication properties of MXenes [163], as well as **b** a demonstration of superlubricity achieved with Ti_3C_2 MXene against a diamond- like carbon-coated steel ball in dry nitrogen environment [177]. **c** Additionally, the mechanical properties in terms of the effective Young's modulus of various 2D materials as obtained by atomic force microscopy nanoindentation measurements are presented and compared [167]. **a** Adapted with permission from [163]. Copyright 2021 American Chemical Society. **b** adapted with permission from [177]. Copyright 2021 Elsevier. **c** adapted with permission from [167]. Copyright 2020 Wiley–VCH

times with an ultralow wear rate of 4×10^{-9} mm^3 N^{-1} m^{-1} [163]. Their beneficial wear resistance was traced back to the formation of highly wear-resistant tribo-layers, which are transferred to the respective counterbody [161, 163, 170–172]. Finally, in polymer composites, the addition of MXenes led to over 70% reduction in both friction [173] and wear rate [174], whereas metallic composites even showed a 95% reduction in wear rate [165] and a decrease in friction by 60% [175].

When considering the COF reached by the use of MXenes, most studies demonstrate a slightly less beneficial behavior when compared with other 2D materials like graphene or h-BN. However, when considering wear, MXenes have been shown to significantly outperform other state-of-the-art 2D nanomaterials [163, 176]. Considering that the research of MXenes' tribological properties is still in its early stages, it can be expected that both friction and wear performance will be improved in the near future, exploiting the variable and tunable properties of these 2D materials. In this context, it is encouraging that superlubricious behaviors with COFs of 0.007 (solid lubricant) [177] and 0.002 (lubricant additive) [178] have been observed on

the macroscale, see also Fig. 7. Almost all studies investigating MXenes' tribological properties have in common that they postulate the formation of a self-lubricating tribofilm responsible for friction and wear reduction [161–163]. However, a more in-depth characterization of this tribofilm by high-resolution techniques needs to be done to understand the mechanisms responsible for the tribological behavior of MXenes.

The interlayer characteristics of MXenes are interesting for micro- or macroscopic applications [179]. However, AFM studies on MXenes show on the nanoscopic scale that the interaction between a tip and a single MXene flake can also produce low friction, which is not related to interlayer sliding but the friction at the interface between AFM tip and the top surface of the MXene flake [179, 180]. Adhesion tests with different MXenes demonstrated a smaller adhesion force between tip and MXenes than between the tip and mica, thus also resulting in friction forces during sliding [179]. Specifically, Nb_2CT_x could significantly reduce friction compared to $Ti_3C_2T_x$ MXenes, which was hypothesized to result from a greater surface charge for $Ti_3C_2T_x$ due to the higher surface dipole moment density [181]. When considering the higher mechanical strength of other Nb-based MXenes ($Nb_4C_3T_x$) in comparison to $Ti_3C_2T_x$, these might be attractive candidates for further macroscale experiments.

Exploring MXenes' mechanical properties is crucial since they are fundamental for their successful application in almost all fields [170]. The mechanical properties of MXenes are essentially governed by the combination of M and X elements and their bonding strength. This bonding is a mixture of ionic, covalent, and metallic bonding [182]. An approximation of the bond stiffness by Wyatt et al., which can be related to the theoretical mechanical properties, demonstrated that bond stiffness of M–C bonds tends to increase with a higher group number of M and *d*-block order, while the trend in bond stiffness for M–N is not as clear [111]. Nevertheless, bond stiffness is maximized in the 3d block of M–N, and the highest bond stiffness was predicated for Mn–N (which has not been made yet) and Ti–N with 21.0 and 20.7 eV/Å^2, respectively. The greater bond stiffness for M–N compared to M–C in the 3*d* block was attributed to the additional electron available for bonding to the *d*-orbitals of the transition metal atom. However, due to the 2D nature of MXenes, the outermost surfaces are not bonded to the X element, thus increasing M–M metallic bonding, which decreases 2D stiffness, in particular, for small flake thickness. In terms of surface termination, especially $–O_2$ terminations tend to enhance 2D stiffness, induced by reducing the contribution of M–M interactions and, thus stronger M–X bond strength. To characterize the mechanical properties under loading conditions, instead of the 2D stiffness, the 3D elastic modulus should be evaluated. Therefore, the monolayer thickness has to be additionally taken into consideration. When analyzing the 3D elastic modulus, it was demonstrated that the thinnest MXenes (i.e., Ti_2X) have the highest values. In terms of experimental findings, there is only very little data available. The 2D stiffness of $Ti_3C_2T_x$ and $Nb_4C_3T_x$ has been measured by nanoindentation, and values of 326 and 486 N m^{-1} have been reached for $Ti_3C_2T_x$ and $Nb_4C_3T_x$, respectively (Fig. 7c) [167]. These values agree with the theoretical predictions in terms of the influence of composition (Nb MXenes were predicted to be higher than Ti-based ones) and flake thickness (M_4C_3 higher than M_3C_2). When

considering the elastic modulus of the tested MXenes, they show the highest values of solution-processable nanomaterials to date with an effective Young's modulus of 386 GPa (compared to 270 GPa for WS_2 and 210 GPa for graphene oxide).

5 Roadmap for the Next Decade

The outstanding properties of MXenes are promising for various technological fields and have a great potential for innovation. However, their utilization in relevant industries strictly depends on critical areas divided into material synthesis, standardization and quality, market introduction, and pricing. A high-quality material supply chain available at a reasonable price is most important in developing a competitive MXene-enhanced product market. The assumed bottlenecks need to be overcome together with crossing critical stages to ensure successful commercialization. Consequently, fundamental research and scientific discoveries must be brought from the research and development stage to the final commercialization and industrial-scale production of MXene-enriched products. Herein, we present the relevant roadmap for the future commercialization of MXenes (Fig. 8).

MXenes are considered as materials of the future due to excellent physical and chemical properties that are well-suited for many applications in almost all technological fields. So far, MXenes have been only demonstrated as an additive to various bulk matrices for different high-tech commercial applications. MXenes can be utilized as feasible building blocks useful for space exploration, quantum computing, batteries, energy storage devices, medicine, or personalized diagnostics and therapy. However, MXene applications will remain in the research, development, and prototyping phase for the following years due to several bottlenecks. Nevertheless, significant market penetration is being envisioned for the next decade.

Their application in low-material-demanding high-tech applications will result in a low global material demand level. The demand growth may pick up while MXenes will prove their applicability in high-material-load bulk applications. Only large-scale application opportunities may allow overcoming the pricing bottleneck. The optimized synthesis routes in the MXene supply industry should appear and support the first largescale production at reasonable material pricing for growing-volume applications. While large companies may hold on with output until reaching the desirable material demand, small-scale companies at a startup level will most probably make the critical step to MXenes commercialization. However, fundraising, up-scaling, and material optimization problems will still make the process difficult and time-consuming.

The ongoing standardization work will create a foundation for enforcement of technical specifications and contribute to defining an ISO standard addressing REACH legislation for MXene. However, a large variation of material parameters and an extraordinary number of MXene-related structures will hamper any legal actions for the following years. It is also noted that for a REACH registration, it is mandatory for any EU-active supplier to produce more than one 1 t per year. Also,

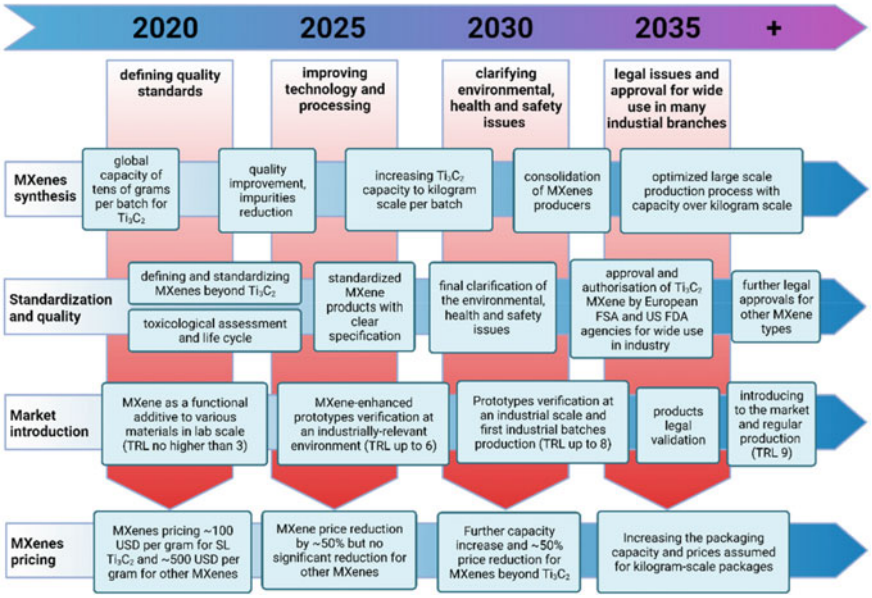

Fig. 8 A roadmap for future commercialization of MXene-enriched products presenting essential areas and processing stages. Identified key areas comprise: MXenes synthesis, standardization and quality, market introduction, and MXenes pricing. Also, crucial process stages that are plausible to evolve through incoming years include: defining quality and standards, improving technology and processing, clarifying environmental, health, and safety issues, legal issues, and approval for wide use in many industrial branches. In the schematic, TRL stands for 'technological readiness level'

the remaining toxicology concerns, both justified and perceived, constitute another bottleneck for the market diffusion of MXenes. Once resolved, the practical application of MXenes may turn into a major driver for a wide range of actual and future markets.

References

1. Barsoum, M., et al.: Compositions comprising free-standing two-dimensional nanocrystals, vol. US9837182B2 (2011)
2. Naguib, M., et al.: Adv. Mater. **23**(37), 4248 (2011)
3. Naguib, M., et al.: Adv. Mater. **26**(7), 992 (2014)
4. Jeitschko, W., et al.: Monatsh. Chem. **95**(1), 178 (1964)
5. Nowotny, V.: Prog. Solid State Chem. **5**, 27 (1971)
6. Jeitschko, W., et al.: Prog. Solid State Chem. **5** (1963)
7. Barsoum, M.W.: Prog. Solid State Chem. **28**(1–4), 201 (2000)
8. Deysher, G., et al.: ACS Nano **14**(1), 204 (2020)
9. Gogotsi, Y., Huang, Q.: ACS Nano **15**(4), 5775 (2021)
10. Mockute, A., et al.: Phys. Rev. B **87**(9) (2013)
11. Li, S.B., et al.: Mater. Sci. Technol. **22**(6), 667 (2013)

12. Qing-He, G., et al.: Comput. Mater. Sci. **118**, 77 (2016)
13. Horlait, D., et al.: Sci. Rep. **6**, 18829 (2016)
14. Tan, T.L., et al.: ACS Nano **11**(5), 4407 (2017)
15. Liu, Z., et al.: Acta Mater. **73**, 186 (2014)
16. Anasori, B., et al.: Scripta Mater. **101**, 5 (2015)
17. Meshkian, R., et al.: Scripta Mater. **108**, 147 (2015)
18. Dahlqvist, M., et al.: Sci. Adv. **3**(7), e1700642 (2017)
19. Dahlqvist, M., et al.: ACS Nano **12**(8), 7761 (2018)
20. Tao, Q., et al.: Nat. Commun. **8**, 14949 (2017)
21. Meshkian, R., et al.: Adv. Mater. **30**(21), e1706409 (2018)
22. Gogotsi, Y., Anasori, B.: ACS Nano **13**(8), 8491 (2019)
23. Zhou, J., et al.: Angew. Chem. Int. Ed. Engl. **55**(16), 5008 (2016)
24. Zha, X.H., et al.: J. Phys. Condens. Matter. **29**(16), 165701 (2017)
25. Gesing, T.-M., et al.: J. Alloy. Compd. **186**(2), 321 (1992)
26. Lin, Z.J., et al.: Acta Mater. **54**(14), 3843 (2006)
27. Ochiai, A., et al. J. Phys. Soc. Jpn. **76**(12) (2007)
28. Fukuda, K., Hisamura, M.: J. Am. Ceram. Soc. **90**(10), 3299 (2007)
29. Iwata, T., et al.: J. Am. Ceram. Soc. **91**(8), 2713 (2008)
30. Iwata, T., et al.: J. Am. Ceram. Soc. **91**(11), 3758 (2008)
31. Sugiura, K., et al.: J. Ceram. Soc. Jpn. **117**(1361), 22 (2009)
32. Sugiura, K., et al.: J. Solid State Chem. **181**(10), 2864 (2008)
33. Fukuda, K., et al.: J. Am. Ceram. Soc. **91**(4), 1342 (2008)
34. He, L.F., et al.: Scripta Mater. **58**(8), 679 (2008)
35. Mockute, A., et al.: Mater. Res. Lett. **3**(1), 16 (2014)
36. Ingason, A.S., et al.: Mater. Res. Lett. **2**(2), 89 (2013)
37. Wang, J., et al.: J. Mater. Res. **22**(10), 2685 (2011)
38. Halim, J., et al.: Adv. Func. Mater. **26**(18), 3118 (2016)
39. Zha, X.H., et al.: Nanoscale **8**(11), 6110 (2016)
40. Zhou, J., et al.: ACS Nano **13**(2), 1195 (2019)
41. Zha, X.H., et al.: Non-MAX phase precursors for mxenes. In: Anasori, B., Gogotsi, Y., (eds.) 2D Metal Carbides and Nitrides (MXenes). Springer (2019)
42. Zhou, J., et al.: ACS Nano **11**(4), 3841 (2017)
43. Zhou, Y.-C., et al.: J. Eur. Ceram. Soc. **33**(15–16), 2831 (2013)
44. Ade, M., Hillebrecht, H.: Inorg. Chem. **54**(13), 6122 (2015)
45. Kota, S., et al.: Int. Mater. Rev. **65**(4), 226 (2019)
46. Alameda, L.T., et al.: J. Am. Chem. Soc. **140**(28), 8833 (2018)
47. Alameda, L.T., et al.: J. Am. Chem. Soc. **141**(27), 10852 (2019)
48. Zhang, H., et al.: J. Mater. Sci. Technol. **35**(8), 1593 (2019)
49. Jakubczak, M., et al.: Adv. Funct. Mater. (2021)
50. Wang, J., et al.: Nat. Commun. **10**(1), 2284 (2019)
51. Fan, M., et al.: Adv. Healthcare Mater. **8**(13) (2019)
52. Jin, Z., et al.: Theranostics **10**(4), 1861 (2020)
53. Chen, D., et al.: Adv. Mater. **33**(16), e2008089 (2021)
54. Chen, N., et al.: Chin. Chem. Lett. **31**(4), 1044 (2020)
55. Halim, J., et al.: Chem Mater **26**(7), 2374 (2014)
56. Rosales, M., et al.: Appl. Mater. Today **20** (2020)
57. Arun, T., et al.: Electrochim. Acta **367** (2021)
58. Blanco, E., et al.: Catal. Commun. **133** (2020)
59. González-Poggini, S., Int. J. Electrochem. Sci. (2021)
60. Hu, T., et al.: J. Phys. Chem. C **121**(35), 19254 (2017)
61. Lu, J., et al.: Nanoscale Adv. **1**(9), 3680 (2019)
62. Li, Y., et al.: Nat. Mater. **19**(8), 894 (2020)
63. Li, M., et al.: ACS Nano **15**(1), 1077 (2021)
64. Kamysbayev, V., et al.: Science **369**(6506), 979 (2020)

65. Persson, I., et al.: Adv. Funct. Mater. **30**(47) (2020)
66. Xie, Y., et al.: ACS Nano **8**(9), 9606 (2014)
67. Mashtalir, O., et al.: J. Mater. Chem. A **2**(35), 14334 (2014)
68. Hu, T., et al.: Phys. Chem. Chem. Phys. **17**(15), 9997 (2015)
69. Tang, Q., et al.: J. Am. Chem. Soc. **134**(40), 16909 (2012)
70. Khazaei, M., et al.: Adv. Func. Mater. **23**(17), 2185 (2013)
71. Khazaei, M., et al.: J. Mater. Chem. C **5**(10), 2488 (2017)
72. Lashgari, H., et al.: Solid State Commun. **195**, 61 (2014)
73. Lei, J.-C., et al.: Front. Phys. **10**(3), 276 (2015)
74. Heyd, J., et al.: J. Chem. Phys. **118**(18), 8207 (2003)
75. Zhao, S., et al.: J. Mater. Chem. C **3**(4), 879 (2015)
76. Guo, X., et al.: J. Phys. Chem. Lett. **7**(24), 5280 (2016)
77. Zhang, X., et al.: J. Mater. Chem. A **3**(9), 4960 (2015)
78. Zhang, X., et al.: Nanoscale **7**(38), 16020 (2015)
79. Hong, L., et al.: Phys. Rev. B **93**(11) (2016)
80. Britnell, L., et al.: Science **335**(6071), 947 (2012)
81. Geim, A.K., Grigorieva, I.V.: Nature **499**(7459), 419 (2013)
82. Ponomarenko, L.A., et al.: Nat. Phys. **7**(12), 958 (2011)
83. Gan, L.-Y., et al.: Phys. Rev. B **87**(24) (2013)
84. Khazaei, M., et al.: Phys. Rev. B **93**(20) (2016)
85. Zhao, H., et al.: J. Appl. Phys. **117**(8) (2015)
86. Lee, Y., et al.: ACS Appl Mater Interfaces **7**(13), 7163 (2015)
87. Ma, Z., et al.: J. Phys. Chem. C **118**(10), 5593 (2014)
88. Rosenkranz, A., et al.: Appl. Surf. Sci. **567** (2021)
89. Zhang, L., et al.: ACS Appl. Energy Mater. **4**(6), 5590 (2021)
90. Nemani, S.K., et al.: ACS Nano (2021)
91. Das, P., et al.: ACS Appl. Mater. Interfaces **13**(26), 31038 (2021)
92. Alhabeb, M., et al.: Chem. Mater. **29**(18), 7633 (2017)
93. Shuck, C.E., et al.: Adv. Eng. Mater. **22**(3) (2020)
94. Abdolhosseinzadeh, S., et al.: Mater. Today (2021)
95. Mohammed Al-Antaki, A.H., et al.: R. Soc. Open Sci. **7**(5), 192255 (2020)
96. Ghazaly, A.E., et al.: ACS Nano **15**(3), 4287 (2021)
97. Jolly, S., et al.: Mater. Today Adv. **10** (2021)
98. Zhou, Y., et al.: Mater. Res. Innov. **2**(3), 142 (2016)
99. Wang, X.H., Zhou, Y.C.: Acta Mater. **50**(12), 3143 (2002)
100. Tzenov, N.V., Barsoum, M.W.: J. Am. Ceram. Soc. **83**(4), 825 (2004)
101. Goc, K., et al.: Ceram. Int. **44**(15), 18322 (2018)
102. Lis, J., et al.: J. Eur. Ceram. Soc. **28**(5), 1009 (2008)
103. Lis, J., et al.: Mater. Lett. **22**(3–4), 163 (1995)
104. Bai, Y., et al.: J. Mater. Res. **24**(8), 2528 (2011)
105. Zhou, A., et al.: Mater. Sci. Eng., A **352**(1–2), 333 (2003)
106. Rozmysłowska-Wojciechowska, A., et al.: Appl. Surf. Sci. **473**, 409 (2019)
107. Shuck, C.E., et al.: ACS Appl. Nano Mater. **2**(6), 3368 (2019)
108. von Treifeldt, J.E., et al.: Mater. Des. **199** (2021)
109. Iqbal, A., et al.: Nano Converg. **8**(1), 9 (2021)
110. Shekhirev, M., et al.: Prog. Mater. Sci. **120** (2021)
111. Wyatt, B.C., et al.: Adv. Mater. **33**(17), e2007973 (2021)
112. Anasori, B., et al.: Nat. Rev. Mater. **2**(2) (2017)
113. Ibragimova, R., et al.: J. Phys. Chem. Lett. **12**(9), 2377 (2021)
114. Wu, Z., et al.: Adv. Sci. (Weinh) **7**(7), 1903077 (2020)
115. Shukla, V.: Mater. Adv. **1**(9), 3104 (2020)
116. Lukatskaya, M.R., et al.: Science **341**(6153), 1502 (2013)
117. Boota, M., et al.: Adv. Mater. **28**(7), 1517 (2016)
118. Mandal, S., et al.: Adv. Funct. Mater. **31**(4) (2020)

119. Lopez, A., Liu, J.: Adv. Intell. Syst. **2**(11) (2020)
120. Gopinath, S.C., Lakshmipriya, T. (eds.): Nanobiosensors for Biomolecular Targeting. Theivasanthi, Thirugnanasambandan (2019)
121. Bandl, C., et al.: J. Appl. Polym. Sci. **138**(30) (2021)
122. Mittal, K.L.: Silanes and Other Coupling Agents. CRC Press (2012)
123. Jayasuriya, C.K.: Interfacial Bonding in Polymer–Ceramic Nanocomposites (2017)
124. Kumar, S., et al.: Biosens Bioelectron **121**, 243 (2018)
125. Wu, Q., et al.: Anal. Chem. **92**(4), 3354 (2020)
126. Ji, J., et al.: FlatChem **17** (2019)
127. Mutin, P.H., et al.: J. Mater. Chem. **15**(35–36) (2005)
128. Sevrain, C.M., et al.: Beilstein J. Org. Chem. **13**, 2186 (2017)
129. Prado, M.C., et al.: ACS Nano **5**(1), 394 (2011)
130. Chen, X., et al.: Chem. Commun. (Camb) **48**(93), 11407 (2012)
131. Mahouche-Chergui, S., et al.: Chem. Soc. Rev. **40**(7), 4143 (2011)
132. Zhang, P., et al.: J. Hazard Mater. **396**, 122731 (2020)
133. Zhang, P., et al.: ACS Appl. Mater. Interfaces **12**(13), 15579 (2020)
134. Ganesh, V., et al.: Chem. Asian J. **6**(10), 2670 (2011)
135. Chandrasekaran, S.: Click Reactions in Organic Synthesis. Wiley-VCH (2016)
136. Gody, G., et al.: J. Am. Chem. Soc. **138**(12), 4061 (2016)
137. McDaniel, R.M., et al.: Chem. Mater. (2021)
138. Yang, Q., et al.: Energy Environ. Mater. **1**(4), 183 (2018)
139. Tontini, G., et al.: J. Phys. Mater. **3**(2) (2020)
140. Li, J., et al.: Adv. Energy Mater. **7**(15) (2017)
141. Lv, G., et al.: Mater. Lett. **219**, 45 (2018)
142. Zhao, M.Q., et al.: Adv. Mater. **27**(2), 339 (2015)
143. Xiu, L., et al.: ACS Nano **12**(8), 8017 (2018)
144. Zhao, M.Q., et al.: Adv. Mater. **29**(37) (2017)
145. Shang, T., et al.: Adv. Funct. Mater. **29**(33) (2019)
146. Naguib, M., Gogotsi, Y.: Acc. Chem. Res. **48**(1), 128 (2015)
147. Dall'Agnese, Y., et al.: J. Power Sour. **306**, 510 (2016)
148. Zhao, M.Q., et al.: Adv. Mater. Technol. **4**(5) (2019)
149. Wu, Y., et al.: ChemElectroChem **4**(6), 1560 (2017)
150. VahidMohammadi, A., et al.: J. Mater. Chem. A **6**(44), 22123 (2018)
151. Ling, Z., et al.: Proc. Natl. Acad. Sci. USA **111**(47), 16676 (2014)
152. Ma, Z., et al.: ACS Appl. Mater. Interfaces **10**(4), 3634 (2018)
153. Liu, J., et al.: Adv. Mater. **29**(38) (2017)
154. Akuzum, B., et al.: ACS Nano **12**(3), 2685 (2018)
155. Barg, S., et al.: Nat. Commun. **5**, 4328 (2014)
156. Bian, R., et al.: Nanoscale **10**(8), 3621 (2018)
157. Shi, S., et al.: Angew. Chem. Int. Ed. Engl. **58**(50), 18171 (2019)
158. Sun, R., et al.: Adv. Funct. Mater. **27**(45) (2017)
159. Bian, R., et al.: J. Mater. Chem. C **7**(3), 474 (2019)
160. Dong, Y., et al.: Nano Energy **44**, 103 (2018)
161. Rosenkranz, A., et al.: Appl. Surf. Sci. **494**, 13 (2019)
162. Lian, W., et al.: Ceram. Int. **44**(16), 20154 (2018)
163. Grutzmacher, P.G., et al.: ACS Nano **15**(5), 8216 (2021)
164. Liu, Y., et al.: J. Mater. Sci. **52**(4), 2200 (2016)
165. Mai, Y.J., et al.: J. Alloy. Compd. **770**, 1 (2019)
166. Zhang, H., et al.: Mater. Des. **92**, 682 (2016)
167. Lipatov, A., et al.: Sci. Adv. **4**(6), eaat0491 (2018)
168. Zhang, H., et al.: RSC Adv. **7**(88), 55912 (2017)
169. Yang, J., et al.: Cryst. Res. Technol. **49**(11), 926 (2014)
170. Marian, M., et al.: Appl. Surf. Sci. **523** (2020)
171. Yin, X., et al.: ACS Appl. Mater. Interfaces **11**(35), 32569 (2019)

172. Yin, X., et al.: Adv. Eng. Mater. **22**(4) (2020)
173. Meng, F., et al.: Friction (2020)
174. Yan, H., et al.: J. Mater. Sci. Technol. **54**, 144 (2020)
175. Hu, J., et al.: Chin. Chem. Lett. **31**(4), 996 (2020)
176. Rosenkranz, A., et al.: Appl. Nanosci. **10**(9), 3353 (2020)
177. Huang, S., et al.: Mater. Today Adv. **9** (2021)
178. Yi, S., et al.: Tribol. Int. **154** (2021)
179. Rodriguez, A., et al.: Appl. Surf. Sci. **535** (2021)
180. Vazirisereshk, M.R., et al.: Lubricants **7**(7) (2019)
181. Zhou, X., et al.: Tribol. Int. **153** (2021)
182. Zhang, Y., et al.: Solid State Commun. **121**(8), 411 (2002)